

# First space-based derivation of the global atmospheric methanol emission fluxes

T. Stavrakou<sup>1</sup>, A. Guenther<sup>2</sup>, A. Razavi<sup>3</sup>, L. Clarisse<sup>3</sup>, C. Clerbaux<sup>4,3</sup>, P.-F. Coheur<sup>3</sup>, D. Hurtmans<sup>3</sup>, F. Karagulian<sup>3,\*</sup>, M. De Mazière<sup>1</sup>, C. Vigouroux<sup>1</sup>, C. Amelynck<sup>1</sup>, N. Schoon<sup>1</sup>, Q. Laffineur<sup>5</sup>, B. Heinesch<sup>5</sup>, M. Aubinet<sup>5</sup>, C. Rinsland<sup>6</sup>, and J.-F. Müller<sup>1</sup>

<sup>1</sup>Belgian Institute for Space Aeronomy, Avenue Circulaire 3, 1180, Brussels, Belgium

<sup>2</sup>Atmospheric Chemistry Division, National Center for Atmospheric Research, 1850 Table Mesa Drive, Boulder Colorado, 80305, USA

<sup>3</sup>Spectroscopie de l'Atmosphère, Service de Chimie Quantique et Photophysique, Université Libre de Bruxelles, Belgium

<sup>4</sup>UPMC Univ. Paris 06, Université Versailles St-Quentin, CNRS/INSU, LATMOS-IPSL, Paris, France

<sup>5</sup>Gembloux Agro-Bio Tech, University of Liège, Unité de Physique des Biosystèmes, Avenue de la Faculté d'Agronomie 8, 5030 Gembloux, Belgium

<sup>6</sup>NASA Langley Research Center, Hampton, Virginia, USA

\* now at: European Commission, Joint Research Centre (JRC), 21027, Ispra, Italy

Received: 3 December 2010 – Published in Atmos. Chem. Phys. Discuss.: 11 February 2011

Revised: 4 May 2011 – Accepted: 19 May 2011 – Published: 25 May 2011

**Abstract.** This study provides improved methanol emission estimates on the global scale, in particular for the largest methanol source, the terrestrial biosphere, and for biomass burning. To this purpose, one complete year of spaceborne measurements of tropospheric methanol columns retrieved for the first time by the thermal infrared sensor IASI aboard the MetOp satellite are compared with distributions calculated by the IMAGESv2 global chemistry-transport model. Two model simulations are performed using a priori biogenic methanol emissions either from the new MEGANv2.1 emission model, which is fully described in this work and is based on net ecosystem flux measurements, or from a previous parameterization based on net primary production by Jacob et al. (2005). A significantly better model performance in terms of both amplitude and seasonality is achieved through the use of MEGANv2.1 in most world regions, with respect to IASI data, and to surface- and air-based methanol measurements, even though important discrepancies over several regions are still present. As a second step of this study, we combine the MEGANv2.1 and the IASI column abundances over continents in an inverse modelling scheme based on the adjoint of the IMAGESv2 model to generate an improved global methanol emission source. The global optimized source totals  $187 \text{ Tg yr}^{-1}$  with a contribution of  $100 \text{ Tg yr}^{-1}$  from plants, only slightly lower than the a priori

MEGANv2.1 value of  $105 \text{ Tg yr}^{-1}$ . Large decreases with respect to the MEGANv2.1 biogenic source are inferred over Amazonia (up to 55 %) and Indonesia (up to 58 %), whereas more moderate reductions are recorded in the Eastern US (20–25 %) and Central Africa (25–35 %). On the other hand, the biogenic source is found to strongly increase in the arid and semi-arid regions of Central Asia (up to a factor of 5) and Western US (factor of 2), probably due to a source of methanol specific to these ecosystems which is unaccounted for in the MEGANv2.1 inventory. The most significant error reductions achieved by the optimization concern the derived biogenic emissions over the Amazon and over the Former Soviet Union. The robustness of the derived fluxes to changes in convective updraft fluxes, in methanol removal processes, and in the choice of the biogenic a priori inventory is assessed through sensitivity inversions. Detailed comparisons of the model with a number of aircraft and surface observations of methanol, as well as new methanol measurements in Europe and in the Reunion Island show that the satellite-derived methanol emissions improve significantly the agreement with the independent data, giving thus credence to the IASI dataset.

## 1 Introduction

Methanol ( $\text{CH}_3\text{OH}$ ) has been identified as one of the major organic compounds in the troposphere, most abundant above forests during the growing season with measured



Correspondence to: T. Stavrakou  
(jenny@aeronomie.be)

concentrations of the order of several ppb (e.g. Williams et al., 2001; Schade and Goldstein, 2006; Karl et al., 2007). Due to its influence on the background tropospheric photochemistry, its influence on OH concentrations in the boundary layer, its contribution to the tropospheric ozone production, and the production of formaldehyde upon its oxidation by OH, methanol became the subject of many literature studies with focus on (i) process-based emission mechanisms (e.g. Macdonald and Fall, 1993; Fall and Benson, 1996; Hüve et al., 2007; Folkers et al., 2008); (ii) modelling studies attempting to derive global methanol budget closures (e.g. Galbally and Kirstine, 2002; Jacob et al., 2005; Millet et al., 2008); (iii) field and aircraft measurements (e.g. Singh et al., 2000; Karl et al., 2003a; Millet et al., 2004; Spirig et al., 2005; Mao et al., 2006).

The above studies have been recently complemented by newly acquired space-based methanol observations in the upper troposphere from the ACE-FTS/SCISAT-1 solar occultation instrument (Dufour et al., 2006), and from the TES/AURA (Beer et al., 2008) and IASI/MetOp-A (Razavi et al., 2011) infrared nadir-looking probes of the lower troposphere.

Although it is agreed that plant emissions represent the major part of the methanol flux from the terrestrial ecosystems, much uncertainty remains concerning their magnitude and global distribution. A number of modelling studies attempting to quantify the plant growth and decay source provided a wide range of values for the global annual emission estimates, from 95 Tg (Singh et al., 2000) up to 280 Tg (Heikes et al., 2002). Aside from the plant source, oceans are hypothesized to constitute an important source of methanol which is required in order to explain observed methanol concentrations in the marine boundary layer (Heikes et al., 2002). This source is, however, outweighed by a more significant ocean sink (Millet et al. (2008), Heikes et al. (2002), this study). In addition to natural emissions from plants and oceans, methanol is also released from anthropogenic activities and biomass burning at much lower rates, contributing less than 10% of the estimated global source. The main methanol removal pathways are oxidation by OH and dry deposition, whereas wet deposition constitutes a minor sink.

In this work we present first a new algorithm (MEGANv2.1) for deriving methanol emissions from plants. As opposed to previous emission models based on the net primary production from the earth ecosystems (Galbally and Kirstine, 2002; Jacob et al., 2005), the MEGANv2.1 model is based on net ecosystem fluxes, and accounts for the effects of light, temperature, and leaf age, in a similar way as for isoprene emissions in the MEGAN model (Guenther et al., 2006). The derived MEGANv2.1 inventory, as well as a previous biogenic methanol emission inventory by Jacob et al. (2005) are implemented in the global IMAGESv2 chemistry-transport model used to simulate methanol concentrations. An inverse modelling experiment is designed using the MEGANv2.1 biogenic

source as a priori and constrained by methanol columns from the newly released global IASI dataset (Razavi et al., 2011) in order to derive updated global methanol emissions. The inversion study is based on the adjoint module of IMAGESv2 (Müller and Stavrakou, 2005), and on the grid-based approach for retrieving emissions of reactive species (Stavrakou and Müller, 2006; Stavrakou et al., 2008, 2009b,c). The initial and updated emissions are compared on the global and regional scale, with focus on seasonal variations of methanol columns, especially over regions (Tropics, Europe, Asia, Africa) where observations from other platforms are either scarce or not available. Furthermore, the model results before and after optimization are evaluated against previous modelling work, available aircraft methanol data, and a compiled set of literature in situ measurements from different continents. Comparisons are also presented with FTIR column data from the Kitt Peak Observatory in the western US, and newly retrieved measurements from a European forested site and FTIR column data from the subtropical site of the Reunion Island in the Indian Ocean.

The article is organized as follows. In Sect. 2 a literature overview on methanol releases by plants is presented, followed by a thorough description of the MEGANv2.1 emission model for methanol emissions, and its implementation in a canopy model to derive global methanol emission estimates. The methanol ocean source and sink are described in Sect. 3. The IMAGESv2 global model used to simulate methanol concentrations and the annual a priori methanol budget are the subject of Sect. 4. Section 5 is dedicated to the presentation of the IASI satellite data used to constrain the inversion, and to a description of the inversion setup. Multi-instrument independent observational methanol data, presented in Sect. 6, are used to evaluate how the model performs before and after optimization and also to validate the satellite dataset. The a priori and inversion results are discussed in Sects. 7 and 8. The errors on the a posteriori IASI-derived fluxes are computed in Sect. 9, and the dependence of the retrieved fluxes on model uncertainties is addressed in Sect. 10. Our main conclusions are drawn in Sect. 11.

## 2 Methanol released by plants

### 2.1 Background

Methanol production is ubiquitous among higher plants, as a result of the demethylation of pectins, complex polysaccharides acting as tissue firming agents in the cell walls of plants. The demethylation is catalyzed by pectin methylesterases, cell wall enzymes involved in plant growth and development (Fall and Benson, 1996), but also in plant defensive response against herbivore attacks (Körner et al., 2009), and produces methanol as a major end-product exiting leaves through stomata during transpiration (Schink and Zeikus,

1980; Nemecek-Marshall et al., 1995; Fall and Benson, 1996). The methanol leaf emission is controlled by leaf temperature and light (Folkers et al., 2008), and by the stomatal conductance and evapotranspiration (Macdonald and Fall, 1993; Niinemets and Reichstein, 2003a,b; Hüve et al., 2007). The emissions exhibit a pronounced diel profile peaking in the morning upon stomatal opening when methanol accumulated at night in the intracellular space is released in the atmosphere (Hüve et al., 2007).

Growing leaves were found to emit about four times more methanol than adult leaves in the case of the Mexican cotton plant (Hüve et al., 2007). Although large methanol emission rates are often associated with young, growing leaves, a substantial portion of the annual emission of methanol from a broadleaf forest is associated with mature and senescing canopies (Karl et al., 2003a). However, the emission generally declined with increasing leaf age after leaf expansion (Nemecek-Marshall et al., 1995). In addition, high amounts of methanol have been reported over agricultural grassland during and after cutting, as well as during the hay drying phase (Davison et al., 2008). Aside from plant growth and development, which are by far the dominant methanol-generating mechanisms, different processes, like e.g. root and fruit growth (Fall and Benson, 1996), or the abiological production of oxidized VOCs from the decay of dead plant material (Warneke et al., 1999) also produce methanol at lower rates. However, literature studies about such processes are generally either limited or lacking.

Bottom-up biogenic methanol emission inventories require extrapolation, often in a crude way, of the limited sets of available laboratory measurements of methanol fluxes from leaves. Guenther et al. (1995) estimated the global annual methanol emission at more than 320 Tg based on flux measurements from Macdonald and Fall (1993), a value close to the value (280 Tg yr<sup>-1</sup>) reported by Heikes et al. (2002). Galbally and Kirstine (2002) assumed that the mass of methanol emitted by a plant over a given time period is linearly related to the net primary carbon production, and estimated the ratio of methanol carbon emission to net primary carbon production at 0.024 % for grasses and to 0.11 % for other higher plants. Their resulting best estimate for the global methanol emission amounts to 100 Tg yr<sup>-1</sup>, three times lower compared to the Tie et al. (2003) estimate. Based on the Galbally and Kirstine (2002) plant model and on the net primary production and heterotrophic transpiration calculated with a biogeochemical model, the plant growth and decay sources of methanol have been estimated at 128 and 23 Tg yr<sup>-1</sup>, respectively (Jacob et al., 2005), whereas a more recent study constrained by aircraft measurements suggested a strong reduction of the plant growth source (by 38 %, Millet et al., 2008) and indicated possible shortcomings in the NPP-based parameterization scheme.

The Model of Emissions of Gases and Aerosols from Nature (MEGAN, Guenther et al., 2006), is extended to include methanol emissions (MEGANv2.1), as described be-

low. The employed modelling approach, different from the one based on the NPP, makes use of the net ecosystem flux that integrates both emission and deposition processes from all ecosystem components including foliage, trunks, leaf litter and soil microbes. The methanol flux algorithm, the observations it is based on, and the implementation of the algorithm in a canopy environment model to generate global methanol emissions from vegetation are the subject of the two following sections.

## 2.2 The MEGANv2.1 algorithm

The net methanol flux,  $F$  (in  $\mu\text{g m}^{-2} \text{h}^{-1}$ ) from a terrestrial landscape into the above canopy atmosphere is estimated as

$$F = E - L, \quad (1)$$

where  $E$  is the methanol emission rate and  $L$  the methanol loss rate. The area average flux within a model grid cell is calculated as the area weighted average of the fluxes in each landcover type (e.g. broadleaf trees, needleleaf trees, shrubs, crops, grass). The methanol loss rate can be calculated from the above canopy methanol concentration and a parameterized dry deposition velocity. A typical value for dry deposition flux is  $50 \mu\text{g m}^{-2} \text{h}^{-1}$ .

The methanol emission rate is estimated as

$$E = \gamma_{\text{age}} \cdot \gamma_{\text{CE}} \cdot \epsilon, \quad (2)$$

where  $\epsilon$  is the emission factor associated with the standard conditions defined in Guenther et al. (2006) ( $800 \mu\text{g m}^{-2} \text{h}^{-1}$  for northern temperate and boreal broadleaf trees, needleleaf trees, shrubs and crops, and  $400 \mu\text{g m}^{-2} \text{h}^{-1}$  for grasses and other broadleaf trees). These emission factors are based on whole ecosystem net methanol flux measurements reported by 17 studies that characterized various ecosystems including tropical forest (Geron et al., 2002; Karl et al., 2004, 2007; Langford et al., 2010), warm conifer forest (Karl et al., 2005), cool temperate conifer forest (Schade and Goldstein, 2001; Baker et al., 2001; Karl et al., 2002), temperate broadleaf forest and plantation (Spirig et al., 2005; Karl et al., 2003a; Jardine et al., 2008), boreal forest (Rinne et al., 2007), croplands (Warneke et al., 2002; Schade and Custer, 2004) and grassland (Kirstine et al., 1998; Fukui and Doskey, 1998; Ruuskanen et al., 2010). Among these studies, Kirstine et al. (1998) and Fukui and Doskey (1998) have used whole ecosystem enclosure techniques with gas chromatography analysis to quantify emissions from grasslands, Schade and Goldstein (2001), Baker et al. (2001) and Geron et al. (2002) used above canopy relaxed eddy accumulation with gas chromatography analysis to measure methanol fluxes above forests, whereas all the other studies used proton-transfer reaction mass spectroscopy (PTR-MS) and the eddy covariance, or disjunct eddy covariance, approach (see Karl et al., 2002). The daytime fluxes reported by these studies for warm, sunny conditions range from no emissions (or a small net uptake) to a net emission of about  $3500 \mu\text{g m}^{-2} \text{h}^{-1}$ .

Methanol emission factors based on the relaxed eddy accumulation approach are a factor of 3 (for broadleaf trees) to 5 (for needleleaf trees) higher than emission factors based on the eddy covariance technique. The average values for northern temperate and boreal broadleaf trees and needleleaf trees are not significantly different and the MEGANv2.1 methanol emission factor for northern forests and all shrublands is based on the median value of these studies. The lower emission rates for tropical broadleaf forests are based on recent measurements indicating lower emissions for these landscapes (Karl et al., 2007; Langford et al., 2010). The few measurements reported for croplands include methanol emission fluxes of alfalfa (Warneke et al., 2002) that are much higher than the forest values, and emission fluxes from ryegrass (Schade and Custer, 2004), that are much lower. Since the MEGAN landcover data do not distinguish between high and low emission crops, the value used for forests is currently used for all crops. The lower emission factor assigned to grasslands is in agreement with the model approach of Galbally and Kirstine (2002). Earlier enclosure studies of grass pastures in US (Fukui and Doskey, 1998) and Australia (Kirstine et al., 1998) reported very low methanol emissions while more than a factor of 3 higher emissions were observed recently from a grassland meadow in Austria using a PTR-MS eddy covariance flux measurement technique (Ruuskanen et al., 2010). The differences could be due to the presence of forbs or different grass species and future methanol modelling efforts may need to distinguish between different grassland types.

Emission variations associated with canopy environment and leaf age are accounted for through the dimensionless emission activity factors  $\gamma_{CE}$  and  $\gamma_{age}$ . The canopy-weighted leaf age emission activity factor for methanol is calculated as

$$\gamma_{age} = F_{new}A_{new} + F_{gro}A_{gro} + F_{mat}A_{mat} + F_{sen}A_{sen}, \quad (3)$$

where the canopy fractions  $F$  of the new, growing, mature, and senescing groups are calculated according to Guenther et al. (2006) and the relative methanol emission rates assigned to each canopy fraction for  $A_{new}$ ,  $A_{gro}$ ,  $A_{mat}$ , and  $A_{sen}$  are equal to 3.5, 3, 1, and 1.2, respectively. The parameters used in the leaf age algorithm are based on the results of Harley et al. (2007) and Karl et al. (2003a). The leaf age activity factor can be applied to both evergreen and deciduous canopies, but will typically be close to 1 for evergreen canopies. The canopy environment activity factor is a function of temperature, photosynthetic photon flux density (PPFD), and leaf area index (LAI), and can be calculated either using a multi-layer canopy environment model that calculates light and temperature for sunlit and shaded leaves or by using parameterized equations for each component (temperature, photosynthetically active radiation, LAI) that are based on simulations with the multi-layer sun/shade canopy

model (Guenther et al., 2006). Using a multi-layer model, the canopy average value is estimated as

$$\gamma_{CE} = C_{CE} \cdot \gamma_{PT} \cdot LAI, \quad (4)$$

where  $C_{CE}$  is equal to 0.58, and  $\gamma_{PT}$  is the weighted average, for all leaves, of activity factors that account for the influence of light and temperature, and LAI is the leaf area index.

Methanol emissions increase exponentially with increasing temperature and tend to have elevated values with higher PPFD (Harley et al., 2007). MEGANv2.1 assumes that all biogenic VOCs can be produced by both light dependent and light independent emission processes. The leaf level temperature and light response is calculated as

$$\gamma_{PT} = (1 - LDF) \cdot \gamma_{T-li} + LDF \cdot \gamma_P \cdot \gamma_{T-id}, \quad (5)$$

where the LDF is the light-dependent fraction of the emissions at standard conditions ( $= 0.8$  for methanol),  $\gamma_P$  is the light response of methanol emissions,  $\gamma_{T-id}$  is the temperature response for the light-dependent fraction of the emissions,  $\gamma_{T-li}$  is the temperature response for the remainder of the emissions that are not light dependent.

The activity factors  $\gamma_P$  and  $\gamma_{T-id}$  for methanol are calculated using the isoprene light and temperature dependent equations described by Guenther et al. (2006), expressed as

$$\gamma_{T-id} = E_{opt} \cdot [C_{T2} \cdot e^{C_{T1} \cdot x} / (C_{T2} - C_{T1} \cdot (1 - e^{C_{T2} \cdot x}))], \quad (6)$$

where for methanol the values of the coefficients are  $C_{T1} = 60$ ,  $C_{T2} = 230$ ,  $x = [(1/T_{opt}) - (1/T)]/0.00831$ , and  $T$  is the leaf temperature (K). At the MEGAN standard conditions,  $E_{opt} = 1.61$  and  $T_{opt} = 313$  K. These may vary with past light and temperature conditions, as is the case for isoprene (Guenther et al., 2006), but are held constant in MEGANv2.1 due to a lack of observations for characterizing these processes. For light independent emissions we have

$$\gamma_{T-li} = \exp(\beta(T - 303)), \quad (7)$$

where  $T$  is the leaf temperature and  $\beta$  is the temperature response factor which is assigned a value of  $0.08 \text{ K}^{-1}$  for methanol. The observed values for  $\beta$  from above canopy field studies ranges from 0.01 to 0.16 with a median value of 0.073. A similar average value of  $0.08 \text{ K}^{-1}$  is reported by Harley et al. (2007), based on controlled enclosure measurements on crops, needleleaf and broadleaf trees.

### 2.3 Global biogenic methanol emission inventory

To determine the height-dependent leaf temperature and radiation fluxes inside the canopy, we use the Model for Hydrocarbon emissions by the CANopy (MOHYCAN) (Müller et al., 2008). The model calculates PPFD and leaf temperature at eight canopy levels based on canopy-top estimates for the visible and near-infrared radiative fluxes (including their diffuse and direct components), air temperature, wind speed, and relative humidity. These estimates are obtained

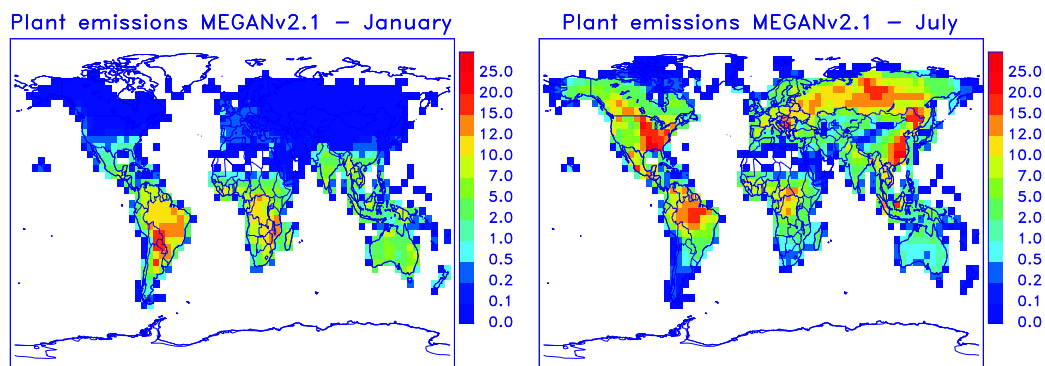


**Fig. 1.** Global biogenic methanol emissions in January and in July calculated using the MEGANv2.1 algorithm and the MOHYCAN canopy model, and downgraded to the IMAGESv2 model resolution ( $4^\circ \times 5^\circ$ ). Units are  $10^{10} \text{ mol cm}^{-2} \text{ s}^{-1}$ .

from ERA-Interim fields for the downward solar radiation, cloud cover fraction, air temperature and wind speed directly above the canopy, provided every 6 h and re-gridded at a resolution of  $0.5^\circ \times 0.5^\circ$  between 2003 and 2009. The emissions are calculated for both cloudy and clear conditions with cloud optical depth being estimated based on the cloud cover fraction and the solar radiation flux. Leaf area index data are obtained from the collection 5 MODIS 8-day product generated by compositing daily Aqua and Terra observations (Shabanov et al., 2007) at  $1 \text{ km}^2$  resolution. This dataset is available between July 2002 and the present date via ftp at the MODIS Land site (<ftp://e4ftl01u.ecs.nasa.gov/MOTA/MCD15A2.005>). The LAI of vegetated areas is determined by dividing the MODIS LAI by the vegetated fraction of the grid cell (Guenther et al., 2006).

Global monthly averaged methanol fluxes are generated at a resolution of  $0.5^\circ$  for all years between 2003 and 2009 and are available at the MOHYCAN model website (<http://tropo.aeronomie.be/models/mohycan.htm>). In the following we present methanol emission fluxes for 2009. The globally estimated source of methanol for this year amounts to 105 Tg. Monthly averaged global methanol fluxes in January and July at  $4^\circ \times 5^\circ$  resolution are illustrated in Fig. 1.

### 3 Modelling the oceanic methanol flux

The parameterization used for the emission and uptake of methanol by the oceans follows the approach of Millet et al. (2008). The flux of methanol is expressed by the Liss and Slater (1974) two-layer model :

$$F = K_w(C_g H^{-1} - C_w) \text{ (mol cm}^{-2} \text{ s}^{-1}), \quad (8)$$

where  $C_g$  and  $C_w$  (in  $\text{mol cm}^{-3}$ ) are the methanol concentrations in the atmosphere and in water, respectively,

$$H^{-1} = K_H RT \quad (9)$$

with  $K_H$  ( $\text{mole l}^{-1} \text{ atm}^{-1}$ ) being the Henry's law constant for methanol (Snider and Dawson, 1985),  $R$  the ideal gas

constant ( $=8.205 \times 10^{-21} \text{ atm mole}^{-1} \text{ K}^{-1}$ ), and  $T$  the water temperature (in K). The term  $K_w$  is expressed by

$$K_w^{-1} = k_w^{-1} + (k_g H)^{-1}, \quad (10)$$

where  $k_g$  and  $k_w$  are the gas phase and liquid phase transfer velocity, respectively, parameterized according to Johnson (2010), based on 6-hourly distributions of surface ocean temperature and wind velocity at 10 m above the ocean obtained from the ECMWF ERA-Interim re-analysis.

Annually averaged oceanic methanol emission fluxes and deposition velocity ( $= (H/k_w + 1/k_g)^{-1}$ ,  $\text{cm s}^{-1}$ ), calculated using the above parameterization are shown in Fig. 2. The global methanol oceanic source amounts to 43 Tg, in good agreement with Heikes et al. (2002) ( $30 \text{ Tg yr}^{-1}$ ), whereas the calculated uptake with the IMAGESv2 model is estimated at 48–56 Tg (Table 1), resulting in a global annual net methanol sink of ca.  $5\text{--}13 \text{ Tg yr}^{-1}$ . This sink is largest ( $>7 \times 10^9 \text{ mol cm}^{-2} \text{ s}^{-1}$ ) near continental coasts, and becomes a weak source over open water regions, in agreement with reported results by Millet et al. (2008). However, the ocean source (and sink) estimated by Millet et al. (2008) is twice as large as our estimate. This difference stems mainly from the use of an older parameterization (Asher, 1997) for the gas-phase transfer coefficient  $k_g$  in Millet et al. (2008). In fact, the use of Millet et al. (2008) parameterization in our model would result in an ocean source estimate of  $90 \text{ Tg yr}^{-1}$ , very close to the Millet et al. (2008) reported value ( $85 \text{ Tg yr}^{-1}$ ).

### 4 Methanol simulated with IMAGESv2

The IMAGESv2 global chemistry-transport model runs at  $4^\circ \times 5^\circ$  resolution and is resolved at 40 vertical levels from the surface up to the pressure of 44 hPa. It calculates the daily averaged concentrations of 100 trace gases using a time step of 1 day, while accounting for the impact of diurnal variations of the chemical compounds through correction factors computed via a diurnal

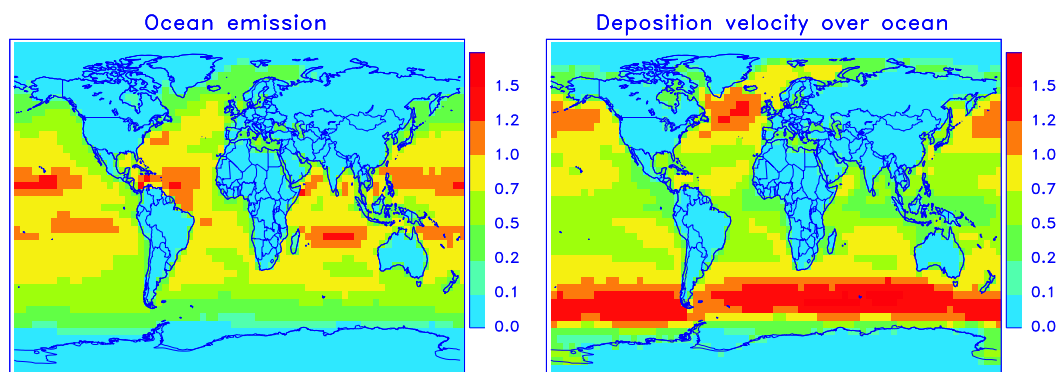


**Fig. 2.** Annually averaged methanol ocean emission fluxes (left, in  $10^{10} \text{ mol cm}^{-2} \text{ s}^{-1}$ ), and deposition velocity over ocean (right), expressed in  $\text{cm s}^{-1}$

**Table 1.** Performed simulations and global a priori and a posteriori annual methanol budgets calculated with IMAGESv2 and comparison with previous work by Millet et al. (2008).

| Performed Simulations           |            |   |            |                      |
|---------------------------------|------------|---|------------|----------------------|
| Forward                         | S1         | uses biogenic source from Jacob et al. (2005) |            |                      |
| Forward                         | S2         | uses the MEGANv2.1 biogenic source            |            |                      |
| Inversion                       | OptS2      | based on S2, is constrained by IASI data      |            |                      |
| Sources ( $\text{Tg yr}^{-1}$ ) |            |   |            |                      |
| Simulations                     | S1         | S2  | OptS2      | Millet et al. (2008) |
| Anthropogenic                   | 9.3        | 9.3   | 9.3        | 17 <sup>a</sup>      |
| Pyrogenic                       | 5.3        | 5.3   | 4.3        |                      |
| Biogenic                        | 151        | 104.7   | 100        | 103 <sup>b</sup>     |
| Oceanic                         | 42.7       | 42.7  | 42.7       | 85                   |
| Atmospheric production          | 30.7       | 30.9  | 31.1       | 37                   |
| <b>Total</b>                    | <b>239</b> | <b>193</b>                                    | <b>187</b> | <b>242</b>           |
| Sinks ( $\text{Tg yr}^{-1}$ )   |            |   |            |                      |
| OH oxidation                    | 131        | 107   | 108        | 88                   |
| Dry dep. land                   | 48         | 34  | 28         | 40                   |
| Dry dep. ocean                  | 56         | 49  | 48         | 101                  |
| Wet deposition                  | 3.6        | 3   | 2.7        | 13                   |
| Lifetime (days)                 | 5.8        | 5.8   | 5.7        | 4.7                  |
| Burden (Tg)                     | 3.7        | 3.0   | 2.9        | 3.1                  |

Notes: <sup>a</sup> refers to the sum of anthropogenic, biomass burning, and biofuel source, <sup>b</sup>: includes a plant growth source of  $80 \text{ Tg yr}^{-1}$  and a plant decay source of  $23 \text{ Tg yr}^{-1}$ .

cycle simulation with a 20-min time step. The model is described thoroughly in a number of previous studies (Müller and Stavrakou, 2005; Stavrakou et al., 2009a,b).

Biogenic emissions of methanol are obtained either from the Jacob et al. (2005) inventory or by the MEGANv2.1 algorithm described in Sect. 2. Jacob et al. (2005) used net primary production and heterotrophic respiration to parameterize the plant growth and decay sources of methanol, with a total annual emission flux that is 44 % higher than in MEGANv2.1 ( $151$  vs.  $104.7 \text{ Tg yr}^{-1}$ ).

Global anthropogenic NMVOC emissions are obtained from the RETRO database for the year 2000 ([http://retro.enes.org/data\\_emissions.shtml](http://retro.enes.org/data_emissions.shtml)). Over Asia, RETRO is replaced by the REAS inventory for anthropogenic NMVOC emissions in 2009 (Ohara et al., 2007). Assuming that methanol represents 100 % of alcohol emission in RETRO and 50 % of the “other hydrocarbons” category in REAS, the global annual anthropogenic source of methanol (including biofuel use) amounts to  $9.3 \text{ Tg yr}^{-1}$ .

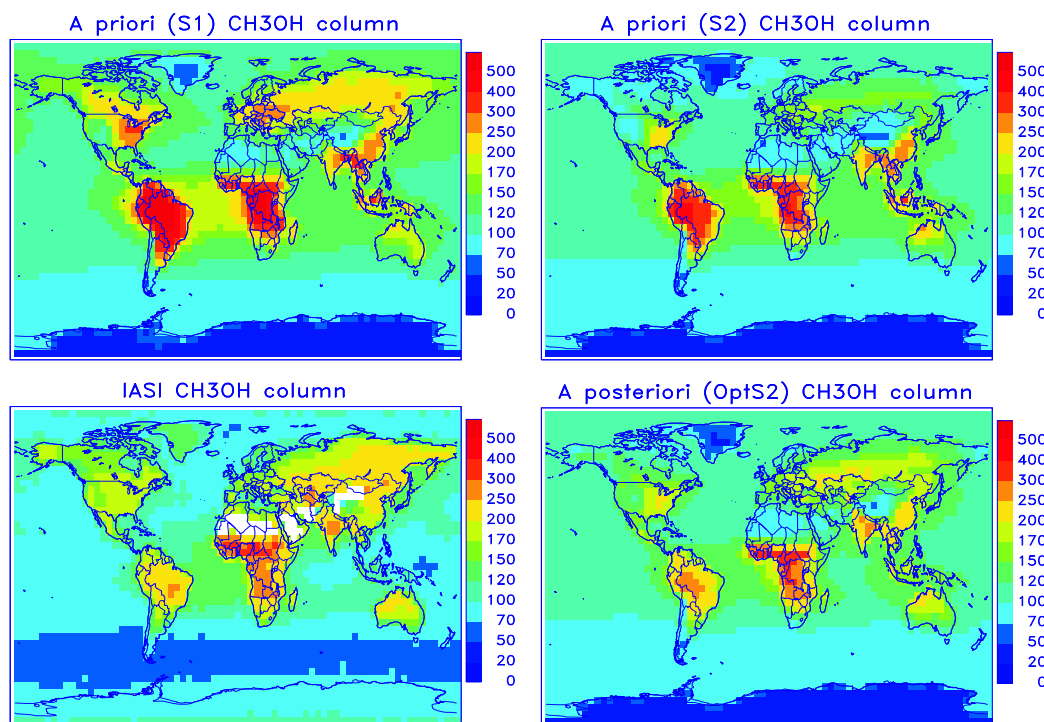


**Fig. 3.** Top panels: a priori global maps of annually averaged methanol columns simulated in S1 and S2 (Table 1). Bottom left: IASI yearly averaged methanol column abundances for 2009 gridded onto a  $4^{\circ} \times 5^{\circ}$  horizontal resolution. Blanks correspond to regions where the quality of the retrievals might be doubtful, mainly due to emissivity problems (Razavi et al., 2011). Bottom right: methanol columns inferred from the OptS2 inversion study (Table 1). Units are  $10^{14} \text{ mol cm}^{-2}$ . Note that modelled columns account for IASI averaging kernels.

Monthly vegetation fire emissions are obtained from the newly released version 3.1 of the Global Fire Emission Database (GFED, <http://www.falw.vu/~gwerf/GFED/index.html>). This dataset comprises a distinction between emissions from savanna, woodland, and forest fires, agricultural waste burning, peatlands, deforestation and degradation fires (van der Werf et al., 2010). Trace gas emissions have been derived from carbon emissions using emission factors obtained from Andreae and Merlet (2001) with updates from M. O. Andreae, personal communication, 2007. The global methanol biomass burning flux is estimated at 5.3 Tg in 2009.

In the atmosphere methanol is formed through reactions of the methylperoxy radical ( $\text{CH}_3\text{O}_2$ ) with itself or through its reactions with other organic peroxy radicals. It is also formed through the photolysis of glycolaldehyde. The atmospheric production source in IMAGESv2 amounts to  $31 \text{ Tg yr}^{-1}$  globally, in good agreement with past modelling studies (Galbally and Kirstine, 2002; Jacob et al., 2005; Millet et al., 2008).

The global methanol emission amounts to  $239 \text{ Tg yr}^{-1}$  in the S1 simulation using the Jacob et al. (2005) emission model, and to  $193 \text{ Tg yr}^{-1}$  in S2 using the MEGANv2.1 source (Table 1).

More than half the atmospheric methanol is removed through OH-oxidation, the remainder through dry deposi-

tion to land and ocean. Wet deposition contributes little to the global sink (Table 1). The dry deposition velocity of methanol to land is parameterized as a function of the leaf area index (LAI), obtained from the MODIS satellite for 2005 (Zhang et al., 2004). It is assumed to increase linearly from 0 to  $0.75 \text{ cm s}^{-1}$  when LAI increases from 0 to  $6 \text{ m}^2 \text{ m}^{-2}$ . A comprehensive description for the wet scavenging parameterization used in IMAGESv2 is given in the Supplement of Stavrou et al. (2009b). The Henry's Law coefficient used for methanol is equal to  $5.8 \times 10^{-6} \exp(5200/T) \text{ mol l}^{-1} \text{ atm}^{-1}$  (Snider and Dawson, 1985; Sander, 1999). The global annual methanol budget is illustrated in Table 1 (first three columns), and simulated a priori methanol columns in S1 and S2 are illustrated in Fig. 3.

## 5 Inversion constrained by IASI methanol columns

### 5.1 Methanol retrievals from IASI

Launched in 2006, the IASI/MetOp-A nadir looking Fourier transform spectrometer probes the Earth's atmosphere in the thermal infrared spectral range. It has a 12-km footprint diameter at nadir and is able to deliver two global earth coverages per day with a very good signal-to-noise ratio. The capabilities of IASI to measure the atmospheric composition

are presented in a number of studies, e.g. Clerbaux et al. (2009); Coheur et al. (2009); George et al. (2009); Boynard et al. (2009). Recently, IASI has been used to derive global tropospheric methanol column distributions, as thoroughly described in Razavi et al. (2011). The retrieval method is briefly presented here.

The method applied to retrieve methanol column data is based on brightness – temperature differences ( $\Delta T_b$ ) between the target channel of  $1033\text{ cm}^{-1}$ , where the methanol absorption in the IASI spectra is the strongest, and contiguous baseline channels at 1019, 1019.5, 1036.25, 1038, 1047 and  $1048.5\text{ cm}^{-1}$ , where the methanol absorption is weak (Razavi et al., 2011). The method then consists in (i) determining global  $\Delta T_b$  values, which provide qualitative information about the strength of the absorption, (ii) applying a correction in order to minimize the impact of ozone and water vapor, and (iii) converting  $\Delta T_b$  to total columns through a radiative transfer model. To reduce computational cost, radiative transfer calculations have been performed over a limited number of world regions, and the conversion factors were derived by matching the retrieved columns on the corresponding  $\Delta T_b$  over land and over ocean. They are applied to deduce total methanol column distributions on the global scale (Razavi et al., 2011). Only daytime (09:30 local time) clear sky scenes are considered in the retrieval and measurements above sand surfaces are filtered out because of emissivity spectral features. Currently, available products are monthly averages. The relative error on the retrieved monthly methanol column is estimated at approximately 50% over continents, although it can be higher in case of low thermal contrast and/or low signal-to-noise ratio. An absolute error of  $10^{16}\text{ mol cm}^{-2}$  is therefore quadratically added to this constant relative error.

The annual methanol column abundances obtained from IASI for 2009 are illustrated in the bottom left panel of Fig. 3. The observed enhanced  $\text{CH}_3\text{OH}$  columns ( $>3 \times 10^{16}\text{ mol cm}^{-2}$ ) are associated with strong emissions from plants and vegetation fires, whereas very low columns are observed over the oceans.

The IMAGESv2 columns are compared with IASI column abundances in 2009 after a 4-month spin-up period starting on 1 September 2008. Mean averaging kernels (separated for land and ocean profiles) were used to account for the vertical sensitivity of the IASI instrument. This is an approximation as the vertical sensitivity is not constant and depends on the temperature and the type of surface. For instance, less information near the ground is usually acquired over ocean or forest surfaces. As shown in Razavi et al. (2011), the IASI total column averaging kernels peak between 5 and 10 km and are very broad, suggesting that IASI measurements are mostly sensitive to free to mid tropospheric columns. The seasonality of the IASI data is compared to the model seasonality for selected large world regions in Figs. 5 and 6. A discussion on these results follows in Sect. 7.

## 5.2 Inverse modelling approach

The inversion scheme used for deriving “top-down” methanol emission updates is based on the adjoint of IMAGESv2 (Müller and Stavrakou, 2005; Stavrakou and Müller, 2006), which has been used in earlier studies to infer emissions of reactive gases constrained by satellite data (Stavrakou et al., 2008, 2009b,c). The adjoint method is used to compute the derivatives of the cost function (misfit between the model and the observations)

$$J(\mathbf{f}) = \frac{1}{2}[(H(\mathbf{f}) - \mathbf{y})^T \mathbf{E}^{-1}(H(\mathbf{f}) - \mathbf{y}) + \mathbf{f}^T \mathbf{B}^{-1} \mathbf{f}], \quad (11)$$

with respect to a number of control variables  $\mathbf{f}$  (emission parameters) allowing to address problems involving a very large number of control variables, like grid-based inversions where fluxes are updated at every model grid cell. In Eq. (11)  $H(\mathbf{f})$  is the model operator acting on the control variables,  $\mathbf{y}$  is the observation vector,  $\mathbf{E}$ ,  $\mathbf{B}$  are the covariance matrices of the errors on the observations and the emission parameters  $\mathbf{f}$ , respectively, and  $^T$  is the transpose of the matrix. The cost function  $J$  is minimized through an iterative descent algorithm which makes use of the forward and the adjoint model of IMAGESv2. A set of updated emission fluxes is determined after ca. 20 iterations (Stavrakou and Müller, 2006).

The methanol concentration in water ( $C_w$ , Eq. (8) is taken equal to  $7.1 \times 10^{13}\text{ mol cm}^{-3}$ , which corresponds to the mean surface ocean concentration of  $118\text{ nmole l}^{-1}$  measured in the tropical Atlantic (Williams et al., 2004).

Two emission categories are optimized, namely the pyrogenic and biogenic emissions, while anthropogenic and ocean emissions are kept at their a priori values (Table 1). The number of unknowns to be determined by the inversion is equal to ca. 15 000 (5000 for biomass burning, 10 000 for biogenic). The errors on the emission parameters, which are represented by the diagonal elements of the  $\mathbf{B}$  matrix, are assumed to be a factor of two for biogenic emissions, and a factor of 2.5 for biomass burning. Spatial and temporal correlations are introduced in the inversion through the off-diagonal elements of the  $\mathbf{B}$  matrix, as in Stavrakou et al. (2009c). The spatial correlations between errors on the emissions from two grid cells are assumed to decay exponentially with the distance  $d$  between the grid cells,  $e^{-d/\ell}$ , with  $\ell = 500\text{ km}$  for both emission categories. Temporal correlations are assumed to decrease linearly between 0.25 for adjacent months and zero for a 6-month time lag.

The inversion study OptS2 (Table 1) is performed using MEGANv2.1 as a priori for plant emissions. The inversion is constrained by IASI columns over continents. Oceanic data are excluded from the inversion due to their large uncertainties. The inferred methanol budget is illustrated in Table 1 (fourth column) and annually averaged global maps of methanol columns are shown in Fig. 3. The derived annual ratio of the optimized to the prior source is illustrated

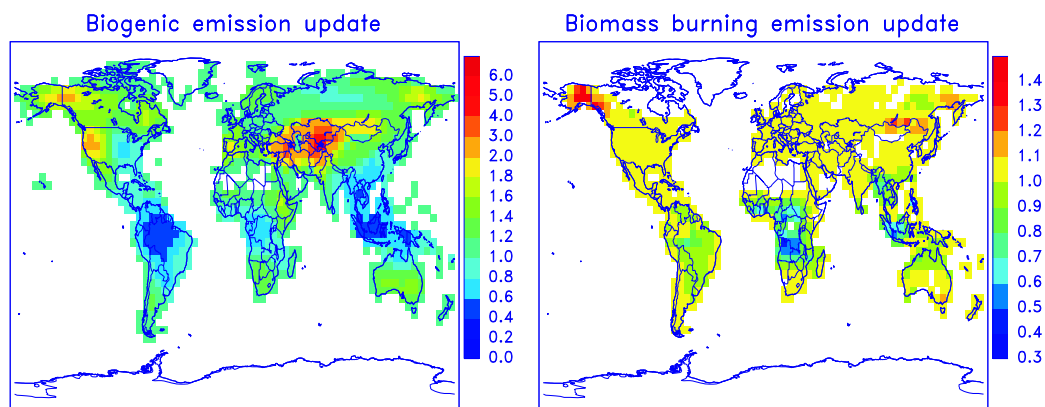


**Fig. 4.** Annual ratios of a posteriori to a priori biogenic (left) and biomass burning (right) emissions inferred by the OptS2 inversion study.

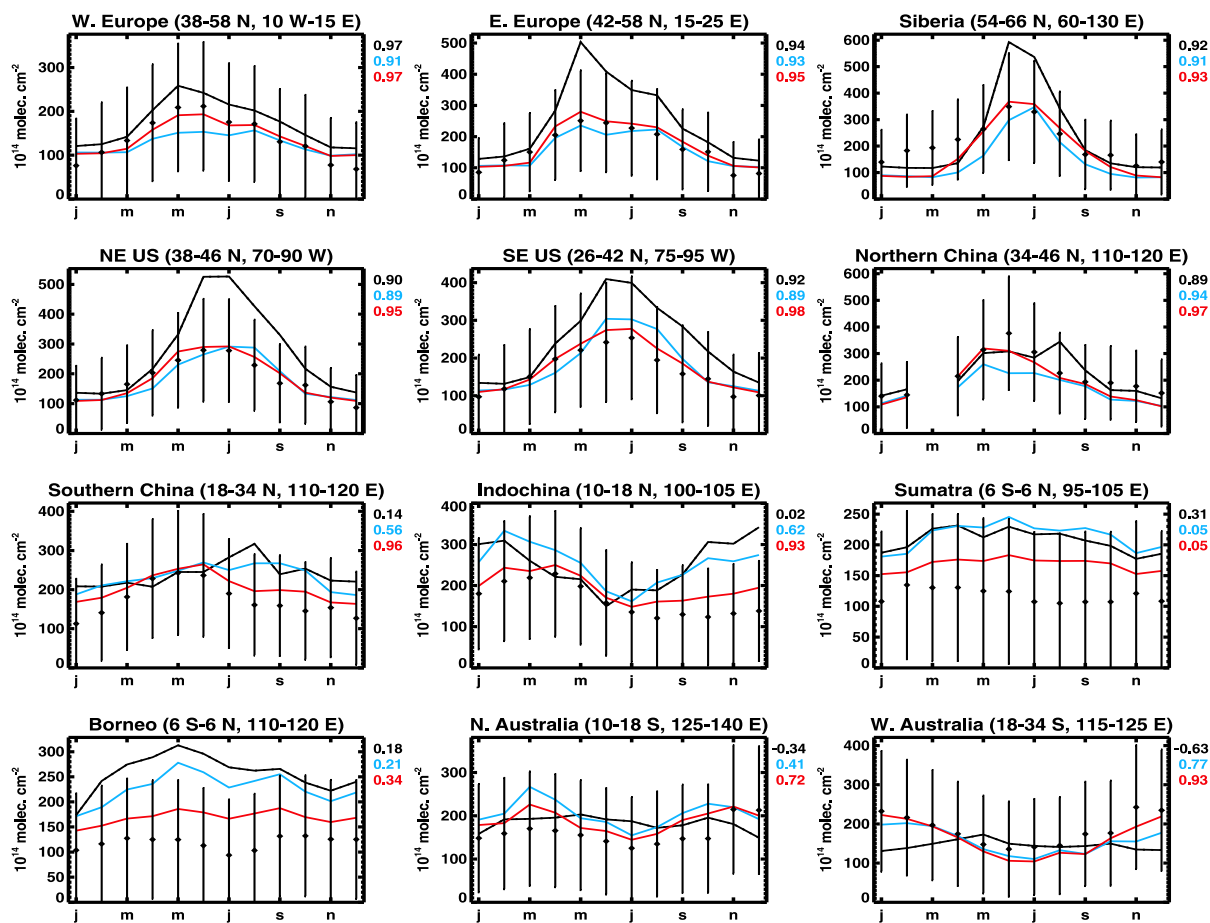


**Fig. 5.** Comparisons over selected regions between monthly averaged IASI methanol columns (black diamonds) with modelled columns of the S1 (black), S2 (blue), and OptS2 (red) simulations of Table 1. Numbers in the right end of each plot correspond to the correlation coefficients calculated for each simulation.

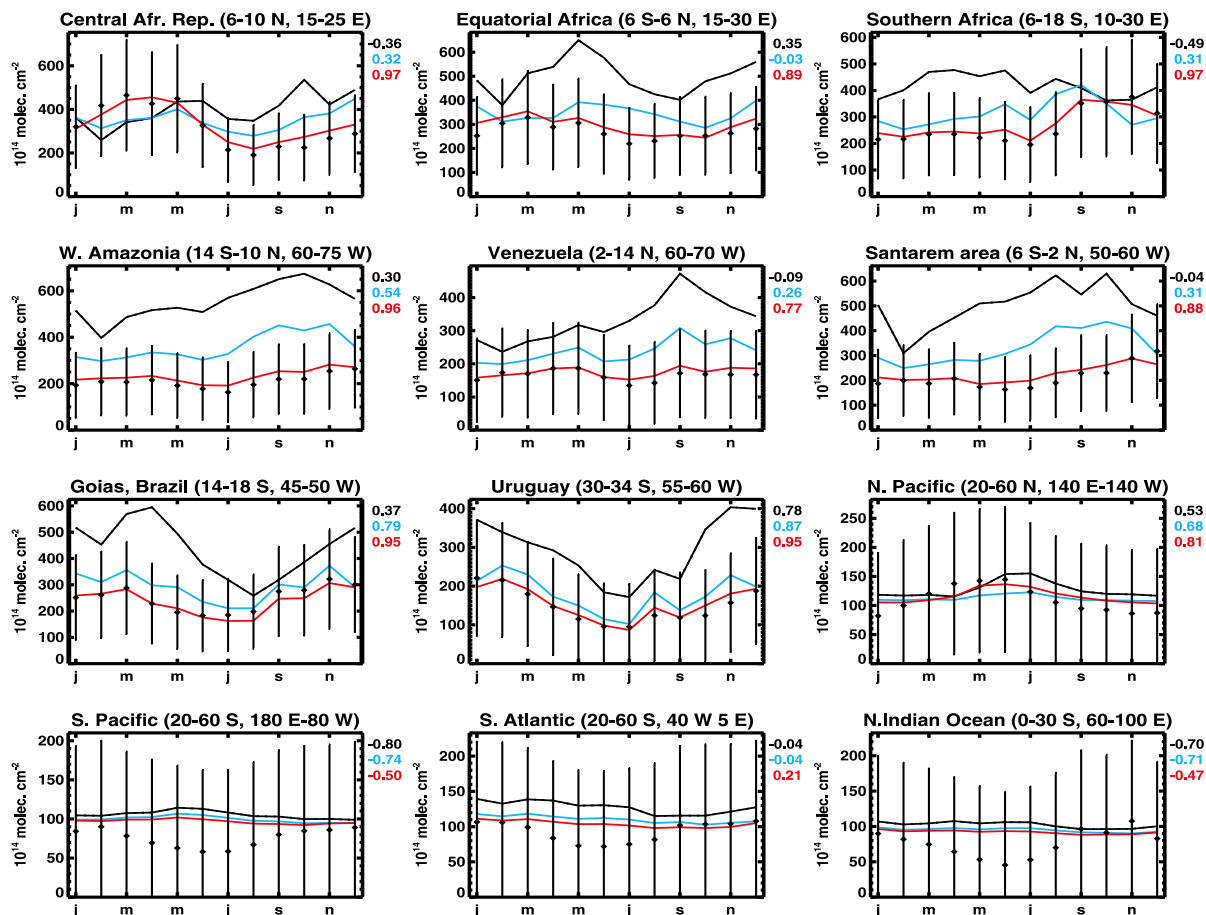


Fig. 6. As in Fig. 5 but for tropical and oceanic regions.

in Fig. 4 and the inferred regional changes in the biogenic source strength are summarized in Table 2.

## 6 Independent methanol observations used for model evaluation

### 6.1 Airborne data

Methanol distributions obtained from different aircraft field campaigns are used to evaluate the model predictive skills for methanol concentrations. More specifically we use:

1. The INTEX-A (Intercontinental Chemical Transport Experiment – North America) mission conducted in the summer of 2004 (1 July to 15 August 2004) over North America and the Atlantic aboard a DC-8 aircraft platform. The plane flew from the US west coast, over the Pacific, moved to mid-America, the Eastern US coast, and the north western Atlantic. The data and flight tracks are available via the NASA INTEX-NA archive (<ftp://ftp-air.larc.nasa.gov>) and an overview of the mission is provided in Singh et al. (2006).

Table 2. Biogenic emission estimates of methanol (in  $\text{Tg yr}^{-1}$ ) in large world regions before and after optimization.

| Regions         | S2    | OptS2 |
|-----------------|-------|-------|
| Europe          | 6.1   | 8.2   |
| North America   | 13.2  | 15.2  |
| South America   | 27.4  | 18.0  |
| Northern Africa | 14.2  | 14.3  |
| Southern Africa | 12.6  | 11.7  |
| South Asia      | 16.2  | 14.0  |
| Global          | 104.7 | 100   |

2. The NOAA WP-3D aircraft platform employed during the NEAQS-ITCT (New England Air Quality Study – Intercontinental Transport and Chemical Transformation) study. The methanol measurements have been obtained between 5 July to 15 August 2004 using a PTR-MS (Proton Transfer Reaction Mass Spectrometer) instrument over the region of the Ohio Valley, the

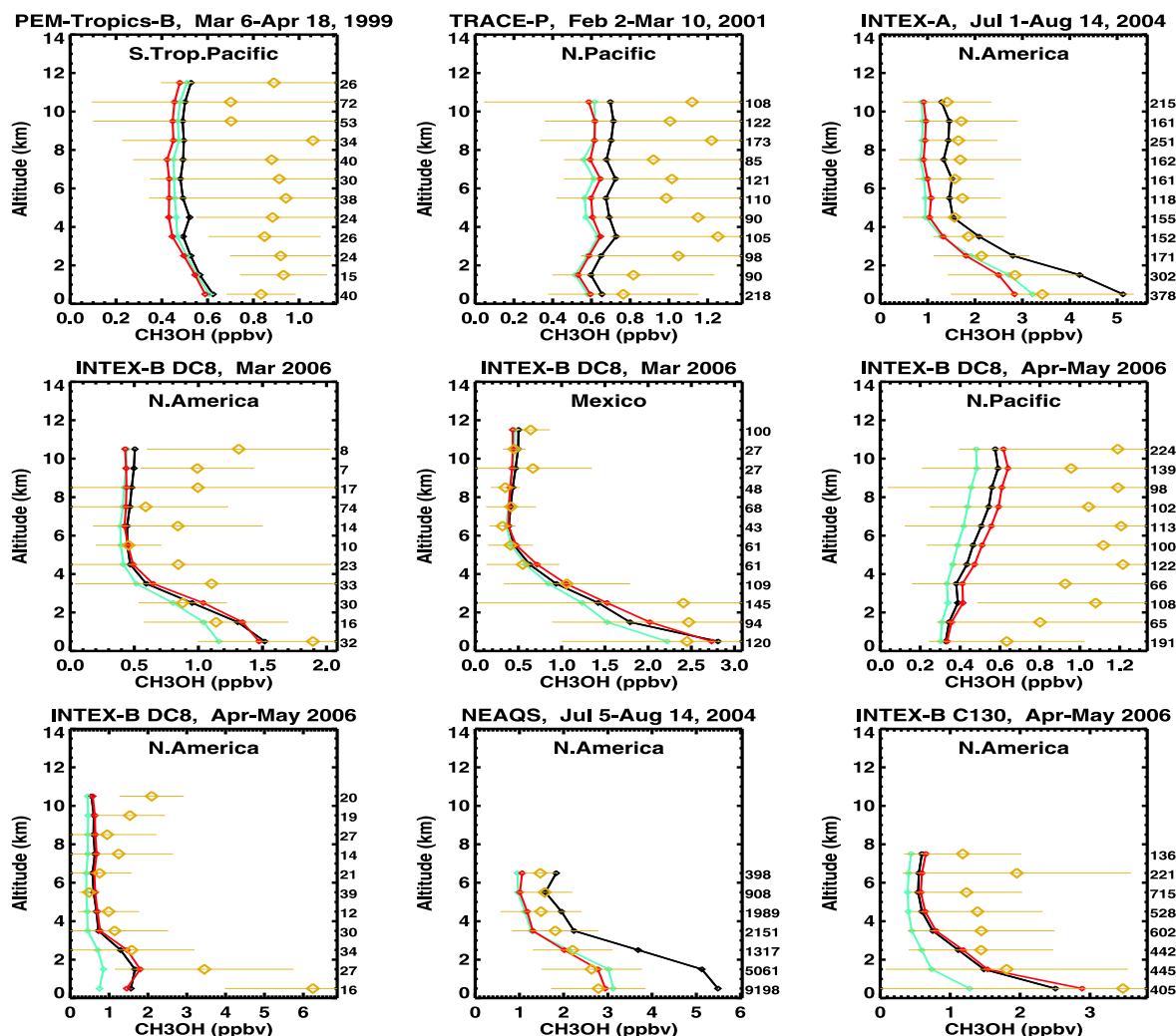


**Fig. 7.** Mean simulated (for 2009) and observed vertical distributions of methanol concentrations during the INTEX-A, NEAQS, INTEX-B, PEM-Tropics-B and TRACE-A aircraft campaigns. Regions are: North America (25–55° N, 45–130° W), Mexico (0–25° N, 85–110° W), N. Pacific (25–55° N, 160–230° E), South Tropical Pacific (0–40° S, 180–275° W). Colored curves correspond to the simulations of Table 1, black for S1, blue for S2, and red for the OptS2 inversion. The number of observations available at each altitude bin is given on the right end of each plot. Error bars are standard deviations.

eastern seaboard, New England and the North Atlantic (<http://www.esrl.noaa.gov/csd/2004/p3platform.shtml>).

3. The INTEX-B two-phase aircraft mission conducted in spring 2006 (1 March to 15 May) over the region of Mexico in March (first phase) and over the Pacific in April and May (second phase). Detailed information on this mission is provided at the INTEX-B web site (<http://www.espo.nasa.gov/intex-b/index.html>) and a large number of studies realized using INTEX-B measurements are included in Molina et al. (2010).
4. The PEM-Tropics B (Pacific Exploratory Mission in the central and eastern regions of the tropical Pacific Ocean basin) and TRACE-P (Transport and Chemical

Evolution over the Pacific) aircraft missions conducted in March–April 1999 and February–March 2001, respectively, as part of NASA's Global Tropospheric Experiment (GTE). Detailed information on these experiments can be found at the GTE page (<http://www-gte.larc.nasa.gov/gte fld.htm>). The data, compiled onto a 5×5 degrees grid with a vertical resolution of 1 km by Emmons et al. (2000), can be accessed through the data composites web page ([http://acd.ucar.edu/~emmons/DATACOMP/camp\\_table.htm](http://acd.ucar.edu/~emmons/DATACOMP/camp_table.htm)).

A compilation of in situ literature measurements of methanol concentrations is also used to evaluate the a priori and optimized model performance. Detailed descriptions of these data can be found in the references of Table 5. The data

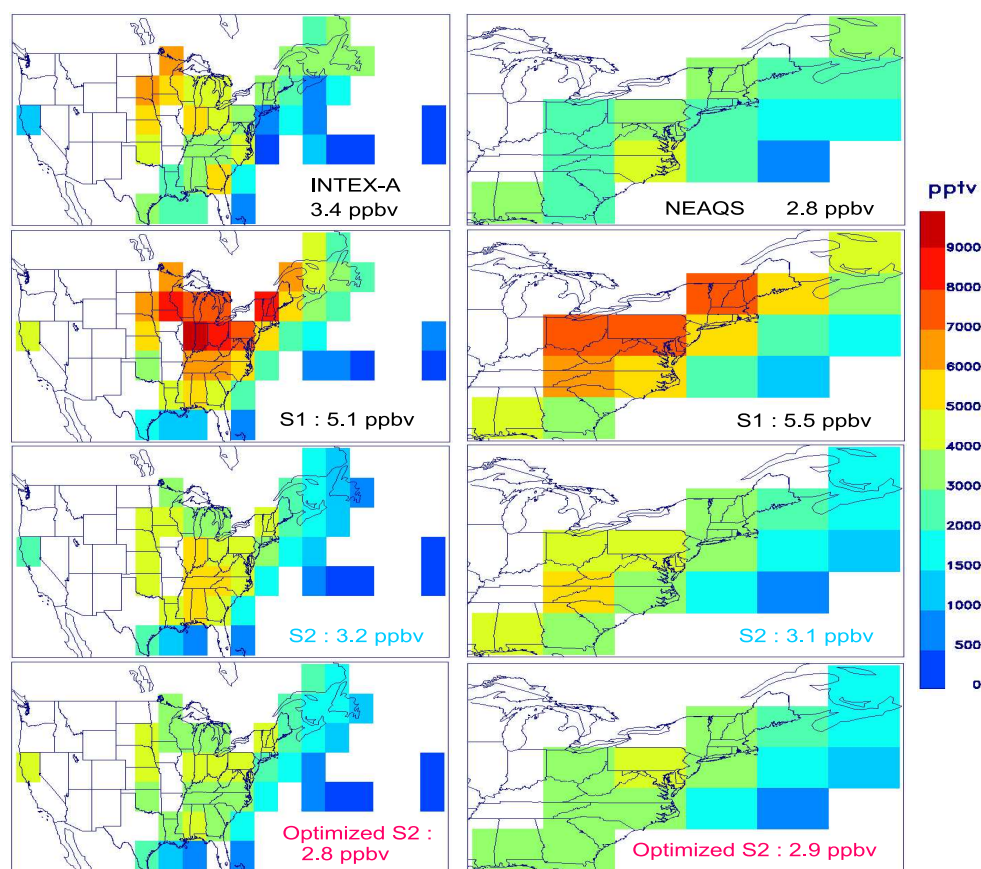


**Fig. 8.** Comparison between data from the INTEX-A and NEAQS campaigns and model concentrations from S1, S2 and OptS2 simulations averaged between the surface and the altitude of 1 km. The mean methanol concentrations over the corresponding aircraft flight domains are provided inset.

are compared with modelled concentrations before and after the inversion averaged for the given measurement duration (Fig. 9). Besides these data, we also evaluate the model using recently retrieved methanol concentrations at a European forest site, and methanol total columns from FTIR (Fourier Transform Infrared) measurements at a southern tropical remote site in the Indian ocean. These datasets are briefly described below.

The Vielsalm measurement site is located in the Belgian Ardenne forest (50.3° N, 6° E, altitude: 450 m). This site has a mixture of coniferous species, mainly Douglas fir, Norway spruce, silver fir, and deciduous species, mainly beech. Long-term BVOC ecosystem-scale flux measurements were performed from a 52 m high tower by the disjunct eddy-covariance technique (see e.g. Spirig et al., 2005) between 26 June and 16 November 2009, and from 25 March until 16 November 2010. A PTR-MS is used for on-line sensitive and fast BVOC concentration measurements. Monitored BVOC are formic and acetic acid, methanol, acetaldehyde, acetone, isoprene, sum of methyl vinyl ketone and methacrolein, C<sub>5</sub> alcohols, and the sum of monoterpenes. A detailed descrip-

tion of the experimental setup can be found in Laffineur et al. (2010). Comparisons of monthly averaged model concentrations in 2009 and measured concentrations between July and September 2009, and between April and September 2010 are shown in Fig. 10.

The FTIR instrument at the Reunion Island (21° S, 55° E) is operating on a quasi-continuous basis since May 2009, whereas three campaigns have been conducted in previous years (Senten et al., 2008; Vigouroux et al., 2009). For this work we focus on the period between June and December 2009. The methanol retrievals are performed in the 1029–1037 cm<sup>-1</sup> spectral range, in the region of the ν<sub>8</sub> Q branch (see also Beer et al., 2008; Coheur et al., 2009). Methanol vertical profiles at Reunion are retrieved using the inversion algorithm SFIT2 Rinsland et al., 1998 (v3.94), and using an a priori volume mixing ratio profile constant at 0.9 ppbv below 12 km, decreasing rapidly above this altitude to reach 0.1 ppbv at 20 km, in consistency with the PEM-Tropics-B aircraft mission (Fig. 7) and ACE-FTS measurements (Dufour et al., 2006). The retrieval is constrained by Tikhonov L1 regularization (Tikhonov, 1963) as in Vigouroux et al.

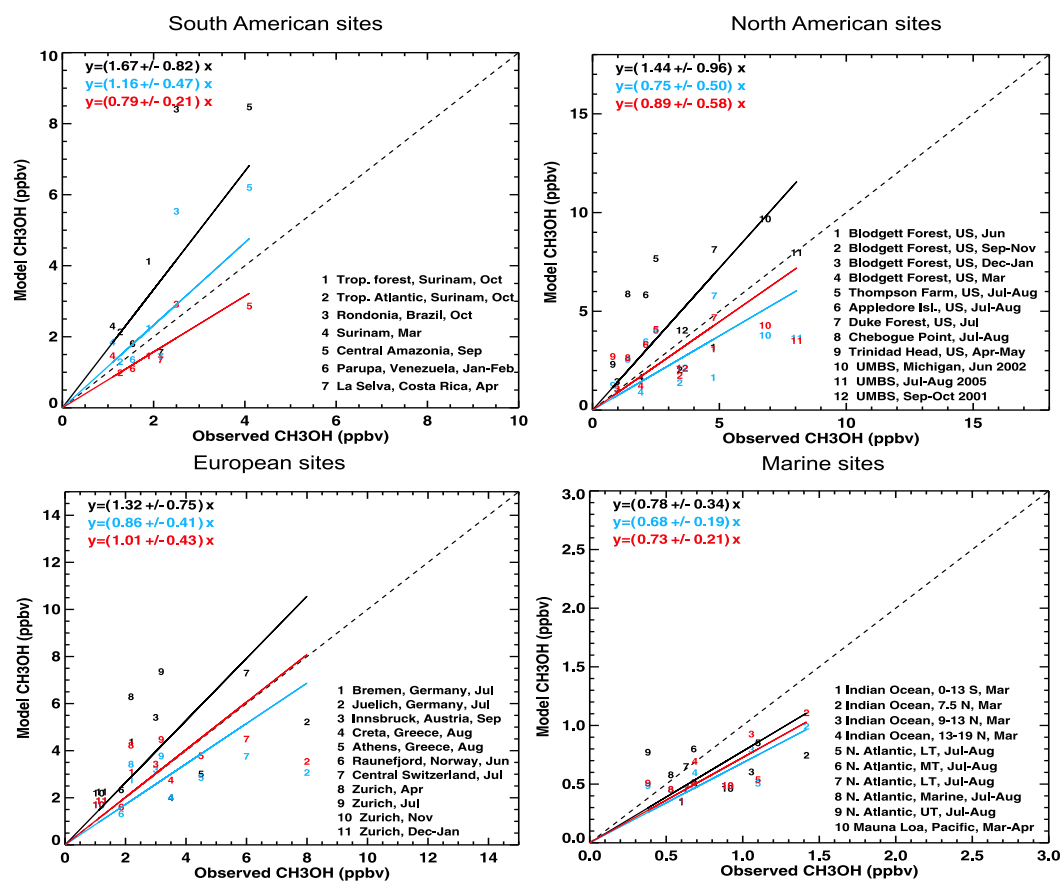


**Fig. 9.** In situ measurements of methanol concentrations shown on Table 5 are compared with the predicted concentrations from simulations S1 (in black), S2 (in blue) and OptS2 (in red). For each simulation, the slopes of the regression lines passing through the origin as well as their standard deviations are illustrated inset respecting the same color code.

(2009). Due to the low degree of freedom for the signal, only total columns are delivered. Monthly averaged model columns are compared with monthly averaged observations in Fig. 11.

## 6.2 Surface-based data

## 7 A priori results – discussion

The use of the NPP-based Jacob et al. (2005) a priori inventory in the S1 experiment leads to significantly higher methanol columns compared to those by the satellite over the majority of continental regions (Fig. 3). On an annual basis, the largest overestimation is found over Amazonia (factor of 2–3), and over Africa and Indonesia (factor of 1.5–2), whereas more moderate overestimations are observed over Europe, Northern America and Australia, and a good overall agreement is found over Siberia. In the S2 simulation, the model output lies closer to IASI data, despite persistent overestimations in the Tropics, which are nevertheless less significant compared to S1.

In Fig. 7 we present comparisons between the mean simulated (using S1, S2, and OptS2) and observed vertical profiles of methanol concentrations above large continental and oceanic regions. The model concentrations have been averaged over the same regions taking into account the location of the measurements. Comparisons between INTEX-A and NEAQS data and modelled concentrations below 1 km are shown in Fig. 8.

A model feature, not corroborated by the comparisons with IASI, is the important difference between methanol columns over eastern and western US (Fig. 3). Another common feature of both simulations is the strong model underestimation over Central Asia (factor of 3), as well as significant underestimations over Western US and Western Australia (up to a factor of 2), due to the very low methanol source estimated by both plant emission models in arid, semi-arid regions or short-grass steppe and limited cropland ecosystems. Supporting evidence for higher-than-predicted methanol concentrations is provided by INTEX-B mission measurements made aboard a C-130 aircraft in April–May 2006 above the westernmost US (Fig. 7). In this case the

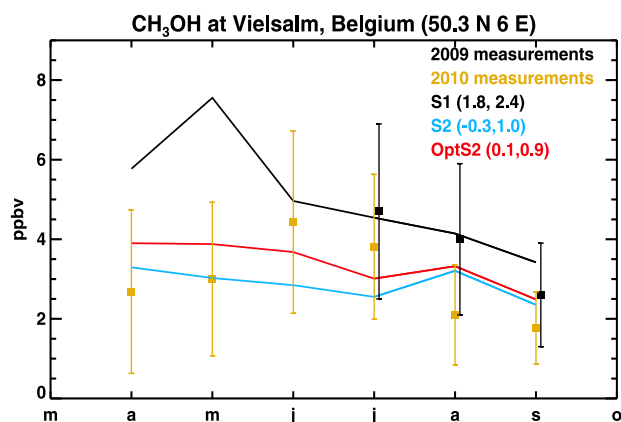


**Fig. 10.** Comparison between measured methanol concentrations near Vielsalm in Belgium (Table 5) and model results from the S1 (in black) and S2 (in blue) a priori simulations and from the OptS2 simulation (in red), see Table 1. Error bars correspond to the standard deviation. The average model/data bias and root mean square deviation are indicated inset in parentheses for each simulation.

model underprediction is, on average near the surface, similar to the one with IASI columns over the same region (factor of 2–3). Furthermore, long-term free tropospheric methanol measurements recorded at Kitt Peak Observatory (31.9° N, 111.6° W) between 2.09 and 14 km (Rinsland et al., 2009) corroborate the IASI measurements both in terms of magnitude and seasonality, showing a similar peak-to-trough amplitude of about 3 between winter and summer, as shown in Fig. 12. The model underestimates the Kitt Peak observed columns by almost a factor of two in summertime, and by 15 % during winter, i.e. the seasonal variation is partly reproduced but is less pronounced. The model underestimation points to the existence of a larger-than-modelled biogenic methanol source in such ecosystems. Geron et al. (2006) investigated biogenic VOC emissions from common desert plants in the southwestern US. The study was focused on terpenoid emissions but some cut branches were analysed with a PTR-MS system so that emissions of methanol and other compounds could be investigated. They observed extremely high methanol rates, 100 to 250  $\mu\text{g g}^{-1} \text{h}^{-1}$ , which is several orders of magnitude higher than typically observed for other plant species. These high rates were attributed to the experimental approach of cutting branches and placing them in water in order to transport the branches for analysis. However, the process by which these plants were able to produce high methanol emission rates was not identified. More recently, Jardine et al. (2010) reported first in-situ measurements of methanol fluxes from a desert shrub, creosote bush, which is a dominant species in the North American Sonoran and Mojave deserts. The average 4.5  $\mu\text{g g}^{-1} \text{h}^{-1}$  emission factor for creosote bush is more than a factor of two higher than the average emission factors of other trees and shrubs (see Harley et al. (2007) and literature reviewed by

Seco et al., 2007), although it is well within the range of these values. Extrapolating the Jardine et al. (2010) measurements to the canopy scale results in a MEGAN methanol emission factor of  $\sim 2 \text{ mg m}^{-2} \text{ h}^{-1}$  for creosote bush, which is more than twice the value used for shrubs in MEGANv2.1. These limited enclosure measurements, along with the IASI satellite observations, suggest that the desert vegetation has a relatively high methanol emission capacity. Above canopy flux measurements are needed to verify this conclusion. The satellite columns remain, however, the only available source of information over Central Asia and western Australia, so that a similar multi-sensor-to-model comparison cannot be conducted.

The Jacob et al. (2005) biogenic emissions used in the S1 simulation lead to modelled methanol columns over northeastern US that are on average by 60 % higher than IASI, while the overestimation reaches 90 % in summertime (Fig. 5). This is consistent with the overestimation reported in Millet et al. (2008) with respect to aircraft observations over the US when the Jacob et al. (2005) plant emissions were used, which was attributed to a possible overestimation of the Galbally and Kirstine (2002) emission factors used to derive the Jacob et al. (2005) methanol emissions. Millet et al. (2008) found that halving the values for all plant functional types, or reducing the emission factors for broadleaf trees and crops by a factor of four, improved significantly the agreement with the observations. On the other hand, the use of MEGANv2.1 greatly improves the comparison with the satellite data: the model overestimates by less than 10 % in both Northeastern and Southeastern US over the entire year, although the overprediction reaches 28 % in summertime southeastern US. Comparisons of S1 results with INTEX-A and NEAQS aircraft data (Sect. 6.1, Fig. 7) present also large overestimations in the boundary layer below 1 km, by 50 % and 95 % for INTEX-A and NEAQS, respectively, while the S2 predicted concentrations agree with the measurements within 10 % (Fig. 8). This result is corroborated by surface measurements at North American sites (most of them in Eastern US), shown in Table 5. As shown in Fig. 9, the S1 predicted concentrations yield a mean overestimation of 44 % at these sites, whereas S2 underpredicts the measurements by ca. 10 %. However, in spite of the better overall model performance near the surface when S2 results are considered, comparisons of modelled to aircraft vertical profiles from INTEX-A, INTEX-B and NEAQS missions above North America show an important underestimation (up to 45 % in the case INTEX-A) of methanol concentrations in the free troposphere (Fig. 7). The reasons for this behaviour are not completely clear and will be addressed in Sect. 10.

The comparisons with aircraft measurements and in situ measurements over ocean point to a general model underestimation over the oceans (Fig. 7, Table 5, Fig. 9), suggesting a more significant ocean source than the one considered in the model (Sect. 3) and/or to an overestimated ocean deposition sink. High concentrations over ocean have

been also reported in earlier aircraft campaign measurements over the Pacific (Singh et al., 1995, 2001). Nevertheless, the model/IASI comparisons over the Pacific, Atlantic and Indian ocean do not confirm these conclusions (Fig. 6). The predicted columns turn out to be higher than IASI observations in almost all regions and months, and they exhibit almost no seasonal variation, as opposed to the observations. It should be noted, however, that the IASI signal over the oceans is weak and large errors are associated to the columns. This issue warrants further study and underscores the need for further measurements at remote oceanic sites.

The MEGANv2.1 inventory reproduces better the magnitude and seasonal variation of the observed columns in most regions. This is also reflected in the correlation coefficients given in Figs. 5 and 6. In Indonesia, the S2 model overprediction with respect to IASI columns (factor of 2, Fig. 5) is in line with comparisons between modelled and observed methanol concentrations obtained during the OP3 campaign conducted in 2008 in the Malaysian rainforest during the wet (April–May) and early dry season (June–July) (Langford et al., 2010). More specifically, the S2 methanol concentrations calculated at the model grid cell comprising the campaign site located in northeastern Borneo ( $5^{\circ}\text{N}$ ,  $118^{\circ}\text{E}$ ) are 2.5 times higher than the concentrations of  $1.2 \pm 0.46$  ppbv, and  $1.5 \pm 0.67$  ppbv observed in the wet and dry season, respectively. This finding could be partly explained by an overestimation of the methanol emission rate assumed in MEGANv2.1 for broadleaf forests ( $400 \mu\text{g m}^{-2} \text{h}^{-1}$ , Sect. 2.2). In fact, flux measurements of methanol reported in Langford et al. (2010) at this rainforest site have a mean value very close to zero and a large variability ( $-33 \pm 300 \mu\text{g m}^{-2} \text{h}^{-1}$ ), suggesting that dry deposition plays an important role. Furthermore, these fluxes over Borneo are much lower than the net fluxes measured in the Amazon rainforest by Karl et al. (2004) ( $500 \mu\text{g m}^{-2} \text{h}^{-1}$ ). Such considerable discrepancies make evident that large variability is associated to measured fluxes even for relatively similar rainforest biomes, and therefore, the use of a single flux value for all broadleaf trees in MEGANv2.1 cannot be but a crude estimate. In Amazonia, the S2 model overestimation with regard to IASI reaches up to 50–70 % depending on the region (Fig. 6), but it is much more significant in the S1 simulation, in line with the findings of Millet et al. (2008). The use of MEGANv2.1 produces a nice agreement with IASI over the Goias province in central Brazil, a region of Brazil covered with woodland savanna, and Uruguay, mainly covered with tall prairie grass plains, lending confidence to the assumed methanol rates for grasslands in MEGANv2.1 (Fig. 6).

Above Africa and Australia, the comparisons of the S2 results with the IASI columns yield a satisfactory agreement both in terms of amplitude and seasonality, whereas the S1 simulation falls short of capturing the observed variations in the columns, as indicated by the negative calculated correlation coefficients. This suggests that the representation of methanol emissions based on net primary production as in Ja-

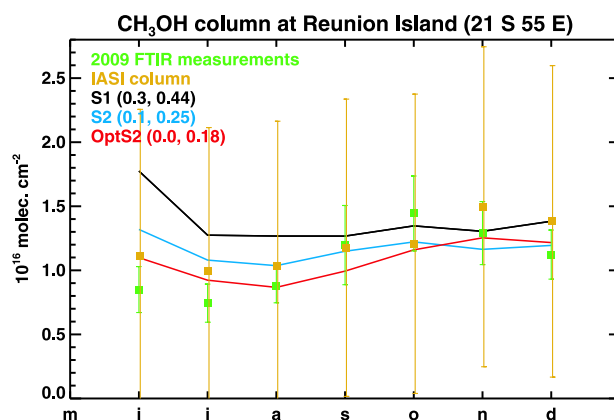


**Fig. 11.** Comparison between FTIR methanol columns at Reunion Island and model results from the S1 (in black) and S2 (in blue) a priori simulations and from the OptS2 simulation (in red), see Table 1. Green and orange error bars correspond to the standard deviation of FTIR measurements and the assumed error on IASI columns, respectively. The average model/FTIR bias and root mean square deviation are indicated inset in parentheses for each simulation.

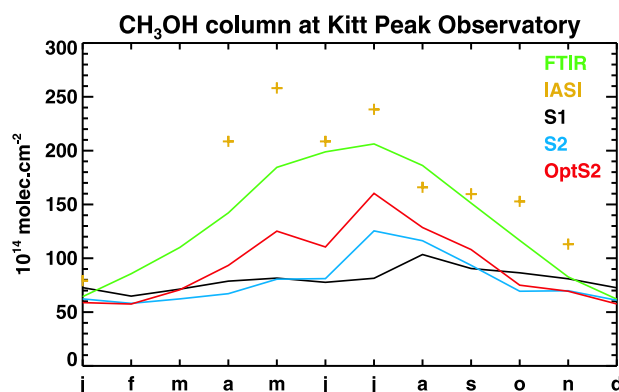


**Fig. 12.** Comparison between (1) monthly averaged FTIR data obtained at the Kitt Peak Observatory ( $31.9^{\circ}\text{N}$ ,  $111.6^{\circ}\text{W}$ , 2.09-km a.s.l.) with a 1-m Fourier transform spectrometer between October 1981 and December 2003 (Rinsland et al., 2009) (in green), (2) IASI columns (in orange), (3) columns simulated by S1, S2 and OptS2 between 2.04 and 14 km. The total uncertainty in the 2.09–14-km FTIR methanol columns due to both random and systematic errors is estimated at less than 20 % (Rinsland et al., 2009). The correlation coefficient between the model and the FTIR data is equal to 0.55 in S1, 0.8 in S2, and 0.94 in OptS2 inversion.

cob et al. (2005) might not be adequate for tropical regions, both in terms of seasonality and magnitude. Over Europe, the S2 run results in a moderate underestimation and to a less marked seasonal cycle compared to IASI (Fig. 5).

## 8 Inversion results – discussion

The global a posteriori biogenic methanol source deduced from the inversion amounts to  $100 \text{ Tg yr}^{-1}$  (OptS2, Table 1) and is very close to the S2 a priori estimate. After optimization, the cost function (Eq. 11) is reduced by a factor of 2.1 globally and its gradient is reduced by a factor of 1200. The optimization yields a significantly better agreement between the model and IASI data, which is carried through substantial changes in the biogenic and biomass burning emission fluxes, as shown in Figs. 3, and 4. Considerable changes of the biogenic source with regard to the a priori MEGANv2.1 database are recorded above Amazonia and Indonesia, with inferred annual reductions of 40–55 % and 45–58 %, respectively, whereas significant reductions are also derived in the Eastern US (20–25 %) and Central Africa (25–35 %). Very significant increases of the biogenic source are deduced above Central Asia (up to a factor of 5), Western US (factor of 2), and the Iberian peninsula (ca. 90 %) (cf. Sect. 7). On the other hand, the methanol source from vegetation fires, although much less significant on the global scale compared to the biogenic source, is also strongly modified by the inversion, with inferred reductions of 35 % above Indonesia, up to 38 % above the Central African Republic, and up to 50 % above Southern Congo.

Note that there might be some conflation of the biogenic and biomass burning source categories, due to the spatiotemporal coexistence of the two sources. However, the simultaneous optimization of two source categories is facilitated by the prescribed spatiotemporal correlations of the a priori errors (**B** matrix in Eq. 11), which tend to preserve the spatiotemporal patterns of the a priori emissions in each category. More importantly, at most locations/times, one of the two sources is largely dominant, and is therefore well constrained by the observations. For example, over Alaska, the large pyrogenic emission increases (Fig. 4) are due to fires in July/August 2009, resulting in methanol emissions about an order of magnitude larger than the biogenic emissions in that region. Conversely, the biogenic emission increases seen in Fig. 4 over Alaska and Yukon are mostly due to a strong enhancement in May–June, when biomass burning emissions are negligible.

Although the reduced plant emissions over the tropical Amazon allow for a very good match with the satellite observations, they lead to model underprediction of about 20 % at 5 of the 7 sites located in South America (Table 5, Fig. 9, red line). The limited set of surface data over this region and the dearth of measurements from other platforms do not allow to draw further conclusions. It is however possible that IASI retrieved columns are low-biased over the tropical Amazon. One tentative explanation is the enhanced presence of clouds in this region. Even though all IASI data is cloud filtered prior to retrieval using the EUMETSAT level 2 data, completely cloud free scenes are extremely rare over tropi-

cal rainforests. It is therefore not unlikely that residual cloud contamination is much larger in this region than in other parts of the world, resulting in lower observed methanol columns. This may also apply to tropical Africa or Asia. Over Indonesia, the emission decreases suggested by IASI bring the model much closer to the OP3 campaign measurements (Sect. 7), i.e. the initial overestimation is reduced from 250 % to approx. 50 %.

Over the Eastern US, the optimized mixing ratios are in good agreement with both INTEX-A and NEAQS campaign measurements below 2 km (Figs. 7, 8). However, a significant underestimation remains in the free troposphere. This is not totally unexpected due to the likely effect of eastward transport from the Western US, where the modelled columns remain underestimated (Figs. 3, 12). In addition, sensitivity calculations indicate that an underestimation of convective fluxes and/or an overestimation of OH simulated concentrations could also partly explain the overestimated methanol gradient between the PBL and the free troposphere (see Sect. 10). The comparison at the marine sites shown in Table 5 is not improved after inversion (Fig. 9). Further, the optimized model concentrations calculated at the North American locations of Table 5 are now, on average, closer to the surface data, although the scatter is still significant (Fig. 9).

Plant emissions in Europe are increased on an annual basis by 35 % (Table 2), with the most important increase found in Spain and Portugal. Further, comparison of the model concentrations from S1, S2 and OptS2 at the Vielsalm forested site (Fig. 10) shows that neither simulation succeeds in representing adequately the seasonality of the surface data. However, in terms of mean bias and root mean square deviation, the optimized results perform significantly better. Furthermore, the OptS2 simulation results in better agreement with the surface observations at different European sites, as depicted in Fig. 9, implying a reasonable consistency between satellite observations and ground-based measurements.

The IASI-derived decreases in pyrogenic and biogenic emissions over the central and Southern Africa are supported by the FTIR columns retrieved at the Reunion Island (Fig. 11). This site, located near Madagascar at a distance of about 2000 km from the continent, is influenced by long-range transport from continental air, given the relatively long methanol lifetime. The presence of strong biogenic emissions throughout the year in Southern Africa and the occurrence of important fire events from June to November have a significant impact on the observed methanol at this site. The inversion suggests reductions to both emission sources in almost all months except in November, when IASI column is at its highest. The observed seasonality is well reproduced by the model, which is also reflected in the low bias and root mean square deviations between the model and the observations.

Finally, the MEGANv2.1 and the optimized global biogenic source are found to be in line with the reported value

by Millet et al. (2008) (Table 1), which was constrained by aircraft data, and are significantly lower compared to the Jacob et al. (2005) source. In opposition to these findings, a strong increase with respect to the Jacob et al. (2005) emissions was invoked by Dufour et al. (2007) during spring and summer in the Northern Hemisphere in order to explain the large mixing ratios sampled over high-latitude regions between 6 and 14 km by the ACE-FTS sensor. Although our model is also found to underpredict methanol concentrations in the free troposphere during the INTEX-A and NEAQS missions (Fig. 7), as well as over the Northern Atlantic (not shown), lower biogenic emissions are supported by both surface and aircraft measurements in the boundary layer. As discussed above, this underestimation might have multiple causes (cf. Sect. 10).

## 9 A posteriori error estimation

The errors on the a posteriori emission estimates are calculated by applying an off-line iterative approximation of the inverse Hessian matrix, which relies on the Davidon-Fletcher-Powell (DFP) updating formula (Fletcher, 1990). When assuming that the model is linear or not too far from being linear, the a posteriori error covariance matrix is related to the Hessian of the cost function  $J$  through the expression:

$$E_{\text{post}} = [(\mathbf{DH})_f^T \mathbf{E}^{-1} (\mathbf{DH})_f + \mathbf{B}^{-1}]^{-1} = (\mathbf{IH})_f, \quad (12)$$

where  $(\mathbf{IH})_f$  is the inverse Hessian matrix evaluated at the point  $f$ ,  $(\mathbf{IH})_f = \mathbf{Hessian}(J)_f^{-1}$ ,  $\mathbf{DH}$  is the Jacobian matrix of the model, and  $\mathbf{E}$  and  $\mathbf{B}$  are as in Eq. 11 (see Müller and Stavrou (2005) for details). The inverse Hessian matrix is estimated iteratively using the new information obtained at each step  $k$  of the minimization procedure through the DFP formula :

$$(\mathbf{IH})_{k+1} = (\mathbf{IH})_k + \frac{s_k s_k^T}{y_k^T s_k} - \frac{(\mathbf{IH})_k y_k y_k^T (\mathbf{IH})_k}{y_k^T (\mathbf{IH})_k y_k}, \quad (13)$$

where  $s_k = f_{k+1} - f_k$ ,  $y_k = (\nabla J)_{f_{k+1}} - (\nabla J)_{f_k}$ ,  $(\nabla J)_{f_k}$  is the gradient of  $J$  at the point  $f_k$ , and the initial inverse Hessian matrix is taken to be equal to  $\mathbf{B}$ . by recursive application of the DFP updating formula to the vectors  $f_k$  and  $(\nabla J)_{f_k}$  calculated by the minimization algorithm (Sect. 5.2), we obtain an approximate inverse Hessian matrix. The square root of the diagonal elements of this matrix are the standard errors associated to the optimized parameter vector  $\mathbf{f}$ . The error reductions, i.e. the ratio of the a priori to the a posteriori errors are given in Table 4 for large continental regions. The largest error reductions are achieved for the biogenic source over regions where forests are dominant, like South America and the Former Soviet Union, where the a posteriori uncertainties are reduced by 50 % and 67 %, respectively. Significant reductions are also found over Europe (40 %) and North America (35 %). The error on the biogenic source is decreased globally by 43 %. Because the biomass burning source represents

only 3 % of the global methanol source, the fire impact of the methanol levels is masked by the contribution of the biogenic source. Lower error reductions are therefore calculated for the vegetation fire source: of the order of 14 % on the global scale, 10–12 % over Africa and southern Asia, and almost negligible error reductions over other regions.

Note that besides the DFP update formula, the BFGS formula (Broyden-Fletcher-Goldfarb-Shanno) for calculating the inverse Hessian matrix is widely used in large-scale problems (Fletcher, 1990). Both expressions have been evaluated against the finite difference approach in Müller and Stavrou (2005). Applied to the OptS2 inversion results, the BFGS formula is found to yield results quite similar to those obtained with the DFP method.

## 10 Sensitivity inversions

Besides the uncertainties on the a posteriori emission fluxes calculated in the previous section, model errors lead to potentially significant uncertainties on the derived methanol fluxes, which are however very difficult to estimate. In this section we propose a tentative assessment of these errors, based on a set of sensitivity inversions conducted to investigate the influence of uncertainties on meteorological parameters, on methanol sink processes, and on the a priori methanol plant emission source. Although this evaluation is not exhaustive, it accounts for the most important uncertainties associated to the model. Table 3 summarizes the performed inversions and provides the corresponding tropical (25° S–25° N), extratropical and global biogenic source inferred in each case study.

In the OptS2-conv inversion a factor of two increase in the convective updraft fluxes used in the model is assumed. Stronger convection leads to a redistribution of trace gases from the boundary layer upwards in the free troposphere, in regions with generally higher horizontal winds resulting in a stronger dispersion and lower methanol columns over source regions. In tropical regions, however, where horizontal winds are weak, this decrease is more than compensated by an increase in the modelled methanol columns calculated with the IASI averaging kernels, because of the higher sensitivity of the retrievals to the higher tropospheric layers. Regionally, the annual biogenic emission change inferred by OptS2-conv lies within 10 % of the standard inversion (Fig. 13), whereas on the global scale the a posteriori biogenic source stays very close to that of the standard inversion. The largest emission changes are found over Amazonia, where about 10 % lower emissions are required to match the IASI columns when convection is enhanced. As expected, the a posteriori column changes are very small (less than 2 %) over source regions, due to the observational constraint. Enhanced transport from source regions to remote areas leads to small methanol column increases over oceans and deserts (Fig. 13). Comparison with the INTEX-A and NEAQS vertical profiles (Fig. 14,

**Table 3.** Performed sensitivity inversions, and corresponding tropical, extratropical and global biogenic methanol source expressed in  $\text{Tg yr}^{-1}$ .

| Description                                      | Name         | Global | Tropical | Extra-tropical |
|--|--------------|--------|----------|----------------|
| Standard   | OptS2        | 100    | 62       | 38             |
| Double convective fluxes                         | OptS2-conv   | 99.4   | 61.2     | 38.2           |
| Methanol dep. velocity increased by 60 %         | OptS2-drydep | 112    | 69       | 43             |
| OH concentrations from Spivakovsky et al. (1990) | OptS2-OH     | 91.5   | 59.5     | 32             |
| Use Jacob et al. (2005) a priori source          | OptS1        | 103.8  | 62.4     | 42.4           |

**Table 4.** Error reduction (ratio of the a priori to the a posteriori error) achieved by the OptS2 optimization calculated annually per source category and region.

| Regions         | Biogenic | Biomass burning |
|-----------------|----------|-----------------|
| North America   | 1.54     | 1               |
| South America   | 2.10     | 1.06            |
| Northern Africa | 1.13     | 1.11            |
| Southern Africa | 1.08     | 1.10            |
| South Asia      | 1.18     | 1.13            |
| Far East        | 1.15     | 1               |
| Europe          | 1.64     | 1               |
| FSU             | 3.00     | 1.03            |
| Global          | 1.74     | 1.16            |

blue) indicates that a stronger convection improves the model profile over the US and leads to higher methanol concentrations in the free troposphere, in better agreement with the observations.

Motivated from recent findings by Karl et al. (2010) suggesting that the removal of oVOCs (oxygenated volatile organic compounds) by dry deposition might be substantially larger than is currently assumed for deciduous ecosystems, owing to their possible loss upon entering leaves through stomata, we carried out an inversion exercise where methanol deposition velocity is increased by 60 % compared to the standard case. For example, the daily averaged deposition velocity for a leaf area index of  $6 \text{ m}^2 \text{ m}^{-2}$  is therefore assumed equal to  $1.2 \text{ cm s}^{-1}$ . Note however that deposition processes for methanol and other oVOCs might be more complex, due to their water solubility and to the potential influence of an aqueous reservoir at the leaf-air interface in humid conditions. An improved representation of oVOC dry deposition will be the subject of further investigations. Due to the larger methanol sink in inversion Opt-drydep, the inferred global biogenic emission fluxes are 12 % higher than in OptS2, but locally, especially over tropical forests, increases of up to 30 % are found. The total column changes

are generally negative, due to the influence of the a priori on the inversion, but always very weak (Fig. 13).

Another important removal process for methanol is the oxidation by OH. By using the prescribed climatological OH fields by Spivakovsky et al. (1990), the OptS2-OH sensitivity inversion acknowledges the large uncertainties that currently exist on modelled OH concentrations, especially over tropical forests, and also in mid-latitude continental regions (Lelieveld et al., 2008; Ren et al., 2008; Hofzumahaus et al., 2009). Note that the Spivakovsky et al. (1990) parameterization ignores completely the depleting effect of isoprene and other biogenic VOC emissions on OH, and therefore might overestimate the OH concentrations over forested areas, whereas isoprene emissions strongly deplete OH levels in IMAGESv2 despite the OH regeneration included in the MIM2+ mechanism used by the model, leading to substantial OH underestimations against campaign measurements over Amazonia and in the Eastern US (Stavrakou et al., 2010). The inferred emission changes, illustrated in Figure 13, reflect directly the differences between the modelled and the prescribed OH fields. In particular, moderate changes in the biogenic emissions are derived over Amazonia, Europe and US (less than 10 %), whereas decreases of up to 30 % are found over central and south Asia. The lower OH concentrations of Spivakovsky et al. (1990) compared to IMAGESv2 at northern mid-latitudes lead to increased methanol lifetime, and consequently, to lower emission fluxes required to match the observations, as also reflected in the weaker vertical gradient of methanol mixing ratios over the US (Fig. 14, red line). Methanol is also more efficiently exported from mid-latitude emitting regions strongly constrained by IASI data, to oceanic or desertic regions where the methanol columns are low and weakly constrained by the observations, as testified by the column increases shown in Fig. 13. The global plant emission is estimated to  $91.5 \text{ Tg yr}^{-1}$ , i.e. by 8 % lower than in the standard case, the decrease being more significant in the extratropics (Table 3).

Finally, in order to assess the influence of the a priori methanol plant emission inventory, we carried out the OptS1 inversion which uses the Jacob et al. (2005) inventory. The

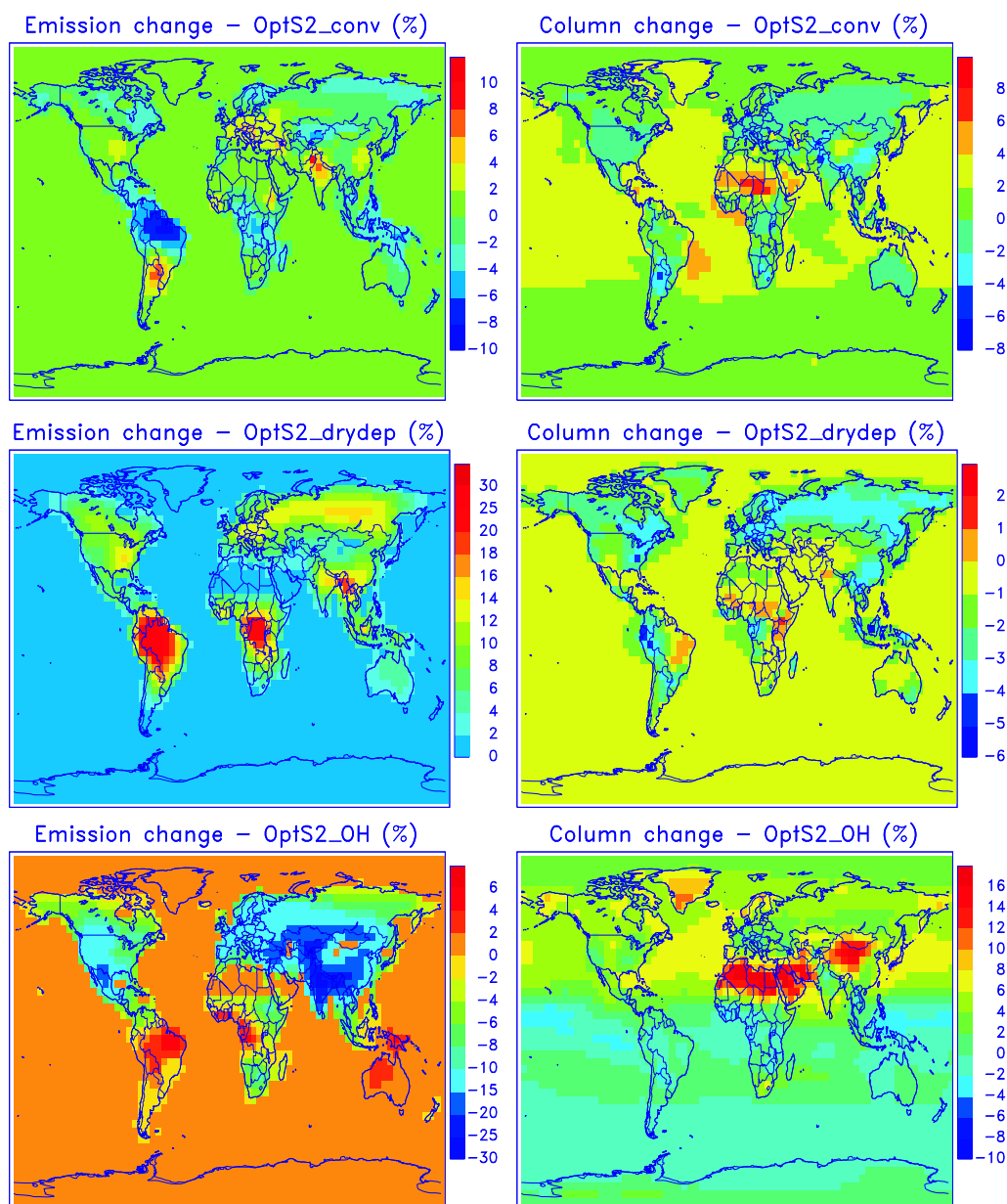


**Fig. 13.** Annual changes of the biogenic methanol emission (left) and methanol total column (right) derived from the three sensitivity inversions, OptS2-conv, OptS2-drydep, and OptS2-OH, described in Table 3, with respect to the standard OptS2 inversion.

results are found to be only moderately different from those deduced with the standard OptS2 inversion (Fig. 15, Table 3). Overall, the inferred emission estimates are found to be quite robust in the different sensitivity cases, with global estimates differing by less than 10 %, although differences of the order of 30 % are found on the regional scale.

## 11 Conclusions

We have introduced a new model (MEGANv2.1) for estimating methanol emissions from the terrestrial biosphere, which is based on net ecosystem flux measurements and accounts for the influence of light, temperature, and leaf age. The MEGANv2.1 methanol emissions and a previous inventory by Jacob et al. (2005) have been used as a priori biogenic emissions in the IMAGESv2 global CTM and compared against multi-sensor methanol measurements. Besides ground-based and airborne methanol observations, a com-

**Table 5.** In situ methanol measurements expressed in pptv.

| Location                | Period       | Coordinates                 | CH <sub>3</sub> OH | Reference                   |
|-------------------------|--------------|-----------------------------|--------------------|-----------------------------|
| Shape South America     |              |                             |                    |                             |
| Surinam rainforest      | Mar 1998     | 2–5° N 303–306° E           | 1100               | Williams et al. (2001)      |
| Parupa, Venezuela       | Jan–Feb 1999 | 5.7° N 298.2° E             | 1540               | Sanhueza et al. (2001)      |
| Rondonia, Brazil        | Oct 1999     | 10.1° S 297.1° E            | 2500               | Kesselmeier et al. (2002)   |
| La Selva, Costa Rica    | Apr–May 2003 | 10.4° N 276.1° E            | 2155               | Karl et al. (2004)          |
| Central Amazonia        | Sep 2004     | 2.6° S 299.8° E             | 4100               | Karl et al. (2007)          |
| Trop. forest, Surinam   | Oct 2005     | 4.5° N 305.0° E             | 1890               | Lelieveld et al. (2008)     |
| Trop. Atlantic, Surinam | Oct 2005     | 5.5° N 308.5° E             | 1270               | id.                         |
| North America           |              |                             |                    |                             |
| UMBS, Michigan          | Jun 2002     | 45.3° N 275.6° E            | 6800               | Karl et al. (2003a)         |
| UMBS, Michigan          | Jul–Aug 2005 | id.                         | 8050               | id.                         |
| UMBS, Michigan          | Sep–Oct 2001 | id.                         | 3530               | id.                         |
| Trinidad Head, US       | Apr–May 2002 | 41.0° N 235.8° E            | 800                | Millet et al. (2004)        |
| Duke Forest, US         | Jul 2003     | 36.0° N 280.1° E            | 4800               | Karl et al. (2005)          |
| Blodgett Forest, US     | Jun 2000     | 38.9° N 239.4° E            | 4760               | Schade and Goldstein (2006) |
| id.                     | Sep–Nov 2000 | id.                         | 3440               | id.                         |
| id.                     | Dec–Jan 2000 | id.                         | 970                | id.                         |
| id.                     | Mar 2001     | id.                         | 1900               | id.                         |
| Thompson Farm, US       | Jul–Aug 2004 | 43.1° N 289.0° E            | 2500               | Mao et al. (2006)           |
| Appledore Isl., US      | id.          | 41.0° N 289.4° E            | 2100               | id.                         |
| Chebogue Point          | id.          | 43.7° N 293.9° E            | 1389               | Millet et al. (2006)        |
| Europe                  |              |                             |                    |                             |
| Innsbruck, Austria      | Sep 1997     | 47.2° N 11.3° E             | 3000               | Holzinger et al. (2001)     |
| Creta, Greece           | Aug 2001     | 35.0° N 25.2° E             | 3500               | de Gouw et al. (2004)       |
| Athens, Greece          | id.          | 38.0° N 24.0° E             | 4500               | id.                         |
| Bremen, Germany         | Jul 2004     | 53.1° N 8.8° E              | 2200               | Solomon et al. (2005)       |
| Juelich, Germany        | Jul 2003     | 50.9° N 6.4° E              | 8000               | Spirig et al. (2005)        |
| Raunefjord, Norway      | Jun 2005     | 60.3° N 5.3° E              | 1860               | Sinha et al. (2007)         |
| Central Switzerland     | Jul 2004     | 47.3° N 7.8° E              | 6000               | Brunner et al. (2007)       |
| Zurich, Switzerland     | Apr 2005     | 47.3° N 8.5° E              | 2180               | Legreid et al. (2007)       |
| id.                     | Jul 2005     | id.                         | 3180               | id.                         |
| id.                     | Nov 2005     | id.                         | 1110               | id.                         |
| id.                     | Dec–Jan 2005 | id.                         | 1210               | id.                         |
| Vielsalm, Belgium       | Jul 2009     | 50.3° N 6.0° E              | 4700               | Sect. 6.2                   |
| id.                     | Aug 2009     | id.                         | 4000               | id.                         |
| id.                     | Sep 2009     | id.                         | 2600               | id.                         |
| id.                     | Apr 2010     | id.                         | 2680               | id.                         |
| id.                     | May 2010     | id.                         | 3000               | id.                         |
| id.                     | Jun 2010     | id.                         | 4430               | id.                         |
| id.                     | Jul 2010     | id.                         | 3810               | id.                         |
| id.                     | Aug 2010     | id.                         | 2100               | id.                         |
| id.                     | Sep 2010     | id.                         | 1770               | id.                         |
| Marine                  |              |                             |                    |                             |
| Indian Ocean, 7.5° N    | Mar 1999     | 7.5° N 70° E                | 1417               | Wisthaler et al. (2002)     |
| Indian Ocean, 9–13° N   | id.          | 9–13° N 67–70° E            | 1057               | id.                         |
| Indian Ocean, 13–19° N  | id.          | 13–19° N 66–70° E           | 687                | id.                         |
| Indian Ocean, 0–13° S   | id.          | 0–13° S 71–73° E            | 600                | id.                         |
| Mauna Loa               | Mar–Apr 2001 | 19.5° N 204.4° E            | 900                | Karl et al. (2003b)         |
| Atlantic 1.7 ± 1.3 km   | Jul–Aug 2004 | 35.8–40.2° N 321.4–332.6° E | 530                | Lewis et al. (2007)         |
| Atlantic 2.4 ± 1.4 km   | id.          | 36–44° N 326–338° E         | 630                | id.                         |
| Atlantic 3.5 ± 1.7 km   | id.          | 40.5–45.5° N 325–335° E     | 1100               | id.                         |
| Atlantic 6.1 ± 1.9 km   | id.          | 36.5–43.5° N 323–341° E     | 680                | id.                         |
| Atlantic 6.7 ± 2.3 km   | id.          | 36.1–41.9° N 319.8–334.2° E | 380                | id.                         |

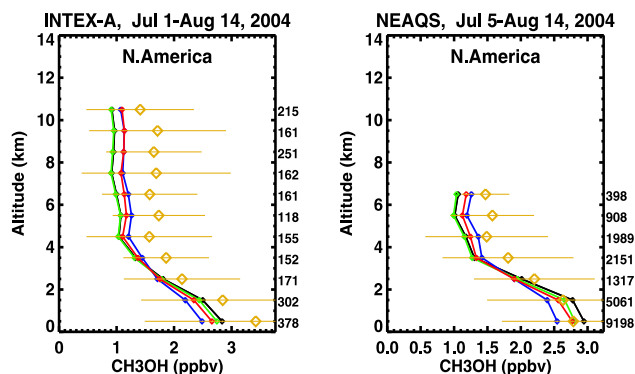


**Fig. 14.** Comparison between vertical profiles measured during the INTEX-A and NEAQS aircraft missions and inferred from the OptS2 (black lines), OptS2-conv (blue), OptS2-drydep (green), and OptS2-OH (red).

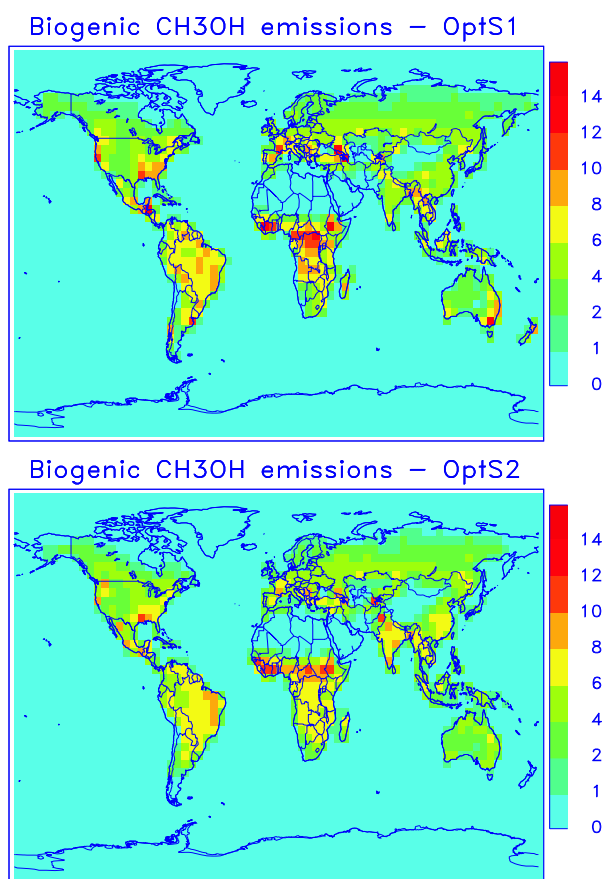


**Fig. 15.** Annually averaged biogenic methanol emissions derived by the inversion OptS1, which uses the Jacob et al. (2005) biogenic sources as a priori, and by the standard OptS2 inversion. Units are  $10^{10} \text{ mol cm}^{-2} \text{ s}^{-1}$ .

plete year of global methanol column abundances retrieved from the IASI sounder has been used in order to evaluate the model in terms of magnitude and seasonal variation of methanol concentrations. The agreement between the IASI columns and the model is considerably improved when MEGANv2.1 is used, compared to the simulation using the Jacob et al. (2005) database. In the latter case, large model overestimations have been found, especially over tropical forests, in line with findings by Millet et al. (2008), whereas poorly reproduced seasonal variations in the Tropics indicate that the parameterization based on net primary productivity is not suitable in these regions. Using MEGANv2.1 as a priori inventory, we have conducted an inverse modelling experiment based on the adjoint of IMAGESv2 and constrained by IASI columns in order to improve the estimates of methanol emissions from plants and vegetation fires. The main conclusions drawn from this study are summarized below.

- The global a posteriori biogenic methanol source deduced from the inversion amounts to  $100 \text{ Tg yr}^{-1}$  and is very close to a priori value of  $105 \text{ Tg yr}^{-1}$ . The methanol source from vegetation fires is also decreased by 20 % globally with respect to the GFEDv3 database, but stronger decreases (up to a factor of two) are inferred over central and Southern Africa.
- Annual reductions of the biogenic methanol source are suggested by the IASI data over Amazonia and Indonesia, by 40–55 % and 45–58 %, respectively. Over Amazonia, the derived source allows for a very satisfactory agreement with the satellite data, yet it leads to a model underprediction of about 20 % with respect to a limited set of available surface methanol measurements. It appears plausible that the IASI columns might be biased low over tropical forests due to possible cloud contamination problems.
- An annual decrease by 20–25 % of the biogenic methanol source is suggested over the Eastern US, leading to a good agreement with aircraft data in the boundary layer, while the model systematically underestimates the methanol concentrations in the free troposphere over land and ocean, in line with previous modelling studies. Possible reasons for this underestimation include an underestimation in the Western US methanol source, an underestimation of convective fluxes, and/or an overestimation of OH simulated concentrations.
- The biogenic methanol source is strongly increased with respect to MEGANv2.1 over arid and semi-arid regions of Central Asia, Western US, and Northern Australia. This might be related to an underestimation of the methanol emission rate from shrub or to an unaccounted source of methanol specific to such environments in the MEGANv2.1 model. Ground-based measurements at Kitt Peak and aircraft measurements over the Western

US confirm these conclusions. This result clearly underscores the need for local measurements in arid regions like Central Asia.

- Comparisons of the optimized methanol concentrations with independent measurements from other instruments show a very good consistency, lending good confidence to IASI columns. The satellite dataset is a valuable tool towards improving our knowledge on methanol sources and sinks on the global scale, and in particular, for many world regions where local measurements are currently missing.
- The most important error reductions are achieved for the biogenic emissions over the Former Soviet Union (67 %), South America (50 %), and globally (43 %). The errors for the vegetation fire source are reduced moderately (14 % on the global scale). Furthermore, the derived emissions are found to be weakly dependent to changes in the meteorology, the a priori emissions, and the methanol sink processes.

*Acknowledgements.* IASI has been developed and built under the responsibility of the Centre National d'Etudes Spatiales (CNES, France). It is flown onboard the Metop satellites as part of the EUMETSAT Polar System. This work has been supported by the PRODEX programme of the European Space Agency funded by the Belgian Science Policy Office and the Fonds National de la Recherche Scientifique (FRS-FNRS F.4511.08).

Edited by: M. Kanakidou

## References

- Andreae, M. O. and Merlet, P.: Emission of trace gases and aerosols from biomass burning, *Global Biogeochem. Cy.*, 15, 955–966, 2001.
- Asher, W.: The sea-surface microlayer and its effect on global air-sea gas transfer, in: *The Sea Surface and Global Change*, edited by: Peter, S. L. and Robert, A. D., Cambridge University Press, Cambridge, UK, 1997.
- Baker, B., Guenther, A., Greenberg, J., and Fall, R.: Canopy level fluxes of 2-methyl-3-buten-2-ol, acetone, and methanol by a portable relaxed eddy accumulation system, *Environ. Sci. Technol.*, 35(9), 1701–1708, 2001.
- Beer, R., Shephard, M. W., Kulawik, S., Clough, S. A., Eldering, A., Bowman, K. W., Sander, S. P., Fisher, B. M., Payne, V. H., Luo, M., Osterman, G. B., and J. R. Worden : First satellite observations of lower tropospheric ammonia and methanol, *Geophys. Res. Lett.*, 35, L09801, doi:10.1029/2008GL033642, 2008.
- Boynard, A., Clerbaux, C., Coheur, P.-F., Hurtmans, D., Turquety, S., George, M., Hadji-Lazaro, J., Keim, C., and Meyer-Arnek, J.: Measurements of total and tropospheric ozone from IASI: comparison with correlative satellite, ground-based and ozonesonde observations, *Atmos. Chem. Phys.*, 9, 6255–6271, doi:10.5194/acp-9-6255-2009, 2009.
- Brunner, A., Ammann, C., Neftel, A., and Spirig, C.: Methanol exchange between grassland and the atmosphere, *Biogeosciences*, 4, 395–410, 2007, <http://www.biogeosciences.net/4/395/2007/>.
- Clerbaux, C., Boynard, A., Clarisse, L., George, M., Hadji-Lazaro, J., Herbin, H., Hurtmans, D., Pommier, M., Razavi, A., Turquety, S., Wespes, C., and Coheur, P.-F.: Monitoring of atmospheric composition using the thermal infrared IASI/MetOp sounder, *Atmos. Chem. Phys.*, 9, 6041–6054, doi:10.5194/acp-9-6041-2009, 2009.
- Coheur, P.-F., Clarisse, L., Turquety, S., Hurtmans, D., and C. Clerbaux : IASI measurements of reactive trace species in biomass burning plumes, *Atmos. Chem. Phys.*, 9, 5655–5667, doi:10.5194/acp-9-5655-2009, 2009.
- Davison, B., Brunner, A., Ammann, C., Spirig, C., Jocher, M., and Neftel, A.: Cut-induced VOC emissions from agricultural grasslands, *Plant Biol.*, 10(1), 76–85, 2008.
- de Gouw, J., Warneke, C., Holzinger, R., Klupfel, T., and Williams, J.: Inter-comparison between airborne measurements of methanol, acetonitrile and acetone using two differently configured PTR-MS instruments, *Inter. J. Mass Spectr.*, 239, 129–137, 2004.
- Dufour, G., Boone, C. D., Rinsland, C. P., and Bernath, P. F.: First space-borne measurements of methanol inside aged southern tropical to mid-latitude biomass burning plumes using the ACE-FTS instrument, *Atmos. Chem. Phys.*, 6, 3463–3470, doi:10.5194/acp-6-3463-2006, 2006.
- Dufour, G., Szopa, S., Hauglustaine, D. A., Boone, C. D., Rinsland, C. P., and Bernath, P. F.: The influence of biogenic emissions on upper-tropospheric methanol as revealed from space, *Atmos. Chem. Phys.*, 7, 6119–6129, doi:10.5194/acp-7-6119-2007, 2007.
- Emmons, L. K., Hauglustaine, D. A., Müller, J.-F., Carroll, M. A., Brasseur, G. P., Brunner, D., Stahelin, J., Thouret, V., and Marengo, A.: Data composites of airborne observations of tropospheric ozone and its precursors, *J. Geophys. Res.*, 105, 20,497–20,538, 2000.
- Fall, R. and Benson, A. A.: Leaf methanol – the simplest natural product from plants, *Trends Plant. Sci.*, 1(9), 296–301, 1996.
- Folkers, A., Hüve, K., Ammann, C., Dindorf, T., Kesselmeier, J., Kleist, E., Kuhn, U., Uerlings, R., and Wildt, J.: Methanol emissions from deciduous tree species: dependence on temperature and light intensity, *Plant Biol.*, 10 (1), 65–75, 2008.
- Fukui, Y., and Doskey, P. V.: Air-surface exchange of nonmethane organic compounds at a grassland site: seasonal variations and stressed emissions, *J. Geophys. Res.*, 103(D11), 13153–13168, 1998.
- Galbally, I. E. and Kirstine, W.: The production of methanol by flowering plants and the global cycle of methanol, *J. Atmos. Chem.*, 43(3), 195–229, 2002.
- George, M., Clerbaux, C., Hurtmans, D., Turquety, S., Coheur, P.-F., Pommier, M., Hadji-Lazaro, J., Edwards, D. P., Worden, H., Luo, M., Rinsland, C., and McMillan, W.: Carbon monoxide distributions from the IASI/METOP mission: evaluation with other space-borne remote sensors, *Atmos. Chem. Phys.*, 9, 8317–8330, doi:10.5194/acp-9-8317-2009, 2009.
- Geron, C., Guenther, A., Greenberg, J., Loeschner, H. W., Clark, D., and Baker, B.: Biogenic volatile organic compound emissions from a lowland tropical wet forest in Costa Rica, *Atmos. Envi-*

- ron., 36, 3793–3802, 2002.
- Geron, C., Guenther, A., Greenberg, J., Karl, T., and Rasmussen, R.: Biogenic volatile organic compound emissions from desert vegetation of the southwestern US, *Atmos. Environ.*, 40, 1645–1660, 2006.
- Guenther, A., Hewitt, C. N., Erickson, D., McKay, W. A., Pierce, T., Scholes, B., Steinbrecher, R., Tallamraju, R., Taylor, J., and Zimmerman, P.: A global model of natural volatile organic compound emissions, *J. Geophys. Res.*, 100(D5), 8873–8892, 1995.
- Guenther, A., Karl, T., Harley, P., Wiedinmyer, C., Palmer, P. I., and Geron, C.: Estimates of global terrestrial isoprene emissions using MEGAN (Model of Emissions of Gases and Aerosols from Nature), *Atmos. Chem. Phys.*, 6, 3181–3210, doi:10.5194/acp-6-3181-2006, 2006.
- Harley, P., Greenberg, J., Niinemets, U., and Guenther, A.: Environmental controls over methanol emission from leaves, *Biogeosciences*, 4(6), 1083–1099, 2007.
- Heikes, B. G., Chang, W., Pilson, M. E. Q., Swift, E., Singh, H. B., Guenther, A., Jacob, D. J., and Brand, L.: Atmospheric methanol budget and ocean implication, *Global Biogeochem. Cy.*, 16, 1133, doi:10.1029/2002GB001895, 2002.
- Hofzumahaus, A., Rohrer, F., Lu, K. Bohn, B., Brauers, T., Chang, C., Fuchs, H., Holland, F., Kita, K., Kondo, Y., Li, X., Lou, S., Shao, M., Zeng, L., Wahner, A., Zhang, Y.: Amplified Trace Gas Removal in the Troposphere, *Science*, 324, 5935, 1702–1704, doi:10.1126/science.1164566, 2009.
- Holzinger, R., Jordan, A., Hansel, A., and Lindinger, W.: Methanol measurements in the lower troposphere near Innsbruck (47° 16' N; 11° 24' E), Austria, *Atmos. Environ.*, 35, 2525–2532, 2001.
- Hüve, K., Christ, M. M., Kleist, E., Uerlings, R., Niinemets, Ü., Walter, A., and Wildt, J.: Simultaneous growth and emission measurements demonstrate an interactive control of methanol release by leaf expansion and stomata, *J. Exp. Bot.*, 58(7), 1783–1793, 2007.
- ITTC Recommended Procedures and guidelines: Testing and Extrapolation Methods, General, Density and viscosity of water, Section 7.5-02-01-03, 2006.
- Fletcher, R.: *Practical Methods in Optimization*, 2nd edn., Wiley, 1990.
- Jacob, D. J., Field, B. D., Li, Q., Blake, D. R., de Gouw, J., Warneke, C., Hansel, A., Wisthaler, A., Singh, H. B., and Guenther, A.: Global budget of methanol: Constraints from atmospheric observations, *J. Geophys. Res.*, 110, D08303, doi:10.1029/2004JD005172, 2005.
- Jardine, K., Harley, P., Karl, T., Guenther, A., Lerdau, M., and Mak, J. E.: Plant physiological and environmental controls over the exchange of acetaldehyde between forest canopies and the atmosphere, *Biogeosciences* 5(6), 1559–1572, 2008.
- Jardine, K., Abrell, L., Kurc, S. A., Huxman, T., Ortega, J., and Guenther, A.: Volatile organic compound emissions from *Larrea tridentata* (creosotebush), *Atmos. Chem. Phys.*, 10, 12191–12206, doi:10.5194/acp-10-12191-2010, 2010.
- Johnson, M. T.: A numerical scheme to calculate temperature and salinity dependent air-water transfer velocities for any gas, *Ocean Sci.*, 6, 913–932, 2010, <http://www.ocean-sci.net/6/913/2010/>.
- Karl, T. G., Spirig, C., Rinne, J., Stroud, C., Prevost, P., Greenberg, J., Fall, R., and Guenther, A.: Virtual disjunct eddy covariance measurements of organic compound fluxes from a subalpine forest using proton transfer reaction mass spectrometry, *Atmos. Chem. Phys.*, 2, 279–291, doi:10.5194/acp-2-279-2002, 2002.
- Karl, T., Guenther, A., Spirig, C., Hansel, A., and Fall, R.: Seasonal variation of biogenic VOC emissions above a mixed hardwood in northern Michigan, *Geophys. Res. Lett.*, 30, 2186, doi:10.1029/2003GL018432, 2003a.
- Karl, T., Hansel, A., Märk, T., Lindinger, W., and Hoffmann, D.: Trace gas monitoring at the Mauna Loa Baseline Observatory using Proton-Transfer Reaction Mass Spectrometry, *Int. J. Mass Spec.*, 223–224, 527–538, 2003b.
- Karl, T., Potosnak, M., Guenther, A., Clark, D., Walker, J., Herrick, J. D., and Geron, C.: Exchange processes of volatile organic compounds above a tropical rain forest: Implications for modelling tropospheric chemistry above dense vegetation, *J. Geophys. Res.*, 109, D18306, doi:10.1029/2004JD004738, 2004.
- Karl, T., Harley, P., Guenther, A., Rasmussen, R., Baker, B., Jardine, K., and Nemitz, E.: The bi-directional exchange of oxygenated VOCs between a loblolly pine (*Pinus taeda*) plantation and the atmosphere, *Atmos. Chem. Phys.*, 5, 3015–3031, doi:10.5194/acp-5-3015-2005, 2005.
- Karl, T., Guenther, A., Yokelson, R. J., Greenberg, J., Potosnak, M., Blake, D. R., and Artaxo, P.: The tropical forest and fire emissions experiment, Emission, chemistry, and transport of biogenic volatile organic compounds in the lower atmosphere over Amazonia, *J. Geophys. Res.*, 112, D18302, doi:10.1029/2007JD008539, 2007.
- Karl, T., Harley, P., Emmons, L., Thornton, B., Guenther, A., Basu, C., Turnipseed, A., and Jardine, K.: Efficient Atmospheric Cleansing of Oxidized Organic Trace Gases by Vegetation, *Science*, 330, 816–819, 2010.
- Kesselmeier, J., Kuhn, U., Rottenberger, S., Biesenthal, T., Wolf, A., Schebeske, G., Andreae, M. O., Ciccioli, P., Brancaleoni, E., Frattoni, M., Oliva, S. T., Botelho, M. L., Silva, C. M. A., and Tavares, T. M.: Concentrations and species composition of atmospheric volatile organic compounds (VOCs) as observed during the wet and dry season in Rondônia (Amazonia), *J. Geophys. Res.*, 107(D20), 8053, doi:10.1029/2000JD000267, 2002.
- Kirstine, W., Galbally, I., Ye, Y., and Hooper, M.: Emissions of volatile organic compounds (primarily oxygenated species) from pasture, *J. Geophys. Res.*, 103(3339), 10605–10619, 1998.
- Körner, E., von Dahl, C. C., Bonaventure, G., and Baldwin, I. T.: Pectin methylesterase NaPMEI contributes to the emission of methanol during insect herbivory and to the elicitation of defence responses in *Nicotiana attenuata*, *J. Exp. Bot.*, 60(9), 2631–2640, doi:10.1093/jxb/erp106, 2009.
- Laffineur, Q., Heinesch, B., Schoon, N., Amelynck, C., Müller, J.-F., Dewulf, J., Van Langenhove, H., Steppe, K., Simpraga, M., and Aubinet, M.: Isoprene and monoterpene emissions from a mixed temperate forest, *Atmos. Environ.*, 45, 3157–3168, 2010.
- Langford, B., Misztal, P. K., Nemitz, E., Davison, B., Helfter, C., Pugh, T. A. M., MacKenzie, A. R., Lim, S. F., and Hewitt, C. N.: Fluxes and concentrations of volatile organic compounds from a South-East Asian tropical rainforest, *Atmos. Chem. Phys.*, 10, 8391–8412, doi:10.5194/acp-10-8391-2010, 2010.
- Legreid, G., Balzani Lööv, J., Staehelin, J., Hueglin, C., Hill, M., Buchmann, B., Prevot, A. S. H., and Reimann, S.: Oxygenated volatile organic compounds (OVOCs) at an urban background site in Zürich (Europe): Seasonal variation and source allocation,

- Atmos. Environ., 41, 8409–8423, 2007.
- Lelieveld, J., Butler, T. M., Crowley, J. N., Dillon, T. J., Fischer, H., Ganzeveld, L., Harder, H., Lawrence, M. G., Martinez, M., Taraborrelli, D., and Williams, J.: Atmospheric oxidation capacity sustained by a tropical forest, *Nature*, 452, 737–740, doi:10.1038/nature06870, 2008.
- Lewis, A. C., Evans, M. J., Methven, J., Watson, N., Lee, J. D., Hopkins, J. R., Purvis, R. M., Arnold, S. R., McQuaid, J. B., Whalley, L. K., Pilling, M. J., Heard, D. E., Monks, P. S., Parker, A. E., Reeves, C. E., Oram, D. E., Mills, G., Bandy, B. J., Stewart, D., Coe, H., Williams, P., Crosier, J.: Chemical composition observed over the mid-Atlantic and the detection of pollution signatures far from source regions, *J. Geophys. Res.*, 112, D10S39, doi:10.1029/2006JD007584, 2007.
- Liss, P. S. and Slater, P. G.: Flux of gases across air-sea interface, *Nature*, 247, 181–184, 1974.
- Macdonald, R. C. and Fall, R.: Detection of substantial emissions of methanol from plants to the atmosphere, *Atmos. Environ.*, 27(11), 1709–1713, 1993.
- Mao, H., Talbot, R., Nielsen, C., and Sive, B.: Controls on methanol and acetone in marine and continental atmospheres, *Geophys. Res. Lett.*, 33, L02803, doi:10.1029/2005GL024810, 2006.
- Millet, D. B., Goldstein, A. H., Allan, J. D., Bates, T. S., Boudries, H., Bower, K. N., Coe, H., Ma, Y., McKay, M., Quinn, P. K., Sullivan, A., Weber, R. J., Worsnop, D. R.: Volatile organic compound measurements at Trinidad Head, California, during ITCT 2K2: Analysis of sources, atmospheric composition, and aerosol residence times, *J. Geophys. Res.*, 109, D23S16, doi:10.1029/2003JD004026, 2004.
- Millet, D. B., Goldstein, A. H., Holzinger, R., Allan, J. D., Jimenez, J. L., Worsnop, D. R., Roberts, J. M., White, A. B., Hudman, R. C., Bertschi, I. T., Stohl, A.: Chemical characteristics of North American surface layer outflow: Insights from Chebogue Point, Nova Scotia, *J. Geophys. Res.*, 111, D23S53, doi:10.1029/2006JD007287, 2006.
- Millet, D. B., Jacob, D. J., Custer, T. G., de Gouw, J. A., Goldstein, A. H., Karl, T., Singh, H. B., Sive, B. C., Talbot, R. W., Warneke, C., and Williams, J.: New constraints on terrestrial and oceanic sources of atmospheric methanol, *Atmos. Chem. Phys.*, 8, 6887–6905, doi:10.5194/acp-8-6887-2008, 2008.
- Molina, L. T., Madronich, S., Gaffney, J. S., Singh, H. B., and U. Pöschl (Eds.): MILAGRO/INTEX-B 2006, Special Issue, *Atmos. Chem. Phys.*, <http://www.atmos-chem-phys.net/special-issue83.html>, 2007–2010.
- Müller, J.-F. and Stavrakou, T.: Inversion of CO and NO<sub>x</sub> emissions using the adjoint of the IMAGES model, *Atmos. Chem. Phys.*, 5, 1157–1186, doi:10.5194/acp-5-1157-2005, 2005.
- Müller, J.-F., Stavrakou, T., Wallens, S., De Smedt, I., Van Roozendael, M., Potosnak, M. J., Rinne, J., Munger, B., Goldstein, A., and Guenther, A. B.: Global isoprene emissions estimated using MEGAN, ECMWF analyses and a detailed canopy environment model, *Atmos. Chem. Phys.*, 8, 1329–1341, doi:10.5194/acp-8-1329-2008, 2008.
- Niinemets, Ü. and Reichstein, M.: Controls on the emission of plant volatiles through stomata : Differential sensitivity of emission rates to stomatal closure explained, *J. Geophys. Res.*, 108, 4208, doi:10.1029/2002JD002620, 2003a.
- Niinemets, Ü. and M. Reichstein : Controls on the emission of plant volatiles through stomata: A sensitivity analysis, *J. Geophys. Res.*, 108, 4211, doi:10.1029/2002JD002626, 2003b.
- Nemecek-Marshall M., MacDonald, R. C., Franzen, J. J., Wojciechowski, C. L., and Fall, R.: Methanol emission from leaves. Enzymatic detection of gas-phase methanol and relation of methanol fluxes to stomatal conductance and leaf development, *Plant Physiol.*, 108, 1359–1368, 1995.
- Ohara, T., Akimoto, H., Kurokawa, J., Horii, N., Yamaji, K., Yan, X., and Hayasaka, T.: An Asian emission inventory of anthropogenic emission sources for the period 1980–2020, *Atmos. Chem. Phys.*, 7, 4419–4444, doi:10.5194/acp-7-4419-2007, 2007.
- Razavi, A., Karagulian, F., Clarisse, L., Hurtmans, D., Coheur, P. F., Clerbaux, C., Müller, J. F., and Stavrakou, T.: Global distributions of methanol and formic acid retrieved for the first time from the IASI/MetOp thermal infrared sounder, *Atmos. Chem. Phys.*, 11, 857–872, doi:10.5194/acp-11-857-2011, 2011.
- Ren, X., Olson, J. R., Crawford, J. H., Brune, W. H., Mao, J., Long, R. B., Chen, Z., Chen, G., Avery, M. A., Sachse, G. W., Barrick, J. D., Diskin, G. S., Huey, L. G., Fried, A., Cohen, R. C., Heikes, B., Wennberg, P. O., Singh, H. B., Blake, D. R., Shetter, R. E.: HO<sub>x</sub> chemistry during INTEX-A 2004: Observation, model calculation, and comparison with previous studies, *J. Geophys. Res.*, 113, D05310, doi:10.1029/2007JD009166, 2008.
- Rinne, J., Taipale, R., Markkanen, T., Ruuskanen, T. M., Hellén, H., Kajos, M. K., Vesala, T., and Kulmala, M.: Hydrocarbon fluxes above a Scots pine forest canopy: measurements and modeling, *Atmos. Chem. Phys.*, 7, 3361–3372, doi:10.5194/acp-7-3361-2007, 2007.
- Rinsland, C. P., Jones, N. B., and Connor, B. J.: Northern and southern hemisphere ground-based infrared spectroscopic measurements of tropospheric carbon monoxide and ethane, *J. Geophys. Res.*, 103(D21), 28,197–28,217, 1998.
- Rinsland, C. P., E. Mahieu, L. Chiou, and H. Herbin : First ground-based infrared solar absorption measurements of free tropospheric methanol (CH<sub>3</sub>OH): Multidecade infrared time series from Kitt Peak (31.9° N 111.6° W): Trend, seasonal cycle, and comparison with previous measurements, *J. Geophys. Res.*, 114, D04309, doi:10.1029/2008JD011003, 2009.
- Ruuskanen, T. M., Müller, M., Schnitzhofer, R., Karl, T., Graus, M., Bamberger, I., Hörtnagl, L., Brilli, F., Wohlfahrt, G., and Hansel, A.: Eddy covariance VOC emission and deposition fluxes above grassland using PTR-TOF, *Atmos. Chem. Phys. Discuss.*, 10, 21,077–21,108, doi:10.5194/acpd-10-21077-2010, 2010.
- Sander, R.: Compilation of Henry's Law Constants for Inorganic and Organic Species of Potential Importance in Environmental Chemistry (Version 3), <http://www.mpch-mainz.mpg.de/%7Esander/res/henry.html>, 1999.
- Sanhueza, E., Holzinger, R., Donoso, L., Santana, M., Fernandez, E., and Romero, J.: Compuestos organicos volatiles en la atmosfera Gran Sabana, concentraciones y quimica atmosferica, *Interciencia*, 26, 597–605, 2001.
- Schade, G. W. and Custer, T. G.: OVOC emissions from agricultural soil in northern Germany during the 2003 European heat wave, *Atmos. Environ.*, 38(36), 6105–6114, 2004.
- Schade, G. W. and Goldstein, A. H.: Fluxes of oxygenated volatile organic compounds from a ponderosa pine plantation, *J. Geophys. Res.*, 106(D3), 3111–3123, 2001.
- Schade, G. W. and Goldstein, A. H.: Seasonal measurements of acetone and methanol: abundances and implications for

- atmospheric budgets, *Global Biogeochem. Cy.*, 20, GB1011, doi:10.1029/2005GB002566, 2006.
- Schink, B. and Zeikus, J. G.: Microbial methanol formation: A major end product of pectin metabolism, *Curr. Microbiol.*, 4(6), 387–389, 1980.
- Seco, R., Peñuelas, J., and Filella, I.: Short-chain oxygenated VOCs: Emission and uptake by plants and atmospheric sources, sinks and concentrations, *Atmos. Environ.*, 41(12), 2477–2499, 2007.
- Senten, C., De Mazière, M., Dils, B., Hermans, C., Kruglanski, M., Neefs, E., Scolas, F., Vandaele, A. C., Vanhaelewyn, G., Vigouroux, C., Carleer, M., Coheur, P. F., Fally, S., Barret, B., Baray, J. L., Delmas, R., Leveau, J., Metzger, J. M., Mahieu, E., Boone, C., Walker, K. A., Bernath, P. F., and Strong, K.: Technical Note: New ground-based FTIR measurements at Ile de La Réunion: observations, error analysis, and comparisons with independent data, *Atmos. Chem. Phys.*, 8, 3483–3508, doi:10.5194/acp-8-3483-2008, 2008.
- Shabanov, N., Samanta, A., Myneni, R. B., Knyazikhin, Y., Votava, P., Nemani, R.: Collection 5 MODIS LAI and FPAR Products, University of Maryland, [http://modis.gsfc.nasa.gov/sci\\_team/meetings/c5meeting/pres/day1/shabanov.pdf](http://modis.gsfc.nasa.gov/sci_team/meetings/c5meeting/pres/day1/shabanov.pdf), 2007.
- Singh, H. B., Kanakidou, M., Krutzen, P. J., and Jacob, D. J.: High concentrations and photochemical fate of oxygenated hydrocarbons in the global troposphere, *Nature*, 378, 50–54, 1995.
- Singh, H. B., Tabazadeh, A., Fukui, Y., Bey, I., Yantosca, R., Jacob, D., Arnold, F., Wohlfrom K., Atlas, E., Flocke, F., Blake, D., Blake, N., Heikes, B., Snow, J., Talbot, R., Gregory, G., Sachse, G., Vay, S., Kondo, Y.: Distribution and fate of selected oxygenated organic species in the troposphere and lower stratosphere over the Atlantic, *J. Geophys. Res.*, 105(D3), 3795–3805, 2000.
- Singh, H. B., Chen, Y., Staudt, A., Jacob, D., Blake, D., Heikes, B., and Snow, J.: Evidence from the Pacific troposphere for large global sources of oxygenated organic compounds, *Nature*, 410, 1078–1081, 2001.
- Singh, H. B., Tabazadeh, A., Evans, M. J., Field, B. D., Jacob, D. J., Sachse, G., Crawford, J. H., Shetter, R., and Brune, W. H.: Oxygenated volatile organic chemicals in the oceans: Inferences and implications based on atmospheric observations and air-sea exchange models, *Geophys. Res. Lett.*, 30(16), 1862, doi:10.1029/2003GL017933, 2003.
- Singh, H. B., Brune, W. H., Crawford, J. H., Jacob, D. J., and Russell, P. B.: Overview of the summer 2004 Intercontinental Chemical Transport Experiment – North America (INTEX-A), *J. Geophys. Res.*, 111, D24S01, doi:10.1029/2006JD007905, 2006.
- Sinha, V., Williams, J., Meyerhöfer, M., Riebesell, U., Paulino, A. I., and Larsen, A.: Air-sea fluxes of methanol, acetone, acetaldehyde, isoprene and DMS from a Norwegian fjord following a phytoplankton bloom in a mesocosm experiment, *Atmos. Chem. Phys.*, 7, 739–755, doi:10.5194/acp-7-739-2007, 2007.
- Snider, J. R., and Dawson, G. A.: Tropospheric light alcohols, carbonyls, and acetonitrile: Concentrations in the southwestern United States and Henry's law data, *J. Geophys. Res.*, 90, 3797–3805, 1985.
- Solomon, S. J., Custer, T., Schade, G., Soares Dias, A. P., and Burrows, J.: Atmospheric methanol measurement using selective catalytic methanol to formaldehyde conversion, *Atmos. Chem. Phys.*, 5, 2787–2796, doi:10.5194/acp-5-2787-2005, 2005.
- Spirig, C., Neftel, A., Ammann, C., Dommen, J., Grabmer, W., Thielmann, A., Schaub, A., Beauchamp, J., Wisthaler, A., and Hansel, A.: Eddy covariance flux measurements of biogenic VOCs during ECHO 2003 using proton transfer reaction mass spectrometry, *Atmos. Chem. Phys.*, 5, 465–481, doi:10.5194/acp-5-465-2005, 2005.
- Spivakovsky, C. M., Yevich, R., Logan, J. A., Wofsy, S. C., McElroy, M. B., and Prather, M. J.: Tropospheric OH in a three-dimensional chemical tracer model: An assessment based on observations of CH<sub>3</sub>CCl<sub>3</sub>, *J. Geophys. Res.*, 95, 18441–18471, doi:10.1029/90JD01299, 1990.
- Stavrakou, T. and Müller, J.-F.: Grid-based versus big region approach for inverting CO emissions using Measurement of Pollution in the Troposphere (MOPITT) data, *J. Geophys. Res.*, 111, D15304, doi:10.1029/2005JD006896, 2006.
- Stavrakou, T., Müller, J.-F., Boersma, F., De Smedt, I., and van der A, R.: Assessing the distribution and growth rates of NO<sub>x</sub> emission sources by inverting a 10-year record of NO<sub>2</sub> satellite columns, *Geophys. Res. Lett.*, 35, L10810, doi:10.1029/2008GL033521, 2008.
- Stavrakou, T., Müller, J.-F., De Smedt, I., Van Roozendaal, M., van der Werf, G. R., Giglio, L., and Guenther, A.: Evaluating the performance of pyrogenic and biogenic emission inventories against one decade of space-based formaldehyde columns, *Atmos. Chem. Phys.*, 9, 1037–1060, doi:10.5194/acp-9-1037-2009, 2009.
- Stavrakou, T., Müller, J.-F., De Smedt, I., Van Roozendaal, M., Kanakidou, M., Vrekoussis, M., Wittrock, F., Richter, A., and Burrows, J. P.: The continental source of glyoxal estimated by the synergistic use of spaceborne measurements and inverse modelling, *Atmos. Chem. Phys.*, 9, 8431–8446, doi:10.5194/acp-9-8431-2009, 2009.
- Stavrakou, T., Müller, J.-F., De Smedt, I., Van Roozendaal, M., van der Werf, G. R., Giglio, L., and Guenther, A.: Global emissions of non-methane hydrocarbons deduced from SCIAMACHY formaldehyde columns through 2003–2006, *Atmos. Chem. Phys.*, 9, 3663–3679, doi:10.5194/acp-9-3663-2009, 2009.
- Stavrakou, T., Peeters, J., and Müller, J.-F.: Improved global modelling of HO<sub>x</sub> recycling in isoprene oxidation: evaluation against the GABRIEL and INTEX-A aircraft campaign measurements, *Atmos. Chem. Phys.*, 10, 9863–9878, doi:10.5194/acp-10-9863-2010, 2010.
- Tie, X., Guenther, A., and Holland, E.: Biogenic methanol and its impacts on tropospheric oxidants, *Geophys. Res. Lett.*, 30(17), 1881, doi:10.1029/2003GL017167, 2003.
- Tikhonov, A.: On the solution of incorrectly stated problems and a method of regularization, *Dokl. Acad. Nauk SSSR*, 151, 501–504, 1963.
- van der Werf, G. R., Randerson, J. T., Giglio, L., Collatz, G. J., Mu, M., Kasibhatla, P. S., Morton, D. C., DeFries, R. S., Jin, Y., and van Leeuwen, T. T.: Global fire emissions and the contribution of deforestation, savanna, forest, agricultural, and peat fires (1997–2009), *Atmos. Chem. Phys.*, 10, 11707–11735, doi:10.5194/acp-10-11707-2010, 2010.
- Vigouroux, C., Hendrick, F., Stavrakou, T., Dils, B., De Smedt, I., Hermans, C., Merlaud, A., Scolas, F., Senten, C., Vanhaelewyn, G., Fally, S., Carleer, M., Metzger, J.-M., Müller, J.-F., Van Roozendaal, M., and De Mazière, M.: Ground-based FTIR and MAX-DOAS observations of formaldehyde at Réunion Island

- and comparisons with satellite and model data, *Atmos. Chem. Phys.*, 9, 9523–9544, doi:10.5194/acp-9-9523-2009, 2009.
- Warneke, C., Karl, T., Judmaier, H., Hansel, A., Jordan, A., Lindinger, W., and Crutzen, P.: Acetone, Methanol, and Other Partially Oxidized Volatile Organic Emissions From Dead Plant Matter by Abiological Processes: Significance for Atmospheric HO<sub>x</sub> Chemistry, *Global Biogeochem. Cy.*, 13(1), 9–17, 1999.
- Warneke, C., Luxembourg, S. L., De Gouw, J. A., Rinne, H. J. I., Guenther, A., and Fall, R.: Disjunct eddy covariance measurements of oxygenated volatile organic compounds fluxes from an alfalfa field before and after cutting, *J. Geophys. Res.*, 107, D8, doi:10.1029/2001JD000594, 2002.
- Williams, J., Pöschl, U., Crutzen, P. J., Hansel, A., Holzinger, R., Warneke, C., Lindinger, W., and Lelieveld, J.: An atmospheric Chemistry interpretation of mass scans obtained from a proton transfer mass spectrometer flown over the tropical rainforest of Surinam, *J. Atmos. Chem.*, 38, 133–166, 2001.
- Williams, J., Holzinger, R., Gros, V., Xu, X., Atlas, E., and Wallace, D. W. R.: Measurements of organic species in air and seawater from the tropical Atlantic, *Geophys. Res. Lett.*, 31, L23S06, doi:10.1029/2004GL020012, 2004.
- Wisthaler, A., Hansel, A., Dickerson, R. R., and Crutzen, P. J.: Organic trace gas measurements by PTR-MS during INDOEX 1999, *J. Geophys. Res.*, 107(D19), 8024, doi:10.1029/2001JD000576, 2002.
- Zhang, P., Anderson, M., Barlow, B., Tan, B., and Myneni, R. B.: Climate-related vegetation characteristics derived from Moderate Resolution Imaging Spectroradiometer (MODIS) leaf area index and normalized difference vegetation index, *J. Geophys. Res.*, 109, D20105, doi:10.1029/2004JD004720, 2004.

# Satellite evidence for a large source of formic acid from boreal and tropical forests

T. Stavrakou<sup>1\*</sup>, J-F. Müller<sup>1</sup>, J. Peeters<sup>2</sup>, A. Razavi<sup>3</sup>, L. Clarisse<sup>3</sup>, C. Clerbaux<sup>3,4</sup>, P-F. Coheur<sup>3</sup>, D. Hurtmans<sup>3</sup>, M. De Mazière<sup>1</sup>, C. Vigouroux<sup>1</sup>, N. M. Deutscher<sup>5,6</sup>, D. W. T. Griffith<sup>5</sup>, N. Jones<sup>5</sup> and C. Paton-Walsh<sup>5</sup>

**Formic acid contributes significantly to acid rain in remote environments<sup>1,2</sup>. Direct sources of formic acid include human activities, biomass burning and plant leaves. Aside from these direct sources, sunlight-induced oxidation of non-methane hydrocarbons (largely of biogenic origin) is probably the largest source<sup>3,4</sup>. However, model simulations substantially underpredict atmospheric formic acid levels<sup>5-7</sup>, indicating that not all sources have been included in the models. Here, we use satellite measurements of formic acid concentrations to constrain model simulations of the global formic acid budget. According to our simulations, 100-120 Tg of formic acid is produced annually, which is two to three times more than that estimated from known sources. We show that 90% of the formic acid produced is biogenic in origin, and largely sourced from tropical and boreal forests. We suggest that terpenoids—volatile organic compounds released by plants—are the predominant precursors. Model comparisons with independent observations of formic acid strengthen our conclusions, and provide indirect validation for the satellite measurements. Finally, we show that the larger formic acid emissions have a substantial impact on rainwater acidity, especially over boreal forests in the summer, where formic acid reduces pH by 0.25–0.5.**

Known sources of formic acid in the atmosphere include fossil fuel and biofuel combustion<sup>8</sup>, biomass burning<sup>9</sup>, plants<sup>10</sup>, dry savanna soils<sup>11</sup>, formicine ants<sup>12</sup>, cloud processing<sup>2</sup>, abiological formation on rock surfaces<sup>13</sup>, and photochemical oxidation of volatile organic precursors<sup>14</sup>. Among these sources, the contributions of savanna soils, ants, rocks, and in-cloud formation are very uncertain, but most probably minor.

On the basis of current inventories, primary formic acid emissions amount to about 10 Tg annually on the global scale (Table 1). The largest contribution to the global formic acid budget is due to the photo-oxidation of non-methane hydrocarbons, representing more than 80% of the secondary source (Table 1). In the base version of the IMAGESv2 global chemistry-transport model<sup>15,16</sup> used in this work to simulate the formic acid budget, the annual production from biogenic precursors is estimated at about 20 Tg, about half of that in a recent modelling study<sup>7</sup>. The major part of this secondary flux is due to isoprene oxidation by OH (8.9 Tg) and by ozone (3.9 Tg), followed by monoterpene oxidation (3 Tg). The contribution of isoprene and

monoterpenes is, however, particularly uncertain owing to the scarcity of laboratory experiments of HCOOH formation under atmospheric conditions. For example, the estimated impact of isoprene is, according to recent studies, largely dependent on the uncertain fate of key intermediates produced at high yields, such as dihydroxy epoxides from HO<sub>2</sub>-reactions of the isoprene peroxy radicals<sup>17</sup> and hydroperoxy-enones from peroxy isomerizations<sup>18</sup>. Formic acid is removed from the atmosphere through oxidation by OH, accounting for 27% of the global sink, and dry and wet deposition (see Supplementary Section S3), resulting in a global lifetime of 3–4 days.

Global models substantially underpredict the observed HCOOH abundances from available ground-based and aircraft measurements<sup>5-7</sup>, pointing to the existence of missing sources. Their quantitative estimation is, however, very difficult owing to the scarcity and limited representativity of these measurements. Recently acquired vertical profiles from two satellite sensors (ACE-FTS and MIPAS; refs 19,20) are of limited usefulness in probing the emissions, as they sample only the upper troposphere and lower stratosphere.

The new generation IASI/MetOp satellite sensor, launched in 2006, measures in the thermal infrared and has two main advantages over its predecessors: high spatial resolution and twice-daily global coverage<sup>21,22</sup>. Recently, global day-time measurements of formic acid have been obtained and are discussed in detail in ref. 23. By limiting the retrieval to clear-sky scenes with a large thermal contrast (>5 K), the theoretical error on the total column does not exceed 60%, but leads to less data from high latitudes and to the exclusion of oceanic observations. Figure 1 and Supplementary Figs S1, S2 illustrate the IASI-retrieved HCOOH monthly column abundances in 2009. The enhanced values observed above the mid- and high latitudes of the Northern Hemisphere during the growing season testify to the existence of a strong source, most probably of biogenic origin, as the biomass burning emission patterns do not generally coincide with enhanced columns (Supplementary Fig. S3). Elevated values are also observed in the tropics, above densely vegetated areas. Comparison of the IASI columns with the IMAGESv2 model predictions (Fig. 1) corroborate earlier studies reporting large model underestimations<sup>5-7</sup>.

To help interpret this discrepancy, we test the impact of two further possible sources: (1) the heterogeneous oxidation of organic aerosols by OH (ref. 7), assumed to form one HCOOH molecule per

<sup>1</sup>Belgian Institute for Space Aeronomy, Avenue Circulaire 3, 1180, Brussels, Belgium, <sup>2</sup>Department of Chemistry, University of Leuven, B-3001, Heverlee, Belgium, <sup>3</sup>Spectroscopie de l'Atmosphère, Service de Chimie Quantique et Photophysique, Université Libre de Bruxelles, Bruxelles 1050, Belgium, <sup>4</sup>UPMC Univ. Paris 6; Université Versailles St.-Quentin; CNRS/INSU, LATMOS-IPSL, 75252 Paris Cedex 05, France, <sup>5</sup>School of Chemistry, University of Wollongong, Wollongong, New South Wales 2522, Australia, <sup>6</sup>Institute of Environmental Physics, University of Bremen, Bremen 28334, Germany.

\*e-mail: Trissevgeni.Stavrakou@aeronomie.be.

**Table 1 | Description of the simulations and inversions performed in this study, and global HCOOH budget calculated with IMAGESv2 and comparison with previous work.**

| Sources (Tg yr <sup>-1</sup> ) | F1   | F2   | F3   | Opt1 | Opt2            | Ref. [ 7]          |
|--------------------------------|------|------|------|------|-----------------|--------------------|
| Anthropogenic                  | 4    | 4    | 4    | 4    | 4               | 2.28*              |
| Pyrogenic                      | 2.9  | 2.9  | 2.9  | 4    | 4               | 1.5                |
| Biogenic primary               | 5.6  | 5.6  | 5.6  | 88   | 5.6             | 4.37 <sup>†</sup>  |
| Photochemical                  |      |      |      |      |                 |                    |
| Biogenic                       | 19.3 | 19.3 | 58.3 | 19.3 | 84 <sup>‡</sup> | 42.2               |
| Anthrop./pyrog.                | 4.2  | 4.2  | 4.2  | 4.6  | 4.6             | 6.35               |
| OA + OH                        | 0    | 27   | 0    | 0    | 0               | (15)               |
| Total                          | 36   | 63   | 75   | 120  | 102             | 56.7 <sup>§</sup>  |
| Sinks (Tg yr <sup>-1</sup> )   |      |      |      |      |                 |                    |
| OH oxidation                   | 9.6  | 19   | 20   | 27   | 28.4            | 10.6               |
| Dry deposition                 | 12.7 | 19.9 | 26.8 | 49.5 | 33.6            | 26.0 <sup>  </sup> |
| Wet deposition                 | 13.7 | 24.1 | 28.2 | 43.4 | 40              | 20.1               |
| Lifetime (days)                | 4    | 4.5  | 3.8  | 3.5  | 4.3             | 3.2                |

\*Includes biofuel burning and cattle emissions. <sup>†</sup>Includes a soil source of 1.8 Tg yr<sup>-1</sup>; <sup>‡</sup>Consists of 19.3 Tg yr<sup>-1</sup> due to known sources and 64.7 Tg yr<sup>-1</sup> due to unidentified precursors. <sup>§</sup>This is an a priori budget, but an estimated extra source of 2 Tmol yr<sup>-1</sup> is invoked to reconcile the model with HCOOH observations. <sup>||</sup>Includes a dust sink of 1.38 Tg yr<sup>-1</sup>. F1: standard simulation. F2: including production of HCOOH in the heterogeneous oxidation of organic aerosols (OA) by OH. F3: including production of HCOOH in the photolysis of hydroperoxy-enones from isoprene. Inversion Opt1: derives a primary HCOOH biogenic source using IASI. Inversion Opt2: derives a secondary HCOOH biogenic source using IASI.

OH lost, and (2) the generation of 0.5 HCOOH in the photolysis of hydroperoxy-enones from isoprene<sup>18</sup>. These hypotheses acknowledge the poor characterization of organic aerosol ageing and the large uncertainty associated with the isoprene oxidation mechanism. The global modelled annual organic aerosol source (~100 Tg) accounts for direct emissions and secondary organic aerosol formation (Supplementary Section S4) and results in an extra global annual HCOOH flux of 27 Tg, whereas a larger source (about 40 Tg) is issued by the hypothesized HCOOH production through the hydroperoxy-enones (Supplementary Section S2). Although both scenarios lead to significant enhancements in the HCOOH columns, allowing for some improvement in the model predictions, especially in tropical regions such as Indonesia and Amazonia, they prove inadequate to reconcile the model with the high observed columns in mid- and high-latitude areas (Fig. 1, Supplementary Fig. S4), underscoring the need for an even larger HCOOH source.

To properly quantify the formic acid source required to reproduce the space-based constraints we use the adjoint source inversion method to infer 'top-down' emissions at the resolution of the global model<sup>24</sup> (see Methods). Two optimization experiments are designed and performed, both constrained by monthly IASI columns. Along with the vegetation fire source, we optimize either a direct HCOOH emission from vegetation (Opt1) or a secondary HCOOH source from the OH oxidation of an as-yet-unidentified biogenic precursor, with a global lifetime taken equal to about one day (Opt2) (Table 1). These simple settings are meant to represent situations in which the missing HCOOH source is due to direct emission or photochemical formation on very short time frames, or through a collection of compounds leading to HCOOH formation after a number of unspecified intermediate steps.

Both optimizations predict the existence of a substantial biogenic source of HCOOH estimated at about 90–110 Tg annually, which is 3.5 times larger than in the a priori budget, as illustrated in Table 1. This brings the contribution of biogenic sources to 90% of the global HCOOH budget, the remainder being due to fires and human activities. The optimization significantly improves the agreement between the model and IASI columns in terms of both column amplitude and seasonality, even at high northern latitudes, where the differences were more pronounced, as shown by comparisons in Fig. 1, Supplementary Figs S1, S2 and Table S1. The extra emission over boreal forests is presumably largely due to oxidation

of biogenic volatile compounds from coniferous trees, for which HCOOH formation pathways remain so far unexplored. A large contribution of primary biogenic HCOOH emissions cannot be excluded, but seems less likely, as high emissions of HCOOH from plants are not corroborated by reported flux measurements<sup>25,26</sup>.

The extra secondary HCOOH source inferred from the Opt2 inversion is estimated at 65 Tg annually, of which tropical ecosystems (30° S–30° N) and extratropical latitudes (30°–90° N) contribute 40 Tg and 24 Tg annually, respectively. The strong contribution of boreal forests seen in its geographical distribution (Fig. 2) clearly suggests that oxidation of terpenoids emitted by these forests generates substantial amounts of HCOOH. The seasonal variation of the extra source exhibits a summertime maximum at high latitudes, which is however less pronounced than in the isoprene and terpene emission inventories used in global models (Supplementary Fig. S5). Interestingly, relatively high emissions are derived also during spring at these latitudes, possibly reflecting higher base emission rates in spring (relative to summer and autumn), as found in recent field studies of monoterpene emissions<sup>27</sup>. In the tropics, the HCOOH precursor emission is largest at the end of the dry season, but is weakly correlated with the vegetation fire source, which is however of low magnitude. Note that, should the entire missing source of HCOOH be attributed to monoterpenes only, a total molar yield of 200% HCOOH in the oxidation of monoterpenes would be required; however, the contribution of terpenoid compounds other than isoprene and monoterpenes might be substantial, as field measurements over boreal forests have suggested the existence of large emissions of undetected short-lived organic compounds<sup>28</sup>.

Both the magnitude and distribution of the source inferred from IASI are found to be only weakly sensitive to model uncertainties, as shown by the results of sensitivity studies detailed in Supplementary Section S8. In particular, we investigated the influence of uncertainties in the wet and dry deposition parameterizations, the chemical scheme, and the assumed errors on the spaceborne data. In most cases, the deduced annual global biogenic source is found to differ by less than 10% from the reference case, confirming the robustness of the inferred estimates.

In an attempt to evaluate the IASI-derived source, we have conducted extensive comparisons of the model with independent HCOOH measurements (Supplementary Section S5). Comparisons

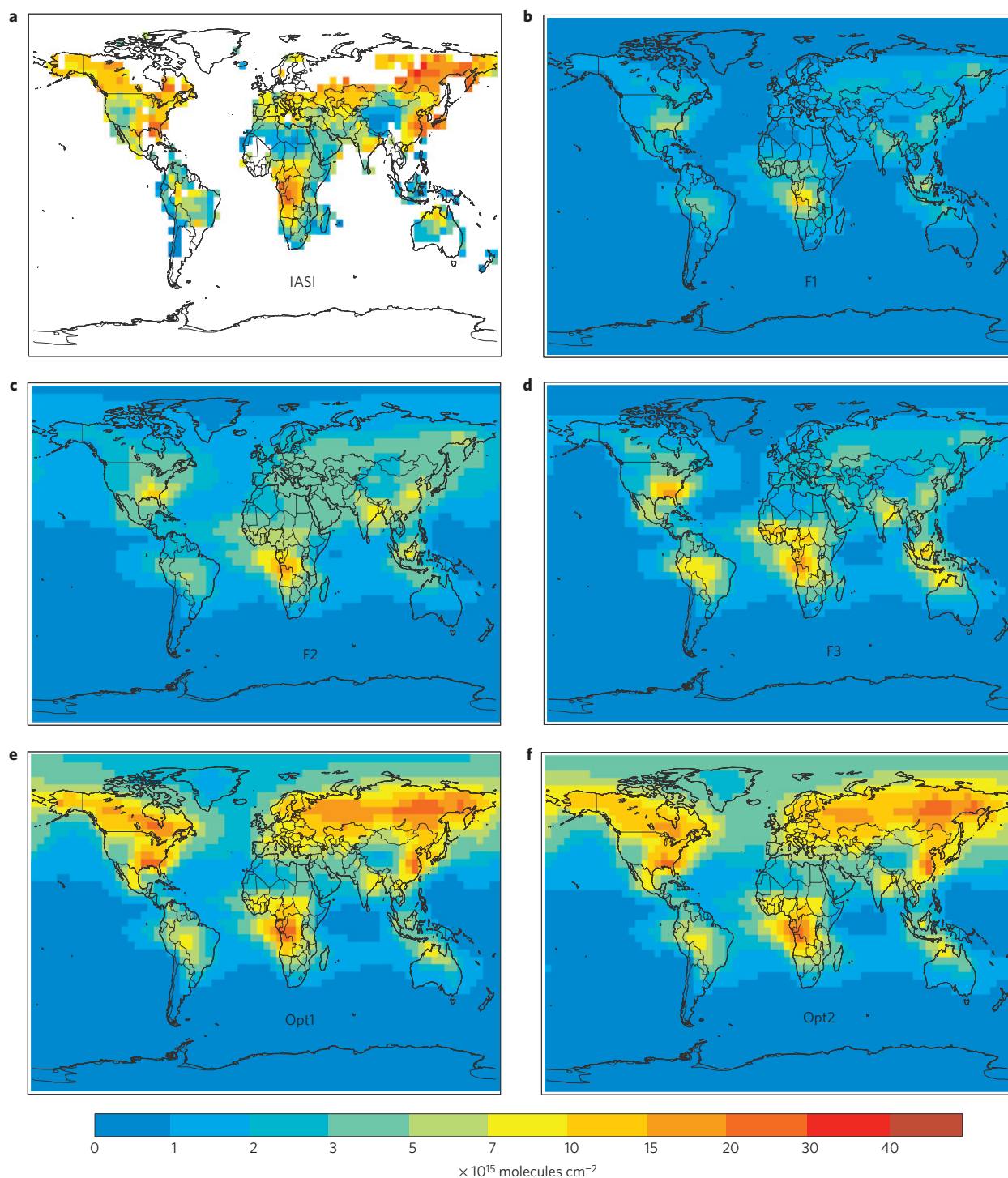


**Figure 1 | Monthly averaged HCOOH columns in June 2009 (expressed in  $10^{15}$  molecules  $\text{cm}^{-2}$ ).** **a**, Observed by IASI. **b**, Simulated by the standard model (F1). **c**, Simulated assuming that HCOOH is produced in the heterogeneous oxidation of organic aerosols by OH (F2). **d**, Simulated accounting for a production of HCOOH in the photolysis of hydroperoxy-enones from isoprene (F3). **e, f**, Inferred from source inversion assuming either a primary (Opt1) (**e**) or a secondary (Opt2) (**f**) biogenic HCOOH source. Details on the model simulations are given in Table 1.

with infrared column measurements using Fourier transform infrared (FTIR) spectroscopy at Wollongong and Reunion Island show substantial improvements after optimization, as seen from the average bias reduction by a factor of three or more at both locations (Fig. 3). At ground level, the a priori model underprediction of HCOOH concentration measurements in air and precipitation by large factors gives way to an a posteriori mean underestimation by a factor of about two or less in all regions (Supplementary Figs S6, S7).

More precisely, the average gas-phase (liquid) concentration is increased from 0.29 ppbv ( $1.32 \mu\text{mol l}^{-1}$ ) in the a priori simulation to 0.78–1.17 ppbv ( $4.0$ – $4.2 \mu\text{mol l}^{-1}$ ) in the optimization runs, as compared with the observed 1.33 ppbv ( $6.7 \mu\text{mol l}^{-1}$ ). Consistent with these results, the optimization also brings the model significantly closer to airborne concentration measurements above North America and the Pacific (Supplementary Fig. S8). Overall, these comparisons lend confidence to the IASI dataset, and therefore

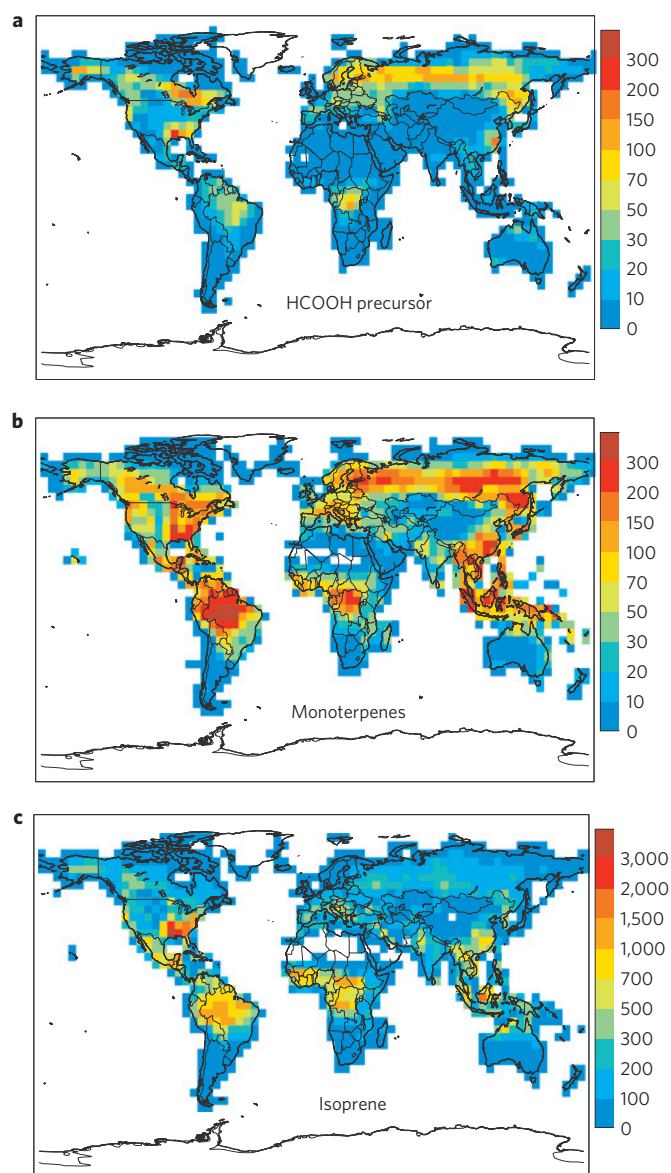


**Figure 2 | Global distribution of biogenic emissions in  $\mu\text{g C m}^{-2} \text{s}^{-1}$  in July 2009. a,** HCOOH precursor as deduced from the Opt2 inversion (Table 1). **b,c,** Emissions from the MEGAN inventory, monoterpene (**b**) and isoprene (**c**), see Supplementary Section S1.

to the strong biogenic source inferred from the optimization. The comparisons, however, also point to a limited ability of the model to capture the observed variability and vertical profile. Although this is largely due to the limited representativity of local measurements, it might also reflect the existence of important shortcomings in the representation of the formic acid sources and sinks.

We quantify the global impact of the IASI-constrained HCOOH source on precipitation acidity using the calculated wet deposition fluxes of nitrate, sulphate, ammonium, formate and acetate ions (Supplementary Section S7). The inferred decrease in pH due to the extra HCOOH source is estimated at 0.25–0.5 over boreal forests in summertime, and 0.15–0.4 above tropical vegetated areas throughout the year (Supplementary Fig. S9). Our model simulations predict that formic acid alone accounts for as much as 60–80% of the rainwater acidity over Amazonia, in accordance with *in situ* measurements<sup>29</sup>, but also over boreal forests during summertime. Its contribution is also substantial at mid-latitudes, in particular over much of the US, where it reaches 30–50% during the summer

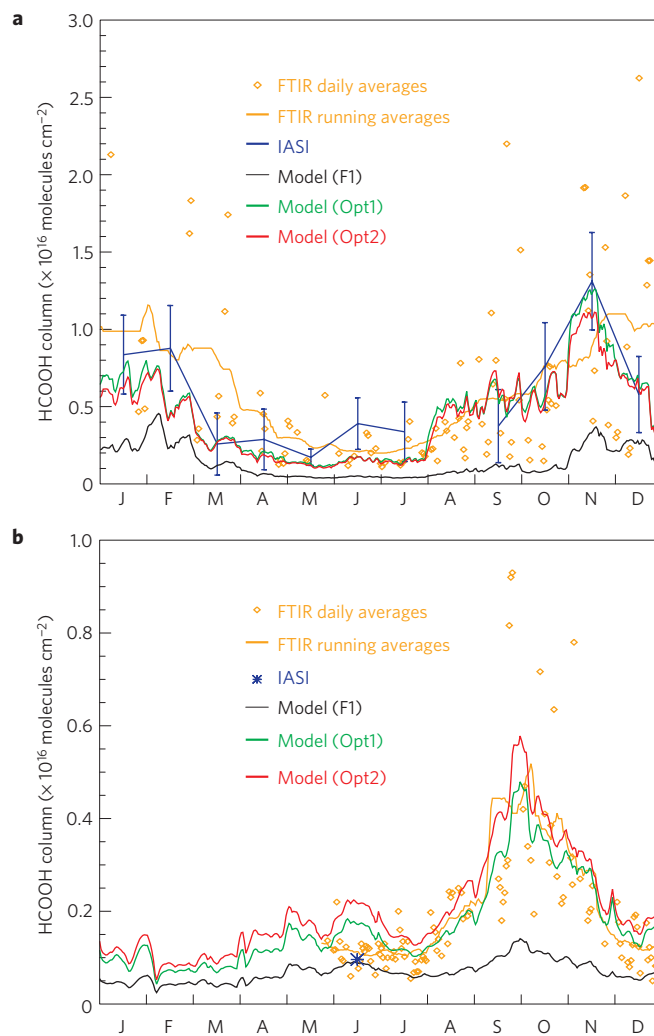


**Figure 3 | Comparisons between FTIR, IASI and modelled HCOOH**

**columns in 2009. a,** Daily and 30-day running FTIR column averages at Wollongong ( $34.41^\circ \text{S}$ ,  $150.88^\circ \text{E}$ ) (orange) and model results from the standard simulation F1 (black) and the two inversions Opt1 (green) and Opt2 (red). Average IASI columns within a radius of 4 degrees around the site and their standard deviations are shown in blue. **b,** Same for Reunion Island ( $21^\circ \text{S}$ ,  $55^\circ \text{E}$ ). Except for June, IASI columns are not available at this site owing to the thermal contrast requirement for their retrieval.

(Supplementary Fig. S10). Given the remaining underestimation of a posteriori modelled HCOOH concentrations against independent measurements (Supplementary Table S5), the large calculated impacts on precipitation acidity are probably conservative estimates. They underscore the importance of HCOOH in acid deposition in different environments, although its consequences for ecosystems are probably limited owing to the assimilation of simple carboxylic acids by the biota<sup>30</sup>.

In this letter we have revisited the formic acid global distribution and budget, using source inversion constrained by space observations. We found a biogenic source of formic acid of the order of 100 Tg annually, much larger than the current state-of-the-art estimates. A large fraction of this source originates in boreal and tropical forests, and although it remains mostly unidentified, it is likely to be of secondary origin. These findings suggest that formic acid is a high-yield product in the oxidation of organic compounds emitted abundantly by plant ecosystems, such as monoterpenes and other terpenoids, and underscore the need for further research on the emissions and chemistry of biogenic precursors.

## Methods

**Modelling.** The simulations are performed with the IMAGESv2 global chemistry transport model for the year 2009, after a four-month spin-up time. The model resolution is  $4^\circ \times 5^\circ$  with 40 vertical levels. The accompanying Supplementary Information includes: details on HCOOH sources and sinks used in the base model (Supplementary Sections S1–S3), a description of the organic aerosol module (Supplementary Section S4), a description of ground-based and aircraft measurements used for validation purposes and comparisons with the model predictions (Supplementary Section S5), discussion on the uncertainties of the IASI columns (Supplementary Section S6), on the impact of formic acid sources on precipitation acidity (Supplementary Section S7), and on the conducted sensitivity inversions (Supplementary Section S8). Results are illustrated in Supplementary Figs S1–S12 and Tables S1–S7.

**Method for source inversion.** The source inversion is realized through minimization of the cost function  $J$ , which measures the misfit between the model and the observations. By using the adjoint model method, the derivatives of the cost function  $J$  are computed with respect to a number of control variables  $\mathbf{f}$  (emission parameters)

$$J(\mathbf{f}) = \frac{1}{2} \left[ (H(\mathbf{f}) - \mathbf{y})^T \mathbf{E}^{-1} (H(\mathbf{f}) - \mathbf{y}) + \mathbf{f}^T \mathbf{B}^{-1} \mathbf{f} \right] \quad (1)$$

where  $H(\mathbf{f})$  is the model operator acting on the control variables,  $\mathbf{y}$  is the observation vector,  $\mathbf{E}$ ,  $\mathbf{B}$  are the covariance matrices of the errors on the observations and the emission parameters  $\mathbf{f}$ , respectively, and  $\mathbf{T}$  is the transpose. The method makes use of a priori distributions for biogenic and pyrogenic emissions, obtained from available inventories (Supplementary Section S1). The adjoint method enables handling of problems with large numbers of control variables, for example emission inversions at the model resolution. The cost function is minimized through an iterative descent algorithm that uses the forward and the adjoint model of IMAGESv2. About 50 iterations are usually needed to reach the minimum and derive the ‘top-down’ emission estimates. The norm of the gradient of the cost function is reduced by a factor  $\geq 1,000$  after optimization. In both optimizations, the pyrogenic and biogenic emission source strengths are updated (about 12,000 emission parameters). The errors on the emission parameters, that is, the square roots of the diagonal elements of  $\mathbf{B}$ , are assumed to be a factor of two for biogenic emissions, and a factor of 2.5 for biomass burning, whereas spatiotemporal correlations are introduced through the off-diagonal elements<sup>24</sup>. The matrix  $\mathbf{E}$  is assumed diagonal. The errors on IASI columns are taken as the quadratic sum of a 30% relative error and a  $4 \times 10^{15}$  molecules  $\text{cm}^{-2}$  absolute error. This estimate does not account for a possible bias in the IASI measured columns. The latter could not be quantified owing to the lack of correlative measurements. At Wollongong, however, we find IASI columns to be biased 30% low compared with FTIR ground-based measurements in 2008–2009, with a high degree of correlation (0.84, Supplementary Section S6). Note also that the model inversions do not account for the heterogeneous vertical sensitivity of IASI. The application of a vertical smoothing to the model columns could potentially decrease the global HCOOH source by about 10%.

Received 5 July 2011; accepted 17 November 2011; published online 18 December 2011

## References

- Galloway, J. N., Likens, G. E., Keene, W. C. & Miller, J. M. The composition of precipitation in remote areas of the world. *J. Geophys. Res.* **87**, 8771–8786 (1982).
- Chameides, W. L. & Davis, D. D. Aqueous-phase source of formic acid in clouds. *Nature* **304**, 427–429 (1983).
- Kavouras, I. G., Mihalopoulos, N. & Stephanou, E. G. Formation of atmospheric particles from organic acids produced by forests. *Nature* **395**, 683–686 (1998).
- Glasius, M. Sources to formic acid studied by carbon isotopic analysis and air mass characterization. *Atmos. Environ.* **34**, 2471–2479 (2000).
- von Kuhlmann, R., Lawrence, M. G., Crutzen, P. J. & Rasch, P. J. A model for studies of tropospheric ozone and nonmethane hydrocarbons: Model evaluation of ozone-related species. *J. Geophys. Res.* **108**, 4729 (2003).
- Ito, A., Sillman, S. & Penner, J. E. Effects of additional nonmethane volatile organic compounds, organic nitrates, and direct emissions of oxygenated organic species on global tropospheric chemistry. *J. Geophys. Res.* **112**, D06309 (2007).
- Paulot, F. *et al.* Importance of secondary sources in the atmospheric budgets of formic and acetic acids. *Atmos. Chem. Phys.* **11**, 1989–2013 (2011).
- Kawamura, K., Ng, L. L. & Kaplan, I. R. Determination of organic acids ( $\text{C}_1$ – $\text{C}_{10}$ ) in the atmosphere, motor exhausts and engine oils. *Environ. Sci. Technol.* **19**, 1082–1086 (1985).
- Andreae, M. O. & Merlet, P. Emission of trace gases and aerosols from biomass burning. *Glob. Biogeochem. Cycles* **15**, 955–966 (2001).
- Gabriel, R., Schäfer, L., Gerlach, C., Rausch, T. & Kesselmeier, J. Factors controlling the emissions of volatile organic acids from leaves of *Quercus ilex* L. (Holm oak). *Atmos. Environ.* **33**, 1347–1355 (1999).

- Sanhueza, E. & Andreae, M. O. Emissions of formic and acetic acids from tropical savanna soils. *Geophys. Res. Lett.* **18**, 1707–1710 (1991).
- Graedel, T. E. & Eisner, T. Atmospheric formic acid from formicine ants: a preliminary assessment. *Tellus B* **40**, 335–339 (1988).
- Ohta, K., Ogawa, H. & Mizuno, T. Abiological formation of formic acid on rocks in nature. *Appl. Geochem.* **15**, 91–95 (2000).
- Neeb, P., Sauer, F., Horie, O. & Moortgat, G. R. Formation of hydroxymethyl hydroperoxide and formic acid in alkene ozonolysis in the presence of water vapor. *Atmos. Environ.* **31**, 1417–1423 (1997).
- Müller, J.-F. & Stavrakou, T. Inversion of CO and NO<sub>x</sub> emissions using the adjoint of the IMAGES model. *Atmos. Chem. Phys.* **5**, 1157–1186 (2005).
- Stavrakou, T. *et al.* Evaluating the performance of pyrogenic and biogenic emission inventories against one decade of space-based formaldehyde columns. *Atmos. Chem. Phys.* **9**, 1037–1060 (2009).
- Paulot, F. *et al.* Unexpected epoxide formation in the gas-phase photooxidation of isoprene. *Science* **325**, 730–733 (2009).
- Peeters, J. & Müller, J.-F. HO<sub>x</sub> radical regeneration in isoprene oxidation via peroxy radical isomerisations, II: Experimental evidence and global impact. *Phys. Chem. Chem. Phys.* **12**, 14227–14235 (2010).
- González Abad, G. *et al.* Global distribution of upper tropospheric formic acid from the ACE-FTS. *Atmos. Chem. Phys.* **9**, 8039–8047 (2009).
- Grutter, M. *et al.* Global distribution and variability of formic acid as observed by MIPAS-ENVISAT. *J. Geophys. Res.* **115**, D10303 (2010).
- Clerbaux, C. *et al.* Monitoring of atmospheric composition using the thermal infrared IASI/MetOp sounder. *Atmos. Chem. Phys.* **9**, 6041–6054 (2009).
- Clarisse, L., Clerbaux, C., Dentener, F., Hurtmans, D. & Coheur, P. F. Global ammonia distribution derived from infrared satellite observations. *Nature Geosci.* **2**, 479–483 (2009).
- Razavi, A. *et al.* Global distributions of methanol and formic acid retrieved for the first time from the IASI/MetOp thermal infrared sounder. *Atmos. Chem. Phys.* **11**, 857–872 (2011).
- Stavrakou, T. *et al.* First space-based derivation of the global atmospheric methanol emission fluxes. *Atmos. Chem. Phys.* **11**, 4873–4898 (2011).
- Kuhn, U. *et al.* Exchange of short-chain monocarboxylic acids by vegetation at a remote tropical forest site in Amazonia. *J. Geophys. Res.* **107**, 8069 (2002).
- Kesselmeier, J., Bode, K., Gerlach, C. & Jork, E. M. Exchange of atmospheric formic and acetic acids with trees and crop plants under controlled chamber and purified air conditions. *Atmos. Environ.* **32**, 1765–1775 (1998).
- Holzinger, R., Lee, A., McKay, M. & Goldstein, A. H. Seasonal variability of monoterpene emission factors for a Ponderosa pine plantation in California. *Atmos. Chem. Phys.* **6**, 1267–1274 (2006).
- Di Carlo, P. *et al.* Missing OH reactivity in a forest: Evidence for unknown reactive biogenic VOCs. *Science* **304**, 722–725 (2004).
- Andreae, M. O., Talbot, R. W., Andreae, T. W. & Harriss, R. C. Formic and acetic acid over the Central Amazon Region, Brazil 1. Dry season. *J. Geophys. Res.* **93**, 1616–1624 (1988).
- Keene, W. C. & Galloway, J. N. Organic acidity in precipitation of North America. *Atmos. Environ.* **18**, 2491–2497 (1984).

## Acknowledgements

This study has been supported by the projects PRODEX A3C of the European Space Agency funded by the Belgian Science Policy Office, and the IBOOT, BIOSOA, AGACC and AGACC-II projects within the ‘Science for a Sustainable Development’ research programme funded by the Belgian Science Policy Office. Financial support by the ‘Actions de Recherche Concertées’ (Communauté Française de Belgique) is also acknowledged. IASI has been developed and built under the responsibility of the Centre National d’Etudes Spatiales (CNES, France). It is flown onboard the Metop satellites as part of the EUMETSAT Polar System. The IASI L1 data are received through the EUMETCast near-real-time data distribution service. L.C. and P.-F.C. are respectively Postdoctoral Researcher and Research Associate with F.R.S.-FNRS. The Australian Research Council (Grant DP110101948) is gratefully acknowledged for their funding of the Wollongong HCOOH measurements. C.V. and M.D.M. are grateful to the BIRA and LACY team members who support the FTIR observations at Reunion Island.

## Author contributions

T.S. and J.-F.M. obtained the results, drafted the manuscript and prepared the figures. J.P. developed the isoprene degradation mechanism used to estimate the photochemical source of formic acid in the model. A.R., L.C., P.-F.C., D.H. and C.C. carried out the first retrievals of formic acid observations from space. C.C. also contributed actively in the development of the IASI sensor. C.V. and M.D.M. retrieved the FTIR data at Reunion Island. N.M.D., D.W.T.G., N.J. and C.P.-W. retrieved the FTIR observations at Wollongong.

## Additional information

The authors declare no competing financial interests. Supplementary information accompanies this paper on [www.nature.com/naturegeoscience](http://www.nature.com/naturegeoscience). Reprints and permissions information is available online at <http://www.nature.com/reprints>. Correspondence and requests for materials should be addressed to T.S.

This discussion paper is/has been under review for the journal Atmospheric Measurement Techniques (AMT). Please refer to the corresponding final paper in AMT if available.

# Tropospheric nitrogen dioxide column retrieval from ground-based zenith-sky DOAS observations

F. Tack<sup>1</sup>, F. Hendrick<sup>1</sup>, F. Goutail<sup>2</sup>, C. Fayt<sup>1</sup>, A. Merlaud<sup>1</sup>, G. Pinardi<sup>1</sup>,  
C. Hermans<sup>1</sup>, J.-P. Pommereau<sup>2</sup>, and M. Van Roozendael<sup>1</sup>

<sup>1</sup>BIRA-IASB, Belgian Institute for Space Aeronomy, Brussels, Belgium

<sup>2</sup>LATMOS, Laboratoire Atmosphères, Milieux, Observations Spatiales, Guyancourt, France

Received: 22 December 2014 – Accepted: 9 January 2015 – Published: 26 January 2015

Correspondence to: F. Tack (frederik.tack@aeronomie.be)

Published by Copernicus Publications on behalf of the European Geosciences Union.

935

## Abstract

We present an algorithm for retrieving tropospheric nitrogen dioxide (NO<sub>2</sub>) vertical column densities (VCDs) from ground-based zenith-sky (ZS) measurements of scattered sunlight. The method is based on a four-step approach consisting of (1) the Differential  
5 Optical Absorption Spectroscopy (DOAS) analysis of ZS radiance spectra using a fixed reference spectrum corresponding to low NO<sub>2</sub> absorption, (2) the determination of the residual amount in the reference spectrum using a Langley-plot-type method, (3) the removal of the stratospheric content from the daytime total measured slant column based  
10 on stratospheric VCDs measured at sunrise and sunset, and simulation of the rapid NO<sub>2</sub> diurnal variation, (4) the retrieval of tropospheric VCDs by dividing the resulting tropospheric slant columns by appropriate air mass factors (AMFs). These steps are fully characterized and recommendations are given for each of them. The retrieval algorithm is applied on a ZS dataset acquired with a Multi-AXis (MAX-) DOAS instrument during the Cabauw (51.97° N, 4.93° E, sea level) Intercomparison campaign for Nitrogen  
15 Dioxide measuring Instruments (CINDI) held from the 10 June to the 21 July 2009 in the Netherlands. A median value of  $7.9 \times 10^{15}$  molec cm<sup>-2</sup> is found for the retrieved tropospheric NO<sub>2</sub> VCDs, with maxima up to  $6.0 \times 10^{16}$  molec cm<sup>-2</sup>. The error budget assessment indicates that the overall error  $\sigma_{\text{TVCD}}$  on the column values is less than 28 %. In case of low tropospheric contribution,  $\sigma_{\text{TVCD}}$  is estimated to be around 39 %  
20 and is dominated by uncertainties in the determination of the residual amount in the reference spectrum. For strong tropospheric pollution events,  $\sigma_{\text{TVCD}}$  drops to approximately 22 % with the largest uncertainties on the determination of the stratospheric NO<sub>2</sub> abundance and tropospheric AMFs. The tropospheric VCD amounts derived from ZS observations are compared to VCDs retrieved from off-axis and direct-sun measurements of the same MAX-DOAS instrument as well as to data from a co-located  
25 Système d'Analyse par Observations Zénithales (SAOZ) spectrometer. The retrieved tropospheric VCDs are in good agreement with the different datasets with correlation coefficients and slopes close to or larger than 0.9. The potential of the presented ZS

936

retrieval algorithm is further demonstrated by its successful application on a 2 year dataset, acquired at the NDACC (Network for the Detection of Atmospheric Composition Change) station Observatoire de Haute Provence (OHP; Southern France).

## 1 Introduction

5 Nitrogen dioxide ( $\text{NO}_2$ ) is an atmospheric trace gas that plays a major role in atmospheric chemistry (Crutzen, 1979). In the troposphere, it is a key precursor in the formation of ozone (Crutzen, 1970) and aerosols (Chan et al., 2010), and can contribute locally to radiative forcing (Solomon et al., 1999), through which it indirectly affects the climate system. As tropospheric  $\text{NO}_2$  abundances mostly coincide with a range of other  
10 pollutants it can be seen as a proxy for air pollution in general. According to a recent study on air pollution published by the World Health Organization (WHO, 2013),  $\text{NO}_2$  can have a direct impact on human health, causing inflammation, airway hyperresponsiveness and lung cell changes in the short term and respiratory and cardiovascular mortality in the long term. Main sources of tropospheric  $\text{NO}_2$  can be of anthropogenic  
15 origin, e.g. industrial burning processes and fossil fuel combustion, and natural origin, e.g. lightning and soil emissions. Tropospheric  $\text{NO}_2$  concentrations can be highly variable in time and space in polluted regions. For the reasons stated, the long-term and accurate monitoring of this trace gas is of great relevance.

Here, we present a retrieval algorithm developed at BIRA-IASB for deriving tropo-  
20 spheric  $\text{NO}_2$  vertical column densities (VCDs) from ground-based (GB) zenith-sky (ZS) observations of scattered sunlight by application of the differential optical absorption spectroscopy (DOAS) technique. DOAS is a well-established remote sensing technique that is able to quantify the abundance of trace gases like  $\text{NO}_2$  in the atmosphere, based on their unique spectral signature (Platt and Stutz, 2008). The main principles  
25 of the DOAS technique are (1) to separate in the measured scattered sunlight spectra, the fine-scale absorption features of trace gases from broad-band absorption due to scattering effects (mainly Rayleigh and Mie scattering), (2) to analyse the remaining

937

absorber narrow-band structures by least-squares spectral fitting on laboratory cross-  
sections. The mathematical and physical fundamentals of the method are extensively described in Platt (1994), and Platt and Stutz (2008). DOAS instruments typically operate in the ultraviolet (UV) and visible (Vis) channels of the solar spectrum. In case  
5 of the GB ZS-DOAS setup, an optical head, connected to a spectrometer coupled to a charge-coupled device (CCD) detector, points permanently to the zenith. This setup exploits the diurnal variation of the solar zenith angle (SZA).

Many studies can be found in the literature discussing the application of the DOAS method for determination of  $\text{NO}_2$  column abundances in the atmosphere based on  
10 observations from ground-based, airborne and spaceborne platforms. Without the intention to be complete, an overview of some relevant studies is provided here. The pioneering works of Brewer et al. (1973) and Noxon (1975) report on observations of  $\text{NO}_2$  concentrations in the atmosphere based on GB ZS measurements. Since more than three decades, these measurements have been commonly performed to monitor trace gases related to the ozone depletion in the stratosphere, such as  $\text{NO}_2$  (e.g. Solomon et al., 1987; McKenzie et al., 1991; Goutail et al., 1994; Hendrick et al., 2004; Denis et al., 2005). More recently, GB Multi-Axis DOAS (MAX-DOAS) has proven to be a suitable and reliable approach to retrieve integrated column amounts of tropo-  
15 spheric trace gases as well as information on their vertical distribution (e.g. Hönninger et al., 2004; Wittrock et al., 2004; Frieß et al., 2006; Clémer et al., 2010; Vlemmix et al., 2011; Wagner et al., 2011; Hendrick et al., 2014). In addition to ZS observations, the GB MAX-DOAS setup measures scattered sunlight from multiple viewing angles towards the horizon (the so-called off-axis geometry), increasing therefore the sensitivity to absorbers present close to the ground, because of the longer light paths  
20 through the lower troposphere. The DOAS method is also applied to assess total and tropospheric  $\text{NO}_2$  columns from nadir-viewing spaceborne sensors like SCIAMACHY (Scanning Imaging Absorption Chartography), GOME (Global Ozone Monitoring Experiment), GOME-2, and OMI (Ozone Monitoring Experiment) (see e.g. Richter and Burrows, 2002; Beirle et al., 2010; Boersma et al., 2011; Hilboll et al., 2011; Valks

938

et al., 2011; Bucseła et al., 2013). Other experiments have been published, presenting approaches to monitor tropospheric NO<sub>2</sub> from car (Johansson et al., 2009; Wagner et al., 2010; Constantin et al., 2013) and airborne platforms (Berg et al., 2012; Merlaud et al., 2012; Popp et al., 2012).

5 Here we describe the different steps of a new ZS retrieval algorithm for tropospheric NO<sub>2</sub> columns. The limitations and possible alternatives for this method are additionally discussed. Although the sensitivity of ZS-DOAS observations to tropospheric NO<sub>2</sub> is lower compared to MAX-DOAS observations, the presented approach offers new perspectives for the exploitation of ZS UV-Vis measurements, especially the historical time series of such observations performed over the last two decades in the framework of NDACC (Network for the Detection of Atmospheric Composition Change). So far, only a few studies have been published focusing on the retrieval of tropospheric NO<sub>2</sub> column amounts solely based on GB ZS-DOAS observations. Chen et al. (2009) presented a retrieval algorithm, applied on ZS observations acquired in Shanghai (China). There are, however, a number of methodological differences with the approach presented here and these will be further discussed in this paper. In Dieudonné et al. (2013), a similar method is applied on ZS observations acquired in Paris (France). However, the retrieval strategy is discussed only very briefly as the focus of the latter publication is on linking retrieved tropospheric NO<sub>2</sub> columns to surface concentrations.

10 The organization of this paper is as follows: Sect. 2 is dedicated to the description of the GB instrument used for the ZS observations, as well as the site where measurements were conducted. Section 3 describes the four main steps of the developed methodology for tropospheric NO<sub>2</sub> VCD retrieval from GB ZS-DOAS observations. Furthermore, the four steps of the retrieval approach are characterised in terms of an error budget analysis. Section 4 presents the retrieval results, including a comparison with correlative MAX-DOAS, direct sun (DS-) DOAS, and SAOZ (Système d'Analyse par Observations Zénithales) data. Section 5 discusses the retrieval approach with a focus on recommendations for application of the method on ZS observations at other stations. In Sect. 6 the application on observations acquired over two years at the NDACC

site of Observatoire de Haute Provence (OHP; Southern France) is demonstrated. The paper concludes with a brief summary.

## 2 Ground-based DOAS observations

The retrieval algorithm is first tested on a dataset acquired from the 10 June to the 21 July 2009 by the BIRA-IASB MAX-DOAS instrument operated in the framework of the international Cabauw Intercomparison campaign for Nitrogen Dioxide measuring Instruments (CINDI). The CINDI campaign took place at Cabauw, the Netherlands (51.97° N, 4.93° E, sea level) at the Cabauw Experimental Site for Atmospheric Research (CESAR; <http://www.cesar-observatory.nl>). It is located in a semi-rural area in the direct proximity of the four largest cities of the Netherlands (i.e. Amsterdam, Rotterdam, Den Haag and Utrecht). One of the main objectives of the campaign was to intercompare and intercalibrate GB instruments measuring NO<sub>2</sub> and determine their performance and accuracy. A more in-depth discussion of the CINDI campaign and results can be found in Roscoe et al. (2010) and Piters et al. (2012).

15 The BIRA-IASB MAX-DOAS instrument consists of three main parts. The optical head, mounted on a suntracker (INTRA manufactured by Brusag), can collect the scattered sunlight over a wide range of elevation (0 to 90°) and azimuth angles (0 to 360°). Optical fibers guide the collected skylight from the output of the optical head to the spectrometers, the latter being placed in a thermo-regulated container to guarantee high stability and minimise thermal stress. The dual-channel system is composed of a UV (ORIEL model MS260i; 1200 grooves mm<sup>-1</sup> grating) and a visible (ORIEL model MS127; 600 grooves mm<sup>-1</sup>) grating spectrometer covering a wavelength range of 300–390 nm and 400–720 nm, respectively. The Gaussian shaped instrument's slit function has a spectral resolution of 0.4 nm full width at half maximum (FWHM) and 0.9 nm FWHM for the UV and visible channels, respectively. Both spectrometers are connected to low-noise thermo-electrically cooled CCD detectors (Princeton Instruments, model PIXIS 2KBVU with 2048 × 512 pixels for the UV channel and Princeton Instruments,

model Spec-10: 100B with  $1340 \times 100$  for the visible channel). A pc unit controls the acquisition and stores all the measured spectral data. The data acquisition is fully automated using a software developed at BIRA-IASB. A full description of the instrument can be found in Clémer et al. (2010). The configuration of the instrument allows to measure scattered sunlight from ZS and off-axis viewing angles, as well as to perform DS observations. Each complete MAX-DOAS scan takes approximately 20 min and comprises ten different elevation angles, including ZS observations.

### 3 Tropospheric NO<sub>2</sub> vertical column retrieval algorithm

The developed methodology for tropospheric NO<sub>2</sub> vertical column retrieval from GB ZS-DOAS observations of scattered sunlight is based on a four-step approach. An overview of the approach is given here while the different steps are described in detail in the following subsections. First, the ZS spectra are analysed by the DOAS spectral fitting (see Sect. 3.1). The direct output of the DOAS analysis is the differential slant column density (DSCD), which is the concentration of the trace gas of interest integrated along the effective light path with respect to a fixed amount of the same absorber in a measured reference spectrum. As many light paths contribute in case of scattered sunlight observations, the measured slant column is a weighted average over all contributions. Air mass factors are calculated in order to model radiative transfer in the atmosphere and to convert slant columns to vertical columns (see Sect. 3.2). Ideally, the concentration of the absorber in the background spectrum should be zero. However, usually it contains low absorption from the measured species itself and therefore the residual amount in the reference spectrum (RSCD) needs to be determined accurately in order to realize the conversion from the DSCD to the total measured slant column density (MSCD) (see Sect. 3.3):

$$\text{MSCD} = \text{DSCD} + \text{RSCD} \quad (1)$$

941

In the next step, the stratospheric slant column density (SSCD) is determined and removed from the total slant column in order to derive the tropospheric slant column density (TSCD) (see Sect. 3.4):

$$\text{TSCD} = \text{MSCD} - \text{SSCD} \quad (2)$$

In the final step, TSCDs are converted to tropospheric vertical column densities (TVCDs) by using appropriate tropospheric air mass factors (TAMFs) (see Sect. 3.5):

$$\text{TVCD} = \frac{\text{TSCD}}{\text{TAMF}} \quad (3)$$

#### 3.1 DOAS analysis of zenith radiance spectra

The ZS observations of scattered sunlight are analysed by the QDOAS spectral fitting tool, developed at BIRA-IASB (Danckaert et al., 2014). The 425–490 nm visible wavelength region is used, as NO<sub>2</sub> is characterised by strongly structured absorption lines in this fitting window enhancing the sensitivity to the absorber, while on the other hand interference with the spectral signature of other absorbers is minimised in this spectral region. In addition to the relevant trace gas cross-sections (NO<sub>2</sub>, O<sub>3</sub>, H<sub>2</sub>O, O<sub>4</sub>), also a synthetic Ring spectrum and a low-order polynomial term are included into the non-linear least-squares fitting. They account for respectively the Ring effect (Grainger and Ring, 1962), i.e. the filling-in of Fraunhofer lines, and the contribution of broad-band absorption and scattering effects (mainly Rayleigh and Mie scattering).

The main DOAS settings used in this study as well as the cross-sections included in the spectral fit are given in Table 1. They have been chosen in accordance with the recommendations made by the NDACC UV-Vis Working Group for the sake of harmonising the different datasets provided to the NDACC database (Van Roozendael and Hendrick, 2012).

DSCDs are the direct output of the QDOAS spectral fitting approach. Prior to further analysis, the NO<sub>2</sub> DSCDs are quality-checked based on: (1) their uncertainty, expressed as SD, and (2) the residual structure of the retrieval fit, expressed as root

942

mean square error (RMS). Both measures of dispersion, which can be interpreted as quality flags for the measurements, are calculated for each DSCD by the QDOAS software. An empirically derived threshold based on the 95 % confidence interval is set for both parameters to determine whether or not a measurement is an outlier, e.g. due to low SNR, and needs to be rejected. On a total of 4226 DSCDs retrieved based on ZS-DOAS observations, 128 were rejected after the quality check.

Beside NO<sub>2</sub> DSCDs, also the oxygen dimer (O<sub>4</sub>) DSCDs have been retrieved. They are essential to determine the presence of aerosols and clouds, which can both affect the tropospheric NO<sub>2</sub> retrieval. O<sub>4</sub> has a well-known and nearly constant column and vertical distribution in the atmosphere, mainly depending on temperature and pressure, and thus on the altitude. This makes the oxygen dimer highly sensitive to the variation of scattering due to aerosols and clouds, and therefore useful to derive information on these parameters, as discussed in Wagner et al. (2004) and Frieß et al. (2006). A high aerosol loading and/or tropospheric clouds can introduce additional multiple scattering, which can significantly enhance the light path, and subsequently the measured NO<sub>2</sub> optical depth. This results in an overestimation of the “true” NO<sub>2</sub> amount. The retrieved NO<sub>2</sub> differential slant columns are screened for this effect according to the following approach: the O<sub>4</sub> diurnal variation is first modeled with the atmospheric radiative transfer model (RTM) UVspec/DISORT (Mayer and Kylling, 2006) and the AFGL standard atmosphere, and then compared with the retrieved O<sub>4</sub> slant columns. The nearly constant concentration of O<sub>4</sub> in the atmosphere results in a diurnal variation characterised by a slow increase at higher SZAs, and therefore by a smooth u-shaped curve in case of a clear and non-polluted day. An empirically derived threshold is set to determine significant offsets from the modeled O<sub>4</sub>, indicating a high aerosol loading and/or the presence of clouds introducing multiple scattering. When this threshold is exceeded, the corresponding NO<sub>2</sub> DSCD spike is identified and rejected. Without the application of the aforementioned filter strategy, a number of outliers could be observed when comparing the retrieved tropospheric NO<sub>2</sub> VCD time series with reference data. For ex-

943

ample for day 187 (6 July 2009), such an NO<sub>2</sub> enhancement event could be observed, as shown in Fig. 1.

### 3.2 Air mass factors

Multiple unknown light paths of scattered sunlight contribute simultaneously to the measured ZS signal. To quantify an effective light path and thus to be able to interpret the observations, radiative transfer in the atmosphere needs to be modeled. Generally the optical path is not expressed in absolute units, e.g. meters, but in terms of an AMF (Solomon et al., 1987), being the ratio of the number of molecules per cm<sup>2</sup> detected in an observation (SCD) and the integrated amount of molecules per cm<sup>2</sup> expected for a single, vertical transect of the atmosphere (VCD):

$$\text{AMF} = \frac{\text{SCD}}{\text{VCD}} \quad (4)$$

AMFs are typically determined by using a radiative transfer model (RTM). It simulates the radiative transfer of electromagnetic radiation through this atmosphere, based on a priori information on the state of the atmosphere (pressure, temperature, absorbers vertical profiles, aerosol loading, cloud cover, and surface albedo). The AMF enhancement factor calculation depends also on the geometry of observation and the position of the sun.

The retrieval approach requires the calculation of stratospheric and tropospheric AMFs (see Sects. 3.4 and 3.5). Equation (4) can be reformulated for the stratosphere and troposphere as follows:

$$\text{SAMF} = \frac{\text{SSCD}}{\text{SVCD}} \quad (5)$$

and

$$\text{TAMF} = \frac{\text{TSCD}}{\text{TVCD}} \quad (6)$$

944

### 3.2.1 Stratospheric AMF

Stratospheric AMFs have been calculated with the RTM package UVspec/DISORT (Mayer and Killing, 2005). This code has been thoroughly validated in the framework of an intercomparison exercise between different RTMs for the interpretation of GB ZS-DOAS and MAX-DOAS observations (Hendrick et al., 2006; Wagner et al., 2007). The radiative transfer equation (RTE) is numerically solved by the discrete ordinate method in a pseudo-spherical geometry and including multiple scattering. The wavelength used here is 457 nm, i.e. the middle of the NO<sub>2</sub> fitting window. Since stratospheric NO<sub>2</sub> is characterised by a strong diurnal variation due to photochemistry, the corresponding changes of the concentration along a given light path complicate the calculation of AMFs, especially at twilight. To account for this effect, the RTM is initialised with NO<sub>2</sub> fields depending on SZA and altitude and generated by a photochemical model. In this study, the stacked box photochemical model PSCBOX (Errera and Fonteyn, 2001; see also Hendrick et al., 2004) is coupled to the RTM UVspec/DISORT. PSCBOX includes 48 variable species, 104 gas-phase and 27 photolysis reactions and is initialised daily with 12:00 UT pressure, temperature, and chemical species profiles from the three-dimensional chemical transport model (3-D CTM) SLIMCAT (Chipperfield, 2006) for the dates and location of interest. Pressure and temperature fields used in SLIMCAT are taken from UKMO (UK Meteorological Office) meteorological analyses. The output time step is 6 min. For the calculation of stratospheric AMFs, UVspec/DISORT parameters for aerosol loading, cloud cover, and surface albedo are respectively set at summer background conditions with a visibility of 20 km, clear-sky, and 0.07. Then, AMFs are interpolated from the calculated NO<sub>2</sub> AMF look-up tables to the date and time/SZA corresponding to the observations.

### 3.2.2 Tropospheric AMF

In contrast to the stratospheric contribution, tropospheric NO<sub>2</sub> concentrations can be highly variable in time and space in polluted regions. For an optimal simulation of tro-

945

pospheric AMFs, realistic a priori profiles that take into account local pollution events are required. Therefore daily NO<sub>2</sub> and aerosol profiles retrieved from the BIRA-IASB MAX-DOAS observations performed during CINDI have been used to derive appropriate tropospheric NO<sub>2</sub> AMFs. These calculations were done with the bePRO package based on the LIDORT RTM (Spurr, 2008). This RT suite, dedicated to the retrieval of trace gas and aerosol vertical profiles, and AMF calculation, based on the Optimal Estimation Method (Rodgers, 2000), is extensively described in Clémer et al. (2010) and Hendrick et al. (2014). Tropospheric NO<sub>2</sub> AMF look-up tables have been generated for morning and afternoon conditions based on the averaging of the daily AMFs calculated for the CINDI campaign period. For the aerosol and NO<sub>2</sub> vertical profile retrievals, the following settings have been used: altitude grid with ten layers of 200 m thickness between 0 and 2 km, two layers of 500 m between 2 and 3 km, and 1 layer between 3 and 4 km, pressure and temperature profiles from US Standard Atmosphere, and a surface albedo of 0.07, which is the yearly mean value extracted at 440 nm for Cabauw from the Koelemeijer et al. (2003) albedo climatology. Regarding the a priori profiles, an exponentially decreasing profile corresponding to an AOD of 0.05 and a scaling height of 1 km has been chosen for the aerosol retrieval. Aerosol single scattering albedo and phase moments were derived as in Clémer et al. (2010) based on co-located AERONET sun photometer measurements. In the case of NO<sub>2</sub>, a profile decreasing linearly from 0.3 ppb at 0 km to 0.01 ppb at 4 km was used as a priori. The a priori covariance matrices for aerosol and NO<sub>2</sub> were constructed as in Clémer et al. (2010). It should be also noted that the stratospheric NO<sub>2</sub> content is removed from the measured DSCDs by taking the zenith measurement of each scan as reference.

### 3.3 Determination of the residual amount in the reference spectrum

In the DOAS analysis, the concentration of NO<sub>2</sub> is determined with respect to a fixed amount of the absorber in a selected reference spectrum. This method is commonly applied to remove the most prominent structures in the measured spectra, the so-called solar Fraunhofer lines, as they blur out the much weaker absorption structures

946

of trace gases. Furthermore, taking the ratio of measured spectra and a Fraunhofer reference spectrum cancels out instrumental effects under the assumption that the characteristics of the instrument remain stable over a sufficiently long period. Usually this background spectrum contains (low) absorption from the measured species itself.

5 This residual amount is, however, unknown and needs to be quantified in order to be able to determine the total measured slant column (see Eq. 1).

It should be mentioned that the concentration of the absorber in the background spectrum would be zero if an observation outside of the Earth's atmosphere could be used. This would avoid the necessity to quantify RSCD. However, as discussed in Herman et al. (2009) accurate matching of an extraterrestrial spectrum measured with a spaceborne instrument to the GB ZS measured spectra has proven to be hard due to the differences between the wavelength-dependent instrument slit functions. Usually an appropriate observation from the GB instrument itself serves as reference. To minimise the NO<sub>2</sub> amount in the background spectrum, the reference is commonly taken on a non-polluted, clear-sky day around local noon, when the sun is high and therefore the atmospheric absorption, especially in the stratosphere, is low. For the analysis of the dataset, a ZS noon spectrum was selected on 21 June 2009 at 12:16 LT (SZA = 29.3°).

To constrain and quantify the residual amount of NO<sub>2</sub> in the reference spectrum, the statistical Minimum-amount Langley-Extrapolation (MLE) method is applied, as described in Herman et al. (2009). The MLE method is based on the assumption that the minimum VCDs are constant or in other words independent from the AMF during a portion of the measurement time. The RSCD can be quantified by plotting the observed DSCDs for the whole dataset in function of the associated AMFs, calculated in Sect. 3.2.1. Based on Eqs. (1) and (4) the relation between these quantities can be formulated as:

$$\text{DSCD} = \text{VCD} \times \text{AMF} - \text{RSCD} \quad (7)$$

947

The MLE plot of the observed DSCDs and associated AMFs is given in Fig. 2. To reduce the impact of uncertainties in the calculation of the AMFs, only observations with an AMF below 5 are taken into account in the analysis. This threshold corresponds to an SZA of approximately 80°. The plotted DSCDs are binned in sets of 30 points per group, starting from the lowest to the highest AMF. Then in each bin, the lowest value is identified and selected. Thereafter, a linear regression is applied on the selected minima. According to Eq. (7), the opposite of the y-intercept gives an approximation for the residual amount in the reference spectrum. In the present case, a value of  $6.2 \times 10^{15} \text{ molec cm}^{-2}$  was determined based on the MLE method. It should be noted that in Chen et al. (2009), the RSCD was determined using a completely different strategy, due to the absence of days without pollution. It was based on measurements performed when the ZS instrument was located in a clean area as close as possible to the polluted site of interest (Shanghai), in combination to co-located long-path DOAS observations.

15 In principle a single reference spectrum can be used for the analysis of long-term measurements if the instrumental properties stay stable. In case of instrumental instability or configuration changes, a drift or/and a bias could be found in the observations, requiring the determination of additional RSCDs for the periods corresponding to the different instrumental conditions. Instrumental stability can be monitored based on the uncertainty on the NO<sub>2</sub> DSCDs and the RMS on the retrieval fit, both a direct product of the DOAS analysis.

20 Despite the limitations to quantify the NO<sub>2</sub> RSCD, it should be mentioned that since a single reference is used for the analysis of the whole dataset, potential errors in the RSCD determination will affect all measurements in the same way. Thus, these RSCD errors scarcely affect the relative variation of the retrieved tropospheric VCDs.

### 3.4 Determination of stratospheric contribution to the total NO<sub>2</sub> column

In order to obtain tropospheric SCDs, stratospheric SCDs need to be removed from the total measured SCDs (see Eq. 2). SSCDs are derived as follows: first, SVCDs

948



the observed spectra itself. According to correlative meteorological observations and in-situ measurements (Piters et al., 2012), day 174 was also identified as a clean, non-overcast day.

Although the temporal variance of the stratospheric  $\text{NO}_2$  content can be assumed to be small over a short time interval, it is characterised by a relatively strong seasonality. Therefore, the above approach can be applied for short-term datasets like the CINDI campaign. In the case of long-term observations, especially at mid- and high-latitudes, reference days for stratospheric  $\text{NO}_2$  correction should be preferably selected at least every month, or better, on a weekly basis.

### 3.4.2 Stratospheric $\text{NO}_2$ diurnal variation modeling between sunrise and sunset

Stratospheric  $\text{NO}_2$  is characterised by a strong diurnal cycle which depends not only on the scattering geometry but predominantly on the photochemistry, as discussed already in Sect. 3.2.1. During nighttime,  $\text{O}_3$  oxidises  $\text{NO}$  to  $\text{NO}_2$  in the absence of sunlight. At sunrise there is a strong decrease of  $\text{NO}_2$  due to photolysis. During daytime at mid-latitude,  $\text{NO}_2$  displays a near-linear increase due to the slow photolysis of  $\text{N}_2\text{O}_5$ . At sunset a rapid increase of  $\text{NO}_2$  occurs due to the progressive absence of photolytic loss.

In this study, the photochemical model PSCBOX described in Sect. 3.2.1 is used to calculate the rapid variation of the  $\text{NO}_2$  concentration at twilight. PSCBOX is initialised with output of the 3-D CTM SLIMCAT based on the date of the selected clean reference day. Then, the simulated  $\text{NO}_2$  diurnal cycle is made consistent with the observations and fitted on the stratospheric VCDs retrieved at twilight for the reference day: a scaling factor is calculated by taking the ratio of the retrieved and simulated stratospheric VCD at  $90^\circ$  SZA for both sunrise and sunset and it is then interpolated for the SZA range in between. Finally, the full  $\text{NO}_2$  diurnal variation is warped on the retrieved stratospheric twilight VCDs by multiplying the simulated  $\text{NO}_2$  diurnal cycle by the varying scaling factor. Obtaining the stratospheric  $\text{NO}_2$  diurnal cycle by combining measurements and a CTM has the advantage that that the model accounts for dynam-

951

ical features in stratospheric  $\text{NO}_2$  while the retrieval does not depend quantitatively on the CTM. Instead it is driven by and in good agreement with the observations. The simulated and measurement-adjusted  $\text{NO}_2$  VCD diurnal cycles are both illustrated in Fig. 4.

In Chen et al. (2009), an assumption is made that the typical  $\text{NO}_2$  diurnal cycle is characterized by a quasi-linear increase and that this can be modeled by a linear interpolation between the retrieved stratospheric  $\text{NO}_2$  VCDs at  $90^\circ$  SZA sunrise and sunset. As illustrated in Fig. 4 by the red dotted curve, this assumption is valid between approximately  $80^\circ$  SZA sunrise and sunset. Applying a linear interpolation between  $90^\circ$  SZA sunrise and sunset leads to an overestimation of the stratospheric content by approximately  $1.0 \times 10^{15}$  molec $\text{cm}^{-2}$  with respect to the simulated diurnal variation, adjusted with measurements at  $90^\circ$  SZA sunrise and sunset. This point is further discussed in Sect. 3.6.

### 3.5 Determination of the $\text{NO}_2$ tropospheric vertical column

Once the daytime SVCDs have been converted into SSCDs using Eq. (5), the retrieval of tropospheric  $\text{NO}_2$  VCDs is straightforward (see Eqs. 2 and 3): SSCDs are removed from MSCDs and resulting TSCDs are converted into TVCDs using appropriate AMFs from the generated look-up tables (TAMFs; see Sect. 3.2.2). TVCDs are retrieved for each day of the dataset between sunrise and sunset with usually a time interval of approximately 20 min. For a number of days the frequency is significantly lower because of instrumental issues or the removal of observations with a large uncertainty, as it was described in Sect. 3.1. As sensitivity to the troposphere is decreasing fast with larger SZAs, tropospheric columns are derived only during daytime for SZAs below  $80^\circ$ .

Despite the fact that this study focuses on retrieval of tropospheric VCDs, the retrieved daytime SVCDs are also a valuable product of the approach. It should be mentioned, however, that the observed spectra are analysed with a  $\text{NO}_2$  cross-section at room temperature (298 K) instead of with a cross-section at 220 K, commonly used for retrieval of stratospheric columns. Therefore, the retrieved SVCD product will be sys-

952



vative value for the uncertainty on modeled stratospheric NO<sub>2</sub> VCDs and profiles (Preston et al., 1997; Bracher et al., 2005).

- iii. The third main error source is the uncertainty on the stratospheric AMFs, which is mainly due to the choice of the RT model settings. Several studies (e.g. Solomon et al., 1987; Van Roozendaal et al., 1994; Ionov et al., 2008) showed that this uncertainty is of about 10 % at 90° SZA.
  - iv. The fourth error source, contributing to the overall SSCD error, results from the selection of a fixed reference day to determine the stratospheric content and the assumption of temporal invariance of stratospheric NO<sub>2</sub>. Although the variation of the stratospheric NO<sub>2</sub> content is small at mid-latitude in summer over a short time interval, like the duration of the CINDI campaign, this error is taken into account by estimating the maximal variation between the simulations of the NO<sub>2</sub> diurnal cycle for all days of the acquisition period. This uncertainty is found to be approximately of  $1.8 \times 10^{14}$  molec cm<sup>-2</sup>.
- Errors in the calculation of the tropospheric AMFs, due to uncertainties in the RT model parameters, are the major error source (4). They affect the retrievals in a systematic way. In Chen et al. (2009) and Wang et al. (2012), a thorough sensitivity study is applied with varying input parameters in the radiative transfer simulations. The influence of parameters such as aerosol and NO<sub>2</sub> layer height, aerosol optical depth (AOD) and NO<sub>2</sub> profile, surface albedo, etc. has been tested. Based on these sensitivity studies, the uncertainty on TAMF is estimated to range between 10 and 20 % for SZAs between 20 and 85°. As in our retrieval approach daily NO<sub>2</sub> and aerosol profiles, retrieved from the MAX-DOAS observations, were utilised instead of model data for the a priori profile shape, it is assumed that  $\sigma_{\text{TAMF}}$  should be definitely within the estimated uncertainties. This is confirmed by the estimation of the uncertainty on the AMFs due to the variability of the NO<sub>2</sub> vertical profiles retrieved during CINDI, which is found to be of 12 % on average.

955

Results of the error budget analysis are summarised in Table 2 and are visualised in Fig. 5. In Table 2, the typical relative errors are presented according to the observed tropospheric NO<sub>2</sub> amount: (1) low (below 33th percentile or  $< 0.6 \times 10^{16}$  molec cm<sup>-2</sup>), (2) moderate (between 33th and 66th percentile or  $0.6$  and  $1.0 \times 10^{16}$  molec cm<sup>-2</sup>), and (3) high (above 66th percentile or  $> 1.0 \times 10^{16}$  molec cm<sup>-2</sup>) NO<sub>2</sub> TVCD values. For each NO<sub>2</sub> TVCD range, the mean relative uncertainty  $\sigma$  is given for both the individual main error sources and the corresponding overall errors.

The error budget indicates that the overall uncertainty  $\sigma_{\text{TVCD}}$  on the retrieved NO<sub>2</sub> TVCDs is on average of 28 %. Larger errors ( $\sim 40$  %) are obtained in case of small TVCD values. In this case, the errors are dominated by uncertainties in the determination of the NO<sub>2</sub> SCD residual amount in the reference spectrum. For moderate and high TVCD values, the corresponding overall relative errors are of 24 and 21 % respectively. In these conditions, the main error sources are the determination of the stratospheric NO<sub>2</sub> abundance and the calculation of tropospheric AMFs. Errors related to the DOAS retrieval ( $\sigma_{\text{DSCD}}$ ) and to the determination of the residual amount ( $\sigma_{\text{RSCD}}$ ) seem to drop in case of larger NO<sub>2</sub> TVCDs, while errors originating from the determination of the stratospheric NO<sub>2</sub> abundance ( $\sigma_{\text{SSCD}}$ ) are not depending significantly on the TVCD values. Errors due to the calculation of tropospheric AMFs ( $\sigma_{\text{TAMF}}$ ), on the other hand, slightly increase with increasing TVCDs. In Fig. 5 the estimated overall absolute and relative errors are plotted in function of the retrieved NO<sub>2</sub> TVCDs. It can be seen that the largest absolute errors are associated with the largest TVCD values as expected. The relative errors, on the other hand, which can be up to 100 % in case of very low tropospheric contributions show a steep and rapid drop in case of increasing TVCDs. The relative error is almost constant ( $\sim 22$  %) for NO<sub>2</sub> TVCDs larger than  $2.0 \times 10^{16}$  molec cm<sup>-2</sup>.

956

## 4 Retrieval results – correlative comparison

The tropospheric NO<sub>2</sub> columns have been compared with correlative datasets in order to thoroughly assess our ZS retrieval algorithm. To ensure comparability of data, and to reduce instrumental and algorithmic differences, a set of measurement requirements were defined in the framework of CINDI, which had to be performed by all instruments to the greatest possible extent (Piters et al., 2012). The same holds for the parameter settings for the trace gas retrieval as well as the relevant cross-sections included in the spectral fit (Roscoe et al., 2010). A first comparison is done with the VCDs obtained from a SAOZ instrument, which has been operated during the CINDI campaign in the close proximity of the BIRA-IASB instrument. Then the retrieval results are compared with VCDs from MAX-DOAS and DS-DOAS observations, also performed with the BIRA-IASB instrument.

### 4.1 ZS-DOAS SAOZ

The ZS-DOAS SAOZ instrument has been developed by CNRS-LATMOS at the end of 1980's. Since then, about 20 SAOZ instruments have been installed at various latitudes on the globe with initially the measurement of stratospheric ozone and NO<sub>2</sub> as main objective. Instrumental set-up has been described in Pommereau and Goutail (1998) and Piters et al. (2012) for the CINDI campaign. During the CINDI campaign, a measurement was done every 2 min, resulting in a high frequency of ZS observations. The retrieval strategy is discussed in Dieudonné et al. (2013).

### 4.2 MAX-DOAS

In addition to zenith-sky observations, the BIRA-IASB MAX-DOAS instrument measured scattered sunlight at different elevation angles towards the horizon, hereby increasing the sensitivity to absorbers present close to the ground. The azimuth was fixed along a west-north-westerly direction (287°) with an unobstructed view down to

957

an elevation angle of 0.5°. Tropospheric NO<sub>2</sub> vertical profiles and corresponding VCDs have been retrieved by applying the bePRO profiling tool (Clémer et al., 2010; Hendrick et al., 2014) to the measured off-axis DSCDs. Retrieval settings are described in Sect. 3.2.2.

### 4.3 DS-DOAS

The BIRA-IASB instrument is also able to perform observations of direct solar irradiance. NO<sub>2</sub> vertical columns can be accurately retrieved based on the DS-DOAS approach as the light path through the atmosphere, and subsequently the AMF, is straightforward to model. The determination of the AMF does not require complex radiative transfer calculations, but can be geometrically derived as the secant of the SZA. This significantly reduces uncertainties in the conversion from slant to vertical columns. The stratospheric contribution, determined as described in Sect. 3.4, is subtracted from the total NO<sub>2</sub> columns in order to obtain tropospheric VCDs. A major drawback of the DS observation is the dependency on clear-sky conditions. As cloud cover was substantial during the CINDI campaign, the acquired DS-DOAS dataset is relatively scarce. The fundamentals of DS-DOAS are extensively discussed in Brewer et al. (1973), Cede et al. (2006), and Herman et al. (2009).

### 4.4 Discussion of the correlative comparison

The comparisons between ZS-DOAS and SAOZ, ZS-DOAS and MAX-DOAS, and ZS-DOAS and DS-DOAS are shown in Fig. 6. A complete scan with the BIRA-IASB instrument, consisting of ten off-axis measurements at different elevation angles including zenith takes approximately 20 min of measurement time. The frequency of ZS measurements is therefore much lower than in case of the SAOZ, which is an instrument dedicated to perform only ZS observations (approximately one measurement every two minutes). To reduce the temporal variability due to different measurement sampling and to intercompare the different datasets in a meaningful way, the retrievals are averaged

958

in 30 min bins. An overall good agreement can be observed between ZS-DOAS, SAOZ, MAX-DOAS and DS-DOAS during the CINDI campaign, demonstrating the robustness and reliability of the presented approach.

Figure 7 shows the scatterplot and linear regression analysis of the binned and averaged  $\text{NO}_2$  TVCDs, retrieved for the whole time series from (a) ZS-DOAS vs. SAOZ, and (b) ZS-DOAS vs. MAX-DOAS, respectively. For both comparisons a correlation coefficient higher than 0.9 can be observed. The linear regression analysis shows slopes within 18 % of unity and intercepts close to zero. In case of small  $\text{NO}_2$  TVCD retrievals, we see a positive bias for the SAOZ with respect to ZS-DOAS retrievals, while the bias gets negative at higher TVCD values.

In Fig. 8 the  $\text{NO}_2$  TVCD daily mean time series, retrieved from (a) ZS-DOAS and SAOZ, and (b) ZS-DOAS and MAX-DOAS, respectively, are compared. A very good consistency can be observed between the ZS-DOAS and SAOZ  $\text{NO}_2$  TVCD retrievals, for both low and high TVCD values. The MAX-DOAS retrievals show similar day-to-day variations with respect to the ZS-DOAS and SAOZ retrievals. However, a positive bias of about 18 % on average can be observed for MAX-DOAS retrievals.

The same feature can be seen in Fig. 9, showing the retrieved  $\text{NO}_2$  TVCD diurnal cycle of two subsequent days in the dataset, i.e. 3 July 2009 (day 184; see Fig. 9a) and 4 July 2009 (day 185; see Fig. 9b). For most retrievals, MAX-DOAS data shows a positive offset while DS-DOAS and SAOZ retrievals are very close to each other. This could be explained by the fact that different air masses were observed because of the different viewing geometries of the multi-axis and zenith-sky approach. It should also be noted that MAX-DOAS has a higher sensitivity to  $\text{NO}_2$  present close to the ground than the other techniques. In Fig. 9, also the DS-DOAS retrievals are plotted. To avoid smoothing due to interpolation between the limited number of retrievals and for a better interpretation of the results, DS-DOAS retrievals are represented as point data. The DS-DOAS retrievals are seen to be in good agreement with the TVCDs retrieved by the other approaches.

959

It is clear from the observations that day to day tropospheric  $\text{NO}_2$  concentrations can have a high variability at the Cabauw site. For day 184 (3 July), many tropospheric  $\text{NO}_2$  pollution events can be observed. On the other hand, day 185 (4 July) is a clean day with low tropospheric  $\text{NO}_2$  values, showing a smooth decrease in the morning and a slow build-up starting from noon. The meteorological parameters have shown that the  $\text{NO}_2$  concentration variability is strongly depending on wind direction. On day 184, there were moderate winds ( $4.3 \text{ ms}^{-1}$ ) from the southwest. The regions north of Cabauw are relatively clean, while there are strong pollution sources in the west (Rotterdam) and the south (industrial Flanders). When the wind is blowing from the south or west, retrievals from the Ozone Monitoring Instrument (OMI) as well as CHIMERE simulations over Cabauw have shown tropospheric  $\text{NO}_2$  columns that are approximately two times higher than on days with winds from the north or east (Piters et al., 2012). On day 185 there was a light breeze ( $2.5 \text{ ms}^{-1}$ ) from the northwest. On this day, the air over Cabauw was dominated by cleaner air originating from the North Sea.

## 5 Discussion and recommendations

In this section, the presented retrieval approach is briefly discussed with a focus on recommendations to improve the applicability on ZS observations acquired at other GB stations. From the error budget analysis can be concluded that reliable  $\text{NO}_2$  TVCDs can be retrieved in case of moderate and strong polluted sites. Cabauw is a typical example of such a site as it is a semi-rural area, in the direct proximity of the four largest cities of the Netherlands. Depending on the meteorological conditions, the city may therefore be subject to substantial pollution events. In case of application of the retrieval approach on ZS observations performed at a station with very low or very high tropospheric content, some recommendations are made below.

Application of chemically-modified Langley plots (Lee et al., 1994), which are frequently used for determination of the  $\text{NO}_2$  residual amount in the reference spectrum, was meaningless in case of the Cabauw dataset. Only the observations in a limited

960

SZA range (90–80°) with low tropospheric sensitivity could be used, since tropospheric pollution events can affect the straight-line fits of the Langley plot method. Along with the low frequency of ZS observations, i.e. each 15 to 20 min, too few data points remained in the plot to be statistically relevant. Furthermore, some tropospheric contamination could still be observed, even at high SZA. Constantin et al. (2013) reported similar issues with the chemically-modified Langley plot method, when applied on observations from a polluted site. For the selection of the SZA interval, a trade-off was discussed between having a sufficiently large set of observations while avoiding tropospheric contamination at lower SZA. In case of low to moderate tropospheric content, it is however strongly recommended to apply both the MLE and the chemically-modified Langley plot methods in order to further constrain the determination of the residual amount in the reference spectrum and to reduce the substantial uncertainties in this step.

Another important error source is the determination of the stratospheric contribution. The assumption that the tropospheric contribution is negligible in case of ZS observations at dawn and dusk does not always count in case of sites where frequent strong pollution events occur. Therefore, an approach was proposed to identify a non-polluted reference day and to assume that the retrieved stratospheric content for this day is representative for the whole dataset. It is recommended, however, to use daily observations (or to take a weekly mean) of the stratospheric NO<sub>2</sub> amount in the absence of frequent tropospheric pollution events in order to reduce the uncertainties introduced by the temporal variance and/or seasonality of the stratospheric NO<sub>2</sub> content.

In Chen et al. (2009) a strategy was applied to determine the stratospheric contribution in case of a heavy polluted site. Due to severe tropospheric contamination at the measurement site in Shanghai (China), no clean reference day could be identified in the dataset. Instead, measurements were done at Chongming Island, which lies to the northeast of Shanghai in the Pacific Ocean. Chongming can be considered as the area with the smallest tropospheric NO<sub>2</sub> pollution in the proximity of Shanghai. The SVCDs determined for a clean day at Chongming Island were eventually used to retrieve the

TVCDs from the observations acquired in Shanghai. This strategy can be, however, an additional error source, because of the spatial and temporal variations of the stratospheric NO<sub>2</sub> content. It makes also difficult its application to any other station due to the need of these additional measurements in a clean site.

## 6 Application at the NDACC site OHP

The potential of the presented ZS retrieval algorithm is also demonstrated by its application on observations acquired at the NDACC station Observatoire de Haute Provence (OHP, 43.94° N, 5.71° E, ~ 650 m a.s.l.), where BIRA-IASB and LATMOS operate a MAX-DOAS (UV channel only) and a SAOZ instrument, respectively. OHP is a mostly remote site at mid-latitude in Southern France, affected from time to time by pollution events coming from the Marseille area (South of OHP). Tropospheric columns are retrieved for a 2 year period from August 2012 to July 2014.

Taken the recommendations of Sect. 5 into account, slightly different strategies are applied in the different steps of the retrieval approach: (1) For the determination of the RSCD, the comparison between the chemically-modified Langley plot and the MLE method shows consistent results when applied on observations acquired at a background station like OHP. Both a higher frequency of ZS observations and the lack of frequent tropospheric contamination results in a sufficiently large and reliable dataset to derive the RSCD by linear least-squares regression in the chemically-modified Langley plot. A single noon spectrum, selected on 31 August 2013 at 11:40 LT, is used for the analysis of the whole time series. For the RSCD, a value of  $2.7 \times 10^{15}$  molec cm<sup>-2</sup> is determined. (2) Due to the absence of frequent tropospheric pollution events at twilight, daily observations of the stratospheric contribution could be performed instead of retrieving the stratospheric content for a number of reference days, representative for parts of the dataset. This strategy reduces the uncertainties introduced by the temporal variance and/or seasonality of the stratospheric NO<sub>2</sub> content. (3) A seasonally-resolved climatology of tropospheric NO<sub>2</sub> AMFs has been generated based on the

lower tropospheric NO<sub>2</sub> vertical profiles retrieved by applying the bePRO algorithm (see Sect. 3.2.2) to the August 2012 to July 2014 MAX-DOAS measurements at OHP. At this station, the MAX-DOAS instrument operates only in the UV at the following elevation angles: 2, 4, 6, 8, 11, 26, and 90° (zenith). Regarding the a priori NO<sub>2</sub> profiles, exponentially decreasing profiles corresponding to the vertical columns determined by the geometrical approximation and a scaling height of 0.5 km has been chosen. In the case of aerosol retrievals, a single extinction profile taken from the LOWTRAN climatology and corresponding to background conditions has been used as a priori. The retrieval altitude grid is one layer of 150 m thickness between 0.65 (altitude of the station) and 0.8 km altitude, 10 layers of 200 m thickness between 0.8 and 3 km, and one layer of 1 km thickness between 3 and 4 km. NO<sub>2</sub> and aerosol extinction profiles have been retrieved at 370 and 360 nm, respectively. In the case of AMF calculation, the following wavelength were selected: 370 and 460 nm. These two sets of UV and visible AMFs have been used for the application of the ZS approach to the MAX-DOAS and SAOZ measurements, respectively. For the calculation of AMFs in the visible, the aerosol profiles retrieved at 360 nm have been converted to 460 nm using the Ångström exponents derived from collocated CIMEL/AERONET sun photometer measurements (<http://aeronet.gsfc.nasa.gov>; see also Wang et al., 2014). MAX-DOAS NO<sub>2</sub> vertical columns involved in the comparison with the ZS method have been derived by integrating the retrieved NO<sub>2</sub> vertical profiles.

The retrieved TVCDs have been compared again with correlative datasets from SAOZ and MAX-DOAS observations and the resulting monthly mean time series are shown in Fig. 10. At OHP, a marked seasonal cycle can be observed with a maximum in winter with mean values close to  $3 \times 10^{15}$  molec cm<sup>-2</sup> and a minimum in summer with mean values around  $1.7 \times 10^{15}$  molec cm<sup>-2</sup>. In general the three datasets are in good agreement for both low and high TVCDs: the correlation coefficients are respectively 0.82 and 0.88 for the comparison of ZS-DOAS with MAX-DOAS and with SAOZ. These results further support the good reliability of the ZS retrieval approach presented in this study.

963

## 7 Summary and conclusions

An algorithm for retrieving tropospheric NO<sub>2</sub> VCDs from GB ZS DOAS measurements has been presented, with a full characterisation of the different retrieval steps. This algorithm has been developed and tested based on ZS observations from the BIRA-IASB MAX-DOAS instrument, acquired during the CINDI campaign at Cabauw, the Netherlands. For the tropospheric VCDs, a median value of  $7.9 \times 10^{15}$  molec cm<sup>-2</sup> can be observed at the Cabauw site with maxima up to  $6.0 \times 10^{16}$  molec cm<sup>-2</sup>. The retrievals are in good agreement when compared to TVCDs retrieved from off-axis and DS observations, and ZS measurements acquired by a co-located SAOZ instrument. For both comparisons a correlation higher than 0.9 can be observed with slopes within 18 % of unity and intercepts close to zero. The main error sources are characterised for the four principal steps of the retrieval approach:

1. Uncertainties due to the DOAS analysis and noise in the spectral measurements result in a relative error of approximately 14 and 3 % for low and high tropospheric VCD retrievals, respectively. It should be noted that DSCDs are quality-checked, including the removal of outliers, and compensated for multiple scattering events prior to the retrieval.
2. The NO<sub>2</sub> SCD residual amount in the fixed reference spectrum, measured on a non-polluted, clear-sky day around local noon, is determined based on the statistical Minimum-amount Langley-Extrapolation method. The related uncertainty can be substantial (22 % on average and up to 40 % in case of low NO<sub>2</sub> TVCDs). However, since a single RSCD is used for the analysis of the whole dataset, potential errors scarcely affect the relative variation of the retrieved tropospheric VCDs.
3. The stratospheric contribution to the total column is determined based on a two-step approach. First, stratospheric VCDs are retrieved for both 90° SZA sunrise and sunset for the selected reference day (23 June 2009). Then the NO<sub>2</sub> diurnal

964

variation between the 90° SZA twilight observations, modeled by the photochemical box-model PSCBOX, is fitted to these observations. The overall error for this step is estimated to be around 19%. It accounts for the uncertainties due to (1) the determination of the effective SZA corresponding to the twilight observations, (2) the modeling of the NO<sub>2</sub> diurnal variation, (3) the simulation of stratospheric AMFs, and (4) the assumption of the temporal invariance of stratospheric NO<sub>2</sub> during the CINDI campaign period.

4. In the last step of the retrieval approach, tropospheric NO<sub>2</sub> slant columns retrieved between 80° SZA sunrise and sunset are converted to vertical columns by using appropriate tropospheric AMFs. Errors on the calculation of the tropospheric AMFs are estimated to range between 10 and 20%, depending on the SZA.

In general, the error budget analysis indicates that tropospheric NO<sub>2</sub> VCDs can be retrieved with the ZS approach with an uncertainty  $\sigma_{\text{TVCD}}$  of less than 28%. In case of low tropospheric content, the relative errors are found to be higher (i.e. in the order of 40%) and are dominated by uncertainties in the determination of the residual amount in the reference spectrum. In case of strong tropospheric pollution events, the overall error drops to approximately 22%. So the TVCD retrievals are generally more reliable in case of large tropospheric contributions, as expected, and for such conditions, the largest uncertainties find their origins in the determination of the stratospheric NO<sub>2</sub> abundance (19%) and the calculation of tropospheric AMFs (15%).

The present study demonstrates that ZS observations, widely used for monitoring of the stratospheric composition since about three decades, are also suitable for the retrieval of tropospheric NO<sub>2</sub> column amounts, despite the lower sensitivity to the troposphere when compared to MAX-DOAS observations. In order to further demonstrate the potential of the presented retrieval algorithm, it has been successfully applied on a 2 year dataset acquired at OHP, being a background site from time to time affected by pollution events. This offers new perspectives for the exploitation of ZS UV-Vis ob-

965

servations at NDACC stations and the applicability of the algorithm on data from other stations as well as longer time series will be further investigated. At present, there are far more ZS-DOAS than MAX-DOAS GB stations at various latitudes and much longer time series of ZS observations are available than for MAX-DOAS, mainly due to the novelty of the latter technique. This makes the ZS retrieval approach relevant for investigating the long-term evolution of tropospheric NO<sub>2</sub>, with a feed-back of more than two decades at some stations.

*Acknowledgements.* The CINDI Campaign was largely funded by the ESA project CEOS (ES-RIN 22202/09/I-EC) and the EU project ACCENT-AT2 (GOCE-CT-2004-505337). We further acknowledge the support of the European Union Seventh Framework Programme via the NORS project (FP7-284421) and the ACTRIS project (FP7-262254). BIRA-IASB is also thankful for the support from the Belgian Federal Science Policy Office through the AGACC-II project (SD/CS/07A). M. P. Chipperfield, from the University of Leeds, is gratefully acknowledged for providing us with the SLIMCAT data. The team of LATMOS wishes to thank the French Centre National d'Etudes Spatiales (CNES) and Institut des Sciences de l'Univers (INSU). The authors also want to express their gratitude to the KNMI staff at Cabauw for their technical support and the offered infrastructure.

## References

- 20 Beirle, S., Köhl, S., Pukite, J., and Wagner, T.: Retrieval of tropospheric column densities of NO<sub>2</sub> from combined SCIAMACHY nadir/limb measurements, *Atmos. Meas. Tech.*, 3, 283–299, doi:10.5194/amt-3-283-2010, 2010.
- Berg, N., Mellqvist, J., Jalkanen, J.-P., and Balzani, J.: Ship emissions of SO<sub>2</sub> and NO<sub>2</sub>: DOAS measurements from airborne platforms, *Atmos. Meas. Tech.*, 5, 1085–1098, doi:10.5194/amt-5-1085-2012, 2012.
- 25 Boersma, K. F., Eskes, H. J., Dirksen, R. J., van der A, R. J., Veeffkind, J. P., Stammes, P., Huijnen, V., Kleipool, Q. L., Sneep, M., Claas, J., Leitão, J., Richter, A., Zhou, Y., and Brunner, D.: An improved tropospheric NO<sub>2</sub> column retrieval algorithm for the Ozone Monitoring Instrument, *Atmos. Meas. Tech.*, 4, 1905–1928, doi:10.5194/amt-4-1905-2011, 2011.

966

- Bogumil, K., Orphal, J., Homann, T., Voigt, S., Spietz, P., Fleischmann, O. C., Vogel, A., Hartmann, M., Bovensmann, H., Frerik, J., and Burrows, J. P.: Measurements of molecular absorption spectra with the SCIAMACHY Pre-Flight Model: instrument characterization and reference spectra for atmospheric remote sensing in the 230–2380 nm region, *J. Photoch. Photobio. A*, 157, 167–184, 2003.
- Bracher, A., Sinnhuber, M., Rozanov, A., and Burrows, J. P.: Using a photochemical model for the validation of NO<sub>2</sub> satellite measurements at different solar zenith angles, *Atmos. Chem. Phys.*, 5, 393–408, doi:10.5194/acp-5-393-2005, 2005.
- Brewer, A. W., McElroy, C. T., and Kerr, J. B.: Nitrogen dioxide concentrations in the atmosphere, *Nature*, 246, 129–133, 1973.
- Bucsela, E. J., Krotkov, N. A., Celarier, E. A., Lamsal, L. N., Swartz, W. H., Bhartia, P. K., Boersma, K. F., Veeffkind, J. P., Gleason, J. F., and Pickering, K. E.: A new stratospheric and tropospheric NO<sub>2</sub> retrieval algorithm for nadir-viewing satellite instruments: applications to OMI, *Atmos. Meas. Tech.*, 6, 2607–2626, doi:10.5194/amt-6-2607-2013, 2013.
- Cede, A., Herman, J., Richter, A., Krotkov, N., and Burrows, J.: Measurements of nitrogen dioxide total column amounts at Goddard Space Flight Center using a Brewer spectrometer in direct sun mode, *J. Geophys. Res.*, 111, D05304, doi:10.1029/2005JD006585, 2006.
- Chan, A. W. H., Chan, M. N., Surratt, J. D., Chhabra, P. S., Loza, C. L., Crouse, J. D., Yee, L. D., Flagan, R. C., Wennberg, P. O., and Seinfeld, J. H.: Role of aldehyde chemistry and NO<sub>x</sub> concentrations in secondary organic aerosol formation, *Atmos. Chem. Phys.*, 10, 7169–7188, doi:10.5194/acp-10-7169-2010, 2010.
- Chance, K. and Kurucz, R. L.: An improved high-resolution solar reference spectrum for Earth's atmosphere measurements in the ultraviolet, visible, and near infrared, available at: <http://www.cfa.harvard.edu/atmosphere> (last access: September 2013), 2010.
- Chance, K. V. and Spurr, R. J. D.: Ring effect studies: rayleigh scattering, including molecular parameters for rotational Raman scattering, and the Fraunhofer spectrum, *Appl. Optics*, 36, 5224–5230, 1997.
- Chen, D., Zhou, B., Beirle, S., Chen, L. M., and Wagner, T.: Tropospheric NO<sub>2</sub> column densities deduced from zenith-sky DOAS measurements in Shanghai, China, and their application to satellite validation, *Atmos. Chem. Phys.*, 9, 3641–3662, doi:10.5194/acp-9-3641-2009, 2009.

- Chipperfield, M. P.: New version of the TOMCAT/SLIMCAT off-line chemical transport model: intercomparison of stratospheric tracer experiments, *Q. J. Roy. Meteor. Soc.*, 132, 1179–1203, doi:10.1256/qj.05.51, 2006.
- Clémer, K., Van Roozendaal, M., Fayt, C., Hendrick, F., Hermans, C., Pinardi, G., Spurr, R., Wang, P., and De Mazière, M.: Multiple wavelength retrieval of tropospheric aerosol optical properties from MAXDOAS measurements in Beijing, *Atmos. Meas. Tech.*, 3, 863–878, doi:10.5194/amt-3-863-2010, 2010.
- Constantin, D.-E., Merlaud, A., Van Roozendaal, M., Voiculescu, M., Fayt, C., Hendrick, F., Pinardi, G., and Georgescu, L.: Measurements of tropospheric NO<sub>2</sub> in Romania using a zenith-sky mobile DOAS system and comparisons with satellite observations, *Sensors*, 13, 3922–3940, doi:10.3390/s130303922, 2013.
- Crutzen, P.: The influence of nitrogen oxides on the atmospheric ozone content, *Q. J. Roy. Meteor. Soc.*, 96, 320–325, 1970.
- Crutzen, P. J.: The role of NO and NO<sub>2</sub> in the chemistry of the troposphere and stratosphere, *Annu. Rev. Earth Pl. Sc.*, 7, 443–472, 1979.
- Danckaert, T., Fayt, C., and Van Roozendaal, M.: QDOAS software user manual 2.108, IASB/BIRA, Uccle, Belgium, 2014, available at [http://uv-vis.aeronomie.be/software/QDOAS/QDOAS\\_manual.pdf](http://uv-vis.aeronomie.be/software/QDOAS/QDOAS_manual.pdf) (last access: 4 November 2014), 2014.
- Denis, L., Roscoe, H. K., Chipperfield, M. P., Van Roozendaal, M., and Goutail, F.: A new software suite for NO<sub>2</sub> vertical profile retrieval from ground-based zenith-sky spectrometers, *J. Quant. Spectrosc. Ra.*, 92, 321–333, doi:10.1016/j.jqsrt.2004.07.030, 2005.
- Dieudonné, E., Ravetta, F., Pelon, J., Goutail, F., and Pommereau, J. P.: Linking NO<sub>2</sub> surface concentration and integrated content in the urban developed atmospheric boundary layer, *Geophys. Res. Lett.*, 40, 1247–1251, doi:10.1002/grl.50242, 2013.
- Errera, Q. and Fonteyn, D.: Four-dimensional variational chemical assimilation of CRISTA stratospheric measurements, *J. Geophys. Res.*, 106, 12253–12265, doi:10.1029/2001JD900010, 2001.
- Frieß, U., Monks, P. S., Remedios, J. J., Rozanov, A., Sinreich, R., Wagner, T., and Platt, U.: MAX-DOAS O<sub>4</sub> measurements: a new technique to derive information on atmospheric aerosols: 2. Modeling studies, *J. Geophys. Res.*, 111, D14203, doi:10.1029/2005JD006618, 2006.
- Goutail, F., Pommereau, J.-P., and Sarkissian, A.: Total nitrogen dioxide at the Arctic Polar Circle since 1990, *Geophys. Res. Lett.*, 21, 1371–740, 1994.



- Irie, H., Johnston, P. V., Kanaya, Y., Kim, Y. J., Klein Baltink, H., Kreher, K., de Leeuw, G., Leigh, R., Merlaud, A., Moerman, M. M., Monks, P. S., Mount, G. H., Navarro-Comas, M., Oetjen, H., Pazmino, A., Perez-Camacho, M., Peters, E., du Piesanie, A., Pinardi, G., Puentedura, O., Richter, A., Roscoe, H. K., Schönhardt, A., Schwarzenbach, B., Shaiganfar, R., Sluis, W., Spinei, E., Stolk, A. P., Strong, K., Swart, D. P. J., Takashima, H., Vlemmix, T., Vrekoussis, M., Wagner, T., Whyte, C., Wilson, K. M., Yela, M., Yilmaz, S., Zieger, P., and Zhou, Y.: The Cabauw Intercomparison campaign for Nitrogen Dioxide measuring Instruments (CINDI): design, execution, and early results, *Atmos. Meas. Tech.*, 5, 457–485, doi:10.5194/amt-5-457-2012, 2012.
- Platt, U.: Differential optical absorption spectroscopy (DOAS), in: *Air Monitoring by Spectroscopic Techniques*, 127, John Wiley & Sons, Hoboken, NJ, USA, 27–83, 1994.
- Platt, U. and Stutz, J.: *Differential Optical Absorption Spectroscopy: Principles and Applications*, Springer-Verlag, Berlin, Germany, 2008.
- Pommereau, J. P. and Goutail, F.: Stratospheric O<sub>3</sub> and NO<sub>2</sub> observations at the Southern Polar Circle in summer and fall 1988, *Geophys. Res. Lett.*, 15, 895–897, doi:10.1029/GL015i008p00895, 1988.
- Popp, C., Brunner, D., Damm, A., Van Roozendael, M., Fayt, C., and Buchmann, B.: High-resolution NO<sub>2</sub> remote sensing from the Airborne Prism EXperiment (APEX) imaging spectrometer, *Atmos. Meas. Tech.*, 5, 2211–2225, doi:10.5194/amt-5-2211-2012, 2012.
- Preston, K. E., Jones, R. L., and Roscoe, H. K.: Retrieval of NO<sub>2</sub> vertical profiles from ground-based UV-visible measurements: method and validation, *J. Geophys. Res.*, 102, 10089–10097, 1997.
- Richter, A. and Burrows, J. P.: Retrieval of tropospheric NO<sub>2</sub> from GOME measurements, *Adv. Space Res.*, 29, 1673–1683, 2002.
- Rodgers, C. D.: *Inverse Methods for Atmospheric Sounding: Theory and Practice*, Ser. Atmos. Oceanic Planet. Phys., Vol. 2, F. W. Taylor, World Sci., Hackensack, NY, USA, 2000.
- Roscoe, H. K., Van Roozendael, M., Fayt, C., du Piesanie, A., Abuhassan, N., Adams, C., Akrami, M., Cede, A., Chong, J., Clémer, K., Friess, U., Gil Ojeda, M., Goutail, F., Graves, R., Griesfeller, A., Grossmann, K., Hemerijckx, G., Hendrick, F., Herman, J., Hermans, C., Irie, H., Johnston, P. V., Kanaya, Y., Kreher, K., Leigh, R., Merlaud, A., Mount, G. H., Navarro, M., Oetjen, H., Pazmino, A., Perez-Camacho, M., Peters, E., Pinardi, G., Puentedura, O., Richter, A., Schönhardt, A., Shaiganfar, R., Spinei, E., Strong, K., Takashima, H., Vlemmix, T., Vrekoussis, M., Wagner, T., Wittrock, F., Yela, M., Yilmaz, S., Boersma, F.,

- Hains, J., Kroon, M., PETERS, A., and Kim, Y. J.: Intercomparison of slant column measurements of NO<sub>2</sub> and O<sub>4</sub> by MAX-DOAS and zenith-sky UV and visible spectrometers, *Atmos. Meas. Tech.*, 3, 1629–1646, doi:10.5194/amt-3-1629-2010, 2010.
- Solomon, S., Schmeltekopf, A. L., and Sanders, R. W.: On the interpretation of zenith sky measurements, *J. Geophys. Res.*, 92, 8311–8319, doi:10.1029/JD092iD07p08311, 1987.
- Solomon, S., Portmann, R. W., Sanders, R. W., Daniel, J. S., Madsen, W., Bartram, B., and Dutton, E. G.: On the role of nitrogen dioxide in the absorption of solar radiation, *J. Geophys. Res.*, 104, 12047–12058, doi:10.1029/1999JD900035, 1999.
- Spurr, R.: LIDORT and VLIDORT: Linearized pseudo-spherical scalar and vector discrete ordinate radiative transfer models for use in remote sensing retrieval problems, in: *Light Scattering Reviews*, edited by: Kokhanovsky, A., Vol. 3, Springer, 2008.
- Valks, P., Pinardi, G., Richter, A., Lambert, J.-C., Hao, N., Loyola, D., Van Roozendael, M., and Emmadi, S.: Operational total and tropospheric NO<sub>2</sub> column retrieval for GOME-2, *Atmos. Meas. Tech.*, 4, 1491–1514, doi:10.5194/amt-4-1491-2011, 2011.
- Vandaele, A.-C., Hermans, C., Simon, P. C., Carleer, M., Colin, R., Fally, S., Mérienne, M.-F., Jenouvrier, A., and Coquart, B.: Measurements of the NO<sub>2</sub> absorption cross-section from 42000 cm<sup>-1</sup> to 10000 cm<sup>-1</sup> (238–1000 nm) at 220 K and 294 K, *J. Quant. Spectrosc. Ra.*, 59, 171–184, 1998.
- Van Roozendael, M. and Hendrick, F.: Recommendations for NO<sub>2</sub> column retrieval from NDACC zenith-sky UV-VIS spectrometers, BIRA-IASB, Uccle, Belgium, 2012, available at: [http://ndacc-uvvis-wg.aeronomie.be/tools/NDACC\\_UVVIS-WG\\_NO2settings\\_v4.pdf](http://ndacc-uvvis-wg.aeronomie.be/tools/NDACC_UVVIS-WG_NO2settings_v4.pdf) (last access: 24 October 2014), 2014.
- Van Roozendael, M., De Mazière, M., and Simon, P. C.: Ground-based visible measurements at the Jungfraujoch station since 1990, *J. Quant. Spectrosc. Ra.*, 52, 231–240, 1994.
- Vlemmix, T., PETERS, A. J. M., Berkhout, A. J. C., Gast, L. F. L., Wang, P., and Levelt, P. F.: Ability of the MAX-DOAS method to derive profile information for NO<sub>2</sub>: can the boundary layer and free troposphere be separated?, *Atmos. Meas. Tech.*, 4, 2659–2684, doi:10.5194/amt-4-2659-2011, 2011.
- Wagner, T., Dix, B., Friedeburg, C. v., Frieß, U., Sanghavi, S., Sinreich, R., and Platt, U.: MAX-DOAS O<sub>4</sub> measurements: a new technique to derive information on atmospheric aerosols – principles and information content, *J. Geophys. Res.*, 109, D22205, doi:10.1029/2004JD004904, 2004.

- Wagner, T., Burrows, J. P., Deutschmann, T., Dix, B., von Friedeburg, C., Frieß, U., Hendrick, F., Heue, K.-P., Irie, H., Iwabuchi, H., Kanaya, Y., Keller, J., McLinden, C. A., Oetjen, H., Palazzi, E., Petritoli, A., Platt, U., Postlyakov, O., Pukite, J., Richter, A., van Roozendaal, M., Rozanov, A., Rozanov, V., Sinreich, R., Sanghavi, S., and Wittrock, F.: Comparison of box-air-mass-factors and radiances for Multiple-Axis Differential Optical Absorption Spectroscopy (MAX-DOAS) geometries calculated from different UV/visible radiative transfer models, *Atmos. Chem. Phys.*, 7, 1809–1833, doi:10.5194/acp-7-1809-2007, 2007.
- Wagner, T., Ibrahim, O., Shaiganfar, R., and Platt, U.: Mobile MAX-DOAS observations of tropospheric trace gases, *Atmos. Meas. Tech.*, 3, 129–140, doi:10.5194/amt-3-129-2010, 2010.
- Wagner, T., Beirle, S., Brauers, T., Deutschmann, T., Frieß, U., Hak, C., Halla, J. D., Heue, K. P., Junkermann, W., Li, X., Platt, U., and Pundt-Gruber, I.: Inversion of tropospheric profiles of aerosol extinction and HCHO and NO<sub>2</sub> mixing ratios from MAX-DOAS observations in Milano during the summer of 2003 and comparison with independent data sets, *Atmos. Meas. Tech.*, 4, 2685–2715, doi:10.5194/amt-4-2685-2011, 2011.
- Wang, S., Zhou, B., Wang, Z., Yang, S., Hao, N., Valks, P., Trautmann, T., and Chen, L.: Remote sensing of NO<sub>2</sub> emission from the central urban area of Shanghai (China) using the mobile DOAS technique, *J. Geophys. Res.*, 117, D13305, doi:10.1029/2011JD016983, 2012.
- Wittrock, F., Oetjen, H., Richter, A., Fietkau, S., Medeke, T., Rozanov, A., and Burrows, J. P.: MAX-DOAS measurements of atmospheric trace gases in Ny-Ålesund – Radiative transfer studies and their application, *Atmos. Chem. Phys.*, 4, 955–966, doi:10.5194/acp-4-955-2004, 2004.
- World Health Organization: Review of Evidence on Health Aspects of Air Pollution (REVIHAAP) – Technical Report, WHO Regional Office for Europe, Copenhagen, Denmark, 302 pp., 2013.

**Table 1.** Main DOAS analysis parameter settings for NO<sub>2</sub> slant column spectral fit, in accordance with the NDACC UV-Vis Working Group recommendations (Van Roozendaal and Hendrick, 2012).

| Parameter                     | Settings   |
|-------------------------------|--|
| Fitting interval              | 425–490 nm   |
| Wavelength calibration method | Calibration based on reference solar atlas (Chance and Kurucz, 2010) |
| Cross-sections                |  |
| NO <sub>2</sub>               | Vandaele et al. (1998), 298 K  |
| O <sub>3</sub>                | Bogumil et al. (2003), 223 K   |
| H <sub>2</sub> O              | Harder and Brault (1997)   |
| O <sub>4</sub>                | Hermans et al. (2003)  |
| Ring effect correction method | Chance and Spurr (1997)  |
| Polynomial term               | Polynomial of order 5  |
| Intensity offset correction   | Slope  |

**Table 2.** Error budget on the retrieved tropospheric NO<sub>2</sub> VCDs. The typical relative and absolute errors (in percent and 10<sup>15</sup> molec cm<sup>-2</sup>, respectively) are given for low (below 33th percentile or < 0.6 × 10<sup>16</sup> molec cm<sup>-2</sup>), moderate (between 33th and 66th percentile or 0.6 and 1.0 × 10<sup>16</sup> molec cm<sup>-2</sup>) and high (above 66th percentile or > 1.0 × 10<sup>16</sup> molec cm<sup>-2</sup>) NO<sub>2</sub> TVCD values, respectively. The last column gives the typical uncertainties on all retrieved TVCDs.

| Error source           | Low TVCD   | Mod TVCD   | High TVCD  | Total TVCD |
|------------------------|------------|------------|------------|------------|
| $\sigma_{\text{DSCD}}$ | 14 % (0.5) | 6 % (0.4)  | 3 % (0.5)  | 8 % (0.5)  |
| $\sigma_{\text{RSCD}}$ | 40 % (1.3) | 16 % (1.3) | 9 % (1.3)  | 22 % (1.3) |
| $\sigma_{\text{SSCD}}$ | 20 % (0.8) | 19 % (1.5) | 19 % (3.1) | 19 % (1.8) |
| $\sigma_{\text{TAMF}}$ | 13 % (0.2) | 14 % (0.2) | 15 % (0.2) | 14 % (0.2) |
| $\sigma_{\text{TVCD}}$ | 38 % (1.3) | 24 % (1.9) | 21 % (3.5) | 28 % (2.2) |

975

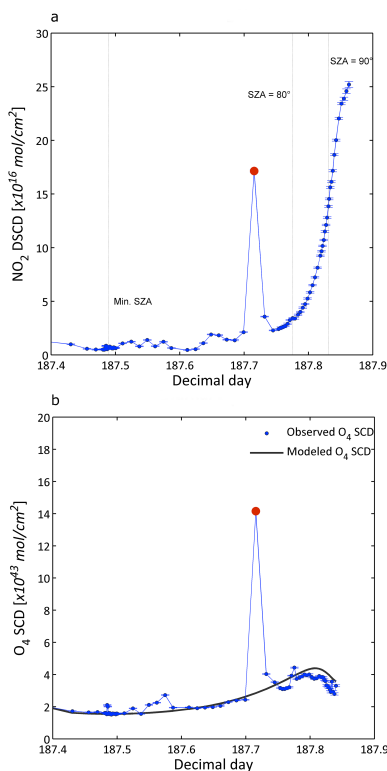


**Figure 1.** Example of a NO<sub>2</sub> enhancement event, due to multiple scattering, on day 187 (6 July 2009). Both **(a)** the NO<sub>2</sub> DSCD and **(b)** the O<sub>4</sub> SCD diurnal cycles show a large spike at approximately 17:10 LT (red dot).

976

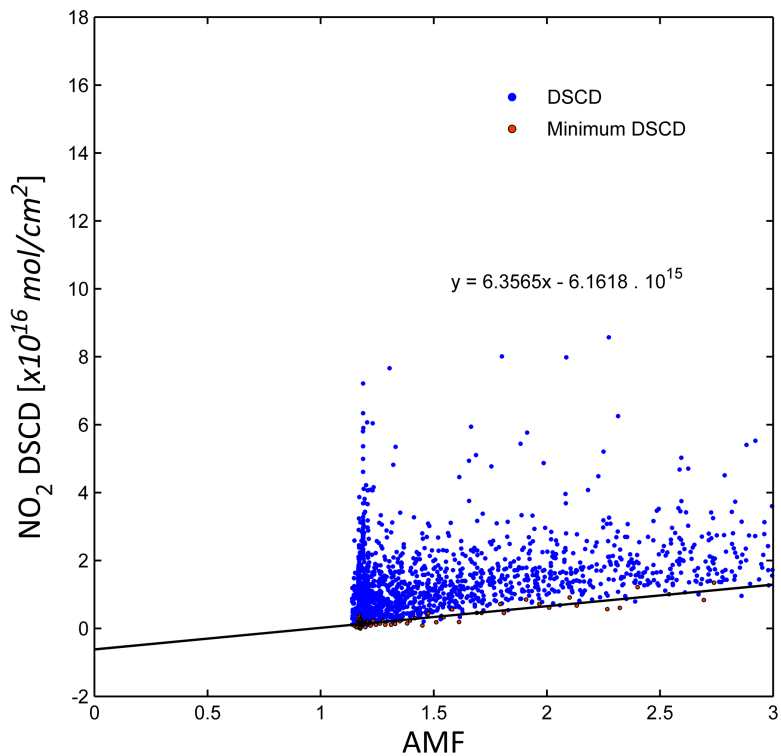


**Figure 2.** A value of  $6.2 \times 10^{15}$  molec $\text{cm}^{-2}$  is determined for the residual amount in the reference spectrum (RSCD) based on application of the MLE method. The ZS noon spectrum was selected on 21 June 2009 at 12:16 LT.

977

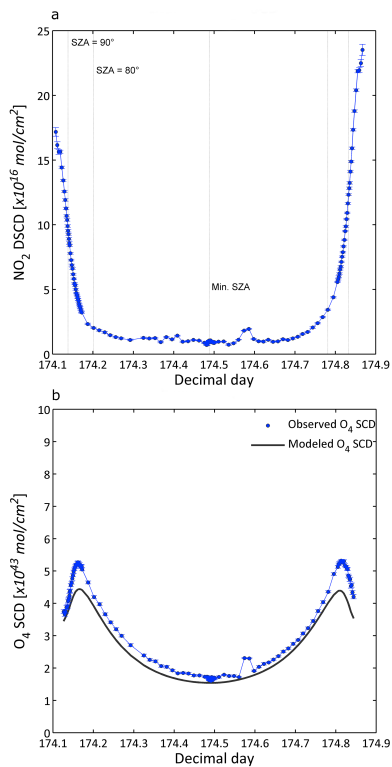


**Figure 3.** NO<sub>2</sub> and O<sub>4</sub> slant column diurnal cycle for the non-polluted, clear-sky reference day 174 (23 June 2009). **(a)** The NO<sub>2</sub> DSCD diurnal cycle, dominated by stratospheric absorption, has a typical u-shape with minimal tropospheric perturbations. **(b)** The observed O<sub>4</sub> SCD diurnal cycle largely follows the smooth curve, modeled with the RTM UVspec/DISORT.

978

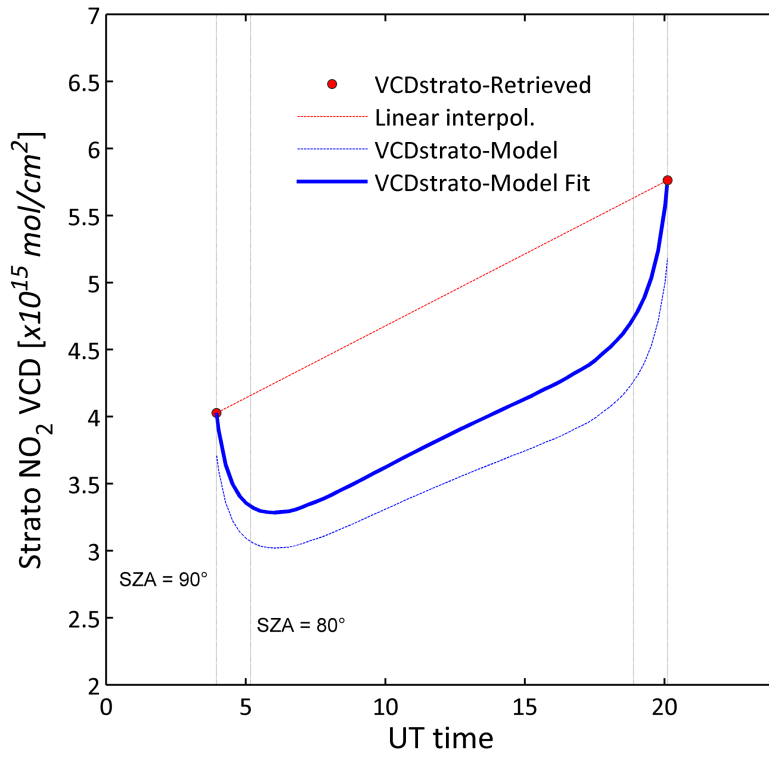


**Figure 4.** Representation of the retrieved stratospheric  $\text{NO}_2$  VCDs at  $90^\circ$  SZA sunrise and sunset for reference day 174 (Sect. 3.4.1) and fit of the  $\text{NO}_2$  diurnal cycle modeled with the photochemical model PSCBOX.

979

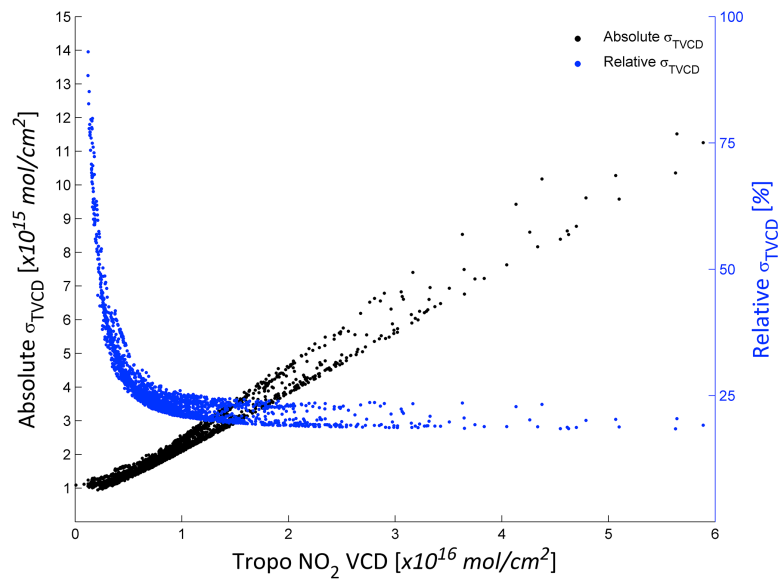


**Figure 5.** Overall absolute and relative errors ( $\sigma_{\text{TVCD}}$ ) on the retrieved  $\text{NO}_2$  TVCDs.

980

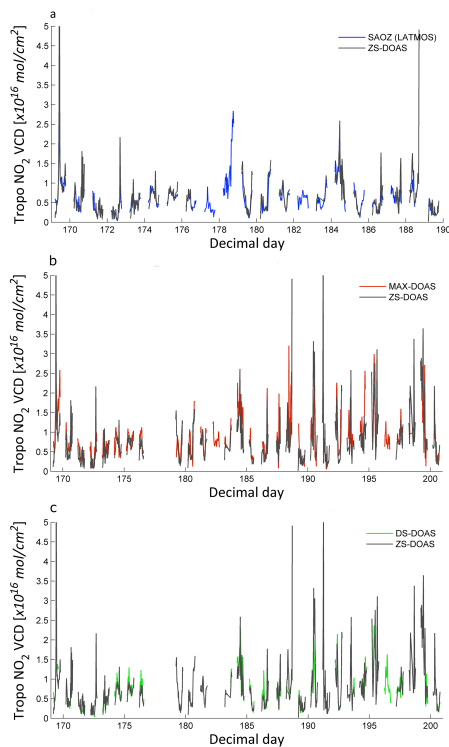


**Figure 6.** Comparisons of the tropospheric NO<sub>2</sub> VCD time series, between (a) ZS-DOAS and SAOZ, (b) ZS-DOAS and MAX-DOAS, and (c) ZS-DOAS and DS-DOAS. TVCDs are binned and averaged in timeslots of 30 min.

981

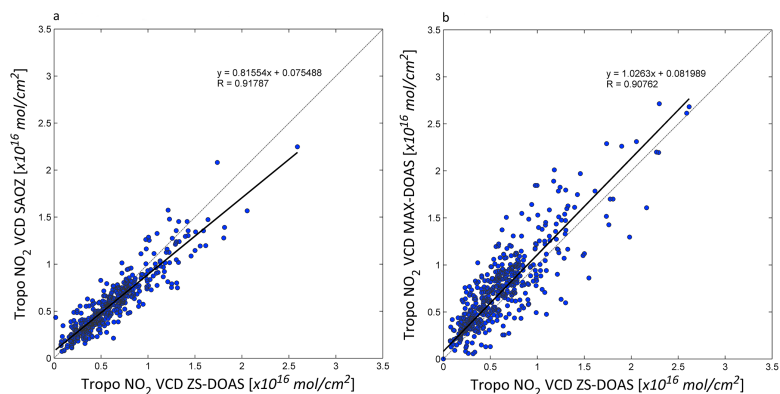


**Figure 7.** Scatter plot and linear regression analysis of the TVCDs retrieved for the whole time series from (a) ZS-DOAS and SAOZ, and (b) ZS-DOAS and MAX-DOAS, respectively. TVCDs are binned and averaged in 30 min bins.

982

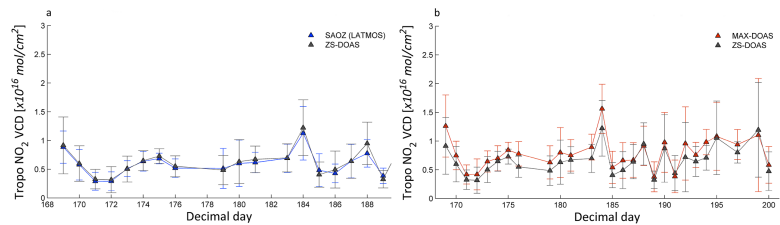


**Figure 8.** TVCD daily mean time series for **(a)** ZS-DOAS and SAOZ, and **(b)** ZS-DOAS and MAX-DOAS, respectively.

983

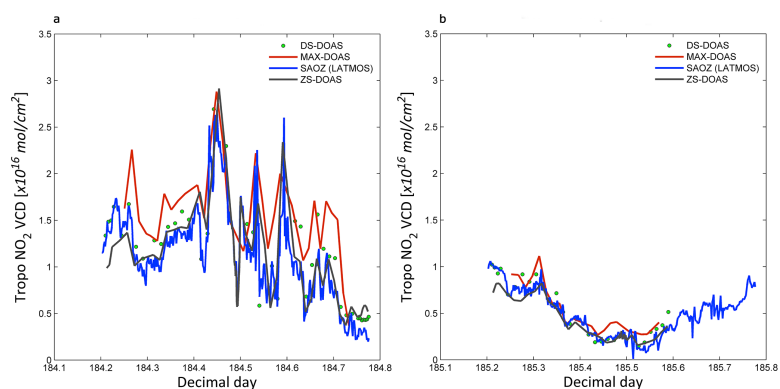


**Figure 9.** TVCD diurnal variation for **(a)** a day with many pollution events (day 184) and **(b)** a non-polluted day (185), respectively. To avoid smoothing due to interpolation between the limited number of retrievals and for a better interpretation of the results, DS-DOAS retrievals are represented as point data here.

984

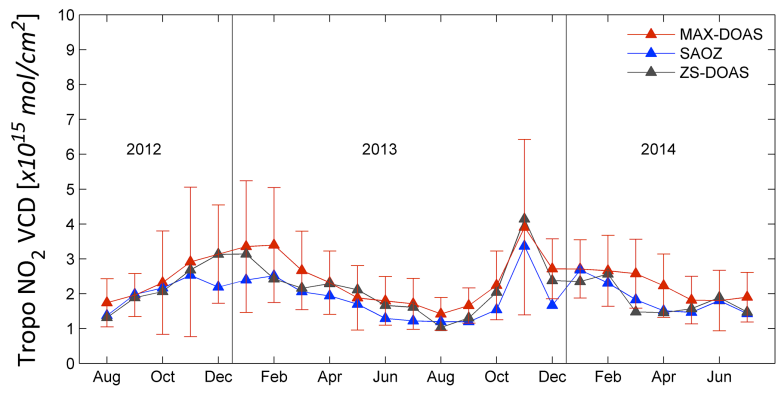


**Figure 10.** TVCD monthly mean time series at the OHP station for ZS-DOAS, SAOZ and MAX-DOAS for the period August 2012–July 2014. The error bars on the MAX-DOAS data points correspond to the one-sigma SD.

## RESEARCH ARTICLE

10.1002/2014JD022657

## Key Points:

- Development of OMI SO<sub>2</sub> vertical column algorithm
- Results are compared to ground-based and satellite data sets
- The algorithm is able to detect weak SO<sub>2</sub> sources

## Supporting Information:

- Readme
- Figure S1
- Figure S2
- Figure S3

## Correspondence to:

N. Theys,  
theys@aeronomie.be

## Citation:

Theys, N., et al. (2015), Sulfur dioxide vertical column DOAS retrievals from the Ozone Monitoring Instrument: Global observations and comparison to ground-based and satellite data, *J. Geophys. Res. Atmos.*, 120, 2470–2491, doi:10.1002/2014JD022657.

Received 2 OCT 2014

Accepted 16 FEB 2015

Accepted article online 20 FEB 2015

Published online 18 MAR 2015

## Sulfur dioxide vertical column DOAS retrievals from the Ozone Monitoring Instrument: Global observations and comparison to ground-based and satellite data

N. Theys<sup>1</sup>, I. De Smedt<sup>1</sup>, J. van Gent<sup>1</sup>, T. Danckaert<sup>1</sup>, T. Wang<sup>1,2</sup>, F. Hendrick<sup>1</sup>, T. Stavrou<sup>1</sup>, S. Bauduin<sup>3</sup>, L. Clarisse<sup>3</sup>, C. Li<sup>4,5</sup>, N. Krotkov<sup>5</sup>, H. Yu<sup>1</sup>, H. Brenot<sup>1</sup>, and M. Van Roozendael<sup>1</sup>

<sup>1</sup>Belgian Institute for Space Aeronomy, Brussels, Belgium, <sup>2</sup>Institute of Atmospheric Physics, Chinese Academy of Sciences, Beijing, China, <sup>3</sup>Spectroscopie de l'Atmosphère, Service de Chimie Quantique et Photophysique, Université Libre de Bruxelles, Brussels, Belgium, <sup>4</sup>Earth System Science Interdisciplinary Center, University of Maryland, College Park, Maryland, USA, <sup>5</sup>NASA Goddard Space Flight Center, Greenbelt, Maryland, USA

**Abstract** We present a new data set of sulfur dioxide (SO<sub>2</sub>) vertical columns from observations of the Ozone Monitoring Instrument (OMI)/AURA instrument between 2004 and 2013. The retrieval algorithm used is an advanced Differential Optical Absorption Spectroscopy (DOAS) scheme combined with radiative transfer calculation. It is developed in preparation for the operational processing of SO<sub>2</sub> data product for the upcoming TROPOspheric Monitoring Instrument/Sentinel 5 Precursor mission. We evaluate the SO<sub>2</sub> column results with those inferred from other satellite retrievals such as Infrared Atmospheric Sounding Interferometer and OMI (Linear Fit and Principal Component Analysis algorithms). A general good agreement between the different data sets is found for both volcanic and anthropogenic SO<sub>2</sub> emission scenarios. We show that our algorithm produces SO<sub>2</sub> columns with low noise and is able to provide accurate estimates of SO<sub>2</sub>. This conclusion is supported by important validation results over the heavily polluted site of Xianghe (China). Nearly 4 years of OMI and ground-based multiaxis DOAS SO<sub>2</sub> columns are compared, and an excellent match is found. We also highlight the improved performance of the algorithm in capturing weak SO<sub>2</sub> sources by detecting shipping SO<sub>2</sub> emissions in long-term averaged data, an unreported measurement from space.

### 1. Introduction

Sulfur dioxide (SO<sub>2</sub>) is emitted to the atmosphere from anthropogenic and natural sources. Anthropogenic emissions are mostly from combustion of fossil fuels (coal and oil) and metal smelting. The main natural source of nonvolcanic sulfur in the boundary layer is the oxidation of biogenic dimethyl sulfide from the oceans, but in the upper troposphere and lower stratosphere (UTLS), volcanic eruptions constitute the largest natural contributor of SO<sub>2</sub>. Sulfur dioxide is depleted in the atmosphere either through deposition or oxidation mechanisms, the latter leading to aerosol formation. The reactive compounds can have adverse effects on surrounding environments (acid rain), air quality [Chin and Jacob, 1996], weather, clouds, and climate [Intergovernmental Panel on Climate Change, 2013]. In the stratosphere, the forcing from sulfate aerosols can have a transient impact on global climate for several years after strong volcanic eruptions [Robock, 2000].

Satellite observations of SO<sub>2</sub> are a key data source for assessing global SO<sub>2</sub> budget and chemistry, studying air pollution, and monitoring volcanic activity and related hazardous clouds. In particular, nadir ultraviolet (UV) sounding is well suited to detect SO<sub>2</sub> from both volcanic and anthropogenic sources, owing to good sensitivity to SO<sub>2</sub> in the lower troposphere. SO<sub>2</sub> has strong absorption bands in the UV spectral range, and the total SO<sub>2</sub> vertical column density (VCD, hereafter expressed in Dobson Unit—1 DU = 2.69 × 10<sup>16</sup> molecules cm<sup>-2</sup>) can be retrieved from satellite measurements of solar backscattered UV radiation, albeit with significant uncertainty. Satellite UV remote sensing of SO<sub>2</sub> VCD has been achieved by the following instruments: Total Ozone Mapping Spectrometer [Krueger et al., 1995; Carn et al., 2004], Global Ozone Monitoring Experiment (GOME-2) [Eisinger and Burrows, 1998; Khokhar et al., 2005], Scanning Imaging Absorption Spectrometer for Atmospheric Chartography (SCIAMACHY) [Richter et al., 2006; Lee et al., 2009], GOME-2 [Richter et al., 2009a;

Nowlan et al., 2011; Rix et al., 2012], Ozone Monitoring Instrument (OMI) [Krotkov et al., 2006; Yang et al., 2007], and Ozone Mapping and Profiler Suite (OMPS) [Yang et al., 2013]. The OMI UV mapper is particularly appealing as it combines hyperspectral measurement capability at high signal-to-noise ratio with high spatial resolution (pixel size is  $13 \times 24 \text{ km}^2$  at nadir) and daily global coverage [Levelt et al., 2006]. Sulfur dioxide retrievals from OMI have been used quite extensively to measure volcanic degassing (a review is provided by Carn et al. [2013]) and anthropogenic emissions [e.g., Carn et al., 2007; Krotkov et al., 2008; Li et al., 2010; Fioletov et al., 2011; Lu et al., 2013]. Recently, Fioletov et al. [2013] showed that long-term averaged  $\text{SO}_2$  retrievals by OMI, GOME-2, and SCIAMACHY were generally in good quantitative agreement over large emission sources, when using consistent assumptions for the radiative transfer and after applying local bias filtration techniques. They also demonstrated the improved detection of small sources by OMI compared to the other sensors.

In this paper, we present a new OMI algorithm to determine  $\text{SO}_2$  columns by applying a multiwindows Differential Optical Absorption Spectroscopy (DOAS) scheme [Platt and Stutz, 2008], which results in robust retrievals with low noise. The presented retrieval scheme will form the basis of the algorithm for the operational level 2  $\text{SO}_2$  data product from the forthcoming TROPospheric Monitoring Instrument (TROPOMI) instrument on board the Sentinel-5 Precursor mission [Veeffkind et al., 2012]. With improved signal-to-noise level and spatial resolution (pixel size  $\sim 7 \times 7 \text{ km}^2$ ) compared to OMI, the TROPOMI sensor will have enhanced capabilities for global  $\text{SO}_2$  measurements. The motivation of this study is to demonstrate the performance of the TROPOMI algorithm using OMI measured spectra for several examples of volcanic and anthropogenic  $\text{SO}_2$  emissions. We evaluate our  $\text{SO}_2$  product through comparisons with other satellite retrievals in the thermal infrared (Infrared Atmospheric Sounding Interferometer, IASI) and ultraviolet. In particular, the new  $\text{SO}_2$  columns are compared to those from the standard OMI  $\text{SO}_2$  products. Presently, two algorithms are employed for the OMI standard products.

1. The Linear Fit (LF) OMI  $\text{SO}_2$  retrieval algorithm [Yang et al., 2007]. This algorithm is used to produce retrievals of  $\text{SO}_2$  total columns for a set of hypothetical  $\text{SO}_2$  profiles with  $\text{SO}_2$  distributed in the lower troposphere, the midtroposphere, and the lower stratosphere (STL), corresponding to  $\text{SO}_2$  plumes from volcanic degassing, modest eruption, and strong eruption, respectively. It exploits the residuals from OMI total column  $\text{O}_3$  retrievals at 10 discrete wavelengths between 310.8 and 360.15 nm. Shorter wavelengths are dropped in the retrievals for large volcanic plumes, in order to reduce negative biases due to saturation of  $\text{SO}_2$  absorption. A sliding median residual correction technique is applied in the LF algorithm to reduce retrieval biases.
2. The new principal component analysis (PCA) OMI  $\text{SO}_2$  retrieval algorithm [Li et al., 2013]. This algorithm applies the PCA technique to OMI-measured radiances between 310.5 and 340 nm to extract principal components (PCs) from each row on an orbital basis. The leading PCs that capture a large fraction of the spectral variance are associated with various processes that interfere with  $\text{SO}_2$  signals, including  $\text{O}_3$  absorption, the Ring effect, etc. These PCs are fitted along with precomputed  $\text{SO}_2$  Jacobians to produce estimates of the  $\text{SO}_2$  total column. No bias correction is currently applied in the PCA algorithm. It has replaced the Band Residual Difference algorithm [Krotkov et al., 2006] as the operational algorithm for the standard OMI planetary boundary layer (PBL)  $\text{SO}_2$  data (assuming  $\text{SO}_2$  mostly in the PBL). Compared with the previous OMI PBL  $\text{SO}_2$  product, the PCA product shows large reduction in both systematic bias and retrieval noise. As shown below, the DOAS and PCA algorithms are in good agreement and have comparable performances, giving confidence to both approaches.

Another important part of the present study is the validation of the retrievals against ground-based multiaxis (MAX-)DOAS measurements at Xianghe (suburban Beijing, China). The long-term MAX-DOAS  $\text{SO}_2$  measurements improve upon previous validation studies based on in situ measurements [Krotkov et al., 2008; Lee et al., 2009; He et al., 2012] that suffer from spatial-temporal sampling and/or extrapolation issues. Finally, the improvements in  $\text{SO}_2$  data are demonstrated using long-term averages that show evidence for  $\text{SO}_2$  pollution from shipping that has not been observed from space before.

In section 2 we give an overview of OMI and the algorithm to retrieve  $\text{SO}_2$  vertical columns. Examples of results and comparison to ground-based and satellite data are presented for cases with  $\text{SO}_2$  from volcanic (section 3.1) and anthropogenic sources (section 3.2). Conclusions are given in section 4.

## 2. Algorithm Description

The Ozone Monitoring Instrument (OMI) is a nadir-viewing instrument on the EOS-Aura satellite of NASA (launched in July 2004) flying in a Sun-synchronous polar orbit with an equator crossing time of about 13:38 local time in the ascending node. OMI is an imaging spectrograph that measures reflected-backscattered sunlight in the ultraviolet-visible range from 270 nm to 500 nm with a spectral resolution of about 0.5 nm [Levelt *et al.*, 2006]. OMI is a CCD (charge-coupled device) push-broom instrument, recording the complete spectrum in along-track direction, and sensing the atmosphere with a 114° field of view, separated in 60 discrete viewing angles, perpendicular to the flight direction (across track). The OMI spatial swath is 2600 km wide allowing complete global coverage in about 1 day. The OMI ground pixel size varies from 13 × 24 km<sup>2</sup> at nadir to 28 × 150 km<sup>2</sup> at the edges of the swath. Since June 2007, the radiance data of OMI are altered at all wavelengths for some particular viewing directions corresponding to specific rows of the 2-D CCD. This so-called row anomaly (see <http://www.knmi.nl/omi/research/product/rowanomaly-background.php>) is due to a partial blockage affecting the nadir-viewing port of the sensor. It changes with time and position on the orbit; from 2008 onward, it affects seriously the quality of some measured spectra and hence reduces the spatial coverage (section 2.2).

The algorithm to retrieve SO<sub>2</sub> vertical columns from OMI measurements is based on three main steps, described in the next sections, that include analysis of the measured spectra, background correction scheme, and radiative transfer simulations.

### 2.1. DOAS Retrieval

OMI radiance measurements from Level 1 data version 2.13 are analyzed using the DOAS method for the determination of the columnar concentration of SO<sub>2</sub> along the effective light path through the atmosphere (hereafter referred as slant column density, SCD). Briefly, absorption cross sections of relevant atmospheric gases are adjusted by a nonlinear least squares fit procedure to the log ratio of a measured earthshine spectrum and a reference spectrum in a given wavelength interval. The DOAS fit also includes additional closure terms for the Ring effect and contributions from broadband and instrumental spectral features.

In practice, SO<sub>2</sub> slant columns have been retrieved with QDOAS [Fayt and Van Roozendaal, 2001; Danckaert *et al.*, 2012], a versatile software for trace gas retrievals in the UV-visible spectral range, which has been adapted for OMI spectra. In particular, each row of OMI is treated in the analysis as a separate detector (hence characterized by a proper wavelength-dependent slit function). This also holds true for the wavelength calibration step.

The DOAS analysis settings used to retrieve SO<sub>2</sub> SCDs are detailed in Table 1. As a baseline, SO<sub>2</sub> is retrieved in the sensitive 312–326 nm window (labeled w1 in the following), which includes strong SO<sub>2</sub> absorption bands (Figure 1). In this interval, the absorption is dominated by total ozone, and two ozone cross sections at 228 K and 243 K are included in the fit. Furthermore, two additional pseudo cross sections are introduced in the analysis to better cope with nonlinear effects due to ozone absorption. Following the formulation of Pukite *et al.* [2010], these spectra correspond to the two terms of the first-order Taylor expansion of the ozone optical depth. This approach allows us to improve the results at high solar zenith angle (SZA; ≥45°) by reducing the fitting residuals (up to a factor of two) and the bias on the SO<sub>2</sub> slant columns (see next section). We have estimated the noise level on the retrieved SO<sub>2</sub> SCDs by the SCD data scatter (1σ value) around the mean for solar zenith angle (SZA) bins and by excluding polluted regions and strong volcanic eruptions. It is typically 0.2–0.5 DU depending on the solar zenith angle. Tests using the 315–326 nm fitting interval [Richter *et al.*, 2006; Rix *et al.*, 2012] increase the data scatter by a factor of 2, as expected by the noninclusion in the fit of the strong SO<sub>2</sub> band peaking at around 313 nm. We have done further tests by extending the fitting window to 310.5–326 nm (including one more SO<sub>2</sub> band), but these show only a small improvement as for the data scatter, probably because of the competing strong ozone absorption in the short UV (Figure 1) causing a drop in intensity (and in signal-to-noise ratio). Therefore, we have not selected the fitting window 310.5–326 nm as the sensitivity to SO<sub>2</sub> absorption in the lower troposphere is somewhat lower than for the 312–326 nm range (mostly because of increasing ozone absorption below 312 nm).

Whereas SO<sub>2</sub> retrieval in w1 is adequate for small SO<sub>2</sub> column amount, it has limited accuracy once the SO<sub>2</sub> signal is large (for scenes with high SO<sub>2</sub> amounts from volcanic eruptions), typically leading to a saturation of

**Table 1.** DOAS Settings Used to Retrieve SO<sub>2</sub> Columns From OMI Spectra<sup>a</sup>

|   |   |
|---|---|
| Fitting Intervals 1 and 2 (UV-2 Channel:307–383 nm) | 312–326 nm (w1), 325–335 nm (w2)  |
| Cross sections                                      | SO <sub>2</sub> 203 K; <i>Bogumil et al.</i> [2003]<br>O <sub>3</sub> 228 K and 243 K with I <sub>0</sub> correction; <i>Brion et al.</i> [1998]<br>Pseudo O <sub>3</sub> cross sections ( $\lambda\sigma_{O_3}$ , $\sigma_{O_3}^2$ ); <i>Puķite et al.</i> [2010]<br>Ring effect: 2 eigenvectors ( <i>Vountas et al.</i> [1998]) generated for 20° and 87° solar zenith angles using LIDORT-RRS; <i>Spurr</i> [2008] |
| Polynomial  | Fifth Order   |
| Fitting interval 3 (VIS channel:349–504 nm)         | 360–390 nm (w3)   |
| Cross sections                                      | SO <sub>2</sub> <i>Hermans et al.</i> [2009] extrapolated at 203 K<br>NO <sub>2</sub> 220 K; <i>Vandaele et al.</i> [1998]<br>O <sub>2</sub> -O <sub>2</sub> ; <i>Greenblatt et al.</i> [1990]<br>Ring effect: single spectrum; <i>Chance and Spurr</i> [1997]  |
| Polynomial  | Fourth order  |
| Intensity offset correction                         | Linear offset   |
| Spectrum shift and stretch                          | Fitted  |
| Spectral spikes removal procedure                   | <i>Richter et al.</i> [2011]  |
| Reference spectrum                                  | Daily averaged earthshine spectrum in Pacific region (10°S–10° N, 160°E–120°W); separate spectrum for each detector row   |
| Fitting interval selection criteria                 | w1: baseline<br>w2: SCD1 > 40 DU or SCD1 > 15 DU if fit residual w1 > 10 <sup>-2</sup><br>SCD2 > SCD1<br>w3: SCD2 > 250 DU and SCD3 > SCD2  |

<sup>a</sup>The cross sections are convolved with the instrumental wavelength-dependent slit functions [*Dobber et al.*, 2006] separately for each of the 60 detector rows.

the retrieved SO<sub>2</sub> SCD due to nonlinear retrieval effects from strong absorption by SO<sub>2</sub> itself [e.g., *Richter et al.*, 2009; *Yang et al.*, 2007]. To overcome this problem, alternative fitting windows (w2 and w3) are considered: 325–335 nm [*Hörmann et al.*, 2013] and 360–390 nm for extreme SO<sub>2</sub> loadings [*Bobrowski et al.*, 2010]. We have conducted several sensitivity tests, based on synthetic and measured spectra, to assess the best use of the different fitting intervals. SCD<sub>*i*</sub> have been retrieved for all w<sub>*i*</sub> (*i* = 1, 2, 3), and the applicability of the three fitting windows was determined empirically by means of scatterplots (see e.g., Figure S1 in the supporting information). The combined use of the three data sets is achieved according to the criteria given in Table 1. Note that SO<sub>2</sub> cross sections are used for a fixed temperature of 203 K, which is valid for a volcanic SO<sub>2</sub> plume in the tropical UTLS. For lower plumes and anthropogenic pollution, the retrievals in w1 tend to underestimate the SO<sub>2</sub> SCDs by up to 15%.

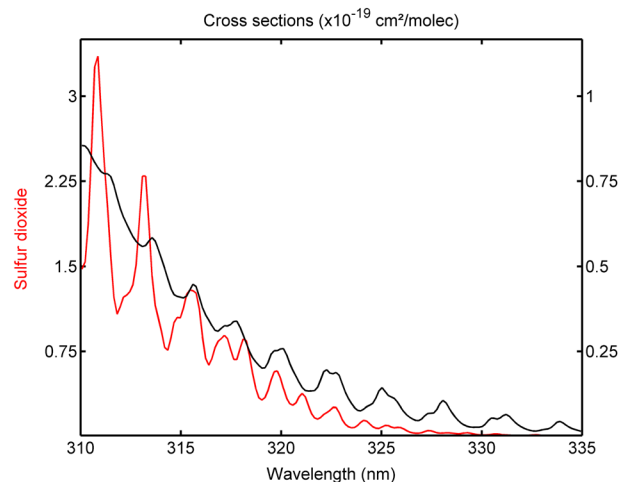


**Figure 1.** Absorption cross sections of SO<sub>2</sub> (203 K) and O<sub>3</sub> (228 K) at the spectral resolution of OMI between 310 and 335 nm.

## 2.2. Treatment of the Row Anomaly and Background Correction

The next step of the algorithm deals with filtering of the pixels affected by the row anomaly. The row anomaly flag included in the OMI operational L1B product has the tendency to classify more pixels as affected than strictly necessary; therefore, we have set up a new identification of row anomaly-affected pixels. We first apply a criterion that removes all data of a given day for certain across-track positions. The selection is based on w1 fitting residuals over a latitude band around the equator (10°S–10°N), which show typically anomalous high values for the affected rows. A given row is

classified as affected by the row anomaly if the mean residual over the equator is larger than the corresponding residual averaged for all rows, by more than 20%. To avoid contamination by a possible strong volcanic SO<sub>2</sub> signal or an artifact (e.g. due to the South Atlantic Anomaly), we only consider the pixels with slant columns less than 5 DU and residuals lower than  $4 \times 10^{-3}$  for the calculation of the averages. After this first selection, we apply a second criterion to filter data affected by the row anomaly. It is a simple selection based on the fitting residuals and is meant for an anomaly corrupting only a part of the orbit: pixels with fitting residuals larger than  $4 \times 10^{-3}$ , but SCDs lower than 5 DU are rejected. The condition on the SCD is used to keep the pixels with real elevated SO<sub>2</sub> (and hence high-fitting residuals). The above-described filtering of the row anomaly proved to be a good compromise between the number of retained observations and the data quality.

After the data filtering step, a background correction is applied to the resulting SCDs. This is particularly important for retrievals in the baseline window. SCDs typically show unphysical nonzero columns over certain clean regions (e.g. the tropical pacific, deserts, and high-altitude regions). While the reason for this behavior is not completely clear, the observed bias is time dependent and is more pronounced for strong ozone absorption (at high latitudes). The correction we use here is based on a parameterization of the background values that are then subtracted from the measurements. The scheme first removes pixels with high SZA (>70°) and SCDs larger than 1.5 DU (measurements with presumably real SO<sub>2</sub>) and then calculates the offset correction by averaging the SO<sub>2</sub> data on an ozone slant column grid. This is done independently for each across-track position and hemisphere, and the correction makes use of measurements averaged over a time period of two weeks around the measurement of interest (to improve the statistics and minimize the impact of a possible extended volcanic SO<sub>2</sub> plume on the averaged values). Figure S2 gives an example of the effect of the background correction and shows that the implemented correction largely solves the SO<sub>2</sub> SCD bias problem.

However, the correction has limitations in its parameterization. The error on the residual SCDs has been estimated by the maximum nonzero SCDs on long-term averaged global maps and is of 0.1–0.15 DU. For the two alternative fitting windows (w2 and w3), the biases are small in comparison to the column amounts expected to be retrieved in these windows (Table 1), but we have, nevertheless, implemented offset corrections using parameterizations of the background slant columns based on latitude, cross-track position, and time (2 weeks moving averages).

### 2.3. Air Mass Factor Calculation

The corrected slant columns are converted into SO<sub>2</sub> vertical column densities by applying air mass factors (AMF = SCD/VCD). The AMFs are calculated using the formulation introduced by *Palmer et al.* [2001]:

$$\text{AMF} = \int_{\text{ground}}^{\text{TOA}} \text{WF}(z)N(z)dz \quad (1)$$

where WF(z) is the so-called scattering-weighting function or box AMF, which characterizes the measurement sensitivity as a function of altitude (z), N(z) is the SO<sub>2</sub> a priori vertical profile shape (normalized SO<sub>2</sub> concentration profile), and the limits of integration are from the ground height to the top of atmosphere.

The weighting functions are determined via a multidimensional linear interpolation of WF look-up tables (three in total, one for each fitting window), generated with the Linearized Discrete Ordinate Radiative Transfer (LIDORT) version 3.3 radiative transfer model [*Spurr*, 2008]. The radiative transfer simulations assume a U.S. standard atmosphere [*Anderson et al.*, 1986] and Lambertian reflectors for the ground and the clouds. The WF look-up tables have six entries, respectively, for the solar zenith angle, viewing zenith angle, relative azimuth angle, surface albedo, effective reflector height (surface or cloud), and total ozone column. The latter is particularly important for accurate sensing of SO<sub>2</sub> in the boundary layer (using the baseline window) where the measurement sensitivity/optical light path is strongly dependent on the absorption of UV radiation by total atmospheric ozone. As a matter of fact, the measurement sensitivity depends on the wavelength, especially in the 312–326 nm range as a result of increased scattering and absorption (see Figure 1 and *Richter* [2009]). We have conducted sensitivity tests to determine effective wavelengths representative of the different fitting intervals. For this, we have generated synthetic spectra for typical observation conditions and SO<sub>2</sub> profiles using the LIDORT model, and we have done closed-loop retrievals (see Figure S3). It turns out from this exercise that calculations at 313, 326, and 375 nm give the best results, for the three fitting windows w1, w2, and w3, respectively. Note that the effective wavelength of 313 nm comes as no surprise because the SO<sub>2</sub> absorption (hence spectral information) is the highest at this wavelength for w1 (Figure 1).

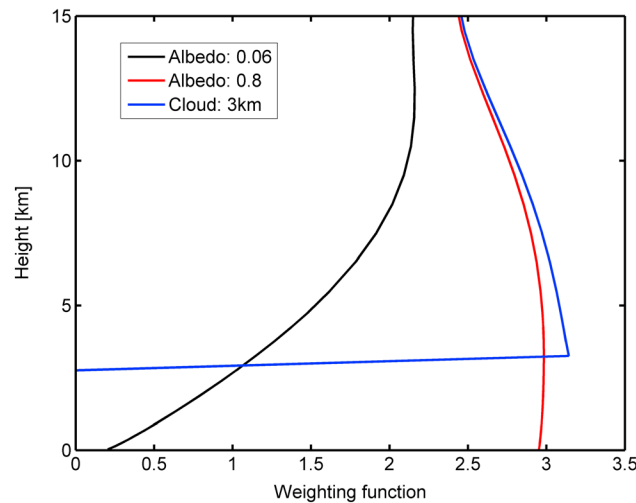


**Figure 2.** Scattering-weighting functions at 313 nm as function of surface albedo (0.06 and 0.8) and for a cloud top at 3 km. Calculations are made for a total ozone column of 385 DU, for a nadir-viewing geometry, and for a solar zenith angle of 40°.

The cloud is considered as a Lambertian reflecting surface, characterized by a single cloud top height and a cloud albedo of 0.8, in line with the assumption made for the OMI cloud product OMCLDO2 [Acarreta et al., 2004]. For partly cloudy pixels, we use the independent pixel approximation:

$$WF(z) = \Phi WF_{cloud}(z) + (1 - \Phi) WF_{clear}(z) \quad (2)$$

where  $\Phi$  is the intensity-weighted cloud radiance fraction [Martin et al., 2002].

$$\Phi = \frac{f_c I_{cloud}}{f_c I_{cloud} + (1 - f_c) I_{clear}} \quad (3)$$

where  $f_c$  is the effective cloud fraction.

The WF look-up tables are used along with the corresponding intensity look-up tables.

An illustration of the weighting functions is given in Figure 2, for clear-sky cases assuming a surface albedo of 0.06 and 0.8, and for a cloudy case with a cloud top height of 3 km. The curves are for a SZA of 40°. Figure 2 shows the typical behavior of the satellite nadir UV measurement sensitivity to an absorber located at different altitudes for various surface albedo situations and for a cloudy scene. Note that the AMF formulation (equations (1) and (2)) accounts implicitly for any SO<sub>2</sub> column below the cloud (the so-called ghost column, not sounded by the satellite) because the integration (equation (1)) is performed down to ground height rather than cloud-top height.

In practice, the WF is evaluated for each pixel based on auxiliary data sets. The total ozone column is from a Level 2 data set of OMI [Bhartia and Wellemeyer, 2002; Koukoulis et al., 2012]. For the surface albedo, we use the climatological monthly minimum Lambertian equivalent reflect (minLER) data from Kleipool et al. [2008]. This database has a spatial resolution of 0.5° × 0.5°. The cloud parameters (cloud fraction and cloud top height) are taken from the OMI operational OMCLDO2 product [Acarreta et al., 2004].

To calculate air mass factors, weighting functions have to be convolved with realistic SO<sub>2</sub> vertical profile shapes (equation (1)). However, the vertical distribution of SO<sub>2</sub> is generally unknown, and it is sometimes even difficult to tell whether the observed SO<sub>2</sub> is of volcanic origin or from pollution. Therefore, the algorithm computes three vertical columns for different hypothetical SO<sub>2</sub> profiles including typical anthropogenic [Krotkov et al., 2006] and volcanic cases. For volcanic SO<sub>2</sub>, we consider two scenarios with 1 km box concentration profiles centered at 7 and 15 km. This approach is similar to other algorithms [Yang et al., 2007; Rix et al., 2012] and aims at representing volcanic plumes injected into the free troposphere and lower stratosphere, respectively. For anthropogenic SO<sub>2</sub>, unlike in previous data, we use daily SO<sub>2</sub> profiles from the global tropospheric chemistry transport model Intermediate Model of the Global and Annual Evolution of Species (IMAGES), extracted at the overpass time of OMI.

The global CTM IMAGESv2 simulates the concentrations of 131 trace gases (among which 41 fast-reacting species) at a horizontal resolution of 2° × 2.5° and at 40 vertical unevenly distributed levels extending from the surface to the lower stratosphere (44 hPa). Details about the current model version are given in Stavrakou et al. [2013]. The model time step is set to 4 h. The effects of diurnal variations in the photolysis rates, kinetic rates, meteorological fields, and the emissions are accounted for through correction factors obtained from a simulation with a 20 min time step [Stavrakou et al., 2009]. These correction factors are then applied to model simulations with longer time steps.

Anthropogenic SO<sub>2</sub> emissions are obtained from the REASv2 inventory [Kurokawa et al., 2013] over Asia, from European Monitoring and Evaluation Programme (EMEP) over Europe (<http://www.ceip.at>), and from the Emissions Database for Global Atmospheric Research (EDGAR3.2) FT2000 inventory for 2000 over the rest of

the world. Emissions of  $\text{SO}_2$  from anthropogenic sources are estimated at 53.8 TgS in 2010 globally. Vegetation fires are obtained from the Global Fire Emissions Database, Version 3 database [van der Werf *et al.*, 2010] and account for 1.3 TgS in 2010. Emissions of  $\text{SO}_2$  and other sulfur compounds from continuously degassing volcanoes are kept constant throughout the years and amount to 7.2 TgS annually [Andres and Kasgnoc, 1998]. Besides direct emissions,  $\text{SO}_2$  is formed through oxidation of sulfur-containing biospheric compounds like dimethyl sulfide, carbonyl sulfide (OCS), carbon disulfide ( $\text{CS}_2$ ), and hydrogen sulfide ( $\text{H}_2\text{S}$ ). The global annual photochemical source is calculated at 18.1 TgS. Dry and wet deposition account for approximately 60% of the global  $\text{SO}_2$  sink, followed by oxidation by OH (20%), and heterogeneous in-cloud reactions of  $\text{SO}_2$  with  $\text{H}_2\text{O}_2$  (18%) and with  $\text{O}_3$ . The aerosol simulation in IMAGESv2 is described in Stavrou *et al.* [2013].

The AMFs calculated with the IMAGES profiles have been compared to the estimates of Lee *et al.* [2009], and we found similar results both in magnitude and for the general patterns. It should be noted that the accuracy of IMAGES-based AMFs over highly polluted regions or for point sources (see section 3.2.3 on validation) is limited due to the relatively coarse resolution of the model.

As can be seen from Figure 2, the measurement sensitivity is strongly dependent on the altitude (at least for the usual low surface reflectance case). Therefore, the algorithm stores the so-called column averaging kernel (CAK =  $\text{WF}/\text{AMF}$ ) [Eskes and Boersma, 2003] as it enables recalculation with alternative profiles estimates or a comparison with other types of data.

### 3. Results

Here we present the  $\text{SO}_2$  column results obtained with the retrieval technique described above. In section 3.1, we illustrate the algorithm for a selection of volcanic events. The results for anthropogenic  $\text{SO}_2$  are presented in section 3.2.

#### 3.1. Volcanic $\text{SO}_2$

In the following, we provide several examples of OMI  $\text{SO}_2$  column retrievals for volcanic plumes typically injected into the UTLS. For such  $\text{SO}_2$  plumes, the exact knowledge of their corresponding altitude is not critical, as the measurement sensitivity is only weakly dependent on the height (above  $\sim 10$  km), even in the presence of clouds underneath the plume (Figure 2). For simplicity (and unless specified otherwise), we have used the  $\text{SO}_2$  vertical columns assuming a box profile centered at 15 km consistent with OMI  $\text{SO}_2$  lower stratosphere STL product. For comparison, we have also used OMI results from the PCA algorithm, assuming a similar lower stratospheric  $\text{SO}_2$  profile centered at  $\sim 17.5$  km. For the PCA retrievals, the same simplified assumptions about solar zenith angle ( $30^\circ$ ), viewing zenith angle ( $0^\circ$ ),  $\text{O}_3$  profile (325 DU, midlatitude profile), and surface albedo (0.05) as those in the OMI standard PBL (planetary boundary layer)  $\text{SO}_2$  product were assumed (see Li *et al.* [2013] for details). The fitting window was iteratively adjusted to longer wavelengths (from 310.5–340 nm to 320.5–340 nm) for pixels with large volcanic  $\text{SO}_2$ . A more complete PCA algorithm with more realistic assumptions for volcanic  $\text{SO}_2$  retrievals is currently underdevelopment.

The first example is for the Kasatochi volcano (Aleutian Islands) that erupted on 7 and 8 August 2008 [Waythomas *et al.*, 2010] and emitted large quantities of  $\text{SO}_2$  in the UTLS [Kristiansen *et al.*, 2010]. The  $\text{SO}_2$  plume could be monitored for several weeks by many satellite instruments [e.g., Richter *et al.*, 2009; Bobrowski *et al.*, 2010; Corradini *et al.*, 2010; Krotkov *et al.*, 2010; Clarisse *et al.*, 2012; Hörmann *et al.*, 2013], as the plume dispersed throughout the Northern Hemisphere. Figure 3 compares our OMI  $\text{SO}_2$  retrievals with the columns from the LF and PCA algorithms, for the first 2 days after the start of the eruption. The retrieved total  $\text{SO}_2$  masses are given inset in Figure 3. For these observations, retrievals are mostly performed in w3 (typically for  $\text{VCD} \gtrsim 100$  DU) and w2 spectral windows.

For both days, the retrievals by DOAS, LF, and PCA are qualitatively consistent, with all three algorithms revealing similar spatial distribution of the volcanic  $\text{SO}_2$  plume. For 8 August, the VCDs retrieved by DOAS and PCA are higher than the VCDs from the LF algorithm, which is to be expected because LF is known to underestimate very high  $\text{SO}_2$  columns [Yang *et al.*, 2007; Krotkov *et al.*, 2010]. The maximum column values are 382, 354, and 222 DU for DOAS, PCA, and LF, respectively. All three retrievals show an apparent increase in the total  $\text{SO}_2$  mass on the following day, suggesting that they probably all underestimate  $\text{SO}_2$  for 8 August, when the volcanic plume is more concentrated with greater  $\text{SO}_2$  loading. This is

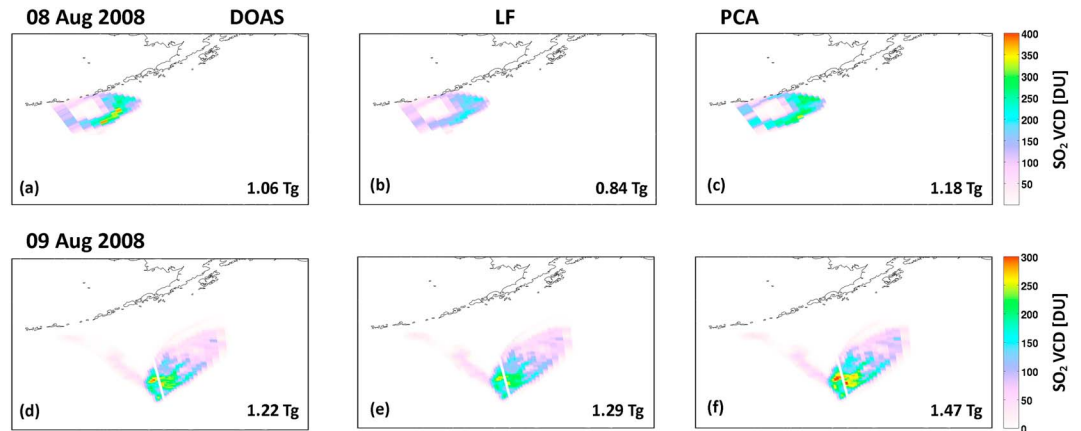


**Figure 3.** OMI SO<sub>2</sub> vertical columns for the plume of Kasatochi for 8 and 9 August 2008 (orbits 21635 and 21650), retrieved by (a, d) DOAS, (b, e) Linear Fit (STL), and (c, f) PCA algorithms. The numbers inset are the retrieved total mass of SO<sub>2</sub>.

supported by other estimates [e.g., Richter et al., 2009; Bobrowski et al., 2010; Clarisse et al., 2012] as well as our tests of the same DOAS algorithm on GOME-2 spectra that yielded column VCD of up to 565 DU (not shown) for the same day. Comparing these three algorithms, we also notice that the percentage increase in SO<sub>2</sub> mass from 8 to 9 August for LF is much greater at over 50%. This implies that LF has a greater relative negative bias for very high SO<sub>2</sub> columns, as also indicated by earlier studies [Yang et al., 2007; Krotkov et al., 2010]. Despite these differences, it is still remarkable that the three algorithms agree within 20–30% in terms of the total SO<sub>2</sub> mass. It should also be mentioned that some of the quantitative discrepancy could be due to different overpass times, ash loadings, viewing angles, or a combination of several effects [Hörmann and Wagner, 2014].

As a second case study, we illustrate our algorithm for the explosive eruption of Sarychev Peak in Russia [Haywood et al., 2010] that emitted large amounts of SO<sub>2</sub> during the 11–19 June 2009 period. Figure 4 shows a comparison between total SO<sub>2</sub> mass time series measured by OMI (DOAS) and the Infrared Atmospheric Sounding Interferometer (IASI) [Clarisse et al., 2012], assuming a representative plume height of 13 km. Here we have summed the contributions of all OMI pixels with columns larger than 0.27 DU (detection limit at the 3σ value level). As can be seen, the OMI results agree fairly well with the IASI data, demonstrating the ability of our algorithm to retrieve SO<sub>2</sub> abundances, for both low- and high-column regimes. We have also

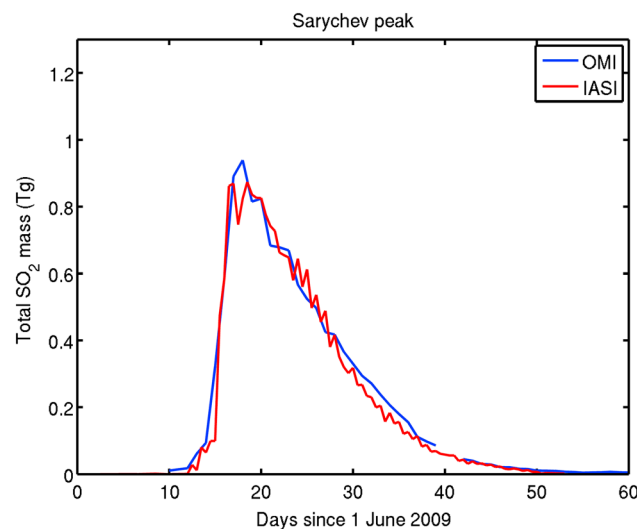


**Figure 4.** Total SO<sub>2</sub> mass measured by OMI and IASI after the eruption of Sarychev in June 2009. A plume height of 13 km is assumed.

estimated the SO<sub>2</sub> amount released by Sarychev during the whole eruption, using a flux determination method described by Theys et al. [2013]. By considering an SO<sub>2</sub> e-folding lifetime of 1 week (compatible with the exponential decay of the total mass in Figure 4), we found a total mass of SO<sub>2</sub> emitted during 11–19 June 2009 of ~1.5 Tg.

The last example is for the eruption of Grímsvötn (Iceland) on 22 and 23 May 2011, which emitted about 0.61 Tg of SO<sub>2</sub> at 5–13 km altitude [Moxnes et al., 2014]. After several weeks, remnants of the volcanic SO<sub>2</sub> emissions could still be detected which allows to illustrate the performances of the algorithms for aged/filamentary plumes. Figure 5 shows a comparison of SO<sub>2</sub> columns over Europe between OMI DOAS, LF,

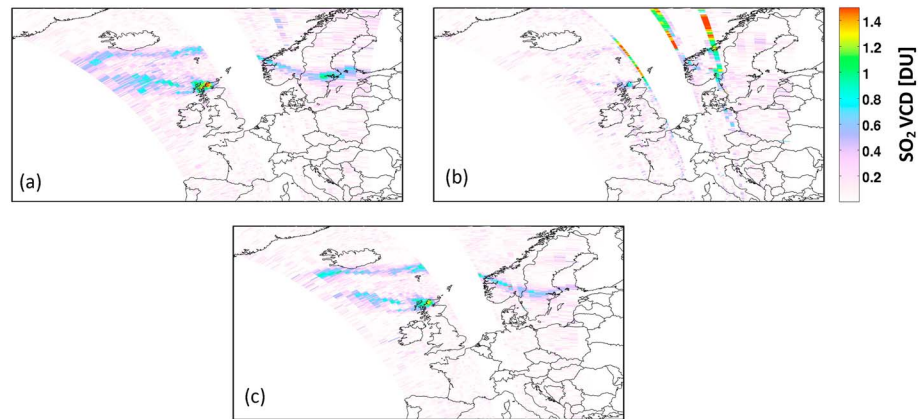


**Figure 5.** OMI SO<sub>2</sub> columns over northern Europe on 13 June 2011, orbit 36759, retrieved using the (a) DOAS, (b) LF (STL) and (c) PCA algorithms.

and PCA algorithms, for measurements performed 3 weeks after the eruption of Grímsvötn. For this example, the treatment of row anomaly pixels described in section 2.2 is applied to all three algorithms.

As can be seen, the plume of SO<sub>2</sub> from Grímsvötn is clearly discernible from the background noise in the DOAS and PCA data set but is hardly detected by the LF algorithm. The reason for this feature is probably related to the failure of the empirical residual correction technique applied to the LF SO<sub>2</sub> band residuals at high latitudes [Yang *et al.*, 2007]. As this correction is based on a sliding group of pixels along the orbit track and since a significant number of those pixels are not SO<sub>2</sub> free (but are classified as such), the band residuals are likely overcorrected. Note also that the DOAS and PCA SO<sub>2</sub> columns seem to be less affected by the row anomaly issue than the LF data. This is likely because LF makes use of radiance measurements only for a few wavelengths, while DOAS and PCA exploit the full spectral information in their respective wavelength ranges. As a test, we applied the row anomaly L1B flag and found that more pixels were discarded with this standard procedure, but the artifacts visible in Figure 5b were effectively removed. Further comparisons between DOAS and PCA results are presented in section 3.2.1 for anthropogenic SO<sub>2</sub>.

### 3.2. Anthropogenic SO<sub>2</sub>

Sulfur dioxide from anthropogenic sources is largely confined in the boundary layer close to the surface. In this altitude region, the accuracy of the retrieved SO<sub>2</sub> columns is directly affected by systematic errors in the AMF input parameters, notably the SO<sub>2</sub> profile shape and surface albedo (as can be deduced from Figure 2). As a consequence, the retrieval uncertainties are large. For many emission sources, the SO<sub>2</sub> signal in the OMI spectra is smaller than the typical noise. Therefore, random sources of error are also significant and spatial-temporal averaging of SO<sub>2</sub> columns is generally needed. In the following (and unless stated otherwise), we have used AMFs calculated with the IMAGES a priori profiles, and only the pixels with effective cloud fractions,  $f_c$ , less than 0.3 have been considered. Even for these relatively clear-sky pixels, the errors on the SO<sub>2</sub> columns due to clouds can be considerable for individual scenes (especially for low clouds), due to propagation of errors in cloud parameters and in SO<sub>2</sub> profile shape (i.e., through the ghost column correction). These effects will be quantified and discussed in more details in a separate paper.

As a first illustration, Figure 6 shows a map of OMI SO<sub>2</sub> columns averaged for multiple years (2004–2009) over Europe and western Asia. It was shown in several papers (Carn *et al.* [2007], Fioletov *et al.* [2011, 2013], McLinden *et al.* [2012], among others) that OMI is able to detect anthropogenic point sources of SO<sub>2</sub> (even small ones), and our results are in line with these studies. In Figure 6, many emission regions are depicted in great details (including several spots with very low SO<sub>2</sub> columns <0.1 DU); these are related to man-made production of SO<sub>2</sub> by coal-fired power plants, cities, oil industry (over the Persian Gulf), and smelters [e.g., Fioletov *et al.*, 2013]. The only natural volcanic source of SO<sub>2</sub> visible on the map is Mount Etna in Sicily, Italy. Over India, emissions of SO<sub>2</sub> from power plants are clearly visible and the retrieved columns are similar to the values of Lu *et al.* [2013]. Outside the geographical area of Figure 6, many other emissions hot spots are

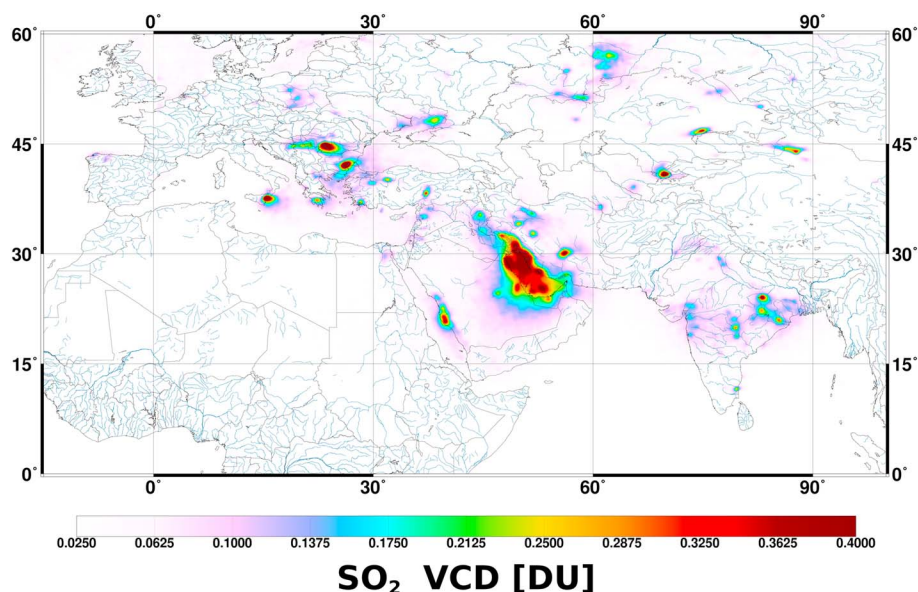


**Figure 6.** OMI SO<sub>2</sub> columns averaged for the 2004–2009 period on a 0.25° × 0.25° grid showing emission hot spots over Europe and western Asia. Cloudy pixels and measurements affected by strong volcanic eruptions are excluded from the analysis.

found and this can be appreciated on a global distribution map of SO<sub>2</sub> columns (Figure 7). We found evidence, in our OMI data set, for even weaker anthropogenic SO<sub>2</sub> signals than those presented in Figures 6 and 7, and this will be illustrated in section 3.2.4.

In the following, we have not applied any ad hoc filtering algorithm, nor had we applied local bias correction as suggested in *Fioletov et al.* [2011] and *McLinden et al.* [2012]. Applying such in the future is expected to enable detection of new point sources with even lower SO<sub>2</sub> signals.

In the next subsections, we evaluate the performances of our algorithm for anthropogenic SO<sub>2</sub> through comparisons with other satellite data sets and validation against ground-based measurements.

### 3.2.1. Comparison to OMI PCA Algorithm

We have compared our DOAS results with the SO<sub>2</sub> columns from the OMI PCA algorithm. Figure 8 shows monthly averaged SO<sub>2</sub> columns from DOAS and PCA, and differences between the results, for August 2006 for the eastern parts of the U.S. and China, which correspond to Figures 3 and S4 from *Li et al.* [2013]. In Figure 8, we have used the same data filtering as described by *Li et al.* [2013], as well as consistent retrieval settings for the AMF calculations. In particular, a summertime eastern U.S. SO<sub>2</sub> profile [*Taubman et al.*, 2006] was used for all AMF computations. Note that, over China, aircraft SO<sub>2</sub> profile by *Krotkov et al.* [2008] indicates a Center of Mass altitude of ~0.9 km, similar to the eastern U.S. SO<sub>2</sub> profiles.

Generally, the SO<sub>2</sub> columns with DOAS have a slightly larger noise level than PCA. Over the equatorial Pacific, we estimate a standard deviation of the DOAS SO<sub>2</sub> VCDs of ~0.6 DU, while the typical value for PCA is 0.5 DU (and ~1 DU for the previous OMI operational PBL product) [*Krotkov et al.*, 2008]. While the DOAS results are retrieved in the 312–326 nm window, the PCA algorithm uses the range 310.5–340 nm. We have done test retrievals by extending our fitting window toward shorter wavelengths (i.e., from 312 to 310.5 nm) and found a standard deviation of the VCDs close to 0.5 DU. Therefore, it is likely that the better performance of PCA compared to DOAS as for the noise is due to the inclusion of the strong SO<sub>2</sub> absorption band peaking around 310.8 nm (Figure 1) which further stabilizes the fit.

When comparing the SO<sub>2</sub> maps, we find that, overall, PCA and DOAS results are fairly close. Both algorithms consistently capture enhanced SO<sub>2</sub> signals over industrialized and densely populated areas. Over the eastern U.S. (Figures 8a and 8c), the absolute differences between DOAS and PCA columns (Figure 8e) are generally less than 0.5 DU and the DOAS algorithm has a tendency to produce more negative values than PCA. Over China, the DOAS and PCA algorithms measure similar patterns (Figures 8b and 8d), but it appears that some

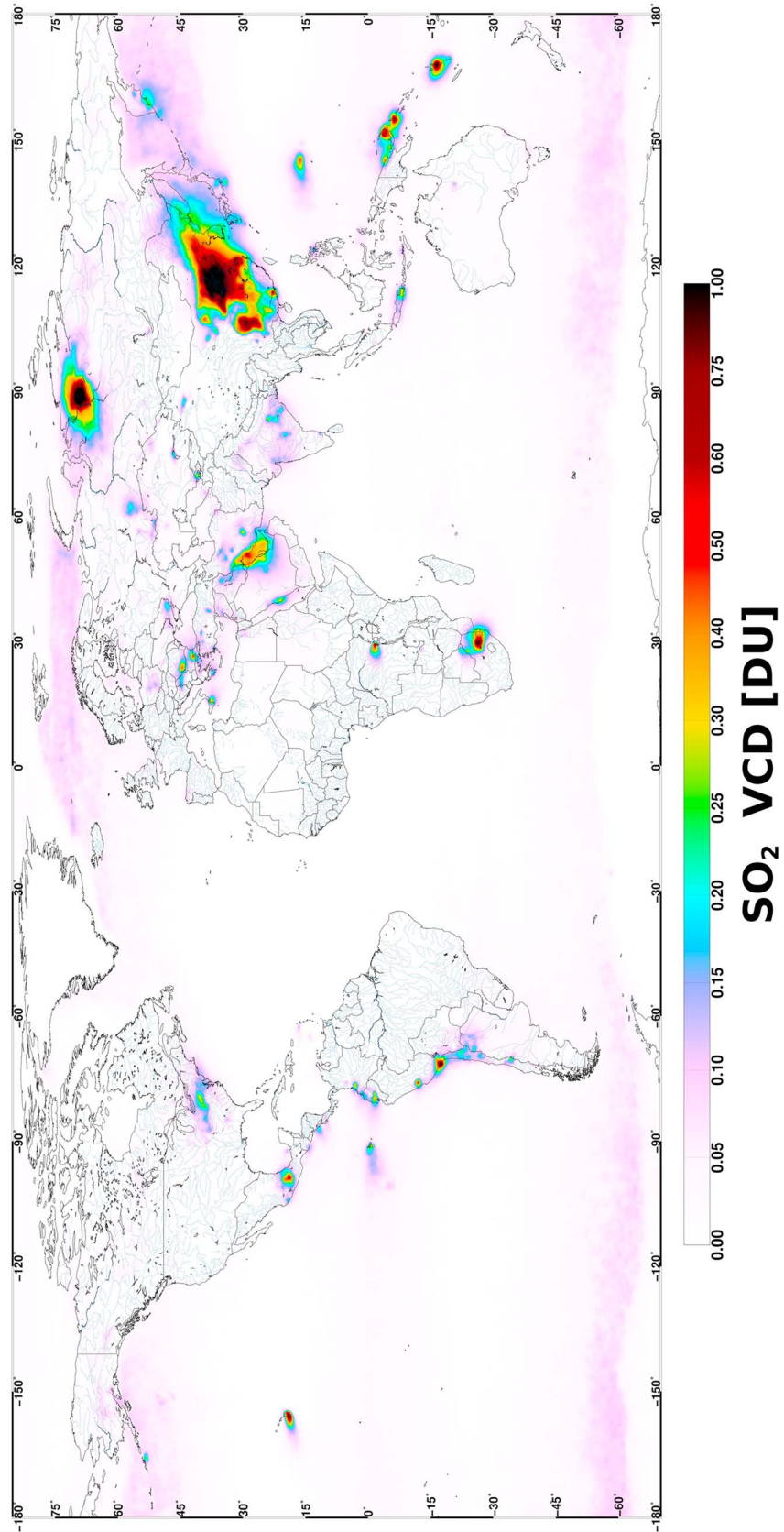


**Figure 7.** Global distribution of SO<sub>2</sub> columns from nearly clear-sky OMI measurements averaged for the 2004–2009 (same as Figure 6). Anthropogenic and volcanic emissions sources are visible. Note the presence of elevated SO<sub>2</sub> values over clean regions at high latitudes due to residual interferences with ozone or the Ring effect.

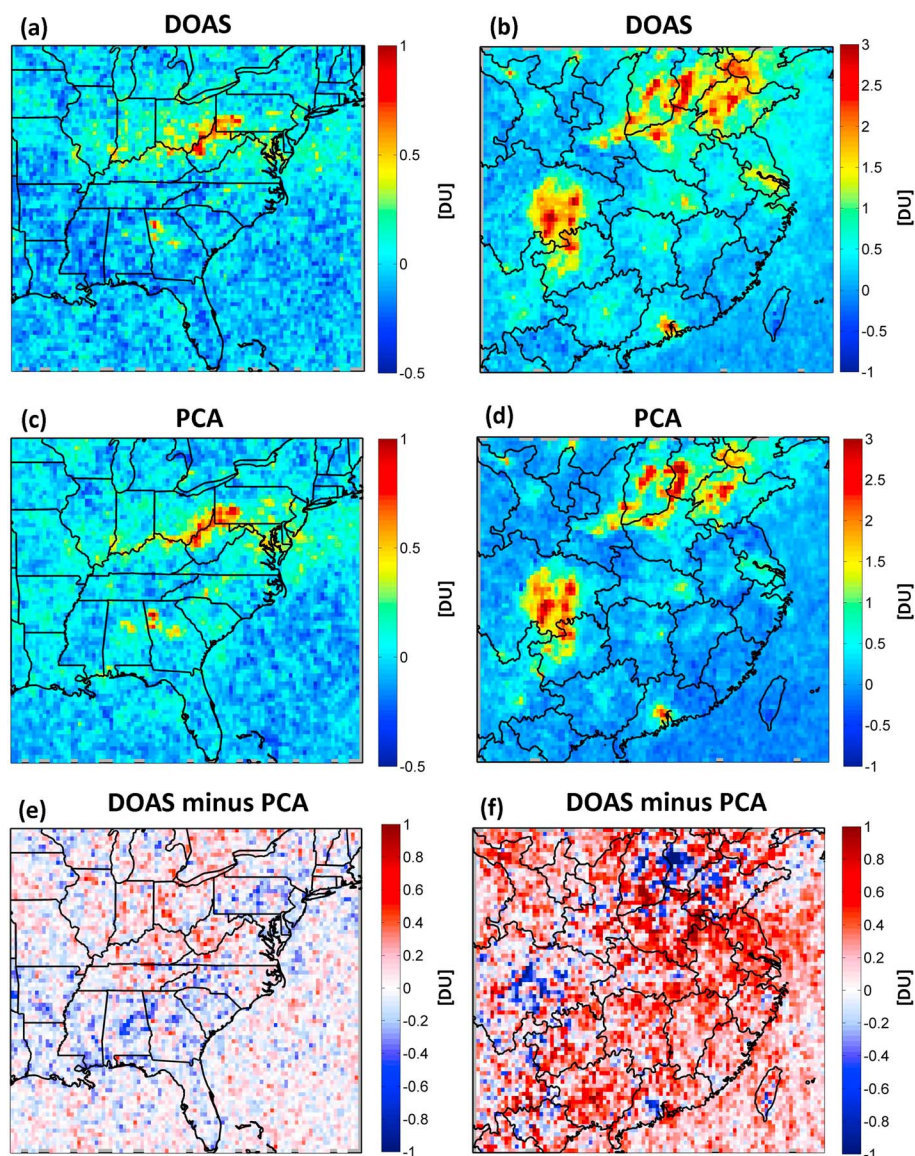


**Figure 8.** OMI SO<sub>2</sub> column maps for August 2006 over (left) eastern U.S. and (right) China retrieved using the (a, b) DOAS and (c, d) PCA algorithms for clear-sky pixels and using a fixed SO<sub>2</sub> profile (see text). (e, f) The SO<sub>2</sub> column differences between DOAS and PCA are shown in the lower maps.

SO<sub>2</sub> point sources are more prominent with DOAS than PCA. We also find that the DOAS retrievals have less negative values than PCA, particularly over southeastern China. Generally, the DOAS columns show larger values than PCA results, and the mean difference is +0.2 DU (Figure 8f).

The reasons for the differences between DOAS and PCA retrievals are unclear but are possibly related to (1) the selection of the wavelength range. The use of different fittings windows leads to different ozone interferences and biases in the SO<sub>2</sub> retrievals, (2) the absence of explicit treatment of aerosols in both DOAS and PCA algorithms, and (3) the use of a background correction scheme in the DOAS algorithm but not in the PCA scheme.

Finally, we have also compared DOAS and PCA results for other geographical regions. We clearly find better performances of the PCA algorithm for high latitudes and clean regions, although no background corrections are made in the PCA retrievals. This is probably due to the large number of principal components used that minimizes spectral misfits.

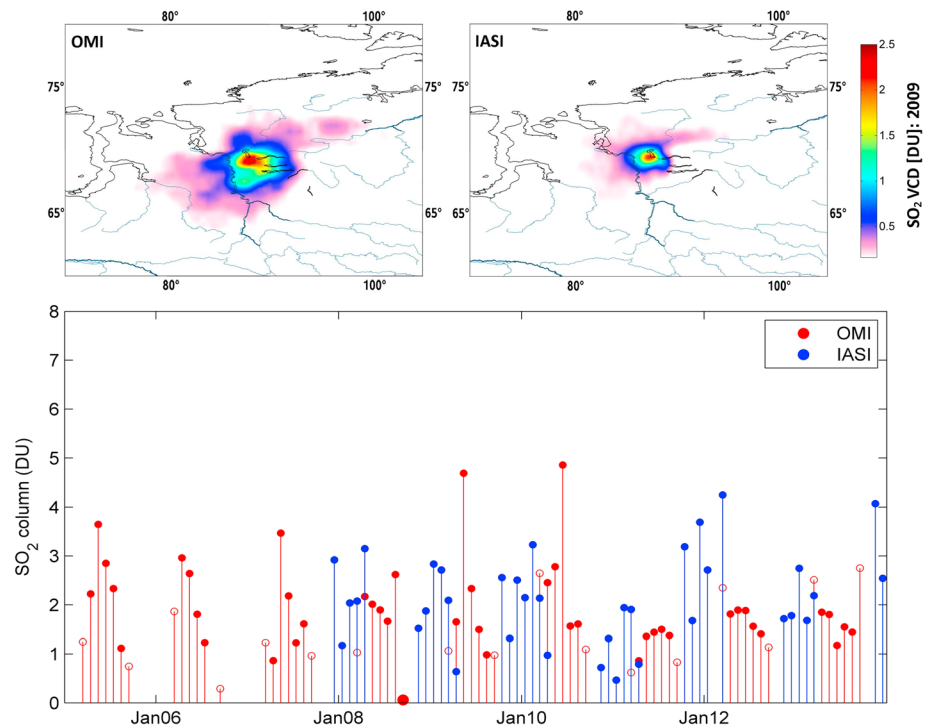


**Figure 9.** (top) Yearly averaged SO<sub>2</sub> columns measured by OMI and IASI over Norilsk for 2009. (bottom) Time series of monthly averaged SO<sub>2</sub> columns from OMI and IASI measurements located within 50 km around Norilsk, for 2005–2013 period. The values for months with less than 5 days of successful measurements are not displayed. The red circles correspond to OMI data with averaged solar zenith angles larger than 65°.

Further comparisons of the DOAS and PCA results are needed. It is important to understand the differences between the algorithms as it opens perspectives for improved and more robust retrievals for the small emission sources.

### 3.2.2. Norilsk—Comparison to IASI Data

Norilsk (69.35°N, 88.2°E) is a heavily polluted industrial city in Siberia due to intense and continuous mining and smelting of heavy metals. With an estimated flux of about 1 Mt of SO<sub>2</sub> per year [Walter *et al.*, 2012], the region of Norilsk produces a strong and persistent signal in the OMI SO<sub>2</sub> data.

Here we compare our OMI SO<sub>2</sub> columns with IASI retrievals. Bauduin *et al.* [2014] demonstrated the ability of a nadir thermal infrared sensor such as IASI to perform measurements of boundary layer SO<sub>2</sub> in the area of Norilsk. This is made possible for conditions with low humidity and large thermal contrast (TC: temperature difference between the surface and the boundary layer), typically encountered at Norilsk in winter. Figure 9 (top) shows maps of SO<sub>2</sub> columns averaged for 2009 by OMI (SZA < 70°) and IASI (0–2 km layer and |TC| > 7 K) over the Norilsk area. Both instruments detect similar distributions of boundary layer SO<sub>2</sub>. However, OMI tends to measure more SO<sub>2</sub>, the spatial pattern being more extended than with IASI. This is probably related to differences in their detection limits for near-surface SO<sub>2</sub>. If one considers a small region around the source, OMI and IASI are then fairly close. For example, for a 50 km circle radius around Norilsk, OMI and IASI averaged SO<sub>2</sub> columns for 2009 are 2.1 and 2.2 DU, respectively. We note however that, strictly speaking, comparing OMI and IASI results is difficult because there are only very few measurements collocated in time; IASI retrievals are mostly successful for wintertime (polar night), while OMI is only able to measure during spring-summer at high latitudes. As an illustration, Figure 9 (bottom) also presents monthly averaged SO<sub>2</sub> columns time series (covering the 2005–2013 period) for OMI and IASI measurements in a 50 km radius circle centered at Norilsk. We found that the OMI and IASI values are in good agreement, and the averaged VCDs are 1.9 and 2.2 DU for OMI and IASI, respectively. The results shown in Figure 9 (bottom) also illustrate the complementarity of UV and thermal infrared soundings in their ability to monitor air pollution in Norilsk. Although it is hard to be conclusive (because measurements are usually not collocated in time), the overall time evolution of the SO<sub>2</sub>

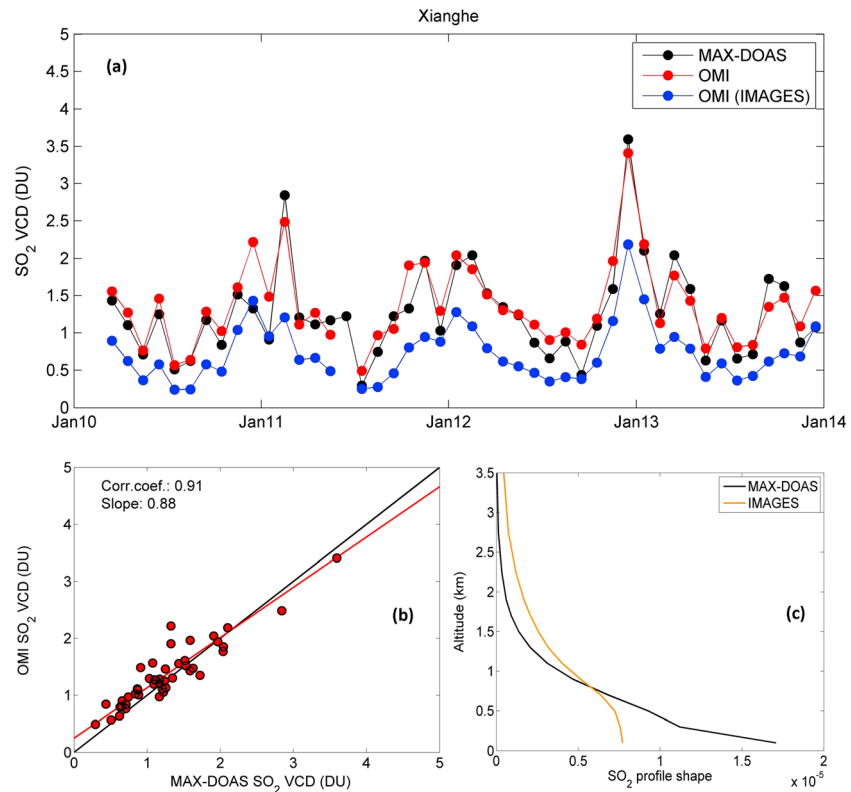


**Figure 10.** (a) Comparison of monthly averaged SO<sub>2</sub> columns at Xianghe for the period 2010–2013 measured by the MAX-DOAS and OMI (pixels falling in a 100 km radius around the station). The SO<sub>2</sub> vertical profiles used in the OMI algorithm are either measured by the MAX-DOAS (red symbols) or modeled by IMAGES (blue symbols). No data are displayed for June 2011 because of the contamination by volcanic SO<sub>2</sub> from the eruption of Nabro. (b) Scatterplot of OMI SO<sub>2</sub> columns (calculated using the MAX-DOAS profiles) versus MAX-DOAS SO<sub>2</sub> columns. Statistical parameters (correlation coefficient and slope of the linear regression (red line)) are given inset. The black line is the 1:1 line. (c) Comparison between the SO<sub>2</sub> profile shapes (expressed in cm<sup>-1</sup>) measured by the MAX-DOAS instrument and modeled by IMAGES (average values for the period March 2010 to December 2013).

columns is similarly captured by OMI and IASI. For example, we notice a decrease in SO<sub>2</sub> columns from the end of 2010 to mid-2011 compared to previous periods. This feature was observed by both OMI and IASI sensors.

### 3.2.3. Validation Over Xianghe, China

The validation of satellite measurements of anthropogenic SO<sub>2</sub> is a challenge for many reasons, one of which being the representativeness (or lack thereof) of the correlative data when compared to the satellite columns. Valuable studies have been undertaken to validate space-based UV SO<sub>2</sub> retrievals, with airborne and surface in situ measurements [e.g., Krotkov *et al.*, 2008; Lee *et al.*, 2009, 2011; Nowlan *et al.*, 2011; He *et al.*, 2012]. Nevertheless, the comparisons presented therein are either limited to short periods of time or rely on assumed vertical distribution of SO<sub>2</sub>. Here we present a comparison of our OMI SO<sub>2</sub> retrievals to ground-based column and profile measurements for nearly 4 years (March 2010 to December 2013), at the suburban site of Xianghe (39.77°N, 117.0°E), China, located at about 50 km south east of Beijing.

The instrument is a multi-axis DOAS (MAX-DOAS) system developed by BIRA-IASB and operated by the Institute of Atmospheric Physics, Chinese Academy of Sciences. Owing to measurements of backscattered UV radiances performed sequentially at several elevation angles above the horizon, the lowermost troposphere is sounded with varying measurement sensitivity, and profile information on SO<sub>2</sub> and aerosol extinction can be retrieved from the MAX-DOAS measurements. The description of the retrieval technique and presentation of the results, including validation against in situ measurements, can be found in Wang *et al.* [2014].

The comparison between the ground-based and OMI SO<sub>2</sub> columns is done as follows: first, all OMI clear-sky pixels ( $f_c$  less than 0.3) within a 100 km radius circle around Xianghe, and surface height less than 500 m

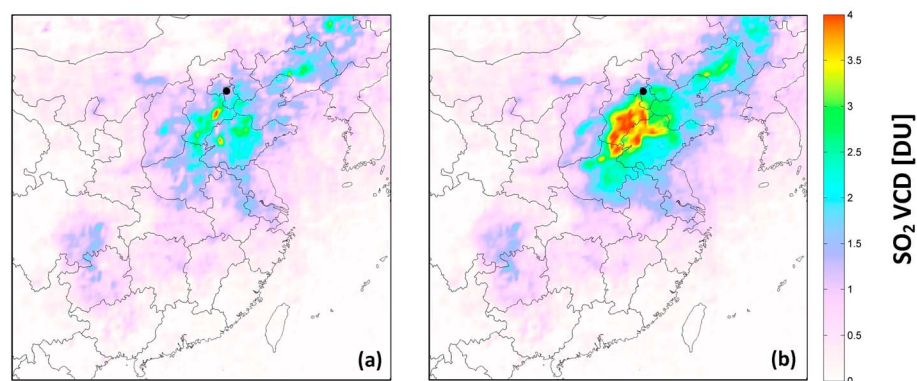


**Figure 11.** OMI SO<sub>2</sub> column maps over China for January 2013 with a selection for (a) clear-sky scenes, and (b) clear-sky and haze scenes (see text). The same AMF calculation is applied to Figures 11a and 11b. It assumes a clear-sky atmosphere and SO<sub>2</sub> profiles from IMAGES. A solar zenith angle cutoff of 70° is considered here. The site of Xianghe is marked by a black circle.

(to exclude observations over clean elevated regions) with solar zenith angles less than 65° are selected. Then, for each OMI pixel, all MAX-DOAS data within  $\pm 90$  min of the OMI overpass time are considered, and a mean SO<sub>2</sub> vertical concentration profile is estimated. To select the best profiles, we have considered only the MAX-DOAS retrievals with degrees of freedom for signal (DFS) larger than 0.7 [Wang *et al.*, 2014]. This criterion removes measurements with high aerosol loadings. Finally, the OMI SO<sub>2</sub> columns are corrected using new AMFs that are evaluated using WFs from OMI and the MAX-DOAS mean SO<sub>2</sub> profile (via equation (1)), doing so allows a consistent comparison between MAX-DOAS and OMI SO<sub>2</sub> VCDs.

It should be noted that the AMF calculation only uses the shape of the MAX-DOAS profile and is therefore independent of the absolute MAX-DOAS concentration values.

Figure 10a shows the comparison between the monthly averaged ground-based (black dots) and coincident OMI SO<sub>2</sub> columns (red dots) for the period March 2010 to December 2013 at Xianghe. One can see that the MAX-DOAS and OMI columns, corrected for the MAX-DOAS profile shape, agree very well, and the seasonal cycle of SO<sub>2</sub> is consistent in both data sets. We have estimated the relevant statistical parameters of the bivariate linear regression OMI versus MAX-DOAS (the scatterplot is shown in Figure 10b). The correlation coefficient is equal to 0.91, and the slope of the linear regression fit is 0.88 (but is very close to 1 if the intercept of the regression is forced to zero). These results depend of course on the accuracy of the retrieved MAX-DOAS SO<sub>2</sub> profile shapes used for the OMI AMFs. Wang *et al.* [2014] presented an error budget on the MAX-DOAS SO<sub>2</sub> retrievals, including the uncertainty related to the a priori profile. We have propagated this error through the OMI retrievals and found an uncertainty on the OMI AMFs of about 20%. This is not negligible and calls for further measurements of SO<sub>2</sub> in the altitude range where the MAX-DOAS has little sensitivity to SO<sub>2</sub>.

Note that the default OMI SO<sub>2</sub> columns using IMAGES a priori profile shapes (displayed in Figure 10a with blue dots) tend to underestimate the MAX-DOAS column values by up to a factor of 2, because the SO<sub>2</sub> profile shapes from IMAGES are peaked at higher altitudes as compared with the MAX-DOAS retrievals (see Figure 10c for a comparison profile shapes). This illustrates the importance of the profiles on the retrievals.

We now proceed further and develop the validation exercise for the specific month of January 2013. During that period, an extreme pollution episode occurred over a large part of North China [e.g., Yang *et al.*, 2013; Boynard *et al.*, 2014; Huang *et al.*, 2014], and several cities were affected by a persistent haze layer. For this event, the measurement of SO<sub>2</sub> pollution by OMI is strongly altered by the high loadings of aerosols that absorb and scatter UV radiation and hence influence the light path through the SO<sub>2</sub> layer. So far, the effect of aerosols has not been considered in our AMF calculation. Another aerosol-related effect affecting the SO<sub>2</sub> column estimates comes from the fact that thick aerosol layers appear as reflecting surfaces (this can be observed, e.g., in true color Moderate Resolution Imaging Spectroradiometer images, <http://neo.sci.gsfc.nasa.gov/>) and are typically considered as clouds in the OMCLD02 cloud product.

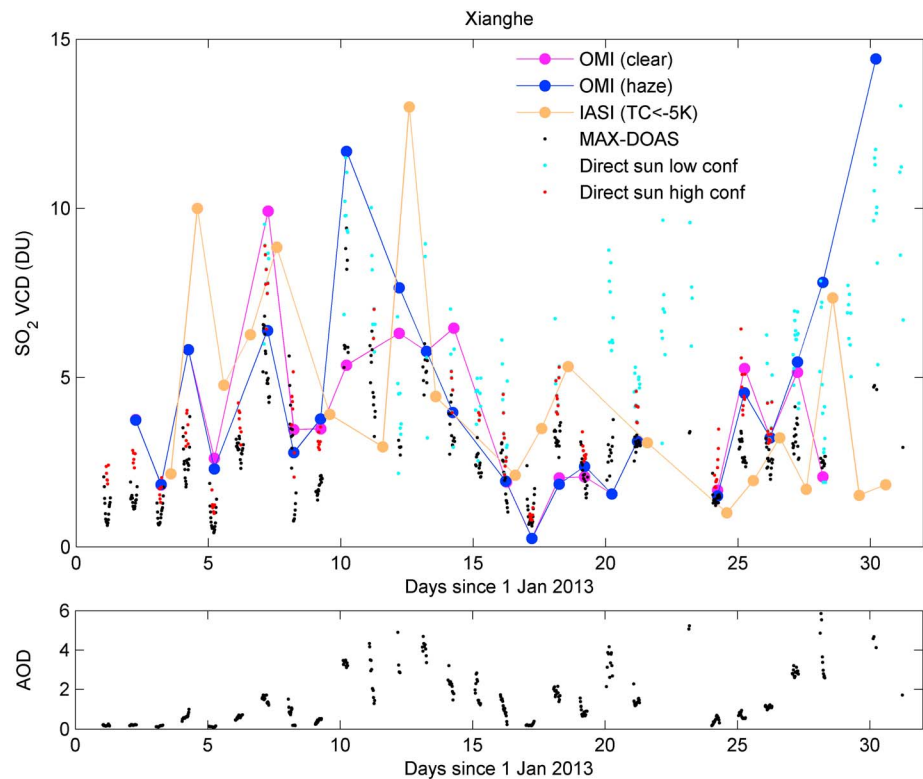


**Figure 12.** (top) Comparison of SO<sub>2</sub> columns from satellites (OMI and IASI daily averages) and ground-based observations for January 2013 at Xianghe. OMI results are displayed for two sets of pixels: clear-sky and haze scenes. For the latter, an aerosol correction based on the retrieved MAX-DOAS extinction profiles is applied. IASI SO<sub>2</sub> column averages have been calculated for pixels with a thermal contrast  $-5$  K and lower and in a circle of 100 km radius around the station. The ground-based SO<sub>2</sub> columns are derived from measurements in multi-axis and direct Sun geometries (see text). (bottom) Time series of aerosol optical depth retrieved from the MAX-DOAS.

To overcome this misclassification issue, we have used a simple empirical selection of OMI pixels to pick up the scenes with thick absorbing aerosol layers close to the surface: the corresponding “haze scenes” are defined by the pixels for which the UV aerosol index is larger than 1.5 and the difference between surface pressure and OMCLDO2 retrieved effective cloud pressure is less than 150 mb. To avoid a double classification, the “clear-sky scenes” are redefined in the following as the pixels with  $f_c$  less than 0.3 and that do not fulfill the haze selection criterion. Figure 11 shows the vertical SO<sub>2</sub> column maps for January 2013 for (Figure 11a) clear-sky pixels and (Figure 11b) clear-sky and haze scenes. The vertical columns are calculated using clear-sky AMFs, and no attempt is made to correct for aerosols (the information on aerosols is not available). The aim of Figure 11 is only to illustrate the impact of the data selection. As can be seen, the SO<sub>2</sub> columns increase by up to a factor of 2 over the North China plain, when considering the haze (SO<sub>2</sub>-enriched) scenes.

Although the city of Xianghe is not the region in China with highest SO<sub>2</sub> pollution (according to Figure 11), we have examined the time evolution of several SO<sub>2</sub> data sets over this site for January 2013 (Figure 12):

1. OMI clear: daily averaged SO<sub>2</sub> columns for clear-sky pixels. This data set is identical to the one in Figure 10, except that haze scenes are excluded and we have relaxed the cutoff value on the SZA to 70° to improve the statistics.
2. OMI clear and haze: same as (1) but including the haze scenes (as defined above). For the latter haze scenes, not only the SO<sub>2</sub> profiles but also the aerosol extinction profiles from the MAX-DOAS are used in the calculation of the AMFs applied to OMI. For this, we have considered a single-scattering albedo for the aerosols equal to 0.9, which is compatible with published estimates [Zhao and Li, 2007] and Aerosol Robotic Network measurements (<http://aeronet.gsfc.nasa.gov/>) at Xianghe, albeit not at UV wavelengths.

3. IASI: half-daily averaged SO<sub>2</sub> columns for pixels within 100 km radius around Xianghe and a thermal contrast of -5 K and lower (mostly nighttime measurements). This data set is identical to the one published in *Boynard et al.* [2014].
4. MAX-DOAS: diurnal cycles of retrieved SO<sub>2</sub> columns. In contrast to Figure 10, no data filtering based on DFS has been applied here, because the aim is to compare the results for various aerosol loadings (the aerosol optical depth (AOD) time series is displayed in Figure 12, bottom).
5. Direct Sun: in addition to its nominal multiaxis mode, the ground-based instrument also operates in the direct Sun geometry. For high aerosol loadings, reduced information to the whole boundary layer SO<sub>2</sub> may be expected for the MAX-DOAS retrievals; and therefore, the direct Sun measurements are deemed to give better results than the MAX-DOAS estimates. The direct Sun vertical columns of SO<sub>2</sub> are obtained by dividing absolute slant columns with air mass factors considering a geometrical light path through the SO<sub>2</sub> layer. The latter assumption is questionable at high AODs, and we have therefore assigned a quality flag to the direct Sun column estimates (labeled “low/high confidence” in Figure 12) as an informative piece on the validity of the geometrical approximation. This flag is evaluated empirically based on concurrent measurements of the oxygen dimer O<sub>2</sub>-O<sub>2</sub>, used here as a proxy of the light path in the atmosphere.

For low AODs, one can see from Figure 12 that the OMI SO<sub>2</sub> columns (clear) agree generally well with the MAX-DOAS estimates. For high AODs (larger than 2), the “clear” and “clear and haze” SO<sub>2</sub> columns are sometimes significantly different and, for these days, the clear and haze column values are commensurate with the direct Sun estimates, suggesting a sensible treatment of the aerosols for the OMI haze data set. Interestingly, most of the differences between the different OMI data arise from the pixels selection (for the haze scenes, as defined above) and not so much from the different AMFs applied. The AMFs, including the aerosols, were found to be on average only 15% (range: -20% to 40%) larger than the aerosol-free AMFs. We have inspected the MAX-DOAS SO<sub>2</sub> and aerosol extinction profiles for January 2013, and found that the profile shapes are quite similar. The explanation is therefore a compensation of enhancement and reduction of the SO<sub>2</sub> signal due to aerosols (in line with the findings of *Leitão et al.* [2010] on the impact of aerosols on satellite NO<sub>2</sub> retrievals). However, we note that the aerosol-corrected AMFs depend strongly on the single-scattering albedo for the aerosols, and the latter is therefore a key parameter that needs to be accurately determined for further validation work.

In Figure 12, the IASI retrievals are also displayed and compare reasonably well with the ground-based and OMI estimates, for the low column values. Conversely, there are often large differences for the SO<sub>2</sub> peaks. For the infrared measurements, the most important source of uncertainty is the thermal contrast (TC)—even small errors in the TC can propagate to large errors in the retrieved column. There are also several other factors that could explain the discrepancies: differences in temporal and vertical sampling of the atmosphere between UV and thermal infrared measurements, dependence of the IASI retrievals on the vertical SO<sub>2</sub> profile, aerosols, and clouds.

To conclude the discussion on the validation exercise at Xianghe, we note that the results of Figures 11 and 12 are not in line with the OMPS retrievals of *Yang et al.* [2013] who reported SO<sub>2</sub> columns over China in January 2013 a factor of 2–4 lower than our estimates.

#### 3.2.4. Detection of Shipping Emissions

International shipping is a significant source of pollutants including CO<sub>2</sub>, nitrogen oxides (NO<sub>x</sub>), sulfur oxides (SO<sub>x</sub>), volatile organic compounds, particulate matter, and black carbon. It is important to monitor those emissions as they are expected to grow in the future. Space-based observations of shipping emissions have focused on NO<sub>2</sub> [e.g., *Beirle et al.*, 2004; *Richter et al.*, 2004, 2011] and also formaldehyde [*Marbach et al.*, 2009], but the detection of SO<sub>2</sub> has hitherto not been reported in the literature. Here we evaluate our OMI SO<sub>2</sub> retrievals to capture the SO<sub>2</sub> emissions from ships.

As the IMAGES model does not include inventories of shipping emissions of SO<sub>x</sub>, the AMFs calculated from the modeled SO<sub>2</sub> profiles are not appropriate for the shipping signal; and therefore, we first concentrate on retrieved slant columns instead of vertical columns. Although the noise level of the retrieved SO<sub>2</sub> SCDs is low (typically 0.25 DU for the standard deviation), the expected shipping signal is well below this detection limit, so we have based our analysis on long-term averages to reduce the data scatter. Five years (2005–2009) of clear-sky data ( $f_c$  less than 0.3) have been considered, and the data affected by volcanic SO<sub>2</sub> from strong eruptions during that period have been filtered out.

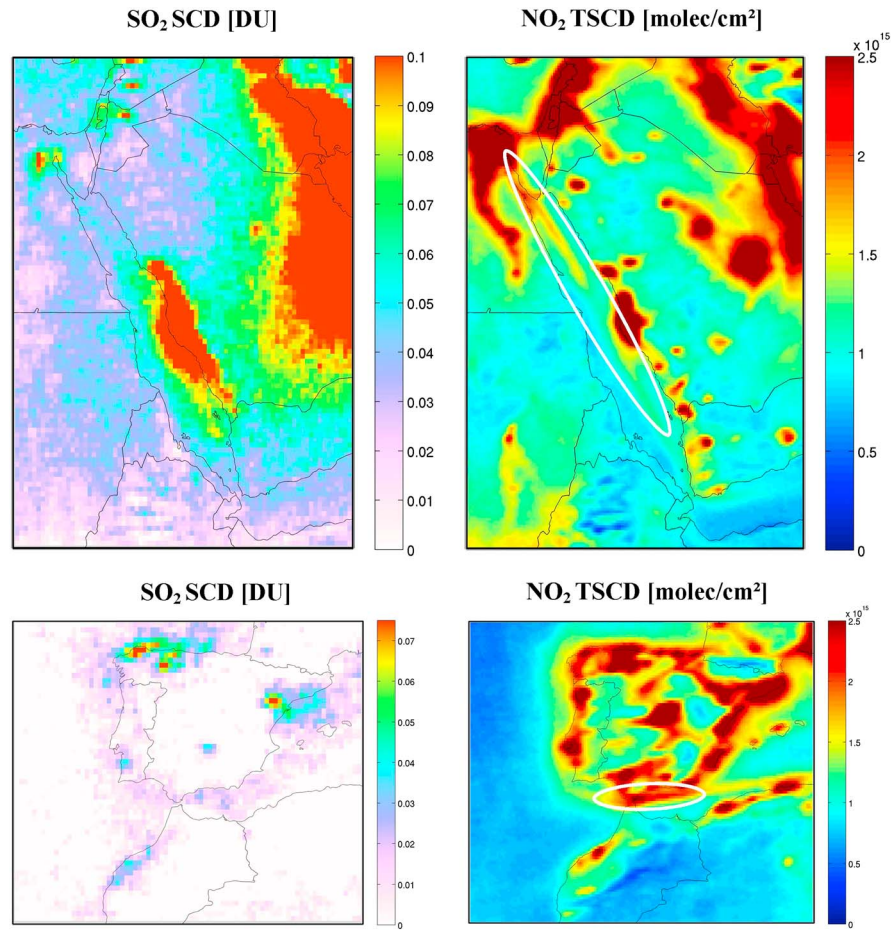


**Figure 13.** (left) Multiannual averaged SO<sub>2</sub> slant columns derived from clear-sky OMI measurements from 2005 to 2009 over the Middle East and Spain-North of Africa. Data strongly affected by volcanic SO<sub>2</sub> have been excluded from the analysis. (right) Tropospheric NO<sub>2</sub> slant columns are measured by OMI over the same period and regions. The shipping lanes in the Red Sea and in the vicinity of the strait of Gibraltar are shown in the NO<sub>2</sub> maps with white ellipses.

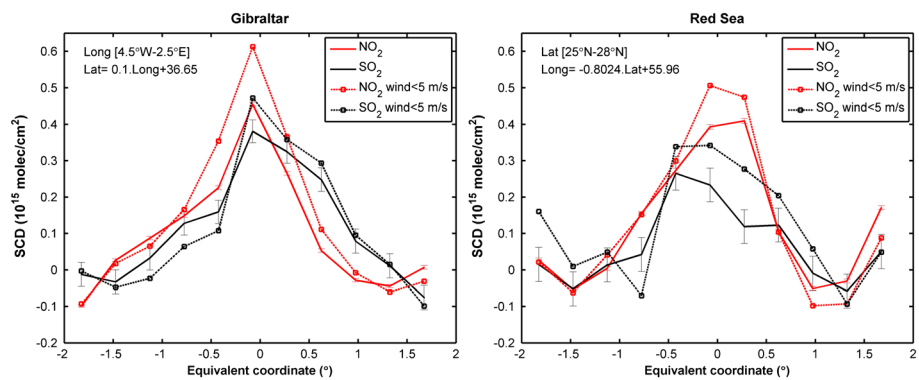


**Figure 14.** OMI multiannual-averaged slant columns of SO<sub>2</sub> (black) and tropospheric NO<sub>2</sub> (red) along ship tracks ((left) strait of Gibraltar and (right) Red Sea) presented in Figure 13. The slant columns are shown as a function of the equivalent coordinate (distance in degree from the shipping lane), and first-order polynomial fits are subtracted from the averages. (inset) The parameterizations used to locate the ship tracks are given. The selection of pixels is identical as in Figure 13, except for the dashed lines that correspond to days with low surface wind speed (less than 5 m/s). The error bars represent the errors on the mean SCDs, i.e., the standard deviation divided by the square root of the number of observations. Note that the error bars for the low wind speed values are not shown for better readability.

The SO<sub>2</sub> results are presented in Figure 13 for two regions, over the Middle East and Spain. Also shown are the corresponding tropospheric NO<sub>2</sub> slant columns measured by OMI (H. Yu et al., manuscript in preparation, 2014) to illustrate the pollution patterns in the corresponding regions. One can see enhanced SO<sub>2</sub> columns in the Red Sea which coincide with the shipping tracks as depicted in the NO<sub>2</sub> map, although the SO<sub>2</sub> column levels over the Red Sea cannot be attributed to ships only as there is a strong contamination by land sources (e.g., refineries near Jeddah in Saudi Arabia). As shown in Figure 13, enhanced SO<sub>2</sub> values are also found near the Gibraltar strait where intense shipping is notorious, as evidenced in the NO<sub>2</sub> data. Nevertheless, for both cases, the signal from ships appears to be close to or at the noise level. To improve the statistics, we have averaged the SO<sub>2</sub> and (tropospheric) NO<sub>2</sub> SCDs along the ship tracks to get a spatial cross section. For this, we have defined for each case (Red Sea or Gibraltar) a parameterization of the shipping lane (a simple latitude-longitude linear relationship), and we have estimated the averaged slant columns of SO<sub>2</sub> and NO<sub>2</sub> (for clear-sky pixels) as a function of the distance from the shipping lane. Compared to the gridded data (Figure 13), this reduces the noise on the SO<sub>2</sub> slant columns by about a factor of 5. To isolate the enhancement due to shipping emissions relative to the background, first-order polynomials were fitted and subtracted from the SO<sub>2</sub> and NO<sub>2</sub> averages.

The SO<sub>2</sub> and NO<sub>2</sub> results are shown in Figure 14, for Gibraltar (left) and Red Sea (right) ship tracks. The error bars on the SO<sub>2</sub> and NO<sub>2</sub> values represent the error on the mean SCDs ( $\sigma/\sqrt{N}$ ;  $\sigma$  is the SCD standard deviation,  $N$  is the number of observations).

For each region, one can see enhanced values of SO<sub>2</sub> and NO<sub>2</sub> well above the detection limit and centered over the middle of the ship track. We have performed these calculations also for low surface wind conditions (i.e., averaged wind speed for the lowest 0–500 m above the surface less than 5 m/s according to data from the European Centre for Medium-Range Weather Forecasts (ECMWF)), and the estimated SCDs (dashed line) increase by about 20–30% both for NO<sub>2</sub> and SO<sub>2</sub> (the corresponding error bars are not shown for better readability but are up to 70% larger than the error bars with no selection on the wind speed). This supports the shipping origin of the observed SO<sub>2</sub> (detection is facilitated by less plume dilution).

Shipping emissions of NO<sub>x</sub> and SO<sub>2</sub> are subject to regulations by the International Maritime Organization, and the monitoring of the effective decrease in fuel sulfur content is of interest. It can be determined by the relative emission of NO<sub>x</sub> (controlled by engine type and operation and temperature of combustion) and SO<sub>2</sub> through the NO<sub>2</sub>/SO<sub>2</sub> ratio. We have estimated the ratio NO<sub>2</sub>/SO<sub>2</sub> based on the measurements in shipping plumes in Figure 14. For this, we have applied a scaling to the NO<sub>2</sub>/SO<sub>2</sub> slant column ratio to account for the difference in measurement sensitivity to NO<sub>2</sub> and SO<sub>2</sub> in the boundary layer. We obtain a typical ratio NO<sub>2</sub>/SO<sub>2</sub> of 0.5–1.0, a range that is compatible, e.g., with the shipping emission estimates from aircraft measurements by Berg et al. [2012].

In addition to the cases shown in Figure 13, we have also looked for other examples of shipping emissions of SO<sub>2</sub>. In the Indian Ocean, several ship tracks are clearly visible in the NO<sub>2</sub> data, but the detection of shipping SO<sub>2</sub> signal was not conclusive there. The reason for this is unclear, but we notice that the NO<sub>2</sub> columns (background corrected) are lower for the Indian Ocean ship tracks than in the Red Sea and near the Gibraltar strait, hence, it might be related to a detection limit issue.

As a final remark, it is worth noting the great ability of our OMI SO<sub>2</sub> algorithm to detect very weak emission sources also over land (sometimes with SCDs lower than 0.05 DU). In Figure 13, we can clearly identify, e.g., the Nile Valley and the coal power plants of Sines (South-West Portugal), El Jadida (Atlantic coast of Morocco), and Puertollano (South-center Spain).

#### 4. Conclusions

We have developed an advanced algorithm to retrieve SO<sub>2</sub> vertical columns from UV-visible measurements and applied it to OMI data from 2004 to 2013. The retrieval scheme includes a DOAS spectral fitting, a background correction, and the calculation of air mass factors and vertical column averaging kernels. We use fixed UTLS SO<sub>2</sub> profiles as input to the algorithm for volcanic SO<sub>2</sub> plumes and simulations from the global chemical transport model IMAGES to represent SO<sub>2</sub> profiles for anthropogenic emissions.

Several examples of volcanic eruptions and comparisons with contemporaneous IASI, OMI Linear Fit, and OMI Principal Component Analysis retrievals demonstrate the ability of our algorithm to detect and quantify volcanic SO<sub>2</sub> plumes for both low and high-column regimes.

The determination of SO<sub>2</sub> columns for anthropogenic sources is notoriously difficult because of the low column amount and reduced measurement sensitivity close to the surface, leading to large retrieval uncertainties. Therefore, intercomparison of satellite SO<sub>2</sub> data and validation against ground-based measurements are especially important for anthropogenic SO<sub>2</sub> sources.

We have made preliminary comparisons of OMI columns retrieved from the DOAS and PCA algorithms over eastern U.S. and eastern China. The results from the two algorithms are in good overall agreement, and we found that they have very good and comparable detection limits (0.5–0.6 DU). However, more work is needed to compare the DOAS and PCA algorithms in a more systematic way to gain confidence in the detection of very weak SO<sub>2</sub> sources.

We have also performed comparisons between OMI columns and recently reported IASI observations of boundary layer SO<sub>2</sub> at Norilsk, and we found a convincing overall agreement, further illustrating the complementarity of ultraviolet and thermal infrared nadir instruments.

We have presented a validation of our OMI data with MAX-DOAS measurements in Xianghe (China) for March 2010 to December 2013. Local air mass factors have been calculated using SO<sub>2</sub> profile shape measurements from the ground-based instrument. We find an excellent agreement between OMI and MAX-DOAS SO<sub>2</sub> columns with consistent seasonal and even short-term variations. On average, the satellite and ground-based SO<sub>2</sub> columns agree within 12%. We have also investigated the extreme pollution case in China for January 2013 and showed that SO<sub>2</sub> columns from ground-based, IASI, and OMI measurements could be as high as 10–15 DU. We found that the selection of OMI pixels corresponding to haze scenes is important to reconcile the OMI and ground-based SO<sub>2</sub> column results. We also briefly discussed the impact of elevated aerosols on the OMI AMFs.

Finally, the ability of our algorithm to detect very weak SO<sub>2</sub> sources has been demonstrated on multiannual averaged SO<sub>2</sub> columns. Using simultaneous observations of tropospheric NO<sub>2</sub> and meteorological wind field data, we, for the first time, present evidence for shipping SO<sub>2</sub> emissions with space-based observations. It is likely that such emissions will be more easily monitored with the next generation of nadir instruments, especially the TROPOMI/Sentinel-5 Precursor instrument, owing to its improved spatial resolution and signal-to-noise ratio.

#### Acknowledgments

This work has been performed in the frame of the TROPOMI project. We acknowledge financial support from ESA S5P and Belgium Prodex TRACE-S5P projects. We also wish to thank support from ESA SEARS and SACS2 projects. MAX-DOAS measurements in Xianghe were funded by Belgian Federal Science Policy Office, Brussels (AGACC-II project), and the EU 7th Framework Programme project NORS (contract 284421). IASI has been developed and built under the responsibility of the Centre National d'Etudes Spatiales (CNES, France). It is flown on board the MetOp satellites as part of the EUMETSAT Polar System. The IASI L1 data are received through the EUMETCast near real-time data distribution service. The research in Belgium was funded by the F.R.S-FNRS, the Belgian State Federal Office for Scientific, Technical, and Cultural Affairs, and the European Space Agency (ESA-Prodex arrangements). S. Bauduin is a Research Fellow with F.R.S-FNRS. N. Krotkov and Can Li acknowledge NASA Earth Science Directorate support of the Aura Science Team. We also thank Marten Sneeep of KNMI for his support with OMI data. The OMI data generated for this paper and ground-based MAX-DOAS data are available at BIRA-IASB (<http://uv-vis.aeronomie.be/>) on request (contacts: [theysa@aeronomie.be](mailto:theysa@aeronomie.be) and [michelv@aeronomie.be](mailto:michelv@aeronomie.be)). The OMI L1 and L2 operational data used for this paper are available from the NASA Goddard Earth Sciences (GES) Data and Information Services Center (<http://disc.sci.gsfc.nasa.gov/Aura/OMI/oms02.shtml>).

#### References

- Acarreta, J. R., J. F. de Haan, and P. Stammes (2004), Cloud pressure retrieval using the O<sub>2</sub>-O<sub>2</sub> absorption band at 477 nm, *J. Geophys. Res.*, *109*, D05204, doi:10.1029/2003JD003915.
- Anderson, G., S. Clough, F. Kneizys, J. Chetwynd, and E. P. Shettle (1986), AFGL atmospheric constituents profiles (0-120 km) Environmental Research Papers No. 954, ADA175173, AFGL-TR 86-0110, U.S. Air Force Geophysics Laboratory, Optical Physics Division.
- Andres, R. J., and A. D. Kasgnoc (1998), A time-averaged inventory of subaerial volcanic sulfur emissions, *J. Geophys. Res.*, *103*(D19), 25,251–25,261, doi:10.1029/98JD02091.
- Bauduin, S., L. Clarisse, C. Clerbaux, D. Hurtmans, and P.-F. Coheur (2014), IASI observations of sulfur dioxide (SO<sub>2</sub>) in the boundary layer of Norilsk, *J. Geophys. Res. Atmos.*, *119*, 4253–4263, doi:10.1002/2013JD021405.
- Beirle, S., U. Platt, R. von Glasow, M. Wenig, and T. Wagner (2004), Estimate of nitrogen oxide emissions from shipping by satellite remote sensing, *Geophys. Res. Lett.*, *31*, L18102, doi:10.1029/2004GL020312.
- Berg, N., J. Mellqvist, J.-P. Jalkanen, and J. Balzani (2012), Ship emissions of SO<sub>2</sub> and NO<sub>2</sub>: DOAS measurements from airborne platforms, *Atmos. Meas. Tech.*, *5*, 1085–1098, doi:10.5194/amt-5-1085-2012.
- Bhartia, P., and C. Wellemeier (2002), TOMS-V8 total O<sub>3</sub> algorithm, OMI algorithm theoretical basis document. [Available at [http://www.knmi.nl/omi/documents/data/OMI\\_ATBD\\_Volume\\_2\\_V2.pdf](http://www.knmi.nl/omi/documents/data/OMI_ATBD_Volume_2_V2.pdf).]
- Bobrowski, N., C. Kern, U. Platt, C. Hörmann, and T. Wagner (2010), Novel SO<sub>2</sub> spectral evaluation scheme using the 360–390 nm wavelength range, *Atmos. Meas. Tech.*, *3*, 879–891, doi:10.5194/amt-3-879-2010.
- Bogumil, K., et al. (2003), Measurements of molecular absorption spectra with the SCIAMACHY Pre-Flight Model: Instrument characterization and reference data for atmospheric remote-sensing in the 230–2380 nm region, *J. Photochem. Photobiol. A*, *157*(2-3), 167–184, doi:10.1016/S1010-6030(03)00062-5.
- Boynard, A., et al. (2014), First space measurements of simultaneous pollutants in the boundary layer from IASI: A case study in the North China Plain, *Geophys. Res. Lett.*, *41*, 1–6, doi:10.1002/2013GL058333.
- Briou, J., A. Chakir, J. Charbonnier, D. Daumont, C. Parisse, and J. Malicet (1998), Absorption spectra measurements for the ozone molecule in the 350–830 nm region, *J. Atmos. Chem.*, *30*, 291–299, doi:10.1023/A:1006036924364.
- Carr, S. A., A. J. Krueger, N. A. Krotkov, and M. A. Gray (2004), Fire at Iraqi sulfur plant emits SO<sub>2</sub> clouds detected by Earth Probe TOMS, *Geophys. Res. Lett.*, *31*, L19105, doi:10.1029/2004GL020719.
- Carr, S. A., A. J. Krueger, N. A. Krotkov, K. Yang, and P. F. Levelt (2007), Sulfur dioxide emissions from Peruvian copper smelters detected by the Ozone Monitoring Instrument, *Geophys. Res. Lett.*, *34*, L09801, doi:10.1029/2006GL029020.

- Carn, S. A., N. A. Krotkov, K. Yang, and A. J. Krueger (2013), Measuring global volcanic degassing with the Ozone Monitoring Instrument (OMI), in *Remote Sensing of Volcanoes and Volcanic Processes: Integrating Observation and Modeling*, edited by D. M. Pyle, T. A. Mather, and J. Biggs, *Geol. Soc. London Spec. Publ.*, 380, 229–257, doi:10.1144/SP380.12.
- Chance, K., and R. J. Spurr (1997), Ring effect studies: Rayleigh scattering including molecular parameters for rotational Raman scattering, and the Fraunhofer spectrum, *Appl. Opt.*, 36, 5224–5230, doi:10.1364/AO.36.005224.
- Chin, M., and D. J. Jacob (1996), Anthropogenic and natural contributions to tropospheric sulfate: A global model analysis, *J. Geophys. Res.*, 101(D13), 18,691–18,699, doi:10.1029/96JD01222.
- Clarisse, L., D. Hurtmans, C. Clerbaux, J. Hadji-Lazaro, Y. Ngadi, and P.-F. Coheur (2012), Retrieval of sulphur dioxide from the infrared atmospheric sounding interferometer (IASI), *Atmos. Meas. Tech.*, 5, 581–594, doi:10.5194/amt-5-581-2012.
- Corradini, S., L. Merucci, A. J. Prata, and A. Piscini (2010), Volcanic ash and SO<sub>2</sub> in the 2008 Kasatochi eruption: Retrievals comparison from different IR satellite sensors, *J. Geophys. Res.*, 115, D00L21, doi:10.1029/2009JD013634.
- Danckaert, T., C. Fayt, M. Van Roozendaal, I. De Smedt, V. Letocart, A. Merlaud, and G. Pinardi (2012), Qdoas Software User Manual, Version 2.1. [Available at [http://uv-vis.aeronomie.be/software/QDOAS/QDOAS\\_manual\\_2.1\\_201212.pdf](http://uv-vis.aeronomie.be/software/QDOAS/QDOAS_manual_2.1_201212.pdf).]
- Dobber, M., et al. (2006), Ozone monitoring instrument calibration, *IEEE Trans. Geosci. Remote Sens.*, 44(5), 1209–1238, doi:10.1109/TGRS.2006.869987.
- Eisinger, M., and J. P. Burrows (1998), Tropospheric sulfur dioxide observed by the ERS-2 GOME instrument, *Geophys. Res. Lett.*, 25(22), 4177–4180, doi:10.1029/1998GL900128.
- Eskes, H. J., and K. F. Boersma (2003), Averaging kernels for DOAS total column satellite retrievals, *Atmos. Chem. Phys.*, 3, 1285–1291, doi:10.5194/acp-3-1285-2003.
- Fayt, C., and M. Van Roozendaal (2001), WinDOAS 2.1, Software User Manual, Belgian Institute for Space Aeronomy, Brussels, Belgium. [Available at <http://bro.aeronomie.be/WinDOAS-SUM-210b.pdf>.]
- Fioletov, V. E., C. A. McLinden, N. Krotkov, M. D. Moran, and K. Yang (2011), Estimation of SO<sub>2</sub> emissions using OMI retrievals, *Geophys. Res. Lett.*, 38, L21811, doi:10.1029/2011GL049402.
- Fioletov, V. E., et al. (2013), Application of OMI, SCIAMACHY, and GOME-2 satellite SO<sub>2</sub> retrievals for detection of large emission sources, *J. Geophys. Res. Atmos.*, 118, 11,399–11,418, doi:10.1002/jgrd.50826.
- Greenblatt, G. D., J. J. Orlando, J. B. Burkholder, and A. R. Ravishankara (1990), Absorption measurements of oxygen between 330 and 1140 nm, *J. Geophys. Res.*, 95(D11), 18,577–18,582, doi:10.1029/JD095iD11p18577.
- Haywood, J. M., et al. (2010), Observations of the eruption of the Sarychev volcano and simulations using the HadGEM2 climate model, *J. Geophys. Res.*, 115, D21212, doi:10.1029/2010JD014447.
- He, H., et al. (2012), SO<sub>2</sub> over central China: Measurements, numerical simulations and the tropospheric sulfur budget, *J. Geophys. Res.*, 117, D00K37, doi:10.1029/2011JD016473.
- Hermans, C., A. C. Vandaele, and S. Fally (2009), Fourier transform measurements of SO<sub>2</sub> absorption cross sections: I. Temperature dependence in the 24 000–29 000 cm<sup>-1</sup> (345–420 nm) region, *J. Quant. Spectrosc. Radiat. Transfer*, 110, 756–765, doi:10.1016/j.jqsrt.2009.10.031.
- Hörmann, C., and T. Wagner (2014), Radiative transfer effects of high SO<sub>2</sub> and aerosol loads during major volcanic eruptions, presentation given at OMI Sc, Team Meeting, Utrecht, March 2014. [Available at [http://www.knmi.nl/omi/research/project/meetings/ostm18/pres\\_ostm18\\_2014.php](http://www.knmi.nl/omi/research/project/meetings/ostm18/pres_ostm18_2014.php).]
- Hörmann, C., H. Sihler, N. Bobrowski, S. Beirle, M. Penning de Vries, U. Platt, and T. Wagner (2013), Systematic investigation of bromine monoxide in volcanic plumes from space by using the GOME-2 instrument, *Atmos. Chem. Phys.*, 13, 4749–4781, doi:10.5194/acp-13-4749-2013.
- Huang, K., G. Zhuang, Q. Wang, J. S. Fu, Y. Lin, T. Liu, L. Han, and C. Deng (2014), Extreme haze pollution in Beijing during January 2013: Chemical characteristics, formation mechanism and role of fog processing, *Atmos. Chem. Phys. Discuss.*, 14, 7517–7556, doi:10.5194/acpd-14-7517-2014.
- Intergovernmental Panel on Climate Change (2013), *Climate Change 2013: The Physical Science Basis. Contribution of Working Group I to the Fifth Assessment Report of the Intergovernmental Panel on Climate Change*, edited by T. F. Stocker et al., 1535 pp., Cambridge Univ. Press, Cambridge, U. K., and New York.
- Khokhar, M. F., C. Frankenberg, M. Van Roozendaal, S. Beirle, S. Kühl, A. Richter, U. Platt, and T. Wagner (2005), Satellite observations of atmospheric SO<sub>2</sub> from volcanic eruptions during the time period of 1996 to 2002, *J. Adv. Space Res.*, 36(5), 879–887, doi:10.1016/j.asr.2005.04.114.
- Kleipool, Q. L., M. R. Dobber, J. F. de Haan, and P. F. Levelt (2008), Earth surface reflectance climatology from 3 years of OMI data, *J. Geophys. Res.*, 113, D18308, doi:10.1029/2008JD010290.
- Koukouli, M., D. Balis, D. Loyola, P. Valks, W. Zimmer, N. Hao, J.-C. Lambert, M. Van Roozendaal, C. Lerot, and R. Spurr (2012), Geophysical validation and long-term consistency between GOME-2/MetOp-A total ozone column and measurements from the sensors GOME/ERS-2, SCIAMACHY/ENVISAT and OMI/Aura, *Atmos. Meas. Tech.*, 5, 2169–2181, doi:10.5194/amt-5-2169-2012.
- Kristiansen, N. I., et al. (2010), Remote sensing and inverse transport modeling of the Kasatochi eruption sulfur dioxide cloud, *J. Geophys. Res.*, 115, D00L16, doi:10.1029/2009JD013286.
- Krotkov, N. A., S. A. Carn, A. J. Krueger, P. K. Bhartia, and K. Yang (2006), Band residual difference algorithm for retrieval of SO<sub>2</sub> from the Aura Ozone Monitoring Instrument (OMI), *IEEE Trans. Geosci. Remote Sens.*, 44(5), 1259–1266, doi:10.1109/TGRS.2005.861932.
- Krotkov, N. A., et al. (2008), Validation of SO<sub>2</sub> retrievals from the Ozone Monitoring Instrument over NE China, *J. Geophys. Res.*, 113, D16540, doi:10.1029/2007JD008818.
- Krotkov, N. A., M. R. Schoeberl, G. A. Morris, S. Carn, and K. Yang (2010), Dispersion and lifetime of the SO<sub>2</sub> cloud from the August 2008 Kasatochi eruption, *J. Geophys. Res.*, 115, D00L20, doi:10.1029/2010JD013984.
- Krueger, A. J., L. S. Walter, P. K. Bhartia, C. C. Schnetzler, N. A. Krotkov, I. Sprod, and G. J. S. Bluth (1995), Volcanic sulfur dioxide measurements from the total ozone mapping spectrometer instruments, *J. Geophys. Res.*, 100(D7), 14,057–14,076, doi:10.1029/95JD01222.
- Kurokawa, J., T. Ohara, T. Morikawa, S. Hanayama, G. Janssens-Maenhout, T. Fukui, K. Kawashima, and H. Akimoto (2013), Emissions of air pollutants and greenhouse gases over Asian regions during 2000–2008: Regional Emission inventory in ASia (REAS) version 2, *Atmos. Chem. Phys.*, 13, 11,019–11,058, doi:10.5194/acp-13-11019-2013.
- Lee, C., R. V. Martin, A. van Donkelaar, G. O'Byrne, N. Krotkov, A. Richter, L. G. Huey, and J. S. Holloway (2009), Retrieval of vertical columns of sulfur dioxide from SCIAMACHY and OMI: Air mass factor algorithm development, validation, and error analysis, *J. Geophys. Res.*, 114, D22303, doi:10.1029/2009JD012123.
- Lee, C., R. V. Martin, A. van Donkelaar, H. Lee, R. R. Dickerson, J. C. Hains, N. Krotkov, A. Richter, K. Vinnikov, and J. J. Schwab (2011), SO<sub>2</sub> emissions and lifetimes: Estimates from inverse modeling using in situ and global, space-based (SCIAMACHY and OMI) observations, *J. Geophys. Res.*, 116, D06304, doi:10.1029/2010JD014758.
- Leitão, J., A. Richter, M. Vrekoussis, A. Kokhanovsky, Q. J. Zhang, M. Beekmann, and J. P. Burrows (2010), On the improvement of NO<sub>2</sub> satellite retrievals—Aerosol impact on the air mass factors, *Atmos. Meas. Tech.*, 3, 475–493, doi:10.5194/amt-3-475-2010.

- Levelt, P. F., G. H. J. van den Oord, M. R. Dobber, A. Mälkki, H. Visser, J. de Vries, P. Stammes, J. Lundell, and H. Saari (2006), The ozone monitoring instrument, *IEEE Trans. Geo. Rem. Sens.*, *44*(5), 1093–1101, doi:10.1109/TGRS.2006.872333.
- Li, C., Q. Zhang, N. Krotkov, D. Streets, K. He, S.-C. Tsay, and J. F. Gleason (2010), Recent large reduction in sulfur dioxide from Chinese power plants observed by the ozone monitoring instrument, *Geophys. Res. Lett.*, *37*, L08807, doi:10.1029/2010GL042594.
- Li, C., J. Joiner, N. A. Krotkov, and P. K. Bhartia (2013), A fast and sensitive new satellite SO<sub>2</sub> retrieval algorithm based on principal component analysis: Application to the ozone monitoring instrument, *Geophys. Res. Lett.*, *40*, 6314–6318, doi:10.1002/2013GL058134.
- Lu, Z., D. G. Streets, B. de Foy, and N. A. Krotkov (2013), Ozone monitoring instrument observations of interannual increases in SO<sub>2</sub> emissions from Indian coal-fired power plants during 2005–2012, *Environ. Sci. Technol.*, *13*(24), 13,993–14,000, doi:10.1021/es4039648.
- Marbach, T., S. Beirle, U. Platt, P. Hoor, F. Wittrock, A. Richter, M. Vrekoussis, M. Grzegorski, J. P. Burrows, and T. Wagner (2009), Satellite measurements of formaldehyde from shipping emissions, *Atmos. Chem. Phys.*, *9*, 8223–8234, doi:10.5194/acp-9-8223-2009.
- Martin, R. V., et al. (2002), An improved retrieval of tropospheric nitrogen dioxide from GOME, *J. Geophys. Res.*, *107*(D20), 4437, doi:10.1029/2001JD001027.
- McLinden, C. A., V. Fioletov, K. F. Boersma, N. Krotkov, C. E. Sioris, J. P. Veefkind, and K. Yang (2012), Air quality over the Canadian oil sands: A first assessment using satellite observations, *Geophys. Res. Lett.*, *39*, L04804, doi:10.1029/2011GL050273.
- Moxnes, E. D., N. I. Kristiansen, A. Stohl, L. Clarisse, A. Durant, K. Weber, and A. Vogel (2014), Separation of ash and sulfur dioxide during the 2011 Grímsvötn eruption, *J. Geophys. Res. Atmos.*, *119*, 7477–7501, doi:10.1002/2013JD021129.
- Nowlan, C. R., X. Liu, K. Chance, Z. Cai, T. P. Kurosu, C. Lee, and R. V. Martin (2011), Retrievals of sulfur dioxide from the Global Ozone Monitoring Experiment 2 (GOME-2) using an optimal estimation approach: Algorithm and initial validation, *J. Geophys. Res.*, *116*, D18301, doi:10.1029/2011JD015808.
- Palmer, P. I., D. J. Jacob, K. Chance, R. V. Martin, R. J. D. Spurr, T. P. Kurosu, I. Bey, R. Yantosca, A. Fiore, and Q. Li (2001), Air mass factor formulation for spectroscopic measurements from satellites: Application to formaldehyde retrievals from the Global Ozone Monitoring Experiment, *J. Geophys. Res.*, *106*(D13), 14,539–14,550, doi:10.1029/2000JD900772.
- Platt, U., and J. Stutz (2008), *Differential Optical Absorption Spectroscopy (DOAS), Principle and Applications*, Springer, Heidelberg, Germany.
- Pukite, J., S. Kühl, T. Deutschmann, U. Platt, and T. Wagner (2010), Extending differential optical absorption spectroscopy for limb measurements in the UV, *Atmos. Meas. Tech.*, *3*, 631–653, doi:10.5194/amt-3-631-2010.
- Richter, A. (2009), Algorithm theoretical basis document for the GOME-2 rapid volcanic SO<sub>2</sub> product, SAVAA project. [Available at <http://savaa.nilu.no/PublicArchive.aspx>.]
- Richter, A., V. Eyring, J. P. Burrows, H. Bovensmann, A. Lauer, B. Sierk, and P. J. Crutzen (2004), Satellite measurements of NO<sub>2</sub> from international shipping emissions, *Geophys. Res. Lett.*, *31*, L23110, doi:10.1029/2004GL020822.
- Richter, A., F. Wittrock, and J. P. Burrows (2006), SO<sub>2</sub> measurements with SCIAMACHY, in *Proceeding of Atmospheric Science Conference, Frascati, Italy, 8–12 May, ESA Publ. SP-628*, ESA/ESRIN, Noordwijk, Netherlands.
- Richter, A., F. Wittrock, A. Schönhardt, and J. P. Burrows (2009), Quantifying volcanic SO<sub>2</sub> emissions using GOME-2 measurements, *Geophys. Res. Abstr.*, EGU2009-7679, EGU General Assembly 2009, Vienna, Austria.
- Richter, A., M. Begoin, A. Hilboll, and J. P. Burrows (2011), An improved NO<sub>2</sub> retrieval for the GOME-2 satellite instrument, *Atmos. Meas. Tech.*, *4*, 1147–1159, doi:10.5194/amt-4-1147-2011.
- Rix, M., et al. (2012), Volcanic SO<sub>2</sub>, BrO and plume height estimations using GOME-2 satellite measurements during the eruption of Eyjafjallajökull in May 2010, *J. Geophys. Res.*, *117*, D00U19, doi:10.1029/2011JD016718.
- Robock, A. (2000), Volcanic eruptions and climate, *Rev. Geophys.*, *38*(2), 191–219, doi:10.1029/1998RG000054.
- Spurr, R. (2008), LIDORT and VLIDORT: Linearized pseudo-spherical scalar and vector discrete ordinate radiative transfer models for use in remote sensing retrieval problems, in *Light Scattering Reviews*, vol. 3, edited by A. Kokhanovsky, Springer, Chichester, U. K.
- Stavrakou, T., J.-F. Müller, I. De Smedt, M. van Roozendaal, G. van der Werf, L. Giglio, and A. Guenther (2009), Evaluating the performance of pyrogenic and biogenic emission inventories against one decade of space-based formaldehyde columns, *Atmos. Chem. Phys.*, *9*, 1037–1060, doi:10.5194/acp-9-1037-2009.
- Stavrakou, T., J.-F. Müller, K. F. Boersma, R. J. van der A, J. Kurokawa, T. Ohara, and Q. Zhang (2013), Key chemical NO<sub>x</sub> sink uncertainties and how they influence top-down emissions of nitrogen oxides, *Atmos. Chem. Phys.*, *13*, 9057–9082, doi:10.5194/acp-13-9057-2013.
- Taubman, B. F., J. C. Hains, A. M. Thompson, L. T. Marufu, B. G. Doddridge, J. W. Stehr, C. A. Piety, and R. R. Dickerson (2006), Aircraft vertical profiles of trace gas and aerosol pollution over the mid- Atlantic United States: Statistics and meteorological cluster analysis, *J. Geophys. Res.*, *111*, D10S07, doi:10.1029/2005JD006196.
- Theys, N., et al. (2013), Volcanic SO<sub>2</sub> fluxes derived from satellite data: A survey using OMI, GOME-2, IASI and MODIS, *Atmos. Chem. Phys.*, *13*, 5945–5968, doi:10.5194/acp-13-5945-2013.
- Vandaele, A.-C., C. Hermans, P. C. Simon, M. Carleer, R. Colin, S. Fally, M. F. Mérienne, A. Jenouvrier, and B. Coquart (1998), Measurements of the NO<sub>2</sub> absorption cross-section from 42000 cm<sup>-1</sup> to 10000 cm<sup>-1</sup> (238–1000 nm) at 220 K and 294 K, *J. Quant. Spectrosc. Radiat. Transfer*, *59*, 171–184, doi:10.1016/S0022-4073(97)00168-4.
- van der Werf, G. R., J. T. Randerson, L. Giglio, G. J. Collatz, M. Mu, P. S. Kasibhatla, D. C. Morton, R. S. DeFries, Y. Jin, and T. T. van Leeuwen (2010), Global fire emissions and the contribution of deforestation, savanna, forest, agricultural, and peat fires (1997–2009), *Atmos. Chem. Phys.*, *10*, 11,707–11,735, doi:10.5194/acp-10-11707-2010.
- Veefkind, P., et al. (2012), TROPOMI on the ESA Sentinel-5 Precursor: A GMES mission for global observations of the atmospheric composition for climate, air quality and ozone layer applications, *Remote Sens. Environ.*, *120*, 70–83, doi:10.1016/j.rse.2011.09.027.
- Vountas, M., V. V. Rozanov, and J. P. Burrows (1998), Ring effect: Impact of rotational Raman scattering on radiative transfer in Earth's atmosphere, *J. Quant. Spectrosc. Radiat. Transfer*, *60*(6), 943–961, doi:10.1016/S0022-4073(97)00186-6.
- Walter, D., K.-P. Heue, A. Rauthe-Schöch, C. A. M. Brenninkmeijer, L. N. Lamsal, N. A. Krotkov, and U. Platt (2012), Flux calculation using CARIBIC DOAS aircraft measurements: SO<sub>2</sub> emission of Norilsk, *J. Geophys. Res.*, *117*, D11305, doi:10.1029/2011JD017335.
- Wang, T., et al. (2014), Evaluation of tropospheric SO<sub>2</sub> retrieved from MAX-DOAS measurements in Xianghe, China, *Atmos. Chem. Phys.*, *14*, 11,149–11,164, doi:10.5194/acp-14-11149-2014.
- Waythomas, C. F., W. E. Scott, S. G. Prejean, D. J. Schneider, P. Izbekov, and C. J. Nye (2010), The 7–8 August 2008 eruption of Kasatochi Volcano, central Aleutian Islands, Alaska, *J. Geophys. Res.*, *115*, B00B06, doi:10.1029/2010JB007437.
- Yang, K., N. A. Krotkov, A. J. Krueger, S. A. Carn, P. K. Bhartia, and P. F. Levelt (2007), Retrieval of large volcanic SO<sub>2</sub> columns from the Aura Ozone Monitoring Instrument: Comparison and limitations, *J. Geophys. Res.*, *112*, D24S43, doi:10.1029/2007JD008825.
- Yang, K., R. R. Dickerson, S. A. Carn, C. Ge, and J. Wang (2013), First observations of SO<sub>2</sub> from the satellite Suomi NPP OMPs: Widespread air pollution events over China, *Geophys. Res. Lett.*, *40*, 4957–4962, doi:10.1002/grl.50952.
- Zhao, F., and Z. Li (2007), Estimation of aerosol single scattering albedo from solar direct spectral radiance and total broadband irradiances measured in China, *J. Geophys. Res.*, *112*, D22S03, doi:10.1029/2006JD007384.



## Improved spectral fitting of nitrogen dioxide from OMI in the 405–465 nm window

J. H. G. M. van Geffen<sup>1</sup>, K. F. Boersma<sup>1,2</sup>, M. Van Roozendael<sup>3</sup>, F. Hendrick<sup>3</sup>, E. Mahieu<sup>4</sup>, I. De Smedt<sup>3</sup>, M. Sneep<sup>1</sup>, and J. P. Veefkind<sup>1,5</sup>

<sup>1</sup>Royal Netherlands Meteorological Institute (KNMI), De Bilt, the Netherlands

<sup>2</sup>Wageningen University (WUR), Wageningen, the Netherlands

<sup>3</sup>Belgium Institute for Space Aeronomy (BIRA-IASB), Brussels, Belgium

<sup>4</sup>University of Liège (ULg), Liège, Belgium

<sup>5</sup>Delft University of Technology (TUDelft), Delft, the Netherlands

Correspondence to: J. H. G. M. van Geffen (geffen@knmi.nl)

Received: 16 June 2014 – Published in Atmos. Meas. Tech. Discuss.: 21 October 2014

Revised: 19 February 2015 – Accepted: 23 March 2015 – Published: 8 April 2015

**Abstract.** An improved nitrogen dioxide (NO<sub>2</sub>) slant column density retrieval for the Ozone Monitoring Instrument (OMI) in the 405–465 nm spectral region is presented. Since the launch of OMI on board NASA's EOS-Aura satellite in 2004, differential optical absorption spectroscopy (DOAS) retrievals of NO<sub>2</sub> slant column densities have been the starting point for the KNMI DOMINO and NASA SP NO<sub>2</sub> vertical column data as well as the OMI NO<sub>2</sub> data of some other institutes. However, recent intercomparisons between NO<sub>2</sub> retrievals from OMI and other UV/Vis and limb spectrometers, as well as ground-based measurements, suggest that OMI stratospheric NO<sub>2</sub> is biased high.

This study revises and, for the first time, fully documents the OMI NO<sub>2</sub> retrieval in detail. The representation of the OMI slit function to convolve high-resolution reference spectra onto the relevant spectral grid is improved. The window used for the wavelength calibration is optimised, leading to much-reduced fitting errors. Ozone and water vapour spectra used in the fit are updated, reflecting the recently improved knowledge of their absorption cross section in the literature. The improved spectral fit also accounts for absorption by the O<sub>2</sub>–O<sub>2</sub> collision complex and by liquid water over clear-water areas.

The main changes in the improved spectral fitting result from the updates related to the wavelength calibration: the RMS error of the fit is reduced by 23 % and the NO<sub>2</sub> slant column by  $0.85 \times 10^{15}$  molec cm<sup>-2</sup>, independent of latitude, solar zenith angle and NO<sub>2</sub> value. Including O<sub>2</sub>–O<sub>2</sub> and liq-

uid water absorption and updating the O<sub>3</sub> and water vapour cross-section spectra further reduces NO<sub>2</sub> slant columns on average by  $0.35 \times 10^{15}$  molec cm<sup>-2</sup>, accompanied by a further 9 % reduction in the RMS error of the fit.

The improved OMI NO<sub>2</sub> slant columns are consistent with independent NO<sub>2</sub> retrievals from other instruments to within a range that can be explained by photochemically driven diurnal increases in stratospheric NO<sub>2</sub> and by small differences in fitting window and approach. The revisions indicate that current OMI NO<sub>2</sub> slant columns suffered mostly from an additive positive offset, which is removed by the improved wavelength calibration and representation of the OMI slit function. It is therefore anticipated that the improved NO<sub>2</sub> slant columns are most important to retrievals of spatially homogeneous stratospheric NO<sub>2</sub> rather than to heterogeneous tropospheric NO<sub>2</sub>.

### 1 Introduction

Nitrogen dioxide (NO<sub>2</sub>) and nitrogen oxide (NO) – together usually referred to as nitrogen oxides (NO<sub>x</sub> = NO + NO<sub>2</sub>) – are important trace gases in the Earth's atmosphere. They enter the atmosphere due to anthropogenic (e.g. fossil fuel combustion, biomass burning) and natural (e.g. microbiological processes in soils, wild fires, lightning) processes. Over remote regions NO<sub>2</sub> is primarily located in the stratosphere. Stratospheric NO<sub>2</sub> columns range from about  $2 \times 10^{15}$  to

$7 \times 10^{15}$  molec  $\text{cm}^{-2}$  between the tropics and high latitudes. For polluted regions, up to 90 % of the total  $\text{NO}_2$  column may be located in the troposphere. Tropospheric  $\text{NO}_2$  columns over polluted areas are usually considerably higher, in places even higher than  $30 \times 10^{15}$  molec  $\text{cm}^{-2}$ . For typical levels of OH, the lifetime of  $\text{NO}_x$  in the lower troposphere is less than 1 day (e.g. Schaub et al., 2007; Beirle et al., 2011).

Boundary layer  $\text{NO}_2$  directly affects human health (WHO, 2003). In addition, nitrogen oxides are essential precursors for the photochemical formation of ozone (Sillman et al., 1990): they influence concentrations of OH and thereby influence the lifetime of methane (Fuglestedt et al., 1999) and other gases.  $\text{NO}_2$  itself is a minor greenhouse gas, but the indirect effects of  $\text{NO}_2$  on global climate change are probably larger, with a presumed net cooling effect mostly driven by oxidation-fuelled aerosol formation (Shindell et al., 2009). Stratospheric  $\text{NO}_2$  originates mainly from oxidation of  $\text{N}_2\text{O}$  in the middle stratosphere, which leads to  $\text{NO}_x$ , which in turn acts as a catalyst for ozone destruction (Crutzen, 1970; Hendrick et al., 2012). Stratospheric  $\text{NO}_x$  can also suppress ozone depletion by converting reactive chlorine and hydrogen compounds into unreactive reservoir species (such as  $\text{ClONO}_2$  and  $\text{HNO}_3$ ; Murphy et al., 1993).

The important role of  $\text{NO}_2$  in both troposphere and stratosphere requires monitoring of its concentration distribution on a global scale. Observations from satellite instruments provide global coverage complementary to sparse measurements by ground-based and in situ (balloon, aircraft) instruments.  $\text{NO}_2$  column densities have been retrieved using the differential optical absorption spectroscopy (DOAS) technique from space since the mid-1990s from data acquired by the nadir-viewing UV/Vis backscatter instruments GOME (Burrows et al., 1999), SCIAMACHY (Bovensmann et al., 1999), OMI (Levelt et al., 2006) and the GOME-2 instruments (Munro et al., 2006) aboard MetOp-A and MetOp-B. TROPOMI (Veefkind et al., 2012), scheduled for launch in 2016, will extend the record of these observations.

The retrieval of  $\text{NO}_2$  from satellite measured spectra with DOAS is certainly possible but not easy: the structure of the  $\text{NO}_2$  differential absorption is weak and there are interfering signals from the surface, atmosphere and instrumental issues. Most retrievals of  $\text{NO}_2$  concentrations are performed in the visible range between 400 and 500 nm, taking into account other absorbers and processes relevant in this wavelength range. Early satellite retrievals of  $\text{NO}_2$  focused on the dominant absorbers  $\text{NO}_2$ , ozone and water vapour, as well as rotational Raman scattering (the so-called “Ring effect”). Recent years have shown continuous improvements in the  $\text{NO}_2$  retrieval by accounting for weaker absorbers, notably the  $\text{O}_2\text{--O}_2$  collision complex and liquid water.

This paper describes a revision of  $\text{NO}_2$  slant column retrieval from level-1b spectra measured by OMI since 2004, performed by a processor named OMNO2A. The study was prompted by the observation, reported first by N. Krotkov at the EOS-Aura meeting in October 2012 (Krotkov et al.,

2012), that OMI stratospheric  $\text{NO}_2$  concentrations are systematically higher than those derived from SCIAMACHY and GOME-2 measurements by  $0.5\text{--}1 \times 10^{15}$  molec  $\text{cm}^{-2}$ , after accounting for the daytime increase in stratospheric  $\text{NO}_2$  (Dirksen et al., 2011). Recently, Belmonte-Rivas et al. (2014) confirmed the high bias in OMI stratospheric columns compared to an ensemble of stratospheric  $\text{NO}_2$  retrievals from satellite-based limb-sounding sensors. Section 3 presents a further comparison of OMI, SCIAMACHY and GOME-2 data, as well as a comparison using ground-based measurements at the Jungfraujoch station, to confirm the high bias in OMI  $\text{NO}_2$  data.

The revision of the OMNO2A settings and input is further motivated by a number of issues regarding the absorption reference spectra (Sect. 4.1): (a) the need to update the spectra of ozone and water vapour; (b) the need to account for the wavelength and row dependency of the OMI slit function in the convolution of the spectra; (c) the need to investigate whether including absorption by  $\text{O}_2\text{--O}_2$  (so far omitted from OMNO2A; cf. Bucselá et al., 2006) and liquid water (cf. Richter et al., 2011; Lerot et al., 2010) improves the  $\text{NO}_2$  retrieval results. In addition, the effects on the DOAS  $\text{NO}_2$  retrieval of the wavelength calibration of the OMI radiance spectra, introduced in OMNO2A following the first appearance of the so-called row anomaly in 2007 but not yet evaluated, has been investigated and the calibration settings have been optimised (Sect. 4.2). Lastly, it was recognised that it is important for users of the OMI  $\text{NO}_2$  data to document the essential elements, both the current and the updated, of the slant column retrieval in one easily referable paper.

## 2 Observations of $\text{NO}_2$ column densities

### 2.1 UV/Vis satellite-based $\text{NO}_2$ observations

The main focus of this paper is  $\text{NO}_2$  data derived from measurements by OMI (Levelt et al., 2006), which are compared to  $\text{NO}_2$  data from the first GOME-2 instrument (Munro et al., 2006) and from SCIAMACHY (Bovensmann et al., 1999). All three instruments measure the backscattered and direct sunlight in the UV and visible ranges from a sun-synchronous polar orbit.

OMI is aboard the EOS-Aura satellite and has been operating since 2004. The overpass is at 13:40 local time (LT), with the satellite flying south to north on the dayside of the Earth. Individual nadir ground pixels are  $13 \times 24 \text{ km}^2$  at the middle of the swath; the size of the pixels increases towards the edges of the swath. The full swath width is about 2600 km and OMI achieves global coverage each day.

The first GOME-2 instrument is aboard the MetOp-A satellite and has been operating since 2007. The overpass is at 09:30 LT, with the satellite flying north to south on the dayside of the Earth. Individual ground pixels are  $40 \times 80 \text{ km}^2$ . The full swath width is about 1920 km and GOME-2 achieves nearly global coverage each day. A sec-

**Table 1.** Main settings of the DOAS retrieval of NO<sub>2</sub> slant column densities of the data versions used in this paper for the satellite instruments OMI, GOME-2 and SCIAMACHY; for OMI the current settings and the settings resulting from the discussion in this paper are given.

|                       | OMI – current                                    | OMI – updated   | GOME-2  | SCIAMACHY   |
|-----------------------|--|---|---|---|
| Wavelength range (nm) | 405–465  | 405–465   | 425–450   | 426.5–451.5   |
| Secondary trace gases | O <sub>3</sub> , H <sub>2</sub> O <sub>vap</sub> | O <sub>3</sub> , H <sub>2</sub> O <sub>vap</sub> , O <sub>2</sub> –O <sub>2</sub> , H <sub>2</sub> O <sub>liq</sub> | O <sub>3</sub> , H <sub>2</sub> O <sub>vap</sub> , O <sub>2</sub> –O <sub>2</sub> | O <sub>3</sub> , H <sub>2</sub> O <sub>vap</sub> , O <sub>2</sub> –O <sub>2</sub> |
| Pseudo-absorbers      | Ring   | Ring  | Ring  | Ring  |
| Degree of polynomial  | 5  | 5   | 3   | 2   |
| Fitting method        | non-linear                                       | non-linear  | linear  | linear  |
| Offset fitted         | no   | no  | yes   | yes   |
| DOAS retrieval code   | OMNO2A   | OMNO2A  | QDOAS   | QDOAS   |
| Retrieval responsible | KNMI   | KNMI  | BIRA-IASB   | BIRA-IASB   |
| Data version used     | DOMINO v2.0                                      | DOMINO v3.0   | TM4NO2A v2.1  | TM4NO2A v2.0  |

ond, identical GOME-2 instrument was launched aboard the MetOp-B satellite in 2012. In this paper, GOME-2 refers to the instrument aboard MetOp-A, sometimes referred to as GOME-2A.

SCIAMACHY is aboard the satellite ENVISAT and operated in the period 2002–2012. The overpass was at 10:00 LT, with the satellite flying north to south on the dayside of the Earth. Individual ground pixels were 30 × 60 km<sup>2</sup>. The full swath width was about 960 km and SCIAMACHY achieved global coverage only once every 6 days, because it measured alternatively in a nadir and limb viewing mode.

The DOAS retrieval technique, described in Sect. 2.2, is applied to the backscattered spectra measured by the three satellite instruments to obtain the NO<sub>2</sub> slant column density (SCD). The SCD is the integrated concentration of NO<sub>2</sub> over light paths from the Sun through the Earth’s atmosphere to the satellite, weighted with their relative contribution to the radiance.

The standard OMI NO<sub>2</sub> SCD data are calculated at NASA by a processor named OMNO2A. The retrieval results of OMNO2A are input for subsequent processing to determine NO<sub>2</sub> vertical column densities (VCDs), e.g. for the DOMINO data product of KNMI (e.g. Boersma et al., 2007, 2011; Dirksen et al., 2011) and NASA’s NO<sub>2</sub> Standard Product (SP; e.g. Bucselo et al., 2006, 2013). For the OMI NO<sub>2</sub> retrieval, the selected spectral fitting window is 405–465 nm, wider than the often used 425–450 nm window in order to improve the effective signal-to-noise ratio.

For GOME-2 and SCIAMACHY NO<sub>2</sub> SCD data, BIRA-IASB uses a processor based on QDOAS (Danckaert et al., 2012), the multi-platform successor of their WinDOAS package; see e.g. Van Roozendaal et al. (2006) and Lerot et al. (2009). The DOAS fit on GOME-2 and SCIAMACHY data uses almost the same wavelength window: 425.0–450.0 and 426.5–451.5 nm respectively (the small difference between the fit windows is related to instrumental issues). The degree of the DOAS polynomial is 3 for GOME-2 and 2 for SCIAMACHY.

Table 1 provides an overview of the details of the DOAS retrieval for the OMI, GOME-2 and SCIAMACHY sensors used in this study.

## 2.2 DOAS retrieval of NO<sub>2</sub> slant column densities

The DOAS (Platt, 1994; Platt and Stutz, 2008) technique matches an analytical function that describes the relevant atmospheric physical processes (scattering, reflection and absorption) to the satellite-measured spectrum. In the OMNO2A setup, the modelled reflectance is expressed in terms of intensities, which leads to a non-linear fit problem and allows the effects of inelastic scattering to be described after a scattering event has occurred:

$$R_{\text{mod}}(\lambda) = P(\lambda) \cdot \exp \left[ - \sum_{k=1}^{N_k} \sigma_k(\lambda) \cdot N_{\text{scd},k} \right] \cdot \left( 1 + C_{\text{Ring}} \frac{I_{\text{Ring}}(\lambda)}{I_0(\lambda)} \right). \quad (1)$$

This physical model contains a low-order polynomial  $P(\lambda)$  of degree  $N_p$  that represents the slowly varying broad-band absorption, as well as Rayleigh and Mie scattering processes in the atmosphere and smooth surface reflection and absorption effects. Furthermore, the physical model includes the spectrally varying absorption signatures  $\sigma_k(\lambda)$  and the slant column amount  $N_{\text{scd},k}$  of relevant absorbers  $k$ , notably NO<sub>2</sub>, ozone (O<sub>3</sub>) and water vapour (H<sub>2</sub>O<sub>vap</sub>).

The physical model accounts for inelastic Raman scattering of incoming sunlight by N<sub>2</sub> and O<sub>2</sub> molecules that leads to filling-in of the Fraunhofer lines in the radiance spectrum – the so-called “Ring effect” (see Grainger and Ring, 1962; Chance and Spurr, 1997) – by describing these effects as a pseudo-absorber, that is, by including a Ring reference absorption spectrum along with the molecular absorption terms. In Eq. (1),  $C_{\text{Ring}}$  is the Ring fitting coefficient and  $I_{\text{Ring}}(\lambda)/I_0(\lambda)$  the sun-normalised synthetic Ring spectrum. The term between parentheses in Eq. (1) describes both the contribution of the direct differential absorption (i.e. the 1) and the modification of these differential structures by in-

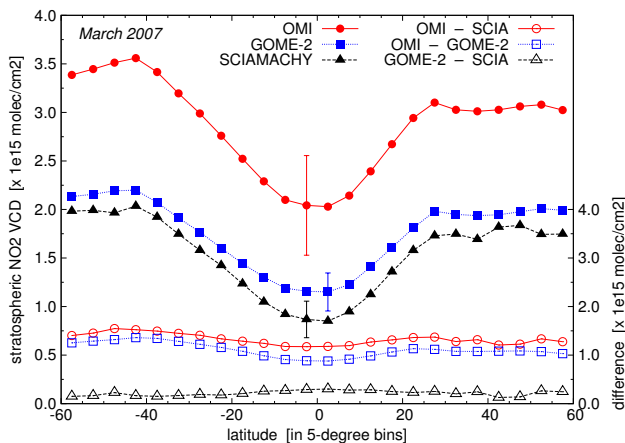


**Figure 1.** Monthly average stratospheric NO<sub>2</sub> VCD values (left axis; filled symbols) and absolute differences (right axis; open symbols) in  $10^{15}$  molec cm<sup>-2</sup> of OMI, GOME-2 and SCIAMACHY in March 2007 over the Pacific Ocean area (60° S–60° N, 140–180° W), as a function of latitude. The error bars at the data points near the equator mark for that latitude bin the average standard deviation of the total VCD (data source: <http://www.temis.nl/>).

elastic scattering (the  $+C_{\text{Ring}} I_{\text{Ring}}(\lambda)/I_0(\lambda)$  term) to the reflectance spectrum.

The DOAS procedure minimises the difference between the measured reflectance spectrum  $R_{\text{meas}}(\lambda)$  and the modelled spectrum  $R_{\text{mod}}(\lambda)$  within a given wavelength window, in the form of minimisation of a chi-squared merit function. The measured reflectance  $R_{\text{meas}}(\lambda)$  is determined from the radiance measured at top-of-atmosphere  $I(\lambda)$  and the measured extraterrestrial solar irradiance spectrum  $I_0(\lambda)$ . Some further details on the OMI NO<sub>2</sub> DOAS slant column retrieval, such as the merit function that is minimised and the definition of the RMS error, can be found in Sect. S1 in the Supplement.

### 3 Intercomparisons of stratospheric NO<sub>2</sub> columns

NO<sub>2</sub> data from OMI, GOME-2 and SCIAMACHY are evaluated for 2007. Stratospheric NO<sub>2</sub> concentrations are best detected over the Pacific Ocean, where tropospheric contributions to the NO<sub>2</sub> column are small in the absence of substantial sources of pollution. The Pacific Ocean area is defined here as the area from 60° S to 60° N and from 140 to 180° W. DOMINO v2.0 data are used for OMI (Boersma et al., 2011), TM4NO2A v2.1 for GOME-2 and TM4NO2A v2.0 for SCIAMACHY (Boersma et al., 2004).

Figure 1 shows the monthly average stratospheric NO<sub>2</sub> column for the three instruments and their mutual differences as a function of latitude for March 2007; for other months (not shown) the comparisons look quite similar. The OMI stratospheric columns are clearly higher than those of GOME-2 by about  $1.0 \times 10^{15}$  molec cm<sup>-2</sup>, consistent with Belmonte-Rivas et al. (2014), who reported a similar high

**Table 2.** Average differences in stratospheric NO<sub>2</sub> columns over the Pacific Ocean area (60° S–60° N, 140–180° W) of 2007 of OMI, GOME-2 and SCIAMACHY, where the averages are computed from monthly latitudinally binned data. The relative difference (right column) is given as percentage of the column values of the second instrument in the difference, e.g. w.r.t. SCIA in the difference OMI – SCIA (data source: <http://www.temis.nl/>).

| Instruments   | Absolute values<br>[ $\times 10^{15}$ molec cm <sup>-2</sup> ] | Relative difference<br>[%] |
|---------------|--|----------------------------|
| OMI – SCIA    | $+1.28 \pm 0.15$   | $+80.1 \pm 9.6$            |
| OMI – GOME-2  | $+1.14 \pm 0.18$   | $+65.6 \pm 10.3$           |
| GOME-2 – SCIA | $+0.14 \pm 0.09$   | $+8.7 \pm 5.8$             |

bias in OMI and low bias in SCIAMACHY data relative to stratospheric NO<sub>2</sub> columns obtained from an ensemble of limb and nadir sensors. The GOME-2 stratospheric columns (not included in the study of Belmonte-Rivas et al., 2014) in turn are higher than those of SCIAMACHY by  $0.1\text{--}0.3 \times 10^{15}$  molec cm<sup>-2</sup>.

Figure 1 shows that there is only a weak variability of the intra-sensor differences with latitude and that the differences are similar to within  $0.2 \times 10^{15}$  molec cm<sup>-2</sup>. This weak variability with latitude and independence of the month indicates that the differences between the instruments is dominated by an additive offset. Table 2 lists the annual averaged 2007 intra-sensor differences over the Pacific Ocean area. The difference of  $1.1\text{--}1.3 \times 10^{15}$  molec cm<sup>-2</sup> between OMI (overpass at 13:40 LT) and the two mid-morning sensors is considerably larger than the increase of stratospheric NO<sub>2</sub> between the respective measurement times. Photochemical models suggest a latitude-dependent increase of 10–30% in stratospheric NO<sub>2</sub> between 09:30 and 13:40 LT. This increase reflects the production of NO<sub>2</sub> from N<sub>2</sub>O<sub>5</sub> photodissociation and corresponds to an increase of  $0.1\text{--}0.6 \times 10^{15}$  molec cm<sup>-2</sup> (Dirksen et al., 2011; Belmonte-Rivas et al., 2014).

The comparison of data from the ground-based SAOZ and FTIR instruments at the Jungfraujoch station with satellite data by Hendrick et al. (2012) was repeated, now also including OMI data and extending the GOME-2 and SCIAMACHY data sets to the end of 2012 (see Sect. S2 in the Supplement). The results of the comparisons also strongly suggest that OMI stratospheric NO<sub>2</sub> is biased high. Since the air-mass factor calculations for NO<sub>2</sub> in the stratosphere are straightforward (with an error of less than 1%), the high bias in OMI stratospheric columns originates from the slant column retrieval. As a result of this finding, the details of the OMI NO<sub>2</sub> spectral fitting OMNO2A were revisited.

## 4 Improvements to the OMI NO<sub>2</sub> retrieval

### 4.1 Reference spectra

The set of reference spectra in the current OMNO2A processing has been introduced in August 2006. Since then a number of improved reference spectra data sets have been reported in the peer-reviewed literature. In addition, the reference spectra used in the current OMNO2A processing have been convolved with the OMI slit function, described by a parametrised broadened Gaussian function (Dirksen et al., 2006), but without taking the wavelength and row dependency (i.e. viewing angle dependency) of the slit function into account.

For these reasons all relevant cross sections are generated anew, based on the latest established absorption spectra, and convolved with the OMI slit function while now taking the wavelength and row dependency of the slit function into account in the form of a row-average slit function. The OMI slit function<sup>1</sup> and the implementation of the convolution are given in Sect. S3 in the Supplement.

Details of the relevant reference spectra used in the current and forthcoming OMNO2A slant column fit are given in Sect. S4. The updated reference spectra are

- solar spectrum  $I_{\text{ref}}(\lambda)$ , from Dobber et al. (2008)
- NO<sub>2</sub> absorption, from Vandaele et al. (1998)
- O<sub>3</sub> absorption, from Bogumil et al. (2000), version 3.0 (Dec. 2004)
- water vapour (H<sub>2</sub>O<sub>vap</sub>) absorption, based on the HITRAN 2012 database (Rothman et al., 2013)
- O<sub>2</sub>–O<sub>2</sub> absorption, from Thalman and Volkamer (2013)
- liquid water (H<sub>2</sub>O<sub>liq</sub>) absorption, from Pope and Fry (1997)
- Ring radiance spectrum  $I_{\text{Ring}}(\lambda)$ , computed following Chance and Spurr (1997).

The reference spectra labelled “v2006” below refer to those used in the current OMNO2A processor (used in, for example, the DOMINO v2.0 data set), while “v2014” refers to the updated reference spectra. The relation between these labels and the official version numbering of OMNO2A is described in Sect. S5.

<sup>1</sup> The full set of the OMI slit function – the slit functions for the 60 individual rows as well as the average slit function, both for the visible (350–500 nm) and UV (310–380 nm) wavelength ranges – is available for download via the OMI website at <http://www.knmi.nl/omi/research/product/>.

### 4.1.1 Other absorption features

Over tropical forests, detectable contributions from glyoxal (CHOCHO) have been reported, and its retrieval requires the inclusion of NO<sub>2</sub> absorption (e.g. Lerot et al., 2010). Conversely, however, glyoxal absorption is only a very minor interference for NO<sub>2</sub> absorption, so that it can be safely neglected.

Richter et al. (2011) have investigated absorption signatures attributable to sand, e.g. over deserts, but this signature is broadband in the OMI NO<sub>2</sub> fit window (any structure in the signature lies well beyond the fit window) and is therefore not accounted for here.

Absorption by vibrational Raman scattering (VRS; e.g. Vasilkov et al., 2002; Vountas et al., 2003) is known to play a role over open waters and thus may have an impact on the NO<sub>2</sub> retrieval; however, it is unclear whether including VRS improves the retrieval results, partly because its signature is apparent over areas where it certainly is not playing a role, e.g. over deserts (A. Richter, personal communication, 2014). In addition, the VRS signature does not seem to be independent from the signature of liquid water absorption (Peters et al., 2014). For these reasons, absorption by VRS is not investigated here.

### 4.2 Wavelength calibration

The measured solar irradiance spectrum  $I_0(\lambda)$  used in the OMI NO<sub>2</sub> DOAS fit has been constructed from a yearly average of daily solar irradiance measurements by OMI during 2005 and has an accurate wavelength calibration.

From the start of the OMI mission, the level-1b radiance spectra  $I(\lambda)$  of OMI are given on an initial assigned wavelength grid (Voors et al., 2006). This assigned wavelength grid – hereafter referred to as “wcA” – was at the time accurate enough for the NO<sub>2</sub> retrieval with OMNO2A. After the onset of the first row anomaly<sup>2</sup> in June 2007 and the subsequent growth of this issue after May 2008, however, the assigned wavelength grid appeared to be less accurate and, consequently, hampered sufficiently accurate NO<sub>2</sub> retrievals in all rows, including those not affected by the row anomaly.

The NO<sub>2</sub> fit results were improved by the introduction of a wavelength calibration in OMNO2A in January 2009. This wavelength calibration determines a wavelength shift for each individual radiance spectrum  $I(\lambda)$  from a fit against the reference solar spectrum  $I_{\text{ref}}(\lambda)$ , taking the Ring effect into account (cf. Voors et al., 2006), starting from the assigned wavelength grid wcA. The wavelength calibration in the current OMNO2A processing, called “wcB” hereafter, uses 408.0–423.0 nm as the calibration window. This window was chosen because it covers some distinct Fraunhofer features in the solar spectrum. Due to the construction of the OMI detector, a squeezing or stretching of the wave-

<sup>2</sup> See <http://www.knmi.nl/omi/research/product/rowanomaly-background.php> for an explanation and details.

**Table 3.** Pacific Ocean test orbit average main results of the wavelength calibration and spectral fit, using the v2014 reference spectra for the wavelength calibration windows mentioned in Sect. 4.2.

| Name | Calib. window |             | Shift<br>$\times 10^{-3}$<br>(nm) | RMS<br>$\times 10^{-4}$<br>(–) | NO <sub>2</sub> error<br>$\times 10^{15}$<br>(molec cm <sup>-2</sup> ) |
|------|---------------|-------------|-----------------------------------|--------------------------------|--|
|      | Begin<br>(nm) | End<br>(nm) |                                   |                                |  |
| wcB  | 408.0         | 423.0       | -3.63                             | 0.97                           | 0.99   |
| wcN  | 409.0         | 428.0       | -4.68                             | 0.95                           | 0.97   |
| wcC  | 425.5         | 443.0       | -7.70                             | 1.09                           | 1.10   |
| wcF  | 405.0         | 465.0       | -6.83                             | 1.02                           | 1.04   |

lengths is unlikely (which is confirmed by ongoing tests on OMI data as preparation for the implementation of a wavelength calibration for TROPOMI which includes the possibility of a squeeze/stretch in the calibration), so that the shift found from the calibration window is representative for the whole NO<sub>2</sub> fit window. The relation between the wavelength calibration labels and the official version numbering of OMNO2A is described in Sect. S5.

With the update of the solar reference spectrum  $I_{\text{ref}}(\lambda)$  and the Ring radiance spectrum  $I_{\text{Ring}}(\lambda)$ , the wavelength shift determined in calibration window wcB turns out to be different from the shift found in the current OMNO2A setup. This change in the wavelength grid of the level-1b spectra directly improves the fit results: both the RMS and the error on the NO<sub>2</sub> SCD are reduced. Using the v2006 reference spectra for NO<sub>2</sub>, O<sub>3</sub> and H<sub>2</sub>O<sub>vap</sub> (and not yet including O<sub>2</sub>-O<sub>2</sub> and H<sub>2</sub>O<sub>liq</sub>), the changes due to the introduction of the new solar and Ring reference spectra in the wcB wavelength calibration, averaged between 60° S and 60° N over the Pacific Ocean test orbit (see Sect. 5.1), are as follows:

- wavelength shift from +0.55 to  $-3.63 \times 10^{-3}$  nm
- RMS error from 1.39 to  $1.15 \times 10^{-4}$  (-17.4 %)
- NO<sub>2</sub> error from 1.29 to  $1.17 \times 10^{15}$  molec cm<sup>-2</sup> (-9.2 %)
- NO<sub>2</sub> SCD from 8.54 to  $8.04 \times 10^{15}$  molec cm<sup>-2</sup> (-5.8 %).

Since the spectral sampling of OMI is about 0.21 nm (Lev-elt et al., 2006), a shift of  $-3.62 \times 10^{-3}$  nm corresponds to 1.7 % of a wavelength pixel.

Given that the NO<sub>2</sub> fit results depend so clearly on the wavelength calibration, it was decided to test a range of calibration windows. Both the starting and end point of the calibration window were varied in steps of 0.5 nm, with a minimum size of 10 nm for the window, over the complete 405–465 nm fit window for a total of 5151 possible calibration windows. The fits were performed on the Pacific Ocean test orbit with all new v2014 reference spectra, including O<sub>2</sub>-O<sub>2</sub> and H<sub>2</sub>O<sub>liq</sub> absorption. From these calculations the “optimal calibration window”, defined as the window that results in

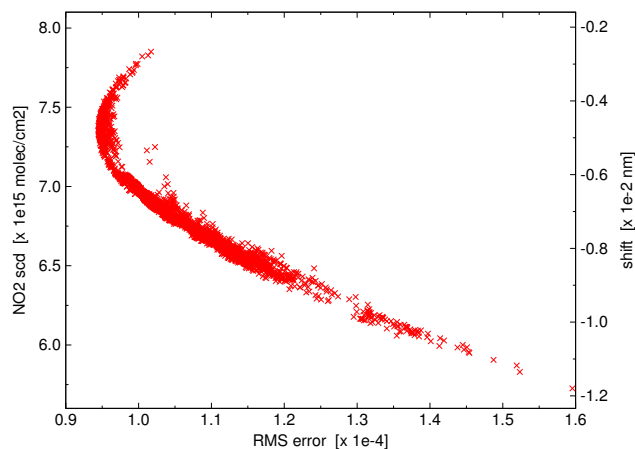


**Figure 2.** Pacific Ocean test orbit average relationship between the RMS error and the NO<sub>2</sub> SCD for the 5151 wavelength calibration windows investigated. The right axis of the main plot is an approximation: it gives the wavelength shift constructed from the linear relationship with the NO<sub>2</sub> SCD mentioned in the text.

the lowest RMS and NO<sub>2</sub> error in the subsequent DOAS fit, was found to be 409.0–428.0 nm. This new calibration window, hereafter “wcN”, covers one more distinct Fraunhofer line than wcB (cf. Fig. S4 in the Supplement).

Table 3 lists the calibration shift and the RMS and NO<sub>2</sub> error of the subsequent DOAS fit for calibration windows wcB and wcN. For comparison, Table 3 also gives the fit results using two other calibration windows: one spanning the full fit window (“wcF”) and one more or less at the centre of the fit window (“wcC”). For the other orbits of the same day (not shown), minimal RMS is achieved either in the wcN window or in a slightly different window, but the difference between that RMS and the RMS of wcN is less than 0.05 %. Hence, wcN is selected as the optimal wavelength calibration window to be implemented in the new version of the OMNO2A processor.

#### 4.2.1 Uncertainty in NO<sub>2</sub> SCD related to calibration

Figure 2 shows the relationship between the RMS error (horizontal axis) and the resulting NO<sub>2</sub> SCD (left axis) for all calibration windows of the Pacific Ocean test orbit. The minimum RMS is achieved for calibration window wcN (409.0–428.0). There are 112 possible calibration windows with an RMS within 0.5 % of the RMS of wcN, and these calibration windows all have an end-wavelength below 430 nm. For these windows, the NO<sub>2</sub> error ranges from 0.97 (the value for wcN) to  $0.98 \times 10^{15}$  molec cm<sup>-2</sup>, and the NO<sub>2</sub> SCD ranges from 7.23 to  $7.47 \times 10^{15}$  molec cm<sup>-2</sup>. The latter variation can be considered a measure for the uncertainty in the NO<sub>2</sub> SCD related to the wavelength calibration:  $0.12 \times 10^{15}$  molec cm<sup>-2</sup> ( $0.05 \times 10^{15}$  molec cm<sup>-2</sup> in terms of the NO<sub>2</sub> VCD when using a geometric air-mass factor).

**Table 4.** Results of the NO<sub>2</sub> SCD fit for the different steps of the updates of the OMNO2A processing for the Pacific Ocean orbit. Case 0 represents the current OMNO2A version (v1) and case 4 is the updated version (v2) settings. Cases 1 through 4 follow the updates listed at the beginning of Sect. 5. The numbers between parentheses are percentage changes w.r.t. case 0. The NO<sub>2</sub> SCD error is given in absolute value and as percentage of the NO<sub>2</sub> SCD column. The NO<sub>2</sub> VCD in the last column is determined from the SCD and the geometric air-mass factor.

| Case | Solar Ring | Calib. window | NO <sub>2</sub> , O <sub>3</sub> H <sub>2</sub> O <sub>vap</sub> | O <sub>2</sub> –O <sub>2</sub> H <sub>2</sub> O <sub>liq</sub> | RMS error (–)         | NO <sub>2</sub> SCD (molec cm <sup>–2</sup> ) | NO <sub>2</sub> SCD error (molec cm <sup>–2</sup> ) | (%)  | NO <sub>2</sub> VCD (molec cm <sup>–2</sup> ) |
|------|------------|---------------|--|--|-----------------------|---|---|------|---|
| 0    | v2006      | wcB           | v2006  | no   | $1.39 \times 10^{-4}$ | $8.54 \times 10^{15}$                         | $1.29 \times 10^{15}$                               | 15.1 | $3.10 \times 10^{15}$                         |
| 1    | v2014      | wcB           | v2006  | no   | 1.15 (–17.4 %)        | 8.04 (–5.8 %)                                 | 1.17 (–9.2 %)                                       | 14.5 | 2.92 (–6.1 %)                                 |
| 2    | v2014      | wcN           | v2006  | no   | 1.13 (–18.7 %)        | 7.75 (–9.2 %)                                 | 1.16 (–10.1 %)                                      | 14.9 | 2.81 (–9.6 %)                                 |
| 3    | v2014      | wcN           | v2014  | no   | 1.06 (–23.6 %)        | 7.96 (–6.8 %)                                 | 1.09 (–15.2 %)                                      | 13.7 | 2.89 (–7.0 %)                                 |
| 4    | v2014      | wcN           | v2014  | yes  | 0.94 (–32.0 %)        | 7.38 (–13.5 %)                                | 0.97 (–24.6 %)                                      | 13.1 | 2.68 (–13.7 %)                                |

There appears to be an almost perfectly linear relationship between the NO<sub>2</sub> SCD and the shift of the calibration for the investigated range of wavelength shifts: NO<sub>2</sub> SCD [ $\times 10^{15}$  molec cm<sup>2</sup>] =  $2.325 \cdot \text{shift} [\times 10^{-2}$  nm] + 8.470, with a correlation coefficient of  $r = 0.99997$ . This linear relationship implies that an error in the wavelength shift of  $1 \times 10^{-3}$  nm (0.5 % of a detector pixel) corresponds to a change in the NO<sub>2</sub> SCD of about  $0.2 \times 10^{15}$  molec cm<sup>–2</sup>. Depending on the desired accuracy of the retrieved NO<sub>2</sub> column, e.g. for future satellite missions, the relationship poses firm requirements on the accuracy of the wavelength grid. The effect of spectral misalignments, i.e. a mismatch between the wavelengths of the measured spectra and the reference spectra, on DOAS fit results has also been investigated, e.g. by Stutz and Platt (1996) and Beirle et al. (2013).

## 5 Results of the OMI NO<sub>2</sub> retrieval improvements

The improvements for the OMNO2A NO<sub>2</sub> SCD retrieval discussed above comprise four steps:

1. the update of the high-resolution solar reference spectrum and the Ring spectrum used for the wavelength calibration;
2. the change of the wavelength calibration window from wcB to wcN;
3. the update of the reference spectra of NO<sub>2</sub>, O<sub>3</sub> and H<sub>2</sub>O<sub>vap</sub>;
4. the inclusion of absorption by the O<sub>2</sub>–O<sub>2</sub> collision complex and by liquid water.

The current OMNO2A processing system is referred to as “v1” below, while the processing using the updated spectral fit settings is named “v2”.

### 5.1 Current vs. updated NO<sub>2</sub> fit results

For the comparison of the current and updated OMNO2A spectra fit results, the OMI orbit over the Pacific Ocean on 1

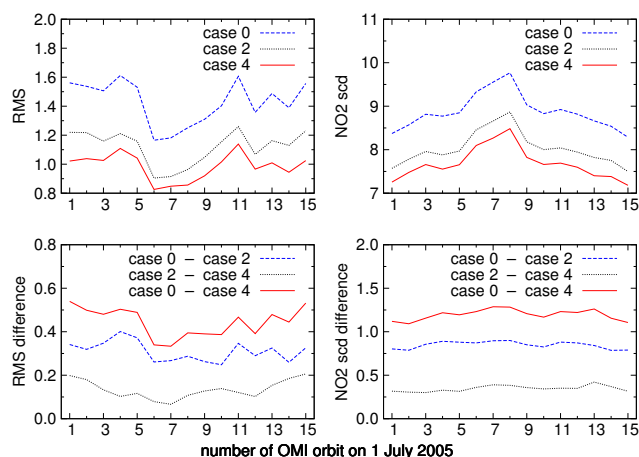


**Figure 3.** Absolute values (top row) and absolute differences (bottom row) of the orbit average RMS error (left column,  $\times 10^{-4}$ ) and NO<sub>2</sub> SCD (right column,  $\times 10^{15}$  molec cm<sup>–2</sup>) as a function of the OMI orbit number on 1 July 2005; the Pacific Ocean orbit is number 14. The case numbers refer to the cases listed in Table 4. The difference “case 0 – case 2” (blue line) refers to the updates of the wavelength calibration, “case 2 – case 4” (black line) to the updates of the reference spectra, and “case 0 – case 4” (red line) to all updates put together.

July 2005 (orbit number 05121) is used. Other orbits of this day and of some other days in 2005 are used to evaluate the robustness of the findings. Only ground pixels with a solar zenith angle less than 75° are considered; in most comparisons using orbit averages, the data are limited to the latitude range [–60° : +60°]. Since stratospheric NO<sub>2</sub> is the main focus of this study, no filtering of cloudy pixels is applied.

Table 4 lists the NO<sub>2</sub> SCD, the NO<sub>2</sub> SCD error and the RMS error values for the step-by-step improvements listed above. The first case in the table represents the current OMNO2A settings for the SCDs used in the DOMINO v2.0 and NASA SP v2.1 NO<sub>2</sub> data products; case 2 represents the improved wavelength calibration; and case 4 the implementation of all updates together, i.e. the updated “v2” version of

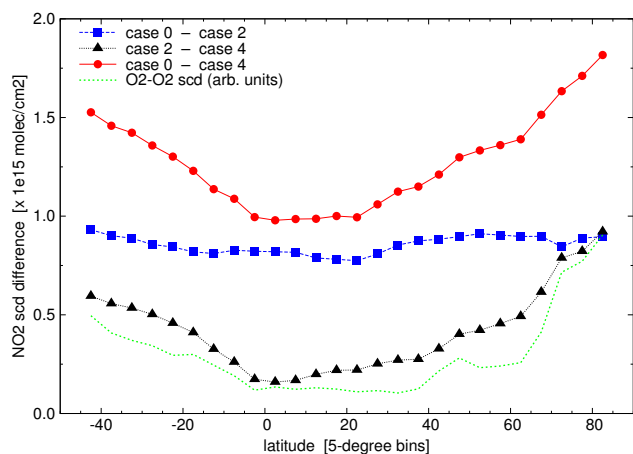


**Figure 4.** Absolute differences in the NO<sub>2</sub> SCD as a function of latitude averaged over all 15 orbits. The case numbers refer to the cases listed in Table 4, similar to the bottom panels of Fig. 3. For comparison, the concentration of O<sub>2</sub>–O<sub>2</sub> as a function of latitude is shown in arbitrary units (green short-dashed line).

OMNO2A. Figure 3 shows the absolute values of and differences between cases 0, 2 and 4 in Table 4 of the RMS error and the NO<sub>2</sub> SCD for all 15 orbits of 1 July 2005.

These results show that the wavelength calibration update (case 2) leads to large improvements in the spectral fitting of OMI NO<sub>2</sub> and the updates of the relevant reference spectra lead to smaller yet still significant improvements of the fit. The lower panels indicate that differences in RMS and NO<sub>2</sub> SCD vary only a little from orbit to orbit. When averaging the 15 orbit averages and giving changes w.r.t. the case-0 averages, the conclusions are that

- the wavelength calibration updates reduce the RMS by 23 % and the SCD by  $0.85 \times 10^{15} \text{ molec cm}^{-2}$ ,
- updates in the reference spectra further reduce the RMS by 9 % and the SCD by  $0.35 \times 10^{15} \text{ molec cm}^{-2}$ ,
- in total the RMS improves by 31 % and the SCD is smaller, on average, by  $1.20 \times 10^{15} \text{ molec cm}^{-2}$ .

The latitudinal dependency of the changes in the NO<sub>2</sub> SCD averaged over the 15 orbits is shown in Fig. 4. The change in NO<sub>2</sub> SCD resulting from the update of the wavelength calibration (blue line with squares) shows little variation with latitude, indicating that the imperfect wavelength calibration likely represents an additive offset of  $0.85 \pm 0.04 \times 10^{15} \text{ molec cm}^{-2}$  in the current “v1 OMNO2A” retrieval.

However, the change in NO<sub>2</sub> SCD due to the update of the trace gas reference spectra and the inclusion of absorption by O<sub>2</sub>–O<sub>2</sub> and H<sub>2</sub>O<sub>liq</sub> (black line with triangles in Fig. 4) depends clearly on latitude in absolute numbers and as a percentage of the NO<sub>2</sub> SCD: the change ranges from  $0.1 \times 10^{15} \text{ molec cm}^{-2}$  (3 %) in the tropics to

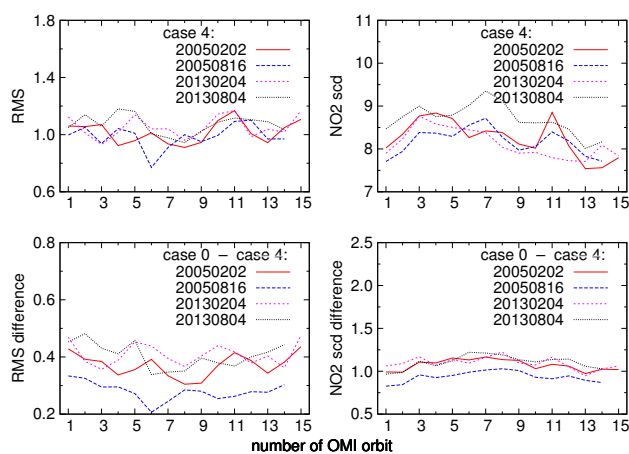


**Figure 5.** Absolute values of the updated data (case 4, top row) and absolute differences between the current and the updated data (bottom row) of the orbit average RMS error (left column,  $\times 10^{-4}$ ) and NO<sub>2</sub> SCD (right column,  $\times 10^{15} \text{ molec cm}^{-2}$ ) as a function of the OMI orbit number on 4 selected days. The case numbers refer to the cases listed in Table 4. Measurements from the rows affected by the row anomaly in the 2013 (rows 25–48 and 53) have been omitted from all data in this comparison.

$0.8 \times 10^{15} \text{ molec cm}^{-2}$  (5 %) at high latitudes. The change in the NO<sub>2</sub> SCD increases with latitude and reflects the inclusion of O<sub>2</sub>–O<sub>2</sub> absorption, which increases poleward as shown by the green short-dashed line in Fig. 4.

Overall, the improved OMNO2A NO<sub>2</sub> SCD is reduced by  $1.0$  to  $1.8 \times 10^{15} \text{ molec cm}^{-2}$  (10 to 16 %), the NO<sub>2</sub> SCD error by  $0.2$  to  $0.3 \times 10^{15} \text{ molec cm}^{-2}$  (16 to 30 %) and the RMS error by 24 to 35 %, depending on latitude.

The above settings of case 0 and case 4 have been evaluated on the 4 test days used in the EU FP7 project QA4ECV<sup>3</sup> to evaluate the robustness of the improvements for other days of the test year (2 February and 16 August 2005) and for more recent OMI data (4 February and 4 August 2013). Figure 5 shows the orbit average values of the RMS error and the NO<sub>2</sub> SCD the updated retrieval values and the differences between the current and the updated values. The other fit coefficients (not shown), such as ozone and water vapour, as well as the associated error terms, show no systematic differences between the results of the current and updated settings either. This comparison confirms that the improvements are robust over time and can therefore be used for reprocessing the entire OMI record.

To facilitate a comparison of the improved spectral fit for OMI with data from SCIAMACHY, the NO<sub>2</sub> slant columns of both instruments are converted to vertical columns with the geometric air-mass factor  $M_{\text{geo}}$ , taking the curvature of the Earth’s atmosphere into account (Leue, 1999). This conversion ensures that the considerable differences in viewing

<sup>3</sup> See <http://www.qa4ecv.eu/>.

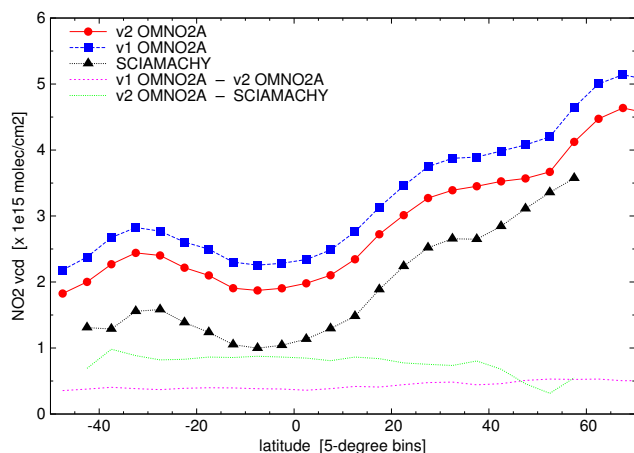


**Figure 6.** Comparison of the  $\text{NO}_2$  VCD values (lines with symbols) of the new v2 OMNO2A (red circles) and old v1 OMNO2A (blue squares) retrieval for the Pacific Ocean orbit of 1 July 2005 and the average SCIAMACHY data (black triangles) over Pacific Ocean of the same day. The two lines without symbols show differences between the  $\text{NO}_2$  VCD values. A comparison between OMI and SCIAMACHY should be limited to latitudes below  $45^\circ$ , because for higher latitudes the instruments cover different geographic areas.

angles between the two instruments do not affect the comparison.

Figure 6 shows a comparison of the OMI Pacific Ocean test orbit using the “v1 OMNO2A” and the “v2 OMNO2A” retrieval and of the SCIAMACHY data over the Pacific Ocean of the same day (lines with symbols). Given SCIAMACHY’s poor geographic coverage, the data of its three orbits over the Pacific are averaged for this comparison. The figure shows that the discrepancy between OMI and SCIAMACHY has been reduced from  $1.2$  to  $0.8 \times 10^{15} \text{ molec cm}^{-2}$ .

The remaining offset between the new v2 OMNO2A and the SCIAMACHY  $\text{NO}_2$  VCDs of  $0.8 \times 10^{15} \text{ molec cm}^{-2}$  can be explained in part by the difference of about  $0.5 \times 10^{15} \text{ molec cm}^{-2}$  expected due to the diurnal cycle of stratospheric  $\text{NO}_2$ . It should, furthermore, be kept in mind that SCIAMACHY has a negative bias of  $0.1$ – $0.2 \times 10^{15} \text{ molec cm}^{-2}$  w.r.t. GOME-2 (Sect. 3; Hendrick et al., 2012) and w.r.t. an ensemble of stratospheric  $\text{NO}_2$  limb sensor measurements (Belmonte-Rivas et al., 2014). In addition, the OMI  $\text{NO}_2$  is retrieved by OMNO2A with a non-linear fit approach in the  $405$ – $465 \text{ nm}$  window, while the SCIAMACHY  $\text{NO}_2$  is retrieved by QDOAS with a linear fit approach in the  $425$ – $450 \text{ nm}$  window (cf. Table 1). The difference in fit window and fit approach explains another  $0.1$ – $0.2 \times 10^{15} \text{ molec cm}^{-2}$  in the difference between OMNO2A and SCIAMACHY, as is shown in Sect. 5.3.

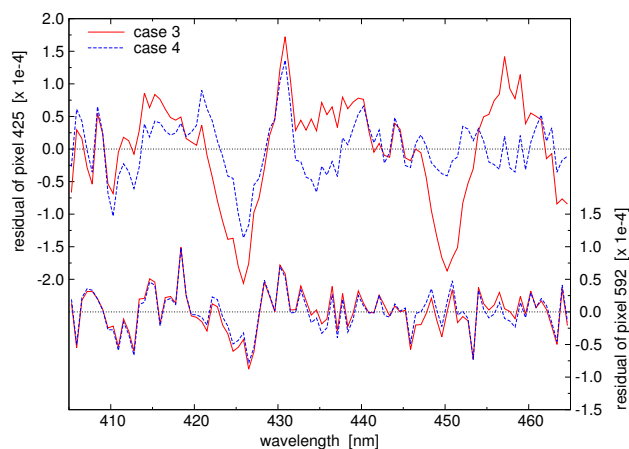


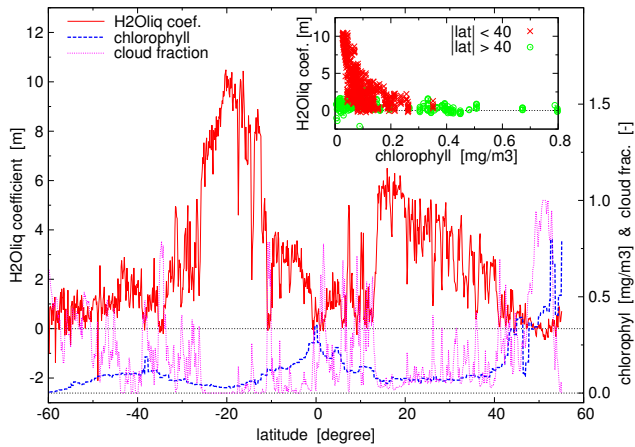
**Figure 7.** Spectral residual of the  $\text{NO}_2$  retrieval fit with the updated reference spectra without (case 3, red solid lines) and with (case 4, blue dashed lines)  $\text{O}_2$ – $\text{O}_2$  and  $\text{H}_2\text{O}_{\text{liq}}$  absorption included for two ground pixels along row 29 (0-based): pixel 425 (located at  $20.2^\circ \text{ S}$ ,  $135.4^\circ \text{ W}$ ; top two curves, left axis) and pixel 592 ( $0.0^\circ \text{ S}$ ,  $139.8^\circ \text{ W}$ ; bottom two curves, right axis) of the Pacific Ocean test orbit. To clarify the graph, the wavelengths of three detector pixels are averaged, thus mimicking the fact that OMI’s spectral resolution is about 3 times its spectral sampling.

## 5.2 About including $\text{O}_2$ – $\text{O}_2$ and liquid water

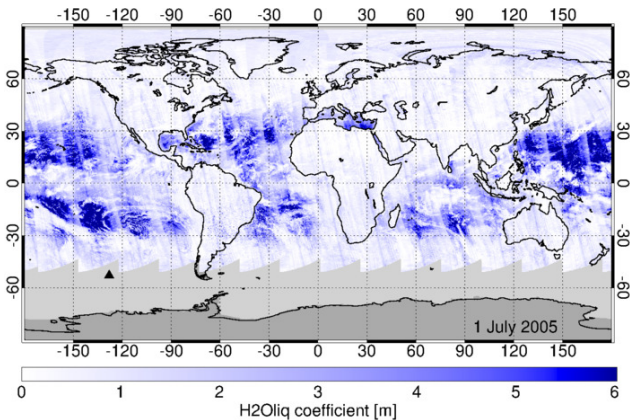
The spectral residual of the  $\text{NO}_2$  retrieval describes the unexplained portion of the measured spectrum after a selected set of absorption signatures is accounted for in the fit model. Figure 7 shows the spectral residual of two cloud-free pixels along row 29 (0-based) of the Pacific Ocean test orbit: pixel 425 and pixel 592 using the updated reference spectra without (case 3, red solid lines) and with (case 4, blue dashed lines) taking absorption of  $\text{O}_2$ – $\text{O}_2$  and  $\text{H}_2\text{O}_{\text{liq}}$  into account. Pixel 425 is over clear open ocean water with a low chlorophyll concentration<sup>4</sup> ( $0.028 \text{ mg m}^{-3}$ ), while pixel 592 is over ocean water with a relatively high chlorophyll concentration ( $0.351 \text{ mg m}^{-3}$ ). An anti-correlation between the chlorophyll concentration and the liquid water absorption coefficient is expected, because the higher the chlorophyll concentration the more opaque the water is and therefore the shorter the penetration depth of light will be.

Figure 7 shows that the residual of pixel 425 has a clear structure in the range  $445$ – $465 \text{ nm}$  in case liquid water absorption is not accounted for, while this structure does not appear for pixel 592. If  $\text{H}_2\text{O}_{\text{liq}}$  is included in the fit, the residual of pixel 425 is much reduced (the RMS decreases by  $-35\%$ ), while there is hardly any change in the residual of pixel 592 (by  $-2\%$ ). For both pixels the  $\text{NO}_2$  SCD reduces by about

<sup>4</sup> Chlorophyll concentrations are extracted from NASA’s daily assimilated total chlorophyll data sets with the Giovanni online data system from NASA GES DISC; data file: NOBM\_DAtot.CR.data.01Jul2005.G3.output.txt.



**Figure 8.** Retrieved  $H_2O_{liq}$  coefficient (in m; red solid line, left axis) as a function of latitude for row 29 of the Pacific Ocean test orbit, showing only ground pixels for which chlorophyll concentration data are available. Also shown, with values along the right axis, are the chlorophyll concentration (in  $mg\ m^{-3}$ ; blue dashed line) and the cloud cover fraction (magenta dotted line). The inset shows the  $H_2O_{liq}$  coefficient as a function of the chlorophyll concentration separately for ground pixels with latitudes between  $\pm 40^\circ$  (red crosses) and higher latitudes (green circles).



**Figure 9.** World map of the  $H_2O_{liq}$  coefficient (in m) based on all 15 OMI orbits of 1 July 2005; the Pacific Ocean test orbit is marked by a black triangle. All ground pixels with solar zenith angle less than  $75^\circ$  are plotted; no filtering for cloudy pixels was applied.

6% and the retrieved  $H_2O_{liq}$  fit coefficients are physically meaningful: for pixel 425 the  $H_2O_{liq}$  fit coefficient is 10.49 m and for pixel 592 it is 0.83 m.

Figure 8 shows the retrieved  $H_2O_{liq}$  coefficient (left axis, red solid line) as a function of latitude for all ground pixels of detector row 29 for which a chlorophyll concentration is available. For comparison the graphs also shows the chlorophyll concentration and the cloud fraction for the same pixels (right axis); cloudiness clearly leads to lower  $H_2O_{liq}$  coefficients, as expected. The inset of Fig. 8 shows the relationship between the  $H_2O_{liq}$  coefficient and the chlorophyll concen-

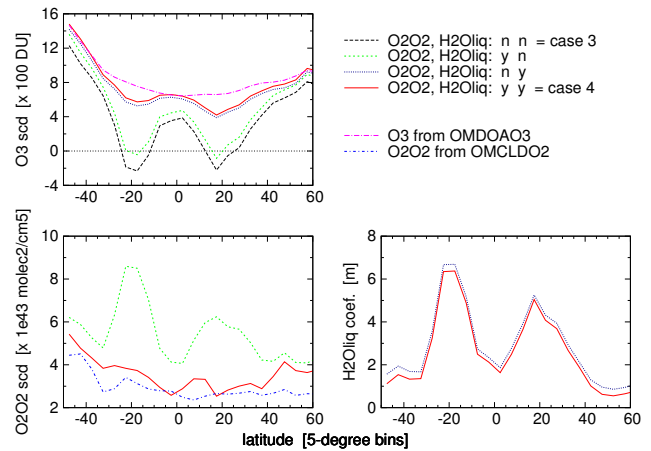


**Figure 10.** Retrieved values for the  $O_3$  SCD (top-left), the  $O_2-O_2$  SCD (bottom-left) and  $H_2O_{liq}$  coefficient (bottom-right) as a function of latitude for the Pacific Ocean test orbit for retrievals without and with absorption by  $O_2-O_2$  and  $H_2O_{liq}$  included in the fit as specified by the legend in the top-right corner; case numbers 3 (black dashed) and 4 (red solid) refer to the cases listed in Table 4. Also plotted are the  $O_3$  SCD value from the OMI ozone slant column product OMDOAO3 (magenta long-dash-dotted) and the  $O_2-O_2$  SCD value from the OMCLDO2 cloud product (blue short-dash-dotted).

tration. The graph makes a distinction between the ground pixels in the latitude range  $40^\circ S$  to  $40^\circ N$  (red crosses) and outside that range (green circles). Pixels at latitudes above  $40^\circ N$  have chlorophyll concentration  $> 0.3\ mg\ m^{-3}$  and for that reason low  $H_2O_{liq}$  coefficients. Pixels at latitudes  $< 40^\circ S$  at high solar zenith angle (above  $70^\circ$ ) have low  $H_2O_{liq}$  coefficients (below about 2 m) even though chlorophyll concentrations are low ( $< 0.2\ mg\ m^{-3}$ ).

Figure 9 shows a global map of the  $H_2O_{liq}$  coefficient retrieved from all OMI orbits of 1 July 2005. Open water areas are clearly visible on the map and land/sea boundaries show up sharply in areas like the Mediterranean Sea, the Gulf of Mexico, around Madagascar and the east coast of South America. Along the west coasts of South America, North America and Africa, for example, the  $H_2O_{liq}$  coefficient is very low, consistent with high chlorophyll concentrations there. Note that since the processing is not optimised for the retrieval of the  $H_2O_{liq}$  coefficient, it is not possible to say how accurate the coefficient is, but overall its values appear realistic. Positive  $H_2O_{liq}$  fit coefficients over areas with little or no liquid water absorption, such as over land or cloudy scenes, are small.

The inclusion of the absorption of  $H_2O_{liq}$  and the  $O_2-O_2$  collision complex in the  $NO_2$  fit is justified since their absorption is known to affect the radiance  $I(\lambda)$  – unless their inclusion would reduce the quality of the  $NO_2$  fit, which is not the case. Figure 10 shows the effect of including  $O_2-O_2$  and  $H_2O_{liq}$  in the retrieved  $O_3$  SCDs. Without either of the two additional absorbers, ozone slant columns are negative

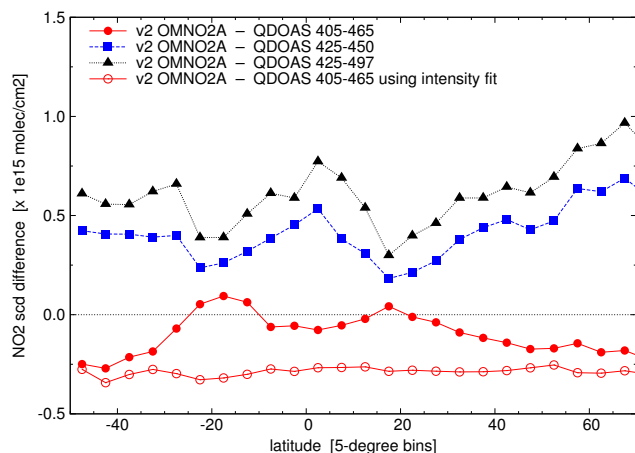


**Figure 11.** Differences of the NO<sub>2</sub> SCD values of the new v2 OMNO2A fit results (i.e. the red line with circles in Fig. 6) with QDOAS retrievals using different fit windows with a linear fitting approach (filled symbols) and using a non-linear fitting approach in the standard fit window (open circles) for the Pacific Ocean test orbit. The size of the steps along the vertical scale is the same as in Fig. 4 to ease comparison of the SCD differences.

in the regions where absorption in open water is taking place. Adding both absorbers brings the retrieved O<sub>3</sub> SCD close to the values given in the official OMI ozone SCD data product OMDOAO3; the improvement is mostly due to including H<sub>2</sub>O<sub>liq</sub> absorption.

Including O<sub>2</sub>–O<sub>2</sub> absorption but not H<sub>2</sub>O<sub>liq</sub> absorption does not result in realistic O<sub>3</sub> SCD values. Furthermore, the retrieved O<sub>2</sub>–O<sub>2</sub> SCD values appear realistic compared to the values given in the official OMI cloud data product OMCLDO2 if H<sub>2</sub>O<sub>liq</sub> is included in the fit. Including O<sub>2</sub>–O<sub>2</sub> absorption has a small effect on the retrieved H<sub>2</sub>O<sub>liq</sub> coefficient (bottom-right panel in Fig. 10).

In summary, (a) including liquid water absorption leads to significant improvements in the NO<sub>2</sub> retrieval fit for pixels over clear open waters, without affecting other pixels, results in physically meaningful H<sub>2</sub>O<sub>liq</sub> and O<sub>3</sub> absorption coefficients; and (b) simultaneously including O<sub>2</sub>–O<sub>2</sub> absorption results in realistic O<sub>2</sub>–O<sub>2</sub> SCDs and improves the fit, especially if light paths are long.

### 5.3 Comparison between OMNO2A and QDOAS

Since the OMI, SCIAMACHY and GOME-2 spectral fits have been done with different fitting approaches and fitting windows (cf. Table 1), the sensitivity of the NO<sub>2</sub> SCD to the spectral fitting approach is studied here. Such estimates are important for satellite intercomparisons and the generation of long-term seamless multi-sensor data records such as the QA4ECV project. The flexible QDOAS package (version 2.105, May 2013), which provides a linear fit approach (cf. the details on DOAS fitting in Sect. S1 in the Supple-

ment), is used for this study with the v2014 reference spectra on the OMI Pacific Ocean test orbit.

Figure 11 shows that the OMNO2A and QDOAS processors, both applied in the 405–465 nm window, result in small differences in the NO<sub>2</sub> SCDs of  $-0.2$  to  $+0.1 \times 10^{15}$  molec cm<sup>-2</sup>. The agreement between these two is therefore quite good considering there are several differences between the processors: the fitting method differs, the Ring effect is included differently and the wavelength calibration of QDOAS differs from the OMNO2A wavelength calibration.

QDOAS has the option to apply a non-linear intensity fitting method instead of the linear optical density fitting method Eq. (S4), similar to the OMNO2A non-linear fitting method Eq. (1) but with the Ring effect treated as a pseudo-absorber; cf. Eq. (S5). The red line with open circles in Fig. 11 shows the difference between the results of this approach and the OMNO2A results, which appears to be larger than the difference with the linear fitting method of QDOAS: about  $-0.3 \times 10^{15}$  molec cm<sup>-2</sup>, almost independent of latitude.

The SCIAMACHY and GOME-2 NO<sub>2</sub> data are retrieved in the fit window 425–450 nm, using a third-degree polynomial. The difference between the OMI orbit processed with QDOAS in this manner and the OMNO2A data is shown by the blue line with squares in Fig. 11. At  $+0.2$ – $0.6 \times 10^{15}$  molec cm<sup>-2</sup>, the difference is clearly larger than for the OMNO2A fit window.

In their study to improve the GOME-2 NO<sub>2</sub> retrieval, Richter et al. (2011) apply the extended fit window 425–497 nm. The black line with triangles in Fig. 11 shows that OMNO2A is higher by  $0.4$ – $0.9 \times 10^{15}$  molec cm<sup>-2</sup> than applying a linear fit in this extended fit window.

The NO<sub>2</sub> SCD differences in Fig. 11 show a clear latitudinal variation around latitudes 20° S and 20° N – areas of the Pacific Ocean where absorption in liquid water plays a role (cf. Sect. 5.2) – for the three curves where QDOAS was used in the linear fitting mode, while for QDOAS’s non-linear fitting mode the differences with OMNO2A are nearly independent of latitude. This may indicate that the linear fitting method deals differently with the polynomial-like signature of H<sub>2</sub>O<sub>liq</sub> and/or O<sub>3</sub> and/or O<sub>2</sub>–O<sub>2</sub> absorption (cf. Fig. S6) than the non-linear fitting method, which is possibly due to interference of the reference spectra with the DOAS polynomial (a few further remarks regarding this issue are given in Sect. S6).

In summary, the selection of the fit window (and with that the degree of the polynomial) and the fitting method determines the NO<sub>2</sub> fit results, i.e. there is no “true” NO<sub>2</sub> SCD but at most a fit window and fit method specific slant column value. Judging from the curves in Fig. 11, the variability in the fit window and fit method selection introduces differences in the retrieved NO<sub>2</sub> SCD between  $-0.3$  and  $+0.6 \times 10^{15}$  molec cm<sup>-2</sup> (i.e. up to  $0.2 \times 10^{15}$  molec cm<sup>-2</sup> in terms of the NO<sub>2</sub> VCD). To better understand the “true”

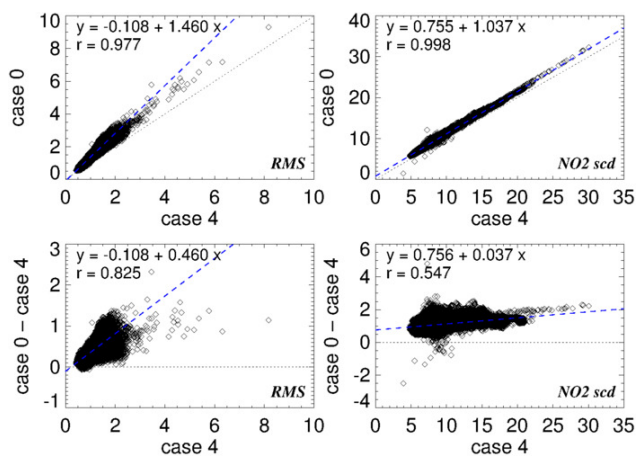


**Figure 12.** Scatter plots of current data (case 0, top row) and absolute differences between the current and the updated data (bottom row) of the RMS error (left column,  $\times 10^{-4}$ ) and NO<sub>2</sub> SCD (right column,  $\times 10^{15}$  molec cm<sup>-2</sup>) as a function of the updated data (case 4) using the July 2005 average gridded data. Dashed blue lines show linear fits through the data; the fit and correlation coefficients are shown in the top-left of each graph.

NO<sub>2</sub> SCD, a comparison with measurements that do not depend on the DOAS technique is needed.

#### 5.4 Reprocessed OMI NO<sub>2</sub> data of 2005

All OMI NO<sub>2</sub> slant column data of the year 2005 have been reprocessed to evaluate the consistency of the proposed improvements. Figure 12 shows the current (case 0) data on the top row and the difference between the current and update data on the bottom row as a function of the updated (case 4) data. The linear relationship between the NO<sub>2</sub> SCD of the current and updated retrieval in the top-right panel shows an offset, reflecting the improved wavelength calibration. The slope of the linear fit is 1.04, which implies that high NO<sub>2</sub> SCD values will decrease more than low SCDs but not by much. This suggests that the effect of the updated retrieval settings on high (tropospheric) NO<sub>2</sub> SCDs will be small compared to the overall decrease of the NO<sub>2</sub> values.

Figure 13 shows a map of the monthly average gridded NO<sub>2</sub> slant columns of the updated (case 4) data and the corresponding difference with the current (case 0) data for July 2005. The RMS error data for the same month are shown in Fig. 14. Similar maps of the month of January 2005 are shown in Sect. S7 in the Supplement. In some areas with high NO<sub>2</sub> levels related to pollution, the decrease of the NO<sub>2</sub> slant column is relatively large, such as for the Highveld area in South Africa in Fig. 13 for July. The average change in the RMS error shown in the lower panel of Fig. 14 is about  $0.33 \times 10^{-4}$ . For clear-sky pixels only (not shown), the decrease of the RMS is much smaller, namely  $0.14 \times 10^{-4}$  on average, while for cloudy pixels (not shown) the decrease is much larger:  $0.80 \times 10^{-4}$  on average. Notably above clouds,

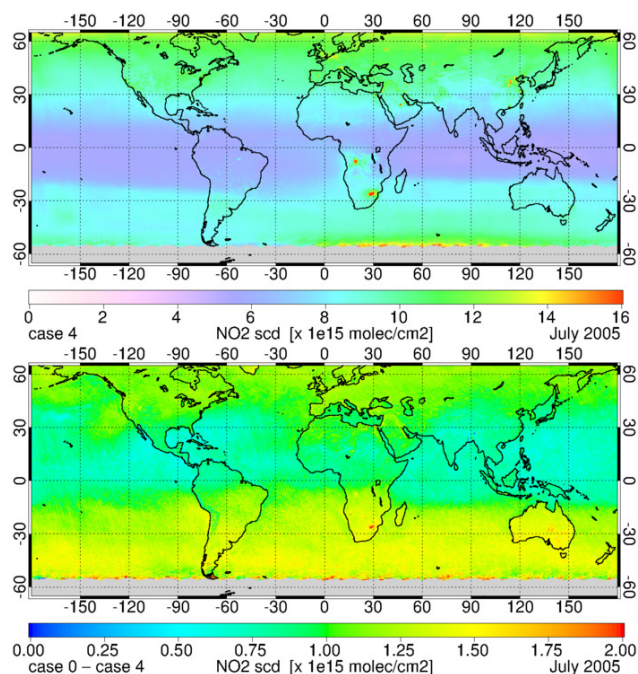


**Figure 13.** Monthly average gridded updated (case 4; top panel) NO<sub>2</sub> slant column data for July 2005 and the corresponding difference with the current (case 0) data (lower panel).

the quality of the fit is evidently improved by the changes made to the OMNO2A retrieval.

Section S7 in the Supplement shows monthly average maps for July 2005 similar to Figs. 13–14 of the results of the other fit parameters.

## 6 Concluding remarks

The OMI NO<sub>2</sub> slant column density retrieval, OMNO2A, lies at the basis of the stratospheric and tropospheric NO<sub>2</sub> vertical column data products of OMI, notably the Dutch OMI NO<sub>2</sub> (DOMINO) and NASA SP data sets. This paper describes important updates for OMNO2A in order to improve the quality of the OMI NO<sub>2</sub> SCD data. The investigation was triggered by the high bias in OMI stratospheric NO<sub>2</sub> columns w.r.t. other satellite sensors and ground-based measurements as well as the need to investigate a number of other elements of the OMNO2A processor. The improvements for the OMNO2A processor are

- implementation of the wavelength and viewing angle dependency of the OMI slit function,
- optimisation of the wavelength calibration window based on minimising RMS and NO<sub>2</sub> errors,
- an update of the reference spectra of the trace gases included in the spectral fit,
- inclusion of absorption by O<sub>2</sub>–O<sub>2</sub> and H<sub>2</sub>O<sub>liq</sub> to further reduce the RMS error.

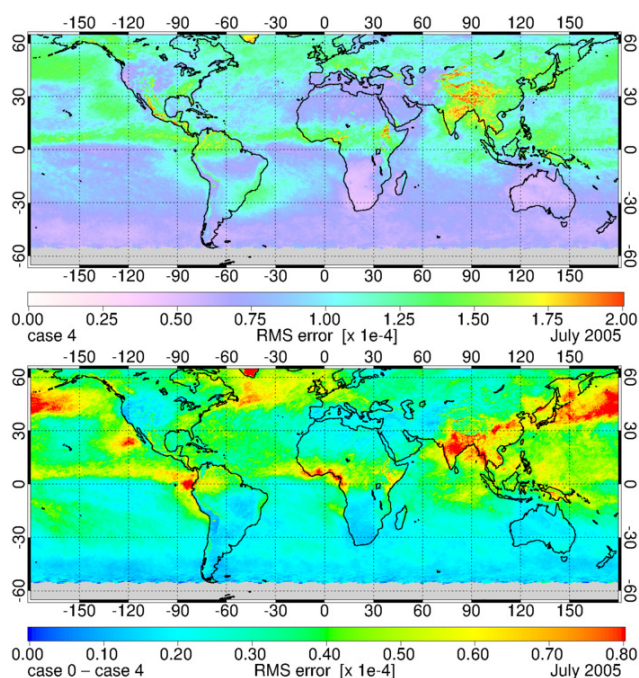


**Figure 14.** Monthly average gridded updated (case 4; top panel) RMS error data for July 2005 and the corresponding difference with the current (case 0) data (lower panel).

The updates of the wavelength calibration have the effect of removing an additive offset in the  $\text{NO}_2$  SCD of  $0.85 \times 10^{15} \text{ molec cm}^{-2}$  and reducing the RMS by about 23 % on average. The updates of trace gas reference spectra and the improved use of the OMI slit function for the convolution of these spectra lead to a reduction of the  $\text{NO}_2$  SCD that depends on latitude, mainly related to the inclusion of  $\text{O}_2\text{-O}_2$  absorption, varying from  $0.2$  to  $0.6 \times 10^{15} \text{ molec cm}^{-2}$  (on average  $0.35 \times 10^{15} \text{ molec cm}^{-2}$ ); the RMS is reduced by about 9 % on average.

Absorption by the  $\text{O}_2\text{-O}_2$  collision complex increases with solar zenith angle due to increased light path length and is therefore important at higher latitudes, and the resulting  $\text{O}_2\text{-O}_2$  SCDs have realistic values. Accounting for absorption by liquid water ( $\text{H}_2\text{O}_{\text{liq}}$ ) is particularly important for pixels over clear open waters with low chlorophyll concentrations and results in marked improvements of the spectral fit and assures that  $\text{O}_3$  SCDs in the fit window have physically realistic values. Inclusion does not deteriorate the spectral fit for other, non-clear water pixels. The values found for the  $\text{H}_2\text{O}_{\text{liq}}$  fit coefficient are physically meaningful for the areas where absorption in liquid water is relevant.

$\text{NO}_2$  SCD retrievals for other satellite and ground-based instruments employ different spectral fit windows and use different implementations of the DOAS technique, which leads to small differences in the resulting SCD values. A short investigation of this using the QDOAS software

(Danckaert et al., 2012) shows that the uncertainty in  $\text{NO}_2$  SCD related to the choice of the fit window and fit method may be as large as  $0.3 \times 10^{15} \text{ molec cm}^{-2}$ .

The combination of improvements to the OMNO2A spectral fit lead to an overall reduction of the  $\text{NO}_2$  SCD by about  $1.2 \times 10^{15} \text{ molec cm}^{-2}$ , a reduction of the  $\text{NO}_2$  fitting error by  $0.2\text{--}0.3 \times 10^{15} \text{ molec cm}^{-2}$  and a reduction of the RMS by 24–35 %. The reduction of the SCD is largely an additive offset, implying that the improvements in OMNO2A will probably affect stratospheric  $\text{NO}_2$  most and smaller effects may be expected on tropospheric  $\text{NO}_2$ .

Comparing the updated OMNO2A data with SCIAMACHY data over the Pacific Ocean shows that the discrepancy between the two instruments is reduced from  $1.2$  to  $0.8 \times 10^{15} \text{ molec cm}^{-2}$ . The remaining difference can be explained largely by the difference expected due to the diurnal cycle of stratospheric  $\text{NO}_2$ , which is higher by about  $0.5 \times 10^{15} \text{ molec cm}^{-2}$  at 13:40 LT (when OMI measures) than at 09:30 (when SCIAMACHY measures), the different choice of the fitting window and the low bias of SCIAMACHY relative to other instruments.

The updates to the OMNO2A retrieval systems are sufficient to remove the bias between the stratospheric  $\text{NO}_2$  columns from OMI and those from other satellite and ground-based instruments. A final test of this requires the conversion of the retrieved SCD to the separate stratospheric and tropospheric  $\text{NO}_2$  columns. This issue will be discussed in a forthcoming study that describes improvements to the data assimilation system of DOMINO, leading to a new DOMINO v3.0 data set for the entire OMI period. The settings of the updated OMNO2A processing will be the initial configuration of the  $\text{NO}_2$  retrieval for TROPOMI for reasons of consistency (van Geffen et al., 2014).

**The Supplement related to this article is available online at doi:10.5194/amt-8-1685-2015-supplement.**

*Acknowledgements.* This work is funded by the Netherlands Space Office (NSO). The authors would like to thank N. Krotkov, S. Marchenko, A. Richter and P. Valks for discussions and information on their approaches and studies. The authors would further like to thank Johan de Haan for discussions on and help with retrieval issues. Folkert Boersma acknowledges funding from NWO (Vidi grant 864.09.001) and support by the EU-FP7 grant QA4ECV (no. 607405). The research at BIRA-IASB (AGACC-II project) and the University of Liège (A3C and ACROSAT projects from the PRODEX program) has been financially supported by the Belgian Federal Science Policy Office (BELSPO), Brussels, and via the EU 7th Framework Programme project NORS (contract 284421). BIRA-IASB is thankful to M. P. Chipperfield (University of Leeds) for providing SLIMCAT data. The authors would also like to thank the International Foundation High Altitude Research Stations Jungfrauoch and Gornergrat (HFSJG, Bern).

Edited by: J. Stutz

## References

- Beirle, S., Boersma, K. F., Platt, U., Lawrence, M. G., and Wagner T.: Megacity emissions and lifetimes of nitrogen oxides probed from space, *Science*, 333, 1737–1739, doi:10.1126/science.1207824, 2011.
- Beirle, S., Sihler, H., and Wagner, T.: Linearisation of the effects of spectral shift and stretch in DOAS analysis, *Atmos. Meas. Tech.*, 6, 661–675, doi:10.5194/amt-6-661-2013, 2013.
- Belmonte-Rivas, M., Veefkind, P., Boersma, F., Levelt, P., Eskes, H., and Gille, J.: Intercomparison of daytime stratospheric NO<sub>2</sub> satellite retrievals and model simulations, *Atmos. Meas. Tech.*, 7, 2203–2225, doi:10.5194/amt-7-2203-2014, 2014.
- Boersma, K. F., Eskes, H. J., and Brinksma, E.J.: Error analysis for tropospheric NO<sub>2</sub> retrieval from space, *J. Geophys. Res.*, 109, D04311, doi:10.1029/2003JD003962, 2004.
- Boersma, K. F., Eskes, H. J., Veefkind, J. P., Brinksma, E. J., van der A, R. J., Sneep, M., van den Oord, G. H. J., Levelt, P. F., Stammes, P., Gleason, J. F., and Bucsela, E. J.: Near-real time retrieval of tropospheric NO<sub>2</sub> from OMI, *Atmos. Chem. Phys.*, 7, 2103–2118, doi:10.5194/acp-7-2103-2007, 2007.
- Boersma, K. F., Eskes, H. J., Dirksen, R. J., van der A, R. J., Veefkind, J. P., Stammes, P., Huijnen, V., Kleipool, Q. L., Sneep, M., Claas, J., Leitão, J., Richter, A., Zhou, Y., and Brunner, D.: An improved tropospheric NO<sub>2</sub> column retrieval algorithm for the Ozone Monitoring Instrument, *Atmos. Meas. Tech.*, 4, 1905–1928, doi:10.5194/amt-4-1905-2011, 2011.
- Bogumil, K., Orphal, J., and Burrows, J. P.: Temperature dependent absorption cross sections of O<sub>3</sub>, NO<sub>2</sub>, and other atmospheric trace gases measured with the SCIAMACHY spectrometer, in *Looking down to Earth in the New Millennium*, Proceedings of the ERS-ENVISAT Symposium, 16–20 October 2000, Gothenburg, Sweden, ESA publication SP-461, 2000.
- Bovensmann, H., Burrows, J. P., Buchwitz, M., Frerick, J., Noel, S., Rozanov, V. V., Chance, K. V., and Goede, A. P. H.: SCIAMACHY: Mission objectives and measurement modes, *J. Atmos. Sci.*, 56, 127–150, 1999.
- Bucsela, E. J., Celarier, E. A., Wenig, M. O., Gleason, J. F., Veefkind, J. P., Boersma, K. F., and Brinksma, E. J.: Algorithm for NO<sub>2</sub> vertical column retrieval from the ozone monitoring instrument, *IEEE Trans. Geosci. Rem. Sens.*, 44, 1245–1258, doi:10.1109/TGRS.2005.863715, 2006.
- Bucsela, E. J., Krotkov, N. A., Celarier, E. A., Lamsal, L. N., Swartz, W. H., Bhartia, P. K., Boersma, K. F., Veefkind, J. P., Gleason, J. F., and Pickering, K. E.: A new stratospheric and tropospheric NO<sub>2</sub> retrieval algorithm for nadir-viewing satellite instruments: applications to OMI, *Atmos. Meas. Tech.*, 6, 2607–2626, doi:10.5194/amt-6-2607-2013, 2013.
- Burrows, J. P., Weber, M., Buchwitz, M., Rozanov, V., Ladstätter-Weißmayer, A., Richter, A., Debeek, R., Hoogen, R., Bramstedt, K., Eichmann, K.-U., Eisinger, M., and Perner, D.: The Global Ozone Monitoring Experiment (GOME): Mission concept and first results, *J. Atmos. Sci.*, 56, 151–175, 1999.
- Chance, K. V. and Spurr, R. J. D.: Ring effect studies: Rayleigh scattering, including molecular parameters for rotational Raman scattering, and the Fraunhofer spectrum, *Appl. Optics*, 36, 5224–5230, 1997.
- Crutzen, P. J.: The influence of nitrogen oxides on the atmospheric ozone content, *Q. J. Roy. Meteor. Soc.*, 96, 320–325, 1970.
- Danckaert, T., Fayt, C., and Van Roozendael, M. QDOAS software user manual, Version 2.1, December 2012, BIRA-IASB, Brussels, Belgium, 2012.
- Dirksen, R., Dobber, M. R., Voors, R., and Levelt, P.: Pre-launch characterization of the Ozone Monitoring Instrument transfer function in the spectral domain, *Appl. Optics*, 45, 3972–3981, doi:10.1364/AO.45.003972, 2006.
- Dirksen, R. J., Boersma, K. F., Eskes, H. J., Ionov, D. V., Bucsela, E. J., Levelt, P. F., and Kelder, H. M.: Evaluation of stratospheric NO<sub>2</sub> retrieved from the Ozone Monitoring Instrument: Intercomparison, diurnal cycle, and trending, *J. Geophys. Res.* 116, D08305, doi:10.1029/2010JD014943, 2011.
- Dobber, M., Voors, R., Dirksen, R., Kleipool, Q., and Levelt, P.: The high-resolution solar reference spectrum between 250 and 550 nm and its application to measurements with the Ozone Monitoring Instrument, *Sol. Phys.*, 249, 281–291, doi:10.1007/s11207-008-9187-7, 2008.
- Fuglestedt, J. S., Berntsen, T., Isaksen, I. S. A., Mao, H., Liang, X.-Z., and Wang, W.-C.: Climatic forcing of nitrogen oxides through changes in tropospheric ozone and methane, *Atmos. Environ.*, 33, 961–977, doi:10.1016/s1352-2310(98)00217-9, 1999.
- Grainger, J. F. and Ring, J.: Anomalous Fraunhofer line profiles, *Nature*, 193, p. 762, doi:10.1038/193762a0, 1962.
- Hendrick, F., Mahieu, E., Bodeker, G. E., Boersma, K. F., Chipperfield, M. P., De Mazière, M., De Smedt, I., Demoulin, P., Fayt, C., Hermans, C., Kreher, K., Lejeune, B., Pinardi, G., Servais, C., Stübi, R., van der A, R., Vernier, J.-P., and Van Roozendael, M.: Analysis of stratospheric NO<sub>2</sub> trends above Jungfraujoch using ground-based UV-visible, FTIR, and satellite nadir observations, *Atmos. Chem. Phys.*, 12, 8851–8864, doi:10.5194/acp-12-8851-2012, 2012.
- Krotkov, N. A., Bucsela, E. J., Celarier, E. A., Lamsal, L. N., and Swartz, W. H.: Improved OMI NO<sub>2</sub> Standard Product: Algorithm, evaluation, and results, EOS Aura Science Team Meeting, Pasadena, CA, USA, 1–3 October, 2012.
- Lerot, C., Van Roozendael, M., van Geffen, J., van Gent, J., Fayt, C., Spurr, R., Lichtenberg, G., and von Barga, A.: Six years of total ozone column measurements from SCIAMACHY nadir observations, *Atmos. Meas. Tech.*, 2, 87–98, doi:10.5194/amt-2-87-2009, 2009.
- Lerot, C., Stavrakou, T., De Smedt, I., Müller, J.-F., and Van Roozendael, M.: Glyoxal vertical columns from GOME-2 backscattered light measurements and comparisons with a global model, *Atmos. Chem. Phys.*, 10, 12059–12072, doi:10.5194/acp-10-12059-2010, 2010.
- Leue, C.: Detektion der troposphärischen NO<sub>2</sub> Daten anhand von GOME, PhD thesis, Univ. Heidelberg, Heidelberg, Germany, 1999.
- Levelt, P. F., van den Oord, G. H. J., Dobber, M. R., Mälkki, A., Visser, H., de Vries, J., Stammes, P., Lundell, J. O. V., and Saari, H.: The Ozone Monitoring Instrument, *IEEE Trans. Geosci. Rem. Sens.*, 44, 1093–1101, doi:10.1109/tgrs.2006.872333, 2006.
- Munro, R., Eisinger, M., Anderson, C., Callies, J., Corpaccioli, E. Lang, R., Lefebvre, A., Livschitz, Y., and Albinana, A. P.: GOME-2 on MetOp, ESA publication SP 628, Paris, France, 2006.
- Murphy, D. M., Fahey, D. W., Proffitt, M. H., Liu, S. C., Chan, K. R., Eubank, C. S., Kawa, S. R., and Kelly, K. K.: Reactive

- nitrogen and its correlation with ozone in the lower stratosphere and upper troposphere, *J. Geophys. Res.*, 98, 8751–8773, 1993.
- Peters, E., Wittrock, F., Richter, A., Alvarado, L. M. A., Rozanov, V. V., and Burrows, J. P.: Liquid water absorption and scattering effects in DOAS retrievals over oceans, *Atmos. Meas. Tech.*, 7, 4203–4221, doi:10.5194/amt-7-4203-2014, 2014.
- Platt, U.: Differential Optical Absorption Spectroscopy (DOAS), in: *Air monitoring by spectroscopic techniques*, edited by: M. W. Sigrist, Chemical Analysis Series, 127, 27–76, Wiley, New York, USA, 1994.
- Platt, U. and Stutz, Z.: *Differential Optical Absorption Spectroscopy, Principles and Applications*, Springer, Heidelberg, Germany, 597 pp., 2008.
- Pope, R. M. and Fry, E. S.: Absorption spectrum (380–700 nm) of pure water. II. Integrating cavity measurements, *Appl. Optics*, 36, 8710–8723, doi:10.1364/AO.36.008710, 1997.
- Richter, A., Begoin, M., Hilboll, A., and Burrows, J. P.: An improved NO<sub>2</sub> retrieval for the GOME-2 satellite instrument, *Atmos. Meas. Tech.*, 4, 1147–1159, doi:10.5194/amt-4-1147-2011, 2011.
- Rothman, L. S., Gordon, I. E., Babikov, Y., Barbe, A., Chris Benner, D., Bernath, P. F., Birk, M., Bizzocchi, L., Boudon, V., Brown, L. R., Campargue, A., Chance, K., Cohen, E. A., Coudert, L. H., Devi, V. M., Drouin, B. J., Fayt, A., Flaud, J.-M., Gamache, R. R., Harrison, J. J., Hartmann, J.-M., Hill C., Hodges, J. T., Jacquemart, D., Jolly, A., Lamouroux, J., Le Roy, R. J., Li, G., Long, D. A., Lyulin, O. M., Mackie, C. J., Massie, S. T., Mikhailenko, S., Müller, H. S. P., Naumenko, O. V., Nikitin, A. V., Orphal, J., Perevalov, V., Perrin, A., Polovtseva, E. R., Richard, C., Smith, M. A. H., Starikova, E., Sung, K., Tashkun, S., Tennyson, J., Toon, G. C., Tyuterev, V. I., and Wagner, G.: The HITRAN 2012 molecular spectroscopic database, *J. Quant. Spectrosc. Ra.*, 130, 4–50, doi:10.1016/j.jqsrt.2013.07.002, 2013.
- Schaub, D., Brunner, D., Boersma, K. F., Keller, J., Folini, D., Buchmann, B., Berresheim, H., and Staehelin, J.: SCIAMACHY tropospheric NO<sub>2</sub> over Switzerland: estimates of NO<sub>x</sub> lifetimes and impact of the complex Alpine topography on the retrieval, *Atmos. Chem. Phys.*, 7, 5971–5987, doi:10.5194/acp-7-5971-2007, 2007.
- Shindell, D. T., Faluvegi, G., Koch, D. M., Schmidt, G. A., Unger, N., and Bauer, S. E.: Improved attribution of climate forcing to emissions, *Science*, 326, 716–718, doi:10.1126/science.1174760, 2009.
- Sillman, S., Logan, J. A., and Wofsy, S. C.: The sensitivity of ozone to nitrogen oxides and hydrocarbons in regional ozone episodes, *J. Geophys. Res.*, 95, 1837–1851, 1990.
- Stutz, J. and Platt, U.: Numerical analysis and estimation of the statistical error of differential optical absorption spectroscopy measurements with least-squares methods, *Appl. Opt.*, 35, 6041–6053, doi:10.1364/AO.35.006041, 1996.
- Thalman, R. and Volkamer, R.: Temperature dependant absorption cross-sections of O<sub>2</sub>-O<sub>2</sub> collision pairs between 340 and 630 nm at atmospherically relevant pressure, *Phys. Chem. Chem. Phys.*, 15, 15371–15381, doi:10.1039/C3CP50968K, 2013.
- van Geffen, J. H. G. M., Boersma, K. F., Eskes, H. J., Maasackers, J. D., and Veefkind, J. P.: TROPOMI ATBD of the total and tropospheric NO<sub>2</sub> data products, Report S5P-KNMI-L2-0005-RP version 0.11.0, 2 October 2014, KNMI, De Bilt, the Netherlands, 2014.
- Van Roozendaal, M., Loyola, D., Spurr, R., Balis, D., Lambert, J.-C., Livschitz, Y., Valks, P., Ruppert, T., Kenter, P., Fayt, C., and Zehner, C.: Ten years of GOME/ERS-2 total ozone data – The new GOME data processor (GDP) version 4: 1. Algorithm description, *J. Geophys. Res.*, 111, D14311, doi:10.1029/2005JD006375, 21 pp., 2006.
- Vandaele, A. C., Hermans, C., Simon, P. C., Carleer, M., Colin, R., Fally, S., Mérienne, M. F., Jenouvrier, A., and Coquart, B.: Measurements of the NO<sub>2</sub> absorption cross-section from 42 000 cm<sup>-1</sup> to 10 000 cm<sup>-1</sup> (238–1000 nm) at 220 K and 294 K, *J. Quant. Spectrosc. Ra.*, 59, 171–184, 1998.
- Vasilkov, A. P., Joiner, J., Gleason, J., and Bhartia, P. K.: Ocean Raman scattering in satellite backscatter UV measurements, *Geophys. Res. Lett.*, 29, 1837–1840, doi:10.1029/2002GL014955, 2002.
- Veefkind, J. P., Aben, I., McMullan, K., Förster, H., de Vries, J., Otter, G., Claas, J., Eskes, H. J., de Haan, J. F., Kleipool, Q., van Weele, M., Hasekamp, O., Hoogeveen, R., Landgraf, J., Snel, R., Tol, P., Ingmann, P., Voors, R., Kruizinga, B., Vink, R., Visser, H., and Levelt, P. F.: TROPOMI on the ESA Sentinel-5 Precursor: A GMES mission for global observations of the atmospheric composition for climate, air quality and ozone layer applications, *Remote Sens. Environ.*, 120, 70–83, doi:10.1016/j.rse.2011.09.027, 2012.
- Voors, R., Dirksen, R., Dobber, M., and Levelt, P.: OMI in-flight wavelength calibration and the solar reference spectrum, in: *Proceedings of the First Convergence on Atmospheric Science*, 8–12 May 2006, ESA publication SP-628, Frascati, Italy, 6 pp., 2006.
- Vountas, M., Richter, A., Wittrock, F., and Burrows, J. P.: Inelastic scattering in ocean water and its impact on trace gas retrievals from satellite data, *Atmos. Chem. Phys.*, 3, 1365–1375, doi:10.5194/acp-3-1365-2003, 2003.
- World Health Organisation: *Health Aspects of Air Pollution with Particulate Matter, Ozone and Nitrogen Dioxide*, World Health Organisation, Bonn, Germany, 98 pp., 2003.



Contents lists available at ScienceDirect

# Journal of Quantitative Spectroscopy & Radiative Transfer

journal homepage: [www.elsevier.com/locate/jqsrt](http://www.elsevier.com/locate/jqsrt)

## Self-broadening coefficients and improved line intensities for the $\nu_7$ band of ethylene near 10.5 $\mu\text{m}$ , and impact on ethylene retrievals from Jungfraujoch solar spectra



J. Vander Auwera<sup>a,\*</sup>, A. Fayt<sup>b</sup>, M. Tudorie<sup>a</sup>, M. Rotger<sup>c</sup>,  
V. Boudon<sup>d</sup>, B. Franco<sup>e</sup>, E. Mahieu<sup>e</sup>

<sup>a</sup> Service de Chimie Quantique et Photophysique, C.P. 160/09, Université Libre de Bruxelles, 50 avenue F.D. Roosevelt, B-1050 Brussels, Belgium

<sup>b</sup> Laboratoire de Spectroscopie Moléculaire, Université Catholique de Louvain, Chemin du cyclotron 2, boîte L7.01.07, B-1348 Louvain-la-Neuve, Belgium

<sup>c</sup> Groupe de Spectrométrie Moléculaire et Atmosphérique, UMR 7331 CNRS-Université de Reims Champagne Ardenne, Moulin de la Housse, B.P. 1039, Cases 16-17, F-51687 Reims Cedex, France

<sup>d</sup> Laboratoire Interdisciplinaire Carnot de Bourgogne, UMR 6303 CNRS-Université de Bourgogne, 9 avenue Alain Savary, BP 47870, F-21078 Dijon Cedex, France

<sup>e</sup> Institute of Astrophysics and Geophysics, Université de Liège, 17 Allée du 6 Août (B5a), B-4000 Liège (Sart-Tilman), Belgium

### ARTICLE INFO

#### Article history:

Received 10 May 2014

Received in revised form

2 July 2014

Accepted 4 July 2014

Available online 14 July 2014

#### Keywords:

Ethylene

High-resolution infrared absorption spectroscopy

Line intensities

Self-broadening coefficients

Atmospheric retrievals

### ABSTRACT

Relying on high-resolution Fourier transform infrared (FTIR) spectra, the present work involved extensive measurements of individual line intensities and self-broadening coefficients for the  $\nu_7$  band of  $^{12}\text{C}_2\text{H}_4$ . The measured self-broadening coefficients exhibit a dependence on both  $J$  and  $K_a$ . Compared to the corresponding information available in the latest edition of the HITRAN spectroscopic database, the measured line intensities were found to be higher by about 10% for high  $J$  lines in the P branch and lower by about 5% for high  $J$  lines of the R branch, varying between these two limits roughly linearly with the line positions. The impact of the presently measured line intensities on retrievals of atmospheric ethylene in the 949.0–952.0  $\text{cm}^{-1}$  microwindow was evaluated using a subset of ground-based high-resolution FTIR solar spectra recorded at the Jungfraujoch station. The use of HITRAN 2012 with line intensities modified to match the present measurements led to a systematic reduction of the measured total columns of ethylene by  $-4.1 \pm 0.1\%$ .

© 2014 Elsevier Ltd. All rights reserved.

## 1. Introduction

Ethylene (ethene,  $\text{C}_2\text{H}_4$ ) is a tropospheric pollutant affecting plants [1], mainly produced by automobiles and in biomass fires [2,3]. In the atmosphere, photochemical

reactions of ethylene with molecular oxygen, nitrogen, the hydroxyl radical, and ozone produce formaldehyde, nitrous oxide and formic acid [4]. Ethylene is also present as a by-product of methane photochemistry in the atmosphere of outer solar system bodies, such as Jupiter and Saturn [5,6], Neptune [7] and Titan [8].

Remote sensing of ethylene in the infrared range relies on the 10  $\mu\text{m}$  region. This spectral range corresponds to the excitation of 7 modes of vibration of  $^{12}\text{C}_2\text{H}_4$ , 4 of which

\* Corresponding author. Tel.: +32 2 650 24 18; fax: +32 2 650 42 32.

E-mail address: [jauwera@ulb.ac.be](mailto:jauwera@ulb.ac.be) (J. Vander Auwera).

<sup>1</sup> Senior research associate with the F.R.S.-FNRS (Belgium).

being infrared active (see Fig. 1 of [9]). The corresponding  $\nu_{10}$ ,  $\nu_7$ ,  $\nu_4$  and  $\nu_{12}$  bands are located near 826, 949, 1026 and 1442  $\text{cm}^{-1}$ , respectively [9]. Among these, the  $\nu_7$  band is the strongest, indeed used for remote sensing measurements of ethylene. Spectral line parameters for the  $\nu_7$  band of  $^{12}\text{C}_2\text{H}_4$ , as well as for the weak  $\nu_{10}$  and  $\nu_4$  bands, were included into the HITRAN database as of the 2000 edition [10]. That information for the 10  $\mu\text{m}$  range was later extended with the addition of line parameters for the  $\nu_{12}$  band [11,12]. No changes occurred for ethylene in the latest edition of HITRAN [13].

The information available in HITRAN for the 10  $\mu\text{m}$  region of ethylene is the result of several efforts. The energy levels structure associated with the 7 modes of vibration of  $^{12}\text{C}_2\text{H}_4$  involved in this region has been extensively studied (see [12,14,15] for reviews). The integrated intensity of the  $\nu_7$  band (thus including the underlying  $\nu_4$  band and R branch of the  $\nu_{10}$  band) has been measured several times [16–19], while measurements of individual intensities have been reported for only 32 lines of the  $\nu_7$  band of  $^{12}\text{C}_2\text{H}_4$ , located near the band origin between 940 and 970  $\text{cm}^{-1}$  [20–25]. Blass et al. [24] mention a database of 510 assigned lines with intensities retrieved from Fourier transform infrared (FTIR) spectra and calibrated using 13 line intensities measured using a tunable diode laser spectrometer. To the best of our knowledge, this database was however not published. The line intensities available in HITRAN for the  $\nu_{10}$ ,  $\nu_7$  and  $\nu_4$  bands of  $^{12}\text{C}_2\text{H}_4$  were generated by matching calculated relative intensities [26] to the intensities reported in [24]. Measurements of self-broadening coefficients have been reported for the  $\nu_7$  band [20,28] and one line of the  $\nu_{10}$  band [29] of  $^{12}\text{C}_2\text{H}_4$ , as well as for a significant number of lines of the  $\nu_7$  band of  $^{13}\text{C}^{12}\text{CH}_4$  [30]. In HITRAN [13], the self-broadening coefficient of all the lines is set to a default value of 0.09  $\text{cm}^{-1} \text{atm}^{-1}$ , except for the  $\nu_{12}$  band for which it is set to 0.125  $\text{cm}^{-1} \text{atm}^{-1}$  [12].

Relying on high-resolution FTIR spectra, the present work involved extensive measurements of individual line intensities and self-broadening coefficients for the  $\nu_7$  band of  $^{12}\text{C}_2\text{H}_4$ . Discrepancies between the measured line intensities and the corresponding information available in HITRAN [13] were observed and modeled empirically. The measured self-broadening coefficients exhibit a dependence with  $J''$  and  $K_a''$ , the quantum numbers respectively associated with the total angular momentum of the molecule in the lower level of the corresponding transition and its projection on the principal axis of inertia  $a$  of the molecule, which was also modeled empirically. Both of these results were used to modify the spectroscopic information available in HITRAN. This work is described in Sections 2–4. The impact of these modifications on retrievals of atmospheric ethylene in the 949.0–952.0  $\text{cm}^{-1}$  microwindow [2,3] was then evaluated using a subset of ground-based high-resolution FTIR solar spectra recorded at the Jungfraujoch station. This work is described in Section 5.

## 2. Experimental details

Six unapodized absorption spectra of a commercial sample of ethylene (Praxair, 99.95% stated purity, used

without further purification) were recorded with an upgraded Bruker IFS120HR Fourier transform spectrometer available in Brussels. The instrument was fitted with a Global source, a KBr beamsplitter, a low-pass optical filter with a cut-off wavenumber at about 2000  $\text{cm}^{-1}$  and a HgCdTe detector. The spectra were recorded at room temperature [295(1) K], stabilized by an air-conditioning system. The sample pressure, absorption path length, maximum optical path difference and diameter of the entrance aperture of the spectrometer used are listed in Table 1. The sample pressure was measured using two MKS Baratron gauges model 690A, of 10 and 1000 Torr full scale range. All the spectra were recorded using a 1.45(2) cm long stainless steel cell located inside the evacuated spectrometer and closed with KBr windows. To avoid saturation of the absorption features, spectra S4–S6 were recorded with two 5-mm thick KBr windows fitted into the cell to reduce the absorption path length. The recorded spectra correspond to the average of 300–742 interferograms. They were corrected for the non-linear response of the MCT detector, using the algorithm implemented in the OPUS software provided by Bruker. A portion of the spectra recorded at the lowest and highest pressures is presented in Fig. 1.

The present effort being focused on measurements of line intensities and self-broadening coefficients, only a

**Table 1**

Sample pressure  $P$ , absorption path length  $\ell$ , maximum optical path difference  $L$  (the corresponding spectral resolution is equal to  $0.9/L$ ) and diameter  $d$  of the entrance aperture of the spectrometer. All the spectra correspond to a temperature of 295(1) K.

| #  | $P$ (hPa)  | $\ell$ (cm)              | $L$ (cm) | $d$ (mm) |
|----|------------|--------------------------|----------|----------|
| S1 | 1.544 (24) | 1.45 (2)                 | 450      | 1.50     |
| S2 | 4.643(36)  | 1.45 (2)                 | 450      | 1.50     |
| S3 | 9.868 (51) | 1.45 (2)                 | 450      | 1.50     |
| S4 | 25.7 (5)   | 0.4322 (15) <sup>a</sup> | 450      | 1.50     |
| S5 | 51.5(5)    | 0.4322 (15) <sup>a</sup> | 150      | 1.50     |
| S6 | 101.4 (8)  | 0.4322 (15) <sup>a</sup> | 150      | 2.50     |

The absolute uncertainties given for the sample pressure  $P$  are the square root of the measurement uncertainty (estimated to be 0.5% of reading) and the peak-to-peak variations during the recordings.

<sup>a</sup> The path length of spectra S4–S6 was included in the least squares fit.

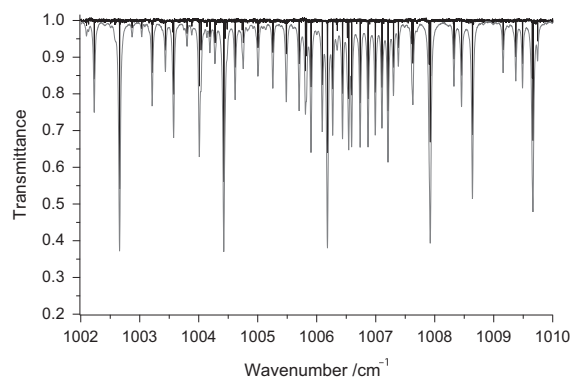


**Fig. 1.** Fourier transform spectra of ethylene near the  $r_{Q_6}$  branch of the  $\nu_7$  band of  $^{12}\text{C}_2\text{H}_4$ , recorded at the lowest (black curve, S1 in Table 1) and highest (gray curve, S6 in Table 1) pressures achieved in the present work.

relative calibration of the spectra was needed. As a different diameter of the entrance aperture of the spectrometer was used for spectrum S6, it had to be calibrated with respect to the other spectra. This was achieved by matching to HITRAN [13] the positions of lines of residual water vapor present in the evacuated spectrometer, measured between 1500 and 1800  $\text{cm}^{-1}$ .

### 3. Measurements

Line intensities and self-broadening coefficients were measured using a multi-spectrum least squares fitting algorithm, developed in Brussels [31]. The program adjusts a synthetic spectrum to each of any number of observed Fourier transform spectra, using a Levenberg–Marquardt least-squares fitting procedure. Each synthetic spectrum, interpolated 4 times with respect to the observed spectrum, is calculated as the convolution of a monochromatic transmission spectrum with an instrumental line shape function, which includes the effects of the finite maximum optical path difference and of the finite size of the entrance aperture in the interferometer as fixed contributions [32]. In the present work, the background in each spectrum was represented by a polynomial expansion up to second order, and the profile of the lines was modeled using a Voigt function [33], with Gaussian width always held fixed to the value calculated for the Doppler broadening. The pressure-induced widths  $b_L$  of the lines was assumed to be proportional to the  $\text{C}_2\text{H}_4$  pressure, with the proportionality factor being identified by the parameter  $b_L^0(\text{self})$  in  $\text{cm}^{-1} \text{atm}^{-1}$ . Self-shift was ignored.

The required initial line parameters were generated as follows. The positions, intensities and assignments of lines belonging to the 3 cold bands ( $\nu_{10}$ ,  $\nu_7$  and  $\nu_4$ ) of  $^{12}\text{C}_2\text{H}_4$  located in the studied range (830–1120  $\text{cm}^{-1}$ ) were obtained from an ongoing global analysis of the 10  $\mu\text{m}$  region [34] using the tensorial formalism developed in Dijon for  $\text{X}_2\text{Y}_4$  asymmetric-top molecules [35,36]. The self-broadening coefficients of these lines were set to values calculated according to

$$b_L^0(\text{self}) = a + bJ'' \quad (1)$$

where  $a = 0.1285(11) \text{ cm}^{-1} \text{atm}^{-1}$  and  $b = -6.42(81) \times 10^{-4} \text{ cm}^{-1} \text{atm}^{-1}$  [throughout the article, numbers between parentheses are the statistical uncertainties ( $1\sigma$ )] were determined by fitting the self-broadening coefficients reported for  $^{13}\text{C}^{12}\text{CH}_4$  by Flaud et al. [30] (neglecting the 5 coefficients lower than  $0.09 \text{ cm}^{-1} \text{atm}^{-1}$ ), with a standard deviation of  $8.3 \times 10^{-3} \text{ cm}^{-1} \text{atm}^{-1}$  (or 6.9% when expressed relative to the calculated values). To account for the hot bands, the positions and intensities of the corresponding lines were measured in spectrum S3 (see Table 1) using the program “WSpectra” [37], giving each line a Voigt profile and including instrumental effects. Their self-broadening coefficients were set to the constant value of  $0.125 \text{ cm}^{-1} \text{atm}^{-1}$ , applied previously to the  $\nu_{12}$  band [12] and agreeing well with the reported values of Flaud et al. [30]. The list thus constructed included 7547 lines in the range between 830 and 1120  $\text{cm}^{-1}$ .

All 6 spectra of Table 1 were fitted simultaneously, varying the positions and intensities of lines having an

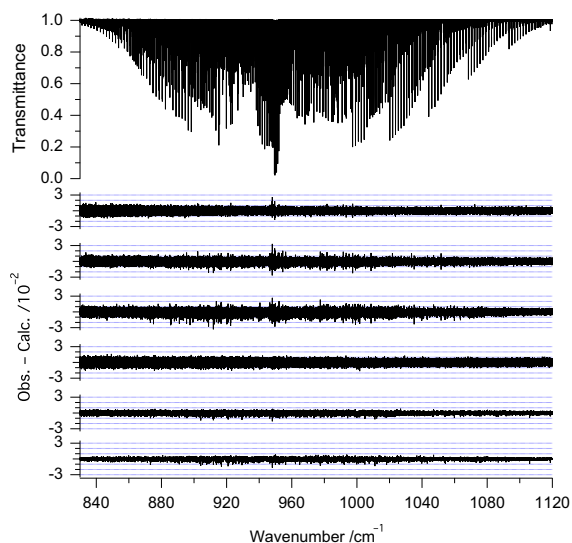


Fig. 2. Fourier transform spectrum of the 10  $\mu\text{m}$  spectral region of ethylene (S2 in Table 1, upper panel) and residuals of the simultaneous fit of spectra S1–S6 in Table 1 (from the top to the bottom of the 6 lower traces). The residuals displayed result from separate fits of 5 adjacent regions (see text for details).

intensity larger than  $3.5 \times 10^{-22} \text{ cm}^{-1}/(\text{mol cm}^{-2})$  at 295 K, as well as the self-broadening coefficients of lines with intensity larger than  $2.0 \times 10^{-21} \text{ cm}^{-1}/(\text{mol cm}^{-2})$ . The measurements were carried out successively for 5 adjacent spectral regions, namely 830–891.5, 891.5–933.2, 933.2–962.5, 962.5–998 and 998–1120  $\text{cm}^{-1}$ , involved from 1178 to 1921 simultaneously fitted parameters, and led to overall standard deviations ranging from 2.4 to  $3.3 \times 10^{-3}$ . The residuals obtained are presented in Fig. 2.

### 4. Results

Only considering the lines of the  $\nu_7$  band of  $^{12}\text{C}_2\text{H}_4$  found in the HITRAN database [13] for which both the intensities and self-broadening coefficients were determined, the present work led to a total of  $2 \times 1221$  measured parameters.

#### 4.1. Line intensities

Fig. 3 displays ratios with data in HITRAN [13] of line intensities measured in the present work and reported in [20,22,24]. The line intensities reported in [25], corresponding to ratios with HITRAN data ranging from 1.36 to 1.78, are not shown. The ratios presented in Fig. 3 show that most of the discrepancies of the present line intensities with HITRAN are in the range between about +10 and –5%, varying roughly linearly with the line positions. Note that the line intensities available in HITRAN for the  $\nu_{10}$ ,  $\nu_7$  and  $\nu_4$  bands of  $^{12}\text{C}_2\text{H}_4$  are characterized by an uncertainty of 5–10% (HITRAN error code=5). We did some test calculations to try and understand the possible origin of such discrepancies, varying the relative signs and values of the transition moments of the  $\nu_{10}$ ,  $\nu_7$  and  $\nu_{12}$  bands (the transition moment of the  $\nu_4$  band was set to

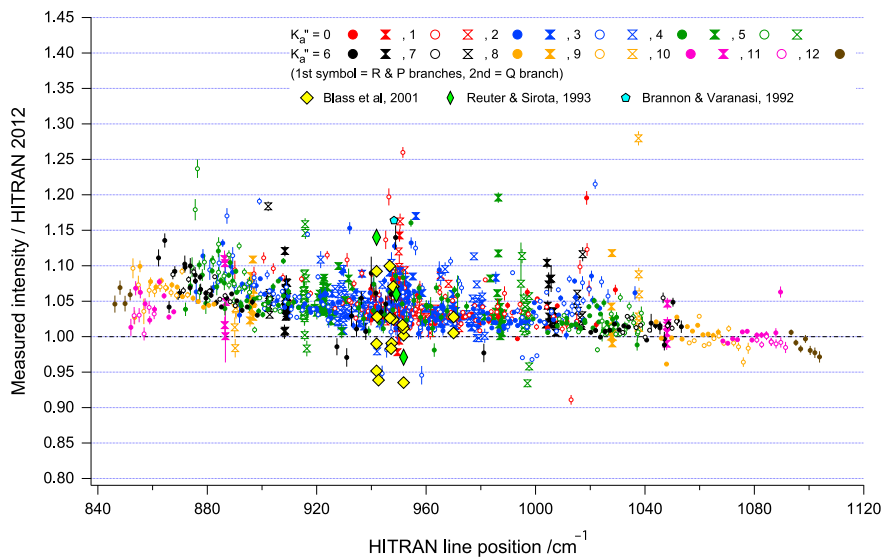


**Fig. 3.** Ratio with data in HITRAN [13] of line intensities measured in the present work for the  $\nu_7$  band of  $^{12}\text{C}_2\text{H}_4$  and reported by Brannon and Varanasi [20], Reuter and Sirota [22] and Blass et al. [24]. The line intensities reported in [25] have ratios with HITRAN data ranging from 1.36 to 1.78 and are not shown. The error bars represent the statistical uncertainty of measurement ( $1\sigma$ ).

zero, as was done when the data in HITRAN were generated). These calculations indicated that the observed discrepancies could result from the relative values of the transition moments used at the time. The ongoing global analysis of the  $10\ \mu\text{m}$  region [34] using the tensorial formalism developed in Dijon for  $\text{X}_2\text{Y}_4$  asymmetric-top molecules [35,36] will hopefully clarify this. In the present work, the observed evolution of the ratios  $R$  presented in Fig. 3 was empirically modeled using the expression

$$R = R_0 F_{HW} \quad (2)$$

where  $F_{HW}$  is a Herman–Wallis factor. Its expression was taken from Eq. (70) of [38] (only the terms involving parameters relevant to the present work are given):

$$F_{HW} = \{1 + A_7^F m_F + A_7^{J(Q)} [\overline{J(J+1)} - m_J^2] + A_7^{J(PR)} m_J^2\}^2 \quad (3)$$

where  $m_J = -J''$ ,  $0$  and  $J''+1$  for P-, Q- and R-branch lines,  $\overline{J(J+1)} = [J'(J'+1) + J''(J''+1)]/2$ ,  $m_F = (F' - F'')/2$ ,  $F$  is the rotational energy within a vibrational level [38], and ' and '' refer to the upper and lower levels of the transition. The subscript "7" indicates that the parameters apply to the  $\nu_7$  band. Note that  $m_J^2 = \overline{J(J+1)}$  for P and R branches and  $m_F$  is equal to half of the separation of the line from the band center [38]. All the 1221 intensity ratios  $R$  of the present work were fitted to Eqs. (2) and (3), with a standard deviation of 0.018. The values of the parameters involved are listed in Table 2 and the corresponding residuals are presented in Fig. 4. Most of the larger residuals are positive, and may result from some weak lines underneath the measured ones.

#### 4.2. Self-broadening coefficients

In this work, self-broadening coefficients were measured for P-, Q- and R-branch lines of the  $\nu_7$  band of  $^{12}\text{C}_2\text{H}_4$ , corresponding to transitions with  $J'' = 0-34$ . Fig. 5 compares

**Table 2**

Values of the parameters [numbers between parentheses are the statistical uncertainties ( $1\sigma$ )] involved in Eqs. (2) and (3), determined by fitting with a standard deviation of 0.018 the ratios with data in HITRAN [13] of 1221 line intensities measured in the present work.

| Parameter     | Value                       |
|---------------|-----------------------------|
| $R_0$         | 1.0312 (9)                  |
| $A_7^F$       | $-3.18 (11) \times 10^{-4}$ |
| $A_7^{J(Q)}$  | $2.05 (21) \times 10^{-5}$  |
| $A_7^{J(PR)}$ | $2.36 (24) \times 10^{-5}$  |

the present measurements with the self-broadening coefficients reported by Brannon and Varanasi [20] and Blanquet et al. [28] using the Voigt profile. Although the agreement is within the error bars stated in [28], the present measurements tend to be systematically higher than reported in Ref. [28]. The coefficients measured in the present work exhibit a dependence on  $J''$  and  $K_a''$ , similar to what was already reported for example for  $\text{CH}_3\text{Br}$  [39] or  $\text{H}_2\text{CO}$  [40]. Following these earlier work, the self-broadening coefficients measured for lines corresponding to the same  $J''$  were fitted to the empirical expression (see Eq. (1) of [40]):

$$b_L^{0J}(\text{self}) = c_0^J + c_5^J K_a''^5 \quad (4)$$

Note that a dependence on the fifth power of  $K_a''$  was found to reproduce the observations better than the dependence on  $K_a''^2$  of Refs. [39,40]. As an example, Fig. 6 presents the results of the fit of the self-broadening coefficients measured for P-, Q- and R-branch lines with  $J'' = 12$ . The corresponding parameters thus determined for  $J'' = 0-30$  are listed in Table 3 and presented in Fig. 7. A  $K_a''$  dependence of the self-broadening coefficients was not observed for  $J'' < 4$  and  $J > 19$ ; the corresponding  $c_5^J$  coefficients were therefore set to zero. Fig. 7 and Table 3 show that  $c_5^J$  tends to zero at high  $J''$ , similar to what was observed for the  $K_a''^2$  coefficient for

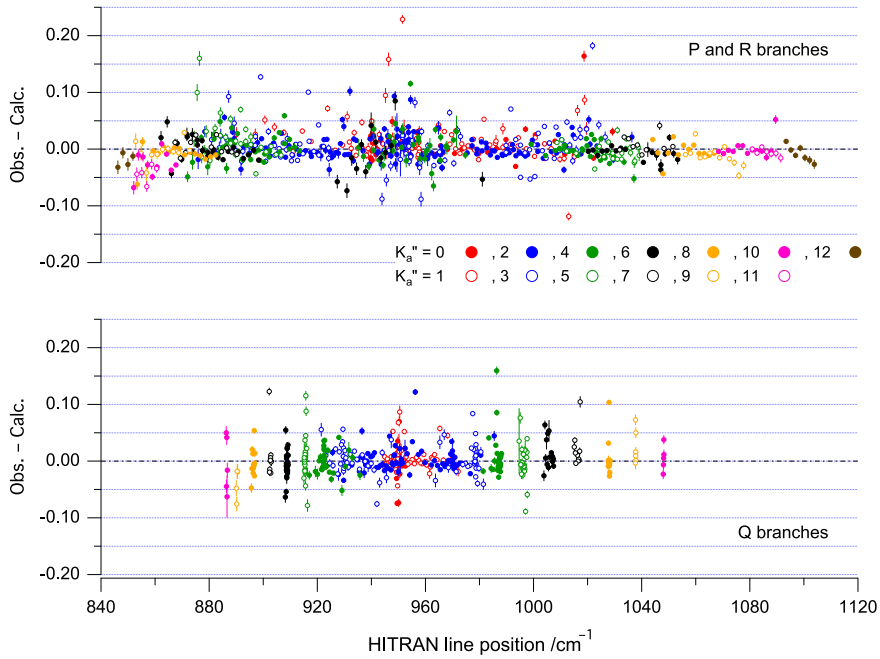


Fig. 4. Residuals of the fit of the ratios with data in HITRAN [13] of line intensities measured in the present work for the R and P (top) and Q (bottom) branches of the  $\nu_7$  band of  $^{12}\text{C}_2\text{H}_4$ . The error bars represent the statistical uncertainty of measurement ( $1\sigma$ ).

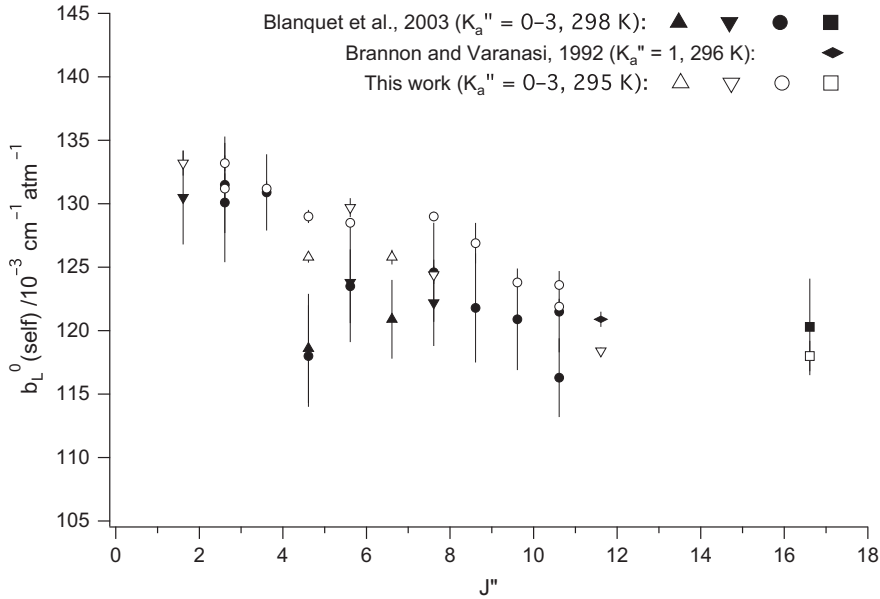


Fig. 5. Comparison between self-broadening coefficients measured for the  $\nu_7$  band of  $^{12}\text{C}_2\text{H}_4$  in this work, by Brannon and Varanasi [20] (296 K) and by Blanquet et al. [28] using the Voigt profile (298 K). The symbols represent the experimental values and the error bars are the statistical errors ( $1\sigma$ ), to which 2–3% of the reported value was added for the data of Ref. [28].

$\text{CH}_3\text{Br}$  [39] or  $\text{H}_2\text{CO}$  [40]. The measured  $c_0^J$  coefficients decrease monotonically with  $J''$ , and seem to tend towards a constant value (if the less precise measurements at  $J'' = 27, 29$  and  $30$  are ignored). This rotational dependence, from  $J'' = 0$  to  $26$ , was fitted to the following empirical expression (inspired from Eq. (5) of [41]):

$$c_0^J = \exp\{a + bJ'' + cJ''^2\} \quad (5)$$

The parameters  $a = -1.993(4)$ ,  $b = -1.18(6) \times 10^{-2}$  and  $c = 2.16(24) \times 10^{-4}$  were thus determined with a standard deviation of 0.8%. The corresponding best-fit values of  $c_0^J$  are also shown in Fig. 7. For  $J'' > 26$ ,  $c_0^J$  is assumed to be equal to the value at  $J'' = 26$ , i.e.  $0.116 \text{ cm}^{-1} \text{ atm}^{-1}$ .

Using Eqs. (2) and (3) together with the values of the parameters involved therein and listed in Table 2, the line intensities available in HITRAN [13] for the  $\nu_7$  band of

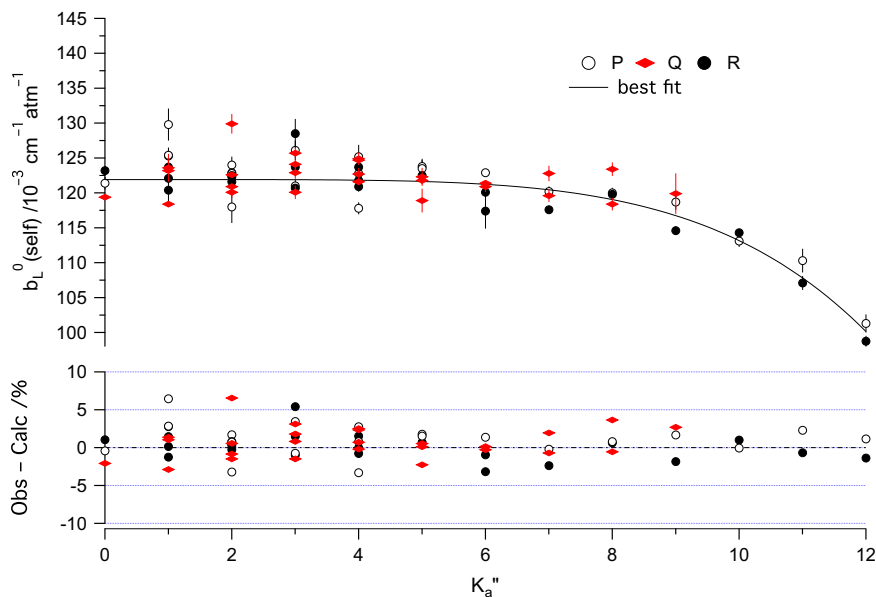


**Fig. 6.** Self-broadening coefficients measured in this work for P-, Q- and R-branch lines with  $J'' = 12$  of the  $\nu_7$  band of  $^{12}\text{C}_2\text{H}_4$ . In the upper panel, the symbols are the experimental values [the error bars represent the statistical uncertainty of measurement ( $1\sigma$ )] and the curve is calculated using Eq. (4) with the parameters listed in Table 3. The differences between the observed and calculated values are presented in the lower panel.

**Table 3**

Values of the parameters  $c_0^J$  and  $c_5^J$  involved in Eq. (4) (in  $\text{cm}^{-1} \text{atm}^{-1}$ ), determined by fitting the self-broadening coefficients measured in the present work for P-, Q- and R-branch lines having the same  $J''$ . Numbers between parentheses are the statistical uncertainties ( $1\sigma$ ).  $K_a''(\text{max})$  is the largest value of  $K_a''$  for which a self-broadening coefficient was measured; no value is given when  $K_a''(\text{max}) = J''$ . # is the number of coefficients included in the fit and  $\sigma_j$  is the corresponding standard deviation.

| $J''$ | $K_a''(\text{max})$ | $c_0^J$     | $c_5^J/10^{-7}$ | #  | $\sigma_j$ (%) |
|-------|---------------------|-------------|-----------------|----|----------------|
| 0     |                     | 0.1323      | 0               | 1  |                |
| 1     |                     | 0.1355 (11) | 0               | 6  | 1.9            |
| 2     |                     | 0.1314 (6)  | 0               | 13 | 2.6            |
| 3     |                     | 0.1312 (5)  | 0               | 21 | 2.3            |
| 4     |                     | 0.1304 (5)  | -43 (12)        | 26 | 2.5            |
| 5     |                     | 0.1293 (5)  | -19 (4)         | 33 | 2.7            |
| 6     |                     | 0.1287 (4)  | -12.9 (11)      | 42 | 2.2            |
| 7     |                     | 0.1273 (4)  | -6.5 (7)        | 48 | 2.4            |
| 8     |                     | 0.1264 (4)  | -4.1 (3)        | 52 | 2.4            |
| 9     |                     | 0.1250 (3)  | -2.6 (2)        | 57 | 2.1            |
| 10    |                     | 0.1237 (3)  | -1.89 (12)      | 61 | 2.2            |
| 11    |                     | 0.1228 (2)  | -1.19 (8)       | 68 | 1.9            |
| 12    |                     | 0.1219 (2)  | -0.88 (6)       | 70 | 2.1            |
| 13    | 12                  | 0.1211 (2)  | -0.62 (7)       | 73 | 2.1            |
| 14    | 12                  | 0.1202 (3)  | -0.50 (8)       | 74 | 2.2            |
| 15    | 12                  | 0.1191 (3)  | -0.39 (9)       | 77 | 2.3            |
| 16    | 12                  | 0.1192 (4)  | -0.54 (15)      | 70 | 2.7            |
| 17    | 12                  | 0.1188 (4)  | -0.50 (15)      | 68 | 3.0            |
| 18    | 12                  | 0.1189 (5)  | -0.62 (23)      | 60 | 2.8            |
| 19    | 10                  | 0.1176 (5)  | -0.61 (30)      | 60 | 2.6            |
| 20    | 10                  | 0.1161 (6)  | 0               | 53 | 4.1            |
| 21    | 10                  | 0.1177 (6)  | 0               | 48 | 3.8            |
| 22    | 10                  | 0.1161 (10) | 0               | 43 | 4.5            |
| 23    | 8                   | 0.1154 (11) | 0               | 27 | 5.1            |
| 24    | 6                   | 0.1170 (7)  | 0               | 25 | 4.2            |
| 25    | 6                   | 0.1167 (9)  | 0               | 14 | 3.8            |
| 26    | 6                   | 0.1169 (12) | 0               | 10 | 3.1            |
| 27    | 4                   | 0.108 (3)   | 0               | 5  | 6.4            |
| 28    | 4                   | 0.1174 (15) | 0               | 5  | 3.7            |
| 29    | 2                   | 0.097 (8)   | 0               | 2  | 19.            |
| 30    | 2                   | 0.105 (4)   | 0               | 3  | 9.8            |

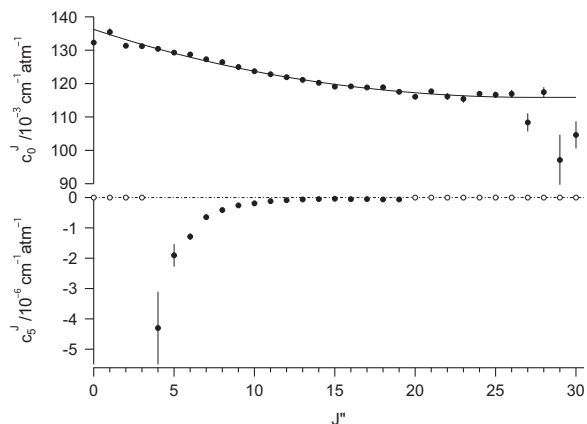


**Fig. 7.** Dependence on  $J''$  of the measured parameters  $c_0^J$  and  $c_5^J$  involved in Eq. (4) (filled circles). The error bars represent the statistical uncertainty of measurement ( $1\sigma$ ). The solid curve represents values of  $c_0^J$ , calculated using Eq. (5).  $c_5^J$  was too small to be measured for  $J'' < 4$  and  $J'' \geq 20$ ; the corresponding values were therefore set to 0 (as indicated by the open circles).

$^{12}\text{C}_2\text{H}_4$  were modified to match the present measurements. In view of the residuals shown in Fig. 4, their uncertainty was estimated to range from 2 to 5% (HITRAN error code=6). Similarly, the self-broadening coefficients of all the transitions of  $^{12}\text{C}_2\text{H}_4$  assigned in HITRAN (the upper vibrational level and rotational levels of some lines in the  $3 \mu\text{m}$  region are not provided) were updated using Eq. (4) with the parameters  $c_0^J$  given by Eq. (5) for  $J'' = 0-26$  and equal to  $0.116 \text{ cm}^{-1} \text{atm}^{-1}$  above, and the values of  $c_5^J$  listed in Table 3 [ $c_5^J = 0 \text{ cm}^{-1} \text{atm}^{-1}$  was assumed for  $J'' > 30$ , and the calculated self-broadening coefficient for  $K_a'' > K_a''(\text{max})$  and  $13 \leq J'' \leq 30$  (see Table 3)

was set to the value calculated for  $K_a''(\text{max})$ . In view of the agreement with previous work [20,28] and comparison between measured and calculated values, the updated self-broadening coefficients are believed to have an uncertainty in the range 5–10% (HITRAN error code=5) when they correspond to measurements (see Table 3). Otherwise, the HITRAN error code was set to 0.

## 5. Impact on ethylene retrievals from Jungfraujoch solar spectra

The impact of the new line parameters on the  $\text{C}_2\text{H}_4$  atmospheric retrievals has been evaluated using high-resolution infrared solar spectra recorded at the Jungfraujoch station (Swiss Alps, 46.5°N, 3580 m a.s.l.). The long-term monitoring of the Earth's atmospheric composition is performed at that site within the framework of the Network for the Detection of Atmospheric Composition Change (NDACC, see <http://www.ndacc.org>), using state-of-the-art instruments, including Fourier Transform Infrared spectrometers (FTIR, see e.g. [42]). The retrieval of  $\text{C}_2\text{H}_4$  from ground-based FTIR spectra is very challenging, given its very weak absorptions for background conditions. Frame A of Fig. 8 illustrates this, showing individual absorptions for the target and main interfering species in the 949.0–952.0  $\text{cm}^{-1}$  microwindow, which encompasses

several lines of the  $\nu_7$  band. The simulation has been performed assuming mean vertical distributions produced by the WACCM model (version 6, Whole Atmosphere Community Climate Model, see [43]), for the Jungfraujoch station under summer conditions and a solar zenith angle (SZA) of 80.0°. The main absorbers are  $\text{CO}_2$ ,  $\text{N}_2\text{O}$ , and  $\text{H}_2\text{O}$ , the latter affecting the local continuum on the left-hand side of the window for wet conditions. In comparison, the  $\text{C}_2\text{H}_4$  absorptions are very weak (even after multiplication by a factor 10 for visibility purpose), with the prominent feature near 949.3  $\text{cm}^{-1}$ , on the wing of a strong  $\text{CO}_2$  line.

About 7000 Jungfraujoch spectra covering the 1998–2012 time period have been systematically fitted in the 949.0–952.0  $\text{cm}^{-1}$  window, using the SFIT-2 (v3.91) retrieval algorithm (e.g. [44]), the HITRAN 2012 line-by-line spectroscopic database [13], pseudoline parameters produced by G.C. Toon (NASA-JPL) from laboratory cross-section spectra (e.g. for  $\text{SF}_6$ ; see e.g. [45]) and daily pressure and temperature information from the NCEP (National Centers for Environmental Prediction, Washington, DC; see <http://www.ncep.noaa.gov>). A priori vertical profiles from WACCM v6 were adopted for all species, except for water vapor which was pre-fitted in a first dedicated run, using the method described in [46]. During the iterative process, the vertical distributions of  $\text{CO}_2$ ,  $\text{H}_2\text{O}$ ,  $\text{N}_2\text{O}$ ,  $\text{O}_3$ ,  $\text{SF}_6$  and  $\text{COF}_2$  were simply scaled while for  $\text{C}_2\text{H}_4$ , a

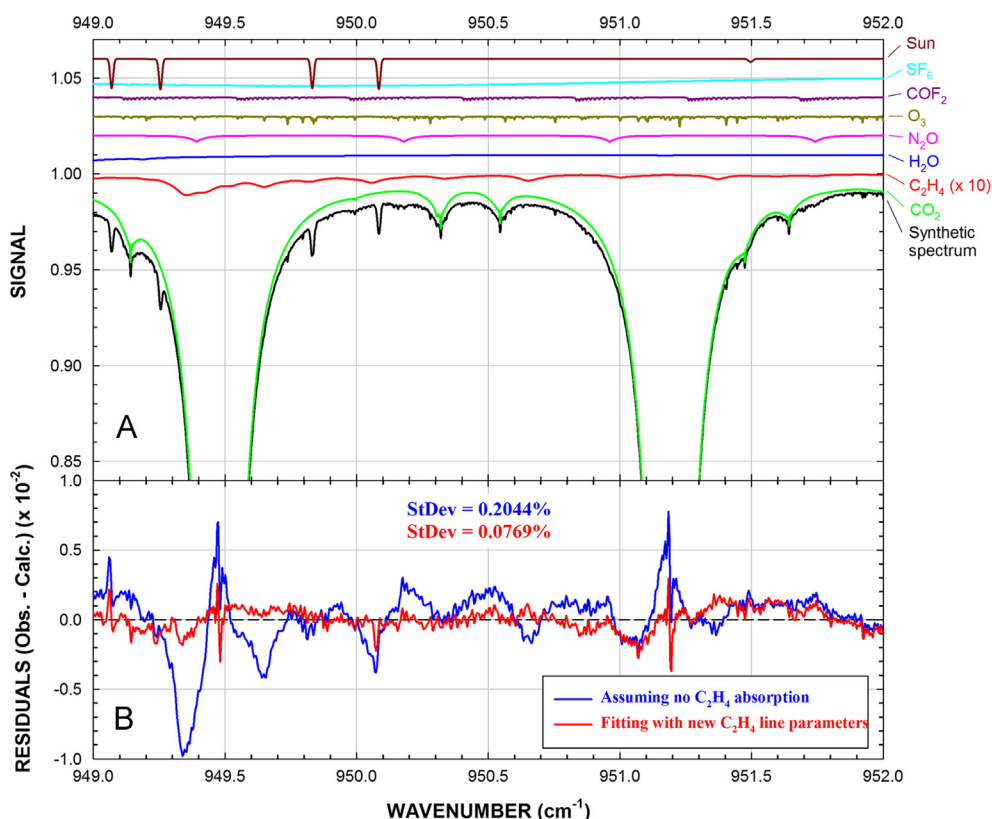


**Fig. 8.** (Frame A) Simulation of the main absorptions in the 949.0–952.0  $\text{cm}^{-1}$  microwindow for a solar zenith angle (SZA) of 80.0° and under summer conditions. The solid black line is the synthetic spectrum representing the total absorption. In this figure, the  $\text{C}_2\text{H}_4$  absorptions have been multiplied by a factor 10 for visibility purpose. (Frame B) Mean residuals (in %) compared to the observations when assuming no  $\text{C}_2\text{H}_4$  in the atmosphere (in blue) and when fitting  $\text{C}_2\text{H}_4$  with the new line parameters (in red). (For interpretation of the references to color in this figure caption, the reader is referred to the web version of this article.)

Tikhonov type  $L_1$  regularization [46] was used, with an alpha parameter (i.e. the regularization strength) set at 50.

The Jungfraujoch time series for  $C_2H_4$  show a clear seasonal signal, with maximum total columns in winter (close to  $1.5 \times 10^{14}$  mol  $cm^{-2}$ ) and minimum values in summer (on average  $0.7 \times 10^{14}$  mol  $cm^{-2}$ ). For the comparisons, we selected the spectra with the largest  $C_2H_4$  absorptions, keeping only the last two percentiles from the retrieved column abundances of ethylene. This subset has the following characteristics: (i) a minimal SZA of  $71.1^\circ$ , (ii) signal-to-noise ratios ranging from about 300 to 4000, (iii) mean standard deviation fitting residuals of 0.077%, and (iv) a mean total column of  $8.34 \times 10^{14}$  mol  $cm^{-2}$ .

This subset has been refitted, using the new line parameters for ethylene derived in the present study. We noted a systematic impact on the total columns which are reduced by  $-4.1 \pm 0.1\%$  (mean of  $8.01 \times 10^{14}$  mol  $cm^{-2}$ ), but no effect on the fitting residuals when compared to the HITRAN 2012 subset. Frame B of Fig. 8 reproduces in red the mean fitting residuals, as obtained when adopting the new line parameters for ethylene. The blue curve shows the mean residuals when assuming no  $C_2H_4$  in the atmosphere, characterized by differences of up to 1% with respect to the red curve.

## 6. Conclusion

Relying on high-resolution Fourier transform infrared spectra, the present work involved extensive measurements of individual line intensities and self-broadening coefficients for the  $\nu_7$  band of  $^{12}C_2H_4$ . Compared to the corresponding information available in the latest edition of the HITRAN spectroscopic database [13], the measured line intensities were found to be higher by about 10% for high  $J$  lines in the P branch and lower by about 5% for high  $J$  lines of the R branch, varying between these two limits roughly linearly with the line positions. Test calculations performed in this work indicated that these discrepancies could result from the relative values of the transition moments of the  $\nu_{10}$ ,  $\nu_7$  and  $\nu_{12}$  bands used when the information provided in HITRAN was generated (the transition moment of the  $\nu_4$  band was set to zero). The measured self-broadening coefficients exhibit a dependence on both  $J$  and  $K_a$ , which was fitted to empirical expressions. The spectroscopic information for ethylene available in HITRAN 2012 was modified to match the present observations. The impact of these modifications on retrievals of atmospheric ethylene was then evaluated via FTIR retrievals in the  $949.0\text{--}952.0$   $cm^{-1}$  microwindow, from a subset of ground-based high-resolution FTIR solar spectra recorded at the Jungfraujoch station. The new line intensities were found to lead to a systematic reduction of the measured total columns of ethylene by  $-4.1 \pm 0.1\%$ , compared to the use of HITRAN 2012.

## Acknowledgments

JVA, MT and EM thank financial support from the Belgian Federal Science Policy Office (contract SD/CS/07A, Advanced exploitation of Ground-based measurements for Atmospheric Chemistry and Climate – II), and VB and MR thank the SpecMo network (GdR CNRS no. 3152). AF

thanks for the computational resources provided by the supercomputing facilities of the Université Catholique de Louvain (CISM/UCL) and the Consortium des Equipements de Calcul Intensif en Fédération Wallonie Bruxelles (CECI) funded by the Fonds de la Recherche Scientifique (F.R.S.-FNRS, Belgium). The Liège team further thanks the F.R.S.-FNRS, the Fédération Wallonie Bruxelles and the International Foundation High Altitude Research Stations Jungfraujoch and Gornergrat (HFSJG, Bern). Thanks are also extended to all people having contributed to FTIR data acquisition at the Jungfraujoch.

## References

- [1] Abeles FB, Heggstad HE. Ethylene: an urban air pollutant. *J Air Pollut Control Assoc* 1973;23:517–21.
- [2] Rinsland CP, Paton-Walsh C, Jones NB, Griffith DWT, Goldman A, Wood SW, et al. High spectral resolution solar absorption measurements of ethylene ( $C_2H_4$ ) in a forest fire smoke plume using HITRAN parameters: tropospheric vertical profile retrieval. *J Quant Spectrosc Radiat Transf* 2005;96:301–9.
- [3] Coheur PF, Herbin H, Clerboux C, Hurtmans D, Wespes C, Carleer M, et al. ACE-FTS observation of a young biomass burning plume: first reported measurements of  $C_2H_4$ ,  $H_2CO$  and PAN by infrared occultation from space. *Atm Chem Phys* 2007;7:5437–46.
- [4] Niki H, Maker PD, Savage CM, Breitenbach LP. Mechanisms for hydroxyl radical initiated oxidation of olefin nitric oxide mixtures in parts per million concentrations. *J Phys Chem* 1978;82:135–7.
- [5] Romani PN, Jennings DE, Bjoraker GL, Sada PV, McCabe GH, Boyle RJ. Temporally varying ethylene emission on Jupiter. *Icarus* 2008;198:420–34.
- [6] Bézard B, Moses JL, Lacy J, Greathouse T, Richter M, Griffith CA. Detection of ethylene ( $C_2H_4$ ) on Jupiter and Saturn in non-auroral regions. *Bull Am Astron Soc* 2001;33:1079.
- [7] Schulz B, Encrenaz T, Bézard B, Romani PN, Lellouch E, Atreya SK. Detection of  $C_2H_4$  in Neptune from ISO/PHT-S observations. *Astron Astrophys* 1999;350:L13–7.
- [8] Coustenis A, Achterberg RK, Conrath BJ, Jennings DE, Marten A, Gautier D, et al. The composition of Titan's stratosphere from Cassini/CIRS mid-infrared spectra. *Icarus* 2007;189:35–62.
- [9] Willaert F, Demaison J, Margulès L, Mäder H, Spahn H, Giesen T, et al. The spectrum of ethylene from microwave to submillimeter-wave. *Mol Phys* 2006;104:273–92.
- [10] Rothman LS, Barbe A, Benner DC, Brown LR, Camy-Peyret C, Carleer M, et al. The HITRAN molecular spectroscopic database: edition of 2000 including updates through 2001. *J Quant Spectrosc Radiat Transf* 2003;82:5–44.
- [11] Rothman LS, Gordon IE, Barbe A, Benner DC, Bernath PF, Birk M, et al. The HITRAN 2008 molecular spectroscopic database. *J Quant Spectrosc Radiat Transf* 2009;110:533–72.
- [12] Rotger M, Boudon V, Vander Auwera J. Line positions and intensities in the  $\nu_{12}$  band of ethylene near  $1450$   $cm^{-1}$ : an experimental and theoretical approach. *J Quant Spectrosc Radiat Transf* 2008;109:952–62.
- [13] Rothman LS, Gordon IE, Babikov Y, Barbe A, Benner DC, Bernath PF, et al. The HITRAN 2012 molecular spectroscopic database. *J Quant Spectrosc Radiat Transf* 2013;130:4–50.
- [14] Rusinek E, Fichoux H, Herlemont F, Legrand J, Fayt A. SubDoppler study of the  $\nu_7$  band of  $C_2H_4$  with a  $CO_2$  laser sideband spectrometer. *J Mol Spectrosc* 1998;189:64–73.
- [15] Ulenikov ON, Gromova OV, Aslapovskaya YuS, Horneman V-M. High resolution spectroscopic study of  $C_2H_4$ : re-analysis of the ground state and  $\nu_4$ ,  $\nu_{10}$  and  $\nu_{12}$  vibrational bands. *J Quant Spectrosc Radiat Transf* 2013;118:14–25.
- [16] Wells AJ, Wilson EB. The experimental determination of the intensities of infra-red vibration-rotation absorption bands of gases. *J Chem Phys* 1941;9:659.
- [17] Thorndike AM, Wells AJ, Wilson EB. The experimental determination of the intensities of infra-red absorption bands. *J Chem Phys* 1947;15:157–65.
- [18] Golike RC, Mills IM, Person WB, Crawford Jr B. Vibrational intensities. VI. Ethylene and its deuterioisotopes. *J Chem Phys* 1956;25:1266–75.
- [19] Nakanaga T, Kondo S, Saeki S. Infrared intensities and Coriolis interactions in ethylene. *J Chem Phys* 1979;70:2471–8.

- [20] Brannon JF, Varanasi P. Tunable diode laser measurements on the  $951.7393\text{ cm}^{-1}$  line of  $^{12}\text{C}_2\text{H}_4$  at planetary atmospheric temperatures. *J Quant Spectrosc Radiat Transf* 1992;47:237–42.
- [21] Brannon JF, Varanasi P. Corrigenda “Tunable diode laser measurements on the  $951.7393\text{ cm}^{-1}$  line of  $^{12}\text{C}_2\text{H}_4$  at planetary atmospheric temperatures”. *J Quant Spectrosc Radiat Transf* 1993;49:695–6.
- [22] Reuter DC, Sirota JM. Absolute intensities and foreign gas broadening coefficients of the  $11_{1,10} \leftarrow 11_{2,10}$  and  $18_{0,18} \leftarrow 18_{1,18}$  lines in the  $\nu_7$  band of  $\text{C}_2\text{H}_4$ . *J Quant Spectrosc Radiat Transf* 1993;50:477–82.
- [23] Blass WE, Jennings L, Ewing AC, Daunt SJ, Weber MC, Senesac L, et al. Absolute intensities in the  $\nu_7$  band of ethylene: tunable laser measurements used to calibrate FTS broadband spectra. *J Quant Spectrosc Radiat Transf* 2001;68:467–72.
- [24] Blass WE, Hillman JJ, Fayt A, Daunt SJ, Senesac LR, Ewing AC, et al.  $10\text{ }\mu\text{m}$  ethylene: spectroscopy, intensities and a planetary modeler's atlas. *J Quant Spectrosc Radiat Transf* 2001;71:47–60.
- [25] Ponurovskii YY, Stepanov EV. Diode laser spectroscopy of the ethylene  $\nu_7$  band in the region of  $960\text{--}1030\text{ cm}^{-1}$ . *Atmos Oceanic Opt* 2002;15:766–70.
- [26] Cauuet I, Walrand J, Blanquet G. Extension to third-order Coriolis terms of the analysis of  $\nu_{10}$ ,  $\nu_7$  and  $\nu_4$  levels of ethylene on the basis of Fourier transform and diode laser spectra. *J Mol Spectrosc* 1990;139:191–214.
- [27] Blanquet G, Bouanich JP, Walrand J, Lepère M. Self-broadening coefficients in the  $\nu_7$  band of ethylene at room and low temperatures. *J Mol Spectrosc* 2003;222:284–90.
- [28] Morozhenko V, Kostiuk T, Buhl D, Hewagama T, Livengood TA, Kollyukh A, et al. Self and nitrogen broadening of the  $\nu_{10} 20_{11,10} \leftarrow 19_{10,9}$  ethylene transition at  $927.01879\text{ cm}^{-1}$ . *J Quant Spectrosc Radiat Transf* 2002;72:101–15.
- [29] Flaud JM, Lafferty WJ, Devi VM, Sams RL, Benner DC. Absolute line intensities and self-broadened half-width coefficients in the ethylene- $1\text{-}^{13}\text{C}$  bands in the  $700\text{--}1900\text{ cm}^{-1}$  region. *J Mol Spectrosc* 2011;267:3–12.
- [30] Tudorie M, Földes T, Vandaele AC, Vander Auwera J.  $\text{CO}_2$  pressure broadening and shift coefficients for the  $1\text{--}0$  band of HCl and DCl. *J Quant Spectrosc Radiat Transf* 2012;113:1092–101.
- [31] Davis SP, Abrams MC, Brault JW. Fourier transform spectrometry, 2001.
- [32] Wells RJ. Rapid approximation to the Voigt/Faddeeva function and its derivatives. *J Quant Spectrosc Radiat Transf* 1999;62:29–48.
- [33] Bourgeois MT, Alkadrou A, Rotger M, Boudon V, Vander Auwera J. Global frequency and intensity analysis of the  $10\text{ }\mu\text{m}$  region of the ethylene spectrum using the  $D_{2h}$  Top Data System. 2014, in preparation.
- [34] Wenger C, Raballand W, Rotger M, Boudon V.  $D_{2h}$  top data system ( $D_{2h}$  TDS) software for spectrum simulation of  $\text{X}_2\text{Y}_4$  asymmetric molecules. *J Quant Spectrosc Radiat Transf* 2005;95:521–38.
- [35] Raballand W, Rotger M, Boudon V, Loëte M. Spectroscopy of  $\text{X}_2\text{Y}_4$  ( $D_{2h}$ ) molecules: tensorial formalism adapted to the  $\text{O}(3) \supset D_{2h}$  chain Hamiltonian and transition operators. *J Mol Spectrosc* 2003;217:239–48.
- [36] Carleer MR. WSpectra: a Windows program to accurately measure the line intensities of high-resolution Fourier transform spectra, in remote sensing of clouds and the atmosphere V. In: Russel JE, Schäfer K, Lado-Bordowsky O, editors. Proceedings of SPIE – The international society for optical engineering, vol. 4168. Barcelona, Spain, 2001. p. 337.
- [37] Watson JKG. Quadratic Herman–Wallis factors for symmetric- and asymmetric-top molecules. *J Mol Spectrosc* 1992;153:211–24.
- [38] Jacquemart D, Kwabia Tchana F, Lacombe N, Kleiner I. A complete set of line parameters for  $\text{CH}_3\text{Br}$  in the  $10\text{--}\mu\text{m}$  spectral region. *J Quant Spectrosc Radiat Transf* 2007;105:264–302.
- [39] Jacquemart D, Laraia A, Kwabia Tchana F, Gamache RR, Perrin A, Lacombe N. Formaldehyde around  $3.5$  and  $5.7\text{--}\mu\text{m}$ : measurement and calculation of broadening coefficients. *J Quant Spectrosc Radiat Transf* 2010;111:1209–22.
- [40] Toth RA, Brown LR, Miller CE, Devi VM, Benner DC. Self-broadened widths and shifts of  $^{12}\text{C}^{16}\text{O}_2$ :  $4500\text{--}7000\text{ cm}^{-1}$ . *J Mol Spectrosc* 2006;239:243–71.
- [41] Zander R, Mahieu E, Demoulin P, Duchatelet P, Roland G, Servais C, et al. Our changing atmosphere: evidence based on long-term infrared solar observations at the Jungfraujoch since 1950. *Sci Total Environ* 2008;391:185–95.
- [42] Chang L, Palo S, Hagan M, Richter J, Garcia R, Riggan R, et al. Structure of the migrating diurnal tide in the Whole Atmosphere Community Climate Model (WACCM). *Adv Space Res* 2008;41:1397–406.
- [43] Rinsland CP, Jones NB, Connor BJ, Logan JA, Pougatchev NS, Goldman A, et al. Northern and southern hemisphere ground-based infrared measurements of tropospheric carbon monoxide and ethane. *J Geophys Res* 1998;103:28197–218.
- [44] Rinsland CP, Mahieu E, Demoulin P, Zander R, Servais C, Hartmann JM. Decrease of the carbon tetrachloride ( $\text{CCl}_4$ ) loading above Jungfraujoch, based on high resolution infrared solar spectra recorded between 1999 and 2011. *J Quant Spectrosc Radiat Transf* 2012;113:1322–9.
- [45] Sussmann R, Borsdorff T, Rettinger M, Camy-Peyret C, Demoulin P, Duchatelet P, et al. Technical note: harmonized retrieval of column-integrated atmospheric water vapor from the FTIR network – first examples for long-term records and station trends. *Atmos Chem Phys* 2009;9:8987–99.



## FTIR time-series of biomass burning products (HCN, C<sub>2</sub>H<sub>6</sub>, C<sub>2</sub>H<sub>2</sub>, CH<sub>3</sub>OH, and HCOOH) at Reunion Island (21° S, 55° E) and comparisons with model data

C. Vigouroux<sup>1</sup>, T. Stavrakou<sup>1</sup>, C. Whaley<sup>2</sup>, B. Dils<sup>1</sup>, V. Dufлот<sup>3,\*</sup>, C. Hermans<sup>1</sup>, N. Kumps<sup>1</sup>, J.-M. Metzger<sup>3</sup>, F. Scolas<sup>1</sup>, G. Vanhalewyn<sup>1,\*\*</sup>, J.-F. Müller<sup>1</sup>, D. B. A. Jones<sup>2</sup>, Q. Li<sup>4</sup>, and M. De Mazière<sup>1</sup>

<sup>1</sup>Belgian Institute for Space Aeronomy (BIRA-IASB), Brussels, Belgium

<sup>2</sup>Department of Physics, University of Toronto, Canada

<sup>3</sup>Laboratoire de l'Atmosphère et des Cyclones (LACy), Université de La Réunion, France

<sup>4</sup>LAGEO, Institute of Atmospheric Physics, Chinese Academy of Sciences, China

\* now at: the Laboratory of Quantic Chemistry and Photophysics, Université Libre de Bruxelles, Belgium

\*\* now at: Department of Solid State Sciences, Ghent University, Belgium

Correspondence to: C. Vigouroux (corinne.vigouroux@aeronomie.be)

Received: 26 March 2012 – Published in Atmos. Chem. Phys. Discuss.: 4 June 2012

Revised: 23 October 2012 – Accepted: 30 October 2012 – Published: 7 November 2012

**Abstract.** Reunion Island (21° S, 55° E), situated in the Indian Ocean at about 800 km east of Madagascar, is appropriately located to monitor the outflow of biomass burning pollution from Southern Africa and Madagascar, in the case of short-lived compounds, and from other Southern Hemispheric landmasses such as South America, in the case of longer-lived species. Ground-based Fourier transform infrared (FTIR) solar absorption observations are sensitive to a large number of biomass burning products. We present in this work the FTIR retrieval strategies, suitable for very humid sites such as Reunion Island, for hydrogen cyanide (HCN), ethane (C<sub>2</sub>H<sub>6</sub>), acetylene (C<sub>2</sub>H<sub>2</sub>), methanol (CH<sub>3</sub>OH), and formic acid (HCOOH). We provide their total columns time-series obtained from the measurements during August–October 2004, May–October 2007, and May 2009–December 2010. We show that biomass burning explains a large part of the observed seasonal and interannual variability of the chemical species. The correlations between the daily mean total columns of each of the species and those of CO, also measured with our FTIR spectrometer at Reunion Island, are very good from August to November ( $R \geq 0.86$ ). This allows us to derive, for that period, the following enhancement ratios with respect to CO: 0.0047, 0.0078, 0.0020, 0.012, and 0.0046 for HCN, C<sub>2</sub>H<sub>6</sub>, C<sub>2</sub>H<sub>2</sub>, CH<sub>3</sub>OH, and HCOOH, respectively. The HCN ground-based

data are compared to the chemical transport model GEOS-Chem, while the data for the other species are compared to the IMAGESv2 model. We show that using the HCN/CO ratio derived from our measurements (0.0047) in GEOS-Chem reduces the underestimation of the modeled HCN columns compared with the FTIR measurements. The comparisons between IMAGESv2 and the long-lived species C<sub>2</sub>H<sub>6</sub> and C<sub>2</sub>H<sub>2</sub> indicate that the biomass burning emissions used in the model (from the GFED3 inventory) are probably underestimated in the late September–October period for all years of measurements, and especially in 2004. The comparisons with the short-lived species, CH<sub>3</sub>OH and HCOOH, with lifetimes of around 5 days, suggest that the emission underestimation in late September–October 2004, occurs more specifically in the Southeastern Africa-Madagascar region. The very good correlation of CH<sub>3</sub>OH and HCOOH with CO suggests that, despite the dominance of the biogenic source of these compounds on the global scale, biomass burning is their major source at Reunion Island between August and November.

## 1 Introduction

Biomass burning is a major source for many atmospheric pollutants released in the atmosphere (Crutzen and Andreae, 1990), especially in the Tropics with a dominant contribution of savanna fires (Andreae and Merlet, 2001; Akagi et al., 2011). Reunion Island (21° S, 55° E), situated in the Indian Ocean at about 800 km east of Madagascar is appropriately located to monitor the biomass burning pollution outflow from Madagascar (Vigouroux et al., 2009), Southern Africa (Randriambelo et al., 2000), and even South America in the case of long-lived species such as CO (Duflo et al., 2010). We have used ground-based FTIR measurements from August to October 2004, May to October 2007, and May 2009 to December 2010 to derive time-series of total columns of five trace gases produced by vegetation fires: hydrogen cyanide (HCN), ethane (C<sub>2</sub>H<sub>6</sub>), acetylene (C<sub>2</sub>H<sub>2</sub>), methanol (CH<sub>3</sub>OH), and formic acid (HCOOH). Considering their long lifetime, hydrogen cyanide (about 5 months in the troposphere, Li et al., 2003), ethane (80 days, Xiao et al., 2008) and acetylene (2 weeks, Xiao et al., 2007) are well-known tracers for the transport of tropospheric pollution, and have already been measured by ground-based FTIR technique at several locations in the Northern Hemisphere (Mahieu et al., 1997; Rinsland et al., 1999; Zhao et al., 2002) and in the Southern Hemisphere, namely in Lauder (New Zealand) at 45° S (Rinsland et al., 2002), in Wollongong (Australia) at 34° S (Rinsland et al., 2001), and in Darwin (Australia) at 12° S (Paton-Walsh et al., 2010). Reunion Island is the only FTIR site located sufficiently close to Southern Africa and Madagascar that it can monitor the outflow of shorter-lived species emitted in these regions. Methanol and formic acid are such shorter-lived species with global lifetimes of 6 days (Stavrakou et al., 2011) and 3–4 days (Paulot et al., 2011; Stavrakou et al., 2012), respectively. Although these species are predominantly biogenic in a global scale (Jacob et al., 2005; Millet et al., 2008; Stavrakou et al., 2011; Paulot et al., 2011; Stavrakou et al., 2012), we show that pyrogenic contributions are important during the more intense biomass burning period at Reunion Island. Only a few ground-based FTIR studies have focused on these two species: methanol has been measured in Wollongong (Paton-Walsh et al., 2008) and Kitt Peak, 32° N (Rinsland et al., 2009), and formic acid mainly in the Northern Hemisphere (Rinsland et al., 2004; Zander et al., 2010; Paulot et al., 2011), but also in Wollongong (Paulot et al., 2011).

Because of its location, Reunion Island is very well situated to evaluate the emission and transport of various biogenic and pyrogenic species in chemical transport models. Previous comparisons of our FTIR measurements of formaldehyde during the 2004 and 2007 campaigns with IMAGES model simulations (Müller and Brasseur, 1995) have shown an overall good agreement, but also suggested that the emissions of formaldehyde precursors at Madagascar might be underestimated by the model (Vigouroux et al., 2009).

Our FTIR measurements of methanol and formic acid at Reunion Island in 2009 were already used to validate an inverse modeling approach of IASI data, which resulted in improved global emission budgets for these species (Stavrakou et al., 2011, 2012, respectively). Also Paulot et al. (2011) used our total column data of formic acid for 2009 for comparison with the GEOS-Chem model. However, in these three studies, the FTIR data were described only briefly. Therefore, a complete description of these methanol and formic acid data is given here, including the retrieval strategies and data characterization. At the same time, we present the more recently retrieved species HCN, C<sub>2</sub>H<sub>6</sub>, and C<sub>2</sub>H<sub>2</sub>. For all these species except HCN, we show comparisons of their daily mean total columns with corresponding IMAGES simulations, for the individual campaigns from 2004 to December 2010. Because IMAGES does not calculate HCN, we compare its daily mean total columns to GEOS-Chem simulations, for the years 2004 and 2007.

To quantify the atmospheric impact of biomass burning in the chemical transport models, the emission factors of the pyrogenic species have to be implemented accurately. As these emission factors depend not only on the species but also on the type of fire and even on the specific conditions prevailing at each fire event, many different values have been reported, for various gases at various locations in the world. Compilations of these numerous data are published regularly in order to facilitate their use by the modeling community (Andreae and Merlet, 2001; Akagi et al., 2011). A common way of deriving an emission factor is the measurement of the emission ratio of the target species relative to a reference species, which is often CO<sub>2</sub> or CO. When the measurement occurs in an aged plume, this same ratio is called “enhancement ratio” by opposition to the emission ratio measured at the source of the fire. These enhancement ratios can be used to interpret the ongoing chemistry within the plume. Recently, there has been an interest in deriving such enhancement ratios from satellite data in the Northern Hemisphere (Rinsland et al., 2007; Coheur et al., 2009) and in the Southern Hemisphere (Rinsland et al., 2006; Dufour et al., 2006; González Abad et al., 2009), or both (Tereschuk et al., 2011). For weakly reactive species, the enhancement ratio should be similar to the emission ratio, as long as the compound is not photochemically produced from the degradation of other pyrogenic NMVOCs. We use our FTIR measurements of CO total columns at Reunion Island (Duflo et al., 2010) to show that during the August–November period the correlation between all the species and CO is very good ( $R \geq 0.86$ ), suggesting that the common predominant source is biomass burning. We can then derive enhancement ratios of HCN, C<sub>2</sub>H<sub>6</sub>, C<sub>2</sub>H<sub>2</sub>, CH<sub>3</sub>OH, and HCOOH from the regression slope of their total column abundance versus that of CO. Considering the relatively long lifetime of these species (5 months to 4 days), we can compare them to emission ratios found in the literature.

Section 2 gives a description of the retrieval strategies optimized for each species, the main difficulties being the weak

absorption signatures of the target gases, especially relative to the strong interference with water vapour lines, in the very humid site of Saint-Denis, Reunion Island. All species are characterized by their averaging kernels and their error budget. The seasonal and interannual variability of the species is discussed in Sect. 3. The correlation with CO and the enhancement ratios relative to CO are then given and compared to literature values in Sect. 4. Finally, we show and discuss the model comparisons in Sect. 5.

## 2 FTIR data: description and characterization

### 2.1 Measurements campaigns

A Bruker 120M Fourier transform infrared (FTIR) spectrometer has been deployed during three campaigns at Saint-Denis in Reunion Island (21° S, 55° E, altitude 50 m), in October 2002, from August to October 2004, and from May to November 2007, and for continuous observations starting in May 2009. The total spectral domain covered by our FTIR solar absorption measurements is 600 to 4500 cm<sup>-1</sup> but, depending on the species, specific bandpass filters and detectors are used (see Senten et al. (2008) for details). The spectrometer was operated in an automatic and remotely controlled way by use of BARCOS (Bruker Automation and Remote Control System) developed at BIRA-IASB (Neefs et al., 2007). More detailed specifications of the 2002 and 2004 experiments are given in Senten et al. (2008). The later experiments are conducted in an almost identical way. In the present work, we will focus on the 2004, 2007, and 2009–2010 time-series.

The volume mixing ratio profiles of target gases are retrieved from the shapes of their absorption lines, which are pressure and temperature dependent. Daily pressure and temperature profiles have been taken from the National Centers for Environmental Prediction (NCEP). The observed absorption line shapes also depend on the instrument line shape (ILS) which is therefore included in the forward model of the retrieval code. In order to characterize the ILS and to verify the alignment of the instrument, a reference low-pressure (2 hPa) HBr cell spectrum is recorded at local noon with the sun as light source, whenever the meteorological conditions allow so, but also each evening using a lamp as light source. The software LINEFIT is used for the analysis of the cell spectra, as described in Hase et al. (1999). In this approach, the complex modulation efficiencies are described by 40 parameters (20 for amplitude and 20 for phase orientation) at equidistant optical path differences.

### 2.2 Retrieval strategies

The FTIR retrievals are performed using the algorithm SFIT2 (Rinsland et al., 1998), version 3.94, jointly developed at the NASA Langley Research Center, the National Center for Atmospheric Research (NCAR) and the National Institute of Water and Atmosphere Research (NIWA). The spectral inver-

sion is based on a semi-empirical implementation of the Optimal Estimation Method (OEM) of Rodgers (2000), which implies the use of an a priori information (a priori profiles and regularization matrix **R**). The retrieved vertical profiles are obtained by fitting one or more narrow spectral intervals (microwindows).

#### 2.2.1 Choice of microwindows and spectroscopic databases

We have used, for all species except C<sub>2</sub>H<sub>6</sub>, the HITRAN 2008 spectroscopic line parameters (Rothman et al., 2009). For C<sub>2</sub>H<sub>6</sub>, we used the pseudo-lines constructed by G. Toon (personal communication, 2010, see <http://mark4sun.jpl.nasa.gov/pseudo.html> for details), based on the recent paper of Harrison et al. (2010).

Table 1 gives the list of microwindows used in this work. All target species have weak absorptions in the infrared. It is therefore important to choose the spectral microwindows in order to minimize the impact of interfering species. The particular difficulty at Saint-Denis is the presence of very strong absorption lines of water vapour in the spectra, in most spectral regions. As can be seen in the table, it is impossible to select spectral regions without interferences of H<sub>2</sub><sup>16</sup>O and/or of isotopologues. In the retrieval process, while a vertical profile is fitted for the target species, a single scaling of their a priori profile is done for the interfering species. For the interfering species having a small impact on the retrievals, a single climatological a priori profile is used for all spectra. For the other ones, such as water vapour, we performed beforehand and independently profile retrievals in dedicated microwindows for each spectrum. These individual retrieved profiles were then used as the a priori profiles in the retrievals of the target species; they are again fitted, but now with only one scaling parameter.

For the retrieval of HCN, we followed the approach of Paton-Walsh et al. (2010) perfectly adapted for humid sites such as Saint-Denis. For humid sites (i.e., tropical sites at low altitude), we do not recommend any of the commonly used micro-windows sets comprising the 3287.248 cm<sup>-1</sup> line (Mahieu et al., 1997; Rinsland et al., 1999; Notholt et al., 2000; Rinsland et al., 2001, 2002; Zhao et al., 2002). Preliminary retrievals of H<sub>2</sub><sup>16</sup>O, H<sub>2</sub><sup>18</sup>O and H<sub>2</sub><sup>17</sup>O were made independently in the 3189.50–3190.45 cm<sup>-1</sup>, 3299.0–3299.6 cm<sup>-1</sup>, and 3249.7–3250.3 cm<sup>-1</sup> spectral intervals, respectively. The H<sub>2</sub><sup>16</sup>O and H<sub>2</sub><sup>18</sup>O retrieval results are also used as a priori profiles for the C<sub>2</sub>H<sub>2</sub> retrievals.

For C<sub>2</sub>H<sub>6</sub>, the widely used (Mahieu et al., 1997; Notholt et al., 2000; Rinsland et al., 2002; Zhao et al., 2002; Paton-Walsh et al., 2010) microwindow around 2976.8 cm<sup>-1</sup> has been fitted together with one of the two other regions suggested in Meier et al. (2004), around 2983.3 cm<sup>-1</sup>, in order to increase the DOFS. We decided to skip the other one, around 2986.7 cm<sup>-1</sup>, also used in Notholt et al. (1997), because of the very strong H<sub>2</sub><sup>16</sup>O line nearby. Independent beforehand

**Table 1.** Microwindows (in  $\text{cm}^{-1}$ ) and interfering species used for the retrievals of HCN,  $\text{C}_2\text{H}_6$ ,  $\text{C}_2\text{H}_2$ , HCOOH, and  $\text{CH}_3\text{OH}$ .

| Target gas             | Microwindows ( $\text{cm}^{-1}$ ) | Interfering species   |
|------------------------|-----------------------------------|---|
| HCN                    | 3268.05–3268.35                   | $\text{H}_2\text{O}$ , $\text{H}_2^{18}\text{O}$ , $\text{H}_2^{17}\text{O}$  |
|                        | 3331.40–3331.80                   | $\text{H}_2\text{O}$ , $\text{H}_2^{17}\text{O}$ , $\text{CO}_2$ , $\text{N}_2\text{O}$<br>solar CO   |
| $\text{C}_2\text{H}_6$ | 2976.66–2976.95                   | $\text{H}_2\text{O}$ , $\text{H}_2^{18}\text{O}$ , $\text{O}_3$   |
|                        | 2983.20–2983.55                   | $\text{H}_2\text{O}$ , $\text{H}_2^{18}\text{O}$ , $\text{O}_3$   |
| $\text{C}_2\text{H}_2$ | 3250.25–3251.11                   | $\text{H}_2\text{O}$ , $\text{H}_2^{18}\text{O}$ , solar CO   |
| $\text{CH}_3\text{OH}$ | 1029.00–1037.00                   | $\text{H}_2\text{O}$ , $\text{O}_3$ , $^{16}\text{O}^{16}\text{O}^{18}\text{O}$ ,<br>$^{16}\text{O}^{18}\text{O}^{16}\text{O}$ , $^{16}\text{O}^{16}\text{O}^{17}\text{O}$ ,<br>$^{16}\text{O}^{17}\text{O}^{16}\text{O}$ , $\text{CO}_2$ , $\text{NH}_3$ |
| HCOOH                  | 1102.75–1106.40                   | HDO, $\text{H}_2\text{O}$ , $\text{H}_2^{18}\text{O}$ , $\text{H}_2^{17}\text{O}$ ,<br>$\text{O}_3$ , $^{16}\text{O}^{16}\text{O}^{18}\text{O}$ , $\text{NH}_3$<br>$\text{CCl}_2\text{F}_2$ , $\text{CHF}_2\text{Cl}$ , $\text{CH}_4$                     |

retrievals of  $\text{H}_2^{16}\text{O}$  were made in the 2924.10–2924.32  $\text{cm}^{-1}$  microwindow. Because of the lower influence of  $\text{H}_2^{18}\text{O}$  and the difficulty of finding an isolated  $\text{H}_2^{18}\text{O}$  line in this spectral region, we simply used the individual retrieved  $\text{H}_2^{16}\text{O}$  profiles also as the a priori for  $\text{H}_2^{18}\text{O}$ . Ozone is a minor interfering species here, we therefore used a single a priori profile for all the spectra, calculated at Reunion Island (J. Hannigan, NCAR, personal communication, 2010) from the Whole Atmosphere Community Climate Model (WACCM<sup>1</sup>, version 5).

For  $\text{C}_2\text{H}_2$ , we have chosen the line at 3250.66  $\text{cm}^{-1}$  following Notholt et al. (2000); Rinsland et al. (2002); Zhao et al. (2002). The other lines suggested in Meier et al. (2004), of which some are used in Notholt et al. (1997); Paton-Walsh et al. (2010), have been tested but gave poorer results. For the CO solar lines, we used the empirical line-by-line model of Hase et al. (2006); the linelist was updated according to Hase et al. (2010).

For HCOOH, we used the Q-branch of the  $\nu_6$  mode, as in other retrievals of satellite (González Abad et al., 2009; Razavi et al., 2011) or ground-based (Rinsland et al., 2004; Zander et al., 2010) infrared measurements. The main difficulty is the HDO absorption overlapping the HCOOH Q-branch. We have therefore performed preliminary retrievals of HDO in the 1208.49–1209.07  $\text{cm}^{-1}$  microwindow, for each spectrum.  $\text{CHClF}_2$  and  $\text{CCl}_2\text{F}_2$  profiles were also retrieved independently in the 828.62–829.35  $\text{cm}^{-1}$  and 1160.2–1161.4  $\text{cm}^{-1}$  spectral intervals, respectively. The  $\text{O}_3$  vertical profiles were also retrieved beforehand using the optimized strategy described in Vigouroux et al. (2008) for

the same spectra (microwindow 1000–1005  $\text{cm}^{-1}$ ). These profiles are used as individual a priori profiles, in the retrieval of HCOOH, not only for  $\text{O}_3$  but also for its isotopologues. Finally,  $\text{H}_2^{16}\text{O}$  was retrieved beforehand in the 834.6–836.6  $\text{cm}^{-1}$  microwindow, and the resulting profiles were used as a priori for all water vapour isotopologues (except HDO). Unique a priori profiles were used for  $\text{CH}_4$  (from WACCMv5) and  $\text{NH}_3$ .

$\text{CH}_3\text{OH}$  has been studied in ground-based infrared measurements only recently (Paton-Walsh et al., 2008; Rinsland et al., 2009), with different choices of microwindows, both around 10  $\mu\text{m}$ . In the case of Saint-Denis, the best sensitivity to  $\text{CH}_3\text{OH}$  is obtained by using the Q-branch of the  $\nu_8$  mode at about 1033  $\text{cm}^{-1}$ , as in Paton-Walsh et al. (2008). The same  $\text{H}_2\text{O}$  and  $\text{O}_3$  individual a priori profiles as for HCOOH are used in the methanol retrievals. Unique a priori profiles were used for  $\text{CO}_2$  (from WACCMv5) and  $\text{NH}_3$ .

### 2.2.2 Choice of a priori profiles and regularization

The a priori profiles adopted in the FTIR retrievals of the target species are shown in Fig. 1.

The HCN a priori profile is the mean of the HCN profiles, calculated at Reunion Island (J. Hannigan, personal communication, 2010) from WACCMv5 from 2004 to 2006. The  $\text{CH}_3\text{OH}$  a priori profile, from the ground to 12 km, is a smoothed approximation of data composites of the airborne experiment PEM-Tropics-B (Raper et al., 2001), as was done for HCHO in Vigouroux et al. (2009): we used the average concentration over the Southern tropical Pacific (0 to 30° S; 160° E to 95° W) based on the data composites available at [http://acd.ucar.edu/~emmons/DATACOMP/camp\\_table.htm](http://acd.ucar.edu/~emmons/DATACOMP/camp_table.htm), which provides an update of the database described in Emmons et al. (2000). The HCOOH a priori profile, from the ground to 7 km, has been constructed from the data composites of the airborne experiment PEM-Tropics-A (Hoell et al., 1999) also available at the previous link, and from ACE-FTS satellite measurements above Reunion Island for the 7–30 km range (González Abad, personal communication, 2010; see González Abad et al., 2009). For  $\text{C}_2\text{H}_6$ , from the ground to 12 km, we used the mean of PEM-Tropics-B and PEM-Tropics-A measurements. For  $\text{C}_2\text{H}_2$ , since the mean of PEM-Tropics-B and PEM-Tropics-A measurements at 7 km was almost two times lower than the value measured by ACE-FTS above Reunion Island (N. Allen, personal communication, 2010), we took the mean of both measurement values at this altitude and used this same value down to the ground; above, we used the ACE measurements but scaled to the value at 7 km. For altitudes above which no information was available, we have decreased the vmr values smoothly to zero.

In the usual OEM, the constraint matrix  $\mathbf{R}$  is the inverse of the a priori covariance matrix  $\mathbf{S}_a$ . Ideally,  $\mathbf{S}_a$  should express the natural variability of the target gas, and thus should be as realistic as possible and evaluated from appropriate

<sup>1</sup>[http://www.cesm.ucar.edu/working\\_groups/WACCM/](http://www.cesm.ucar.edu/working_groups/WACCM/)

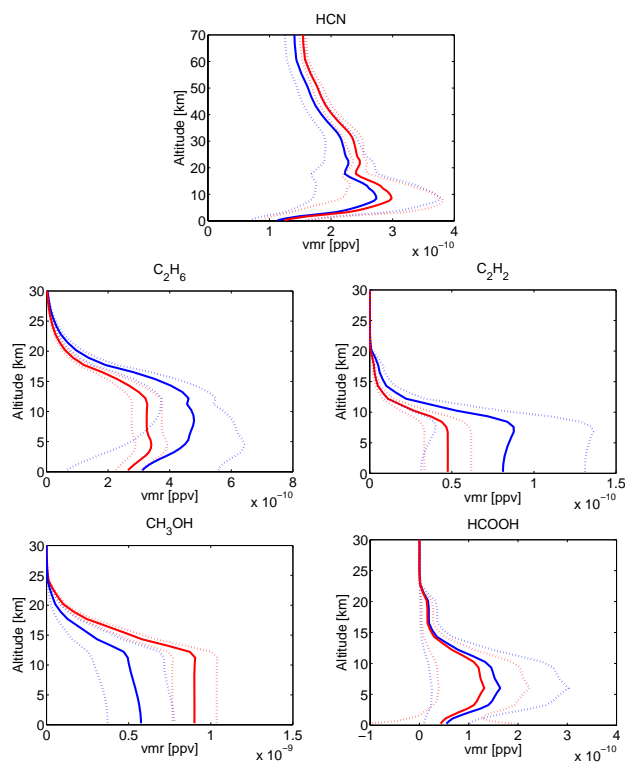


**Fig. 1.** A priori vertical profiles (red lines; Sect. 2.2.2) and variability used for smoothing error calculation (red dashed lines; Sect. 2.3) of the five retrieved species (in vmr, ppv). The HCN a priori profile is given by the WACCM, v5 model. The a priori profiles of the other species have been constructed using a combination of airborne and ACE-FTS measurements (see text for details). The means (blue lines) and standard deviations (blue dashed lines) of the retrieved FTIR profiles over the whole dataset are also shown for comparison.

climatological data (Rodgers, 2000). However, for our target species at Reunion Island, this information is poorly available and therefore we have opted for Tikhonov  $L_1$  regularization (Tikhonov, 1963) as in Vigouroux et al. (2009), i.e., the constraint matrix is defined as  $\mathbf{R} = \alpha \mathbf{L}_1^T \mathbf{L}_1$ , with  $\alpha$  the regularization strength and  $\mathbf{L}_1$  the first derivative operator. For determining the strength of the constraint ( $\alpha$ ), we have followed the method illustrated in Fig. 4 of Steck (2002): we have chosen, for each target species, the parameter  $\alpha$  that minimizes the total error (measurement noise + smoothing error).

The vertical information contained in the FTIR retrievals are characterized by the averaging kernel matrix  $\mathbf{A}$  and its trace gives the degrees of freedom for signal (DOFS). We obtain mean DOFS of about  $1.50 \pm 0.15$  for HCN,  $1.60 \pm 0.19$  for  $\text{C}_2\text{H}_6$ , and  $1.05 \pm 0.02$  for  $\text{C}_2\text{H}_2$ , HCOOH and  $\text{CH}_3\text{OH}$ . We therefore use only total column results in our comparisons with the model. It is worth noticing that the total column results shown in this paper are representative of the tropospheric columns of the species, since the cold-point

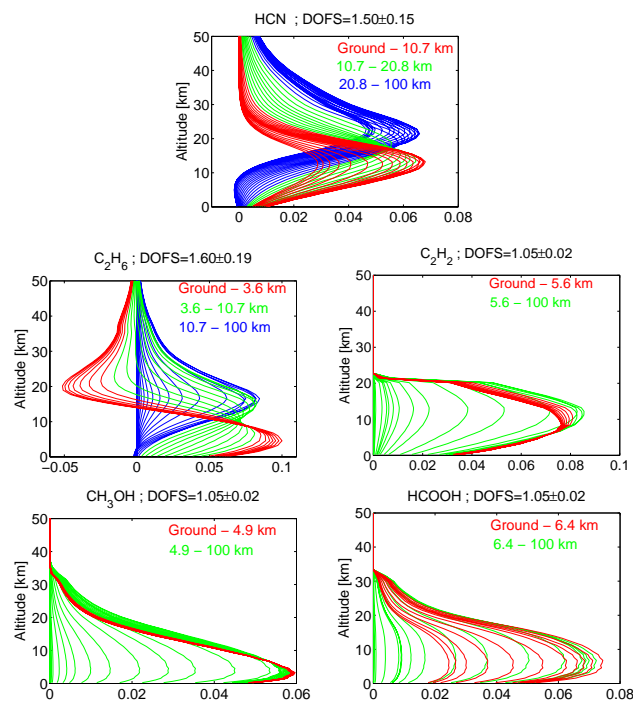


**Fig. 2.** FTIR volume mixing ratio averaging kernels ( $\text{ppv ppv}^{-1}$ ) of the five retrieved species. The total DOFS for each species is given in the titles. Each line corresponds to the averaging kernel at a given altitude, the retrievals being made with a 47 layers grid. We have used the same color for the averaging kernels at altitudes lying in a partial column for which we have about a DOFS of 0.5. The partial columns boundaries are given in the legends.

tropopause lies around 17 km at Reunion Island (Sivakumar et al., 2006) and the partial columns from the ground up to 17 km represent more than 98 % of the total column amounts for all species, except HCN (91 %).

The means of the averaging kernels (rows of  $\mathbf{A}$ ) for each molecule are shown in Fig. 2. As expected with DOFS close to one (except for  $\text{C}_2\text{H}_6$  and HCN), we can see that the averaging kernels are not vertically resolved. For each species, they all peak at about the same altitude (around 10 km for  $\text{C}_2\text{H}_2$ ; 5 km for HCOOH; and 3 km for  $\text{CH}_3\text{OH}$ ). For  $\text{C}_2\text{H}_6$  and HCN, we obtain two maxima: at about 5 and 15 km, and at about 13 and 21 km, respectively. Since we discuss total column results, we also show in Fig. 3 the total column averaging kernel for each species.

### 2.3 FTIR error budget

The error budget is calculated following the formalism of Rodgers (2000), and can be divided into three different error sources: the smoothing error expressing the uncertainty due to the limited vertical resolution of the retrieval, the forward model parameters error, and the measurement noise error.

The smoothing error covariance is calculated as  $(\mathbf{I} - \mathbf{A})\mathbf{S}_{\text{var}}(\mathbf{I} - \mathbf{A})^T$ , where  $\mathbf{S}_{\text{var}}$  is the best possible estimate of the

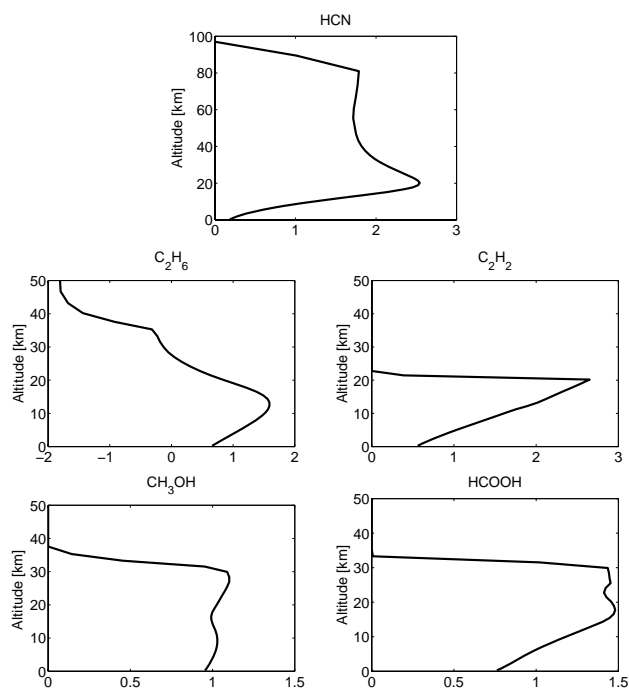


**Fig. 3.** FTIR total column averaging kernels ( $\text{molec cm}^{-2}/\text{molec cm}^{-2}$ ) of the five retrieved species.

natural variability of the target molecule. For HCN, we use the full covariance matrix constructed with the same modeled profiles from WACCMv5 as for the HCN a priori profile. The vertical resolution of the WACCMv5 model used in this work is less than 1 km below 13 km, and less than 1 km below 30 km. The diagonal elements of the covariance matrix correspond to a variability of about 30 % at the ground increasing up to 40 % at 3 km, and then decreasing rapidly (24 % at 10 km and 5 % at 20 km and above). The off-diagonal elements correspond approximately to a Gaussian correlation with a correlation length of 6 km. For the other species, the diagonal elements of  $\mathbf{S}_{\text{var}}$  are estimated from the average observed variability in  $5^\circ \times 5^\circ$  pixels during PEM-Tropics-B and PEM-Tropics-A. The vertical resolution of these aircraft data is 1 km. For  $\text{C}_2\text{H}_6$  and  $\text{C}_2\text{H}_2$ , approximately constant values of 15 % and 30 % are observed, respectively, at all altitudes up to 12 km. For HCOOH, the variability decreases rapidly from 350 % at the surface to about 70 % at 2.5 km up to 12 km. For  $\text{CH}_3\text{OH}$ , the observed variability seems unrealistic (below 1 % at the surface up to only 2 % at 12 km), but the number of measurements for this species is much smaller. We have therefore decided to use a constant 15 % value as for  $\text{C}_2\text{H}_6$ , since the standard deviations observed by our FTIR measurements are similar for both species. For the latter four species, the off-diagonal elements of  $\mathbf{S}_{\text{var}}$  are estimated using a Gaussian correlation between the layers, with a correlation length of 4 km. Our smoothing error estimation is based on our best current knowledge of the variability of the

**Table 2.** Mean error budget on individual total columns. The mean standard deviations (SD) of daily means, for the days when the number of measurements were equal or greater than three, are also given. The total error includes the smoothing error.

| Errors (in %) | HCN | $\text{C}_2\text{H}_6$ | $\text{C}_2\text{H}_2$ | $\text{CH}_3\text{OH}$ | HCOOH |
|---------------|-----|------------------------|------------------------|------------------------|-------|
| Smoothing     | 9   | 2                      | 3                      | 0.3                    | 7     |
| Random        | 2   | 5                      | 16                     | 10                     | 11    |
| SD            | 3   | 6                      | 14                     | 8                      | 15    |
| Systematic    | 14  | 5                      | 7                      | 9                      | 15    |
| Total error   | 17  | 7                      | 17                     | 13                     | 19    |

species, calculated here with respect to the vertical resolution of WACCMv5 (for HCN) and of aircraft data (for the other species), but it should be corrected once this knowledge will be improved. We see from Fig. 1, that the variability obtained by our FTIR measurements (blue dashed lines) is larger than the one we assumed for the smoothing error calculation, for all species but especially for  $\text{C}_2\text{H}_2$ . So our smoothing error budget given in Table 2 might be underestimated.

All the details on the calculation of the measurement noise error and the forward model parameters error can be found in Vigouroux et al. (2009). The only difference concerns the error due to interfering species: in the present work, the  $\mathbf{S}_b$  matrix (covariance matrix of the vector of model parameters) has been constructed according to a constant (vs altitude) variability of 10 % and a Gaussian correlation between the layers with a 3 km correlation length.

The largest contributions to the model parameters random error are due to the temperature, the interfering species and the ILS uncertainties. The model parameters giving rise to a systematic error are the spectroscopic parameters: the line intensities and the pressure broadening coefficients of the absorption lines present in our micro-windows.

Table 2 summarizes, for the total columns of each species, the smoothing error, the total random and the total systematic error budget. The dominant contribution to the random error is, for each species, the random noise, except for methanol for which the temperature error contribution is the largest. We give also in Table 2 the mean of the standard deviations of each daily means for the days when the number of measurements were equal or greater than three. As we do not expect our target species total columns to vary much during the day, these standard deviation values give an estimation of the random error made on an individual total column retrieval. Indeed, the standard deviations are in good agreement with the total random errors given in the table.

### 3 FTIR time-series: seasonality and interannual variability

The time-series of the FTIR daily means total columns of HCN, C<sub>2</sub>H<sub>6</sub>, C<sub>2</sub>H<sub>2</sub>, CH<sub>3</sub>OH, and HCOOH are shown in Fig. 4 (blue circles). In addition, we show the CO time-series, also measured with our FTIR spectrometer at Reunion Island (see Dufлот et al. (2010) for details on the CO retrievals), because we discuss the correlation between CO and the five target species in the next section. The number of measurements within a day varies from 1 to 20, but with a median value of only 2. The smoothing error is not included in the error bars shown in Fig. 4 since we will discuss in Sect. 5 the comparisons with the model data that have been smoothed by the FTIR averaging kernels.

First, we observe maximum total column amounts in October for all species, as we already found for CO (Dufлот et al., 2010), and as was observed also for ozone from radiosoundings (Randriambelo et al., 2000) at Reunion Island. It has been estimated that the biomass burning emission peak occurs in September in the Southern Hemisphere as a whole (Duncan et al., 2003). This is illustrated in Fig. 5 (top panel), where we show the CO emissions from the Global Fire Emission Database GFED2 and GFED3 for the whole Southern Hemisphere. However, there are important seasonal differences between different regions, depending on the timing of the dry season (Cooke et al., 1996). While the peak occurs generally in September in Southern Africa, the east coast (Mozambique) shows strong emissions also in October and to a lesser extent in November (Duncan et al., 2003). At Madagascar, the peak of the biomass burning emissions occurs in October (Cooke et al., 1996; Randriambelo et al., 1998). The latter two studies noted a peak fire displacement from the west coast of Madagascar in August (savanna), to the east coast in October (rain forest). The strong emissions in the eastern part of Southern Africa and Madagascar explain the peak in October observed for the species with a short lifetime (6 and 4 days for methanol and formic acid, respectively), while for the long-lived species HCN and C<sub>2</sub>H<sub>6</sub> (5 and 2 months lifetime, respectively), the accumulation due to the September peak in South America (Duncan et al., 2003) and global Southern Africa also plays a role.

Concerning the interannual variability, the annual carbon emission estimates over 1997–2009 (Table 7 of van der Werf et al., 2010) show a high variability in South America ( $1-\sigma$  standard deviation of 51 %), and a low variability in Southern Africa ( $1-\sigma = 10\%$ ). The interannual variability of CO emissions in the Southern Hemisphere, shown in Fig. 5 (top panel), is therefore mainly due to the South American tropical forest fires. The low variability of Southern Africa emissions is illustrated in Fig. 5 (middle panel). Table 7 of van der Werf et al. (2010), updated for the year 2010<sup>2</sup>, shows annual

carbon emissions that are 9 % and 3 % above the 1997–2010 mean values for South America and Southern Africa, respectively, in 2004; and 91 % above and 5 % below, respectively, in 2007. In 2009, they are 70 % and 3 % below the 1997–2010 mean values for South America and Southern Africa, respectively; and in 2010, 125 % and 10 % above, respectively. It has been shown that biomass burning from South America yields an important contribution to the CO columns above Reunion Island in 2007, especially in September and October (Fig. 15 of Dufлот et al., 2010). Since ethane has a similar lifetime as CO, and HCN an even longer one, one expects to observe larger values of the two species amounts in September and October 2007 compared to 2004 and 2009. This is indeed the case, as can be observed in Fig. 4: larger values are obtained in October 2007 compared to October 2004, and in September 2007 compared to September 2009. The lack of data in October 2009 does not allow conclusion for this month. Larger values are observed in December 2010 compared to December 2009 for these two species. We can therefore conclude that the interannual variability of biomass burning emissions in the Southern Hemisphere is well observed at Reunion Island in the C<sub>2</sub>H<sub>6</sub> and HCN total column amounts. However, if an interannual variability is indeed observed, its amplitude is well below the variability observed in the fire emission estimates in South America, suggesting that the influence of South American fires is present but is diluted at Reunion Island, possibly partly hidden by higher contributions from nearer fires.

On the contrary, we do not observe significant interannual differences for methanol and formic acid. Although biomass burning emissions are only a small source of methanol and formic acid, even in the Southern Hemisphere, when annual means are concerned (Sect. 5.1.2), they represent a significant contribution in the August–October period. To illustrate this, the model simulations obtained when the biomass burning contribution is removed is plotted for the two species in Fig. 4 (black solid line when removed from the standard run; red solid line from the optimized run using IASI data in 2009). Due to the short lifetime of these two species, biomass burning emissions in South America have little influence on the total columns above Reunion Island. The low interannual variability observed in the FTIR total columns during this period therefore reflects the low variability of the biogenic and photochemical contributions to the total budget of these compounds (see Sect. 5.1.2) and the weak variability of biomass burning emissions in Southern Africa ( $1-\sigma = 10\%$  as seen above). However, these two species are highly sensitive to specific biomass burning events as shown by the presence of many outliers in their time-series, especially in October. To confirm that these extreme values are indeed related to biomass burning events, we show the correlation between the total columns of our target species and CO in the next section.

<sup>2</sup>at [http://www.falw.vu/~gwerf/GFED/GFED3/tables/emis.C\\_absolute.txt](http://www.falw.vu/~gwerf/GFED/GFED3/tables/emis.C_absolute.txt)

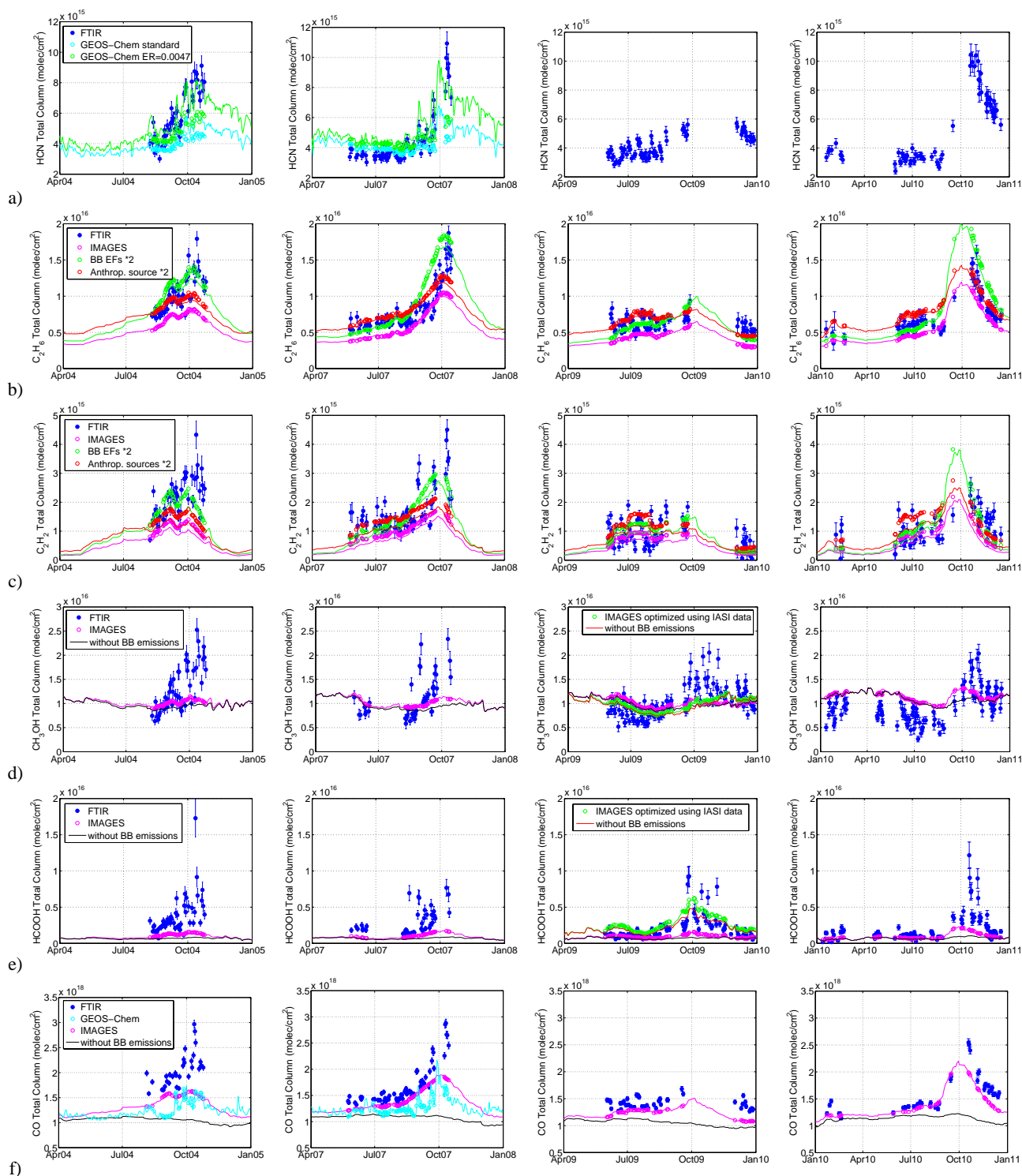


**Fig. 4.** Time-series of daily mean total columns at Reunion Island from: FTIR and GEOS-Chem HCN (a), FTIR and IMAGES  $C_2H_6$  (b),  $C_2H_2$  (c),  $CH_3OH$  (d), and HCOOH (e). We also show the time-series of CO from Duflot et al. (2010), extended to 2009 and 2010 (f). From left to right, the columns cover the years 2004, 2007, 2009, and 2010. The FTIR data are represented by the blue filled circles, different model simulations with the coloured lines (cyan and magenta for the standard runs of GEOS-Chem and IMAGES, respectively; green and red for the sensitivity tests: see Sect. 5), and the model data smoothed with the FTIR averaging kernels with the open circles. For  $CH_3OH$  and HCOOH, the model simulations obtained when the biomass burning contribution is removed are shown in black for the standard run, and in red for the inversion using IASI data. (BB: biomass burning; ER: emission ratio; EF: emission factor; Anthrop.: anthropogenic).

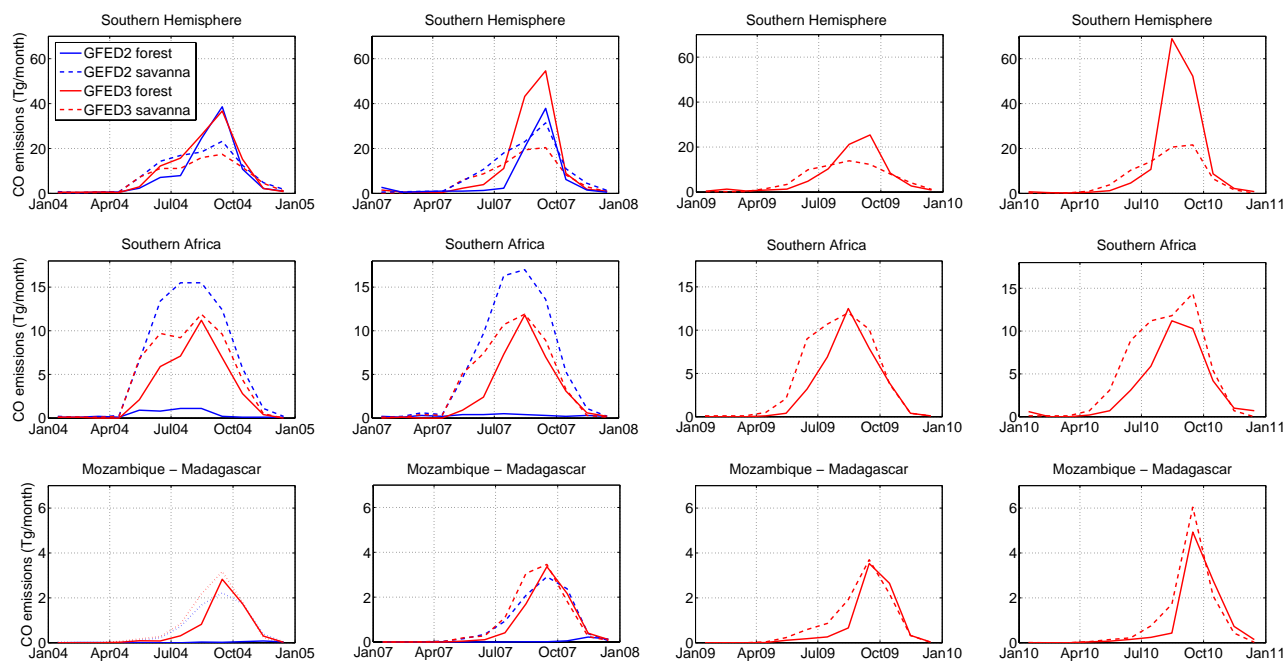


**Fig. 5.** CO emissions ( $\text{Tg month}^{-1}$ ) from the GFED2 (in blue) and GFED3 (in red) inventories, for the southern Hemisphere (top panel), Southern Africa (middle panel), and the region of Mozambique and Madagascar (bottom panel). The contribution from forests (solid lines) and savannas (dashed lines) are distinguished.

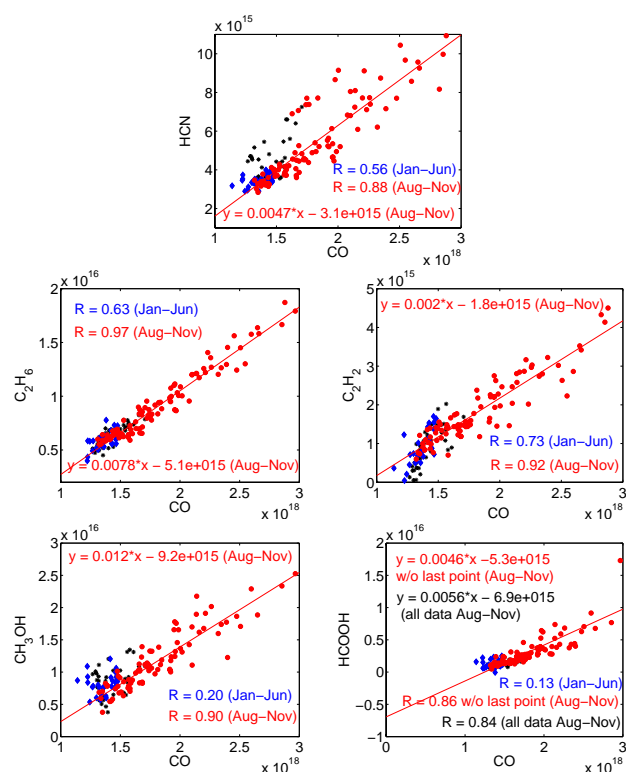
#### 4 Correlation with CO and enhancement ratios

Figure 6 shows the correlation plots between the daily mean total columns of each of the five species discussed in this paper and those of CO (Duflo et al., 2010). We see from Fig. 6 that the correlation is very good ( $R \geq 0.86$ ) for all species during the biomass burning period observed in Reunion Island (August–November, see previous section). This result indicates that CO and the five species share a common emission source, most probably biomass burning, which is responsible for most of their observed variability at Reunion Island during this period. Although the oxidation of methane and other organic compounds is a large source of CO, especially in the Tropics, its variability is low in comparison with vegetation fires, as reflected by the high correlation between CO and compounds such as HCN,  $\text{C}_2\text{H}_6$  and  $\text{C}_2\text{H}_2$ , which are not produced photochemically in the atmosphere. Similarly, the biogenic source and the photochemical production of  $\text{CH}_3\text{OH}$  and  $\text{HCOOH}$  are unlikely to contribute significantly to the high correlation with CO.

The vertical columns sampled at Reunion Island represent a mix of airmasses with different ages since the time of emission. The highest columns are due to a predominance of fresh emissions in the sampled airmasses, and therefore to backward trajectories which were most often in the direct vicinity of emission regions in the previous days. Lower column values are more influenced by older emissions which might therefore originate in more distant areas. Distant fires (from

e.g., South America) clearly cannot cause significant enhancements in  $\text{CH}_3\text{OH}$  and  $\text{HCOOH}$  (due to their short lifetimes). Their good correlation with CO confirms that those distant fires have a probably smaller impact on the variability of CO and other long-lived compounds than the nearby fires in Southern Africa and Madagascar. From backward trajectory simulations using FLEXPART, Duflo et al. (2010) concluded that the biomass burning emission contribution to the CO columns at Reunion Island from South America dominates the contribution of the Africa-Madagascar region in September–October 2007 (their Fig. 15). Our findings suggest however that, as far as short-term variability is concerned, Southern Africa and Madagascar fires have a major contribution at Reunion Island. This does not exclude a contribution of South American fires to the background levels of the long-lived pyrogenic compounds in the Southern Hemisphere, including Reunion Island, as suggested by the observed interannual variability of HCN and  $\text{C}_2\text{H}_6$  (Sect. 3). It is noteworthy that there are large uncertainties residing in backward trajectory calculations, and also that the biomass burning emission inventory used in Duflo et al. (2010) (GFED2) could underestimate the emissions in the vicinity of Reunion Island (Southeastern Africa-Madagascar). Section 5 seems to confirm this conclusion.

We also evaluated the slope  $\Delta X/\Delta \text{CO}$  for the measurements obtained during the August–November period for each species X. If we assume that, during this period, the excess total columns of X and CO are due to the biomass burning



**Fig. 6.** Correlation plots of daily mean total columns of the five retrieved species versus CO (molec cm<sup>-2</sup>). The correlation coefficient ( $R$ ) is given for the periods from January to June (blue), and from August to November (red). For the latter period, the slope ( $\Delta X/\Delta CO$ ) and the intercept from a linear least-squares fit of the data are also given.

events, then following Hornbrook et al. (2011) these slopes represent the “normalized excess mixing ratios” (also called the “enhancement ratios” as the plumes are far from the emission sources, as opposed to the emission ratios at the source, as defined in Andreae and Merlet, 2001). Given the relatively low reactivity and therefore long lifetimes of the species (from 5 months for HCN to 4 days for HCOOH), our “enhancement ratios” can be compared to the emission ratios (ER) obtained in previous studies. Indeed, from aircraft measurements of biomass burning plumes ranging from recent emissions to plumes aged of about one week, very little difference was observed between the emission ratio obtained at the source region and the enhancement ratios measured in plumes aged for methanol (Hornbrook et al., 2011). Also, the enhancement ratios of all our species measured by ACE-FTS in plumes aged of 5–6 days are very similar (and equal within the given standard deviations) to those obtained in plumes aged of 1–2 days (Table 2 in Tereszchuk et al., 2011).

Therefore, we compare in Table 3, the enhancement ratios obtained from our measurements between August and November, to emission ratios obtained from aircraft measurements of savanna fires in Southern Africa (Sinha et al.,

2003), and to emission ratios derived from the latest compilation of emission factors (EF) by Akagi et al. (2011), for savanna and tropical forest. Following Andreae and Merlet (2001), we derive the “Akagi ER” from the equation:

$$ER\left(\frac{X}{CO}\right) = \frac{EF_X}{EF_{CO}} \frac{MW_{CO}}{MW_X},$$

where  $MW_X$  and  $MW_{CO}$  are the molecular weights of the species  $X$  and the reference species CO in our case.

For the two long-lived species HCN and C<sub>2</sub>H<sub>6</sub>, our FTIR-derived enhancement ratios agree well with the compilation of Akagi et al. (2011), especially when the tropical forest values are considered. This could evidence for an influence of tropical forest fire emissions in South America to the observed concentrations of these long-lived species. But as noted previously and illustrated in Fig. 5 (bottom panel), the eastern part of Madagascar is also dominated by tropical forest, and woodland fires are also widespread in Mozambique/Zambia/Tanzania according to the GFED3 inventory (van der Werf et al., 2010). Moreover, the uncertainties on the emission factors given in Akagi et al. (2011) are quite large (40–60 % for HCN and C<sub>2</sub>H<sub>6</sub>), so this very good agreement should be interpreted with caution. For HCN, our enhancement ratio agrees very well with the value of  $0.0047 \pm 0.0005$  obtained by Rinsland et al. (2002), using the same FTIR technique for the period July–September, at Lauder, New Zealand (45° S, 170° E). In the case of long-lived tracers, the emission ratios derived from the dry season measurements at Reunion Island reflect a mix of different vegetation types in the Southern Hemisphere, with however a strong influence of nearby regions (Madagascar and South-eastern Africa) as suggested by the good correlation between CH<sub>3</sub>OH and HCOOH with CO. This kind of mixed emission (enhancement) ratios can be useful for models which do not include individual emission factors for different vegetation/fire types. This has been used in Sect. 5.2.1 when we compare FTIR HCN time-series with GEOS-Chem: replacing the HCN/CO ratio with our 0.0047 value significantly improved the agreement between data and model.

The enhancement ratio obtained for C<sub>2</sub>H<sub>2</sub> ( $0.0020 \pm 0.0001$ ) does not agree with Sinha et al. (2003) nor with Akagi et al. (2011), but considering the 41 % and 80 % uncertainties in the emission factors given in Akagi et al. (2011) for savanna and tropical forest, respectively, we are still in the expected range of values. Indeed, one of the references used by Akagi et al. (2011) in the evaluation of the average emission factor for the tropical forest is the work of Ferek et al. (1998), who obtain a value of  $0.0024 (\pm 0.0004)$  from 19 airborne measurements in Brazil. Also Paton-Walsh et al. (2010) obtain an emission ratio of  $0.0024 (\pm 0.0003)$ , from FTIR measurements of Australian savanna fire products, thus from a different vegetation type than Ferek et al. (1998). On the other hand, we obtain different values than Paton-Walsh et al. (2010) for HCN and C<sub>2</sub>H<sub>6</sub>.

**Table 3.** Enhancement ratios with respect to CO from this work. Also listed for comparison, the emission ratios with respect to CO from aircraft measurements over savanna fires in Southern Africa (Sinha et al., 2003), and derived from emission factors given in Akagi et al. (2011) (see text for details). The approximate tropospheric global lifetimes of each species are also given. The lifetime of CO is about 2 months (Xiao et al., 2007).

| Species                       | Global lifetime | This work       | Akagi et al. (2011)<br>Tropical forest | Akagi et al. (2011)<br>Savanna | Sinha et al. (2003)<br>Savanna Southern Africa |
|-------------------------------|-----------------|-----------------|--|--------------------------------|--|
| HCN                           | 5 months        | 0.0047 ± 0.0003 | 0.0047                                 | 0.0067                         | 0.0085 ± 0.0029                                |
| C <sub>2</sub> H <sub>6</sub> | 2 months        | 0.0078 ± 0.0002 | 0.0071                                 | 0.0098                         | 0.0026 ± 0.0002                                |
| C <sub>2</sub> H <sub>2</sub> | 2 weeks         | 0.0020 ± 0.0001 | 0.0051                                 | 0.0041                         | 0.0043 ± 0.0013                                |
| CH <sub>3</sub> OH            | 6 days          | 0.0116 ± 0.0006 | 0.0229                                 | 0.0164                         | 0.015 ± 0.003                                  |
| HCOOH                         | 4 days          | 0.0046 ± 0.0003 | 0.0052                                 | 0.0020                         | 0.0059 ± 0.0022                                |

We see that the agreement is very good between our work and the measurements of savanna fires in Southern Africa (Sinha et al., 2003) for the two species with a shorter lifetime, formic acid and methanol. The agreement is also reasonable with the values of Akagi et al. (2011). Note that the HCOOH outlier at about  $17 \times 10^{15}$  molec cm<sup>-2</sup> (Fig. 6) has been removed in the derivation of the enhancement ratio given in Table 3. This measurement is clearly seen in Fig. 4 in 2004 and corresponds to a day (12 October) where very high values are also observed in other species (C<sub>2</sub>H<sub>6</sub>, C<sub>2</sub>H<sub>2</sub>, HCHO in Vigouroux et al., 2009). The reason why this point is an outlier in the correlation plot, in contrast with the corresponding measurements for C<sub>2</sub>H<sub>6</sub> and C<sub>2</sub>H<sub>2</sub> is not clear at present, and may originate from the type of fire on that specific day. Trajectory calculations could possibly help to determine the origin of the air mass and possibly the fire type responsible for the observed enhancement.

However, the comparisons given in Table 3 and discussed above are only indicative, because we use all the measurements within the August–November period to derive the correlation plots, without making any distinction according to the origin of the different air masses, i.e. forest or savanna. When the whole Southern Hemisphere is concerned, we see from Fig. 5 (top panel) that the peak of the emissions is dominated by the forest source. When considering Southern African emissions, we see an important difference between GFED2 and GFED3: the former includes almost no emission from the forest source, while for the latter the forest source is about as high as the savanna source (Fig. 5, middle and bottom panels). Trusting the GFED3 inventory, it is not possible to know, without precise quantitative backward trajectories, if our FTIR measurements are representative of forest or savanna emissions. Such backward trajectories analysis is beyond the scope of the paper. More insights will be obtained after additional years of measurements, in order to improve the statistics and to make a more quantitative study.

## 5 Comparisons with chemical transport models

### 5.1 Models description

#### 5.1.1 HCN simulated in GEOS-Chem

GEOS-Chem (<http://www.geos-chem.org/>) is a global 3-D chemical transport model driven by assimilated meteorological fields from the Goddard Earth Observing System (GEOS-5) of the NASA Global Modeling and Assimilation Office. The HCN simulation in GEOS-Chem was first described by Li et al. (2003). We use version v8-02-01 of the model, with updates to the HCN simulation based on Li et al. (2009). We employ the meteorological fields at a horizontal resolution of  $2 \times 2.5$  degrees, degraded from their native resolution of  $0.5 \times 0.67$  degrees. The model has 47 vertical layers ranging from the surface to 0.01 hPa. Biomass burning emissions, the primary source of HCN, are specified based on monthly mean biomass burning emissions of CO from the Global Fire Emission Database v2 (GFED2), with an assumed HCN/CO emission scale factor of 0.27% (Li et al., 2003). Monthly mean biofuel emissions of HCN are based on CO emissions from Streets et al. (2003), following Li et al. (2009), with an HCN/CO emission scale factor of 1.6% (Li et al., 2003). The global annual source of HCN simulated in the model between 2001 and 2008 varied between 0.56 and 0.77 Tg N yr<sup>-1</sup> (Li et al., 2009). The main sink of HCN is ocean uptake, which is estimated at 0.73 Tg N yr<sup>-1</sup> (Li et al., 2003). Loss of HCN through reaction with OH in the atmosphere is captured using specified OH fields from a full-chemistry simulation of the model (Li et al., 2009). To remove the influence of the initial conditions on the HCN fields presented here, we spun up the model for two years, between 2002–2003, using an earlier version of the meteorological fields, GEOS-4, that were available for that period.

#### 5.1.2 Organic compounds simulated in IMAGESv2

The IMAGESv2 global chemistry transport model is run at a horizontal resolution of  $2 \times 2.5$  degrees and is discretized vertically in 40 levels from the surface to the lower

stratosphere. A detailed description of the model can be found in Müller and Brasseur (1995); Müller and Stavroukou (2005); Stavroukou et al. (2009). Here we describe the atmospheric budget of  $C_2H_6$ ,  $C_2H_2$ ,  $CH_3OH$  and  $HCOOH$  as simulated by IMAGESv2.

Fossil fuel and biofuel NMVOC emissions are obtained from the RETRO database (Schultz et al., 2008) for the year 2000 and are overwritten by the REAS inventory over Asia (Ohara et al., 2007) for each corresponding year of simulation. Vegetation fire emissions are obtained from the GFED3 inventory (van der Werf et al., 2010), through application of updated (in 2007) emission factors (Andreae and Merlet, 2001). The large-scale fire emissions are distributed over six layers from the surface to 6 km according to Dentener et al. (2006). Isoprene emissions are obtained from the MEGAN-ECMWF inventory (Müller et al., 2008) and amount to 416, 423, 424 and 437 Tg annually on the global scale, in 2004, 2007, 2009, and 2010, respectively. Meteorological fields are obtained from ECMWF ERA-Interim analyses.

About 70% of the global source of  $C_2H_2$  and  $C_2H_6$ , estimated at about 5 and 10 Tgyr<sup>-1</sup>, respectively, is due to anthropogenic activities, the remainder to biomass burning events. The emission factors for tropical forest, extratropical forest and savanna burning emissions are 0.402, 0.260 and 0.269 g of  $C_2H_2$  per kg of dry matter, and 1.202, 0.733, and 0.325 g of  $C_2H_6$  per kg of dry matter, respectively. Both gases are removed from the troposphere through oxidation by OH. In the case of ethane, a small fraction of about 5% is removed through reaction with chlorine radicals in the lower stratosphere. The global lifetime is calculated at about 2 weeks for  $C_2H_2$  and 2 months for  $C_2H_6$ . The impact of changing their biomass burning or anthropogenic emission sources is investigated through sensitivity studies (see Sect. 5.2.2).

Both methanol and formic acid have direct emissions from anthropogenic activities, fires and vegetation, as well as a secondary production source. The methanol source, in the standard simulation with the IMAGESv2 model, is estimated at about 200 Tgyr<sup>-1</sup> globally, and is mostly due to the terrestrial vegetation (54%), oceans (22%), and photochemistry (16%) (Millet et al., 2008; Stavroukou et al., 2011). The global source of formic acid in the standard run amounts to 36 Tgyr<sup>-1</sup>, of which two thirds is due to secondary production (Paulot et al., 2011; Stavroukou et al., 2012). The emission factors for tropical forest, extratropical forest and savanna burning per kg of dry matter are, respectively, 1.984, 1.798, and 1.47 g of  $CH_3OH$ , and 1.13, 2.43 and 0.63 g of  $HCOOH$ . Methanol emitted from vegetation is obtained from the MEGANv2.1 emission model (Stavroukou et al., 2011, [http://accent.aero.jussieu.fr/database\\_table\\_inventories.php](http://accent.aero.jussieu.fr/database_table_inventories.php)), and direct emissions of formic acid from plant leaves are taken from Lathièrre et al. (2006). Methanol and formic acid are removed through OH oxidation, and wet and dry deposition, and their global lifetimes are estimated as about 6 and 4 days, respectively.

**Table 4.** Sources of  $C_2H_6$ ,  $C_2H_2$ ,  $CH_3OH$  and  $HCOOH$  in the Southern Hemisphere in Tg yr<sup>-1</sup>, as implemented in the standard simulation of the IMAGES model, for the different categories (Categ.): anthropogenic (Anthr.), biomass burning (BB), biogenic (Biog.), and photochemical (Phot.). The Southern Hemispheric emission ratios (ER), from IMAGESv2, of the species relative to CO are also given in mole/mole.

| Species  | Categ. | 2004 | 2007 | 2009 | 2010 | ER     |
|----------|--------|------|------|------|------|--------|
| $C_2H_6$ | Anthr. | 1.48 | 1.49 | 1.50 | 1.50 |        |
|          | BB     | 1.67 | 1.94 | 1.15 | 2.21 | 0.0085 |
| $C_2H_2$ | Anthr. | 0.48 | 0.48 | 0.49 | 0.49 |        |
|          | BB     | 0.77 | 0.86 | 0.55 | 0.95 | 0.0043 |
|          | Anthr. | 2.8  | 2.8  | 2.8  | 2.8  |        |
| $CH_3OH$ | BB     | 4.0  | 4.44 | 2.91 | 4.86 | 0.018  |
|          | Biog.  | 66.3 | 65.9 | 66.2 | 67.8 |        |
|          | Phot.  | 14.9 | 15.0 | 15.3 | 14.0 |        |
|          | Anthr. | 2.59 | 2.59 | 2.59 | 2.59 |        |
| $HCOOH$  | BB     | 2.00 | 2.26 | 1.45 | 2.49 | 0.0065 |
|          | Phot.  | 12.8 | 13.0 | 12.6 | 11.9 |        |

Two source inversion studies of  $CH_3OH$  and  $HCOOH$  emissions have been performed based on the IMAGESv2 model constrained by one complete year of satellite column measurements retrieved from the IASI sounder in 2009 (Razavi et al., 2011; Stavroukou et al., 2011, 2012). The global optimized methanol source totals 187 Tg yr<sup>-1</sup>, close to the a priori, but large decreases in the biogenic sources were inferred over tropical forests of South America and Indonesia. Both biogenic and pyrogenic emissions were decreased by the inversion over Central and Southern Africa compared to the a priori inventories. Regarding  $HCOOH$ , a strong increase is deduced from the inversion using IASI  $HCOOH$  column data. It is found that 100–120 Tg of formic acid is produced annually, i.e. two to three times more than estimated from known sources (Stavroukou et al., 2012). The source increase is attributed to biogenic sources, either due to direct emission or to the oxidation of biogenic volatile organic compounds. The biomass burning source inferred from the inversion remains close to the a priori. The results were validated by extensive comparisons with (mostly ground-based)  $HCOOH$  concentration measurements. The modeled columns at Reunion Island before and after source inversion are presented in Sect. 5.2.3.

The Southern Hemispheric emissions of the discussed compounds in the different years are given in Table 4. Regarding biomass burning, the average emission ratios of these species with respect to CO in the Southern Hemisphere are also given in the table.

## 5.2 Comparisons of modeled and observed FTIR columns

We show comparisons between FTIR total columns and model total columns *c*. Since the FTIR total column

averaging kernels  $\mathbf{a}$  (Fig. 3) are not ideal ( $= 1$  at all altitudes), we degrade the model vertical profile to the FTIR vertical resolution, in order to obtain the model “smoothed” total column  $c_{\text{smoothed}}$ , which represents what the FTIR would measure if the model profile was the true state. We follow Eq. (25) of Rodgers and Connor (2003):

$$c_{\text{smoothed}} = c_a + \mathbf{a}(\mathbf{pc}_{\text{model}} - \mathbf{pc}_a), \quad (1)$$

$\mathbf{pc}_{\text{model}}$  and  $\mathbf{pc}_a$ , being respectively the model and the FTIR a priori vertical profiles expressed in partial columns ( $\text{molec cm}^{-2}$ ) and  $c_a$  the FTIR a priori total column.

### 5.2.1 Hydrogen cyanide (HCN)

We show in Fig. 4 the FTIR time-series of HCN daily mean total columns measured at Reunion Island, together with, for the years 2004 and 2007, the GEOS-Chem HCN total columns, before and after the smoothing with the FTIR total column averaging kernel (Eq. 1). We do not show, for HCN, the model results for the years 2009 and 2010, because the fire database GFED3 (van der Werf et al., 2010) was not implemented in v8-02-01 of GEOS-Chem and the GFED2 currently used does not provide data after 2008. The standard GEOS-Chem run underestimates the HCN total columns at Reunion Island during September–October. As seen in Sect. 5.1.1, the standard model uses a global HCN/CO emission scale factor of 0.27 % for biomass burning emissions of HCN. As a sensitivity test, a simulation was conducted with a biomass burning emission ratio HCN/CO in the Southern Hemisphere equal to 0.47 %, i.e., the value derived from our FTIR measurements (see Sect. 4). The agreement between the model and the FTIR data is greatly improved, especially when comparing the model output before smoothing it by the FTIR averaging kernels.

The agreement between the model and FTIR data is supposed to be improved by the use of the FTIR averaging kernels, whereas the opposite behaviour is observed here. This can be understood by considering the shape of the HCN total column averaging kernel (Fig. 3), and the shape of the model profile simulated during the biomass burning season given in Fig. 7, which is very different from the FTIR a priori and retrieved profiles. The model profile shows a biomass burning enhancement peak at about 4 km, while the peak is located at 6–7 km in the FTIR data. Due to the low sensitivity of the FTIR retrieval to altitudes below 5 km (Fig. 3), the smoothed model profile in the biomass burning season is strongly reduced below 5 km, and therefore also the total column. However, in May–July, the smoothed model total columns are similar to the direct model total columns, in agreement with the profile shapes shown in Fig. 7. This implies that if an enhancement in HCN does occur below 5 km, our FTIR measurements would underestimate it. The FTIR a priori profile, taken from the model WACCMv5 (Sect. 2.2.2), peaks at a higher altitude, about 5–7 km.

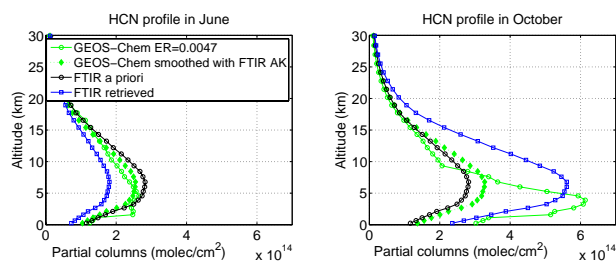


**Fig. 7.** Example of FTIR and GEOS-Chem HCN profiles (in Partial Columns,  $\text{molec cm}^{-2}$ ) in June and October.

The difference between the WACCM and GEOS-Chem models could reflect differences in the vertical transport in the models. Ott et al. (2009) compared the convective transport in a single column version of the GEOS-5 model with that of a cloud-resolving model and found that GEOS-5 underestimated the convective mass fluxes, which resulted in weaker vertical transport. Liu et al. (2010) showed that, in October 2004 and 2005, upward transport over Southern Africa was weaker in GEOS-5 than in the previous version of the GEOS model, GEOS-4. They also found that convective transport over South America was weaker in GEOS-5 than in GEOS-4 in October 2005.

However, based on the comparisons between the FTIR and the model “smoothed” total columns, the model still underestimates HCN in October, both in 2004 and 2007, suggesting an underestimation of the biomass burning emission inventory (GFED2 in GEOS-Chem) during these months. This seems to be confirmed by the same underestimation of CO from GEOS-Chem compared to FTIR data (Fig. 4, lower panel).

Table 5 provides mean differences between FTIR and model “smoothed” total columns,  $\text{mean}(\text{FTIR} - \text{model})/\text{mean}(\text{FTIR})$ , and standard deviations ( $\sigma$ ),  $\text{std}(\text{FTIR} - \text{model})/\text{mean}(\text{FTIR})$ , in percentage, for the different species and the different sensitivity tests, together with the correlation coefficients ( $R$ ). We see again that for HCN the agreement is significantly improved using a corrected HCN/CO emission ratio of 0.47 %, especially regarding the  $\sigma$  and  $R$  values. Despite the positive values of the annual mean differences seen in Table 5, the bias is negative outside the intense biomass burning period ( $-12 \pm 7\%$  and  $-22 \pm 7\%$  for the standard and sensitivity runs, respectively), and larger than the systematic error on the FTIR columns (14.5 %) for the sensitivity case, suggesting that the HCN emissions are overestimated in the model during the January–July 2007 period.

### 5.2.2 Ethane ( $\text{C}_2\text{H}_6$ ) and acetylene ( $\text{C}_2\text{H}_2$ )

The modeled time-series of  $\text{C}_2\text{H}_6$  and  $\text{C}_2\text{H}_2$  are compared with the FTIR measurements in Fig. 4. The interannual variability of the biomass burning emissions (from GFED3, see

**Table 5.** Relative (%) mean differences ( $D$ ) between FTIR and model total columns,  $\text{mean}(\text{FTIR-model})/\text{mean}(\text{FTIR})$ , and standard deviations ( $\sigma$ ),  $\text{std}(\text{FTIR-model})/\text{mean}(\text{FTIR})$  for the different species and the different sensitivity tests, together with the correlation coefficients  $R$ . The model total columns have been smoothed to the FTIR vertical resolution using Eq. (1).

|                                   | Annual         |      | Jan–Jul        |      | Aug–Nov        |      |
|-----------------------------------|----------------|------|----------------|------|----------------|------|
|                                   | $D \pm \sigma$ | $R$  | $D \pm \sigma$ | $R$  | $D \pm \sigma$ | $R$  |
| <b>HCN</b>                        |                |      |                |      |                |      |
| Standard                          | 20 ± 32        | 0.77 | −12 ± 7        | 0.20 | 27 ± 28        | 0.86 |
| ER = 0.0047                       | 7 ± 26         | 0.89 | −22 ± 7        | 0.19 | 12 ± 24        | 0.89 |
| <b>C<sub>2</sub>H<sub>6</sub></b> |                |      |                |      |                |      |
| Standard                          | 26 ± 20        | 0.85 | 28 ± 15        | 0.24 | 23 ± 21        | 0.80 |
| BB EF doubled                     | −12 ± 28       | 0.87 | 10 ± 15        | 0.34 | −23 ± 22       | 0.83 |
| Anthr. doubled                    | −4 ± 22        | 0.81 | −15 ± 16       | 0.19 | −1 ± 22        | 0.77 |
| <b>C<sub>2</sub>H<sub>2</sub></b> |                |      |                |      |                |      |
| Standard                          | 35 ± 45        | 0.62 | 23 ± 43        | 0.09 | 38 ± 40        | 0.48 |
| BB EF doubled                     | 0 ± 41         | 0.69 | −2 ± 44        | 0.18 | −1 ± 38        | 0.55 |
| Anthrop. doubled                  | 4 ± 50         | 0.46 | −29 ± 49       | 0.01 | 15 ± 43        | 0.31 |
| <b>CH<sub>3</sub>OH</b>           |                |      |                |      |                |      |
| Standard all years                | 0 ± 37         | 0.17 | −38 ± 23       | 0.30 | 15 ± 32        | 0.44 |
| Standard 2009                     | 1 ± 31         | 0.17 | −30 ± 20       | 0.38 | 17 ± 25        | 0.70 |
| Optimized 2009                    | 5 ± 26         | 0.55 | −15 ± 20       | 0.37 | 19 ± 23        | 0.64 |
| <b>HCOOH</b>                      |                |      |                |      |                |      |
| Standard all years                | 58 ± 79        | 0.64 | 30 ± 42        | 0.23 | 64 ± 66        | 0.51 |
| Standard 2009                     | 53 ± 79        | 0.61 | 20 ± 30        | 0.16 | 66 ± 63        | 0.57 |
| Optimized 2009                    | −34 ± 57       | 0.74 | −74 ± 46       | 0.10 | −18 ± 52       | 0.62 |

Table 4) is reflected by lower model columns of C<sub>2</sub>H<sub>6</sub> and C<sub>2</sub>H<sub>2</sub> in 2009, and higher columns in 2010.

Doubling the pyrogenic source, by doubling the C<sub>2</sub>H<sub>6</sub> and C<sub>2</sub>H<sub>2</sub> emission factors, is found to improve the overall agreement with FTIR data, as evidenced by the slightly higher correlation coefficient in this case (Table 5). But, the Southern Hemispheric emission ratio C<sub>2</sub>H<sub>6</sub>/CO in the standard IMAGESv2 model (0.0085, Table 4) is very close to the FTIR derived value (0.0078), and the C<sub>2</sub>H<sub>2</sub> emission ratio is already larger (0.0043) than the FTIR value (0.002), implying that the CO pyrogenic emissions are also underestimated in the GFED3 inventory used in IMAGESv2. This is confirmed by the CO comparisons between IMAGESv2 and FTIR (Fig. 4, bottom panel). Additional considerations confirm that the emission factors are not the cause of the disagreement. First, the standard deviation is higher with doubled emission factors for C<sub>2</sub>H<sub>6</sub>. This is well explained by examining the time-series of Fig. 4: while the peak in October is well reproduced for C<sub>2</sub>H<sub>6</sub> by this sensitivity run, the model overestimates the C<sub>2</sub>H<sub>6</sub> columns during August–mid-September, and again in November 2010. The strong underestimation in late September–October of the standard run is also observed in C<sub>2</sub>H<sub>2</sub> and CO. Since the lifetime of C<sub>2</sub>H<sub>2</sub> is only 12 days in the Tropics, this suggests that very high biomass burning emissions occurred around late September–October that are underestimated in the GFED3 inventory.

Finally, the simulation using doubled anthropogenic emissions of C<sub>2</sub>H<sub>6</sub> and C<sub>2</sub>H<sub>2</sub> overestimates the observations during the January–July period and leads to a weaker correlation with the data. However, if the underestimation of biomass burning emissions occurs indeed mainly in late September–October, Table 5 and Fig. 4 during January–July suggest an underestimation of anthropogenic emissions, even if it is well below the factor of two that has been simulated.

### 5.2.3 Methanol (CH<sub>3</sub>OH) and formic acid (HCOOH)

The modeled time-series of CH<sub>3</sub>OH and HCOOH are shown in Fig. 4. As expected by the lower contribution of biomass burning emissions compared to the biogenic and photochemical sources (Table 4), the interannual variability of methanol and formic acid is smaller than for C<sub>2</sub>H<sub>6</sub> and C<sub>2</sub>H<sub>2</sub>. But still, the modeled values in late September–October are higher (by about 30 % in the case of methanol) in 2010 than in 2009, reflecting the interannual variability of biomass burning emissions. The similar modeled values in 2004 and 2007 are explained by the fact that the more intense biomass burning season in 2007 occurred only in South America, with little impact on the relatively short-lived compounds considered here, while the 2010 year shows enhanced biomass burning emissions also in Southern Africa (van der Werf et al., 2010, and Sect. 3). In contrast to the model, the FTIR data show enhanced values in 2004, not only for C<sub>2</sub>H<sub>6</sub> and C<sub>2</sub>H<sub>2</sub>, but also for CH<sub>3</sub>OH and HCOOH. This leads to the conclusion that the underestimation of biomass burning emissions in September–October 2004, occurs more specifically in the Southeastern Africa–Madagascar region. As in the case of C<sub>2</sub>H<sub>2</sub> and C<sub>2</sub>H<sub>6</sub>, the underestimation of the modeled CH<sub>3</sub>OH and HCOOH during the fire season can not be due to the emission factors used in the model, since the ratios CH<sub>3</sub>OH/CO and HCOOH/CO have slightly larger values in IMAGESv2 (0.018 and 0.0065, respectively) than in the FTIR observations (0.012 and 0.0056, respectively). From Fig. 4, we see that the standard model IMAGESv2 simulates better the CH<sub>3</sub>OH and HCOOH columns in October 2010 compared to 2009, as a consequence of the higher emissions in 2010 in Southern Africa and Madagascar. The fact that the observed CH<sub>3</sub>OH and HCOOH columns were roughly as high in 2009 as in 2010 suggests that the biomass burning emissions in Southern Africa–Madagascar should be comparable for both years, if indeed biomass burning is responsible for the high columns observed for these two species during the dry season. The possible underestimation of GFED3 emissions in 2009 could unfortunately not be confirmed by comparisons with the other species, because of the lack of FTIR measurements during that period in the required spectral ranges.

The standard model overestimates the observed CH<sub>3</sub>OH columns during the January–July period by about 40 %. The optimization of methanol sources using IASI data over the continents inferred a reduction of biogenic emissions

(Stavrakou et al., 2011), leading to some improvement in the modeled seasonal cycle in comparison with FTIR data in 2009, with a reduction of the negative bias observed in the January–July period (Table 5). Still, the IASI-derived emissions appear too low during the fire season. Monthly means comparisons between IASI at Reunion Island and our FTIR data are shown in Fig. 11 of Stavrakou et al. (2011). Considering the large error bars of IASI, the datasets are in agreement, but the amplitude of the seasonal cycle in IASI is lower than in the FTIR data, and the value for October is 15–20 % lower in IASI. The model overestimation between January and July/August is stronger in 2010 than in 2007 and 2009, for unknown reasons. It could be due to an overestimation of biogenic sources, but also possibly to a misrepresentation of the ocean–atmosphere exchanges in the model. The magnitude and even the sign of this exchange is determined by methanol concentrations in ocean water which are not well constrained. This ocean–atmosphere exchange could not be constrained by the inversion using IASI data, because oceanic IASI data were excluded from the inversion, due to large uncertainties (low signal-to-noise ratio, low thermal contrast). Note however that the overestimation of CH<sub>3</sub>OH concentrations by the model in the January–July period is at odds with comparisons of IMAGESv2 with aircraft data in the South Tropical Pacific in March–April 1999 (PEM-Tropics-B campaign, Stavrakou et al., 2011), which suggested the existence of a significant ocean source at these latitudes.

Concerning formic acid, underestimated pyrogenic and biogenic emissions in the model are likely responsible for the general model underestimation of the FTIR columns. As shown in Fig. 4, the use of continental 2009 IASI column data to constrain the model in a source inversion scheme using IMAGESv2 (Stavrakou et al., 2012) brings the simulated columns closer to the FTIR data during the dry season and increases the correlation (Table 5). This column enhancement is realized primarily through the introduction of a large source due to the photochemical degradation of biogenic NMVOCs. The inversion also increases the biomass burning source in Southeastern Africa, but this appears to have little influence on the simulated HCOOH columns at Reunion Island (Fig. 4: the red solid line shows the inversion results without the biomass burning source). The fact that biomass burning plays only a minor role in the inversion is a consequence of the dominance of biogenic/photochemical sources over the continental Tropics. The inversion is driven by elevated IASI HCOOH columns over widespread areas in Southern Africa, in regions (e.g., Congo/Angola, see Fig. (S2) in Stavrakou et al., 2012) where biomass burning emissions are small in September and October.

During the January–July period, however, the inversion leads to a significant overestimation of HCOOH columns, for reasons yet unclear. It appears possible that the model overestimates the transport, or underestimates the sink of HCOOH from biogenic emission areas to Reunion Island. Model

transport is especially sensitive to fire injection heights, boundary layer mixing, deep convection and horizontal advection, which all have significant (but difficult to quantify) uncertainties. It is worth noting that models have in particular difficulties in reproducing the HCOOH vertical profiles in the upper troposphere, where the modeled mixing ratios are often overestimated (Paulot et al., 2011; Stavrakou et al., 2012), with possibly important consequences for long-range transport, since horizontal winds are usually stronger at those higher altitudes. These issues require further investigation.

Note that the apparent model underestimation of the role of biomass burning as the main driver for HCOOH and CH<sub>3</sub>OH variability at Reunion Island does not imply that the global impact of biomass burning on the budget of those species is underestimated by the model. In fact, the enhancement ratios obtained within this study confirm previous estimations and lead to global pyrogenic emission estimates of the order of 5 Tg CH<sub>3</sub>OH and 3 Tg HCOOH yr<sup>-1</sup>, to be compared with total source estimates exceeding 100 Tg yr<sup>-1</sup> for both compounds.

Finally, Paulot et al. (2011) has shown that a good agreement between the HCOOH columns modeled by GEOS-Chem and the FTIR measurements at Reunion Island can be obtained by assuming that the oxidation of organic aerosol generates a diffuse source of formic acid associated with aerosol aging. Since organic aerosols come primarily from biomass burning in the South Hemisphere, this study confirms our finding, based on our very good correlation between HCOOH and CO, that biomass burning is a dominant source of HCOOH at Reunion Island during the August–November period.

## 6 Conclusions

We have performed FTIR measurements and retrieval analyses of five important biomass burning products (HCN, C<sub>2</sub>H<sub>6</sub>, C<sub>2</sub>H<sub>2</sub>, CH<sub>3</sub>OH, and HCOOH) at Reunion Island. The time-series obtained during three measurement campaigns allow the determination of both the seasonality and interannual variability of each species. The influence of biomass burning in the total columns of the target species is clearly observed and, in particular, the correlation with the CO FTIR total columns is very high ( $R \geq 0.86$ ) during the peak of the biomass burning season (August–November). From the correlation plots of the target species versus CO, we have derived enhancement ratios, which are in agreement with previous values reported in the literature: we obtain 0.0047, 0.0078, 0.0020, 0.012, and 0.0046 for HCN, C<sub>2</sub>H<sub>6</sub>, C<sub>2</sub>H<sub>2</sub>, CH<sub>3</sub>OH, and HCOOH, respectively.

The HCN ground-based data have been compared to the chemical transport model GEOS-Chem, while the other species have been compared to the IMAGESv2 model. We show that using our derived HCN/CO ratio of 0.0047, instead of the 0.0027 value used in the standard GEOS-Chem simulations, improves the agreement between GEOS-Chem and FTIR data. The comparisons between the FTIR HCN total columns and the total columns obtained when the model is “smoothed” with the FTIR averaging kernels suggest an underestimation of the biomass burning emissions in the inventory used in the model (GFED2) in October. This seems to be confirmed by the higher underestimation of CO from GEOS-Chem compared to FTIR during October. We have seen also that an underestimation could result from the lower altitude (4 km) of the peak of HCN simulated in GEOS-Chem compared to the one of the a priori profile used for the FTIR retrievals (6–7 km), which comes from the WACCMv5 model. It suggests that the altitude of the biomass burning outflow over Southern Africa may be too low in the GEOS-Chem model. This should be investigated in the future.

The comparisons between IMAGESv2 and FTIR for the long-lived species  $C_2H_6$  and  $C_2H_2$  lead to the conclusion that the biomass burning emission inventory (GFED3) is probably underestimated in the late September–October period for all years of measurements, and particularly in 2004. The comparisons with  $CH_3OH$  and  $HCOOH$ , having a lifetime of 6 and 4 days, respectively, show that the underestimation in late September–October 2004, occurs more specifically in the Southeastern Africa-Madagascar region. Note that this result confirms also the underestimation of GFED2 emissions, since the emissions in GFED2 are even lower than in GFED3, especially in this region (Fig. 5). The  $CH_3OH$  IASI-derived emissions remain too low during the fire season, suggesting that IASI may underestimate  $CH_3OH$  in this period in the Southeastern Africa-Madagascar region. The standard model overestimates the observed  $CH_3OH$  columns during the January–July period by about 40 %, and still by 15 % after the inversion using IASI data, possibly due to an overestimation of biogenic sources and/or a misrepresentation of the ocean-atmosphere exchanges in the model.

Although the IMAGESv2 optimization of  $HCOOH$  sources using IASI data greatly improves the agreement with FTIR data during the fire season, the model strongly overestimates  $HCOOH$  during the January–July period after inversion. However, this better agreement is achieved with only a minor contribution from biomass burning, the dominant one being the introduction of a large source due to the photochemical degradation of biogenic NMVOCs. This specific result at Reunion Island is not in agreement with our finding, based on our very good correlation between  $HCOOH$  and CO, that biomass burning is a dominant source of  $HCOOH$  and CO, at Reunion Island during the August–November period. However, our finding is consistent with the study of Paulot et al. (2011), who have shown that a good agreement between the  $HCOOH$  columns modeled by GEOS-Chem and the FTIR

measurements at Reunion Island can be achieved by assuming that organic aerosol oxidation generates a diffuse source of formic acid.

We have demonstrated that Reunion Island, close to Africa and Madagascar, is very well located to assess the ability of the chemical transport models to reproduce the biogenic and biomass burning emissions of various species and to evaluate model input parameters such as emission factors and biomass burning emission inventories.

*Acknowledgements.* This study has been supported by the ESA PRODEX project A3C, as well as the BIOSOA and AGACC-II projects within the “Science for a Sustainable Development” research program funded by the Belgian Science Policy Office. One of the co-authors (G. V.) was funded by the EU Integrated project GEOMON. Work at the University of Toronto was supported by the Natural Sciences and Engineering Research Council of Canada.

Edited by: G. Stiller

## References

- Akagi, S. K., Yokelson, R. J., Wiedinmyer, C., Alvarado, M. J., Reid, J. S., Karl, T., Crouse, J. D., and Wennberg, P. O.: Emission factors for open and domestic biomass burning for use in atmospheric models, *Atmos. Chem. Phys.*, 11, 4039–4072, doi:10.5194/acp-11-4039-2011, 2011.
- Andreae, M. O. and Merlet, P.: Emission of trace gases and aerosols from biomass burning, *Global Biogeochem. Cy.*, 15, 955–966, 2001.
- Coheur, P.-F., Clarisse, L., Turquety, S., Hurtmans, D., and Clerbaux, C.: IASI measurements of reactive trace species in biomass burning plumes, *Atmos. Chem. Phys.*, 9, 5655–5667, doi:10.5194/acp-9-5655-2009, 2009.
- Cooke, W. F., Koffi, B., and Grégoire, J. M.: Seasonality of vegetation fires in Africa from remote sensing data and application to a global chemistry model, *J. Geophys. Res.*, 101, 21051–21065, doi:10.1029/96JD01835, 1996.
- Crutzen, P. J. and Andreae, M. O.: Biomass burning in the tropics: impact on atmospheric chemistry and biogeochemical cycles, *Science*, 250, 1669–1678, 1990.
- Dentener, F., Kinne, S., Bond, T., Boucher, O., Cofala, J., Geroso, S., Ginoux, P., Gong, S., Hoelzemann, J. J., Ito, A., Marelli, L., Penner, J. E., Putaud, J.-P., Textor, C., Schulz, M., van der Werf, G. R., and Wilson, J.: Emissions of primary aerosol and precursor gases in the years 2000 and 1750 prescribed data-sets for AeroCom, *Atmos. Chem. Phys.*, 6, 4321–4344, doi:10.5194/acp-6-4321-2006, 2006.
- Duflot, V., Dils, B., Baray, J.-L., De Mazière, M., Attié, J.-L., Vanhaelewyn, G., Senten, C., Vigouroux, C., Clain, G., and Delmas, R.: Analysis of the origin of the distribution of CO in the subtropical Southern Indian Ocean in 2007, *J. Geophys. Res.*, 115, D22106, doi:10.1029/2010JD013994, 2010.
- Dufour, G., Boone, C. D., Rinsland, C. P., and Bernath, P. F.: First space-borne measurements of methanol inside aged southern tropical to mid-latitude biomass burning plumes using

- the ACE-FTS instrument, *Atmos. Chem. Phys.*, 6, 3463–3470, doi:10.5194/acp-6-3463-2006, 2006.
- Duncan, B. N., Martin, R. V., Staudt, A. C., Yevich, R., and Logan, J. A.: Interannual and seasonal variability of biomass burning emissions constrained by satellite observations, *J. Geophys. Res.*, 108, 4100, doi:10.1029/2002JD002378, 2003.
- Emmons, L. K., Hauglustaine, D. A., Müller, J.-F., Carroll, M. A., Brasseur, G. P., Brunner, D., Staehelin, J., Thouret, V., Marengo, A.: Data composites of airborne observations of tropospheric ozone and its precursors, *J. Geophys. Res.*, 105, 20497–20538, 2000.
- Ferek, R. J., Reid, J. S., Hobbs, P. V., Blake, D. R., and Liousse, C.: Emission factors of hydrocarbons, halocarbons, trace gases and particles from biomass burning in Brazil, *J. Geophys. Res.*, 103, 32107–32118, doi:10.1029/98JD00692, 1998.
- González Abad, G., Bernath, P. F., Boone, C. D., McLeod, S. D., Manney, G. L., and Toon, G. C.: Global distribution of upper tropospheric formic acid from the ACE-FTS, *Atmos. Chem. Phys.*, 9, 8039–8047, doi:10.5194/acp-9-8039-2009, 2009.
- Harrison, J. J., Allen, N. D. C., and Bernath, P. F.: Infrared absorption cross sections for ethane ( $C_2H_6$ ) in the  $3\ \mu m$  region, *J. Quant. Spectros. Radiat. Transfer*, 111, 357–363, 2010.
- Hase, F., Blumenstock, T., and Paton-Walsh, C.: Analysis of the instrumental line shape of high-resolution Fourier transform IR spectrometers with gas cell measurements and new retrieval software, *Appl. Opt.*, 38, 3417–3422, 1999.
- Hase, F., Demoulin, P., Sauval, A. J., Toon, G. C., Bernath, P. F., Goldman, A., Hannigan, J. W., and Rinsland, C. P.: An empirical line-by-line model for the infrared solar transmittance spectrum from 700 to  $5000\ cm^{-1}$ , *J. Quant. Spectros. Radiat. Transfer*, 102, 450–463, 2006.
- Hase, F., Wallace, L., McLeod, S. D., Harrison, J. J., and Bernath, P. F.: The ACE-FTS atlas of the infrared solar spectrum, *J. Quant. Spectros. Radiat. Transfer*, 111, 521–528, 2010.
- Hoell, J. M., Davis, D. D., Jacob, D. J., Rodgers, O., Newell, R. E., Fuelberg, H. E., McNeal, R. J., Raper, J. L., and Bendura, R. J.: Pacific Exploratory Mission in the Tropical Pacific: PEM-Tropics A, August–September 1996, *J. Geophys. Res.*, 104, 5567–5583, doi:10.1029/1998JD100074, 1999.
- Hornbrook, R. S., Blake, D. R., Diskin, G. S., Fried, A., Fuelberg, H. E., Meinardi, S., Mikoviny, T., Richter, D., Sachse, G. W., Vay, S. A., Walega, J., Weibring, P., Weinheimer, A. J., Wiedinmyer, C., Wisthaler, A., Hills, A., Riemer, D. D., and Apel, E. C.: Observations of nonmethane organic compounds during ARCTAS – Part 1: Biomass burning emissions and plume enhancements, *Atmos. Chem. Phys.*, 11, 11103–11130, doi:10.5194/acp-11-11103-2011, 2011.
- Jacob, D. J., Field, B. D., Li, Q., Blake, D. R., de Gouw, J., Warneke, C., Hansel, A., Wisthaler, A., Singh, H. B., and Guenther, A.: Global budget of methanol: constraints from atmospheric observations, *J. Geophys. Res.*, 110, D08303, doi:10.1029/2004JD005172, 2005.
- Lathière, J., Hauglustaine, D. A., Friend, A. D., De Noblet-Ducoudré, N., Viovy, N., and Folberth, G. A.: Impact of climate variability and land use changes on global biogenic volatile organic compound emissions, *Atmos. Chem. Phys.*, 6, 2129–2146, doi:10.5194/acp-6-2129-2006, 2006.
- Li, Q., Jacob, D. J., Yantosca, R. M., Heald, C. L., Singh, H. B., Koike, M., Zhao, Y., Sachse, G. W., and Streets, D. G.: A global three-dimensional model analysis of the atmospheric budgets of HCN and  $CH_3CN$ : constraints from aircraft and ground measurements, *J. Geophys. Res.*, 108, 8827, doi:10.1029/2002JD003075, 2003.
- Li, Q., Palmer, P. I., Pumphrey, H. C., Bernath, P., and Mahieu, E.: What drives the observed variability of HCN in the troposphere and lower stratosphere?, *Atmos. Chem. Phys.*, 9, 8531–8543, doi:10.5194/acp-9-8531-2009, 2009.
- Liu, J., Logan, J. A., Jones, D. B. A., Livesey, N. J., Megretskaja, I., Carouge, C., and Nedelec, P.: Analysis of CO in the tropical troposphere using Aura satellite data and the GEOS-Chem model: insights into transport characteristics of the GEOS meteorological products, *Atmos. Chem. Phys.*, 10, 12207–12232, doi:10.5194/acp-10-12207-2010, 2010.
- Mahieu, E., Zander, R., Delbouille, L., Demoulin, P., Roland, G., and Servais, C.: Observed trends in total vertical column abundances of atmospheric gases from IR solar spectra recorded at the Jungfraujoch, *J. Atmos. Chem.*, 28, 227–243, 1997.
- Meier, A., Toon, G. C., Rinsland, C. P., Goldman, A., and Hase, F.: Spectroscopic Atlas of Atmospheric Microwindows in the Middle Infra-Red, 2nd revised edition, IRF Technical Report 048, ISSN 0284-1738, IRF Institutet för Rymdfysik, Kiruna, Sweden, 2004.
- Millet, D. B., Jacob, D. J., Custer, T. G., de Gouw, J. A., Goldstein, A. H., Karl, T., Singh, H. B., Sive, B. C., Talbot, R. W., Warneke, C., and Williams, J.: New constraints on terrestrial and oceanic sources of atmospheric methanol, *Atmos. Chem. Phys.*, 8, 6887–6905, doi:10.5194/acp-8-6887-2008, 2008.
- Müller, J.-F. and Brasseur, G.: A three-dimensional chemical transport model of the global troposphere, *J. Geophys. Res.*, 100, 16445–16490, 1995.
- Müller, J.-F. and Stavrakou, T.: Inversion of CO and  $NO_x$  emissions using the adjoint of the IMAGES model, *Atmos. Chem. Phys.*, 5, 1157–1186, doi:10.5194/acp-5-1157-2005, 2005.
- Müller, J.-F., Stavrakou, T., Wallens, S., De Smedt, I., Van Roozendaal, M., Potosnak, M. J., Rinne, J., Munger, B., Goldstein, A., and Guenther, A. B.: Global isoprene emissions estimated using MEGAN, ECMWF analyses and a detailed canopy environment model, *Atmos. Chem. Phys.*, 8, 1329–1341, doi:10.5194/acp-8-1329-2008, 2008.
- Neefs, E., De Mazière, M., Scolas, F., Hermans, C., and Hawat, T.: BARCOS, an automation and remote control system for atmospheric observations with a Bruker interferometer, *Rev. Sci. Instrum.*, 78, 035109-1–0035109-9, 2007.
- Notholt, J., Toon, G. C., Lehmann, R., Sen, B., and Blavier, J.-F.: Comparison of Arctic and Antarctic trace gas column abundances from ground-based Fourier transform infrared spectrometry, *J. Geophys. Res.*, 102, 12863–12869, 1997.
- Notholt, J., Toon, G. C., Rinsland, C. P., Pougatchev, N. S., Jones, N. B., Connor, B. J., Weller, R., Gautrois, M., and Schrems, O.: Latitudinal variations of trace gas concentrations measured by solar absorption spectroscopy during a ship cruise, *J. Geophys. Res.*, 105, 1337–1349, 2000.
- Ohara, T., Akimoto, H., Kurokawa, J., Horii, N., Yamaji, K., Yan, X., and Hayasaka, T.: An Asian emission inventory of anthropogenic emission sources for the period 1980–2020, *Atmos. Chem. Phys.*, 7, 4419–4444, doi:10.5194/acp-7-4419-2007, 2007.

- Ott, L. E., Bacmeister, J., Pawson, S., Pickering, K., Stenchikov, G., Suarez, M., Huntrieser, H., Loewenstein, M., Lopez, J., and Xueref-Remy, I.: Analysis of Convective Transport and Parameter Sensitivity in a Single Column Version of the Goddard Earth Observation System, Version 5, General Circulation Model, *J. Atmos. Sci.*, 66, 627–646, 2009.
- Paton-Walsh, C., Wilson, S. R., Jones, N. B., and Griffith, D. W. T.: Measurement of methanol emissions from Australian wildfires by ground-based solar Fourier transform spectroscopy, *Geophys. Res. Lett.*, 35, L08810, doi:10.1029/2007GL032951, 2008.
- Paton-Walsh, C., Deutscher, N. M., Griffith, D. W. T., Forgan, B. W., Wilson, S. R., Jones, N. B., and Edwards, D. P.: Trace gas emissions from savanna fires in Northern Australia, *J. Geophys. Res.*, 115, D16314, doi:10.1029/2009JD013309, 2010.
- Paulot, F., Wunch, D., Crouse, J. D., Toon, G. C., Millet, D. B., DeCarlo, P. F., Vigouroux, C., Deutscher, N. M., González Abad, G., Notholt, J., Warneke, T., Hannigan, J. W., Warneke, C., de Gouw, J. A., Dunlea, E. J., De Mazière, M., Griffith, D. W. T., Bernath, P., Jimenez, J. L., and Wennberg, P. O.: Importance of secondary sources in the atmospheric budgets of formic and acetic acids, *Atmos. Chem. Phys.*, 11, 1989–2013, doi:10.5194/acp-11-1989-2011, 2011.
- Randriambelo, T., Baldy, S., Bessafi, M. Petit, M., and Despinoy, M.: An improved detection and characterization of active fires and smoke plumes in Southeastern Africa and Madagascar, *Int. J. Remote Sensing*, 19, 2623–2638, 1998.
- Randriambelo, T., Baray, J.-L., and Baldy, S.: Effect of biomass burning, convective venting, and transport on tropospheric ozone over the Indian Ocean: Reunion Island field observations, *J. Geophys. Res.*, 105, 11813–11832, doi:10.1029/1999JD901097, 2000.
- Raper, J., Kleb, M., Jacob, D., Davis, D., Newell, R., Fuelberg, H., Bendura, R., Hoell, J., and McNeal, R.: Pacific Exploratory Mission in the Tropical Pacific: PEM-Tropics B, March–April 1999, *J. Geophys. Res.*, 106, 32401–32425, 2001.
- Razavi, A., Karagulian, F., Clarisse, L., Hurtmans, D., Coheur, P. F., Clerbaux, C., Müller, J. F., and Stavrakou, T.: Global distributions of methanol and formic acid retrieved for the first time from the IASI/MetOp thermal infrared sounder, *Atmos. Chem. Phys.*, 11, 857–872, doi:10.5194/acp-11-857-2011, 2011.
- Rinsland, C. P., Jones, N. B., Connor, B. J., Logan, J. A., Pougatchev, N. S., Goldman, A., Murcray, F. J., Stephen, T. M., Pine, A. S., Zander, R., Mahieu, E., and Demoulin, P.: Northern and Southern Hemisphere ground-based infrared spectroscopic measurements of tropospheric carbon monoxide and ethane, *J. Geophys. Res.*, 103, 28197–28217, 1998.
- Rinsland, C. P., Goldman, A., Murcray, F. J., Stephen, T. M., Pougatchev, N. S., Fishman, J., David, S. J., Blatherwick, R. D., Novelli, P. C., Jones, N. B., and Connor, B. J.: Infrared solar spectroscopic measurements of free tropospheric CO, C<sub>2</sub>H<sub>6</sub>, and HCN above Mauna Loa, Hawaii: seasonal variations and evidence for enhanced emissions from the Southeast Asian tropical fires of 1997–1998, *J. Geophys. Res.*, 104, 18667–18680, doi:10.1029/1999JD900366, 1999.
- Rinsland, C. P., Meier, A., Griffith, D. W. T., and Chiou, L. S.: Ground-based measurements of tropospheric CO, C<sub>2</sub>H<sub>6</sub>, and HCN from Australia at 34° S latitude during 1997–1998, *J. Geophys. Res.*, 106, 20913–20924, doi:10.1029/2000JD000318, 2001.
- Rinsland, C. P., Jones, N. B., Connor, B. J., Wood, S. W., Goldman, A., Stephen, T. M., Murcray, F. J., Chiou, L. S., Zander, R., and Mahieu, E.: Multiyear infrared solar spectroscopic measurements of HCN, CO, C<sub>2</sub>H<sub>6</sub>, and C<sub>2</sub>H<sub>2</sub> tropospheric columns above Lauder, New Zealand (45° S latitude), *J. Geophys. Res.*, 107, 4185, doi:10.1029/2001JD001150, 2002.
- Rinsland, C. P., Mahieu, E., Zander, R., Goldman, A., Wood, S., and Chiou, L.: Free tropospheric measurements of formic acid (HCOOH) from infrared ground-based solar absorption spectra: retrieval approach, evidence for a seasonal cycle, and comparison with model calculations, *J. Geophys. Res.*, 109, D18308, doi:10.1029/2004JD004917, 2004.
- Rinsland, C. P., Boone, C. D., Bernath, P. F., Mahieu, E., Zander, R., Dufour, G., Clerbaux, C., Turquety, S., Chiou, L., McConnell, J. C., Neary, L., and Kaminski, J. W.: First space-based observations of formic acid (HCOOH): Atmospheric Chemistry Experiment austral spring 2004 and 2005 Southern Hemisphere tropical-mid-latitude upper tropospheric measurements, *Geophys. Res. Lett.*, 33, L23804, doi:10.1029/2006GL027128, 2006.
- Rinsland, C. P., Dufour, G., Boone, C. D., Bernath, P. F., Chiou, L., Coheur, P. F., Turquety, S., and Clerbaux, C.: Satellite boreal measurements over Alaska and Canada during June–July 2004: Simultaneous measurements of upper tropospheric CO, C<sub>2</sub>H<sub>6</sub>, HCN, CH<sub>3</sub>Cl, CH<sub>4</sub>, C<sub>2</sub>H<sub>2</sub>, CH<sub>3</sub>OH, HCOOH, OCS, and SF<sub>6</sub> mixing ratios, *Global Biogeochem. Cy.*, 21, GB3008, doi:10.1029/2006GB002795, 2007.
- Rinsland, C. P., Mahieu, E., Chiou, L., and Herbin, H.: First ground-based infrared solar absorption measurements of free tropospheric methanol (CH<sub>3</sub>OH): multidecade infrared time series from Kitt Peak (31.9° N 111.6° W): trend, seasonal cycle, and comparison with previous measurements, *J. Geophys. Res.*, 114, D04309, doi:10.1029/2008JD011003, 2009.
- Rodgers, C. D.: *Inverse Methods for Atmospheric Sounding: Theory and Practice*, Series on Atmospheric, Oceanic and Planetary Physics – Vol. 2, World Scientific Publishing Co., Singapore, 2000.
- Rodgers, C. D. and Connor, B. J.: Intercomparison of remote sounding instruments, *J. Geophys. Res.*, 108, 4116–4129, 2003.
- Rothman, L. S., Gordon, I. E., Barbe, A., Benner, D. C., Bernath, P. F., Birk, M., Boudon, V., Brown, L. R., Campargue, A., Champion, J.-P., Chance, K., Coudert, L. H., Danaj, V., Devi, V. M., Fally, S., Flaud, J.-M., Gamache, R. R., Goldman, A., Jacquemart, D., Kleiner, I., Lacombe, N., Lafferty, W. J., Mandin, J.-Y., Massie, S. T., Mikhailenko, S. N., Miller, C. E., Moazzen-Ahmadi, N., Naumenko, O. V., Nikitin, A. V., Orphal, J., Perevalov, V. I., Perrin, A., Predoi-Cross, A., Rinsland, C. P., Rotger, M., Šimečková, M., Smith, M. A. H., Sung, K., Tashkun, S. A., Tennyson, J., Toth, R. A., Vandaele, A. C., and Vander Auwera, J.: The HITRAN 2008 molecular spectroscopic database, *J. Quant. Spectrosc. Radiat. Transfer*, 110, 533–572, 2009.
- Schultz, M. G., Heil, A., Hoelzemann, J. J., Spessa, A., Thonicke, K., Goldammer, J. G., Held, A. C., Pereira, J. M. C., and van het Bolscher, M.: Global wildland fire emissions from 1960 to 2000, *Global Biogeochem. Cy.*, 22, GB2002, doi:10.1029/2007GB003031, 2008.
- Senten, C., De Mazière, M., Dils, B., Hermans, C., Kruglanski, M., Neefs, E., Scolas, F., Vandaele, A. C., Vanhaelewyn, G.,

- Vigouroux, C., Carleer, M., Coheur, P. F., Fally, S., Barret, B., Baray, J. L., Delmas, R., Leveau, J., Metzger, J. M., Mahieu, E., Boone, C., Walker, K. A., Bernath, P. F., and Strong, K.: Technical Note: New ground-based FTIR measurements at Ile de La Réunion: observations, error analysis, and comparisons with independent data, *Atmos. Chem. Phys.*, 8, 3483–3508, doi:10.5194/acp-8-3483-2008, 2008.
- Sinha, P., Hobbs, P. V., Yokelson, R. J., Bertschi, I. T., Blake, D. R., Simpson, I. J., Gao, S., Kirchstetter, T. W., and Novakov, T.: Emissions of trace gases and particles from savanna fires in Southern Africa, *J. Geophys. Res.*, 108, 8487, doi:10.1029/2002JD002325, 2003.
- Sivakumar, V., Baray, J.-L., Baldy, S., and Bencherif, H.: Tropopause characteristics over a southern subtropical site, Reunion Island (21° S, 55° E): using radiosonde-ozonesonde data, *J. Geophys. Res.*, 111, D19111, doi:10.1029/2005JD006430, 2006.
- Stavrakou, T., Müller, J.-F., De Smedt, I., Van Roozendaal, M., van der Werf, G. R., Giglio, L., and Guenther, A.: Evaluating the performance of pyrogenic and biogenic emission inventories against one decade of space-based formaldehyde columns, *Atmos. Chem. Phys.*, 9, 1037–1060, doi:10.5194/acp-9-1037-2009, 2009.
- Stavrakou, T., Guenther, A., Razavi, A., Clarisse, L., Clerbaux, C., Coheur, P.-F., Hurtmans, D., Karagulian, F., De Mazière, M., Vigouroux, C., Amelynck, C., Schoon, N., Laffineur, Q., Heinesch, B., Aubinet, M., Rinsland, C., and Müller, J.-F.: First space-based derivation of the global atmospheric methanol emission fluxes, *Atmos. Chem. Phys.*, 11, 4873–4898, doi:10.5194/acp-11-4873-2011, 2011.
- Stavrakou, T., Müller, J.-F., Peeters, J., Razavi, A., Clarisse, L., Clerbaux, C., Coheur, P.-F., Hurtmans, D., De Mazière, M., Vigouroux, C., Deutscher, N. M., Griffith, D. W. T., Jones, N., and Paton-Walsh, C.: Satellite evidence for a large source of formic acid from boreal and tropical forests, *Nature Geosci.*, 5, 26–30, doi:10.1038/ngeo1354, 2012.
- Steck, T.: Methods for determining regularization for atmospheric retrieval problems, *Appl. Opt.*, 41, 1788–1797, 2002.
- Streets, D. G., Bond, T. C., Carmichael, G. R., Fernandes, S. D., Fu, Q., He, D., Klimont, Z., Nelson, S. M., Tsai, N. Y., Wang, M. Q., Woo, J.-H., Yarber, K. F.: An inventory of gaseous and primary aerosol emissions in Asia in the year 2000, *J. Geophys. Res.*, 108, 8809, doi:10.1029/2002JD003093, 2003.
- Tereszczuk, K. A., González Abad, G., Clerbaux, C., Hurtmans, D., Coheur, P.-F., and Bernath, P. F.: ACE-FTS measurements of trace species in the characterization of biomass burning plumes, *Atmos. Chem. Phys.*, 11, 12169–12179, doi:10.5194/acp-11-12169-2011, 2011.
- Tikhonov, A.: On the solution of incorrectly stated problems and a method of regularization, *Dokl. Acad. Nauk SSSR*, 151, 501–504, 1963.
- Vigouroux, C., De Mazière, M., Demoulin, P., Servais, C., Hase, F., Blumenstock, T., Kramer, I., Schneider, M., Mellqvist, J., Strandberg, A., Velazco, V., Notholt, J., Sussmann, R., Stremme, W., Rockmann, A., Gardiner, T., Coleman, M., and Woods, P.: Evaluation of tropospheric and stratospheric ozone trends over Western Europe from ground-based FTIR network observations, *Atmos. Chem. Phys.*, 8, 6865–6886, doi:10.5194/acp-8-6865-2008, 2008.
- Vigouroux, C., Hendrick, F., Stavrakou, T., Dils, B., De Smedt, I., Hermans, C., Merlaud, A., Scolas, F., Senten, C., Vanhaelewyn, G., Fally, S., Carleer, M., Metzger, J.-M., Müller, J.-F., Van Roozendaal, M., and De Mazière, M.: Ground-based FTIR and MAX-DOAS observations of formaldehyde at Réunion Island and comparisons with satellite and model data, *Atmos. Chem. Phys.*, 9, 9523–9544, doi:10.5194/acp-9-9523-2009, 2009.
- van der Werf, G. R., Randerson, J. T., Giglio, L., Collatz, G. J., Mu, M., Kasibhatla, P. S., Morton, D. C., DeFries, R. S., Jin, Y., and van Leeuwen, T. T.: Global fire emissions and the contribution of deforestation, savanna, forest, agricultural, and peat fires (1997–2009), *Atmos. Chem. Phys.*, 10, 11707–11735, doi:10.5194/acp-10-11707-2010, 2010.
- Xiao, Y., Jacob, D. J., and Turquety, S.: Atmospheric acetylene and its relationship with CO as an indicator of air mass age, *J. Geophys. Res.*, 112, D12305, doi:10.1029/2006JD008268, 2007.
- Xiao, Y., Logan, J. A., Jacob, D. J., Hudman, R. C., Yantosca, R., and Blake, D. R.: Global budget of ethane and regional constraints on US sources, *J. Geophys. Res.*, 113, D21306, doi:10.1029/2007JD009415, 2008.
- Zander, R., Duchatelet, P., Mahieu, E., Demoulin, P., Roland, G., Servais, C., Auwera, J. V., Perrin, A., Rinsland, C. P., and Crutzen, P. J.: Formic acid above the Jungfrauoch during 1985–2007: observed variability, seasonality, but no long-term background evolution, *Atmos. Chem. Phys.*, 10, 10047–10065, doi:10.5194/acp-10-10047-2010, 2010.
- Zhao, Y., Strong, K., Kondo, Y., Koike, M., Matsumi, Y., Irie, H., Rinsland, C. P., Jones, N. B., Suzuki, K., Nakajima, H., Nakane, H., and Murata, I.: Spectroscopic measurements of tropospheric CO, C<sub>2</sub>H<sub>6</sub>, C<sub>2</sub>H<sub>2</sub>, and HCN in Northern Japan, *J. Geophys. Res.*, 107, 4343, doi:10.1029/2001JD000748, 2002.



# Trends of ozone total columns and vertical distribution from FTIR observations at eight NDACC stations around the globe

C. Vigouroux<sup>1</sup>, T. Blumenstock<sup>2</sup>, M. Coffey<sup>3</sup>, Q. Errera<sup>1</sup>, O. García<sup>4</sup>, N. B. Jones<sup>5</sup>, J. W. Hannigan<sup>3</sup>, F. Hase<sup>2</sup>, B. Liley<sup>6</sup>, E. Mahieu<sup>7</sup>, J. Mellqvist<sup>8</sup>, J. Notholt<sup>9</sup>, M. Palm<sup>9</sup>, G. Persson<sup>8</sup>, M. Schneider<sup>4</sup>, C. Servais<sup>7</sup>, D. Smale<sup>6</sup>, L. Thölix<sup>10</sup>, and M. De Mazière<sup>1</sup>

<sup>1</sup>Department of Atmospheric Composition, Belgian Institute for Space Aeronomy (BIRA-IASB), Brussels, Belgium

<sup>2</sup>Karlsruhe Institute of Technology (KIT), Institute for Meteorology and Climate Research (IMK-ASF), Karlsruhe, Germany

<sup>3</sup>Atmospheric Chemistry Division, National Center for Atmospheric Research (NCAR), Boulder, Colorado, USA

<sup>4</sup>Izaña Atmospheric Research Centre (IARC), Agencia Estatal de Meteorología (AEMET), Santa Cruz de Tenerife, Spain

<sup>5</sup>Centre for Atmospheric Chemistry, University of Wollongong, Wollongong, Australia

<sup>6</sup>Department of Atmosphere, National Institute of Water and Atmospheric Research Ltd (NIWA), Lauder, New Zealand

<sup>7</sup>Institute of Astrophysics and Geophysics, University of Liège (ULg), Liège, Belgium

<sup>8</sup>Department of Earth and Space Science, Chalmers University of Technology, Göteborg, Sweden

<sup>9</sup>Institute of Environmental Physics, University of Bremen, Bremen, Germany

<sup>10</sup>Climate Research, Finnish Meteorological Institute (FMI), Helsinki, Finland

Correspondence to: C. Vigouroux (corinne.vigouroux@aeronomie.be)

Received: 11 July 2014 – Published in Atmos. Chem. Phys. Discuss.: 25 September 2014

Revised: 19 February 2015 – Accepted: 23 February 2015 – Published: 16 March 2015

**Abstract.** Ground-based Fourier transform infrared (FTIR) measurements of solar absorption spectra can provide ozone total columns with a precision of 2% but also independent partial column amounts in about four vertical layers, one in the troposphere and three in the stratosphere up to about 45 km, with a precision of 5–6%. We use eight of the Network for the Detection of Atmospheric Composition Change (NDACC) stations having a long-term time series of FTIR ozone measurements to study the total and vertical ozone trends and variability, namely, Ny-Ålesund (79° N), Thule (77° N), Kiruna (68° N), Harestua (60° N), Jungfraujoch (47° N), Izaña (28° N), Wollongong (34° S) and Lauder (45° S). The length of the FTIR time series varies by station but is typically from about 1995 to present. We applied to the monthly means of the ozone total and four partial columns a stepwise multiple regression model including the following proxies: solar cycle, quasi-biennial oscillation (QBO), El Niño–Southern Oscillation (ENSO), Arctic and Antarctic Oscillation (AO/AAO), tropopause pressure (TP), equivalent latitude (EL), Eliassen–Palm flux (EPF), and volume of polar stratospheric clouds (VPSC).

At the Arctic stations, the trends are found mostly negative in the troposphere and lower stratosphere, very mixed in the middle stratosphere, positive in the upper stratosphere due to a large increase in the 1995–2003 period, and non-significant when considering the total columns. The trends for mid-latitude and subtropical stations are all non-significant, except at Lauder in the troposphere and upper stratosphere and at Wollongong for the total columns and the lower and middle stratospheric columns where they are found positive. At Jungfraujoch, the upper stratospheric trend is close to significance ( $+0.9 \pm 1.0$  % decade<sup>-1</sup>). Therefore, some signs of the onset of ozone mid-latitude recovery are observed only in the Southern Hemisphere, while a few more years seem to be needed to observe it at the northern mid-latitude station.

## 1 Introduction

While the past negative trend in the ozone layer has been successfully attributed to the increase of ozone depleting substances and reproduced by chemistry–climate models, under-

standing and predicting the current and future ozone layer, and especially attributing an ozone recovery to the positive effect of the Montreal Protocol and its Amendments and Adjustments, is still a challenge. This results from natural variability, observation uncertainties, and changes in dynamics and temperature induced by the increase of greenhouse gases (WMO, 2010). Long-term measurements of total and vertical ozone are required to understand the ozone response to different natural and anthropogenic forcings. Since the long-term satellite experiments ceased to operate (i.e., SAGE, HALOE), the satellite community is working on merging the past records to the new measurements performed by a number of satellite instruments launched since 2000 (e.g., Bodeker et al., 2013; Kyrölä et al., 2013; Sioris et al., 2014; Chehade et al., 2014). Reliable data from stable instruments are needed to validate these satellite-extended data sets, and to offer an alternative determination of ozone total and vertical changes. Ground-based (Dobson, Umkehr) and ozonesonde data are traditionally used for these studies, already reporting trends in the 1985 ozone report (WMO, 1985) and followed in 1998 by lidar and microwave measurements (WMO, 1998). Ground-based FTIR (Fourier transform infrared) measurements derived from high-resolution solar absorption spectra provide an additional ozone data set; they were first used for trend studies in Vigouroux et al. (2008) with 10 years of data (1995–2004) at several European stations and then were updated in the WMO (2010) report. Additional similar studies have been performed at individual stations (Mikuteit, 2008; García et al., 2012). These measurements have their own advantages. First, for atmospheric gases such as ozone, which have very narrow absorption lines, the ozone absorption signatures are self-calibrated with the reference being the surrounding continuum. Therefore, the derived absolute ozone columns depend mainly on the employed spectroscopic parameters which dominate the systematic uncertainty budget. Second, they can provide not only ozone total columns with a precision of 2 %, but also low vertical resolution profiles, obtained from the temperature and pressure dependence of the absorption line shapes. This leads to about four independent partial columns, one in the troposphere and three in the stratosphere up to about 45 km, with a precision of about 5–6 %. The instrumental line shape (ILS), which depends on the alignment of the spectrometer, impacts the absorption line shape on which the ozone profile retrievals are based. Hence, it is important to have accurate knowledge of the ILS in order to derive correct ozone profiles and trends.

The work discussed in this paper expands on the previous study of Vigouroux et al. (2008): it is based on longer time series, it includes FTIR data from stations outside of Europe, and it uses a stepwise multiple linear regression model including several explanatory variables for the trend evaluation. It is presented as follows: Sect. 2 provides information about the FTIR ozone observations (retrieval strategies, characterization of the vertical information, time series and

seasonality). Section 3 describes the stepwise multiple linear regression model applied to the ozone time series. Section 4 presents and discusses the trend results as well as the explained part of ozone variability. Section 5 summarizes the conclusions.

## 2 Ground-based FTIR ozone observations

### 2.1 FTIR monitoring

Table 1 identifies the ground-based FTIR stations, all part of NDACC (Network for the Detection of Atmospheric Composition Change), that contribute to the present work. The latitudinal coverage is good: from 79° N to 45° S. These stations perform regular solar absorption measurements, under clear-sky conditions and over a wide spectral range (around 600–4500 cm<sup>-1</sup>); the derived time series of total column abundances of many atmospheric species are available in the NDACC database (<http://www.ndacc.org>). While the stations are all currently active, they started their regular monitoring activities at different times. The period of measurement used for ozone trend analysis at each station is summarized in Table 1, together with the instrument manufacturer and type. Some of the stations performed measurements even earlier but these older spectra, taken with different spectrometers, have to be carefully reanalyzed first before being included in a trend study. The instruments currently used are the high-resolution spectrometers Bruker 120 M, 125 M, 120 HR, and 125 HR, which can achieve a spectral resolution of 0.0035 cm<sup>-1</sup> or better. The Bomem DA8 used in the first years of Wollongong measurements has a spectral resolution of 0.004 cm<sup>-1</sup>.

### 2.2 FTIR retrieval strategy

We refer to Vigouroux et al. (2008) for more details on the ozone FTIR inversion principles, which are based on the optimal estimation method (Rodgers, 2000). The effort of retrieval homogenization initiated in Vigouroux et al. (2008) has been pursued and we report in Table 2 the common retrieval parameters. The spectroscopic database has been updated to HITRAN 2008 (Rothman et al., 2009). All stations are employing the daily pressure and temperature profiles from NCEP (National Centers for Environmental Prediction). A common source for the ozone a priori profiles is used: the model WACCM4 (Whole Atmosphere Community Climate Mode; Garcia et al., 2007) calculated at each FTIR station, except at Harestua where a climatology based on ozonesondes and HALOE measurements is used. Finally, the interfering species fitted in the ozone retrievals, usually with a simple scaling of their a priori profile, are the same for all stations, except Harestua, namely, H<sub>2</sub>O, CO<sub>2</sub>, C<sub>2</sub>H<sub>4</sub>, and the ozone isotopologues <sup>668</sup>O<sub>3</sub> and <sup>686</sup>O<sub>3</sub>. At Harestua, only H<sub>2</sub>O and CO<sub>2</sub> are fitted.

**Table 1.** Characteristics of the FTIR stations that contribute to the present work: location and altitude (in km a.s.l.), time period covered by the ozone measurements used in the present trend analysis, and instrument type.

| Station      | Latitude | Longitude | Altitude (km) | Time period | Instrument    |
|--------------|----------|-----------|---------------|-------------|---------------|
| Ny-Ålesund   | 79° N    | 12° E     | 0.02          | 1995–2012   | Bruker 120 HR |
| Thule        | 77° N    | 69° W     | 0.22          | 1999–2012   | Bruker 120 M  |
| Kiruna       | 68° N    | 20° E     | 0.42          | 1996–2007   | Bruker 120 HR |
|              |          |           |               | 2007–2012   | Bruker 125 HR |
| Harestua     | 60° N    | 11° E     | 0.60          | 1995–2009   | Bruker 120 M  |
|              |          |           |               | 2009–2012   | Bruker 125 M  |
| Jungfraujoch | 47° N    | 8° E      | 3.58          | 1995–2012   | Bruker 120 HR |
| Izaña        | 28° N    | 16° W     | 2.37          | 1999–2005   | Bruker 120 M  |
|              |          |           |               | 2005–2012   | Bruker 125 HR |
| Wollongong   | 34° S    | 151° E    | 0.03          | 1996–2007   | Bomem DA8     |
|              |          |           |               | 2007–2012   | Bruker 125 HR |
| Lauder       | 45° S    | 170° E    | 0.37          | 2001–2012   | Bruker 120 HR |

Some retrieval parameters still differ from station to station, either for historical reasons or for the inherent specificities of the different locations. They are also summarized in Table 2.

First, two different profile retrieval algorithms are widely used depending on each team's expertise: PROFFIT9 (Hase, 2000) at Kiruna and Izaña and SFIT2 (Pougatchev et al., 1995) at the six other stations. It has been demonstrated in Hase et al. (2004) that the profiles and total column amounts retrieved from these two different algorithms under identical conditions are in excellent agreement.

Second, the microwindow sets involve some common lines at all stations, which ensures that only a small bias is expected due to the different microwindow choices. Either some additional thin microwindows are used together with the 1000–1005 cm<sup>-1</sup> or, at Kiruna and Izaña, a different choice was led by the priority given to avoid the more intense H<sub>2</sub>O lines while still having a high DOFS (degrees of freedom for signal). All choices of microwindows lead to the required 4–5 DOFS, thanks to the numerous ozone lines with different intensities which give information both in the stratosphere and the troposphere. The test has been made at Kiruna and Ny-Ålesund to use the 1000–1005 cm<sup>-1</sup> window only and, as expected, only little impact has been observed: except for Ny-Ålesund's tropospheric trends (1.4%/decade), we obtained small trend differences of between 0.0 and 0.8 % decade<sup>-1</sup>, which is in all cases well below the uncertainty on the trends (see Section 4). However, it is planned, within the InfraRed Working Group of NDACC, to fix a common choice of microwindows for future improved homogenization.

Third, the main interfering species in this spectral region is water vapor, and it has been dealt with differently depending on the station: at the Wollongong and Lauder stations, the H<sub>2</sub>O profile is retrieved simultaneously with the ozone profile, adding the microwindow of 896.4–896.6 cm<sup>-1</sup> for a better H<sub>2</sub>O determination. At Kiruna, Izaña and Jungfrau-

joch, the H<sub>2</sub>O a priori profiles are only scaled in the ozone retrieval but these a priori profiles have been preliminarily retrieved in dedicated H<sub>2</sub>O microwindows for each spectrum (Schneider et al. (2006) for Kiruna and Izaña; Sussmann et al. (2009) for Jungfraujoch). For the very dry Jungfraujoch site, it has been found that preliminary H<sub>2</sub>O retrievals do not improve the quality of the ozone retrievals. At Ny-Ålesund and Thule, water vapor is treated as the other interfering species: only a scaling of a single a priori profile from WACCM4 is made. Therefore, except at the two latter stations, the H<sub>2</sub>O profile variability has been well taken into account. This may be a future improvement to be done in Ny-Ålesund and Thule strategies. However, the random uncertainties due to the water vapor interference are not dominating the ozone error budget (see Sect. 2.3), and we expect a negligible impact on the ozone trends due to the H<sub>2</sub>O treatment.

Fourth, the choice of the regularization (a priori covariance matrix,  $\mathbf{S}_a$ , and signal to noise ratio, SNR) cannot be easily homogenized because it depends on the real variability of ozone which is different at each station location and on the real SNR achieved by each spectrometer. In optimal estimation, the choice of the a priori covariance matrix  $\mathbf{S}_a$  is an important parameter of the inversion process and, together with the measurement noise error covariance matrix  $\mathbf{S}_\epsilon$ , it will lead to the following averaging kernel matrix  $\mathbf{A}$  (Rodgers, 2000):

$$\mathbf{A} = (\mathbf{K}^T \mathbf{S}_\epsilon^{-1} \mathbf{K} + \mathbf{S}_a^{-1})^{-1} \mathbf{K}^T \mathbf{S}_\epsilon^{-1} \mathbf{K}, \quad (1)$$

where  $\mathbf{K}$  is the weighting function matrix that links the measurement vector  $\mathbf{y}$  to the state vector  $\mathbf{x}$ :  $\mathbf{y} = \mathbf{K}\mathbf{x} + \boldsymbol{\epsilon}$ , with  $\boldsymbol{\epsilon}$  representing the measurement error. In our retrievals, we assume  $\mathbf{S}_\epsilon$  to be diagonal, in which case the diagonal elements are the inverse square of the SNR. The diagonal elements of  $\mathbf{S}_a$  represent the assumed variability of the target gas volume mixing ratio (VMR) at a given altitude, and the non-diagonal elements represent the correlation between the VMR at different altitudes. We can see in Table 2 that, ex-

**Table 2.** Summary of the ozone retrieval parameters. All microwindow (mw) limits are given in per centimeter units. Ny: Ny-Ålesund; Th: Thule; Ha: Harestua; Ju: Jungfraujoch.

| Parameters                                       | Ny-Ålesund/Thule  | Harestua/Jungfraujoch   | Kiruna/Izaña   | Wollongong/Lauder  |
|--|---|---|--|--|
| Spectroscopic database                           | HITRAN 2008   | HITRAN 2008   | HITRAN 2008  | HITRAN 2008  |
| Pressure and temperature                         | NCEP  | NCEP  | NCEP   | NCEP   |
| Ozone a priori profiles                          | WACCM4  | WACCM4 (Ju)<br>climatology based on<br>sondes and HALOE (Ha)  | WACCM4   | WACCM4   |
| Retrieval code                                   | SFIT2 <sup>a</sup> v3.94  | SFIT2 <sup>a</sup> v3.94  | PROFIT9 <sup>b</sup>   | SFIT2 <sup>a</sup> v3.94   |
| Microwindows                                     | 1000–1005<br>782.56–782.86 (Ny)<br>788.85–789.37 (Ny)<br>993.3–993.8 (Ny)   | 1000–1005   | 991.25–993.80<br>1001.47–1003.04<br>1005.0–1006.9<br>1007.347–1009.003<br>1011.147–1013.553  | 1000–1005<br>782.56–782.86<br>788.85–789.37<br>993.3–993.8<br>896.4–896.6 (H <sub>2</sub> O)   |
| Interfering species                              | H <sub>2</sub> O, CO <sub>2</sub> , C <sub>2</sub> H <sub>4</sub> ,<br><sup>668</sup> O <sub>3</sub> , <sup>686</sup> O <sub>3</sub>                          | H <sub>2</sub> O, CO <sub>2</sub> , C <sub>2</sub> H <sub>4</sub> ,<br><sup>668</sup> O <sub>3</sub> , <sup>686</sup> O <sub>3</sub> (Ju)<br>H <sub>2</sub> O, CO <sub>2</sub> (Ha) | H <sub>2</sub> O, CO <sub>2</sub> , C <sub>2</sub> H <sub>4</sub> ,<br><sup>668</sup> O <sub>3</sub> , <sup>686</sup> O <sub>3</sub> | H <sub>2</sub> O, CO <sub>2</sub> , C <sub>2</sub> H <sub>4</sub> ,<br><sup>668</sup> O <sub>3</sub> , <sup>686</sup> O <sub>3</sub> |
| H <sub>2</sub> O treatment<br>– a priori profile | One single profile (Ny)<br>Preliminary retrievals in<br>dedicated H <sub>2</sub> O mws (Th)   | One single profile (Ha)<br>Preliminary retrievals in<br>dedicated H <sub>2</sub> O mws (Ju)   | Preliminary retrievals<br>in dedicated H <sub>2</sub> O mws  | One single profile   |
| – fit in ozone mw                                | Scaling retrieval only  | Scaling retrieval only  | Scaling retrieval only   | Profile retrieval  |
| Regularization:<br>– S <sub>a</sub>              | Diagonal: 20 % (Ny)<br>Diagonal: 30 % (Th)<br>No interlayer correlation   | Diagonal: 5–11 % (Ha)<br>Diagonal: 10 % (Ju)<br>No interlayer correlation (Ha)<br>Interlayer correlation:<br>Gaussian decay 4 km (Ju)   | Tikhonov regularization<br>L1  | Diagonal: 10 %<br><br>Interlayer correlation:<br>exponential decay 4 km  |
| – SNR  | Real SNR (depending on<br>each spectrum), except <sup>c</sup><br>regions at<br>1000.85–1001.45<br>1003.16–1004.5<br>set to SNR = 1 (Ny)<br>Constant = 50 (Th) | Constant = 100 (Ju)<br>Constant = 200 (Ha)  | Depending on<br>each spectrum  | Constant = 150   |
| Instrumental<br>Line Shape                       | Fixed ideal (Ny)<br>Fixed from LINEFIT<br>(Th)  | Fixed from LINEFIT (Ha)<br>second-order polynomial fit<br>of EAP (Ju)   | Fixed ideal (Kiruna)<br>Fixed from LINEFIT<br>(Izaña)  | Fixed ideal<br>except Bomem spectra:<br>fourth-order polynomial fit<br>of EAP  |

<sup>a</sup> Pougatchev et al. (1995);<sup>b</sup> Hase (2000);<sup>c</sup> in order to mask strong H<sub>2</sub>O absorptions.

cept at Harestua, Kiruna and Izaña, the stations are using an a priori covariance matrix with diagonal elements constant with altitude corresponding to 10, 20 or 30 % variability, the largest variability taking place at the high latitude stations Ny-Ålesund and Thule. At Harestua, the diagonal elements of S<sub>a</sub> correspond to 11 % in the stratosphere, de-

creasing down to 6 % in the troposphere and to 5 % above 35 km. Except at Ny-Ålesund, the SNR value is not the real one coming from each individual spectrum but an effective SNR that is used as a regularization parameter. This effective SNR is smaller than the value derived from the inherent noise in the spectra, since the residuals in a spectral fit are

not only coming from pure measurement noise but also from uncertainties in the model parameters. At Kiruna and Izaña, the regularization is made using the Tikhonov L1 constraint (Tikhonov, 1963). The regularization choice ( $S_a$  and SNR) is made at each station in order to obtain stable retrievals with reasonable DOFS. The regularization, via the  $A$  matrix, will impact, together with the real natural variability of ozone, the smoothing uncertainty which is the dominant source for the tropospheric and lower stratospheric columns. However, this is mainly a random uncertainty source and it has been shown at Izaña that using Tikhonov regularization or a  $S_a$  matrix obtained from ozone climatological measurements does not impact the ozone trends significantly (García et al., 2012).

The last important parameter is the instrumental line shape (ILS). As already mentioned, the ILS impacts the absorption line shape on which the ozone profile retrievals are based. Hence, if it is not properly included in the forward model or in the retrieval process, and if the alignment of the instrument is changing over time, this could impact the derived ozone trends (García et al., 2012). There are three options for considering the ILS and the choice is led by the type of spectrometer and the availability of cell measurements. A perfect alignment of the instrument would provide an “ideal” ILS: the modulation efficiency amplitude (also called the effective apodization parameter, EAP, at the maximum optical path difference) and the phase error remain equal to 1 and 0, respectively, along the optical path differences (OPDs). This perfect alignment can usually be achieved and maintained over time by the stable Bruker 120 or 125 HR. Even when those spectrometers are used, the alignment must be controlled by HBr or  $N_2O$  absorption measurements in a low-pressure gas cell and the use of the LINEFIT code, as described in Hase et al. (1999). In this approach, the loss of modulation efficiency and the phase error can be described (1) by 40 parameters (20 for each) at equidistant OPDs, or (2) simply by 2 parameters assuming a linear decline of the modulation efficiency with OPD and a constant phase error. At all stations using the 120 or 125 HR spectrometers, and where the cell measurements were available for the whole period and taken at least twice a year (Ny-Ålesund, Kiruna, Lauder, Wollongong from 2007), the ILS retrieved from LINEFIT was found good and stable: less than 2 % of loss in modulation efficiency at the maximum OPD. It has been therefore considered and fixed as ideal in the forward model. For the stations where the cell measurements were available and where the ILS could not be considered ideal, which was the case for the stations running a Bruker 120 M instrument, the ILS was fixed in the forward model to the parameters obtained by LINEFIT using either option (1) at Thule and Izaña or option (2) at Harestua. At Jungfraujoch up to the early 2000’s, and at Wollongong, when the Bomem instrument was used, no cell measurements were performed; hence, it is not possible to use the LINEFIT results in the forward model. To take into account that the ILS may not be ideal, the modulation efficiency is retrieved simultaneously with the ozone

profiles by using a polynomial fit of order 2 (Jungfraujoch) or 4 (Wollongong). The phase error has been neglected, i.e., it is treated as ideal. An argument against the use of the ozone absorption line shape to retrieve simultaneously the ozone profiles and the ILS is that a change on the ozone concentration at a given altitude may be interpreted wrongly as a change in the ILS. However, it was found that at Jungfraujoch the fitting of the ILS, instead of assuming that it is ideal, improved the agreement with correlative ozone profiles measurements (Barret et al., 2002), leading to the conclusions that there was enough information in the absorption line shapes to isolate correctly the ILS effect. We conducted the test at Ny-Ålesund to use a polynomial fit (order 2) of the modulation efficiency instead of a fixed ideal ILS. We found very small impact on the trends (less than  $0.6\%$  decade<sup>-1</sup> for all layers). Of course the situation may differ for stations with worse alignment if this one cannot be reproduced by a polynomial fit of the modulation efficiency. Another solution to deal with periods without cell measurements would be to retrieve independently the ILS using  $N_2$  and  $CO_2$  lines in the historical solar spectra, since these gases have very well-known vertical profiles, and then fix the ILS to these preliminary derived values in the ozone retrievals.

### 2.3 Vertical information in FTIR retrievals

The vertical information contained in the FTIR retrievals can be characterized by the averaging kernel matrix  $A$  (Eq. 1), as described in detail in Vigouroux et al. (2008). It has been shown in this previous paper that the ozone retrievals provide 4–5 DOFS, depending on the station. Therefore, in addition to total column trends, we provide ozone trends in four independent partial column layers, corresponding to the vertical information. The layer limits have been chosen such that the DOFS is at least 1.0 in each associated partial column. The adopted layers are independent according to the resolution of the averaging kernels, as can be seen in Fig. 1 where the partial column averaging kernels of the four layers in the case of Jungfraujoch and Izaña are shown. Similar averaging kernels are obtained at each station (not shown). Also shown is the sensitivity which is, at each altitude  $k$ , the sum of the elements of the corresponding averaging kernel  $\sum_i A_{ki}$  and represents roughly the fraction of the retrieval that comes from the measurement rather than from the a priori information. At Izaña, the sensitivity does not decrease towards 0 at about 50 km (Fig. 1) because of the use of Tikhonov regularization instead of optimal estimation (García et al., 2012). In the present work, small changes have been made in the partial column limits in comparison to Vigouroux et al. (2008): we avoid the tropopause region at each station, in order to have a better separation between the layer that we call the “tropospheric” layer and the lower stratospheric layer. Due to the high tropopause heights at Izaña (14.9 km) and Wollongong (13.8 km), compared to mid- and high-latitude stations (from 10.1 km at Ny-Ålesund to 11.8 km at Jungfraujoch), we use

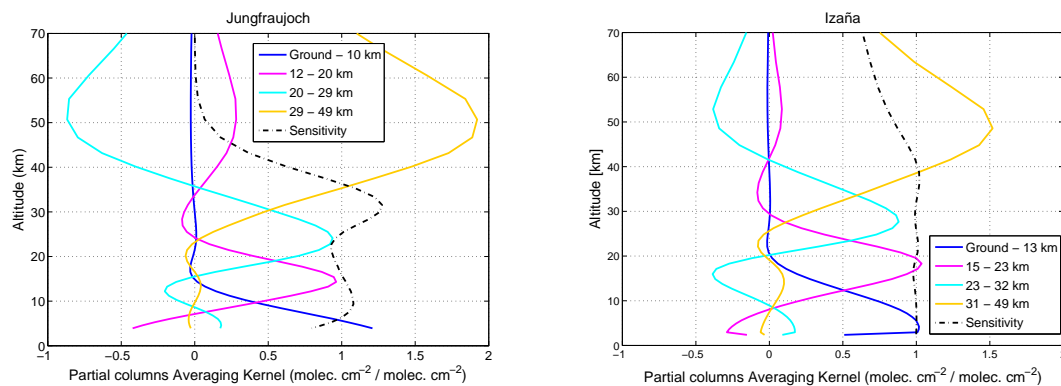


**Figure 1.** Partial column averaging kernels ( $\text{molec cm}^{-2} (\text{molec cm}^{-2})^{-1}$ ) for ozone retrievals at Jungfraujoch (left) and Izaña (right) stations.

different partial column limits for these two stations. The upper limit of the upper layer is here 49 km, the altitude above which the DOFS is small (from about 0.01 to 0.04 depending on station), instead of 42 km in Vigouroux et al. (2008), chosen as the altitude above which the sensitivity was below 0.5. We still gain from 0.06 (Jungfraujoch) up to 0.23 (Lauder) DOFS in this 7 km wide range with poorer sensitivity. For Harestua, the chosen layer limits give a DOFS of only 0.9 and 0.75 in the ground–10 km and in the 29–49 km layers, respectively.

We provide in Table 3, for each station, the partial column limits of the four defined layers (Trop: troposphere; LowS: lower stratosphere; MidS: middle stratosphere; UppS: upper stratosphere). The detailed error budget for ozone FTIR retrievals has been described in Vigouroux et al. (2008) and more recently in García et al. (2012) for Izaña; we only just summarize in Table 3 the total random uncertainties obtained for the present choice of layers and for the total columns (TotC). As obtained in the two previous papers, and not shown here, the smoothing error is the dominant random error source for the tropospheric and lower stratospheric layer, while the temperature dominates the random error budget for the middle and upper stratospheric layers and for total columns. Also found in these two papers, and not repeated here, is the validation of the FTIR total and partial columns with correlative data (Dobson, Brewer, UV–Vis, ozonesondes, lidar).

## 2.4 FTIR ozone time series

Figure 2 displays the time series of ozone total columns at each ground-based FTIR station. Because we consider only solar absorption measurements, the time series at Ny-Ålesund, Thule, and Kiruna cover only the mid-March–September, late-February–mid-October and mid-January–mid-November periods, respectively. The seasonal variation is isolated in Fig. 3, which shows the monthly mean total columns over the periods of measurements. We clearly see the well-known seasonal cycle of ozone total column having

**Table 3.** Partial column (PC) limits for the four altitude layers containing at least one DOFS. The random uncertainties are given for each partial column. Trop: troposphere; LowS: lower stratosphere; MidS: middle stratosphere; UppS: upper stratosphere; TotC: total columns; Gd: ground; Err.: total random uncertainties.

| Layers | Stations         | PC limits   | Err. |
|--------|------------------|-------------|------|
| Trop   | Izaña/Wollongong | Gd–13/12 km | 6 %  |
|        | Other stations   | Gd–9/10 km  | 5 %  |
| LowS   | Izaña/Wollongong | 15–23 km    | 5 %  |
|        | Other stations   | 12–20 km    | 4 %  |
| MidS   | Izaña/Wollongong | 23–32 km    | 5 %  |
|        | Other stations   | 20–29 km    | 5 %  |
| UppS   | Izaña/Wollongong | 31–49 km    | 5 %  |
|        | Other stations   | 29–49 km    | 5 %  |
| TotC   | Izaña/Wollongong | –           | 2 %  |
|        | Other stations   | –           | 2 %  |

a maximum in spring at all stations, and the higher amplitude of the seasonal variation at higher latitudes (Brasseur and Solomon, 1984).

Figure 3 shows also the monthly means of the four partial columns defined in the previous section (Table 3). In the upper stratospheric layer, the ozone maximum occurs in summer (early summer at high latitudes shifting to late summer with decreasing latitude), in agreement with higher photochemical production of ozone during this season. In the lower stratospheric layer, the ozone maximum is in late winter/early spring at all latitudes. The situation is more variable for the middle stratospheric layer: still late winter/early spring for Harestua, Jungfraujoch, Lauder and Wollongong, but the latter shows a second maximum in late summer, and a small amplitude of the seasonal cycle. For the three higher latitude stations – Ny-Ålesund, Thule and Kiruna – the maximum is still in spring, extending to May for the two latter stations. At Izaña, the maximum is in summer in the mid-

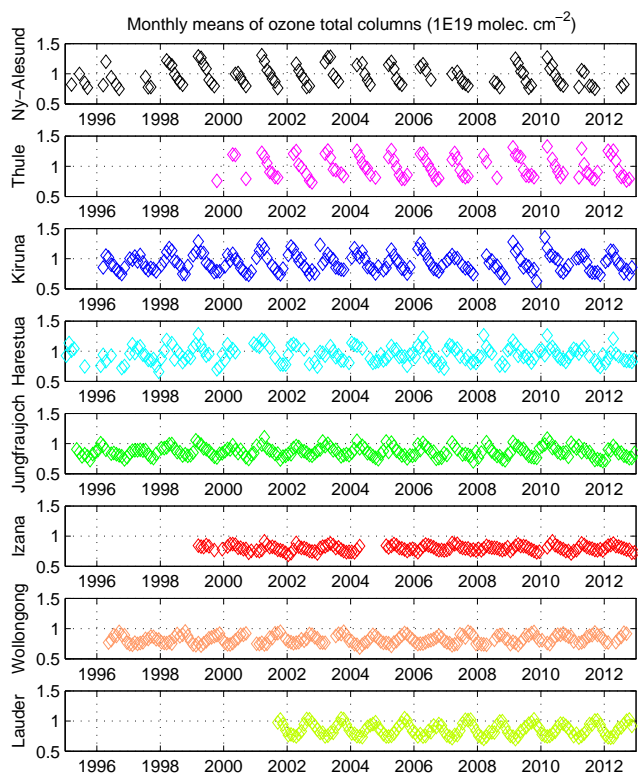


**Figure 2.** Time series of monthly means of ozone total columns at each station.

dle stratosphere. For the tropospheric column, we observe a maximum in spring at all stations, but at Jungfraujoch it extends also into summer.

### 3 Multiple regression model

The ozone FTIR total and partial column trends in Vigouroux et al. (2008); WMO (2010); García et al. (2012) were calculated with a bootstrap resampling method, applied to the daily means time series. In these studies, only the seasonal cycle and a linear trend were taken into account, the remaining natural ozone variability was then an additional noise in the ozone trend determination. To reduce the uncertainties on the trends and to better understand what drives ozone variability and trends, we use in the present study a multiple linear regression (MLR) model. To reduce the auto-correlation in the residuals, we use here the monthly means time series. Furthermore, to account for the still significant auto-correlation in the residuals, a Cochrane–Orcutt transformation (Cochrane and Orcutt, 1949) is applied to the final model. This gives more reliable confidence intervals for the regression parameters.

The following regression model is applied to the monthly means of ozone total and partial column time series  $Y(t)$ :

$$Y(t) = A_0 + A_1 \cdot \cos(2\pi t/12) + A_2 \cdot \sin(2\pi t/12) + A_3 \cdot \cos(4\pi t/12) + A_4 \cdot \sin(4\pi t/12) + A_5 \cdot t + \sum_{k=6}^n A_k \cdot X_k(t) + \epsilon(t), \quad (2)$$

where  $A_0$  is the intercept, the  $A_1$ – $A_4$  parameters describe the ozone seasonal cycle,  $A_5$  is the annual trend,  $X_k(t)$  are the explanatory variables (proxies time series) and  $A_k$  their respective coefficient, and  $\epsilon(t)$  represents the residuals.

To select the final regression model, we have included several proxies, which represent processes that are known to impact ozone, in a stepwise regression procedure that keeps or rejects each proxy: the initial model (seasonal cycle and trend) is fitted first. Second, iteratively, if any proxies, not already in the model, have  $p$  values smaller than an entrance tolerance (0.05), i.e., if it is unlikely that they would have a 0 coefficient if added to the model, then we add the one with the smallest  $p$  value. Otherwise, if any proxies in the model have  $p$  values greater than an exit tolerance (0.10), we remove the one with the largest  $p$  value and we repeat the whole process until no single step improves the model. Hence, the final set of parameters can vary with the station and with the partial columns concerned. In this paper, a proxy is called “non-significant” when it has not been retained by the stepwise procedure. This choice of not using a fixed model for all stations and partial columns avoids overfitting the data and is justified by the large latitudinal range of the stations (e.g., the VPSC or ENSO proxies will not impact the stations in the same way) and by the different processes driving ozone variability at different altitudes.

The proxies that have been tested in the stepwise regression procedure are summarized in Table 4. The two most common explanatory variables found in the literature are the solar radio flux at F10.7 cm (SOLAR) which represents the 11-year solar cycle (following e.g., Newchurch et al., 2003; Randel and Wu, 2007), and the zonal winds measured at Singapore at 30 and 10 hPa (following e.g., Brunner et al., 2006) which represent the quasi-biennial oscillation (QBO). The proxy used for the El Niño–Southern Oscillation (ENSO) is the multivariate ENSO index (MEI), following Randel et al. (2009). Different time lags (from 0 to 4 months) between ENSO and ozone time series have been tested. The other dynamical proxies that have been explored are the tropopause pressure (TP) at each station (following e.g., Appenzeller et al., 2000), the equivalent latitude (EL) at three altitude levels around each station, the Arctic Oscillation (AO) or the Antarctic Oscillation (AAO) indices depending on the station location (e.g., Appenzeller et al., 2000; Frossard et al., 2013), and the vertical component of the Eliassen–Palm flux (EPF) at 100 hPa averaged over 45–75° north and south, as a proxy for the Brewer–Dobson circulation (e.g., Brunner et al., 2006). These dynamical proxies are connected, e.g. the

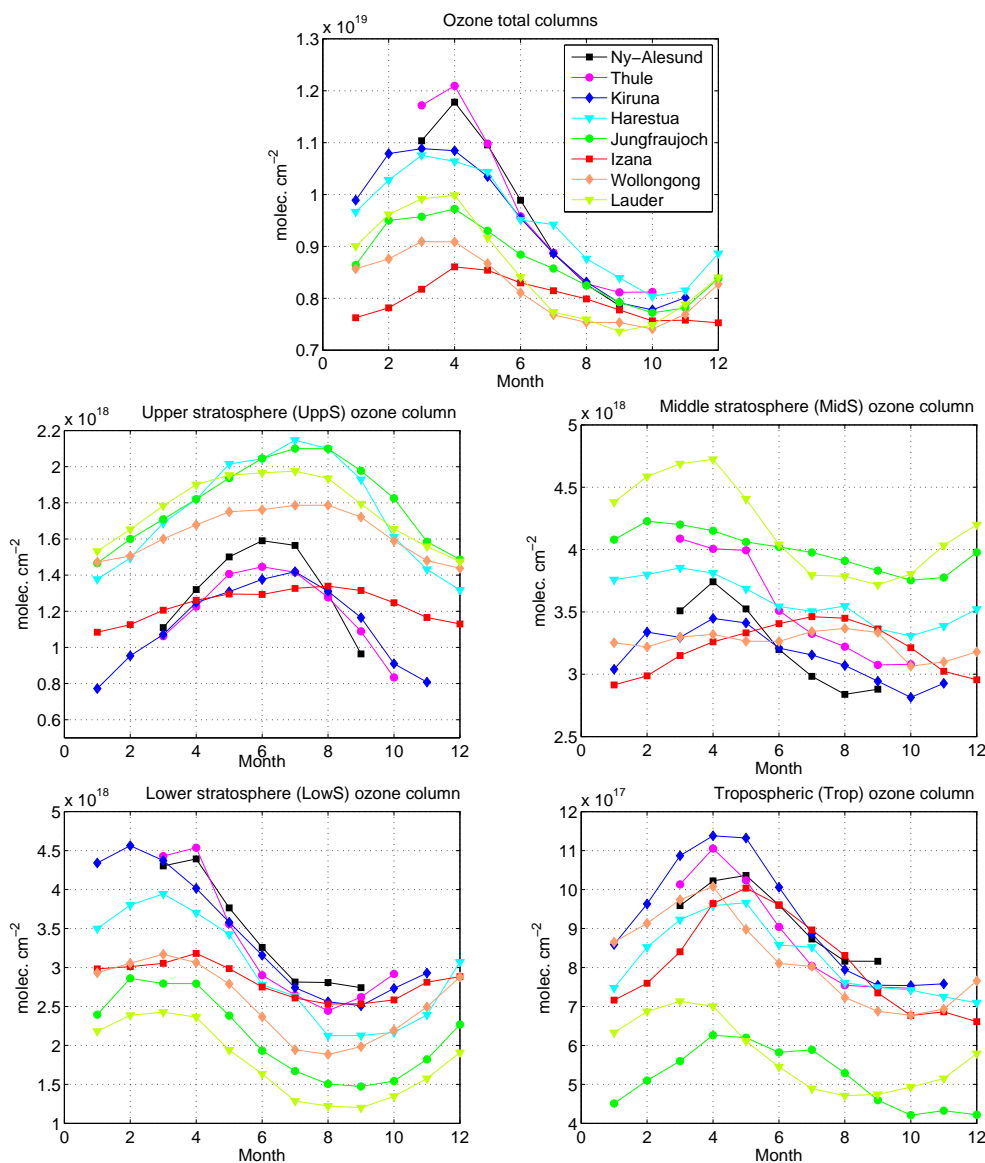


**Figure 3.** Monthly means of ozone total and partial columns for the whole periods of measurements. See Table 3 for the limits of the partial columns at each station. The seasonal cycle for Southern Hemisphere stations, Wollongong and Lauder, has been shifted by 6 months for better comparison.

NAO (North Atlantic Oscillation, closely related to AO) and the tropopause pressure (Appenzeller et al., 2000), the eddy heat flux (proportional to EPF) and the AO (Weber et al., 2011), but we let the stepwise regression model choose the most adapted proxy for each station and partial column. Concerning the equivalent latitude, we did not construct an integrated equivalent proxy valuable for the whole ozone “integrated” total column as in Wohltmann et al. (2005). Here, we simply use the equivalent latitude calculated from ERA Interim reanalysis (Dee et al., 2011) at three altitude levels corresponding approximately to the middle of our three stratospheric layers (ELL for LowS, ELM for MidS, and ELU for UppS; see Table 3 for the layer limits), namely at 370, 550,

and 950 K, respectively, for all stations except Izaña and Wollongong (460, 700, and 1040 K, respectively).

Lastly, the volume of polar stratospheric clouds (VPSC) is used as a proxy for polar ozone loss (e.g., Brunner et al., 2006). The VPSC proxy has been multiplied by the effective equivalent stratospheric chlorine (EESC) time series calculated with a mean age of air of 5.5 years, in order to take into account the time for the ozone-depleting substances to reach the poles ([http://acdb-ext.gsfc.nasa.gov/Data\\_services/automailer/index.html](http://acdb-ext.gsfc.nasa.gov/Data_services/automailer/index.html)). To account for the cumulative effect over months of the EPF and the VPSC\*EESC proxies on ozone, we have followed the approach of Brunner et al.

**Table 4.** Name, short description, and source of the proxies that have been tested in the stepwise regression model.

| Name      | Description   | Source  |
|-----------|---|---|
| SOLAR     | solar radio flux at 10.7 cm   | ftp://ftp.ngdc.noaa.gov/STP/SOLAR_DATA/SOLAR_RADIO/FLUX/Penticton_Adjusted/monthly/MONTHLY.ADJ                            |
| QBO30     | zonal winds measured at Singapore at 30 hPa   | http://www.geo.fu-berlin.de/en/met/ag/strat/produkte/qbo/index.html   |
| QBO10     | zonal winds measured at Singapore at 10 hPa   | http://www.geo.fu-berlin.de/en/met/ag/strat/produkte/qbo/index.html   |
| ENSO      | multivariate ENSO index (MEI)   | http://www.esrl.noaa.gov/psd/enso/mei/  |
| AO/AAO    | Arctic Oscillation  | http://www.cpc.ncep.noaa.gov/products/precip/CWlink/daily_ao_index/monthly.ao.index.b50.current.ascii                     |
|           | Antarctic Oscillation   | http://www.cpc.ncep.noaa.gov/products/precip/CWlink/daily_ao_index/aa0/monthly.aa0.index.b79.current.ascii                |
| TP        | tropopause pressure   | http://www.esrl.noaa.gov/psd/data/gridded/data.ncep.reanalysis.tropopause.html  |
| EL(L/M/U) | equivalent latitude at three altitude levels:<br>370, 550, and 950 K: high-/mid-latitude stations<br>460, 700, and 1040 K: subtropical stations | calculated at BIRA from ERA interim reanalysis  |
| EPF       | vertical component of the EP flux   | http://www.awi.de/en/research/research_divisions/climate_science/atmospheric_circulations/projects/candidoz/ep_flux_data/ |
| VPSC      | volume of polar stratospheric clouds  | calculated at FMI   |

(2006) (see their Eq. 4), with the same dependence of their constant  $\tau$  on season and latitude of the station.

For the two QBO proxies (30 and 10 hPa), if retained in the stepwise procedure, four seasonal parameters can be added to the model. The  $A_k \cdot X_k(t)$  term of Eq. (2) is then replaced by

$$(A_k + A_{k+1} \cdot \cos(2\pi t/12) + A_{k+2} \cdot \sin(2\pi t/12) + A_{k+3} \cdot \cos(4\pi t/12) + A_{k+4} \cdot \sin(4\pi t/12)) \cdot X_k(t). \quad (3)$$

Depending on the station and on the layer, none, one or both of the two proxies QBO30 and QBO10 will be retained in the model, with or without their additional seasonal parameters. We will call from here on “QBO contribution” the sum of all possible contributions of QBO30 and QBO10.

Since the time series involved in the present study start at the earliest in 1995, we do not include two commonly used explanatory variables: the aerosol optical thickness needed to represent the effect on ozone of the large volcanic eruptions of El Chichón (1982) and Mount Pinatubo (1991), and the EESC proxy which can be used as direct proxy for the halogen loading of the stratosphere instead of the piecewise linear trend (PWLTL) with a turnaround in 1996/1997 often used in time series starting well before this turnaround point (WMO, 2010). Our linear-trend estimates are therefore better comparable to the studies which use the PWLTL method. At polar stations, the turnaround is occurring a few years later, so that the use of the EESC proxy could be an alternative to the simple linear trend for these stations. However, we preferred to adopt the same approach for all the stations. It is possible that when the FTIR record is longer, one will be able to distinguish between the EESC impact on ozone and a possible additional trend due to processes that are not represented in the model.

## 4 Results and discussion

In Fig. 4, we show the individual contribution  $C_{\text{frac}}$  of each proxy retained by the stepwise procedure to the coefficient of determination  $R^2 = \sum C_{\text{frac}}$ , for each station and partial column. The individual contribution  $C_{\text{frac}}$  of a proxy is the product of the standardized regression coefficient of this proxy with the correlation coefficient between the proxy and the observations (Scherrer, 1984). In Fig. 4, the seasonal parameters’ contribution ( $A_1$ –  $A_4$  in Eq. 2), which gives in most cases the very dominant part of the explained variability, is not shown for better clarity of the other proxies’ contribution. However, we give it for completeness in Table 5, together with  $R^2$ . In the following discussion, we will highlight some selected features which are visible in the ozone time series and which can be attributed to a specific proxy. The final MLR model is the sum of all the significant proxies and, therefore, the effect of a specific proxy can be visible in the plots in some years, but masked in other years.

In Table 6, we give the annual ozone trend at each station for each layer obtained with the stepwise multiple linear regression model. The uncertainties on the trends correspond to the 95 % confidence interval. A trend is considered significant if it is larger than the uncertainty.

### 4.1 High latitude stations

In addition to the three Arctic stations Ny-Ålesund, Thule and Kiruna, we will consider Harestua (60° N) as a high latitude station since, in terms of trends, Harestua appears to behave similarly to the Arctic stations.

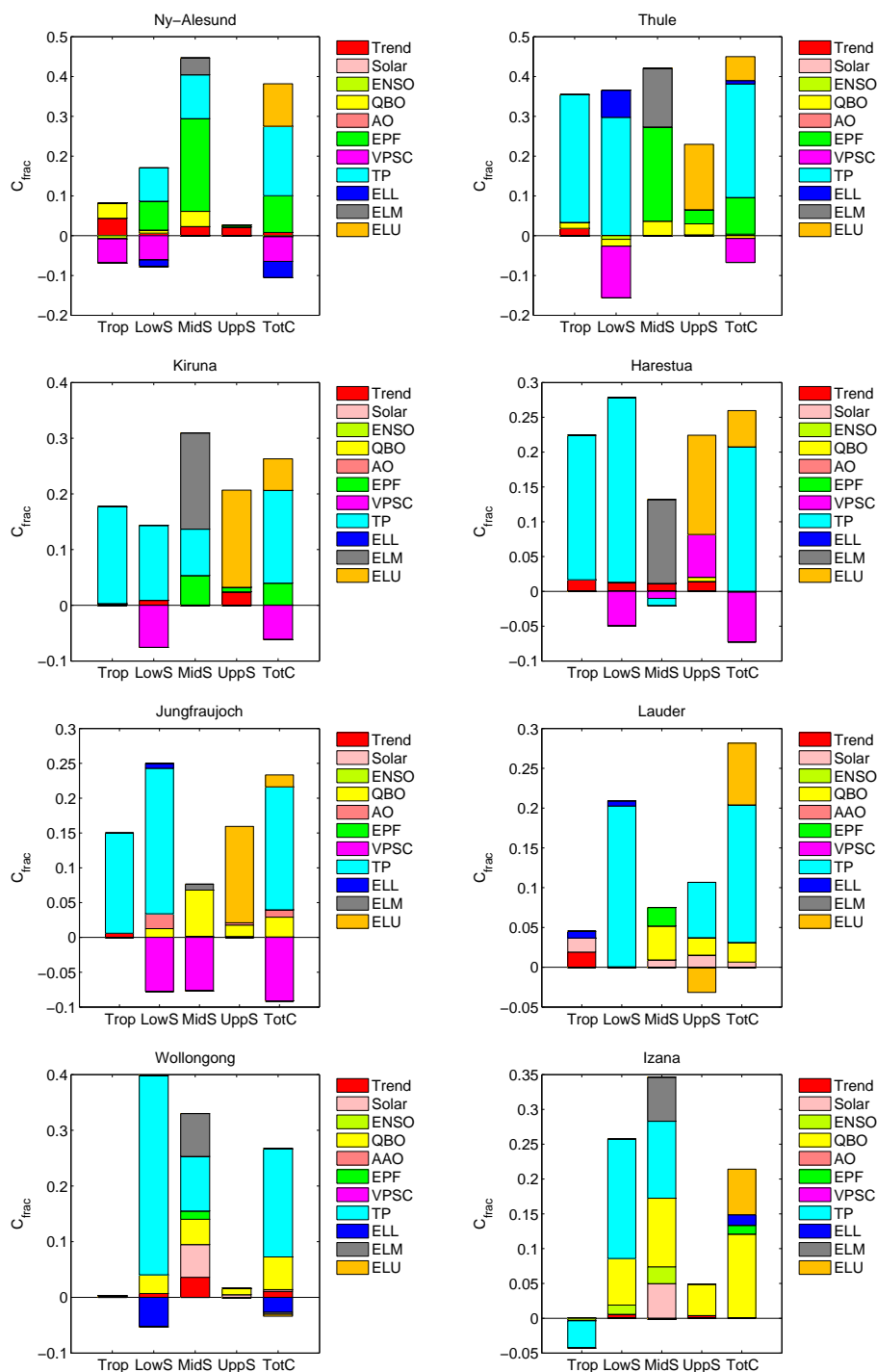


**Figure 4.** Individual contributions  $C_{\text{frac}}$  of the proxies to the coefficient of determination  $R^2$ .  $R^2$  and the dominant contribution of the seasonal cycle  $C_{\text{seas}}$  are given in Table 5.

#### 4.1.1 Tropospheric (Trop) columns

In the troposphere, the high latitude stations, except Kiruna, show negative significant ozone trends (Table 6). The spatial and temporal variability in the Arctic and the different

sampling at the stations Thule/Ny-Ålesund due to polar night (see Fig. 2) makes it difficult to compare the trend results. We see in Fig. 5 that at Ny-Ålesund the negative trend occurs in the second part of the period (2004–2012), which is also observed at Thule (not shown). On the contrary, at Harestua, the

**Table 5.** Coefficient of determination  $R^2$  and contribution of the seasonal cycle  $C_{\text{seas}}$  determined within the final model. See Table 3 for the limits of the layers, different for subtropical stations and mid-/high-latitude stations.

| FTIR station | Trop                                     | LowS                                     | MidS                                     | UppS                                     | Total columns                            |
|--------------|--|--|--|--|--|
| Ny-Ålesund   | $R^2 = 0.75$<br>$C_{\text{seas}} = 0.73$ | $R^2 = 0.92$<br>$C_{\text{seas}} = 0.82$ | $R^2 = 0.72$<br>$C_{\text{seas}} = 0.27$ | $R^2 = 0.74$<br>$C_{\text{seas}} = 0.72$ | $R^2 = 0.95$<br>$C_{\text{seas}} = 0.68$ |
| Thule        | $R^2 = 0.86$<br>$C_{\text{seas}} = 0.50$ | $R^2 = 0.92$<br>$C_{\text{seas}} = 0.71$ | $R^2 = 0.83$<br>$C_{\text{seas}} = 0.41$ | $R^2 = 0.81$<br>$C_{\text{seas}} = 0.58$ | $R^2 = 0.96$<br>$C_{\text{seas}} = 0.58$ |
| Kiruna       | $R^2 = 0.85$<br>$C_{\text{seas}} = 0.67$ | $R^2 = 0.89$<br>$C_{\text{seas}} = 0.82$ | $R^2 = 0.54$<br>$C_{\text{seas}} = 0.23$ | $R^2 = 0.78$<br>$C_{\text{seas}} = 0.58$ | $R^2 = 0.89$<br>$C_{\text{seas}} = 0.69$ |
| Harestua     | $R^2 = 0.77$<br>$C_{\text{seas}} = 0.54$ | $R^2 = 0.74$<br>$C_{\text{seas}} = 0.51$ | $R^2 = 0.36$<br>$C_{\text{seas}} = 0.25$ | $R^2 = 0.67$<br>$C_{\text{seas}} = 0.45$ | $R^2 = 0.75$<br>$C_{\text{seas}} = 0.56$ |
| Jungfraujoch | $R^2 = 0.73$<br>$C_{\text{seas}} = 0.58$ | $R^2 = 0.83$<br>$C_{\text{seas}} = 0.66$ | $R^2 = 0.53$<br>$C_{\text{seas}} = 0.53$ | $R^2 = 0.93$<br>$C_{\text{seas}} = 0.77$ | $R^2 = 0.81$<br>$C_{\text{seas}} = 0.67$ |
| Izaña        | $R^2 = 0.83$<br>$C_{\text{seas}} = 0.87$ | $R^2 = 0.72$<br>$C_{\text{seas}} = 0.46$ | $R^2 = 0.80$<br>$C_{\text{seas}} = 0.45$ | $R^2 = 0.69$<br>$C_{\text{seas}} = 0.64$ | $R^2 = 0.77$<br>$C_{\text{seas}} = 0.56$ |
| Wollongong   | $R^2 = 0.69$<br>$C_{\text{seas}} = 0.69$ | $R^2 = 0.86$<br>$C_{\text{seas}} = 0.52$ | $R^2 = 0.42$<br>$C_{\text{seas}} = 0.09$ | $R^2 = 0.77$<br>$C_{\text{seas}} = 0.75$ | $R^2 = 0.87$<br>$C_{\text{seas}} = 0.63$ |
| Lauder       | $R^2 = 0.89$<br>$C_{\text{seas}} = 0.85$ | $R^2 = 0.94$<br>$C_{\text{seas}} = 0.73$ | $R^2 = 0.78$<br>$C_{\text{seas}} = 0.70$ | $R^2 = 0.89$<br>$C_{\text{seas}} = 0.82$ | $R^2 = 0.95$<br>$C_{\text{seas}} = 0.66$ |

**Table 6.** Annual trend (in % decade<sup>-1</sup>) and their 95 % uncertainty ranges. Due to polar night, the measurements at Ny-Ålesund, Thule and Kiruna cover only the mid-March–September, late-February–mid-October, and mid-January–mid-November periods, respectively. All time series end in September/December 2012 for the present study. The time of start is repeated for each station. See Table 3 for the limits of the layers, different for subtropical stations and mid-/high-latitude stations. Trends indicated in bold are significant.

| FTIR station   | Trop              | LowS              | MidS              | UppS              | Total columns     |
|----------------|-------------------|-------------------|-------------------|-------------------|-------------------|
| Ny-Ålesund     | <b>-5.8 ± 3.2</b> | <b>-4.2 ± 3.1</b> | <b>-5.5 ± 3.8</b> | <b>+6.7 ± 5.3</b> | <b>-3.0 ± 1.5</b> |
| 1995           |                   |                   |                   |                   |                   |
| Thule          | <b>-5.3 ± 4.4</b> | -0.4 ± 6.3        | +0.2 ± 4.4        | -2.3 ± 6.5        | -2.1 ± 2.6        |
| 1999 (October) |                   |                   |                   |                   |                   |
| Kiruna         | -0.9 ± 2.5        | <b>-3.9 ± 2.6</b> | +0.4 ± 2.6        | <b>+7.4 ± 3.4</b> | -0.3 ± 1.6        |
| 1996           |                   |                   |                   |                   |                   |
| Harestua       | <b>-3.1 ± 2.0</b> | <b>-5.3 ± 4.6</b> | <b>+4.8 ± 4.3</b> | <b>+7.8 ± 5.5</b> | +1.0 ± 2.2        |
| 1995           |                   |                   |                   |                   |                   |
| Jungfraujoch   | -2.5 ± 2.7        | -0.5 ± 3.3        | -0.6 ± 1.2        | +0.9 ± 1.0        | -0.4 ± 1.2        |
| 1995           |                   |                   |                   |                   |                   |
| Izaña          | +0.7 ± 2.8        | -1.7 ± 2.2        | -0.1 ± 2.0        | +1.6 ± 2.6        | +0.5 ± 1.2        |
| 1999           |                   |                   |                   |                   |                   |
| Wollongong     | -2.2 ± 2.8        | <b>+3.1 ± 2.7</b> | <b>+4.0 ± 2.0</b> | +0.2 ± 1.6        | <b>+1.9 ± 1.1</b> |
| 1996           |                   |                   |                   |                   |                   |
| Lauder with /  | <b>+7.7 ± 3.5</b> | -3.8 ± 4.1        | -0.2 ± 3.5        | <b>+2.8 ± 2.4</b> | -0.3 ± 1.8        |
| without SOLAR  | <b>+5.0 ± 4.4</b> | –                 | -1.1 ± 3.4        | +1.7 ± 2.4        | -0.6 ± 1.9        |
| 2001           |                   |                   |                   |                   |                   |

negative trend is occurring in the 1999–2007 period (Fig. 5, lower left panel). The second line of Fig. 5 shows the partial columns where the seasonal cycle is removed to emphasize

the interannual variability, and the effect of individual proxies showing interannual differences. We have added in the third line of Fig. 5 the VPSC signal, i.e., the VPSC proxy

time series multiplied by the corresponding parameter obtained in the MLR process ( $A_k \cdot X_k(t)$  in Eq. 2). We see that the particular low tropospheric values in 1995, 2005 and 2011 at Ny-Ålesund can be related to the VPSC proxy and, therefore, by the influence of lower stratospheric ozone variability on the tropospheric columns. At the three other stations, this VPSC impact was not found to be significant, and the main driver of tropospheric variability is found to be the tropopause pressure TP (Fig. 4). The larger VPSC value in 1996 does not lead to a larger decrease in tropospheric ozone because it is compensated by a positive QBO signal, while the small ozone value in 2004 is related to a negative QBO signal (not shown).

As expected, the large VPSC values in 1995, 2005 and 2011 have also a significant impact on the lower stratospheric (LowS) values at Ny-Ålesund (middle column of Fig. 5), as well as in 1996, since the negative effect is not compensated by the QBO signal as in Trop. We can note that the VPSC impact is 10 times larger in LowS than in Trop (different scales in Fig. 5).

#### 4.1.2 Lower stratospheric (LowS) columns

The VPSC proxy is found significant at the four high latitude stations for the lower stratospheric columns, being the main driver of ozone variability after TP (Fig. 4). We give the example of Ny-Ålesund and Kiruna in Fig. 5, where the effect of large amount of VPSC in 1996, 2005, and 2011 is clearly visible in both monthly means and deseasonalized time series. We show in addition the EPF and TP signals at Ny-Ålesund and Kiruna, respectively, in the bottom panel. It can be seen that the TP signal at Kiruna in 2005 also contributed to even lower ozone that particular year. The larger LowS values at Ny-Ålesund in 1999 are due to a combination of the TP (not shown) and EPF signals.

In the lower stratosphere, at all high latitude stations, except Thule, we observe significant negative trends (Table 6). At Thule, the shorter time period associated with the high variability of this layer at high latitude gives a large uncertainty on the trend.

#### 4.1.3 Middle stratospheric (MidS) columns

The results are mixed for the middle stratospheric layers, as noticed previously for the seasonal cycles. The trend is significantly negative at Ny-Ålesund and non-significant at Thule. The trend is non-significant at Kiruna, and significantly positive at Harestua. The EPF proxy explains about 25 % of the variability at Ny-Ålesund and Thule, and about 5 % at Kiruna (Fig. 4). This is illustrated in Fig. 6 for Ny-Ålesund and Thule, where we see nicely the same features at both stations in the middle stratospheric columns (e.g., higher columns in 2009, 2010; lower columns in 2011), associated with the EPF time series.

#### 4.1.4 Upper stratospheric (UppS) columns

In the upper stratosphere, the three stations with similar time periods show a significant positive trend. In the three cases, the increase in ozone partial columns occurs in the 1995–2003 period, after which a leveling off is observed (Fig. 7). If we run the MLR model on the same time period as Thule (October 1999–2012), all the stations show non-significant trends. Since the EESCs were still increasing until about 2000 at polar regions (WMO, 2010), the significant positive trends obtained at high latitude stations in the upper stratosphere cannot be explained by the effect of the Montreal Protocol on ozone depleting substances. At present we do not have an explanation for this increase in ozone during the 1995–2003 period. The 11-year solar cycle might contribute to it, since the increase in solar activity from 1996 to its maximum in 2001–2002 is in phase with the ozone increase during the same period. The solar cycle signal at Ny-Ålesund, shown in Fig. 7 as an illustration, turns out to be non-significant after the Cochrane–Orcutt transformation is applied, so its contribution is small and not visible in Fig. 4. The solar cycle might be found non-significant at the other stations because the expected decrease of ozone during the declining phase of the solar cycle (2002–2009) is not observed. This could be a sign that this decrease is compensated by a positive linear trend, which could be due to the declining EESCs, but also to the increase of greenhouse gases (WMO, 2010). More years are needed to understand unequivocally the increase in 1995–2003, followed by a leveling off, and distinguish between the ozone responses due to solar cycle, EESCs and other possible proxies not included in the present study.

#### 4.1.5 Total columns

We observe that the total column ozone trends are small and non-significant at all high latitude stations, except at Ny-Ålesund ( $-3.0 \pm 1.5 \%$  decade<sup>-1</sup> or  $-10.8 \pm 5.6$  DU decade<sup>-1</sup>). The negative trend at Ny-Ålesund occurs in the 2003–2012 period, as for the lowest altitude layers. At all stations, the dominant contributions to the total column variability are the TP, the VPSC, the ELU, and, except at Harestua, the EPF proxies. We see nicely in Table 5, how well the proxies explained the additional variability at the Arctic stations, e.g., at Ny-Ålesund  $R^2 = 0.95$ , compared to the contribution of the seasonal cycle  $C_{\text{seas}} = 0.68$ .

#### 4.2 Mid-latitude and subtropical stations

In this study, we have two mid-latitude stations (Jungfraujoch at 47° N and Lauder at 45° S) and two subtropical stations (Izaña at 28° N and Wollongong 34° S).

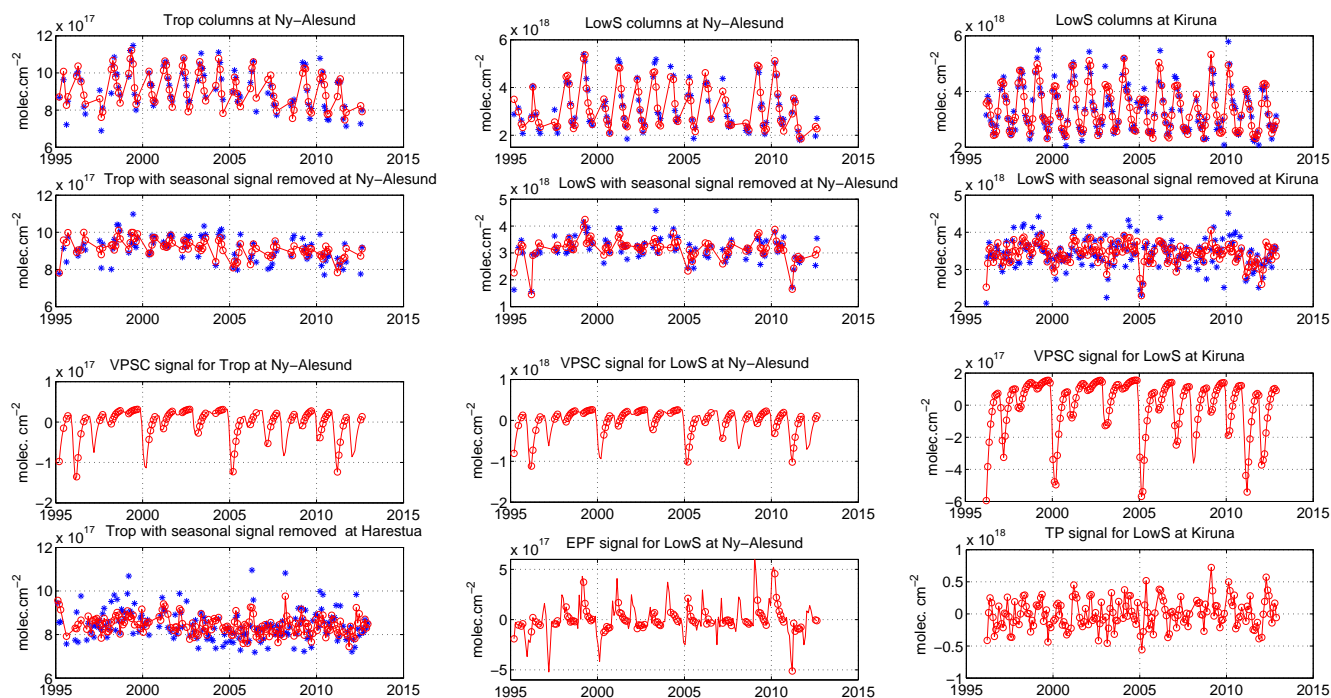


**Figure 5.** Left (top to bottom panels): (1) monthly means of the tropospheric columns (Trop) at Ny-Ålesund (blue: FTIR, red: MLR model); (2) same but with the seasonal signal removed; (3) the VPSC signal obtained from the MLR model for Trop at Ny-Ålesund, for each month of the period (red line), and at each FTIR observed month (red circle); (4) monthly means of Trop at Harestua with the seasonal cycle removed. Middle panels: (1–3) same as left panels but for the lower stratospheric columns (LowS) at Ny-Ålesund; (4) the EPF signal obtained for the LowS at Ny-Ålesund. Right panels: (1–3) same as middle panels but at Kiruna; (4) the tropopause pressure (TP) signal obtained for the LowS at Kiruna.

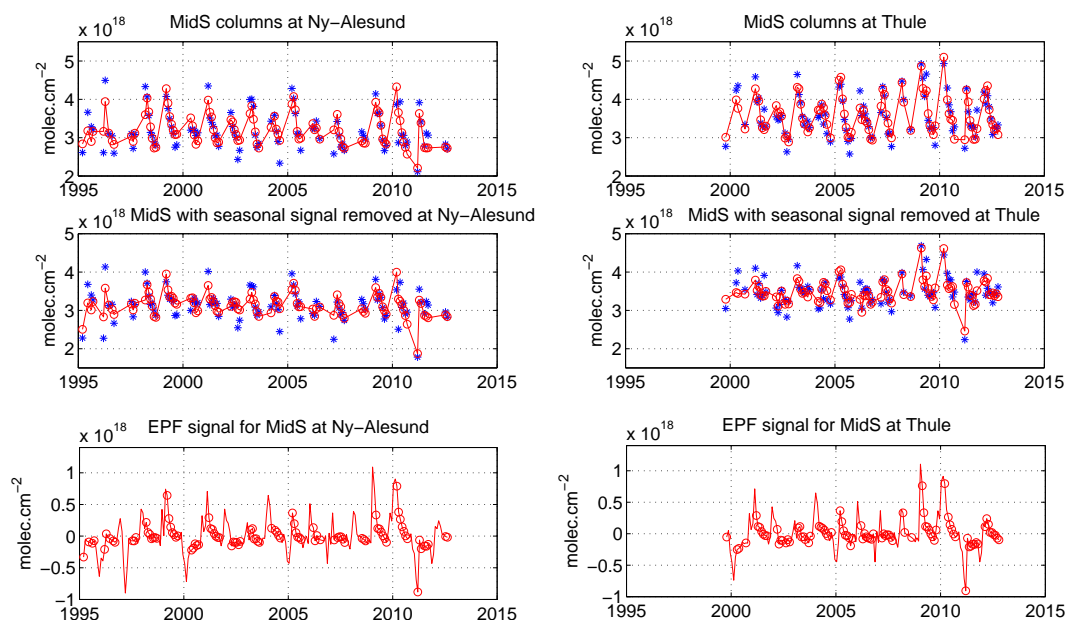


**Figure 6.** Top panels: monthly means of the middle stratospheric columns (MidS) at Ny-Ålesund (left) and Thule (right) (blue: FTIR, red: MLR model). Middle panels: same but with the seasonal signal removed. Bottom panels: the EPF signal obtained in each case from the MLR model, for each month of the period (red line), and at each FTIR observed month (red circle).

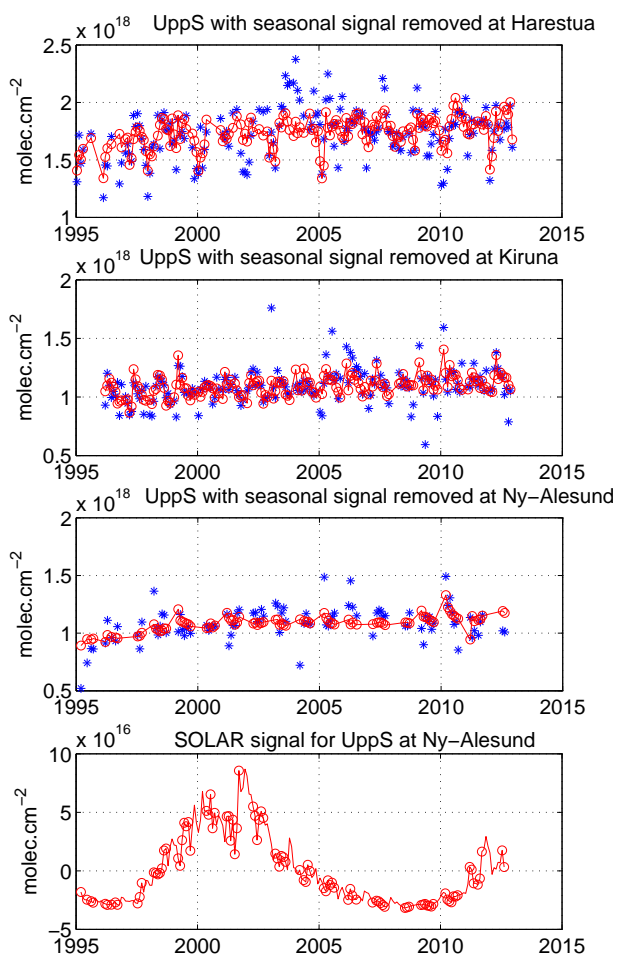


**Figure 7.** Monthly means of the upper stratospheric columns (UppS) with the seasonal cycle removed at, from top to bottom: Harestua, Kiruna and Ny-Ålesund (blue: FTIR, red: MLR model). Bottom panel: the solar cycle signal obtained at Ny-Ålesund from the MLR model, before the Cochrane–Orcutt transformation.

#### 4.2.1 Tropospheric (Trop) columns

The tropospheric trends are non-significant at Jungfraujoch, Izaña and Wollongong, and significantly positive at Lauder. The trend at Jungfraujoch is  $-2.5 \pm 2.7 \%$  decade $^{-1}$ ; however, we see in Fig. 8 that the tropospheric columns are increasing up to 1999 and then show a linear decrease, in agreement with aircraft and surface alpine sites in the study of Logan et al. (2012). If we limit our time period to the 1998–2008 period as in Logan et al. (2012), we also find a significant negative trend ( $-6.3 \pm 4.9 \%$  decade $^{-1}$ ). However, this is largely due to the high ozone values 1998–1999, and for the period 2000–2012 we obtain still a non-significant trend of  $-2.9 \pm 3.4 \%$  decade $^{-1}$ . At Izaña, the tropospheric trends derived from ozonesondes were found non-significant in García et al. (2012), in agreement with our study, but the uncertainties were large. The situation is more mixed in the Southern Hemisphere: the tropospheric trend at Wollongong

is not significant while it is significantly positive at Lauder ( $+7.7 \pm 3.5 \%$  decade $^{-1}$ ). The trend at Lauder is in agreement with the study of Oltmans et al. (2013), who obtain about  $+5 \%$  decade $^{-1}$  in the lower and middle troposphere with ozonesonde measurements at Lauder. We find a significant positive impact of the solar cycle at Lauder and it is clearly seen in Fig. 8. This is not in agreement with Chandra et al. (1999), in which the solar cycle shows a strong but negative impact on tropospheric columns for a non-polluted region. At Lauder, presently only a short time period (2001–2012) is available for trend studies, and we hope to have more clarification on this subject with more years of data. However, if we remove the solar cycle proxy from the MLR model, we still obtain a significant trend of  $+5.0 \pm 4.4 \%$  decade $^{-1}$ . For this short time series, we have added in Table 6 the trends that are obtained if the solar cycle is removed from the model.

#### 4.2.2 Lower stratospheric (LowS) columns

The trends in the lower stratosphere are non-significant at Jungfraujoch, Izaña and Lauder, and significantly positive at Wollongong. The cause of the significant positive trend at Wollongong is not fully explained at present. A part of it is due to a small negative trend in the ELL proxy. If we remove this proxy from the MLR model, we observe a non-significant positive trend of  $+2.4 \pm 2.8 \%$  decade $^{-1}$ .

The dominant proxy is TP for all stations. At the Jungfraujoch station, the VPSC proxy, which in the case of Jungfraujoch corresponds to the transport of polar ozone loss to mid-latitudes, explains about 8 % of the variability (Fig. 4). The VPSC proxy is non-significant at the southern hemispheric station Lauder, in agreement with the more stable and isolated vortex in the Antarctic compared to the Arctic. The AO proxy is found significant at Jungfraujoch while the corresponding AAO proxy is non-significant at Lauder.

We show the time series of the lower stratospheric columns at Jungfraujoch in Fig. 9 together with the AO and QBO signals. We see that in 2010 ozone shows larger values and that this is explained by the combination of a very negative AO index (the corresponding parameter in the MLR is negative and gives the positive signal in 2010 shown in Fig. 9) and easterly phase of the QBO. This is in agreement with Nair et al. (2013), who applied a MLR model to the mean of ozone anomalies at Observatoire de Haute-Provence (OHP) from different instruments (lidar, ozonesondes and satellites). However, we did not find a significant contribution from the EPF proxy, which according to Nair et al. (2013) also contributed to the high ozone values in 2010. We can state that our vertical and total column ozone trends are in agreement with the Nair et al. (2013) results when taking the error bars into account, but the latter study found significant positive trends at OHP while our trends at Jungfraujoch are all non-significant.

As expected, the QBO contribution to ozone variability is more important at the subtropical station Izaña, which is

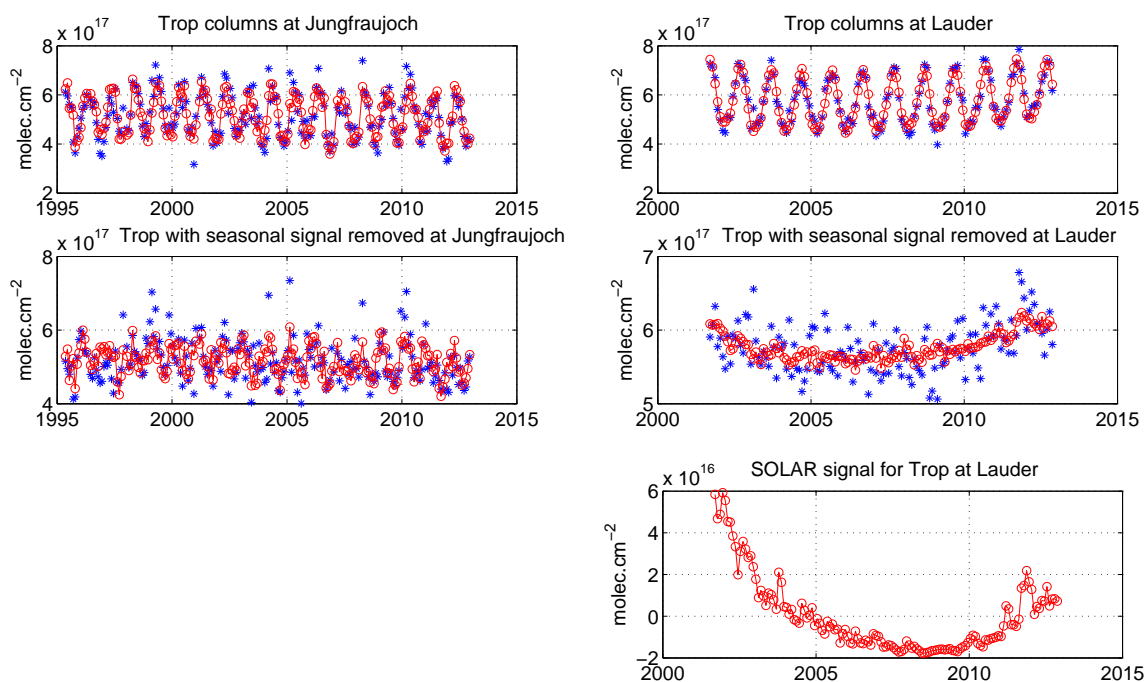


**Figure 8.** Top panels: monthly means of the tropospheric columns (Trop) at Jungfraujoch (left) and Lauder (right) (blue: FTIR, red: MLR model). Middle panels: same but with the seasonal signal removed. Bottom panel: the solar cycle signal obtained at Lauder from the MLR model.

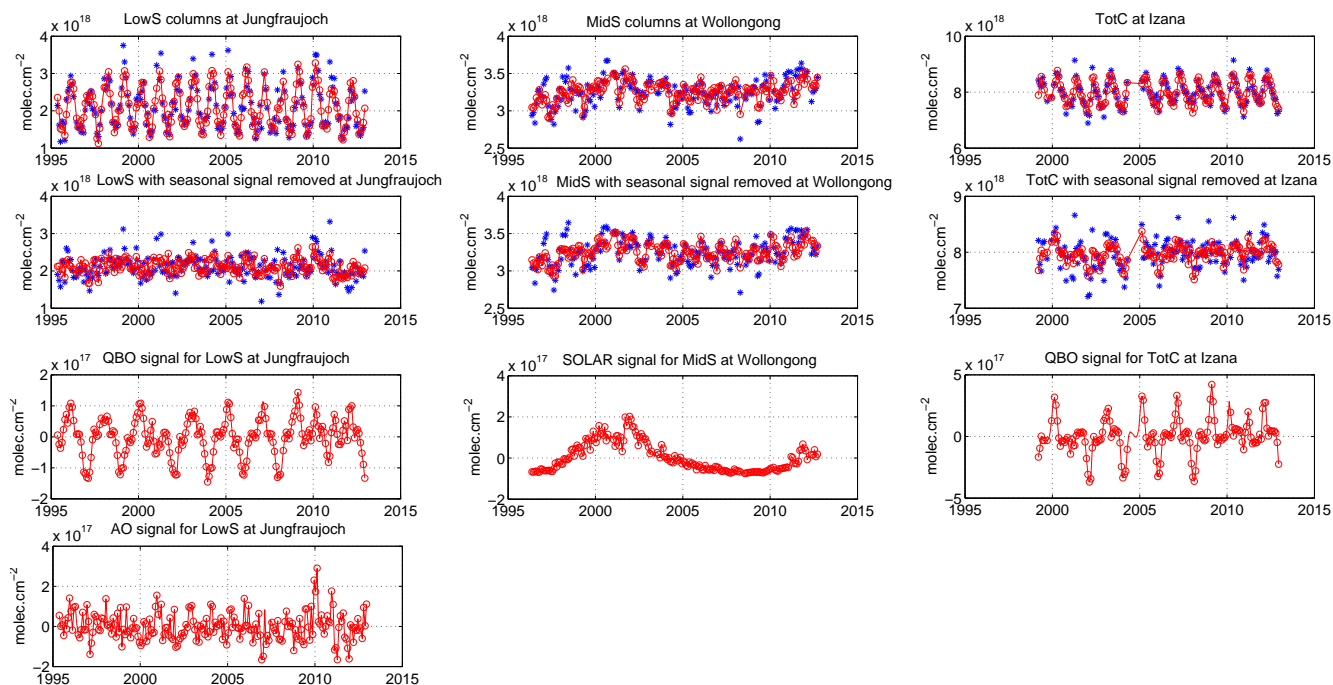


**Figure 9.** Top panels: monthly means of the lower stratospheric columns (LowS) at Jungfraujoch (left), middle stratospheric columns (MidS) at Wollongong (middle), and total columns (TotC) at Izaña (right) (blue: FTIR, red: MLR model). Middle panels: same but with the seasonal signal removed. Bottom panels: QBO and AO signals obtained from the MLR model at Jungfraujoch (left), SOLAR signal at Wollongong (middle), and QBO signal at Izaña (right).

also the only station where the ENSO proxy was found to make a significant, but small, contribution to the variability (Fig. 4). We illustrate the QBO effect at Izaña in Fig. 9 for total columns.

#### 4.2.3 Middle stratospheric (MidS) columns

The situation for the middle stratosphere is very similar to that of the lower stratosphere: all trends are found non-significant except at Wollongong where it is positive. It is in this 23–32 km layer for subtropical stations that the solar cycle shows the most important contribution (Fig. 4). This is not what has been reported in Randel and Wu (2007) and Tourpali et al. (2007), where the ozone response to the solar cycle was maximum in the tropical lower and upper stratosphere, and minimum in the middle stratosphere. At Wollongong, the middle stratospheric ozone response is about 6 % between solar minimum and solar maximum (see Fig. 9) while values of 1 % have been reported (Sioris et al., 2014) at about 25 km. However, the recent work of Chiodo et al. (2014) shows that the apparent solar cycle signal in the tropical lower stratosphere for the period 1960–2004 is due to the two volcanic eruptions of El Chichón in 1982 and Mt. Pinatubo in 1991, and the authors find robust solar cycle signals only in the middle and upper stratosphere. In the upper stratospheric layer at Wollongong, the response to the solar cycle is indeed also significant and is about 2.5 % between solar minimum and solar maximum which is in agreement with previous studies (WMO, 2010). At Izaña, the solar contribution is found negative in the 23–32 km layer, which seems doubtful. Again, this concerned one of the shortest time series of the study (1999–2012) and could be corrected with future measurements.

#### 4.2.4 Upper stratospheric (UppS) columns

The trends in the upper stratospheric layer are all positive in these latitudes but significant only at Lauder ( $+2.8 \pm 2.4 \%$  decade<sup>-1</sup>). Our trend at Jungfraujoch station ( $+0.9 \pm 1.0 \%$  decade<sup>-1</sup>) corresponds well to the observed trend ( $+1.5 \%$  decade<sup>-1</sup>) at OHP in Nair et al. (2013) in the 31–39 km range, although it is found significant in this latter study. The MLR model explains 93 % of the variability at Jungfraujoch ( $R^2 = 0.93$ ), namely, 77 % of the variability comes from the seasonality and the remaining 16 % from the proxies, mainly the ELU and QBO (see Fig. 4). At Lauder, the trend in the 30–40 km range from lidar measurements is also found significantly positive for the period 2000–2012 with trend values ( $+2$ – $3 \%$  decade<sup>-1</sup>) similar to FTIR (W. Steinbrecht, personal communication, 2013). If we remove the solar cycle signal in the MLR for the short time series of Lauder, the trend becomes smaller and non-significant ( $+1.7 \pm 2.4 \%$  decade<sup>-1</sup>). More years of data will improve the confidence in the solar cycle signal in the short time series.

#### 4.2.5 Total columns

The total column trends are non-significant at the mid-latitude stations ( $-0.4 \pm 1.2 \%$  decade<sup>-1</sup> or  $-1.4 \pm 3.8$  DU decade<sup>-1</sup> at Jungfraujoch;  $-0.3 \pm 1.8 \%$  decade<sup>-1</sup> or  $-1.1 \pm 5.9$  DU decade<sup>-1</sup> at Lauder), non-significant at Izaña ( $+0.5 \pm 1.2 \%$  decade<sup>-1</sup> or  $+1.4 \pm 3.6$  DU decade<sup>-1</sup>), and significantly positive at Wollongong ( $+1.9 \pm 1.1 \%$  decade<sup>-1</sup> or  $+5.8 \pm 3.5$  DU decade<sup>-1</sup>). The total column trend at Jungfraujoch is in agreement within error bars with the result of Nair et al. (2013) at OHP when they use the PWLT method ( $+5.5 \pm 3.3$  DU decade<sup>-1</sup>), but again the trend at OHP is found significantly positive. When the EESC proxy is used in their study a trend of  $+4.2 \pm 0.8$  DU decade<sup>-1</sup> is found. The same behavior is seen more globally in a recent study using merged satellite data from 1979 to 2012 (Chehade et al., 2014): for the latitude of Jungfraujoch, the trends are about  $+3$ – $4$  DU decade<sup>-1</sup> for the 1997–2012 period and non-significant if the PWLT method is used, while significant when the EESC proxy is used, which decreases the uncertainty on the trends. It seems that at Jungfraujoch, our time series is still too short to observe this positive trend. At the latitude of Izaña, the merged satellite data set shows a  $+3$ – $4$  DU decade<sup>-1</sup> for the 1997–2012 period, with the more recent SBUV/SBUV-2 MOD v8.6, non-significant using the PWLT (in agreement with our study) and significant using the EESC proxy. Since our time series start at best in 1995, the EESC proxy is not really “separable” from a linear trend study at our mid-latitude and subtropical stations. When more years of data are available, the same sensitivity study (PWLT vs. EESC) could be tested at least for polar stations where the turnaround point is expected around 2000.

It is also interesting to note that, using the PWLT method, at the latitude of Wollongong, Chehade et al. (2014) found a positive significant trend of about  $+3$  DU decade<sup>-1</sup>, while at the latitude of Lauder the trend is decreased to about  $+1$  DU decade<sup>-1</sup> (non-significant) in good agreement with what FTIR observed. When they use the EESC proxy, the trend is increasing with latitude so that at the Lauder latitude it reaches about  $4$ – $5$  DU decade<sup>-1</sup>.

Our non-significant trends at Jungfraujoch, Izaña and Lauder, and positive trend at Wollongong are also in agreement with the recent study of Coldewey-Egbers et al. (2014), which provides trends using a similar period (1995–2013) of merged satellite data sets. For Wollongong, since the total column positive trend is due to the ozone trends in the lower and middle stratosphere, it cannot be attributed unambiguously to the EESCs decline.

## 5 Conclusions

We have exploited the time series of ozone total and partial columns (Trop, LowS, MidS, UppS) at eight NDACC FTIR stations (Ny-Ålesund, 79° N; Thule, 77° N; Kiruna, 68° N;

Harestua, 60° N; Jungfraujoch, 47° N; Izaña, 28° N; Wollongong, 34° S; Lauder, 45° S) to derive vertically resolved trends, using a MLR model including the main proxies well-known for impacting the ozone variability.

After the seasonal variation, the TP proxy is the dominant driver of ozone variability at all stations, mainly for the troposphere, lower stratosphere and total columns, while the EL proxy is an important contributor to the middle and upper stratosphere, as well as to the total column variabilities. At the highest latitude stations (68–79° N), the EPF proxy contributes substantially to the middle stratospheric and total column variabilities. The VPSC proxy for polar ozone loss contributes to the lower stratosphere and total column variabilities at the Arctic stations but also at Jungfraujoch, while it is non-significant at the southern hemispheric station Lauder. At the mid-latitude and subtropical stations, the QBO proxy is a substantial contributor to ozone variability, especially at the lowest latitude station, Izaña. The AO/AAO and ENSO proxies are significant only at Jungfraujoch and Izaña, respectively. At Wollongong, the 2.5 % ozone response to solar cycle in the upper layer is in agreement with previous studies, but the response in the middle stratosphere (~ 6 %) is much larger than previously reported (~ 1 %). The 11-year solar cycle effect is still subject of debate (WMO, 2010; Chiodo et al., 2014), so that an additional decade of measurements would help in fixing its real impact on ozone. This is particularly true for our shortest time series of Lauder, Izaña and Thule.

The trends at the high latitude stations are negative in the troposphere, except at Kiruna where it is non-significant. Except at Thule, the high latitude stations show significant negative trends in the lower stratosphere. The situation is mixed in the middle stratosphere where the trend is significantly negative at Ny-Ålesund, non-significant at Thule and Kiruna, and significantly positive at Harestua. The trends of the three high latitude stations with a similar time period are all positive in the upper stratosphere, but this increase is taking place during the 1995–2003 period while the EESC trends were still increasing until about 2000 in the polar region (WMO, 2010). However all four stations give non-significant trends in the upper stratosphere for the October 1999–2012 period, which could be the onset of the upper stratospheric ozone recovery at high latitude. The total column trends are non-significant at all high latitude stations, except at Ny-Ålesund where it is negative. This is in agreement (except at Ny-Ålesund) with model predictions that the Arctic March ozone recovery to 1980 levels will occur around 2026 (WMO, 2010). However, the high year-to-year total column variability at these latitudes, driven mainly by lower stratospheric variability due to the polar temperature variations, does not allow yet to draw conclusions from the current trends for Arctic total ozone in the coming few years.

The trends for mid-latitude and subtropical stations are all non-significant, except at Lauder in the troposphere and upper stratosphere and at Wollongong for the total columns and the lower and middle stratospheric columns. Some signs of the onset of ozone mid-latitude recovery are observed only in the Southern Hemisphere, while a few more years seem to be needed to observe it at the northern stations.

To conclude, among the numerous available satellite and ground-based data sets measuring vertical distributions of ozone that are useful for ozone trend evaluations (Hassler et al., 2014), the NDACC ground-based FTIR measurements have their particular assets. Indeed, several stations, well distributed around the globe, are now reaching almost 20 years of measurements and will continue measuring ozone in the future: to the eight stations of this work could be added, after homogenization of the retrieval analysis and/or few more years of data, Eureka (80°N), Rikubetsu (44°N), Bremen (53°N), Mauna Loa (20°N), and Arrival Heights (78°S). This provides long time series of ozone that are reliable over time, provided that the ILS is properly taken into account. This is also the only data set, with Umkehr measurements, that provides simultaneously total columns, tropospheric columns and three stratospheric columns that reach 40–45 km. This data set is suitable for an alternative determination of ozone vertical changes, as demonstrated in this study, but also for validation of the satellite-merged data sets and detection of possible drifts.

*Acknowledgements.* The National Center for Atmospheric Research is supported by the National Science Foundation. The observation program at Thule, Greenland, is supported under contract by the National Aeronautics and Space Administration and the site is also supported by the NSF Office of Polar Programs. We wish to thank the Danish Meteorological Institute for support at Thule. We would like to thank U. Raffalski and P. Völger for technical support at IRF Kiruna. The University of Liège team acknowledges the support of the F.R.S. – FNRS, the Fédération Wallonie-Bruxelles, the International Foundation High Altitude Research Stations Jungfraujoch and Gornergrat (HFSJG, Bern) and Meteoswiss. The NIWA Lauder MIR-FTIR project is core-funded through New Zealand's Ministry of Business, Innovation and Employment. We are grateful to the many colleagues having contributed to FTIR data acquisition at the various sites. We wish to thank S. Godin-Beekmann and M. Pastel (LATMOS) for useful discussions on equivalent latitude proxy, and R. Kivi (KMI) for discussion on ozonesonde trends in the Arctic. This study has been supported by the EU FP7 project NORS, the ESA PRODEX project A3C, as well as the AGACC-II project within the Science for a Sustainable Development research program funded by the Belgian Science Policy Office.

Edited by: M. Dameris

## References

- Appenzeller, C., Weiss, A. K., and Staehelin, J.: North Atlantic Oscillation modulates total ozone winter trends, *Geophys. Res. Lett.*, 27, 1131–1134, 2000.
- Barret, B., De Mazière, M., and Demoulin, P.: Retrieval and characterization of ozone profiles from solar infrared spectra at the Jungfraujoch, *J. Geophys. Res.*, 107, 4788, doi:10.1029/2001JD001298, 2002.
- Bodeker, G. E., Hassler, B., Young, P. J., and Portmann, R. W.: A vertically resolved, global, gap-free ozone database for assessing or constraining global climate model simulations, *Earth Syst. Sci. Data*, 5, 31–43, doi:10.5194/essd-5-31-2013, 2013.
- Brasseur, G. and Solomon, S.: *Aeronomy of the Middle Atmosphere*, 441 pp., D. Reidel Publishing Company, Dordrecht, Holland, 1984.
- Brunner, D., Staehelin, J., Maeder, J. A., Wohltmann, I., and Bodeker, G. E.: Variability and trends in total and vertically resolved stratospheric ozone based on the CATO ozone data set, *Atmos. Chem. Phys.*, 6, 4985–5008, doi:10.5194/acp-6-4985-2006, 2006.
- Chandra, S., Ziemke, J. R., and Stewart, R. W.: An 11-year solar cycle in tropospheric ozone from TOMS measurements, *Geophys. Res. Lett.*, 26, 185–188, 1999.
- Chehade, W., Weber, M., and Burrows, J. P.: Total ozone trends and variability during 1979–2012 from merged data sets of various satellites, *Atmos. Chem. Phys.*, 14, 7059–7074, doi:10.5194/acp-14-7059-2014, 2014.
- Chiodo, G., Marsh, D. R., Garcia-Herrera, R., Calvo, N., and García, J. A.: On the detection of the solar signal in the tropical stratosphere, *Atmos. Chem. Phys.*, 14, 5251–5269, doi:10.5194/acp-14-5251-2014, 2014.
- Cochrane, D. and Orcutt, G. H.: Application of least squares regression to relationships containing auto-correlated error terms, *J. Am. Stat. Assoc.*, 44, 32–61, 1949.
- Coldewey-Egbers, M., Loyola, D. G., Braesicke, P., Dameris, M., van Roozendaal, M., Lerot, C., and Zimmer, W.: A new health check of the ozone layer at global and regional scales, *Geophys. Res. Lett.*, 41, 4363–4372, doi:10.1002/2014GL060212, 2014.
- Dee, D. P., Uppala, S. M., Simmons, A. J., Berrisford, P., Poli, P., Kobayashi, S., Andrae, U., Balmaseda, M. A., Balsamo, G., Bauer, P., Bechtold, P., Beljaars, A. C. M., van de Berg, L., Bidlot, J., Bormann, N., Delsol, C., Dragani, R., Fuentes, M., Geer, A. J., Haimberger, L., Healy, S. B., Hersbach, H., Hólm, E. V., Isaksen, I., Kållberg, P., Köhler, M., Matricardi, M., McNally, A. P., Monge-Sanz, B. M., Morcrette, J.-J., Park, B.-K., Peubey, C., de Rosnay, P., Tavolato, C., Thépaut, J.-N., and Vitart, F.: The ERA-Interim reanalysis: configuration and performance of the data assimilation system, *Q. J. Roy. Meteor. Soc.*, 137, 553–597, doi:10.1002/qj.828, 2011.
- Frossard, L., Rieder, H. E., Ribatet, M., Staehelin, J., Maeder, J. A., Di Rocco, S., Davison, A. C., and Peter, T.: On the relationship between total ozone and atmospheric dynamics and chemistry at mid-latitudes – Part 1: Statistical models and spatial fingerprints of atmospheric dynamics and chemistry, *Atmos. Chem. Phys.*, 13, 147–164, doi:10.5194/acp-13-147-2013, 2013.
- García, O. E., Schneider, M., Redondas, A., González, Y., Hase, F., Blumenstock, T., and Sepúlveda, E.: Investigating the long-term evolution of subtropical ozone profiles applying ground-based FTIR spectrometry, *Atmos. Meas. Tech.*, 5, 2917–2931, doi:10.5194/amt-5-2917-2012, 2012.
- García, R. R., Marsh, D. R., Kinnison, D. E., Boville, B. A., and Sassi, F.: Simulation of secular trends in the middle atmosphere, 1950–2003, *J. Geophys. Res.*, 112, D09301, doi:10.1029/2006JD007485, 2007.
- Hase, F., Blumenstock, T., and Paton-Walsh, C.: Analysis of the instrumental line shape of high-resolution Fourier transform IR spectrometers with gas cell measurements and new retrieval software, *Appl. Optics*, 38, 3417–3422, 1999.
- Hase, F.: *Inversion von Spurengasprofilen aus hochaufgelösten bodengebundenen FTIR-Messungen in Absorption*, Dissertation, Wissenschaftliche Berichte Forschungszentrum Karlsruhe, FZKA 6512; ISSN 0947–8620, Forschungszentrum Karlsruhe, Karlsruhe, Germany, 2000.
- Hase, F., Hannigan, J. W., Coffey, M. T., Goldman, A., Höpfner, M., Jones, N. B., Rinsland, C. P., and Wood, S. W.: Intercomparison of retrieval codes used for the analysis of high-resolution, ground-based FTIR measurements, *J. Quant. Spectrosc. Ra.*, 87, 25–52, 2004.
- Hassler, B., Petropavlovskikh, I., Staehelin, J., August, T., Bhartiya, P. K., Clerbaux, C., Degenstein, D., Mazière, M. De, Dinelli, B. M., Dudhia, A., Dufour, G., Frith, S. M., Froidevaux, L., Godin-Beekmann, S., Granville, J., Harris, N. R. P., Hoppel, K., Hubert, D., Kasai, Y., Kurylo, M. J., Kyrölä, E., Lambert, J.-C., Levelt, P. F., McElroy, C. T., McPeters, R. D., Munro, R., Nakajima, H., Parrish, A., Raspollini, P., Remsberg, E. E., Rosenlof, K. H., Rozanov, A., Sano, T., Sasano, Y., Shiotani, M., Smit, H. G. J., Stiller, G., Tamminen, J., Tarasick, D. W., Urban, J., van der A, R. J., Veeffkind, J. P., Vigouroux, C., von Clarmann, T., von Savigny, C., Walker, K. A., Weber, M., Wild, J., and Zawodny, J. M.: Past changes in the vertical distribution of ozone – Part 1: Measurement techniques, uncertainties and availability, *Atmos. Meas. Tech.*, 7, 1395–1427, doi:10.5194/amt-7-1395-2014, 2014.
- Kyrölä, E., Laine, M., Sofieva, V., Tamminen, J., Päiväranta, S.-M., Tukiainen, S., Zawodny, J., and Thomason, L.: Combined SAGE II–GOMOS ozone profile data set for 1984–2011 and trend analysis of the vertical distribution of ozone, *Atmos. Chem. Phys.*, 13, 10645–10658, doi:10.5194/acp-13-10645-2013, 2013.
- Logan, J. A., Staehelin, J., Megretskaia, I. A., Cammas, J.-P., Thouret, V., Claude, H., De Backer, H., Steinbacher, M., Scheel, H.-E., Stübi, R., Fröhlich, M., and Derwent, R.: Changes in ozone over Europe: Analysis of ozone measurements from sondes, regular aircraft (MOZAIC) and alpine surface sites, *J. Geophys. Res.*, 117, D09301, doi:10.1029/2011JD016952, 2012.
- Mikuteit, S.: *Trendbestimmung stratosphärischer Spurengase mit Hilfe bodengebundener FTIR-Messungen*, Dissertation, Forschungszentrum Karlsruhe, FZK Report No. 7385, Germany, 2008.
- Nair, P. J., Godin-Beekmann, S., Kuttippurath, J., Ancellet, G., Goutail, F., Pazmiño, A., Froidevaux, L., Zawodny, J. M., Evans, R. D., Wang, H. J., Anderson, J., and Pastel, M.: Ozone trends derived from the total column and vertical profiles at a northern mid-latitude station, *Atmos. Chem. Phys.*, 13, 10373–10384, doi:10.5194/acp-13-10373-2013, 2013.
- Newchurch, M. J., Yang, E.-S., Cunnold, D. M., Reinsel, G. C., Zawodny, J. M., and Russell III, J. M.: Evidence for slowdown in

- stratospheric ozone loss: First stage of ozone recovery, *J. Geophys. Res.*, 108, 4507, doi:10.1029/2003JD003471, 2003.
- Oltmans, S. J., Lefohn, A. S., Shadwick, D., Harris, J. M., Scheel, H. E., Galbally, I., Tarasick, D. W., Johnson, B. J., Brunke, E.-G., Claude, H., Zeng, G., Nichol, S., Schmidlin, F., Davies, J., Cuevas, E., Redondas, A., Naoe, H., Nakano, T., Kawasato, T.: Recent tropospheric ozone changes – a pattern dominated by slow or no growth, *Atmos. Environ.*, 67, 331–351, 2013.
- Pougatchev, N. S., Connor, B. J., and Rinsland, C. P.: Infrared measurements of the ozone vertical distribution above Kitt Peak, *J. Geophys. Res.*, 100, 16689–16697, 1995.
- Randel, W. J., and Wu, F.: A stratospheric ozone profile data set for 1979–2005: Variability, trends, and comparisons with column ozone data, *J. Geophys. Res.*, 112, D06313, doi:10.1029/2006JD007339, 2007.
- Randel, W. J., Garcia, R. R., Calvo, N., and Marsh, D.: ENSO influence on zonal mean temperature and ozone in the tropical lower stratosphere, *Geophys. Res. Lett.*, 36, L15822, doi:10.1029/2009GL039343, 2009.
- Rodgers, C. D.: Inverse methods for atmospheric sounding: Theory and Practice, Series on Atmospheric, Oceanic and Planetary Physics – Vol. 2, World Scientific Publishing Co., Singapore, 2000.
- Rothman, L. S., Gordon, I. E., Barbe, A., Benner, D. C., Bernath, P. F., Birk, M., Boudon, V., Brown, L. R., Campargue, A., Champion, J.-P., Chance, K., Coudert, L. H., Danaj, V., Devi, V. M., Fally, S., Flaud, J.-M., Gamache, R. R., Goldman, A., Jacquemart, D., Kleiner, I., Lacome, N., Lafferty, W. J., Mandin, J.-Y., Massie, S. T., Mikhailenko, S. N., Miller, C. E., Moazzen-Ahmadi, N., Naumenko, O. V., Nikitin, A. V., Orphal, J., Perevalov, V. I., Perrin, A., Predoi-Cross, A., Rinsland, C. P., Rotger, M., Šimečková, M., Smith, M. A. H., Sung, K., Tashkun, S. A., Tennyson, J., Toth, R. A., Vandaele, A. C., and Vander Auwera, J.: The Hitran 2008 molecular spectroscopic database, *J. Quant. Spectrosc. Ra.*, 110, 533–572, 2009.
- Scherrer, B.: Biostatistique, Gaëtan Morin, Chicoutimi, 1984.
- Schneider, M., Hase, F., and Blumenstock, T.: Ground-based remote sensing of HDO/H<sub>2</sub>O ratio profiles: introduction and validation of an innovative retrieval approach, *Atmos. Chem. Phys.*, 6, 4705–4722, doi:10.5194/acp-6-4705-2006, 2006.
- Sioris, C. E., McLinden, C. A., Fioletov, V. E., Adams, C., Zawodny, J. M., Bourassa, A. E., Roth, C. Z., and Degenstein, D. A.: Trend and variability in ozone in the tropical lower stratosphere over 2.5 solar cycles observed by SAGE II and OSIRIS, *Atmos. Chem. Phys.*, 14, 3479–3496, doi:10.5194/acp-14-3479-2014, 2014.
- Sussmann, R., Borsdorff, T., Rettinger, M., Camy-Peyret, C., Demoulin, P., Duchatelet, P., Mahieu, E., and Servais, C.: Technical Note: Harmonized retrieval of column-integrated atmospheric water vapor from the FTIR network – first examples for long-term records and station trends, *Atmos. Chem. Phys.*, 9, 8987–8999, doi:10.5194/acp-9-8987-2009, 2009.
- Tikhonov, A.: On the solution of incorrectly stated problems and a method of regularization, *Dokl. Acad. Nauk SSSR*, 151, 501–504, 1963.
- Tourpali, K., Zerefos, C. S., Balis, D. S., and Bais, A. F.: The 11-year solar cycle in stratospheric ozone: comparison between Umkehr and SBUVv8 and effects on surface erythemal irradiance, *J. Geophys. Res.*, 112, D12306, doi:10.1029/2006JD007760, 2007.
- Vigouroux, C., De Mazière, M., Demoulin, P., Servais, C., Hase, F., Blumenstock, T., Kramer, I., Schneider, M., Mellqvist, J., Strandberg, A., Velasco, V., Notholt, J., Sussmann, R., Stremme, W., Rockmann, A., Gardiner, T., Coleman, M., and Woods, P.: Evaluation of tropospheric and stratospheric ozone trends over Western Europe from ground-based FTIR network observations, *Atmos. Chem. Phys.*, 8, 6865–6886, 2008, <http://www.atmos-chem-phys.net/8/6865/2008/>.
- Weber, M., Dikty, S., Burrows, J. P., Garny, H., Dameris, M., Kubin, A., Abalichin, J., and Langematz, U.: The Brewer-Dobson circulation and total ozone from seasonal to decadal time scales, *Atmos. Chem. Phys.*, 11, 11221–11235, doi:10.5194/acp-11-11221-2011, 2011.
- Wohlmann, I., Rex, M., Brunner, D., and Mäder: Integrated equivalent latitude as a proxy for dynamical changes in ozone column, *Geophys. Res. Lett.*, 32, L09811, doi:10.1029/2005GL022497, 2005.
- World Meteorological Organization: Atmospheric Ozone: 1985, Global Ozone Research and Monitoring Project – Report No. 16, Geneva, 1998.
- World Meteorological Organization: Scientific Assessment of Ozone Depletion: 1998, Global Ozone Research and Monitoring Project – Report No. 44, Geneva, 1998.
- World Meteorological Organization: Scientific Assessment of Ozone Depletion: 2010, Global Ozone Research and Monitoring Project – Report No. 52, Geneva, 2011.



# MAX-DOAS observations of aerosols, formaldehyde and nitrogen dioxide in the Beijing area: comparison of two profile retrieval approaches

T. Vlemmix<sup>1,2</sup>, F. Hendrick<sup>2</sup>, G. Pinardi<sup>2</sup>, I. De Smedt<sup>2</sup>, C. Fayt<sup>2</sup>, C. Hermans<sup>2</sup>, A. Piters<sup>3</sup>, P. Wang<sup>4</sup>, P. Levelt<sup>3,1</sup>, and M. Van Roozendaal<sup>2</sup>

<sup>1</sup>Delft University of Technology (TU-Delft), Delft, the Netherlands

<sup>2</sup>Belgian Institute for Space Aeronomy (IASB-BIRA), Brussels, Belgium

<sup>3</sup>Royal Netherlands Meteorological Institute (KNMI), De Bilt, the Netherlands

<sup>4</sup>Institute of Atmospheric Physics, Chinese Academy of Sciences, Beijing, China

Correspondence to: T. Vlemmix (t.vlemmix@tudelft.nl)

Received: 27 July 2014 – Published in Atmos. Meas. Tech. Discuss.: 19 September 2014

Revised: 22 December 2014 – Accepted: 30 December 2014 – Published: 25 February 2015

**Abstract.** A 4-year data set of MAX-DOAS observations in the Beijing area (2008–2012) is analysed with a focus on NO<sub>2</sub>, HCHO and aerosols. Two very different retrieval methods are applied. Method A describes the tropospheric profile with 13 layers and makes use of the optimal estimation method. Method B uses 2–4 parameters to describe the tropospheric profile and an inversion based on a least-squares fit. For each constituent (NO<sub>2</sub>, HCHO and aerosols) the retrieval outcomes are compared in terms of tropospheric column densities, surface concentrations and “characteristic profile heights” (i.e. the height below which 75 % of the vertically integrated tropospheric column density resides).

We find best agreement between the two methods for tropospheric NO<sub>2</sub> column densities, with a standard deviation of relative differences below 10 %, a correlation of 0.99 and a linear regression with a slope of 1.03. For tropospheric HCHO column densities we find a similar slope, but also a systematic bias of almost 10 % which is likely related to differences in profile height. Aerosol optical depths (AODs) retrieved with method B are 20 % high compared to method A. They are more in agreement with AERONET measurements, which are on average only 5 % lower, however with considerable relative differences (standard deviation ~ 25 %). With respect to near-surface volume mixing ratios and aerosol extinction we find considerably larger relative differences:  $10 \pm 30$ ,  $-23 \pm 28$  and  $-8 \pm 33$  % for aerosols, HCHO and NO<sub>2</sub> respectively. The frequency distri-

butions of these near-surface concentrations show however a quite good agreement, and this indicates that near-surface concentrations derived from MAX-DOAS are certainly useful in a climatological sense. A major difference between the two methods is the dynamic range of retrieved characteristic profile heights which is larger for method B than for method A. This effect is most pronounced for HCHO, where retrieved profile shapes with method A are very close to the a priori, and moderate for NO<sub>2</sub> and aerosol extinction which on average show quite good agreement for characteristic profile heights below 1.5 km.

One of the main advantages of method A is the stability, even under suboptimal conditions (e.g. in the presence of clouds). Method B is generally more unstable and this explains probably a substantial part of the quite large relative differences between the two methods. However, despite a relatively low precision for individual profile retrievals it appears as if seasonally averaged profile heights retrieved with method B are less biased towards a priori assumptions than those retrieved with method A. This gives confidence in the result obtained with method B, namely that aerosol extinction profiles tend on average to be higher than NO<sub>2</sub> profiles in spring and summer, whereas they seem on average to be of the same height in winter, a result which is especially relevant in relation to the validation of satellite retrievals.

## 1 Introduction

Multi-Axis Differential Optical Absorption Spectroscopy (MAX-DOAS) is a ground-based passive remote sensing technique that is used to detect tropospheric trace gases such as nitrogen dioxide (NO<sub>2</sub>), formaldehyde (HCHO), sulfur dioxide (SO<sub>2</sub>), nitrous acid (HONO), iodine oxide (IO), glyoxal (CHOCHO), bromine oxide (BrO) and aerosols (aerosol extinction) (e.g. Wittrock et al., 2004; Wagner et al., 2004, 2009; Irie et al., 2011; Coburn et al., 2011; Pinardi et al., 2013; Hendrick et al., 2014; Wang et al., 2014). MAX-DOAS instruments take spectral measurements of scattered sunlight in the ultraviolet (UV) and visible (Vis) part of the electromagnetic spectrum. Profile information is obtained from a scan which comprises spectral measurements at different elevation angles but in the same azimuthal direction. The main retrieval products are tropospheric column densities, concentrations near the surface and estimates of the vertical profile shape.

Because of this versatility MAX-DOAS is complementary to ground-based in situ observations (in a spatial sense) as well as to satellite observations (in a temporal and spatial sense, i.e. the vertical) and it can play an important role in bridging the gap between those techniques (Richter et al., 2013). Knowledge of the relationship between surface concentrations and integrated tropospheric column densities (in urban, suburban and rural regions) is important for the use of satellite observations in studies of air quality (e.g. Boersma et al., 2009; Mendolia et al., 2013).

MAX-DOAS has great potential to be used in regional or global networks similar to the AERONET (sun photometer) and EARLINET (lidar) networks because of its versatility, the relatively low cost per instrument, the fact that a radiometric calibration is not required, and the fact that instruments can operate autonomously. Long-term data sets can be used for e.g. air quality monitoring, validation of chemical transport models, validation of satellite tropospheric column density retrievals and potentially as input in data assimilation systems for air quality forecasts. With respect to satellite validation it is interesting to note that MAX-DOAS can provide not only tropospheric trace gas column densities for direct comparison, but also profile shape estimates for trace gases and aerosol extinction. These can replace the a priori profile shapes assumed for the satellite retrieval, such that one can assess the impact of the a priori profile shape assumption (both for aerosols and for the trace gas of interest) on the satellite retrieval accuracy (Rodgers and Connor, 2003). Proper knowledge of the accuracy of the profile shape assumptions that are used in the satellite retrieval is crucial for a realistic estimate of the potential biases in the retrieved tropospheric column density.

Mostly in the last decade, much progress has been made with respect to the quantitative interpretation of MAX-DOAS observations (e.g. Wagner et al., 2007; Roscoe et al., 2010), and MAX-DOAS instrumentation or similar (like

PANDORA Herman et al., 2009) has been used for a wide range of gases and applications. In comparison to surface concentrations and profile shapes, tropospheric column densities are the most robust retrieval product. Several MAX-DOAS data sets have been used for validation of satellite observations of tropospheric column densities, predominantly for NO<sub>2</sub> (e.g. Irie et al., 2008b; Halla et al., 2011; Ma et al., 2013; Lin et al., 2014; Kanaya et al., 2014). Near-surface concentrations are generally associated with higher uncertainties (primarily because of the quite limited vertical resolution of MAX-DOAS measurements), but nevertheless some studies have shown promising comparisons compared to independent ground-based in situ instrumentation, (see e.g. Wagner et al., 2011; Li et al., 2013). Most challenging is the retrieval of vertical tropospheric profiles, and also their validation.

Quite some groups have developed algorithms for the vertical profiles of aerosol extinction and trace gases (e.g. Frieß et al., 2006; Irie et al., 2008a; Clémer et al., 2010; Li et al., 2010; Wagner et al., 2011; Vlemmix et al., 2011; Sinreich et al., 2013). Especially in relation to satellite validation there is a great need for simultaneously measured trace gas and aerosol extinction profiles, and MAX-DOAS is one of the few remote sensing methods which can satisfy this need. At the same time it is well known that the MAX-DOAS profiles are only first-order estimates, due to the fact that the information content of MAX-DOAS observations with respect to the vertical distribution of aerosols and trace gases is very limited: the degrees of freedom for signal typically varies from 1 to 3, see Sect. 2.5 and Vlemmix et al. (2011).

Comparatively few studies have been published however which directly address the quality of MAX-DOAS tropospheric profiles obtained from real observations. This is largely due to the fact that suitable long-term (multi-year) data sets which can serve as golden standard in a comparison (e.g. profiles measured with high vertical resolution) do not exist. In turn, the lack of a thorough validation of MAX-DOAS profiles limits their usefulness in validation studies where MAX-DOAS itself would be the reference.

The present study is highly motivated by the need for further assessment of the quality of MAX-DOAS profiles. Our approach is based on three pillars. First, the use of two very different profile retrieval algorithms, both run with various a priori profile shape assumptions. Second, the use of a 4-year data set covering a wide range of conditions (e.g. pollution levels, seasons, meteorological conditions). Third, analysis of profiles for three different components: formaldehyde, NO<sub>2</sub> and aerosols (aerosol extinction profile). With this we address in this work the following specific questions: how consistent are the retrievals of individual profiles with different algorithms? How consistent are the retrievals on average? Do the column densities and profiles – on average – show a diurnal and seasonal variation? How strong or weak is the dependence on a priori assumptions? Which atmospheric conditions most critically limit the quality of the profile re-

retrieval? What is the agreement between the profile shapes retrieved for the different constituents?

The two profile retrieval methods that are compared in this study do not retrieve profiles on the same vertical grid. One way to perform a profile comparison would be to interpolate profiles retrieved with both methods to a common vertical grid. A comparison performed in this way would give results for all layers which define the common grid. Such an approach would probably be favourable if the vertical resolution of the measurements (and therefore the DOFS) was high, but this is not the case for MAX-DOAS measurements, as noted above. Because of the low DOFS (1–3), it was decided to derive from each profile three suitable quantities and to compare the two profile retrieval methods based on those quantities: tropospheric column density, near-surface concentration and “characteristic profile heights”  $H_{75}$ . The latter quantity is defined as the height below which 75 % of the integrated profile resides (75 % of the tropospheric column density). An advantage of this quantity (a scalar) is that it allows a first-order description of the profile shape of pollutants which reside primarily in the atmospheric boundary layer.

The paper is structured as follows: in Sect. 2 we describe the data set of MAX-DOAS observations that is used: the instrument characteristics and measurement sites; the settings of the DOAS fitting procedures for the UV and Vis; the two MAX-DOAS profile retrieval algorithms, both of which are run with different “internal” settings to test the dependence on a priori assumptions. The last part of this section describes the criteria that are applied to select data with sufficient quality. Results for selected days and the statistical analysis based on the entire data set are shown and discussed in Sect. 3. Section 4 contains a discussion, and the conclusions are in the last section.

## 2 MAX-DOAS measurements and profile retrieval algorithms

The retrieval of vertical profiles from spectral measurements with MAX-DOAS typically consists of three steps. First, differential slant column densities (of  $O_4$ ,  $NO_2$  and HCHO) are derived by applying the DOAS spectral fitting technique to the measured spectra. Second, differential slant column densities of  $O_4$  are used as input for the aerosol extinction profile retrieval algorithms. Third, differential slant column densities of the trace gas of interest (in this work:  $NO_2$  and HCHO) are used as input for the trace gas profile retrieval algorithm, together with the estimated aerosol extinction profile. In this section each of those steps is described in more detail.

### 2.1 Instrument and measurement site

The MAX-DOAS instrument used in this study has been designed and assembled by the Belgian Institute for Space

Aeronomy (BIRA-IASB), see Clémer et al. (2010). It consists essentially of a telescope mounted on a sun-tracker (which can point at any elevation and in any azimuthal direction) combined with two spectrographs: one for the UV (300–390 nm), and one for the Vis (400–720 nm). Although the instrument is also capable of taking direct sun observations, we use here only the scattered sunlight observations taken towards the north. The retrievals described below are based on sequential observations at 2, 4, 6, 8, 10, 12, 15, 30 and 90° elevation. During the period analysed in this work (2008–2012), the instrument was stationed at two different sites. First it was stationed in Beijing city centre, at the Institute of Atmospheric Physics (IAP) of the Chinese Academy of Sciences (39.98° N, 116.38° E). From 2010 until present, the instrument was stationed about 55 km away to the east-southeast, at the meteorological observatory in Xianghe (39.75° N, 116.96° E). Compared to Beijing this site has a more suburban character.

### 2.2 DOAS retrieval of differential slant column densities

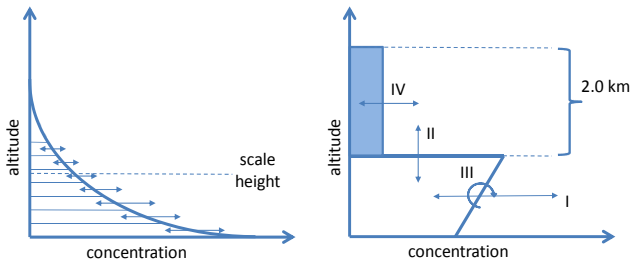
The DOAS spectral fitting method (Platt and Stutz, 2008) is applied to the spectra measured with the UV and Vis spectrometers. The DOAS analysis is performed with the QDOAS software that has been developed at BIRA (Fayt et al., 2011). Table 1 gives for some relevant parameters the values used in both of the channels. More details of the DOAS settings used can be found in Pinardi et al. (2013) for the UV channel, and Hendrick et al. (2014) for the Vis channel. Note that a scaling factor of 0.8 is applied to the measured differential slant  $O_4$  column densities (see Clémer et al., 2010) in order to obtain sufficient agreement between simulations and measurements. This scaling factor is used for both methods A and B. After the DOAS analysis the differential slant column densities corresponding to each elevation are linearly interpolated in time (with a 20 min sampling), such that as input for the profile retrieval code one “scan” can be provided, as if the measurements were performed at the same time. Since the DOAS analysis is performed with the zenith-noon spectrum as a reference, the (interpolated) zenith differential slant column densities of a scan is subtracted from all the differential slant column densities. This procedure reduces the sensitivity to trace gases in the stratosphere and upper part of the free troposphere to almost zero.

### 2.3 Method A – algorithm developed at BIRA

The first algorithm (method A) has been developed at BIRA (Clémer et al., 2010; Hendrick et al., 2014; Wang et al., 2014) and makes use of the optimal estimation method (Rodgers, 2000). Forward simulations of differential slant column densities and weighting functions are performed using the LI-DORT radiative transfer model (Spurr, 2008). Trace gas and aerosol extinction profiles are described by partial columns

**Table 1.** DOAS settings used for the UV and Vis. For more details, see Pinaridi et al. (2013) for the UV and Hendrick et al. (2014) for the Vis.

|                       | UV  | Vis  |
|-----------------------|---|--|
| Wavelength range (nm) | 336.5–359   | 425–490  |
| Cross-sections        | HCHO, O <sub>4</sub> , O <sub>3</sub> , NO <sub>2</sub> , BrO, Ring | NO <sub>2</sub> , O <sub>4</sub> , O <sub>3</sub> , H <sub>2</sub> O, Ring |
| Polynomial            | 3rd order   | 3rd order  |

**Figure 1.** Schematic of profile parameterizations for methods A (left) and B (right). Method A uses 13 layers (not drawn) between 0 and 4 km. The number of free variables for method B varies, see Table 2.

of 13 layers in a fixed altitude grid: the first 10 layers (below 2 km) each have a vertical extent of 200 m, between 2 and 3 km there are two layers of 0.5 km, and the uppermost layer of the profile goes from 3 to 4 km. An important input parameter for retrieval model A is the a priori profile, which is the initial profile from which the profile retrieval code iteratively searches for a more optimal solution. Retrieved profile shapes can in principle be very different from the a priori, but only if the information content of the measurements is sufficiently high (depending on trace gas and measurement conditions). If this is not the case, the retrieved profile shape will be very similar to the a priori. In the original implementation of the retrieval code (Cl mer et al., 2010) this a priori profile concentration profile  $n(z)$  was described by an exponential function which is characterized by a specific a priori scale height  $H_s^{\text{prior}}$ :

$$n(z) = \frac{N_{\text{prior}}^V}{H_s^{\text{prior}}} \cdot \exp\left(-\frac{z}{H_s^{\text{prior}}}\right). \quad (1)$$

For trace gases, the profile shape is scaled such that the integrated profile corresponds to the first-order estimate of the tropospheric trace gas column density ( $N_{\text{prior}}^V$ ), namely the differential slant column density measurement at 30° elevation. The corresponding geometrical differential air mass factor (see e.g. Brinksmas et al., 2008) is equal to one. For aerosols the initial column estimate (the AOD, aerosol optical depth) was set to 0.15 for all retrievals.

A second important input parameter is the a priori error estimate for each layer. Tests have shown that setting this value high – this would give the algorithm most flexibility

to realize diverse profile shapes – leads to frequent retrievals of profile shapes showing oscillations that are not likely to be realistic. For this reason a relatively low value (20 %) of the a priori is chosen, although this limits the potential of the algorithm to deviate significantly from the a priori, see also the discussion in Sect. 4.2.

Tests performed prior to the study presented here have shown that the interplay between the a priori profile and its error estimate, combined with the fact that the sensitivity of MAX-DOAS decreases with altitude, leads to an undesired effect for relatively high a priori scale heights (> 1.5 km), namely that the retrieved tropospheric trace gas column or AOD in the case of aerosol extinction retrieval is systematically too high.

This unwanted mechanism works as follows: for a priori scale heights higher than 1.5 km, the exponentially decreasing a priori profile does not go to (almost) zero in the upper part of the altitude grid (4 km). Because above approximately 1.5 km the information content of the observation is low, the retrieval will have a tendency to stay close to the a priori and not be allowed to go to zero. As a consequence, the retrieved profiles will have a considerable fraction of the partial column above ~ 1.5 km, even when this is not the case in reality. This effect will lift up the mean profile height, and this goes together with a systematic overestimation of the integrated trace gas column (or AOD).

By modifying the definition of the a priori profile shape such that it decreases to zero at the top of the altitude grid, the overestimation of columns and AOD is greatly reduced. The following profile shape definition is forced to low values above 1.5 km and even zero at the top of the altitude grid:

$$n(z) = \left[ \frac{N_{\text{prior}}^V}{H_s^{\text{prior}}} \cdot \exp\left(-\frac{z}{H_s^{\text{prior}}}\right) \right] \cdot (4 - z). \quad (2)$$

Figure 2 shows a priori profile shapes obtained with this definition, for  $H_s^{\text{prior}} = \{0.5, 1.0, 1.5\}$  km. Note that the range in terms of  $H_{75}$  is different:  $\{0.6, 1.0, 1.3\}$  km.

The impact of the a priori profile shape on the retrieved profile can be quite high. For this reason the profile retrieval with method A is performed with three different a priori scale heights ( $H_s^{\text{prior}} = \{0.5, 1.0, 1.5\}$ ), leading to three versions: A1, A2 and A3. The final product that is compared to method B is a composite of the retrievals with these three a priori: for each retrieval quantity (see Sect. 2.6) the mean of the values obtained with A1–A3 is taken as the solution,

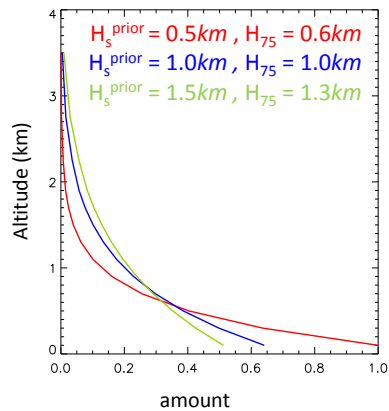


**Figure 2.** Method A is run with three different a priori profile shapes (see Eq. 2), each with a different characteristic profile height ( $H_{75}$ ).

and the difference between the maximum and minimum as the uncertainty. The reason to follow this approach is that the impact of the a priori is substantial and there is no external information available instead which justifies the choice for one specific a priori. Tests have indicated that errors estimated in this way are in general considerably larger than the smoothing error, a commonly used parameter in the optimal estimation framework to quantify the impact of the a priori on the retrieval error (Rodgers, 2000). The relative smoothing error per layer is typically less than 20 %, for both the aerosol extinction and the trace gas retrieval. The a priori based error is about 1.6 times higher in case of the aerosol extinction retrieval and about 4.8 times higher in case of the  $\text{NO}_2$  retrieval (both numbers are median values).

## 2.4 Method B – algorithm developed at KNMI

The profile retrieval approach of method B (Vlemmix et al., 2011) is quite different from method A: it makes use of a profile shape parameterization with just a few (2–4) free parameters; forward simulations are performed by making use of a look-up table which has been created with the Doubling Adding KNMI (DAK) radiative transfer model (De Haan et al., 1987; Stammes et al., 1989); a standard least-squares algorithm is used, without any form of regularization. The main reason to use a low number of free parameters is that the information content of MAX-DOAS observations with respect to the vertical distribution of aerosols and trace gases is quite limited (see Fig. 3). With a suitable choice of free parameters a sufficiently wide range of possible profile shapes can be retrieved, especially in combination with the ensemble approach described below. Compared to the description in Vlemmix et al. (2011) the algorithm has been modified in the following ways: the profile shape parameterization is slightly different, this is described below; the look-up table is compiled to allow for more extreme aerosol optical thicknesses ( $\tau$ ) needed in China with  $\tau = 3.2$  as maximum; the look-up table is expanded with a UV component (central wave-

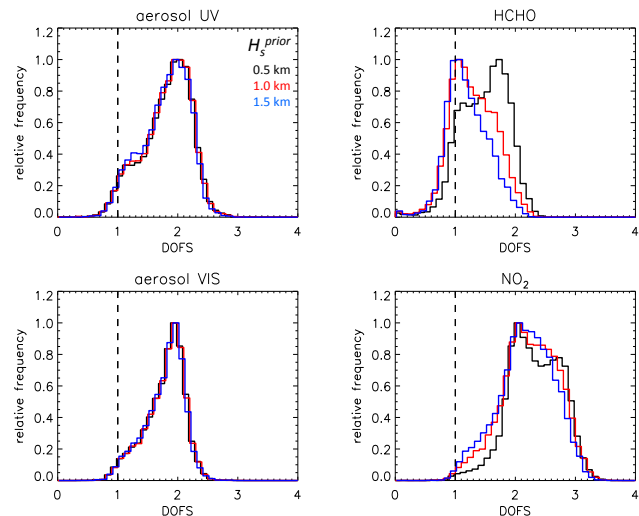


**Figure 3.** Histograms showing the degrees of freedom for signal (DOFS) for the profile fits obtained with methods A1–A3, based on all MAX-DOAS scans analysed for the Xianghe station. The upper row shows results for the UV, the bottom row shows results for the Vis. The dashed line indicates the threshold that is used for the quality control: retrievals with  $\text{DOFS} < 1$  are excluded from the comparison.

length: 360 nm); no correction is applied to compensate for the temperature dependence of the differential cross-section of  $\text{NO}_2$  (similar strategy for method A) – a fixed temperature is used (296 K). This will affect the accuracy of both retrieval methods similarly. The up to four free parameters that are used to parameterize the profile (see Fig. 2) are: (i) the tropospheric column density for trace gases and the AOD in case of aerosols; (ii) the top height of the mixing layer; (iii) the “shape parameter”, which determines the linear increase or decrease of the trace gas concentration or aerosol extinction in the mixing layer; (iv) the fraction of the total trace gas column density which resides (uniformly distributed) in the layer starting at the top of the mixing layer up to 2 km above. The vertical extent of this layer varies with parameter (ii). Parameter (iv) replaces the free tropospheric layer which in the earlier version of the algorithm (Vlemmix et al., 2011) was put at a fixed altitude. Parameter (iii), already tested and introduced as part of a sensitivity study in Vlemmix et al. (2011) is also newly applied here.

An important characteristic of this profile shape parameterization is that with parameter (ii) it can mimic the dynamic behaviour of the cloud-free boundary layer, which can be very shallow in the morning (especially after a cold, cloud-free night with little wind) and become quite deep during the day, especially in summer. Parameter (iii) is included especially to allow for profile shapes which peak at higher altitudes (e.g. somewhere near the top of the mixing layer). With parameter (iv) elevated trace gas concentrations at higher altitudes can be described. From Vlemmix et al. (2011) it is

known that the accuracy of this part of the profile is generally low. For the aerosol extinction profile retrieval, parameter (iv) is not used for practical reasons (computation time). As a consequence it is not possible to perform accurate aerosol extinction profile retrievals under measurement conditions with elevated aerosol layers above the mixing layer – aerosol extinction profiles which peak near the top of the mixing layer can be described with the shape parameter (iii). Such cases are however indicated by high values of  $\chi^2$  and can therefore be flagged (or excluded), see below. The cost function used for method B is defined as

$$\chi^2 = \sum_{i=1}^8 \left( \frac{\Delta N_{\alpha_i}^S - \widehat{\Delta N_{\alpha_i}^S}}{\epsilon_{\alpha_i}} \right)^2, \quad (3)$$

where  $\Delta N_{\alpha_i}^S$  is the measured differential slant column density for elevation  $i$ ,  $\widehat{\Delta N_{\alpha_i}^S}$  is the simulated differential slant column density and  $\epsilon_{\alpha_i}$  is the error estimate for the differential slant column density. Due to the low number of free parameters used in method B (2 to 4), it is more difficult to get optimal agreement between simulations and measurements (i.e. to obtain low residuals) than with method A (13 profile layers). Therefore, and also because there is no a priori to fall back on, the individual retrievals with method B tend to be more unstable with respect to one or more retrieval parameters.

It is important to note that this instability is not necessarily an unwanted effect: it is an expression of the fact that (under some conditions) the MAX-DOAS observations contain very limited information about the profile shape. For such conditions it is desirable to have a good estimate of the uncertainty. This is obtained by making use of an ensemble approach: the retrieval code is run 50 times, each time with slightly different input. The differential slant column density measurements are perturbed by adding Gaussian noise with a standard deviation corresponding to 10 % of the original differential slant column density (obtained with the semi-simultaneous zenith measurement). For each scan an ensemble of solutions is obtained, and for each retrieval quantity the median is taken as the final result. The width of the distribution for each parameter (e.g. described by the end of the first and beginning of the fourth quartile) provides an estimate for the retrieval uncertainty. Note however, that this retrieval uncertainty does not account for the uncertainty with respect to the profile shape parameterization. For this reason the retrieval is run for several profile shape parameterizations at the same time (see Table 2) and a composite retrieval product is constructed a posteriori. A posteriori selection of plausible profile shape parameterizations (among B1–B4) is done by considering the distribution of the reduced  $\chi^2$  ( $\chi_v^2$ ). This parameter is defined as

**Table 2.** Retrieval with method B is performed for different combinations of free parameters which describe the profile shape. See also Fig. 1.

| Profile parameterization | Free parameters included |
|--------------------------|--------------------------|
| B1                       | I, II                    |
| B2                       | I, II, III               |
| B3                       | I, II, IV                |
| B4                       | I, II, III, IV           |

$$\chi_v^2 = \frac{\chi^2}{(N - M)}, \quad (4)$$

where  $N$  is the number of observations (differential slant column densities at various elevations) minus the number of model parameters (i.e. 2 to 4). If the median value of the  $\chi_v^2$  distribution (after 50 runs) for a certain profile shape parameterization is approximately equal to one, then the selected retrieval model is capable of producing simulations that agree with the observations within the estimated measurement error.

After the algorithm is run 50 times for all four models, it is determined which models are included in the a posteriori composite retrieval product, namely all models which have a median  $\chi_v^2 < 1.5$ . For each model individually the retrieval outcomes for a certain quantity (e.g. surface concentration) is defined as the median value of the distribution (after 50 runs) for that particular quantity. The lower limit of the corresponding uncertainty estimate is defined as the value which marks the transition from the first to the second quartile of the distribution. The upper limit is defined similarly as the value which marks the transition from the third to the fourth quartile of the distribution. This implies that 50 % of the retrievals is within the error bar. The composite product is constructed simply by averaging the medians of the selected models, and the error bars are constructed by averaging the lower limits and upper limits separately. The procedure that is followed here (including all models among B1–B4 which have sufficiently low median of  $\chi_v^2$ ) yields a more realistic uncertainty estimate than if only the model with lowest median  $\chi_v^2$  would be used, because it takes into account the uncertainty with respect to the profile shape.

## 2.5 Selection criteria and uncertainty estimates

Comparison of methods A and B is done only for profile pairs which satisfy three criteria: they should pass the quality control criteria of method A, and those of method B, and they should coincide with AERONET observations. The third criterion provides an indirect way of selecting cloud-free periods. MAX-DOAS profiles are only included in the comparison if at least three AERONET level 2.0 (cloud screened,

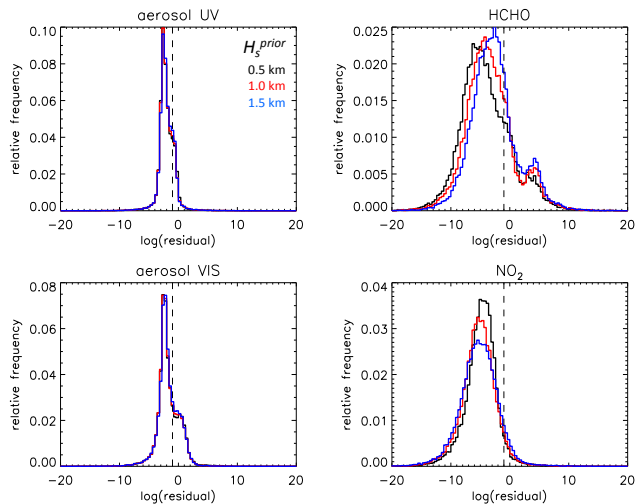


**Figure 4.** Histograms of residuals of the profile fits obtained with methods A1–A3, based on all MAX-DOAS scans analysed for the Xianghe station. The upper row shows results for the UV, the bottom row shows results for the Vis. The dashed line indicates the threshold (0.1, or  $-1$  on a logarithmic scale) that is used for the quality control: retrievals with residuals above this threshold are excluded from the comparison.

quality controlled) measurements are taken within an hour around the MAX-DOAS measurement. Quality control for method A is based on two quantities: the size of the residual of the profile fit and the degrees of freedom for signal (DOFS, see Rodgers, 2000). The residuals are defined as the sum of squared differences between simulations and measurements, divided by the simulated differential slant column density for an elevation of  $30^\circ$  (this quantity provides a first-order estimate of the tropospheric vertical column density):

$$\delta = \sum_{i=1}^8 \left( \frac{\Delta N_{\alpha_i}^S - \widehat{\Delta N_{\alpha_i}^S}}{\widehat{\Delta N_{\alpha_i=8}^S}} \right)^2. \quad (5)$$

Figures 3 and 4 show the histograms of these two parameters before the quality control is applied. These figures illustrate clearly that in general profile retrieval is more challenging for HCHO than for  $\text{NO}_2$ : the DOFS for HCHO are often well below 2, whereas for  $\text{NO}_2$  the DOFS are often  $> 2$ . Also the residuals for HCHO are considerably higher for a considerable fraction of all data (note that Fig. 4 shows the logarithm of the residual). The same is illustrated in Fig. 5: the averaging kernels for HCHO are lower than for  $\text{NO}_2$  and are less orthogonal with respect to one another. Profile pairs of A and B are excluded from the comparison if the minimum value of the DOFS is  $< 1$  for one or more of the models A1–A3. Also they are excluded if the maximum residual of A1–A3 is larger than 0.1. Quality control for method B consists of selecting only those profiles where the median value of the reduced  $\chi_V^2$  for the profile fit of method B is  $< 1.5$ . For aerosol

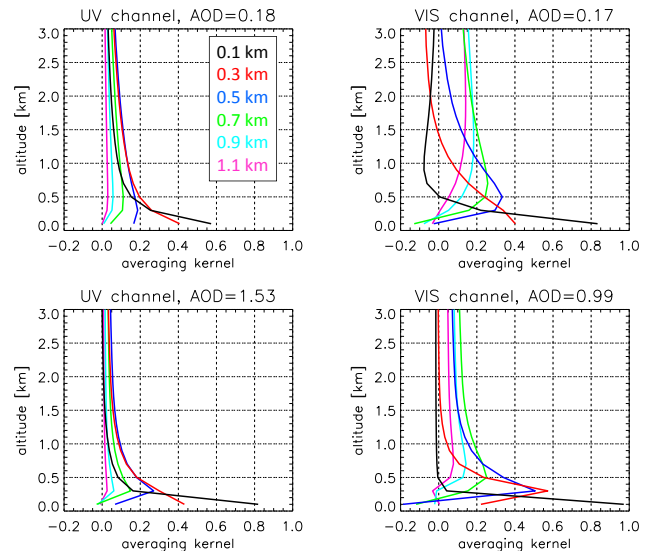


**Figure 5.** Examples of averaging kernels for retrievals performed with method A, both for the UV (left column) and Vis (right column). The upper row shows averaging kernels for low AOD (representative for the winter season), the bottom row for high AOD (representative for the summer season).

extinction only the median  $\chi_V^2$  of the aerosol extinction profile fits is considered, for the trace gas retrieval also the median  $\chi_V^2$  of the trace gas profile fits.

The impact of the quality control criteria defined above is discussed in Sect. 4.1.

## 2.6 Retrieval quantities

We compare results mostly based on three quantities: the tropospheric vertical column densities ( $N^V$ ), the concentration ( $n_{\text{surf}}$ ) or volume mixing ratio ( $X_{\text{surf}}$ ) of trace gases near the surface and the characteristic height (or  $H_{75}$ , see Sect. 1) of the retrieved profile. Similar quantities are used in the case of aerosols: aerosol optical depth ( $\tau_{\text{aer}}$ ), aerosol extinction near the surface  $e_{\text{surf}}$ , and  $H_{75}$ . A fourth quantity that is used is the a posteriori scale height (not to be confused with the scale height of the a priori profile of method A ( $H_s^{\text{prior}}$ ), see Sect. 2.3). This a posteriori scale height  $H_s^{\text{post}}$  is a first-order profile height estimate derived from column density (or AOD) and surface concentration (or aerosol extinction):

$$H_s^{\text{post}} = \frac{N^V}{n_{\text{surf}}} \quad (6)$$

for the trace gases, and

$$H_s^{\text{post}} = \frac{\tau}{e_{\text{surf}}} \quad (7)$$

for aerosols. The reason to consider this first-order profile height estimate in addition to  $H_{75}$  is that, as will be shown in Sect. 3.2, for method A it depends less on the a priori

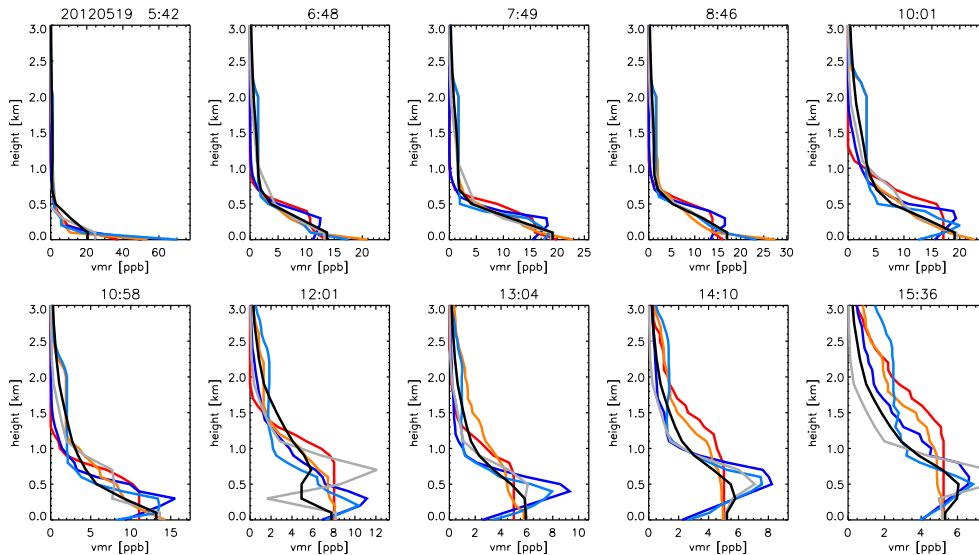


**Figure 6.** Examples of  $\text{NO}_2$  profiles retrieved with method A – grey ( $H_s = 0.5$  km) and black ( $H_s = 1.5$  km) – and method B – parameterizations B1–B4 (see Fig. 1 and Table 2) shown in red, blue, orange and light blue respectively.

than  $H_{75}$ . This indicates to some extent that the measurements contain information about the profile height that is not extracted in an optimal manner in this particular retrieval set-up.

### 3 Results

#### 3.1 Example day

Figures 6–8 show retrieval results for 19 May 2012. The individual profiles obtained with method A and B (Fig. 6) show good agreement in the sense that in the morning they are all quite low, and in the afternoon they are all quite high. Nevertheless, this example also illustrates that retrieved profile shapes can be very different: not only do the four versions of method B show considerable differences but so do the two versions of method A, especially those retrieved after 12:00 p.m. LT (bottom row).

Time lines for the different quantities that can be derived from the profile retrieval are shown in Fig. 7 for the same example day. Both for the aerosol extinction retrieval (left column) and the  $\text{NO}_2$  retrieval (right column) the  $\chi^2_v$  are quite low for most of the day, indicating a good quality of fit. On this particular day, the retrievals agree quite well for most quantities, especially for the column densities (row 1) and surface concentrations (row 3). Agreement is worst for  $H_{75}^{\text{NO}_2}$  and  $H_s^{\text{NO}_2}$  in the afternoon, where method B occasionally shows much higher values. This is a consequence of the fact that the retrieval is not regularized, in combination with relatively low surface concentrations in the afternoon. Because the surface concentration is the denominator in Eq. (6), one can understand that a small change (error) in the surface con-

centration can lead to a much larger change in  $H_s^{\text{NO}_2}$ . This figure also clearly demonstrates the potential impact of different profile shape assumptions on  $H_{75}^{\text{NO}_2}$ .

Figure 8 shows results for the same day, but this time for the aerosol extinction and HCHO retrieval in the UV. In general there is much more disagreement compared to  $\text{NO}_2$ . There is on this day almost no retrieval where the agreement is good for all quantities at the same time. The agreement between most quantities is especially low between 10:00 a.m. and 4:00 p.m. LT. High values for  $\chi^2_v$  in the aerosol extinction retrieval indicate that the retrieval with method B is not successful and therefore this period is flagged with grey bars on top of each figure. Quite remarkable is the disagreement in terms of HCHO column densities in the remaining part of the day (before 10:00 a.m. and after 4:00 p.m.). In the morning of this day the higher column densities (for method B compared to A) seem to go along with higher  $H_{75}^{\text{HCHO}}$ .

#### 3.2 Statistical analysis

Results of both retrieval methods are compared for 16 quantities in terms of correlation, slope and intercept of linear fit, and median, mean and standard deviation of relative differences, see Table 3. The comparison of 12 of these quantities is also shown in Figs. 10, 14, 15 and 21. We will discuss these results separately in terms of tropospheric column densities (AOD for aerosols), profile heights and surface concentrations (or aerosol extinction).

##### 3.2.1 Tropospheric column densities

Figure 9 shows the monthly median values for the column quantities: AOD, tropospheric  $\text{NO}_2$  and HCHO column den-

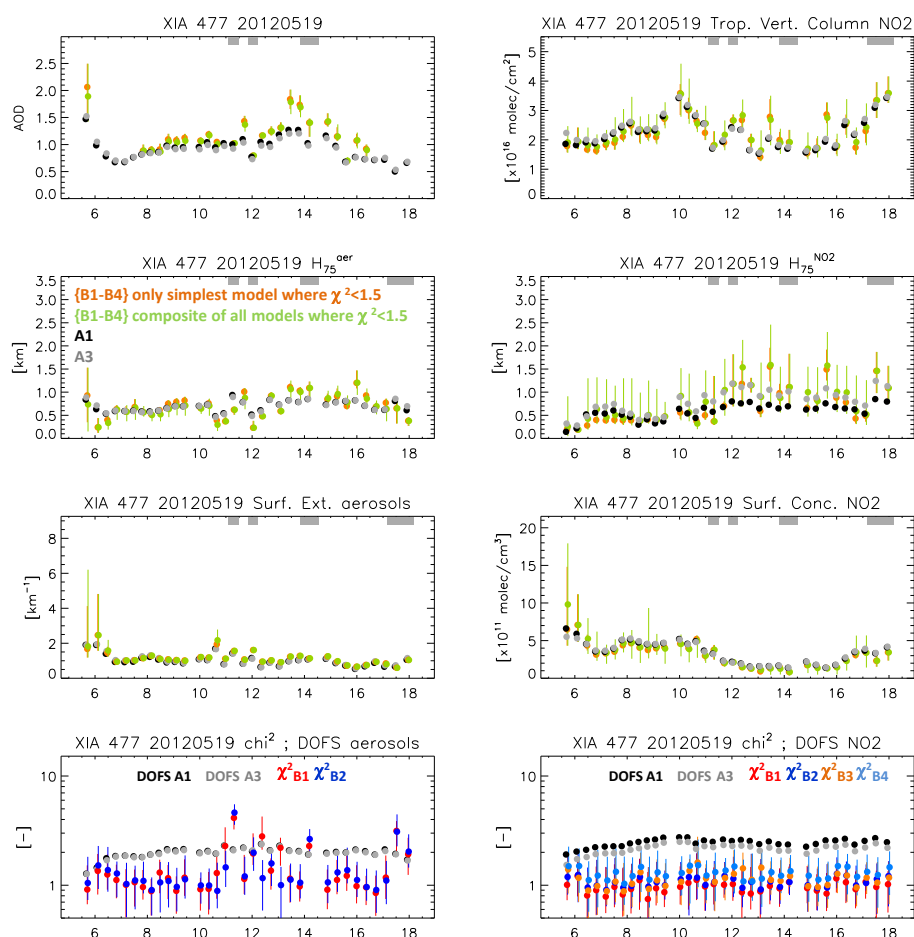


**Figure 7.** Example of quantities derived from the profile retrieval in the Vis (Xianghe, 19 May 2012). The left column shows the results of the aerosol retrieval, the right column shows results for the NO<sub>2</sub> retrieval. Grey horizontal bars above each panel indicate periods that are flagged because of high values of  $\chi^2$  in the aerosol or in the trace gas retrieval.

sities. Note that measurements before 2010 are made in Beijing. From 2010 onwards, the observations are made in Xianghe. A clear seasonal cycle with a winter minimum of about  $5 \times 10^{15}$  molec cm<sup>-2</sup> and a summer maximum roughly five times as high can be seen for HCHO. Compared to NO<sub>2</sub> and aerosols, the variability per month is quite small. A weaker, but similar seasonal cycle can be seen for aerosols, with typical winter values around 0.2 and a summer median between 0.5 and 1.0. For NO<sub>2</sub> the seasonal cycle of monthly median values is quite weak as well. Winter medians are roughly between  $20 \times 10^{15}$  and  $30 \times 10^{15}$  molec cm<sup>-2</sup>, summer medians between  $10 \times 10^{15}$  and  $20 \times 10^{15}$  molec cm<sup>-2</sup>. Noteworthy is the fact that especially the peak values in winter can be high with values above  $100 \times 10^{15}$ . Peaks in tropospheric NO<sub>2</sub> column densities in midsummer do not exceed  $30 \times 10^{15}$ . Figure 10 and Table 3 show that very good agreement is found for tropospheric NO<sub>2</sub> column densities. The standard deviation of relative differences is however considerable: almost 10%. The third and fourth columns of Fig. 10 show that the relative difference increases with in-

creasing tropospheric column density and with increasing profile height. Also for tropospheric HCHO column densities the agreement is good. Relative differences are however considerably larger than for NO<sub>2</sub>. The dependence of relative differences on the tropospheric column density itself (second row, third column) shows opposite behaviour as for NO<sub>2</sub>, whereas the dependence of relative differences on the profile height shows a similar increase as for NO<sub>2</sub>. Despite the quite high correlation found for the AOD, the agreement between method A and B is moderate, with slopes 1.20 (UV) and 1.39 (Vis) and substantial mean relative differences. Figure 10 (bottom row) shows for the Vis that these differences in AOD are strongly related to the difference in aerosol extinction profile height, but also tend to increase with the AOD itself. The agreement between method B and AERONET is much better, which provides confidence in the AOD retrievals obtained with method B. The frequency distributions of AERONET and AODs retrieved with method B show good agreement and differ with respect to method A in the fact that they include much more cases with AOD between 1.5 and

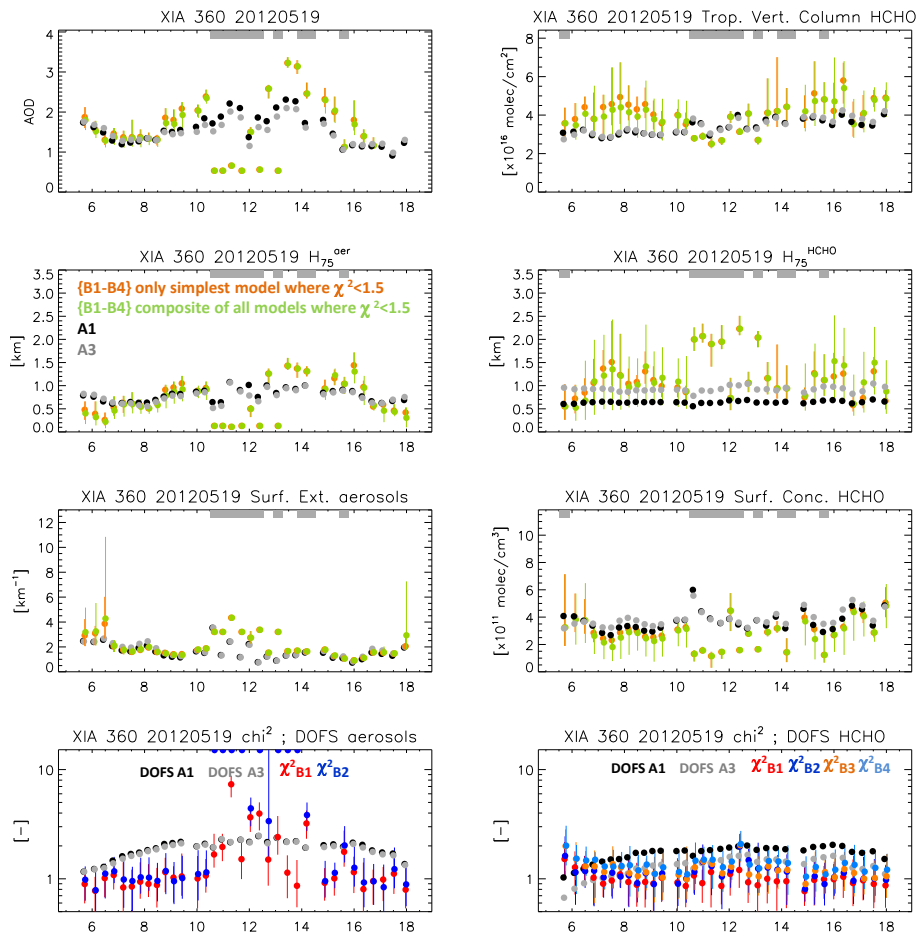


**Figure 8.** Example of quantities derived from the profile retrieval in the UV (Xianghe, 19 May 2012). The left column shows the results of the aerosol retrieval, the right column shows results for the HCHO retrieval. Grey horizontal bars above each panel indicate periods that are flagged because of high values of  $\chi^2$  in the aerosol or in the trace gas retrieval.

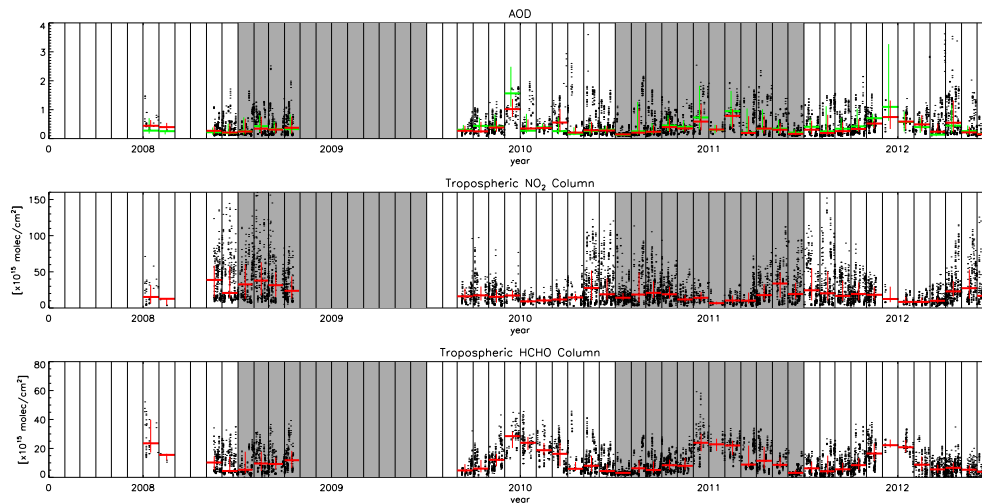


**Figure 9.** Time series of individual data points and monthly medians of AOD (Vis), and tropospheric column densities of NO<sub>2</sub> and HCHO, obtained with method A. The black dots refer to individual profiles and the red lines refer to monthly medians. AOD from AERONET is shown in green (upper row). In 2008/2009 the instrument was installed in Beijing; from 2010 onwards it was stationed in Xianghe.

**Table 3.** Statistical comparison of methods A and B. The last two columns refer to median, mean and standard deviation (SD) of percentage relative differences (RD). The linear fit results are defined for method A on the abscissa. Relative differences have a sign determined by B – A. Note that the intercepts have unit km for  $H_{75}$  and  $H_s^{\text{post}}$ , unit  $10^{15}$  molec  $\text{cm}^{-2}$  for the tropospheric column densities, unit ppb for the volume mixing ratio (vmr) near the surface, and unit  $\text{km}^{-1}$  for the aerosol extinction near the surface.

| Quantity                | $N$  | Corr. | Slope | Interc. | Median (mean) of RD (%) | SD of RD (%) |
|-------------------------|------|-------|-------|---------|-------------------------|--------------|
| UV, aerosols            |      |       |       |         |                         |              |
| AOD                     | 2734 | 0.92  | 1.20  | −0.02   | 17.16 (22.81)           | 24.92        |
| $H_{75}$                | 2723 | 0.77  | 4.08  | −2.42   | 7.55 (6.69)             | 47.17        |
| $H_s^{\text{post}}$     | 2735 | 0.88  | 1.50  | −0.37   | 10.92 (10.25)           | 25.91        |
| Extinction near surface | 2734 | 0.93  | 1.12  | 0.01    | 11.44 (14.93)           | 20.07        |
| UV, HCHO                |      |       |       |         |                         |              |
| Trop. column density    | 2509 | 0.95  | 1.02  | 0.67    | 9.64 (9.43)             | 12.14        |
| $H_{75}$                | 2498 | 0.67  | 7.47  | −5.33   | 22.34 (15.65)           | 36.93        |
| $H_s^{\text{post}}$     | 2498 | 0.77  | 3.01  | −1.47   | 41.96 (37.87)           | 35.57        |
| vmr near surface        | 2504 | 0.80  | 0.95  | −0.32   | −23.03 (−20.70)         | 27.71        |
| Vis, aerosols           |      |       |       |         |                         |              |
| AOD                     | 4001 | 0.91  | 1.39  | −0.05   | 18.26 (23.07)           | 23.54        |
| $H_{75}$                | 3936 | 0.62  | 2.82  | −1.31   | 5.67 (2.74)             | 43.63        |
| $H_s^{\text{post}}$     | 3821 | 0.63  | 1.20  | 0.11    | 12.65 (14.40)           | 36.64        |
| Extinction near surface | 3907 | 0.93  | 1.33  | −0.08   | 11.24 (10.27)           | 30.43        |
| Vis, NO <sub>2</sub>    |      |       |       |         |                         |              |
| Trop. column density    | 3360 | 0.99  | 1.03  | −0.56   | 0.51 (0.25)             | 9.26         |
| $H_{75}$                | 3298 | 0.76  | 1.44  | −0.20   | 8.71 (6.51)             | 33.18        |
| $H_s^{\text{post}}$     | 3309 | 0.80  | 1.79  | −0.35   | 18.71 (17.30)           | 38.03        |
| vmr near surface        | 3313 | 0.76  | 1.16  | −2.25   | −11.82 (−7.92)          | 32.97        |

3.5. But for the highest 25 % of characteristic profile heights, method B seems to overestimate the AOD systematically by about 20 %. Figure 11 shows for NO<sub>2</sub> and HCHO the relation between AOD (as measured by AERONET) and tropospheric trace gas column densities for different seasons. There are clear seasonal differences with largest differences for NO<sub>2</sub> vs. AOD between summer and winter. The two models show good agreement, with only moderate systematic differences for HCHO column densities in spring and summer. This is in line with the example day (Fig. 8) which shows considerable differences between tropospheric HCHO column densities retrieved by methods A and B. Note that on this example day the AOD is high, and the differences in characteristic HCHO profile height are considerable. The quite linear relationship between NO<sub>2</sub> and AOD, and HCHO and AOD illustrate that trace gas emissions are often accompanied by aerosol emissions. From that perspective the flattening of the curves for high AODs (mainly in summer and autumn) is remarkable. Possibly this is related to aerosols from natural sources (dust), emissions of which do not go along with emissions of trace gases. Another explanation would be that high AODs cause systematic underestimation of the tropospheric column density, but the flattening of the curves is not seen in winter and spring, even for higher AODs.

### 3.2.2 Profile heights

Figures 12 and 13 show for methods A and B monthly median values of characteristic heights, with a distinction between retrievals before 10:00 a.m. (red) and retrievals after 12:00 p.m. (blue). For all three species and both retrieval methods, we find higher profiles in the afternoon than in the morning, especially with method B. Only for  $H_{75}^{\text{HCHO}}$  obtained with method A are the differences between morning and afternoon negligible. This is most likely an artefact, which is also seen in Fig. 14, and which is discussed in Sect. 4.2. The morning–afternoon differences found in all other cases are qualitatively in agreement with the expected diurnal variation in the mixing layer height, and provide a first-order check to see if the algorithms behave as expected. Variability per month and between months is however much larger with method B. Highest monthly median characteristic profile heights are found with method B for aerosol extinction profiles in summer. This is in agreement with the general expectation that mixing layers are more shallow in winter and grow deeper in summer (see e.g. Luo et al., 2014). That this effect is weaker for NO<sub>2</sub> might be related to the shorter lifetime of NO<sub>2</sub> in summer which limits the effective transport of NO<sub>2</sub> from the surface to the

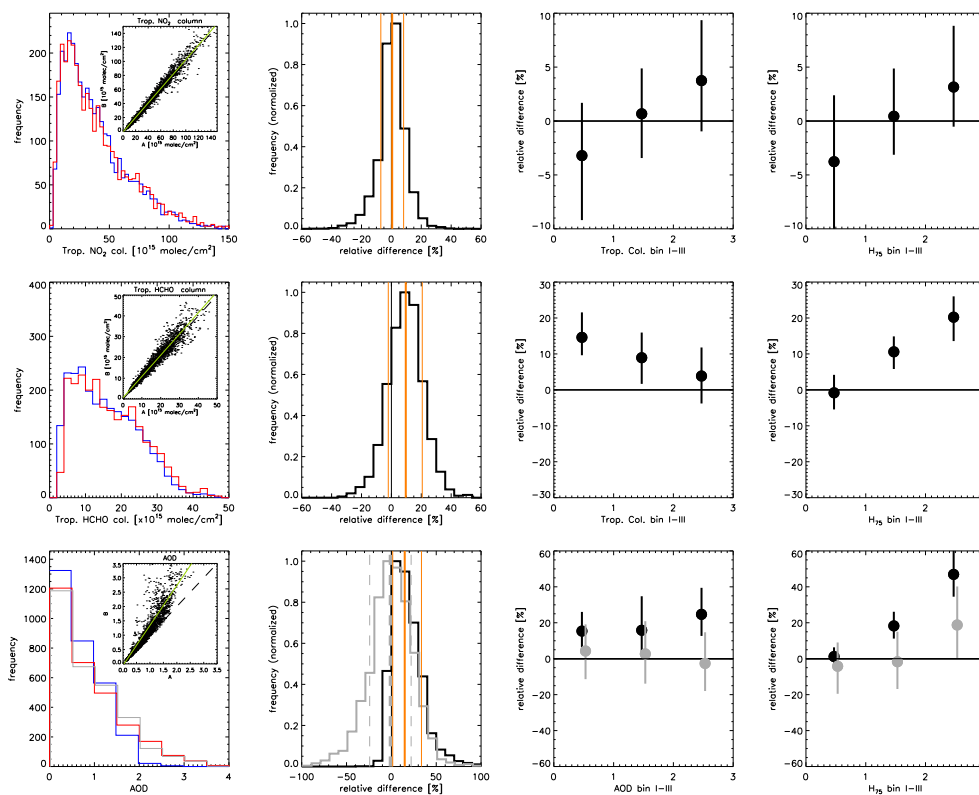


**Figure 10.** Statistics of column density retrievals. The three rows refer to tropospheric column densities of  $\text{NO}_2$ , HCHO and aerosols respectively. Left column: frequency distributions obtained with method A (blue) and B (red). Second column: frequency distribution of relative differences (B minus A). Lines in orange indicate the quartiles. Column 3: relative difference sorted as a function of the tropospheric column density (AOD for row 3) where the three bins refer to the lowest 25 %, middle 50 % and highest 25 % respectively. Column 4: similar to column 3, but here sorted as a function of the profile height ( $H_{75}$ ). The grey line on the bottom row refers to AODs from AERONET. The relative differences indicated in grey (bottom row, columns 2–4) refer to method B minus AERONET.

higher parts of the mixing layer, see also Halla et al. (2011) and Mendolia et al. (2013). Figure 14 and Table 3 show that the agreement between the two methods in terms of profile heights is considerably lower than the agreement in terms of column densities, which is to be expected because the information content of MAX-DOAS with respect to the vertical distribution is limited. The best agreement is found again for  $\text{NO}_2$ , with for the profile heights correlation 0.76, slope 1.44, intercept  $-0.20$  km, and mean relative difference 6.51 %. The standard deviation of relative differences is high: 33.18 %. It can be seen in Fig. 14 that the dynamic range of  $\text{NO}_2$  profile heights found with method A is somewhat lower than with method B. In particular, the fraction of profiles with height above 1 km is significantly higher with method B. For the HCHO profile height we have correlation 0.62. This is quite surprising because the dynamic range of profile heights found with method A is very small compared to method B and this also explains the exceptional slope (7.47) and intercept ( $-5.33$  km). Even though no independent data are available, it is quite safe to conclude that this very limited dynamic range is unrealistic, and therefore these HCHO pro-

files should be used and interpreted with great care. As a result of this effect, it is difficult to judge the quality of the HCHO profile heights obtained with method B. One can see that here the dynamic range is comparable to that of  $\text{NO}_2$  and aerosols, but the mode of the histogram has shifted to higher altitudes compared to  $\text{NO}_2$ . Also for aerosols (Vis) the dynamic range found with method A is limited compared to method B. The correlation (0.62) is somewhat lower than for  $\text{NO}_2$  and HCHO, but the slope and intercept are less extreme than for HCHO (2.82 and  $-1.31$  respectively). Figure 15 demonstrates that in terms of the other estimator of the average profile height ( $H_s^{\text{post}}$ ) the agreement between methods A and B is better. Especially for HCHO, the slope is less extreme for  $H_s^{\text{post}}$  than for  $H_{75}$  which is in line with the higher dynamic range seen for method A in Fig. 15 compared to Fig. 14. We see a similar effect for aerosols. This might indicate a retrieval artefact for method A which means that information about the profile height that is actually contained in the MAX-DOAS measurements is not efficiently converted into a noticeable effect on  $H_{75}^{\text{NO}_2}$ .

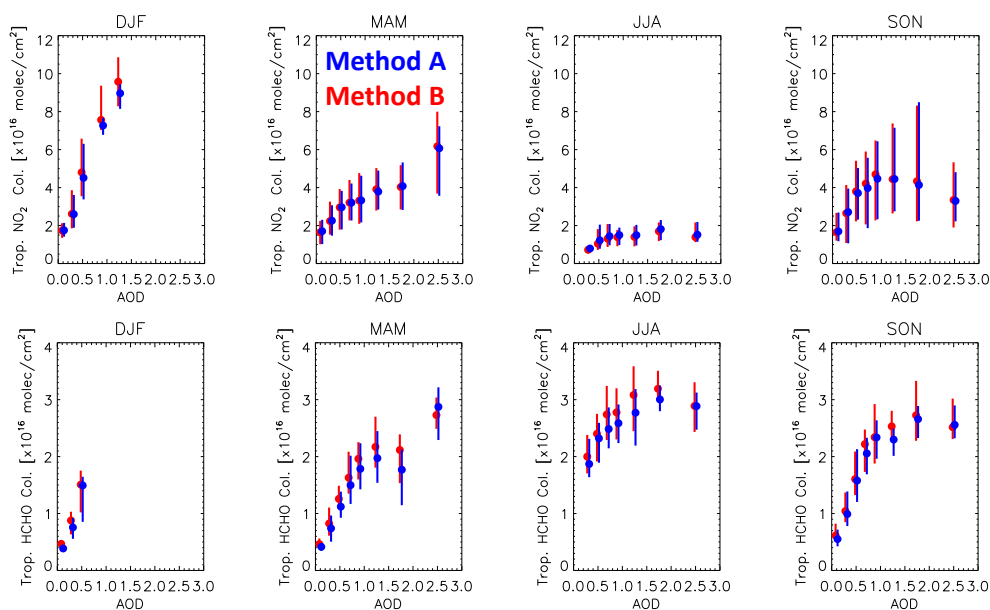


**Figure 11.** Median values of the tropospheric NO<sub>2</sub> column (upper row) and HCHO column (bottom row) for a range of AOD bins, specified per season.

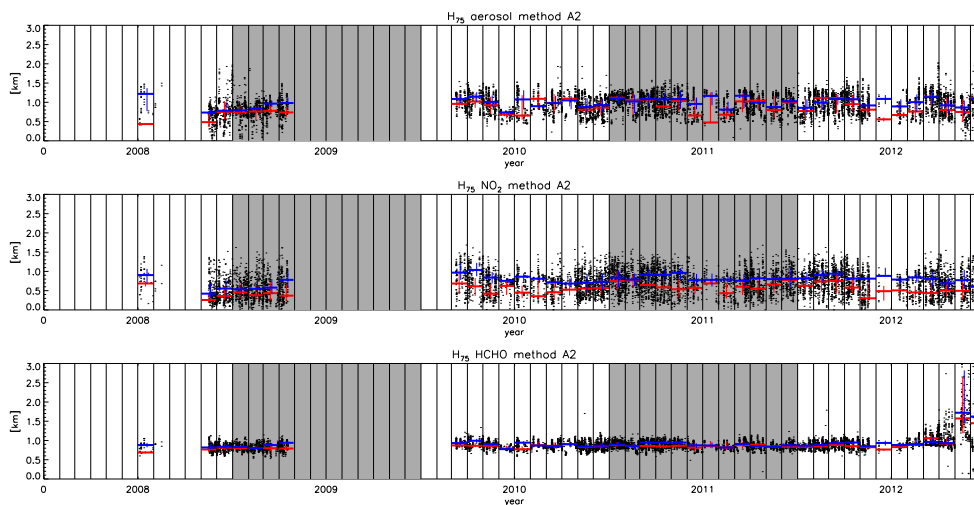


**Figure 12.** Time series of individual data points and monthly medians of profile heights ( $H_{75}$ ) for aerosol (Vis), NO<sub>2</sub> and HCHO obtained with method A. The black dots refer to individual profiles. The red and blue lines refer to monthly medians for the morning (all observations before 10:00 a.m.) and afternoon respectively (all observations after 12:00 p.m.).

A different view on the quality of the profile height retrieval obtained with both methods is given by Fig. 16. From the left panel we can conclude that for both methods the internal consistency (UV vs. Vis) of aerosol extinction profile heights below 1.5 km is quite good, especially for method A. Above 1.5 km we have only very few cases with method A, and all of these cases show a strong bias between UV and Vis. For method B the bias appears to be quite constant over the entire range, with UV profiles that are approximately 25 % lower than profiles in the Vis. The middle panel of Fig. 16

shows a comparison of NO<sub>2</sub> and aerosol extinction profiles. In contrast to aerosols, we do not expect a strong agreement beforehand. What we hope to see, and this is partially the case, is that the general pattern is similar for both methods. Below 1.5 km the agreement is remarkably good, and this is certainly a confirmation that the results obtained with both methods make some sense. As mentioned before, the limited dynamical range of method A makes it almost impossible to draw conclusions on the reliability of profile heights above 1.5 km found with method B. Nevertheless, a possible expla-

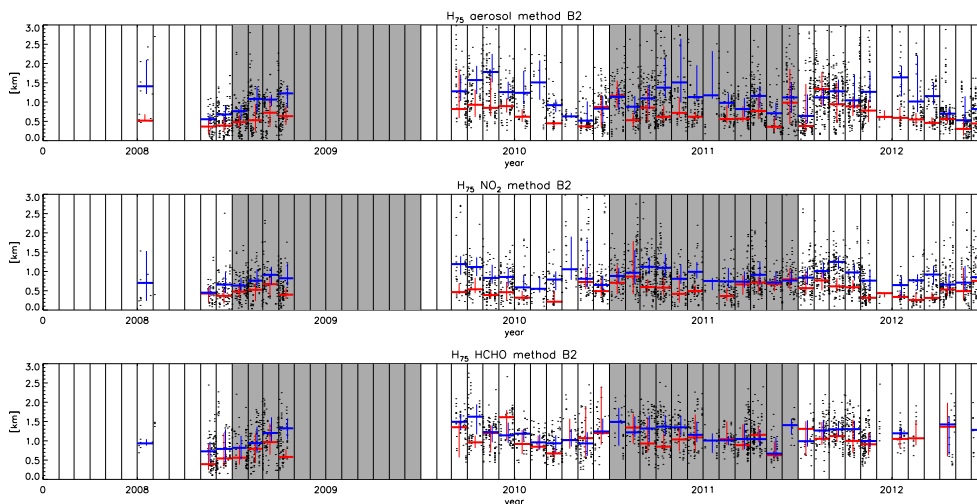


Figure 13. Similar to Fig. 12, but now for method B.

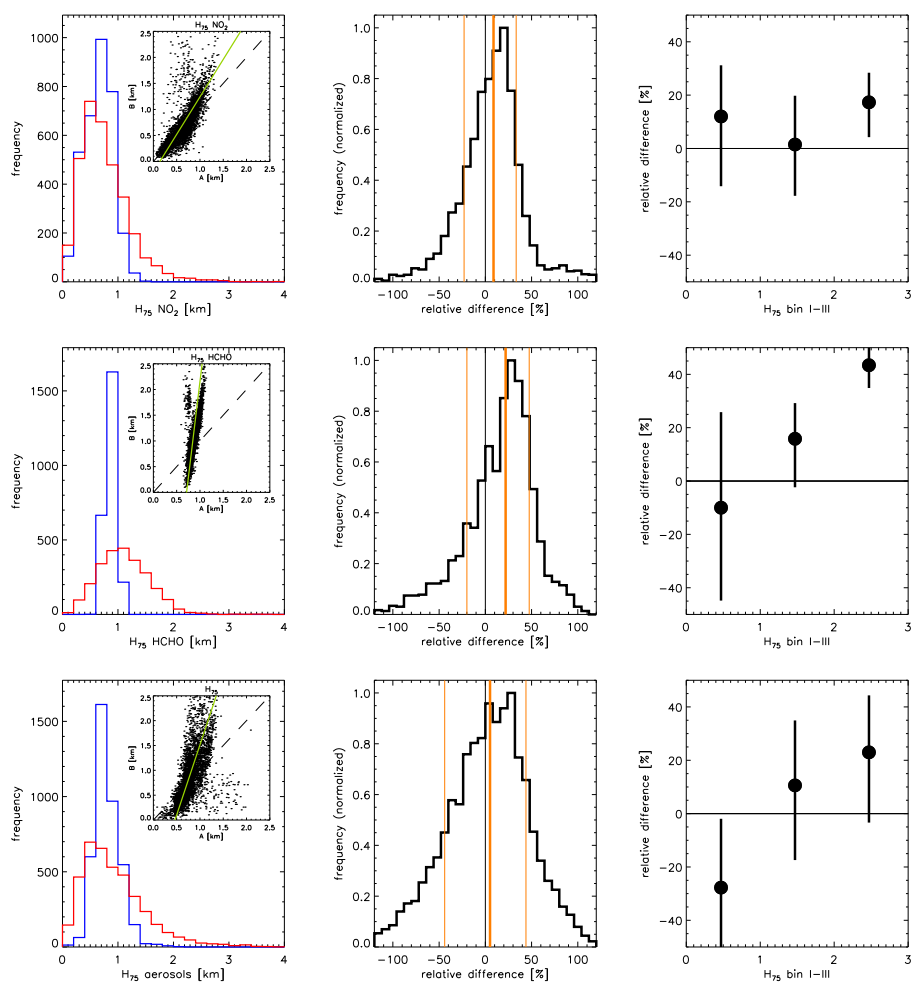
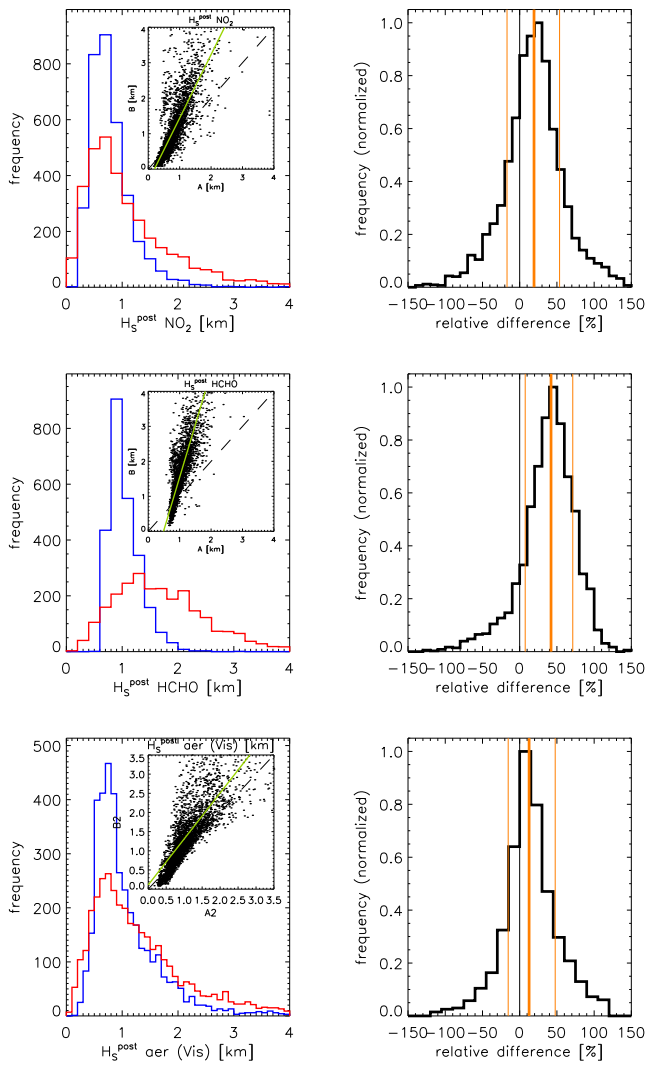


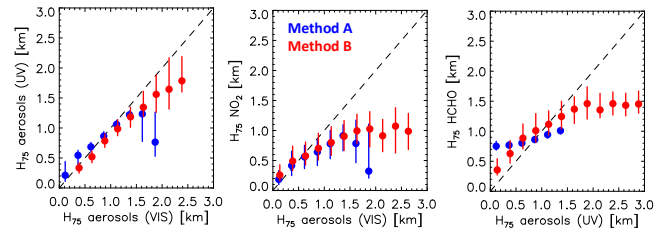
Figure 14. Statistics of characteristic profile height retrievals. The three rows refer to profile heights ( $H_{75}$ ) of  $\text{NO}_2$ , HCHO and aerosols respectively. Left column: frequency distributions obtained with method A (blue) and B (red). Second column: frequency distribution of relative differences (B minus A). Lines in orange indicate the quartiles. Column 3: relative difference sorted as a function of  $H_{75}$  where the three bins refer to the lowest 25 %, middle 50 % and highest 25 % respectively.



**Figure 15.** Similar to Fig. 14, but here for the a posteriori scale height ( $H_s^{\text{post}}$ , Eqs. 6 and 7). The three rows refer  $\text{NO}_2$ , HCHO and aerosols respectively. Left column: frequency distributions obtained with method A (blue) and B (red). Second column: frequency distribution of relative differences (B minus A). Lines in orange indicate the quartiles.

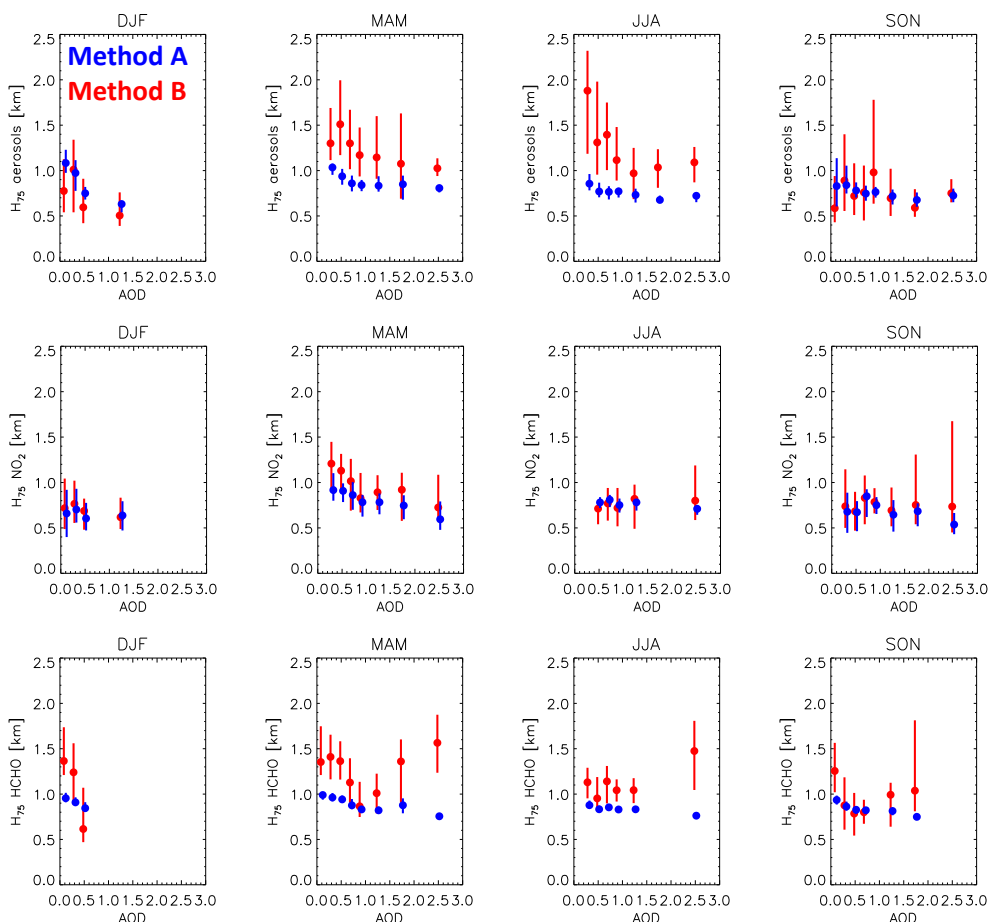
nation for the bias between  $\text{NO}_2$  and aerosol extinction profile heights in this regime is the same as mentioned earlier: higher aerosol extinction profiles occur in summer, but then the lifetime of  $\text{NO}_2$  can be very short, which leads to more shallow  $\text{NO}_2$  profiles.

Figure 17 shows for different seasons the characteristic aerosol extinction,  $\text{NO}_2$  and HCHO profile heights as a function of the AOD. For aerosol extinction profile heights, we see a much stronger seasonal cycle with method B than with method A. In principle a seasonal cycle is also expected: higher boundary layers occur in summer, when the thermal convection is strongest. A possible interpretation of the results seen on the top row (decline of  $H_{75}^{\text{aer}}$  with increasing



**Figure 16.** Three binned scatter plots: aerosol profile heights retrieved in the Vis, vs. profile heights retrieved in the UV (left), aerosol profile height retrieved in the Vis vs.  $\text{NO}_2$  profile heights (middle), aerosol profile heights retrieved in the UV vs. HCHO profile heights (right). Note that models A and B have very different frequency distributions of characteristic profile heights for the three constituents, see Fig. 14.

AOD) is that growth of the boundary layer through convection is weakened by the presence of high aerosol loadings (see also Barbaro et al., 2013). Without independent simultaneous observations with other techniques, it can however not be excluded that this effect is related to the measurement technique itself (i.e. a retrieval artefact). Method B shows a weaker seasonal variation in  $\text{NO}_2$  than in aerosol extinction profile heights and highest  $\text{NO}_2$  profiles occur in spring. This might be due to the fact that in spring the  $\text{NO}_2$  lifetime is not as short as in summer (allowing more time for vertical transport), whereas at the same time vertical transport through convection is stronger than in winter. Results for HCHO are more difficult to interpret. Because the lifetime is longer than for  $\text{NO}_2$ , and because formaldehyde sources can be biogenic and anthropogenic (the relative contribution varies by season) the profile shapes can be very different from those of  $\text{NO}_2$ . A quantity that is especially important in the context of satellite validation and satellite retrievals is the relative difference in  $\text{NO}_2$  and aerosol extinction profile height. The impact of the relative characteristic profile heights on the slant column density measurement can be high, and lead to systematic biases if not accounted for in the retrieval. This quantity is shown for both methods as a function of season in Fig. 18 (also for HCHO). Similar as for the characteristic heights themselves, we see in Fig. 18 a higher dynamic range for method B than for method A. This is partly explained by the lower stability of method B, but also by the ability to retrieve a wider range of profile heights. Both methods detect in spring higher characteristic aerosol than  $\text{NO}_2$  profile heights. In summer method B finds systematically higher values for  $H_{75}^{\text{aer}} - H_{75}^{\text{NO}_2}$  than method A. In winter and autumn, the systematic bias between  $H_{75}^{\text{aer}}$  and  $H_{75}^{\text{NO}_2}$  is smaller. As argued above, results for HCHO are more difficult to interpret (because of the artefact affecting the retrieval with method A). However, based on the results obtained with method B it appears as if aerosol extinction profiles are higher than HCHO profiles in spring and summer, and lower in fall and winter.



**Figure 17.** Median values of the characteristic profile height ( $H_{75}$ ) for aerosols (upper row),  $\text{NO}_2$  (middle row) and HCHO column (bottom row) for a range of AOD bins, specified per season.

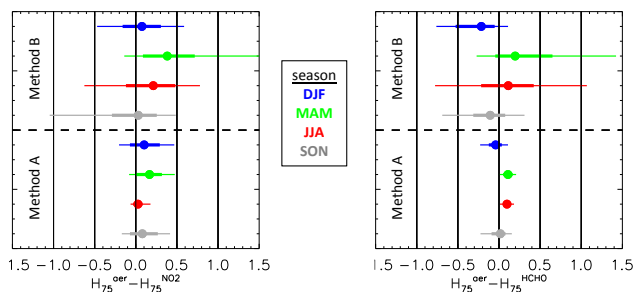


**Figure 18.** Box plots of difference between aerosol and trace gas profile heights ( $\text{NO}_2$  left, HCHO right), specified per season and retrieval method.

### 3.2.3 Aerosol extinction and trace gas volume mixing ratios near the surface

Seasonal variations of volume mixing ratios and aerosol extinction near the surface are shown in Figs. 19 and 20 for methods A and B respectively. For  $\text{NO}_2$  a systematic difference is seen between morning and afternoon values, and this

is clearly related to the dynamics of the mixing layer. For aerosols a similar effect is found. For HCHO however, this contrast is almost absent. This is related to fact that HCHO profiles shapes retrieved with method A show almost no deviation from the a priori (Sect. 3.2.2). As a consequence, the main driver of the surface concentration is the tropospheric column density of HCHO. This explains why for HCHO retrieval with method A the seasonal variation in volume mixing ratios is so similar to the seasonal variation in column densities. For method B (not shown) the results are quite different in winter months, when morning values are about three to four times higher than afternoon values of the HCHO volume mixing ratio. In summer months, this effect appears to be less pronounced, unlike for  $\text{NO}_2$ . It is difficult to draw conclusions based on method B only, but this weaker diurnal variation in HCHO surface volume mixing ratios compared to winter could indicate that in summer local emissions on the surface have a relatively small impact. Based on this data set only, it can however not be excluded that absence of a strong morning–afternoon contrast for HCHO volume mixing ratios in summer is an artefact of the retrieval. Fig-

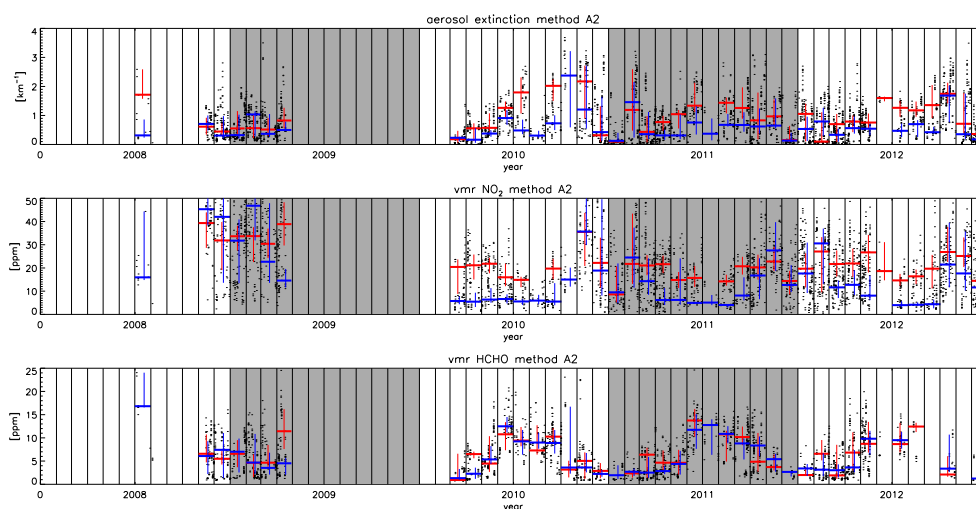


**Figure 19.** Time series of individual data points and monthly medians of near-surface aerosol extinction (upper row) and volume mixing ratios for  $\text{NO}_2$  and HCHO (bottom row), retrieved with method A. Red refers to morning observations, blue to afternoon observations.

ure 21 shows the results of the comparison of methods A and B in terms of trace gas volume mixing ratios and aerosol extinction near the surface (lowest profile layer). In contrast with the results found for the profile heights, the agreement is reasonable, with quite similar histograms for all three constituents. Nevertheless, the systematic relative differences are considerable. For  $\text{NO}_2$  we have a mean relative difference of  $-7.92\%$  with a standard deviation of  $32.97\%$ . For HCHO the relative differences are larger ( $-20.70, \pm 27.71\%$ ) which is mostly explained by the differences in profile shape, because in terms of column densities the relative difference is smaller and of opposite sign ( $9.43\%$ ). With respect to aerosol extinction near the surface, the agreement between methods A and B is good, with correlation  $0.93$ , slope  $1.33$  and intercept  $-0.08$ . The mean relative difference is however considerable ( $10.27\%$ ) and the standard deviation of relative differences is high:  $30.43\%$ .

## 4 Discussion

In this section we address the main question of this paper: what can be concluded on the quality of aerosol extinction and trace gas profiles retrieved from MAX-DOAS observations. We begin with a discussion of strength and weaknesses of both profile retrieval methods, draw conclusions, and then give recommendations for improvements and use.

### 4.1 Impact of quality control

The ideal selection of high-quality data for this comparison study would be based on a validated cloud screening method which performs well under a wide range of aerosol conditions. Such a method was not available when this study was started (in the meantime promising results have been pub-

lished by Wagner et al., 2014, and Gielen et al., 2014). Therefore a pragmatic approach was chosen, see Sect. 2.5. A disadvantage of this approach is that a high number of retrievals is rejected. For example, there are many cases where the trace gas retrieval is rejected (despite a proper  $\chi_v^2$ ) because the  $\chi_v^2$  in the aerosol extinction retrieval is not sufficiently low. The criterion used might be more appropriate for a quality control intended for profiles – and for that reason it is used in this work – but it is probably too strict for a quality control intended for column densities only. Several tests have been performed to check the robustness of findings reported in this paper after changing the selection criteria. For example, the criterion on  $\chi_v^2$  has been relaxed to  $\chi_v^2 < 5$  and the number of AERONET observations in the same hour is lowered from 3 or more to 2 or more. This leads roughly to two times more aerosol extinction profile pairs (see second column of Table 3) and roughly two and a half and three times more profile pairs for HCHO and  $\text{NO}_2$  respectively. The impact of these relaxed settings is considerable for the aerosol extinction retrieval (e.g. mean relative difference in  $H_{75}^{\text{aer}}$  increases from  $2.74$  to  $12.35\%$ ), but quite small for the trace gas retrieval. For example, the mean relative difference in  $H_{75}^{\text{NO}_2}$  increases from  $8.71$  to  $9.85\%$ , and the mean relative difference in the volume mixing ratio for  $\text{NO}_2$  decreases from  $-7.92$  to  $-4.4\%$ , which is a small change compared to the standard deviation ( $32.97\%$ ). There are no sign changes for quantities in Table 3 that are significantly different from zero. It should be noted that the results for the aerosol extinction retrieval obtained with these relaxed constraints are clearly considered to be less representative for ideal clear sky conditions. With every set of quality criteria, the results presented here will change slightly (largely due to a different the sampling of the full data set), however the settings used here are considered to be a reasonable balance between maintain-

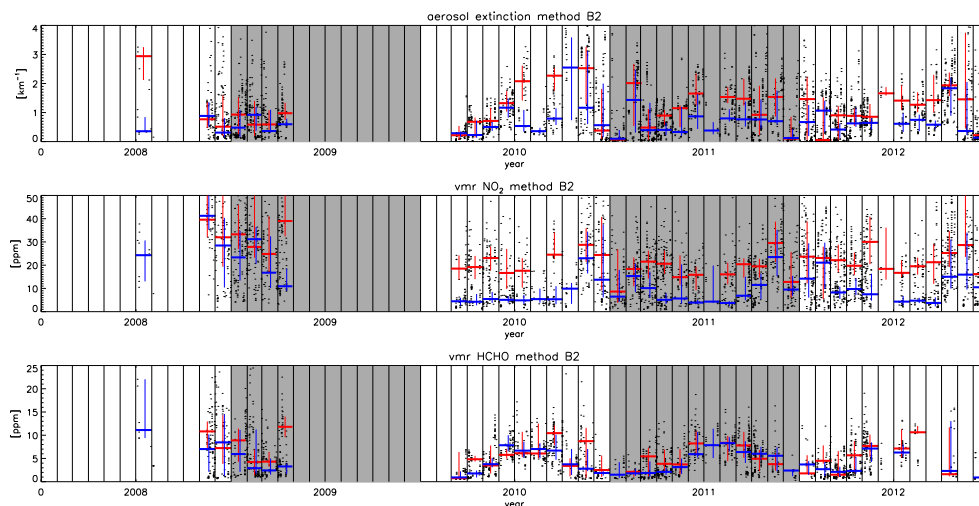


**Figure 20.** Time series of individual data points and monthly medians of near-surface aerosol extinction (upper row) and volume mixing ratios for NO<sub>2</sub> (middle row) and HCHO (bottom row), retrieved with method B. Red refers to morning observations, blue to afternoon observations.

ing sufficient data pairs and rejection of data pairs which are likely to be affected through clouds.

#### 4.2 Strength and weaknesses

In Sect. 3.2 it was shown that both methods show good agreement in terms of tropospheric NO<sub>2</sub> and HCHO column densities: the correlation is high, the slopes of linear fit are close to 1 and the intercepts are relatively close to zero. The agreement of characteristic profile heights is reasonable for NO<sub>2</sub> and aerosols, despite clear biases, especially above 1.5 km. The main strength of method A is its robustness (stability). This is a clear advantage especially when differential slant column densities are close to the detection limit, or when the assumptions that are made about fixed parameters (or cloud-free conditions) do not hold. In such cases, the retrieval can rely on the a priori. The characteristic profile height retrieval with method B is only stable under cloud-free conditions, and if assumptions about fixed parameters are not too far from the truth. The number of profiles which passes the quality control (Sect. 2.5) for method B is significantly smaller than for method A. A disadvantage of method A is that the combination of a profile parameterization based on 13 layers and a relatively low information content of the MAX-DOAS observations forces one to take measures to stabilize the retrieval. These measures are: (1) a relatively conservative estimate of the a priori error (for each profile layer 20 % of the a priori profile estimate) and (2) a profile which decreases to zero rapidly above 1 km. A consequence of this approach is that the absolute values of the a priori error estimate become very low above 1 km. This is believed to be the main reason why it is almost impossible to retrieve profiles with a characteristic height ( $H_{75}$ ) much higher than that of the a priori. In most cases sufficient agreement between observations and

simulations can be achieved by modifying the profile shape (compared to the a priori) only below 1.0 km. This explains why for retrieved NO<sub>2</sub> profiles reduction of  $H_{75}$  compared to the a priori is seen much more often than increase. This is not seen for HCHO. For HCHO it appears that the information content is too low to obtain profiles (with method A) which deviate much from the a priori. A strong aspect of method B is that it can realize a high range of quite different profile shapes, with just a few free parameters. It can more easily realize profiles which have a characteristic height ( $H_{75}$ ) well above 1.0 km. In this study, it is however not possible to fully judge the quality of these profiles because these cannot be retrieved with method A. Nevertheless, the monthly averaged morning to afternoon difference in profile height and the seasonal cycle of aerosol extinction profile heights (Fig. 13) correspond to the expected behaviour and this is at least an indirect indication of the quality of the profiles obtained with method B. Independent (e.g. lidar) observations at the same measurement site would be needed to say more about the quality of individual profiles.

This study also makes clear that the main disadvantage of method B is its instability, despite the limited number of free parameters and the ensemble approach. Note however that the retrieval is certainly not always unstable, see for example the retrievals in the Vis on 15 May 2012 (Fig. 7). The advantage of the ensemble approach taken with method B is that most often the instabilities go along with high-uncertainty estimates, and this provides a means for additional quality control. Unlikely retrievals with a low-uncertainty estimate occur also, but these can most often be excluded based on high values for  $\chi^2$ , either in the aerosol or in the trace gas part of the retrieval.

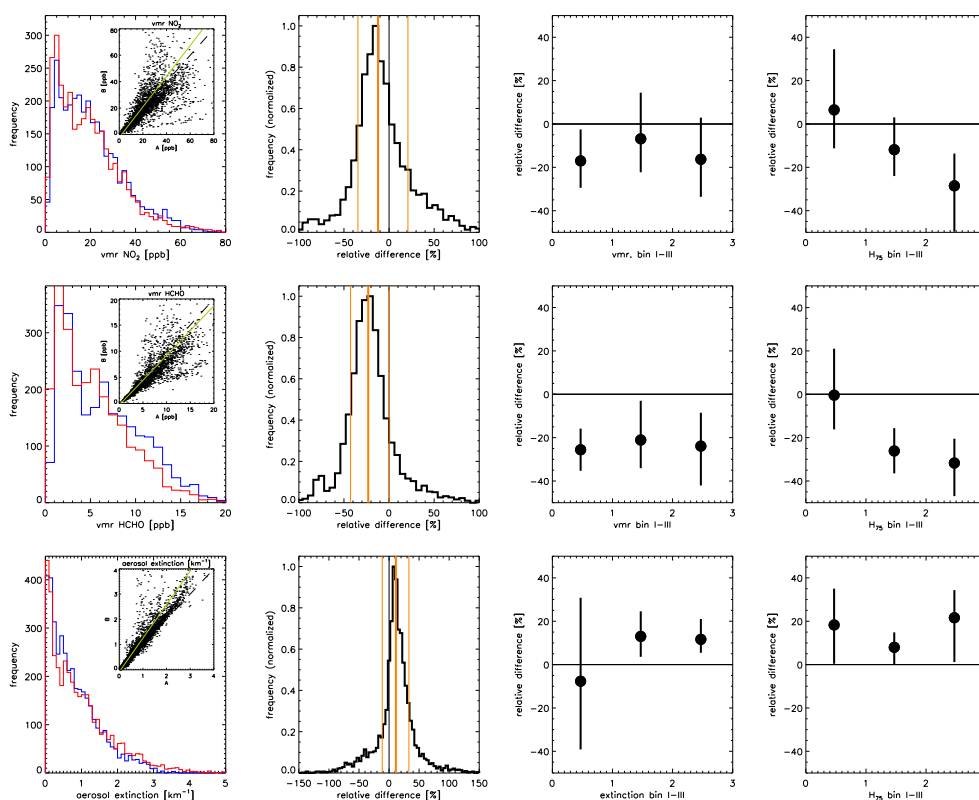


**Figure 21.** Statistics of near-surface concentration retrievals. The three rows refer to volume mixing ratios of  $\text{NO}_2$  (row 1) and  $\text{HCHO}$  (row 2) and aerosol extinction (row 3). Left column: frequency distributions obtained with method A (blue) and B (red). Second column: frequency distribution of relative differences (B minus A). Lines in orange indicate the quartiles. Column 3: relative differences sorted as a function of the volume mixing ratio (rows 1 and 2) and aerosol extinction (row 3). Column 4: relative difference sorted as a function of  $H_{75}$  where the three bins refer to the lowest 25 %, middle 50 % and highest 25 % respectively.

#### 4.3 Recommendations for algorithm improvements and further validation

Both profile retrieval algorithms have specific strengths and weaknesses, as described above. The challenge for improved algorithms is to combine the stability and precision of method A with the ability of method B to retrieve a high dynamic range of characteristic profile heights. A possible but not so practical solution could be to use method B to obtain an initial estimate of the a priori scaling height for method A and then as a next step to perform a retrieval with method A. This will work however only under strict cloud-free conditions because of the limitations for method B. Also it would transfer the impact of instabilities (for individual cases) from method B to method A. An alternative is to use the profile parameterization of method B in the framework of the optimal estimation method. Such a retrieval algorithm could be better capable of retrieving a wide range of profile heights and at the same time be more stable than the present implementation of method B. This would also lead to an algorithm which is considerably faster because there would be no need for an ensemble approach. Improving the

stability of the retrieval by making use of a priori data (in combination with the optimal estimation approach) brings a certain risk, which is that systematic biases in the a priori climatology remain present in the a posteriori climatology. An advantage of more simple retrieval schemes (e.g. method B) is that they are predominantly driven by the observations themselves and therefore less prone to inheritance of systematic biases in the a priori, despite a low precision. It is almost impossible to make a choice which combines the best of both worlds: a very stable retrieval (i.e. precision of individual profiles) without introducing systematic biases in a climatological sense. Stability is important for comparison with satellite observations if the number of available cases is very limited; accuracy over a wide range of profile heights is important if MAX-DOAS would be used to provide a climatology of profile heights for better a priori estimates in the satellite retrieval. The recent work by Hartl and Wenig (2013) provides indications that the Phillips–Tikhonov regularization method can be used for MAX-DOAS profile retrievals which are more stable and at the same time (potentially) less biased in a climatological sense. To our best knowledge, their method has not yet been applied to a long data set of real

observations with a similar focus on the ability to retrieve accurate (first order) profile height estimates. The present study has demonstrated the benefit of having a large data set covering a wide range of measurement conditions. Based on a small data set it would have been very difficult to entangle differences in accuracy and precision. More thorough validation requires simultaneous co-located observations with other techniques (lidar, NO<sub>2</sub> sonde). Such validation efforts are especially useful if a sufficiently large data set is available. In the presence of large differences in spatial representativity (this is very different for satellite, MAX-DOAS and in situ techniques) and a high variability in possible NO<sub>2</sub> and aerosol extinction profile shapes, it is almost impossible to draw conclusions about the accuracy of MAX-DOAS profile shapes based on a quite limited number of co-located observations, even if the precision and accuracy of the other techniques are high.

## 5 Summary and conclusions

A 4-year data set of MAX-DOAS observations in the Beijing area is analysed with two different methods for the retrieval of tropospheric NO<sub>2</sub>, HCHO and aerosol extinction profiles. The objective of this study is firstly to assess for each constituent (NO<sub>2</sub>, HCHO, aerosols) and retrieval quantity (AOD or tropospheric column density, characteristic profile height ( $H_{75}$ ), aerosol extinction or surface concentration) the mutual consistency of the retrievals with both methods, and secondly to identify the mechanisms causing the differences. The two profile retrieval methods differ in many respects. Method A uses a profile parameterization with 13 layers (up to 4 km), on-line forward simulations with the LIDORT radiative transfer model and an inversion based on optimal estimation. Method B uses a profile parameterization based on 2 to 4 parameters to describe the profile shape and a look-up table created with the DAK radiative transfer model. The inversion is based on a least-squares minimization and an ensemble approach is used to improve stability of the solutions and to estimate uncertainties. In the following we summarize the results of the comparison, first in a qualitative sense, then quantitatively. The strength of method A is the stability of the profile shape retrieval, even under cloudy conditions, which is a consequence of the relatively conservative estimate of the uncertainty of the a priori profile. The choice for stability is advantageous for the retrieval of tropospheric column densities and volume mixing ratios near the surface. A negative side effect of this conservative estimate of the uncertainty of the a priori appears to be that the retrieved characteristic profile heights have a relatively small dynamic range. This is most evident for the HCHO profiles retrieved in the UV, but also for aerosol extinction and NO<sub>2</sub> retrieved in the Vis. Method B is generally less stable, and this affects the precision of individual retrievals. The tropospheric column density is least

sensitive to instabilities in the profile retrieval, whereas the characteristic profile height and volume mixing ratio near the surface are most sensitive. The most pronounced difference with method A is the higher dynamic range of retrieved profile heights for aerosols, HCHO and NO<sub>2</sub>. Although the higher dynamic range is partly a consequence of the instability of the retrieval (and therefore not necessarily meaningful), diurnal and seasonal patterns that show up after averaging many profiles give some confidence that the retrievals are meaningful. For example, we see low characteristic profile heights in the morning, and higher values in the afternoon, especially for aerosol extinction in summer. This can be related to the periodical cycles of the boundary layer. Also we find in spring and summer lower aerosol extinction profile heights with decreasing aerosol optical thickness. Although it cannot be excluded that this is a retrieval artefact, this might also be real (and therefore add to the credibility of method B), namely that higher aerosol loads reduce the thermal convection in the boundary layer and therefore lead to lower aerosol extinction profile heights. More quantitatively, we find best agreement for the tropospheric NO<sub>2</sub> column densities (correlation 0.99), with almost no systematic bias (slope 1.03, intercept  $-0.56 \times 10^{15}$  molec cm<sup>-2</sup>) and comparatively small relative differences (mean 0.25 % and standard deviation 9.3 %). For formaldehyde column densities we find a high correlation (0.95) and slope close to one (1.02), but also find that method B is systematically higher than method A: mean relative difference is 9.4 % and standard deviation of relative differences is 12.1 %. Relative differences in formaldehyde column densities are found to be related to differences in profile height: overestimations of the tropospheric column density (for method B compared to method A) often correspond to overestimations of the characteristic profile height (for method B compared to method A). Volume mixing ratios near the surface are systematically lower for method B compared to method A:  $\sim 8$  % relative difference for NO<sub>2</sub> and  $\sim 21$  % for HCHO. The differences can again be related to the differences in profile heights between methods A and B. The standard deviation of relative differences of surface volume mixing ratios is much higher than for tropospheric column densities: 33 % for NO<sub>2</sub> and 28 % for HCHO. Characteristic profile heights are systematically higher for method B than for method A. The mean relative differences are 6.5 % for NO<sub>2</sub>, 15.7 % for HCHO and 2.7 % for aerosols (Vis). The high standard deviation of relative differences (33, 37 and 44 % for NO<sub>2</sub>, HCHO and aerosols respectively) shows that the precision of characteristic profile heights is low. We find with method B that in spring and summer aerosol extinction profiles are systematically higher than NO<sub>2</sub> profiles. Also we find that in winter and summer mornings HCHO profiles are systematically higher than aerosol extinction profiles, and vice versa in summer afternoons. Note however that these findings are only indicative, because the limitations with method A prevent confirmation of the results obtained with method B. Altogether,

this study gives some indications about the quality of tropospheric column densities, surface concentrations and profile heights retrieved with MAX-DOAS. Since this study is based solely on MAX-DOAS observations the scope is limited and a more thorough validation is needed. In order to obtain robust validation results which can entangle differences related to accuracy and/or precision for a wide range of pollution and sky conditions, it is recommended to station MAX-DOAS instruments close to continuously monitoring surface in situ monitors (e.g. for NO<sub>2</sub>), sun photometers and lidars which are sufficiently sensitive to boundary layer aerosols.

*Acknowledgements.* This research was financially supported at IASB-BIRA by the Belgian Federal Science Policy Office, Brussels (AGACC-II project) and the EU 7th Framework Programme projects NORS (contract 284421) and SHIVA (contract 226224). The authors would like to acknowledge R. Spurr for providing the LIDORT package, and P. Stammes and P. Wang for providing DAK. We thank Pucai Wang, Hong-Bin Chen and Philippe Goloub for their effort in establishing and maintaining the Xianghe and Beijing AERONET sites. Furthermore we would like to thank Trissevgeni Stavrakou from IASB-BIRA for her contributions to this work.

Edited by: H. Worden

## References

- Barbaro, E., Vilà-Guerau de Arellano, J., Krol, M., and Holtslag, A.: Impacts of aerosol shortwave radiation absorption on the dynamics of an idealized convective atmospheric boundary layer, *Bound.-Lay. Meteorol.*, 148, 31–49, 2013.
- Boersma, K. F., Jacob, D. J., Trainic, M., Rudich, Y., DeSmedt, I., Dirksen, R., and Eskes, H. J.: Validation of urban NO<sub>2</sub> concentrations and their diurnal and seasonal variations observed from the SCIAMACHY and OMI sensors using in situ surface measurements in Israeli cities, *Atmos. Chem. Phys.*, 9, 3867–3879, doi:10.5194/acp-9-3867-2009, 2009.
- Brinksma, E. J., Pinardi, G., Volten, H., Braak, R., Richter, A., Schoenhardt, A., Van Roozendaal, M., Fayt, C., Hermans, C., Dirksen, R. J., Vlemmix, T., Berkhout, A. J. C., Swart, D. P. J., Oetjes, H., Wittrock, F., Wagner, T., Ibrahim, O., de Leeuw, G., Moerman, M., Curier, R. L., Celarier, E. A., Cede, A., Knap, W. H., Veefkind, J. P., Eskes, H. J., Allaart, M., Rothe, R., PETERS, A. J. M., and Levelt, P. F.: The 2005 and 2006 DANDELIONS NO<sub>2</sub> and aerosol intercomparison campaigns, *J. Geophys. Res.*, 113, D16S46, doi:10.1029/2007JD008808, 2008.
- Clémer, K., Van Roozendaal, M., Fayt, C., Hendrick, F., Hermans, C., Pinardi, G., Spurr, R., Wang, P., and De Mazière, M.: Multiple wavelength retrieval of tropospheric aerosol optical properties from MAXDOAS measurements in Beijing, *Atmos. Meas. Tech.*, 3, 863–878, doi:10.5194/amt-3-863-2010, 2010.
- Coburn, S., Dix, B., Sinreich, R., and Volkamer, R.: The CU ground MAX-DOAS instrument: characterization of RMS noise limitations and first measurements near Pensacola, FL of BrO, IO, and CHOCHO, *Atmos. Meas. Tech.*, 4, 2421–2439, doi:10.5194/amt-4-2421-2011, 2011.
- De Haan, J. F., Bosma, P. B., and Hovenier, J. W.: The adding method for multiple scattering calculations of polarized light, *Astron. Astrophys.*, 183, 371–393, 1987.
- Fayt, C., De Smedt, I., Letocart, V., Merlaud, A., Pinardi, G., and Van Roozendaal, M.: QDOAS Software user manual, available at: <http://uv-vis.aeronomie.be/software/QDOAS/index.php> (last access: 30 June 2013), 2011.
- Gielen, C., Van Roozendaal, M., Hendrick, F., Pinardi, G., Vlemmix, T., De Bock, V., De Backer, H., Fayt, C., Hermans, C., Gillotay, D., and Wang, P.: A simple and versatile cloud-screening method for MAX-DOAS retrievals, *Atmos. Meas. Tech.*, 7, 3509–3527, doi:10.5194/amt-7-3509-2014, 2014.
- Halla, J. D., Wagner, T., Beirle, S., Brook, J. R., Hayden, K. L., O'Brien, J. M., Ng, A., Majonis, D., Wenig, M. O., and McLaren, R.: Determination of tropospheric vertical columns of NO<sub>2</sub> and aerosol optical properties in a rural setting using MAX-DOAS, *Atmos. Chem. Phys.*, 11, 12475–12498, doi:10.5194/acp-11-12475-2011, 2011.
- Hartl, A. and Wenig, M. O.: Regularisation model study for the least-squares retrieval of aerosol extinction time series from UV/Vis MAX-DOAS observations for a ground layer profile parameterisation, *Atmos. Meas. Tech.*, 6, 1959–1980, doi:10.5194/amt-6-1959-2013, 2013.
- Hendrick, F., Müller, J.-F., Clémer, K., Wang, P., De Mazière, M., Fayt, C., Gielen, C., Hermans, C., Ma, J. Z., Pinardi, G., Stavrakou, T., Vlemmix, T., and Van Roozendaal, M.: Four years of ground-based MAX-DOAS observations of HONO and NO<sub>2</sub> in the Beijing area, *Atmos. Chem. Phys.*, 14, 765–781, doi:10.5194/acp-14-765-2014, 2014.
- Herman, J., Cede, A., Spinei, E., Mount, G., Tzortziou, M., and Abuhassan, N.: NO<sub>2</sub> column amounts from ground-based Pandora and MFDOAS spectrometers using the direct-sun DOAS technique: Intercomparisons and application to OMI validation, *J. Geophys. Res.*, 114, D13307, doi:10.1029/2009JD011848, 2009.
- Irie, H., Kanaya, Y., Akimoto, H., Iwabuchi, H., Shimizu, A., and Aoki, K.: First retrieval of tropospheric aerosol profiles using MAX-DOAS and comparison with lidar and sky radiometer measurements, *Atmos. Chem. Phys.*, 8, 341–350, doi:10.5194/acp-8-341-2008, 2008a.
- Irie, H., Kanaya, Y., Akimoto, H., Tanimoto, H., Wang, Z., Gleason, J. F., and Bucsela, E. J.: Validation of OMI tropospheric NO<sub>2</sub> column data using MAX-DOAS measurements deep inside the North China Plain in June 2006: Mount Tai Experiment 2006, *Atmos. Chem. Phys.*, 8, 6577–6586, doi:10.5194/acp-8-6577-2008, 2008b.
- Irie, H., Takashima, H., Kanaya, Y., Boersma, K. F., Gast, L., Wittrock, F., Brunner, D., Zhou, Y., and Van Roozendaal, M.: Eight-component retrievals from ground-based MAX-DOAS observations, *Atmos. Meas. Tech.*, 4, 1027–1044, doi:10.5194/amt-4-1027-2011, 2011.
- Kanaya, Y., Irie, H., Takashima, H., Iwabuchi, H., Akimoto, H., Sudo, K., Gu, M., Chong, J., Kim, Y. J., Lee, H., Li, A., Si, F., Xu, J., Xie, P.-H., Liu, W.-Q., Dzhola, A., Postlyakov, O., Ivanov, V., Grechko, E., Terpugova, S., and Panchenko, M.: Long-term MAX-DOAS network observations of NO<sub>2</sub> in Russia and Asia (MADRAS) during the period 2007–2012: instrumentation, elucidation of climatology, and comparisons with OMI satellite observations and global model simulations, *At-*

- mos. Chem. Phys., 14, 7909–7927, doi:10.5194/acp-14-7909-2014, 2014.
- Li, X., Brauers, T., Shao, M., Garland, R. M., Wagner, T., Deutschmann, T., and Wahner, A.: MAX-DOAS measurements in southern China: retrieval of aerosol extinctions and validation using ground-based in-situ data, *Atmos. Chem. Phys.*, 10, 2079–2089, doi:10.5194/acp-10-2079-2010, 2010.
- Li, X., Brauers, T., Hofzumahaus, A., Lu, K., Li, Y. P., Shao, M., Wagner, T., and Wahner, A.: MAX-DOAS measurements of NO<sub>2</sub>, HCHO and CHOCHO at a rural site in Southern China, *Atmos. Chem. Phys.*, 13, 2133–2151, doi:10.5194/acp-13-2133-2013, 2013.
- Lin, J.-T., Martin, R. V., Boersma, K. F., Sneep, M., Stammes, P., Spurr, R., Wang, P., Van Roozendaal, M., Clémer, K., and Irie, H.: Retrieving tropospheric nitrogen dioxide from the Ozone Monitoring Instrument: effects of aerosols, surface reflectance anisotropy, and vertical profile of nitrogen dioxide, *Atmos. Chem. Phys.*, 14, 1441–1461, doi:10.5194/acp-14-1441-2014, 2014.
- Luo, T., Yuan, R., and Wang, Z.: Lidar-based remote sensing of atmospheric boundary layer height over land and ocean, *Atmos. Meas. Tech.*, 7, 173–182, doi:10.5194/amt-7-173-2014, 2014.
- Ma, J. Z., Beirle, S., Jin, J. L., Shaiganfar, R., Yan, P., and Wagner, T.: Tropospheric NO<sub>2</sub> vertical column densities over Beijing: results of the first three years of ground-based MAX-DOAS measurements (2008–2011) and satellite validation, *Atmos. Chem. Phys.*, 13, 1547–1567, doi:10.5194/acp-13-1547-2013, 2013.
- Frieß, U., Monks, P. S., Remedios, J. J., Rozanov, A., Sinreich, R., Wagner, T., and Platt, U.: MAX-DOAS O<sub>4</sub> measurements: a new technique to derive information on atmospheric aerosols: 2. Modeling studies, *J. Geophys. Res.*, 111, D14203, doi:10.1029/2005JD006618, 2006.
- Mendolia, D., D'Souza, R. J. C., Evans, G. J., and Brook, J.: Comparison of tropospheric NO<sub>2</sub> vertical columns in an urban environment using satellite, multi-axis differential optical absorption spectroscopy, and in situ measurements, *Atmos. Meas. Tech.*, 6, 2907–2924, doi:10.5194/amt-6-2907-2013, 2013.
- Pinardi, G., Van Roozendaal, M., Abuhassan, N., Adams, C., Cede, A., Clémer, K., Fayt, C., Frieß, U., Gil, M., Herman, J., Hermans, C., Hendrick, F., Irie, H., Merlaud, A., Navarro Comas, M., Peters, E., PETERS, A. J. M., Puente-dura, O., Richter, A., Schönhardt, A., Shaiganfar, R., Spinei, E., Strong, K., Takashima, H., Vrekoussis, M., Wagner, T., Wittrock, F., and Yilmaz, S.: MAX-DOAS formaldehyde slant column measurements during CINDI: intercomparison and analysis improvement, *Atmos. Meas. Tech.*, 6, 167–185, doi:10.5194/amt-6-167-2013, 2013.
- Platt, U. and Stutz, J.: *Differential Optical Absorption Spectroscopy*, Springer-Verlag, Berlin, Heidelberg, 2008.
- Richter, A., Weber, M., Burrows, J., Lambert, J.-C., and van Gijssels, A.: Validation strategy for satellite observations of tropospheric reactive gases, *Ann. Geophys.-Italy*, 56, doi:10.4401/ag-6335, 2013.
- Rodgers, C. D.: *Inverse Methods For Atmospheric Sounding: Theory and Practice*, Ser. Atmos. Oceanic Planet. Phys., World Scientific Publishing, 2000.
- Rodgers, C. D. and Connor, B. J.: Intercomparison of remote sounding instruments, *J. Geophys. Res.*, 108, 4116, doi:10.1029/2002JD002299, 2003.
- Roscoe, H. K., Van Roozendaal, M., Fayt, C., du Piesanie, A., Abuhassan, N., Adams, C., Akrami, M., Cede, A., Chong, J., Clémer, K., Friess, U., Gil Ojeda, M., Goutail, F., Graves, R., Griesfeller, A., Grossmann, K., Hemerijckx, G., Hendrick, F., Herman, J., Hermans, C., Irie, H., Johnston, P. V., Kanaya, Y., Kreher, K., Leigh, R., Merlaud, A., Mount, G. H., Navarro, M., Oetjen, H., Pazmino, A., Perez-Camacho, M., Peters, E., Pinardi, G., Puente-dura, O., Richter, A., Schönhardt, A., Shaiganfar, R., Spinei, E., Strong, K., Takashima, H., Vlemmix, T., Vrekoussis, M., Wagner, T., Wittrock, F., Yela, M., Yilmaz, S., Boersma, F., Hains, J., Kroon, M., PETERS, A., and Kim, Y. J.: Intercomparison of slant column measurements of NO<sub>2</sub> and O<sub>4</sub> by MAX-DOAS and zenith-sky UV and visible spectrometers, *Atmos. Meas. Tech.*, 3, 1629–1646, doi:10.5194/amt-3-1629-2010, 2010.
- Sinreich, R., Merten, A., Molina, L., and Volkamer, R.: Parameterizing radiative transfer to convert MAX-DOAS dSCDs into near-surface box-averaged mixing ratios, *Atmos. Meas. Tech.*, 6, 1521–1532, doi:10.5194/amt-6-1521-2013, 2013.
- Spurr, R.: LIDORT and VLIDORT: linearized pseudo-spherical scalar and vector discrete ordinate radiative transfer models for use in remote sensing retrieval problems, in: *Light Scattering Reviews*, 3, edited by: Kokhanovsky, A., 2008.
- Stammes, P., de Haan, J. F., and Hovenier, J. W.: The polarized internal radiation field of a planetary atmosphere, *Astron. Astrophys.*, 225, 239–259, 1989.
- Vlemmix, T., PETERS, A. J. M., Berkhout, A. J. C., Gast, L. F. L., Wang, P., and Levelt, P. F.: Ability of the MAX-DOAS method to derive profile information for NO<sub>2</sub>: can the boundary layer and free troposphere be separated?, *Atmos. Meas. Tech.*, 4, 2659–2684, doi:10.5194/amt-4-2659-2011, 2011.
- Wagner, T., Dix, B., von Friedeburg, C., Frieß, U., Sanghavi, S., Sinreich, R., and Platt, U.: MAX-DOAS O<sub>4</sub> measurements: a new technique to derive information on atmospheric aerosols – principles and information content, *J. Geophys. Res.*, 109, D22205, doi:10.1029/2004JD004904, 2004.
- Wagner, T., Burrows, J. P., Deutschmann, T., Dix, B., von Friedeburg, C., Frieß, U., Hendrick, F., Heue, K.-P., Irie, H., Iwabuchi, H., Kanaya, Y., Keller, J., McLinden, C. A., Oetjen, H., Palazzi, E., Petritoli, A., Platt, U., Postlyakov, O., Pukite, J., Richter, A., van Roozendaal, M., Rozanov, A., Rozanov, V., Sinreich, R., Sanghavi, S., and Wittrock, F.: Comparison of box-air-mass-factors and radiances for Multiple-Axis Differential Optical Absorption Spectroscopy (MAX-DOAS) geometries calculated from different UV/visible radiative transfer models, *Atmos. Chem. Phys.*, 7, 1809–1833, doi:10.5194/acp-7-1809-2007, 2007.
- Wagner, T., Deutschmann, T., and Platt, U.: Determination of aerosol properties from MAX-DOAS observations of the Ring effect, *Atmos. Meas. Tech.*, 2, 495–512, doi:10.5194/amt-2-495-2009, 2009.
- Wagner, T., Beirle, S., Brauers, T., Deutschmann, T., Frieß, U., Hak, C., Halla, J. D., Heue, K. P., Junkermann, W., Li, X., Platt, U., and Pundt-Gruber, I.: Inversion of tropospheric profiles of aerosol extinction and HCHO and NO<sub>2</sub> mixing ratios from MAX-DOAS observations in Milano during the summer of 2003 and comparison with independent data sets, *Atmos. Meas. Tech.*, 4, 2685–2715, doi:10.5194/amt-4-2685-2011, 2011.

- Wagner, T., Apituley, A., Beirle, S., Dörner, S., Friess, U., Remmers, J., and Shaiganfar, R.: Cloud detection and classification based on MAX-DOAS observations, *Atmos. Meas. Tech.*, 7, 1289–1320, doi:10.5194/amt-7-1289-2014, 2014.
- Wang, T., Hendrick, F., Wang, P., Tang, G., Clémer, K., Yu, H., Fayt, C., Hermans, C., Gielen, C., Müller, J.-F., Pinardi, G., Theys, N., Brenot, H., and Van Roozendaal, M.: Evaluation of tropospheric SO<sub>2</sub> retrieved from MAX-DOAS measurements in Xianghe, China, *Atmos. Chem. Phys.*, 14, 11149–11164, doi:10.5194/acp-14-11149-2014, 2014.
- Wittrock, F., Oetjen, H., Richter, A., Fietkau, S., Medeke, T., Rozanov, A., and Burrows, J. P.: MAX-DOAS measurements of atmospheric trace gases in Ny-Ålesund – Radiative transfer studies and their application, *Atmos. Chem. Phys.*, 4, 955–966, doi:10.5194/acp-4-955-2004, 2004.



# Evaluation of tropospheric SO<sub>2</sub> retrieved from MAX-DOAS measurements in Xianghe, China

T. Wang<sup>1,2</sup>, F. Hendrick<sup>2</sup>, P. Wang<sup>1</sup>, G. Tang<sup>1</sup>, K. Clémer<sup>2,\*</sup>, H. Yu<sup>2</sup>, C. Fayt<sup>2</sup>, C. Hermans<sup>2</sup>, C. Gielen<sup>2</sup>, J.-F. Müller<sup>2</sup>, G. Pinardi<sup>2</sup>, N. Theys<sup>2</sup>, H. Brenot<sup>2</sup>, and M. Van Roozendael<sup>2</sup>

<sup>1</sup>Institute of Atmospheric Physics, Chinese Academy of Sciences, Beijing, China

<sup>2</sup>Belgian Institute for Space Aeronomy, Brussels, Belgium

\* now at: Instituut voor Sterrenkunde, Katholieke Universiteit Leuven, Leuven, Belgium

Correspondence to: F. Hendrick (franch@oma.be)

Received: 7 January 2014 – Published in Atmos. Chem. Phys. Discuss.: 11 March 2014

Revised: 15 September 2014 – Accepted: 15 September 2014 – Published: 23 October 2014

**Abstract.** Ground-based multi-axis differential optical absorption spectroscopy (MAX-DOAS) measurements of sulfur dioxide (SO<sub>2</sub>) have been performed at the Xianghe station (39.8° N, 117.0° E) located at ~ 50 km southeast of Beijing from March 2010 to February 2013. Tropospheric SO<sub>2</sub> vertical profiles and corresponding vertical column densities (VCDs), retrieved by applying the optimal estimation method to the MAX-DOAS observations, have been used to study the seasonal and diurnal cycles of SO<sub>2</sub>, in combination with correlative measurements from in situ instruments, as well as meteorological data. A marked seasonality was observed in both SO<sub>2</sub> VCD and surface concentration, with a maximum in winter (February) and a minimum in summer (July). This can be explained by the larger emissions in winter due to the domestic heating and, in case of surface concentration, by more favorable meteorological conditions for the accumulation of SO<sub>2</sub> close to the ground during this period. Wind speed and direction are also found to be two key factors in controlling the level of the SO<sub>2</sub>-related pollution at Xianghe. In the case of east or southwest wind, the SO<sub>2</sub> concentration does not change significantly with the wind speed, since the city of Tangshan and heavy polluting industries are located to the east and southwest of the station, respectively. In contrast, when wind comes from other directions, the stronger the wind, the less SO<sub>2</sub> is observed due to a more effective dispersion. Regarding the diurnal cycle, the SO<sub>2</sub> amount is larger in the early morning and late evening and lower at noon, in line with the diurnal variation of pollutant emissions and atmospheric stability. A strong correlation with correlation coefficients between

0.6 and 0.9 is also found between SO<sub>2</sub> and aerosols in winter, suggesting that anthropogenic SO<sub>2</sub>, through the formation of sulfate aerosols, contributes significantly to the total aerosol content during this season. The observed diurnal cycles of MAX-DOAS SO<sub>2</sub> surface concentration are also in very good agreement (correlation coefficient close to 0.9) with those from collocated in situ data, indicating the good reliability and robustness of our retrieval.

## 1 Introduction

Sulfur dioxide (SO<sub>2</sub>), one of the most common air pollutants, is of major concern in pollution control acts (Gauderman et al., 2000). In China, the Ministry of Environmental Protection (MEP) lists SO<sub>2</sub> as one of the three conventional pollutants, together with NO<sub>2</sub> and PM<sub>10</sub>, and daily averaged SO<sub>2</sub> concentrations were used as an indicator to quantify the level of pollution (Yan et al., 2010). This trace gas is predominantly produced by the burning of fossil fuels including oil and coal, and the smelting of mineral ores that contain sulfur (Yan et al., 2005; Zhao et al., 2012). SO<sub>2</sub> contributes to a large extent to the process of acidification resulting in acid rain and to the formation of sulfate aerosols, both of which cause human health damages, building surface corrosion, and visibility reduction. In particular, the secondary pollutant sulfate aerosols generated by SO<sub>2</sub> are the primary source of fine solid particles in cities, which are also responsible for severe air pollution issues (Meng et al., 2009). In addition, the ongoing industrial development, population growth, and heavy

traffic contribute to higher energy consumption and, therefore, to an increase in SO<sub>2</sub> emissions into the atmosphere (Wu et al., 2013). Consequently, in order to meet the urgent demand to improve and control air quality in China, as well as to promote sustainable development, it is of the greatest importance to study the evolution of a pollutant like SO<sub>2</sub> and to identify its possible origins.

So far, the SO<sub>2</sub> surface concentration has been monitored using in situ and long-path DOAS (differential optical absorption spectroscopy) instruments (Meng et al., 2009), while satellite sensors like GOME, SCIAMACHY, GOME-2, OMI, OMPS, and IASI have shown their ability to measure the SO<sub>2</sub> vertical column density (VCD) over polluted areas (see, e.g., Eisinger and Burrows, 1998; Krotkov et al., 2006; Lee et al., 2009; Nowlan et al., 2011; Fioletov et al., 2013; Yang et al., 2013; Boynard et al., 2014). During the last decade, a new remote sensing technique called MAX-DOAS (multi-axis differential optical absorption spectroscopy) has been developed, providing information on both VCD and vertical distribution of trace gases in the troposphere (Hönninger et al., 2004; Platt and Stutz, 2008). It is based on the measurement of sunlight scattered at multiple elevation angles towards the horizon, thus increasing the sensitivity to absorbers present close to the ground compared to the zenith viewing geometry (Hönninger et al., 2004). MAX-DOAS studies published so far have been mainly focused on the retrieval of NO<sub>2</sub> (e.g., Wittrock et al., 2004; Vlemmix et al., 2010; Frins et al., 2012; Hendrick et al., 2014; Ma et al., 2013; Wang et al., 2014), halogen oxides like BrO and IO (e.g., Frieß et al., 2011; Großmann et al., 2013), formaldehyde (e.g., Heckel et al., 2005; Wagner et al., 2011), and aerosols (e.g., Wagner et al., 2004; Frieß et al., 2006; Clémer et al., 2010). A lot of work has been done on MAX-DOAS measurements of volcanic SO<sub>2</sub> (e.g., Bobrowski et al., 2007; Galle et al., 2010), but so far only a few studies deal with MAX-DOAS observations of this species in polluted areas (e.g., Irie et al., 2011; Lee et al., 2008; Wu et al., 2013), despite the fact that, as for other trace gases like NO<sub>2</sub>, HCHO, and BrO, the combination of both surface concentration and VCD retrievals makes MAX-DOAS a useful technique for validating SO<sub>2</sub> satellite data.

Here we present 3 years (March 2010–February 2013) of continuous MAX-DOAS SO<sub>2</sub> observations at the Xianghe Observatory, China (39.8° N, 117.0° E), located at about 50 km southeast of Beijing, at the borders among Beijing, Tangshan and Tianjin (see Fig. 1). The station is operated by the Institute of Atmospheric Physics (IAP)/Chinese Academy of Sciences (CAS) while the MAX-DOAS instrument was developed by the Belgian Institute for Space Aeronomy (BIRA-IASB) and validated in several intercomparison exercises, in particular as part of the international Cabauw Intercomparison of Nitrogen Dioxide measuring Instruments (CINDI, Roscoe et al., 2010) and more recently a national Chinese MAX-DOAS instrument intercomparison campaign held in Xianghe (Wang et al., 2013). SO<sub>2</sub> MAX-

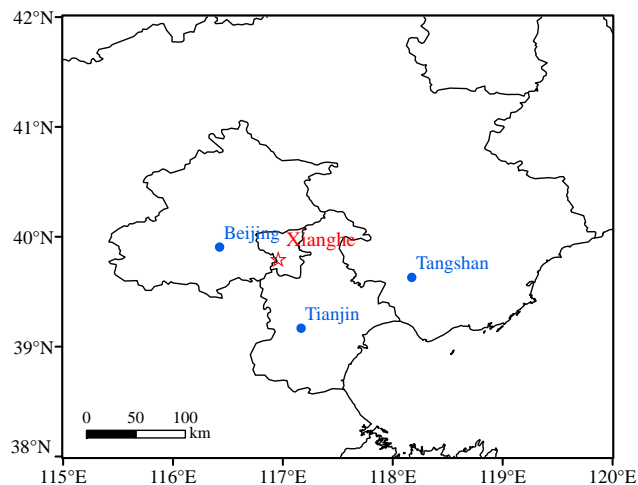


**Figure 1.** Location of the Xianghe Observatory (red star) and major neighborhood cities.

DOAS observations are used here in combination with in situ measurements as well as conventional meteorological data (temperature, humidity, wind direction and speed) to investigate the seasonal and diurnal cycles of SO<sub>2</sub> vertical profiles and VCDs. The paper is divided into three main sections. In Sect. 2, the SO<sub>2</sub> measurements are described, including the DOAS analysis, vertical profile retrieval, and retrieval verification through comparison with in situ data. The seasonal and diurnal cycles of SO<sub>2</sub>, and the relationship between SO<sub>2</sub> and aerosols are investigated in Sect. 3. Finally, conclusions are given Sect. 4.

## 2 Data

### 2.1 Instrument

The MAX-DOAS instrument operated at the Xianghe Observatory consists of three components: a thermo-regulated box containing two spectrometers, an optical head mounted on a sun tracker, and two computers for instrument control and data storage (Clémer et al., 2010). The optical head and the two spectrometers are linked by two-way splitter optical fibers (Clémer et al., 2010; Wang et al., 2013). This setup is capable of measuring scattered as well as direct sunlight. One spectrometer works in the UV region (300 to 390 nm) and its instrumental function is close to a Gaussian with a full width at half maximum (FWHM) of 0.4 nm. The other spectrometer covers the visible wavelength range from 400 to 720 nm with a FWHM equal to 0.9 nm. During the observation, the azimuth direction of the telescope is fixed to the north. A full MAX-DOAS scan consists of nine elevation viewing angles (2, 4, 6, 8, 10, 12, 15, 30, and 90°) and lasts about 15 min (Clémer et al., 2010). The 3-year data set investigated in this study covers the March 2010 to February 2013 period.

**Table 1.** Settings used for the SO<sub>2</sub> and O<sub>4</sub> DOAS analysis.

| Parameter         | Data source                         | Fitting interval nm          |                                 |
|-------------------|-------------------------------------|------------------------------|---------------------------------|
|                   |                                     | 338–370 nm (O <sub>4</sub> ) | 305–317.5 nm (SO <sub>2</sub> ) |
| NO <sub>2</sub>   | Vandaele et al. (1998) 220 K, 294 K | x                            | x (only 294 K)                  |
| SO <sub>2</sub>   | Vandaele et al. (1994) 294 K        |                              | x                               |
| O <sub>3</sub>    | Bogumil et al. (2003) 223 K, 243 K  | x (only 223 K)               | x                               |
| O <sub>4</sub>    | Hermans et al. (2003) 296 K         | x                            |                                 |
| BrO               | Fleischmann et al. (2004) 223 K     | x                            |                                 |
| H <sub>2</sub> CO | Meller and Moortgat (2000) 293 K    | x                            |                                 |
| Ring              | Chance and Spurr (1997)             | x                            | x                               |
| Polynomial degree |                                     | 5                            | 5                               |

## 2.2 DOAS analysis

Scattered-sunlight spectra measured at different elevation angles (EVAs) are analyzed using the DOAS technique (Platt and Stutz, 2008) where high-frequency molecular absorption structures in the UV and visible regions of the spectrum are exploited to detect and quantify a number of key atmospheric gases such as SO<sub>2</sub>.

In this work, the spectra obtained from MAX-DOAS observations are analyzed using the QDOAS spectral-fitting software suite developed at BIRA-IASB (<http://uv-vis.aeronomie.be/software/QDOAS/>). QDOAS calculates the SO<sub>2</sub> differential slant column densities (DSCDs), which are defined as the difference between the trace-gas concentration integrated along the effective light path and the amount of the absorber in a measured reference spectrum. (MAX-)DOAS is recognized as a “self-calibrating” technique because differential absorptions are measured and therefore the impact of possible instrumental degradations can be largely removed by using appropriate reference spectra. In contrast, in situ instruments need to be optically and/or chemically calibrated on a regular basis, especially when performing long-term measurements. For tropospheric studies, a zenith spectrum is frequently chosen as reference, in this way also removing the contribution of the stratosphere in off-axis DSCDs.

The SO<sub>2</sub> DOAS settings have been investigated through sensitivity tests on several key parameters, such as wavelength interval, choice of absorption cross sections, polynomial order, and intensity off-set terms. The selected settings are summarized in Table 1 and described in the next section.

SO<sub>2</sub> fitting windows ranging between 303 and 325 nm have generally been used in previous studies (Bobrowski and Platt, 2007; Lee et al., 2008; Galle et al., 2010; Irie et al., 2011). At wavelengths shorter than 303 nm, the limiting factor is the strong ozone absorption which interferes with SO<sub>2</sub>, leading to lower signal to noise ratio. At wavelengths longer than 325 nm, the SO<sub>2</sub> differential absorption signal becomes too weak. In order to identify the wavelength interval which minimizes both random and systematic uncertainties on SO<sub>2</sub> retrieval, six wavelength intervals have been investigated. The results of these sensitivity tests for 2 ex-

ample days are presented in Figs. 2 and 3. On the first day (1 October 2011), the SO<sub>2</sub> content is minimum and stable in time. On the second day (4 October 2011), large variations of the SO<sub>2</sub> content occur, so the ability of the different intervals to give consistent and stable values can be verified. As can be seen, the 305–317.5 nm interval provides the lowest fitting errors throughout the day and the smallest dependence on the solar zenith angle (SZA) for both days. Due to the larger absorption and therefore interference by O<sub>3</sub> at large SZAs, it has been decided to exclude measurements taken at SZAs larger than 75°. For these tests, the following spectral signatures have been included: SO<sub>2</sub>, O<sub>3</sub>, NO<sub>2</sub>, and the Ring effect (Grainger and Ring, 1962; Chance and Spurr, 1997). Daily zenith-sky radiance spectra recorded around local noon have been selected as reference. To account for the temperature dependence of the ozone absorption, cross sections at two different temperatures (223 and 243 K) were used according to Van Roozendaal et al. (2006). A fifth-order polynomial is applied to fit the low-frequency spectral structure due to Rayleigh and Mie scattering and instrumental effects. Attempts to further adjust these settings, e.g., by adding BrO cross section or by including additional ozone correction terms according to Pukite et al. (2010), were not successful (less stable retrievals with larger noise on the SO<sub>2</sub> DSCDs).

Figure 4 shows a typical example of a DOAS fit for SO<sub>2</sub> at 43° SZA. We see that fitting residuals range in between  $-2 \times 10^{-3}$  and  $2 \times 10^{-3}$ , corresponding to a root mean square (rms) of  $9 \times 10^{-4}$ , which appears to be small in comparison to the SO<sub>2</sub> differential structures presented in the lowest panel of the figure. The typical fitting uncertainty in SO<sub>2</sub> DSCDs is of about  $1-6 \times 10^{15}$  molec cm<sup>-2</sup> (less than 10%) and, for the case illustrated here, corresponds to 2%. For near-noon conditions, the detection limit on the SO<sub>2</sub> DSCD can be conservatively estimated as 3 times the  $1\sigma$  uncertainty in the slant column, which means approximately  $3 \times 10^{15}$  molec cm<sup>-2</sup>. This detection limit is similar for the vertical columns estimated using the geometrical approximation at 30° elevation (see Sect. 2.3). Vertical columns derived from the full inversion generally have a smaller detection limit, owing to the gain in sensitivity obtained when including near horizontal viewing measurements.

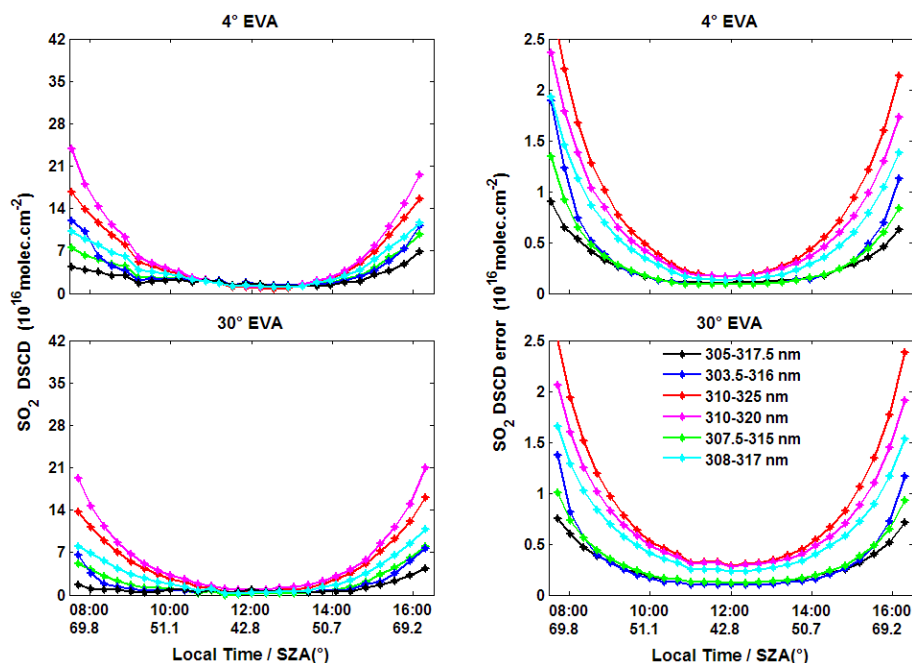


**Figure 2.** SO<sub>2</sub> DSCDs (first column) and corresponding fitting uncertainties (second column) retrieved at 4° (upper plots), 30° (lower plots) elevation (EVA) for different wavelength intervals on 1 October 2011. Local time (h) and corresponding SZA (°) are given on the *x* axis.

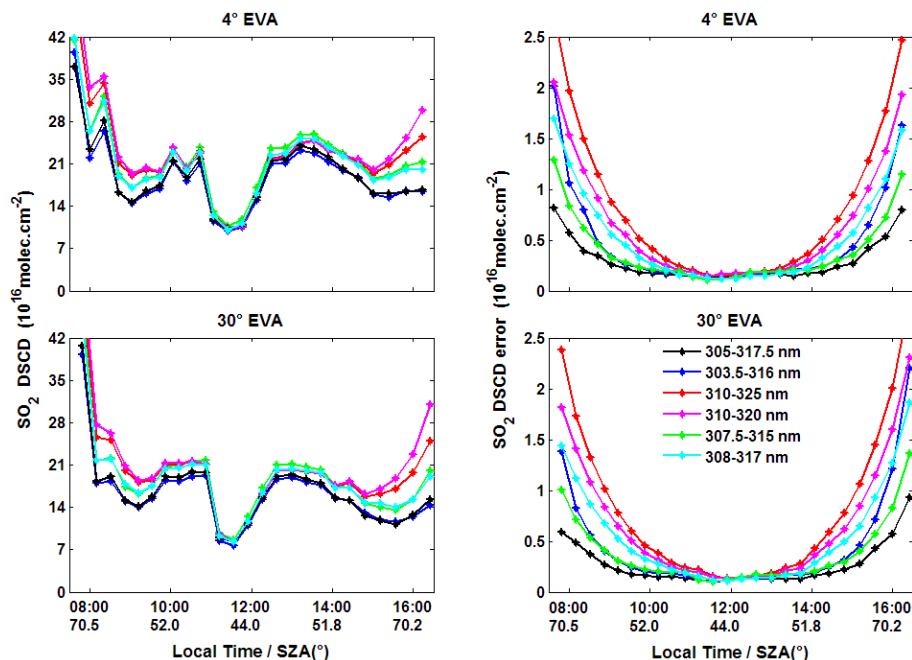


**Figure 3.** Same as Fig. 2, but for 4 October 2011.

### 2.3 Profile retrieval

SO<sub>2</sub> vertical profiles are retrieved for each MAX-DOAS scan by using the bePRO profiling tool developed at BIRA-IASB (Clémer et al., 2010; see also Hendrick et al., 2014). It is based on the optimal estimation method (Rodgers, 2000) and

includes the LIDORT radiative transfer model (RTM) as a forward model. A two-step approach is implemented in bePRO: first, aerosol extinction profiles are retrieved from measured O<sub>4</sub> DSCDs. This step is needed because the aerosols strongly influence the effective light path in the atmosphere and therefore the optical density of trace gases like SO<sub>2</sub>.

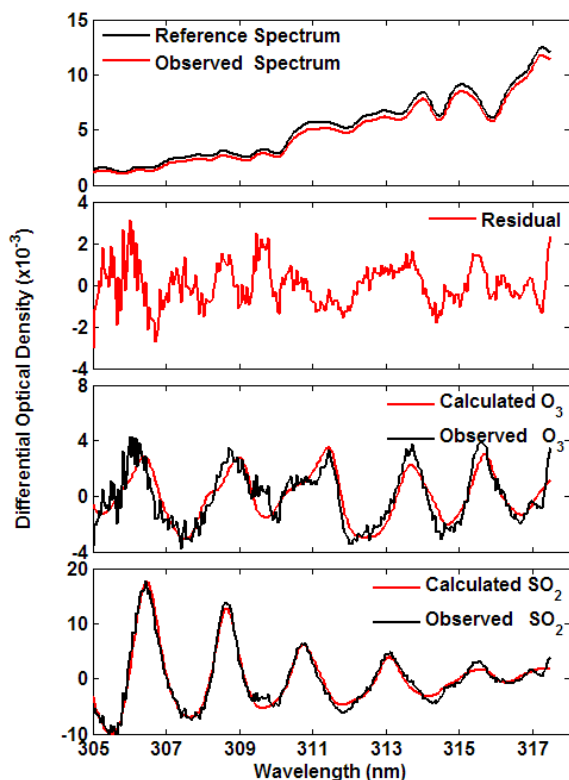


**Figure 4.** Example of DOAS fit result for SO<sub>2</sub>. It corresponds to 29 September 2010 at ~11:20 LT. SZA and EVA values are 43 and 30°, respectively.

Secondly, bePRO is applied to measured trace-gas DSCDs using the retrieved aerosol extinction profiles for the radiative transfer calculations (see below). Since the DOAS analysis is performed using daily zenith radiance spectra around noon as reference, bePRO is fed for each scan with SO<sub>2</sub> and O<sub>4</sub> DSCDs obtained by taking the difference between off-axis DSCDs and the zenith DSCD interpolated at the time of each off-axis measurement using the zenith DSCDs of two consecutive scans. Proceeding this way allows properly removing the contributions of the stratosphere from the measurements and is similar, at least for SZA < 75°, to taking the zenith spectrum of each scan as reference for the DOAS analysis.

Both linear and nonlinear iterative approaches have been implemented in our profiling algorithm. For weak absorbers like NO<sub>2</sub>, HCHO and SO<sub>2</sub>, the linear method is selected (see, e.g., Hendrick et al., 2004). In case of strong absorbers like O<sub>4</sub>, the nonlinear iterative approach is used:

$$\mathbf{x}_{i+1} = \mathbf{x}_i + (\mathbf{S}_a^{-1} + \mathbf{K}_i^T \mathbf{S}_\varepsilon^{-1} \mathbf{K}_i)^{-1} \cdot [\mathbf{K}_i^T \mathbf{S}_\varepsilon^{-1} (\mathbf{y} - F(\mathbf{x}_i)) - \mathbf{S}_a^{-1} (\mathbf{x}_i - \mathbf{x}_a)], \quad (1)$$

where  $\mathbf{y}$  is the observation vector with the DSCDs at the different EVAs,  $F$  is the forward model describing the physics of the measurements,  $\mathbf{K}$  is the weighting function, expressing

the sensitivity of the measurements to changes in the aerosol extinction or SO<sub>2</sub> vertical profile and calculated online by the LIDORT RTM,  $\mathbf{S}_\varepsilon$  is the measurement uncertainty covariance matrix,  $\mathbf{x}_a$  and  $\mathbf{S}_a$  are the a priori vertical profile and its corresponding error covariance matrix. A priori information is needed in the OEM method in order to indirectly reject unrealistic solutions compatible with the measurements. Another important quantity in the OEM is the averaging kernel matrix  $\mathbf{A}$ , which represents the sensitivity of the retrieval to the true state. More specifically, each element  $\mathbf{A}_{ij}$  in the matrix  $\mathbf{A}$  describes the sensitivity of the retrieval at  $i$ th level to the true states at the different altitude levels  $j$ . Furthermore, the trace of the matrix  $\mathbf{A}$  gives the degrees of freedom of signal (DFS), which corresponds to the number of independent pieces of information contained in the measurements. Due to the nonlinearity of the inverse problem in case of aerosols, the solution to Eq. (1) must be iterated until satisfactory convergence is achieved between measured DSCDs and those calculated using the retrieved aerosol extinction vertical profile.

Regarding the choice of the a priori profile  $\mathbf{x}_a$ , exponentially decreasing a priori SO<sub>2</sub> and aerosol extinction profiles with a fixed scaling height of 0.5 km have been constructed according to the following expression:

$$\mathbf{x}_a(z) = \frac{\text{VCD}_a}{\text{SH}} e^{-\frac{z}{\text{SH}}}, \quad (2)$$

where  $\mathbf{x}_a(z)$  is the a priori profile, SH the scaling height (0.5 km), and VCD<sub>a</sub> (AOD<sub>a</sub>) is the a priori vertical column density (aerosol optical depth). For each scan, VCD<sub>a</sub> is derived using the geometrical approximation method; that is, the SO<sub>2</sub> layer is assumed to be located below the scattering altitude at 30° EVA, so that tropospheric SO<sub>2</sub> VCDs can be derived by applying a geometrical air mass factor (AMF) to measured 30° EVA DSCDs (Hönninger et al., 2004; Brinkma et al., 2008; see also Hendrick et al., 2014). In case of aerosols, a fixed AOD of 0.2 is used. Since the DOAS fitting intervals are different for SO<sub>2</sub> and aerosols, the aerosol extinction profiles utilized as input for the calculation of SO<sub>2</sub> weighting functions have been derived by directly converting the aerosol profiles retrieved in the 338–370 nm wavelength range to the 305–317.5 nm interval using the Ångström exponents (Cachorro et al., 2000) retrieved from collocated CIMEL/AERONET sun photometer measurements (Holben et al., 1998; see <http://aeronet.gsfc.nasa.gov>):

$$\text{extinction}(z, 313 \text{ nm}) = \text{extinction}(z, 360 \text{ nm}) \times (313/360)^{-\alpha}, \quad (3)$$

where  $z$  is the altitude and  $\alpha$  is the Ångström exponent.

The 340–440 nm exponents are used in a first approximation since values for a wavelength range closer to the SO<sub>2</sub> fitting interval (305–317.5 nm) are not available yet. The corresponding mean scaling factor for the March 2010–February 2013 period is of  $1.16 \pm 0.06$ . The single scattering albedo

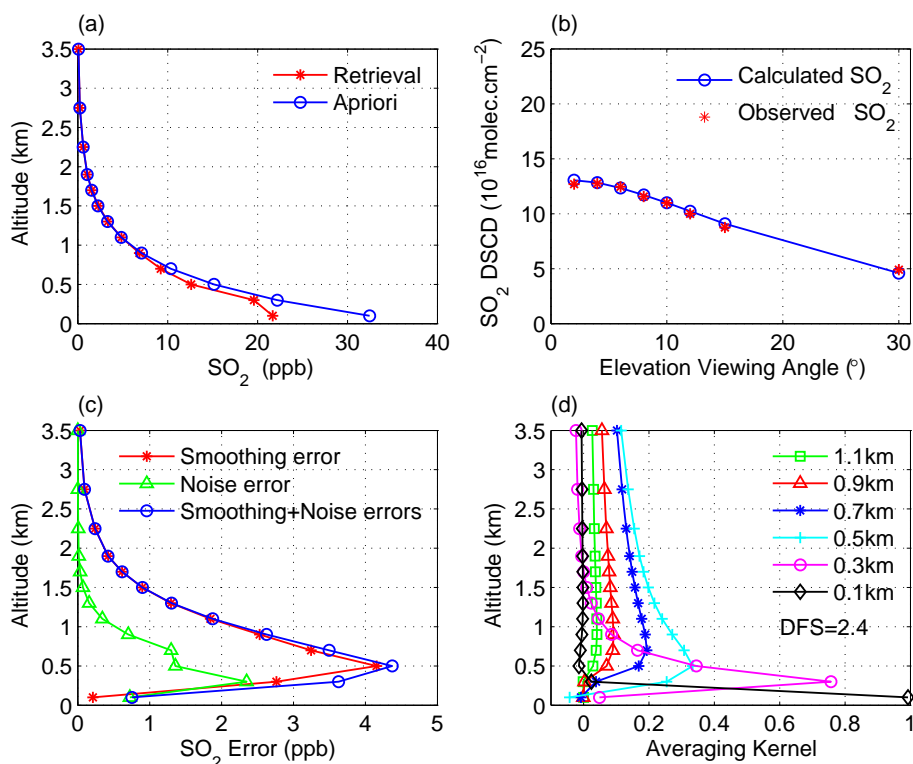


**Figure 5.** Example of SO<sub>2</sub> vertical profile retrieval from MAX-DOAS measurements at Xianghe (29 September, 2010 at 10:15 LT). (a) A priori (blue) and retrieved profile (red); (b) observed (red) and calculated (blue) DSCD (c) smoothing error (red), noise error (green) and sum of these two (blue); (d) averaging kernels.

**Table 2.** Error budget of retrieved SO<sub>2</sub> concentration (0–200 m) and VCD.

| Uncertainty (%)                              | Concentration (0–200 m) | VCD       |
|--|-------------------------|-----------|
| Smoothing + noise errors                     | 16                      | 11        |
| Uncertainty related to aerosols              | 16                      | 5         |
| Uncertainty related to the a priori          | 8                       | 19        |
| Uncertainty in SO <sub>2</sub> cross section | 5                       | 5         |
| <b>Total uncertainty</b>                     | <b>24</b>               | <b>23</b> |

and phase function of aerosols at 360 nm required by bePRO for retrieving aerosol extinction profiles are calculated offline based on the aerosol size distribution and refractive index retrieved from the same CIMEL/AERONET sun photometer measurements as above. The temperature–pressure profiles are obtained from the US standard atmosphere.  $\mathbf{S}_\varepsilon$  and  $\mathbf{S}_a$  matrices are similar as in Cl  mer et al. (2010) and Hendrick et al. (2014).  $\mathbf{S}_\varepsilon$  is a diagonal matrix, with variances equal to the square of the DOAS fitting error. For  $\mathbf{S}_a$ , the diagonal element corresponding to the lowest layer,  $\mathbf{S}_a(1.1)$ , is set equal to the square of a scaling factor  $\beta$  times the maximum partial VCD (AOD) of the profiles. Here  $\beta = 0.4$  for SO<sub>2</sub> and 0.2 for aerosol. The other diagonal elements decrease linearly with

altitude down to  $0.2 \times \mathbf{S}_a(1.1)$ . The off-diagonal terms in  $\mathbf{S}_a$  were set using Gaussian functions as follows:

$$\mathbf{S}_a(i, j) = \sqrt{\mathbf{S}_a(i, i)\mathbf{S}_a(j, j)} \exp\left(-\ln(2) \left(\frac{z_i - z_j}{\gamma}\right)^2\right), \quad (4)$$

where  $z_i$  and  $z_j$  are the altitudes of  $i$ th and  $j$ th levels, respectively. The correlation length is set to 0.1 km for SO<sub>2</sub> and 0.05 km for aerosol in order to optimize the DFS.

The retrieval altitude grid is also the same as in Cl  mer et al. (2010) and Hendrick et al. (2014), i.e., 10 layers of 200 m thickness between 0 and 2 km, 2 layers of 500 m between 2 and 3 km and 1 layer between 3 and 4 km.

Figure 5 shows an example of a SO<sub>2</sub> profile retrieval (Xianghe, 29 September 2010, 10:15 LT). Figure 5a compares the a priori and retrieved profiles; Fig. 5b shows an example of fit results, i.e., the comparison between measured DSCDs and those calculated from the retrieved profile. The quality of the profile retrieval is checked for each scan by calculating the relative root mean square error (RMSE) between observed and calculated DSCDs. This RMSE corresponds to the standard RMSE expressed in molec cm<sup>−2</sup> divided by the mean DSCD of the scan. All retrievals based on the following selection criteria have been selected: RMSE < 15 %, DFS > 0.7, and negative values not allowed. For each year,

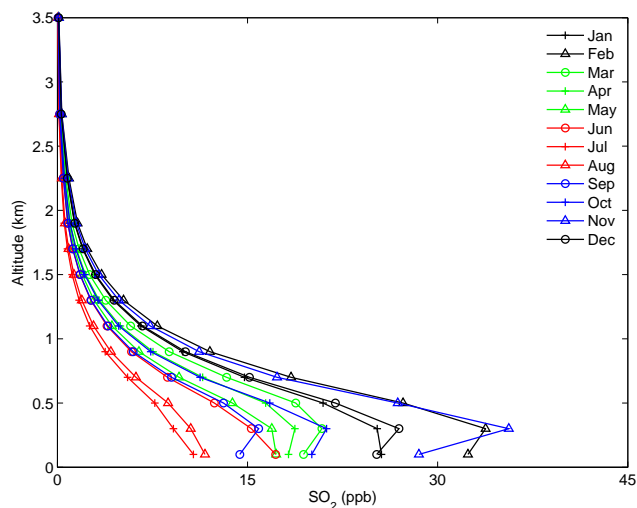


**Figure 6.** Monthly averaged SO<sub>2</sub> concentration vertical profiles for the March 2010–February 2013 period.

the number of selected retrievals using these criteria reaches  $\sim 70\%$  of the total number of scans.

Also shown in Fig. 5 are the smoothing and noise errors (c) and the averaging kernels (d). Regarding the errors, the smoothing error limits the ability of the retrieval to obtain solutions far from the a priori, while the noise error is related to the propagation of the noise in the measurements into the retrieval (Rodgers, 2000). From Fig. 5c, we see that the smoothing error is significantly larger than the noise error, except in the 0–200 m layer. The averaging kernels show that the retrieval is mainly sensitive to the layer close to the surface in addition to the total vertical column. In this example, the DFS is about 2.4, suggesting that two independent pieces of information can be determined from the measurements.

The error budget is presented in Table 2. Uncertainty related to aerosols is estimated by retrieving SO<sub>2</sub> profiles using wavelength-converted retrieved aerosol profiles plus their corresponding error (i.e., the sum of smoothing and noise errors plus a 20% error due to the uncertainty in the O<sub>4</sub> cross sections; see Cl  mer et al., 2010) as input and comparing the results to the standard retrievals. The uncertainty in the SO<sub>2</sub> cross sections is set to 5%, as suggested by Vandaele et al. (1994). The uncertainty in the a priori profiles is estimated by taking SH = 1 km in Eq. (2) instead of 0.5 km in the standard retrieval. The total uncertainty is calculated by adding the different terms in Gaussian quadrature.

Monthly-mean SO<sub>2</sub> profiles are shown in Fig. 6. There is a maximum SO<sub>2</sub> concentration in the 200–400 m layer for each profile, except in summer where the maximum is located near the surface. The largest vertical gradient is observed in February and November, the minimum in July and August. This is mainly due to the fact that the SO<sub>2</sub> emissions are the highest in February and November. This will be discussed in detail below.

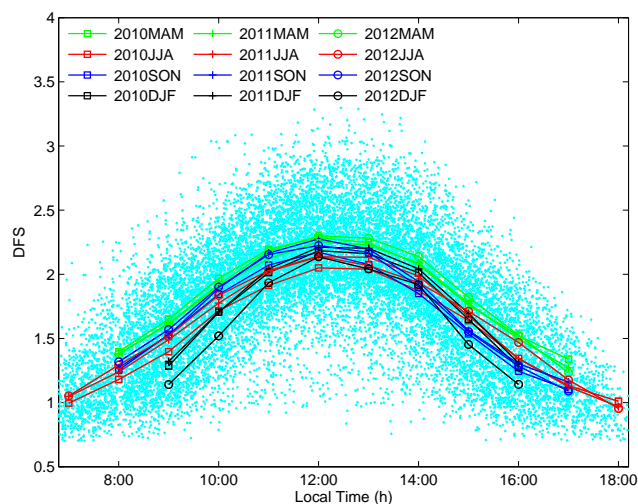


**Figure 7.** Seasonally averaged DFS diurnal cycles corresponding to the SO<sub>2</sub> profile retrievals.

Figure 7 shows the seasonal mean of diurnal cycle of DFS. The diurnal distribution in any season shows a single peak at midday due to the fact that the retrieval error at late evening or early morning overweights that at noon. If we compare the DFS around noon among the different seasons, values in summer are lower compared to the other seasons due to the lower SO<sub>2</sub> amounts associated with larger uncertainties observed during this period.

## 2.4 SO<sub>2</sub> surface concentration retrieval verification

For verification purposes, our retrieved SO<sub>2</sub> surface concentrations have been compared to measurements from a modified commercial in situ instrument, based on pulsed UV fluorescence technology (Thermo Environmental Instruments Model 43C) (Li et al., 2007). Comparison results for December 2011 when the in situ instrument was freshly calibrated are shown in Fig. 8. Hourly and daily averages of SO<sub>2</sub> concentration are plotted in Fig. 8a and b, respectively. A good agreement is obtained with a correlation coefficient of 0.86 and a slope of 0.95.

In Fig. 9, the daytime variations of the MAX-DOAS and in situ SO<sub>2</sub> surface concentration are compared for 9 continuous days. A very good agreement is found between both data sets, indicating the good overall reliability and the robustness of our MAX-DOAS retrievals.

## 3 Results and discussion

Based on the SO<sub>2</sub> profiles retrieved for the period from March 2010 to February 2013, we have investigated the daily and seasonal variations of the SO<sub>2</sub> VCD and surface concentration and the possible influence of meteorological conditions, including atmospheric stability, wind direction and

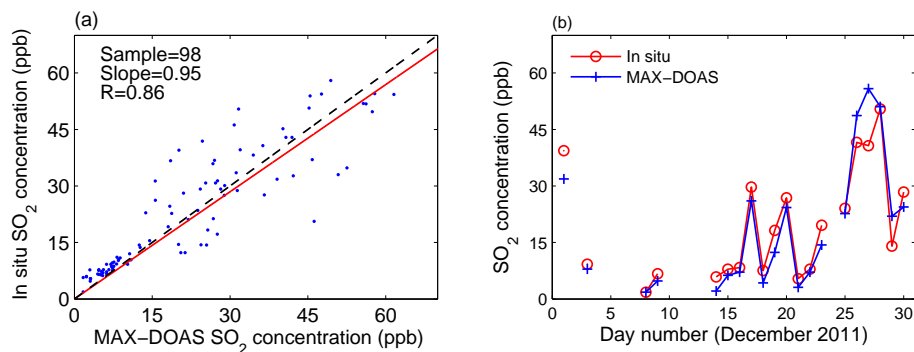


**Figure 8.** (a) Scatterplot of in situ SO<sub>2</sub> surface concentrations (0–200 m layer) against MAX-DOAS data for December 2011 (hourly averaged concentrations). The red line denotes the linear least-squares fit to the data. (b) Temporal evolution of daily averaged MAX-DOAS and in situ SO<sub>2</sub> concentrations during December 2011. Gaps in the data series are due to missing MAX-DOAS measurements.

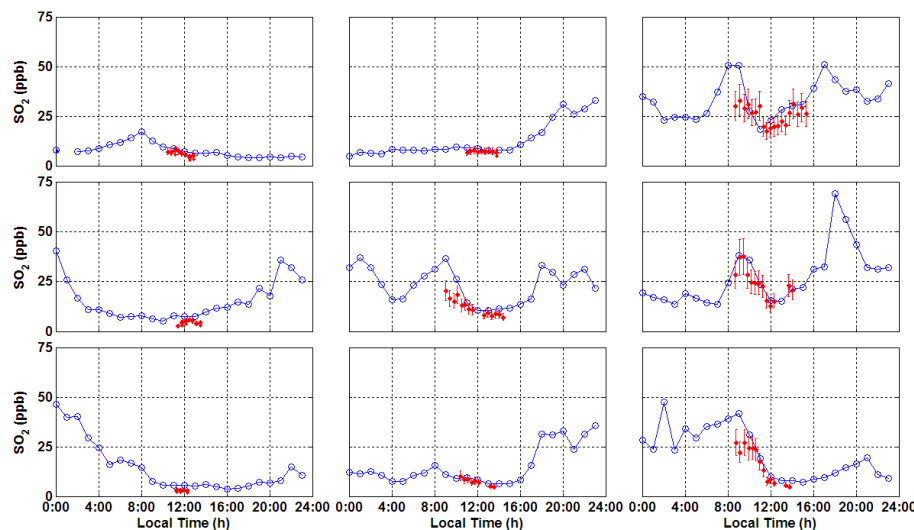


**Figure 9.** Comparison between in situ (blue, hourly means) and MAX-DOAS SO<sub>2</sub> surface concentrations (red, each point represents the retrieval from one scan) for the 15–23 December 2011 period (upper plots are for 15–17 December, middle plots for 18–20 December, and lower plots for 21–23 December).

speed. We have adopted the following convention for the seasons: MAM, JJA, SON, and NJF for spring, summer, autumn, and winter, respectively.

### 3.1 Seasonal variation of SO<sub>2</sub>

Figure 10a shows that the SO<sub>2</sub> VCD is highly correlated with concentration close to the ground (correlation coefficient of 0.85). From Fig. 10b, we see that the temporal evolutions of SO<sub>2</sub> VCD and concentration are very similar, consistent with the fact that the SO<sub>2</sub> emission sources are located near the ground.

The monthly averaged SO<sub>2</sub> VCD and surface concentrations are shown in Fig. 11. Both show a marked seasonal signature with a maximum in winter and a minimum in summer, implying that SO<sub>2</sub> originates mainly from human sources rather than natural ones (Lin et al., 2011). Generally, the fluctua-

tions of any atmospheric pollutant in a region of interest can be mainly attributed to three factors: emission level, residence time, and atmospheric transport (Wang et al., 2010; Lin et al., 2011). From the perspective of emission level, firstly, owing to enhanced domestic heating and associated coal and oil consumption in winter, the heating-related emissions of SO<sub>2</sub> are much larger during this period than in summer. Secondly, the residence time, defined as the rate of removal mechanisms, also plays an important role in determining the seasonal variation of SO<sub>2</sub> concentrations (Lee et al., 2011). Processes responsible for the removal of SO<sub>2</sub> involve dry and wet deposition and homogeneous or inhomogeneous gas-phase reactions leading to the production of H<sub>2</sub>SO<sub>4</sub> or sulfate (Tu et al., 2004). As shown in Fig. 12, the relative humidity is lower in winter, so that the removal of SO<sub>2</sub> through wet deposition is not as substantial as in summer. Thirdly, the transport can also influence the evolution of SO<sub>2</sub> at a given

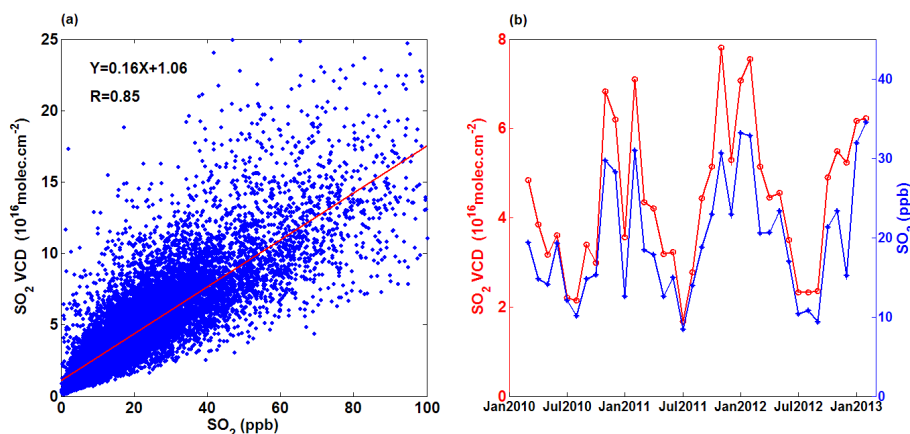


**Figure 10.** (a) Scatterplot of SO<sub>2</sub> VCD against surface concentration. The red line represents the linear least-squares fit to the data. (b) Temporal evolutions of monthly mean VCD and concentration from March 2010 to February 2013.

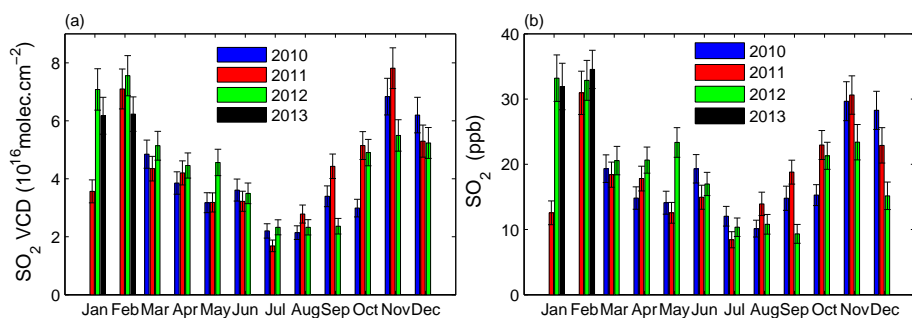


**Figure 11.** Monthly mean SO<sub>2</sub> VCD (a) and surface concentration (b) for the March 2010–February 2013 period.

location. Although in winter the wind is stronger at Xianghe, the emissions also increase during the same period. In addition, the reduced atmospheric boundary layer height and frequent temperature inversion events result in larger surface concentrations due to an accumulation of SO<sub>2</sub> in the lower troposphere (Meng et al., 2009). In summary, the aforementioned three factors jointly lead to the observed seasonal pattern of SO<sub>2</sub> concentration in Xianghe.

From Fig. 11, we see that the amount of SO<sub>2</sub> strongly increases in November with respect to October, as a consequence of increasing domestic heating (November is the beginning of the domestic heating season). Moreover, the higher wind speed observed in December (see Fig. 12) leads to a decrease of SO<sub>2</sub> during this month due to more efficient diffusion and dilution effects. Finally, it is also noticeable that SO<sub>2</sub> in January 2011 is remarkably lower than that in other years. This will be further discussed below.

### 3.2 Impact of meteorological conditions

Because of the high correlation coefficient and similar seasonal variations of the SO<sub>2</sub> VCD and concentration, we decided to investigate the impact of meteorological conditions on VCDs only. The variation of the SO<sub>2</sub> VCD is

closely linked not only to the spatial distribution of emission sources but also to meteorological conditions including wind (speed and direction) and precipitation. As shown in Fig. 12, in general, the variations of temperature and humidity appear to exhibit similar behavior from year to year. This suggests that the contribution of the wind speed and direction as drivers of the SO<sub>2</sub> VCD variation is probably different over the different years investigated here. We further explore the relationship between SO<sub>2</sub> and wind (speed and direction), as displayed in Fig. 13. It can be seen that the amount of SO<sub>2</sub> is strongly dependent on the wind direction (Fig. 13a): high VCDs are prominent when the winds blow from the east, because Tangshan, a heavy industrial city releasing large amounts of SO<sub>2</sub>, is situated to the east of Xianghe (see Fig. 1); in contrast, the northwest direction corresponds to a minimum in SO<sub>2</sub> VCD, since it is a mountain area, characterized by much fewer emissions than in Xianghe. The wind therefore contributes significantly to the dispersion of the pollutants, as expected. Regarding the dependence of the SO<sub>2</sub> VCD on wind speed, Fig. 13b shows that the VCD is almost constant with wind speed for the E and SW, which means that no good dispersion happens with the wind from these directions, since high-emission industrial areas and Tangshan are located to the southwest and

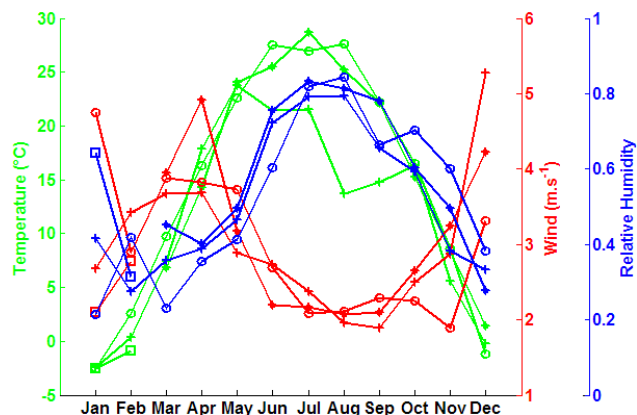


**Figure 12.** Seasonal cycles (monthly means) of temperature, humidity, and wind speed in 2010 (marker: star), 2011 (plus), 2012 (circle), and 2013 (square).

east of Xianghe, respectively. In contrast, an anticorrelation is observed for NE/NNE, NW, and SE, which means that the wind from these directions corresponding to less polluted areas can efficiently disperse pollutants. In addition, the SO<sub>2</sub> content at Xianghe is more sensitive to the emission sources in Tangshan (E) than in Beijing (WNW), which is consistent with the fact that Beijing has taken regulatory actions to reduce air pollution through traffic-control measures and the closure of heavy polluting industries initiated before the 2008 Olympic Games (Yu et al., 2010).

The annual cycles of SO<sub>2</sub> are generally in good agreement among the different years. However, the SO<sub>2</sub> VCD in January 2011 drastically deviates by up to 30 % from the values during the same month in 2012 and 2013, which is also the case in May 2012. Wind roses in Fig. 14 reveal that the inter-annual variability of wind speed and direction is responsible for the significantly different SO<sub>2</sub> VCD in January 2011. During that month, the frequency of north-west winds reaches 70 % and wind speed predominantly exceeds 5 m s<sup>-1</sup>. As mentioned above, the strong north-westerly wind favors the atmospheric dispersion of pollutants. Consequently, the SO<sub>2</sub> VCDs are generally lower than  $4 \times 10^{16}$  molec cm<sup>-2</sup>. For January 2012 and 2013, uniformly distributed wind on each side and low velocity (< 5 m s<sup>-1</sup>, frequency > 50 %) jointly result in relatively high SO<sub>2</sub> VCDs compared to January 2011. Similar features can explain the May 2012 case.

### 3.3 Diurnal cycle

In Fig. 15, we further compare the diurnal cycles of SO<sub>2</sub> VCDs for the different seasons. Since the sunshine duration is different in the four seasons, the available time period for MAX-DOAS observations also differs: 07:30–17:30 in spring and autumn, 06:30–18:30 in summer, and 08:30–16:30 in winter. As can be seen, the diurnal cycles for all years are very consistent, especially in summer. The retrieved

SO<sub>2</sub> VCDs in autumn 2011 and spring 2012 are significantly higher than those during the same period of the other years due to the anomalous VCD values in November 2011 and May 2012. Furthermore, the amplitude of the SO<sub>2</sub> VCD diurnal cycle, which shows a minimum at noon and a maximum in the morning and late afternoon, is larger in winter. This can be explained by a strengthened diurnal variation of emission sources during this period (Meng et al., 2009).

It should be noted that similar investigations have been done for NO<sub>2</sub> (Wang et al., 2014). One can conclude that both NO<sub>2</sub> and SO<sub>2</sub> display a similar seasonal variation and are impacted in the same way by meteorological conditions. However, SO<sub>2</sub> abundances are always higher than NO<sub>2</sub> ones and their diurnal cycles are different, especially in winter and summer: SO<sub>2</sub> has a more pronounced diurnal cycle than NO<sub>2</sub> in winter which is in line with the known diurnal cycle of burning of fossil fuels for heating and atmospheric stability, and the photochemical reaction activity leads to an obvious decrease of NO<sub>2</sub> during daytime in summer (Wang et al., 2008; Meng et al., 2009; Lin et al., 2011).

### 3.4 Relationship between SO<sub>2</sub> and aerosols

SO<sub>2</sub> is known as a major aerosol precursor in the Beijing area through its conversion into sulfates and sulfuric acid by reaction with OH (see, e.g., Ma et al., 2012; Zhang et al., 2013). Since aerosol extinction profiles are retrieved in the first step of the SO<sub>2</sub> retrieval (see Sect. 2.3), our data set offers a unique opportunity to investigate the relationship between SO<sub>2</sub> emission and aerosol production in suburban Beijing. This will be done through a correlation study as in Lu et al. (2010) and Veeffkind et al. (2011).

Figure 16 shows monthly scatterplots of the SO<sub>2</sub> concentration versus aerosol extinction coefficient retrieved in the 0–200 m layer for the March 2010–February 2013 period. In all plots, data points correspond to MAX-DOAS scans satisfying the selection criteria based on the quality of the retrievals (see Sect. 2.3). A strong correlation (Pearson correlation coefficients in the 0.6–0.9 range) is obtained in January–March and October–December while a significantly lower correlation is observed in late spring/summer with correlation coefficients around 0.3 in June–August. Similar features are found from the scatterplots of SO<sub>2</sub> VCD versus AOD but also when outliers outside the 95 % confidence interval are removed and/or the uncertainties on both SO<sub>2</sub> and aerosol data are taken into account (not shown here). The marked seasonality of the correlation between SO<sub>2</sub> and aerosols is further illustrated in Fig. 17 where monthly correlation coefficients for both surface concentration and integrated column are reported. The positive correlation (> 0.2) observed throughout the year indicates that, in most cases, high pollution events in Xianghe are associated with enhanced SO<sub>2</sub> and aerosol levels (Chan and Yao, 2008; Li et al., 2007). The higher correlation coefficients obtained in winter (> 0.6) suggest that anthropogenic SO<sub>2</sub>, through the formation of sulfate

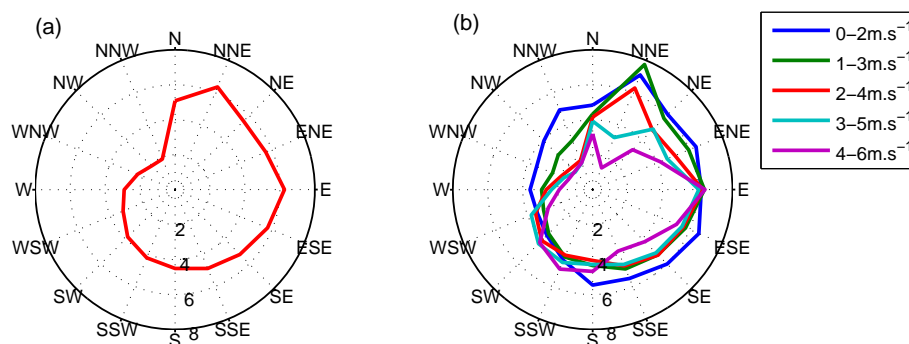


**Figure 13.** (a) Wind rose showing the SO<sub>2</sub> VCD ( $10^{16}$  molec  $\text{cm}^{-2}$ ) as a function of the wind direction (average for all wind speed). (b) Dependence of SO<sub>2</sub> VCD ( $10^{16}$  molec  $\text{cm}^{-2}$ ) on wind direction for different wind speeds.

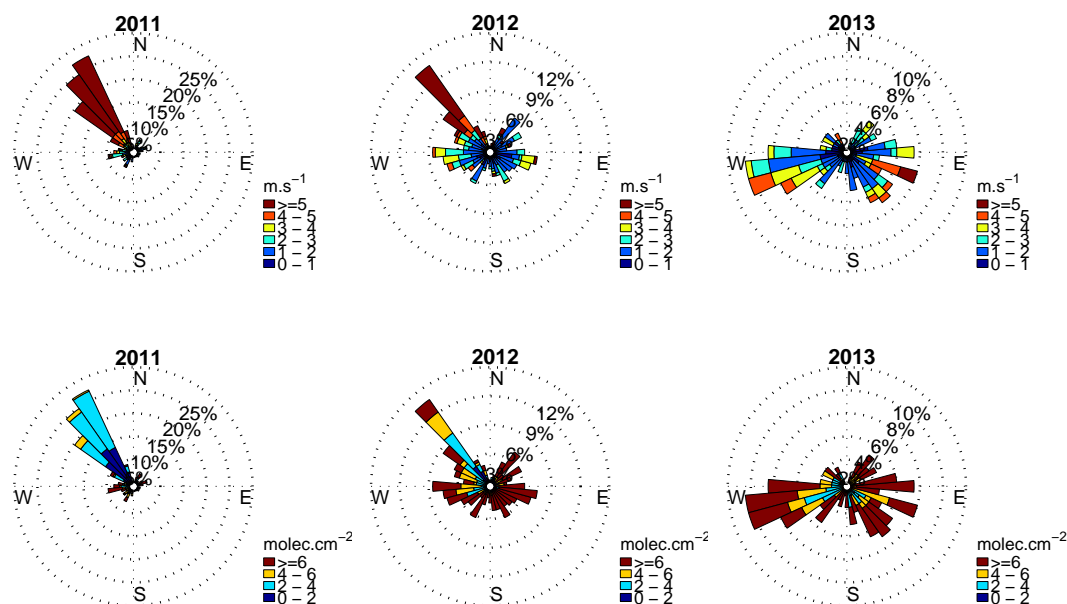


**Figure 14.** Wind rose for wind speed (first row;  $\text{m s}^{-1}$ ) and SO<sub>2</sub> VCD (second row;  $10^{16}$  molec  $\text{cm}^{-2}$ ) for January 2011 (first column), 2012 (second column), and 2013 (third column).

aerosols, is a major contributor to the total aerosol content during this period of the year. In late spring/summer, the Beijing area is strongly influenced by other sources of aerosols, especially particles emitted from massive agricultural fires in the surrounding region (Xia et al., 2013) as well as dust particles transported from the Kumutage and Taklimakan deserts in western China and from the Mongolian deserts (Yu et al., 2009). These perturbations by other aerosol sources combined with lower SO<sub>2</sub> emissions, shorter lifetime of SO<sub>2</sub> due to a more efficient oxidation, and different meteorological conditions could likely explain the significantly weaker correlation between anthropogenic SO<sub>2</sub> and aerosols obtained in June–August. The intercept values much larger than zero found in summer scatterplots (see Fig. 16) further support the fact that aerosol sources other than anthropogenic ones play a significant role in summer, as also suggested by Lu

et al. (2010) from a correlation study between SO<sub>2</sub> emission inventories and AODs measured by the MODIS satellite instrument. It is however important to note that co-located measurements of the chemical composition of aerosols in Xianghe as well as additional investigations on the type and photochemical age of the air masses probed by the MAX-DOAS instrument would be needed to confirm our findings.

#### 4 Summary and conclusions

Tropospheric SO<sub>2</sub> vertical profiles and corresponding column densities at the Xianghe station have been retrieved by applying an OEM-based profiling tool to continuous ground-based MAX-DOAS observations from March 2010 to February 2013. The 305–317.5 nm wavelength range was found to be the most suitable fitting window for near-noon DOAS

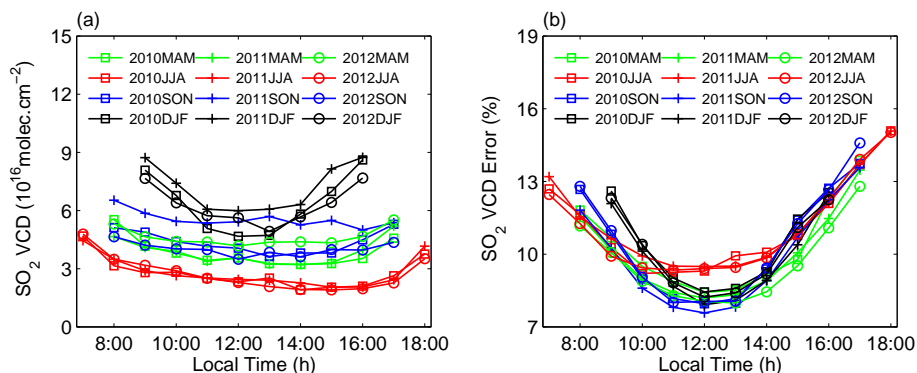


**Figure 15.** (a) Seasonally averaged SO<sub>2</sub> VCD diurnal cycles and (b) corresponding errors. Data points represent hourly means.

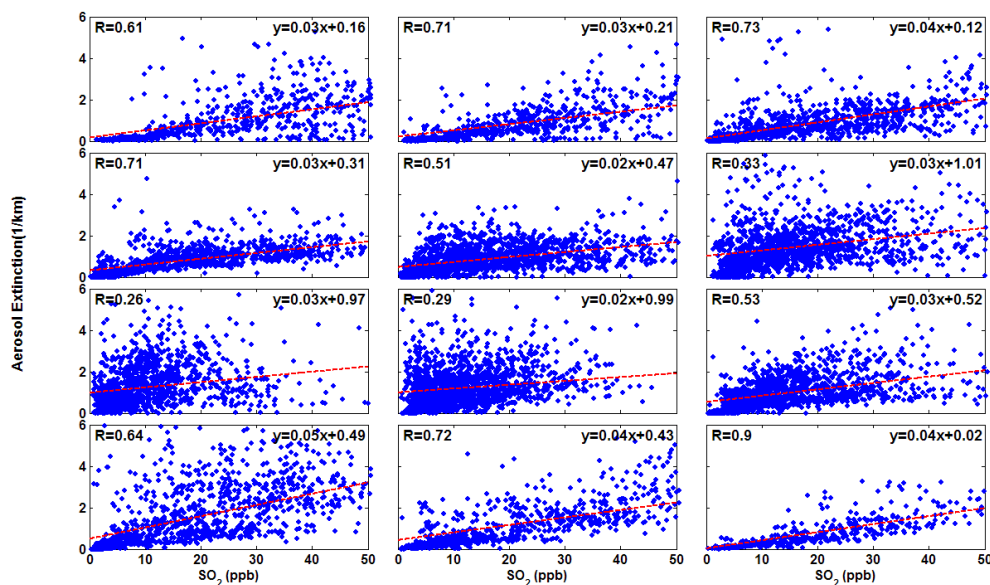


**Figure 16.** Scatterplots of aerosol extinction coefficient versus SO<sub>2</sub> concentration in the 0–200 m layer for months 1–12 of the March 2010–February 2013 period (first row from left to right is for January–March, respectively; second row for April–June; third row for July–September; fourth row for October–December). The data points correspond to the different MAX-DOAS scans. The red line denotes the linear least-squares fit to the data.

analysis of SO<sub>2</sub>. For verification purpose, retrieved SO<sub>2</sub> surface concentrations have been compared to collocated in situ data. An excellent agreement was found, with correlation coefficient and slope close to 0.9, indicating the good reliability and robustness of our retrievals.

These MAX-DOAS measurements have been used to investigate the seasonal and diurnal cycles of SO<sub>2</sub> vertical columns and surface concentrations, in combination with conventional meteorological data (temperature, humidity, and wind speed and direction). Regarding the seasonal variation, both VCD and surface concentrations exhibit the same patterns, with a maximum in winter (February) and a minimum in summer (July), in accordance with the large emissions due to domestic heating in winter. The high levels of SO<sub>2</sub> during the cold season are further enhanced by the

weakness of the wet deposition mechanism and, in case of surface concentration, by the frequent temperature-inversion events occurring during this period, favoring the accumulation of SO<sub>2</sub> in the atmospheric layers close to the ground. The variation of the SO<sub>2</sub> amount in Xianghe is also found to be largely driven by wind speed and direction. In the case of east or southwest wind, the VCD at the station remains almost constant with the increase of wind speed, since the city of Tangshan and heavy polluting industries are located to the east and southwest of Xianghe, respectively. In contrast, an anticorrelation between SO<sub>2</sub> VCD and wind speed is observed for NE/NNE, NW, and SE directions, which means the wind from these directions can efficiently disperse the pollution in Xianghe. With respect to the diurnal cycle, larger SO<sub>2</sub> amounts are obtained in the early morning

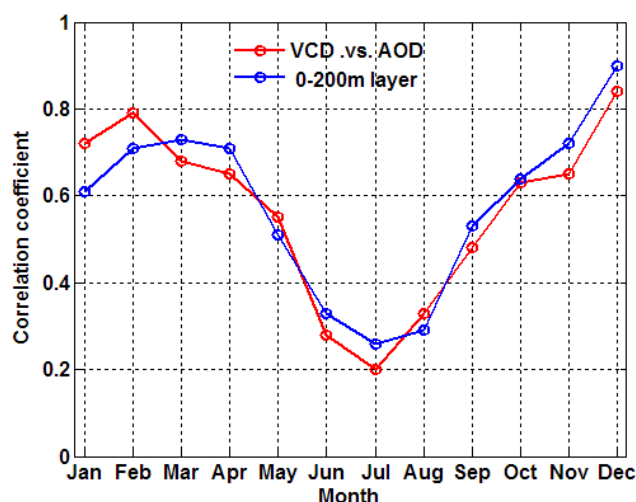


**Figure 17.** Seasonal variation of the correlation coefficient between SO<sub>2</sub> and aerosols over the March 2010–February 2013 period. The red curve corresponds to VCD versus AOD and the blue curve to SO<sub>2</sub> concentration versus aerosol extinction coefficient in the 0–200 m layer.

and late evening with a minimum around noon, in line with the diurnal variation of pollutant emission and atmospheric state. Moreover, the diurnal cycle is more pronounced during wintertime, mainly due to the more marked diurnal variation of emission sources during this season. The relationship between SO<sub>2</sub> and aerosols has been also investigated. A strong correlation between both is found in winter but not in summer. This seasonality could be related to the fact that, in the Beijing area in winter, the aerosol content depends significantly on anthropogenic SO<sub>2</sub> through the formation of sulfate aerosols while, in spring/summer, dust and biomass burning particles, which are much less SO<sub>2</sub>-dependent, are also important aerosol sources. It is however worth noting that such kind of correlation analysis should be combined to aerosol composition measurements in order to definitely conclude whether the conversion of SO<sub>2</sub> to sulfate is a dominant aerosol source or not.

These 3-year MAX-DOAS SO<sub>2</sub> measurements in Xianghe constitute a unique data set for validating and improving spaceborne observations over China, which is the region in the world where anthropogenic SO<sub>2</sub> emissions are the largest (Yang et al., 2013; Boynard et al., 2014). In particular, retrieved SO<sub>2</sub> vertical profiles can be used as a priori information for the AMF calculation in satellite retrievals. Moreover, the combination of both integrated columns and surface concentrations could provide useful information to make explicitly the link between measured satellite columns and surface concentrations.

**Acknowledgements.** This work was supported by China Scholarship Council, the Special Scientific Research Fund of Meteorological Public Welfare Profession of China (grant no. GYHY201106045-52), and the National Natural Science Foundation of China (grant no. 41175030). We acknowledge the Belgian Federal Science Policy Office, Brussels (AGACC-II project), and the funding obtained from the EU 7th Framework Programme project NORS (contract 284421) and the ESA CEOS Intercalibration project (ESA/ESRIN contract 22202/09/I-EC). We would like also to thank J. Z. Ma (Chinese Academy of Meteorological Sciences, Beijing; Editor of this paper) and two anonymous referees for their helpful comments.

Edited by: J. Ma

## References

- Bobrowski, N. and Platt, U.: SO<sub>2</sub>/BrO ratios studied in five volcanic plumes, *J. Volcanol. Geotherm. Res.*, 166, 147–160, 2007.
- Bobrowski, N., von Glasow, R., Aiuppa, A., Inguaggiato, S., Louban, I., Ibrahim, O. W., and Platt, U.: Reactive halogen chemistry in volcanic plumes, *J. Geophys. Res.*, 112, D06311, doi:10.1029/2006JD007206, 2007.
- Bogumil, K., Orphal, J., Homann, T., Voigt, S., Spietz, P., Fleischmann, O. C., Vogel, A., Hartmann, M., Bovensmann, H., Frerik, J., and Burrows, J. P.: Measurements of molecular absorption spectra with the SCIAMACHY Pre-Flight Model: Instrument characterization and reference spectra for atmospheric remote sensing in the 230–2380 nm region, *J. Photoch. Photobio. A*, 157, 167–184, 2003.
- Boynard, A., Clerbaux, C., Clarisse, L., Safieddine, S., Pommier, M., Van Damme, M., Bauduin, S., Oudot, C., Hadji-Lazaro, J., Hurtmans, D., and Coheur, P.-F.: First simultaneous space measurements of atmospheric pollutants in the boundary layer from IASI: a case study in the North China Plain, *Geophys. Res. Lett.*, 41, 645–651, doi:10.1002/2013GL058333, 2014.
- Brinkma, E. J., Pinardi, G., Volten, H., Braak, R., Richter, A., Schonhardt, A., van Roozendaal, M., Fayt, C., Hermans, C., Dirksen, R. J., Vlemmix, T., Berkhout, A. J. C., Swart, D. P. J., Oetjen, H., Wittrock, F., Wagner, T., Ibrahim, O. W., de Leeuw, G., Moerman, M., Curier, R. L., Celarier, E. A., Cede, A., Knap, W. H., Veefkind, J. P., Eskes, H. J., Allaart, M., Rothe, R., Peters, A. J. M., and Levelt, P. F.: The 2005 and 2006 DANDELIONS NO<sub>2</sub> and aerosol intercomparison campaigns, *J. Geophys. Res.*, 113, D16S46, doi:10.1029/2007jd008808, 2008.
- Cachorro, V. E., Durán, P., Vergaz, R., and de Frutos, A. M.: Measurements of the atmospheric turbidity of the north-centre continental area in Spain: Spectral aerosol optical depth and Ångström turbidity parameters, *J. Aerosol Sci.*, 31, 687–702, 2000.
- Chan, C. K. and Yao, X.: Air pollution in mega cities in China, *Atmos. Environ.*, 42, 1–42, 2008.
- Chance, K. V. and Spurr, R. J.: Ring effect studies: Rayleigh scattering, including molecular parameters for rotational Raman scattering, and the Fraunhofer spectrum, *Appl. Optics*, 36, 5224–5230, 1997.
- Clémer, K., Van Roozendaal, M., Fayt, C., Hendrick, F., Hermans, C., Pinardi, G., Spurr, R., Wang, P., and De Mazière, M.: Multiple wavelength retrieval of tropospheric aerosol optical proper-

- ties from MAXDOAS measurements in Beijing, *Atmos. Meas. Tech.*, 3, 863–878, doi:10.5194/amt-3-863-2010, 2010.
- Eisinger, M. and Burrows, J. P.: Tropospheric sulfur dioxide observed by the ERS-2/GOME instrument, *Geophys. Res. Lett.*, 25, 4177–4180, doi:10.1029/1998GL900128, 1998.
- Fioletov, V. E., McLinden, C. A., Krotkov, N., Yang, K., Loyola, D. G., Valks, P., Theys, N., Van Roozendael, M., Nowlan, C. R., Chance, K., Liu, X., Lee, C., and Martin, R. V.: Application of OMI, SCIAMACHY, and GOME-2 satellite SO<sub>2</sub> retrievals for detection of large emission sources, *J. Geophys. Res.-Atmos.*, 118, 11399–11418, doi:10.1002/jgrd.50826, 2013.
- Fleischmann, O. C., Hartmann, M., Burrows, J. P., and Orphal, J.: New ultraviolet absorption cross-sections of BrO at atmospheric temperatures measured by time-windowing Fourier transform spectroscopy, *J. Photoch. Photobio. A: Chemistry*, 168, 117–132, 2004.
- Frieß, U., Monks, P. S., Remedios, J. J., Rozanov, A., Sinreich, R., Wagner, T., and Platt, U.: MAX-DOAS O<sub>4</sub> measurements: A new technique to derive information on atmospheric aerosols: 2. Modeling studies, *J. Geophys. Res.*, 111, D14203, doi:10.1029/2005jd006618, 2006.
- Frieß, U., Sihler, H., Sander, R., Pöhler, D., Yilmaz, S., and Platt, U.: The vertical distribution of BrO and aerosols in the Arctic: Measurements by active and passive differential optical absorption spectroscopy, *J. Geophys. Res.*, 116, D00R04, doi:10.1029/2011JD015938, 2011.
- Frins, E., Osorio, M., Casaballe, N., Belsterli, G., Wagner, T., and Platt, U.: DOAS-measurement of the NO<sub>2</sub> formation rate from NO<sub>x</sub> emissions into the atmosphere, *Atmos. Meas. Tech.*, 5, 1165–1172, doi:10.5194/amt-5-1165-2012, 2012.
- Galle, B., Johansson, M., Rivera, C., Zhang, Y., Kihlman, M., Kern, C., Lehmann, T., Platt, U., Arellano, S., and Hidalgo, S.: Network for Observation of Volcanic and Atmospheric Change (NOVAC)-A global network for volcanic gas monitoring: Network layout and instrument description, *J. Geophys. Res.*, 115, D05304, doi:10.1029/2009JD011823, 2010.
- Gauderman, W. J., McConnell, R., Gilliland, F., London, S., Thomas, D., Avol, E., Vora, H., Berhane, K., Rappaport, E. B., and Lurmann, F.: Association between air pollution and lung function growth in southern California children, *Am. J. Resp. Crit. Care.*, 162, 1383–1390, 2000.
- Grainger, J. and Ring, J.: Anomalous Fraunhofer line profiles, *Nature*, 193, p. 762, 1962.
- Großmann, K., Frieß, U., Peters, E., Wittrock, F., Lampel, J., Yilmaz, S., Tschirner, J., Sommariva, R., von Glasow, R., Quack, B., Krüger, K., Pfeilsticker, K., and Platt, U.: Iodine monoxide in the Western Pacific marine boundary layer, *Atmos. Chem. Phys.*, 13, 3363–3378, doi:10.5194/acp-13-3363-2013, 2013.
- Hönninger, G., von Friedeburg, C., and Platt, U.: Multi axis differential optical absorption spectroscopy (MAX-DOAS), *Atmos. Chem. Phys.*, 4, 231–254, doi:10.5194/acp-4-231-2004, 2004.
- Heckel, A., Richter, A., Tarsu, T., Wittrock, F., Hak, C., Pundt, I., Junkermann, W., and Burrows, J. P.: MAX-DOAS measurements of formaldehyde in the Po-Valley, *Atmos. Chem. Phys.*, 5, 909–918, doi:10.5194/acp-5-909-2005, 2005.
- Hendrick, F., Barret, B., Van Roozendael, M., Boesch, H., Butz, A., De Mazière, M., Goutail, F., Hermans, C., Lambert, J.-C., Pfeilsticker, K., and Pommereau, J.-P.: Retrieval of nitrogen dioxide stratospheric profiles from ground-based zenith-sky UV-visible observations: validation of the technique through correlative comparisons, *Atmos. Chem. Phys.*, 4, 2091–2106, doi:10.5194/acp-4-2091-2004, 2004.
- Hendrick, F., Müller, J.-F., Clémer, K., Wang, P., De Mazière, M., Fayt, C., Gielen, C., Hermans, C., Ma, J. Z., Pinardi, G., Stavrou, T., Vlemmix, T., and Van Roozendael, M.: Four years of ground-based MAX-DOAS observations of HONO and NO<sub>2</sub> in the Beijing area, *Atmos. Chem. Phys.*, 14, 765–781, doi:10.5194/acp-14-765-2014, 2014.
- Hermans, C., Vandaele, A., Fally, S., Carleer, M., Colin, R., Coquart, B., Jenouvrier, A., and Merienne, M.-F.: Absorption cross-section of the collision-induced bands of oxygen from the UV to the NIR, in: *Weakly interacting molecular pairs: unconventional absorbers of radiation in the atmosphere*, Springer, 193–202, 2003.
- Holben, B., Eck, T., Slutsker, I., Tanre, D., Buis, J., Setzer, A., Vermote, E., Reagan, J., Kaufman, Y., and Nakajima, T.: AERONET-A federated instrument network and data archive for aerosol characterization, *Remote Sens. Environ.*, 66, 1–16, 1998.
- Irie, H., Takashima, H., Kanaya, Y., Boersma, K. F., Gast, L., Wittrock, F., Brunner, D., Zhou, Y., and Van Roozendael, M.: Eight-component retrievals from ground-based MAX-DOAS observations, *Atmos. Meas. Tech.*, 4, 1027–1044, doi:10.5194/amt-4-1027-2011, 2011.
- Krotkov, N. A., Carn, S. A., Krueger, A. J., Bhartia, P. K., and Yang, K.: Band Residual Difference Algorithm for Retrieval of SO<sub>2</sub> From the Aura Ozone Monitoring Instrument (OMI), *IEEE, Trans. Geosci. Remote Sens.*, 44, 1259–1266, 2006.
- Lee, C., Richter, A., Lee, H., Kim, Y. J., Burrows, J. P., Lee, Y. G., and Choi, B. C.: Impact of transport of sulfur dioxide from the Asian continent on the air quality over Korea during May 2005, *Atmos. Environ.*, 42, 1461–1475, 2008.
- Lee, C., Martin, R. V., van Donkelaar, A., O'Byrne, G., Krotkov, N., Richter, A., Huey, L. G., and Holloway, J. S.: Retrieval of vertical columns of sulfur dioxide from SCIAMACHY and OMI: Air mass factor algorithm development, validation, and error analysis, *J. Geophys. Res.*, 114, D22303, doi:10.1029/2009JD012123, 2009.
- Lee, C., Martin, R. V., van Donkelaar, A., Lee, H., Dickerson, R. R., Hains, J. C., Krotkov, N., Richter, A., Vinnikov, K., and Schwab, J. J.: SO<sub>2</sub> emissions and lifetimes: Estimates from inverse modeling using in situ and global, space-based (SCIAMACHY and OMI) observations, *J. Geophys. Res.*, 116, D06304, doi:10.1029/2010JD014758, 2011.
- Li, C., Marufu, L. T., Dickerson, R. R., Li, Z., Wen, T., Wang, Y., Wang, P., Chen, H., and Stehr, J. W.: In situ measurements of trace gases and aerosol optical properties at a rural site in northern China during East Asian Study of Tropospheric Aerosols: An International Regional Experiment 2005, *J. Geophys. Res.*, 112, D22S04, doi:10.1029/2006JD007592, 2007.
- Lin, W., Xu, X., Ge, B., and Liu, X.: Gaseous pollutants in Beijing urban area during the heating period 2007–2008: variability, sources, meteorological, and chemical impacts, *Atmos. Chem. Phys.*, 11, 8157–8170, doi:10.5194/acp-11-8157-2011, 2011.
- Lu, Z., Streets, D. G., Zhang, Q., Wang, S., Carmichael, G. R., Cheng, Y. F., Wei, C., Chin, M., Diehl, T., and Tan, Q.: Sulfur dioxide emissions in China and sulfur trends in East Asia since 2000, *Atmos. Chem. Phys.*, 10, 6311–6331, doi:10.5194/acp-10-6311-2010, 2010.

- Ma, J. Z., Xu, X. B., Zhao, C. S., and Yan, P.: A review of atmospheric chemistry research in China: Photochemical smog, haze pollution, and gas-aerosol interactions, *Adv. Atmos. Sci.*, 29, 1006–1026, 2012.
- Ma, J. Z., Beirle, S., Jin, J. L., Shaiganfar, R., Yan, P., and Wagner, T.: Tropospheric NO<sub>2</sub> vertical column densities over Beijing: results of the first three years of ground-based MAX-DOAS measurements (2008–2011) and satellite validation, *Atmos. Chem. Phys.*, 13, 1547–1567, doi:10.5194/acp-13-1547-2013, 2013.
- Meller, R. and Moortgat, G. K.: Temperature dependence of the absorption cross sections of formaldehyde between 223 and 323 K in the wavelength range 225–375 nm, *J. Geophys. Res.*, 105, 7089–7101, 2000.
- Meng, X., Wang, P., Wang, G., Yu, H., and Zong, X.: Variation and transportation characteristics of SO<sub>2</sub> in winter over Beijing and its surrounding areas, *Climatic and Environmental Research (in Chinese)*, 14, 309–317, 2009.
- Nowlan, C. R., Liu, X., Chance, K. V., Cai, Z., Kurosu, T. P., Lee, C., and Martin, R. V.: Retrievals of sulfur dioxide from the Global Ozone Monitoring Experiment 2 (GOME-2) using an optimal estimation approach: Algorithm and initial validation, *J. Geophys. Res.*, 116, D18301, doi:10.1029/2011JD015808, 2011.
- Platt, U. and Stutz, J.: *Differential Optical Absorption Spectroscopy (DOAS): Principles and applications*, ISBN 978-3-540-21193-8, Springer, Berlin-Heidelberg, 2008.
- Puķite, J., Kūhl, S., Deutschmann, T., Platt, U., and Wagner, T.: Extending differential optical absorption spectroscopy for limb measurements in the UV, *Atmos. Meas. Tech.*, 3, 631–653, doi:10.5194/amt-3-631-2010, 2010.
- Rodgers, C. D.: *Inverse methods for atmospheric sounding: theory and practice*, World Scientific Publishing, Singapore-New Jersey-London-Hong Kong, 2000.
- Roscoe, H. K., Van Roozendaal, M., Fayt, C., du Piesanie, A., Abuhassan, N., Adams, C., Akrami, M., Cede, A., Chong, J., Clémer, K., Friess, U., Gil Ojeda, M., Goutail, F., Graves, R., Griesfeller, A., Grossmann, K., Hemerijckx, G., Hendrick, F., Herman, J., Hermans, C., Irie, H., Johnston, P. V., Kanaya, Y., Kreher, K., Leigh, R., Merlaud, A., Mount, G. H., Navarro, M., Oetjen, H., Pazmino, A., Perez-Camacho, M., Peters, E., Pinardi, G., Puentedura, O., Richter, A., Schönhardt, A., Shaiganfar, R., Spinei, E., Strong, K., Takashima, H., Vlemmix, T., Vrekoussis, M., Wagner, T., Wittrock, F., Yela, M., Yilmaz, S., Boersma, F., Hains, J., Kroon, M., PETERS, A., and Kim, Y. J.: Intercomparison of slant column measurements of NO<sub>2</sub> and O<sub>4</sub> by MAX-DOAS and zenith-sky UV and visible spectrometers, *Atmos. Meas. Tech.*, 3, 1629–1646, doi:10.5194/amt-3-1629-2010, 2010.
- Tu, F. H., Thornton, D. C., Bandy, A. R., Carmichael, G. R., Tang, Y., Thornhill, K. L., Sachse, G. W., and Blake, D. R.: Long-range transport of sulfur dioxide in the central Pacific, *J. Geophys. Res.*, 109, D15S08, doi:10.1029/2003JD004309, 2004.
- Vandaele, A., Simon, P. C., Guillemot, J. M., Carleer, M., and Colin, R.: SO<sub>2</sub> absorption cross section measurement in the UV using a Fourier transform spectrometer, *J. Geophys. Res.*, 99, 25599–25605, 1994.
- Vandaele, A. C., Hermans, C., Simon, P. C., Carleer, M., Colin, R., Fally, S., Merienne, M.-F., Jenouvrier, A., and Coquart, B.: Measurements of the NO<sub>2</sub> absorption cross-section from 42 000 cm<sup>-1</sup> to 10 000 cm<sup>-1</sup> (238–1000 nm) at 220 and 294 K, *J. Quant. Spectrosc. Ra.*, 59, 171–184, 1998.
- Van Roozendaal, M., Loyola, D., Spurr, R., Balis, D., Lambert, J.-C., Livschitz, Y., Valks, P., Ruppert, T., Kenter, P., Fayt, C., and Zehner, C.: Ten years of GOME/ERS-2 total ozone data – The new GOME data processor (GDP) version 4: 1. Algorithm description, *J. Geophys. Res.*, 111, D14311, doi:10.1029/2005JD006375, 2006.
- Veefkind, J. P., Boersma, K. F., Wang, J., Kurosu, T. P., Krotkov, N., Chance, K., and Levelt, P. F.: Global satellite analysis of the relation between aerosols and short-lived trace gases, *Atmos. Chem. Phys.*, 11, 1255–1267, doi:10.5194/acp-11-1255-2011, 2011.
- Vlemmix, T., PETERS, A. J. M., Stammes, P., Wang, P., and Levelt, P. F.: Retrieval of tropospheric NO<sub>2</sub> using the MAX-DOAS method combined with relative intensity measurements for aerosol correction, *Atmos. Meas. Tech.*, 3, 1287–1305, doi:10.5194/amt-3-1287-2010, 2010.
- Wagner, T., Dix, B., von Friedeburg, C., Friess, U., Sanghavi, S., Sinreich, R., and Platt, U.: MAX-DOAS O<sub>4</sub> measurements: A new technique to derive information on atmospheric aerosols – Principles and information content, *J. Geophys. Res.*, 109, D22205, doi:10.1029/2004jd004904, 2004.
- Wagner, T., Beirle, S., Brauers, T., Deutschmann, T., Frieß, U., Hak, C., Halla, J. D., Heue, K. P., Junkermann, W., Li, X., Platt, U., and Pundt-Gruber, I.: Inversion of tropospheric profiles of aerosol extinction and HCHO and NO<sub>2</sub> mixing ratios from MAX-DOAS observations in Milano during the summer of 2003 and comparison with independent data sets, *Atmos. Meas. Tech.*, 4, 2685–2715, doi:10.5194/amt-4-2685-2011, 2011.
- Wang, T., Nie, W., Gao, J., Xue, L. K., Gao, X. M., Wang, X. F., Qiu, J., Poon, C. N., Meinardi, S., Blake, D., Wang, S. L., Ding, A. J., Chai, F. H., Zhang, Q. Z., and Wang, W. X.: Air quality during the 2008 Beijing Olympics: secondary pollutants and regional impact, *Atmos. Chem. Phys.*, 10, 7603–7615, doi:10.5194/acp-10-7603-2010, 2010.
- Wang, T., Wang, P., Yu, H., Zhang, X., Zhou, B., Si, F., Wang, S., Bai, W., Zhou, H., and Zhao, H.: Intercomparison of slant column measurements of NO<sub>2</sub> by ground-based MAX-DOAS, *Acta Phys. Sin.*, 62, 054206, doi:10.7498/aps.62.054206, 2013.
- Wang, T., Wang, P., Yu, H., and Sun, L.: Analysis of the characteristics of tropospheric NO<sub>2</sub> in Xianghe based on MAX-DOAS measurement, *Climatic and Environmental Research (in Chinese)*, 19, 51–60, 2014.
- Wang, W., Chai, F., Zhang, K., Wang, S., Chen, Y., Wang, X., and Yang, Y.: Study on ambient air quality in Beijing for the summer 2008 Olympic Games, *Air Qual, Atmos. Health*, 1, 31–36, 2008.
- Wittrock, F., Oetjen, H., Richter, A., Fietkau, S., Medeke, T., Rozanov, A., and Burrows, J. P.: MAX-DOAS measurements of atmospheric trace gases in Ny-Ålesund – Radiative transfer studies and their application, *Atmos. Chem. Phys.*, 4, 955–966, doi:10.5194/acp-4-955-2004, 2004.
- Wu, F. C., Xie, P. H., Li, A., Chan, K. L., Hartl, A., Wang, Y., Si, F. Q., Zeng, Y., Qin, M., Xu, J., Liu, J. G., Liu, W. Q., and Wenig, M.: Observations of SO<sub>2</sub> by mobile DOAS in the Guangzhou eastern area during the Asian Games 2010, *Atmos. Meas. Tech.*, 6, 2277–2292, doi:10.5194/amt-6-2277-2013, 2013.
- Xia, X., Zong, X., and Sun, L.: Exceptionally active agricultural fire season in mid-eastern China in June 2012 and its impact on atmospheric environment, *J. Geophys. Res. Atmos.*, 118, 9889–9900, doi:10.1002/jgrd.50770, 2013.

- Yan, P., Huang, J., and Draxler, R.: The long-term simulation of surface SO<sub>2</sub> and evaluation of contributions from the different emission sources to Beijing city, *Science in China Series D (Earth Sciences)*, 48, 196–208, 2005.
- Yan, P., Wang, X., Wang, Z., and Wu, Q.: Analysis of decreases in NO<sub>2</sub> concentrations during Beijing Olympic Games in 2008, *Climatic and Environmental Research*, 15, 609–615, 2010 (in Chinese).
- Yang, K., Dickerson, R. R., Carn, S. A., Ge, C., and Wang, J.: First observations of SO<sub>2</sub> from satellite Suomi NPP OMPS: Widespread air pollution events over China, *Geophys. Res. Lett.*, 40, 4957–4962, doi:10.1002/grl.50952, 2013.
- Yu, H., Wang, P., Zong, X., Li, X., and Lü, D.: Change of NO<sub>2</sub> column density over Beijing from satellite measurement during the Beijing 2008 Olympic Games, *Chinese Sci. Bull.*, 55, 308–313, 2010.
- Yu, X., Zhu, B., and Zhang, M.: Seasonal variability of aerosol optical properties over Beijing, *Atmos. Environ.*, 43, 4095–4101, 2009.
- Zhang, R., Jing, J., Tao, J., Hsu, S.-C., Wang, G., Cao, J., Lee, C. S. L., Zhu, L., Chen, Z., Zhao, Y., and Shen, Z.: Chemical characterization and source apportionment of PM<sub>2.5</sub> in Beijing: seasonal perspective, *Atmos. Chem. Phys.*, 13, 7053–7074, doi:10.5194/acp-13-7053-2013, 2013.
- Zhao, B., Wang, P., Ma, J. Z., Zhu, S., Pozzer, A., and Li, W.: A high-resolution emission inventory of primary pollutants for the Huabei region, China, *Atmos. Chem. Phys.*, 12, 481–501, doi:10.5194/acp-12-481-2012, 2012.